Transactions of the ASME®

Journal of Fluids Engineering

Published Quarterly by The American Society of Mechanical Engineers

VOLUME 118 • NUMBER 4 • DECEMBER 1996

(Contents continued on p. 705)

FLUIDS ENGINEERING DIVISION
Technical Editor
DEMETRI P. TELIONIS (1999)
Executive Secretary
PAT WHITE (1999)
Assistants to the Editor
N. W. SCHAEFFLER
J. E. POWELL
Calendar Editor
M. F. ACKERSON

Associate Technical Editors
P. R. BANDYOPADHYAY (1997)
S. BANERJEE (1999)
P. W. BEARMAN (1998)
M. DHAUBHADEL (1999)
J. EATON (1999)
F. GIRALT (1997)
H. HASHIMOTO (1996)
J. A. C. HUMPHREY (1997)
F. HUSSAIN (1998)
O. JONES (1996)
J. KATZ (1998)
J. KIM (1996)
L. NELIK (1996)
M. W. REEKS (1996)
B. SCHIAVELLO (1999)
O. SIMONIN (1998)
P. M. SOCKOL (1998)
M. W. SINDIR (1997)
M. SOMMERFELD (1999)
D. E. STOCK (1996)
M. S. TRIANTAFYLLOU (1998)
S. P. VANKA (1996)

BOARD ON COMMUNICATIONS
Chairman and Vice-President
R. MATES

OFFICERS OF THE ASME
President, **R. J. GOLDSTEIN**
Exec. Director
D. L. BELDEN
Treasurer
J. A. MASON

PUBLISHING STAFF
Managing Director, Engineering
CHARLES W. BEARDSLEY
Director, Technical Publishing
PHILIP DI VIETRO
Managing Editor, Technical Publishing
CYNTHIA B. CLARK
Managing Editor, Transactions
CORNELIA MONAHAN
Production Assistant
MARISOL ANDINO

Transactions of the ASME, Journal of Fluids Engineering (ISSN 0098-2202) is published quarterly (Mar., June, Sept., Dec.) for $185.00 per year by The American Society of Mechanical Engineers, 345 East 47th Street, New York, NY 10017. Periodicals postage paid at New York, NY and additional mailing offices. POSTMASTER: Send address changes to Transactions of the ASME, Journal of Fluids Engineering, c/o THE AMERICAN SOCIETY OF MECHANICAL ENGINEERS, 22 Law Drive, Box 2300, Fairfield, NJ 07007-2300.

CHANGES OF ADDRESS must be received at Society headquarters seven weeks before they are to be effective. Please send old label and new address.

PRICES: To members, $40.00, annually: to nonmembers, $185.00. Add $30.00 for postage to countries outside the United States and Canada.

STATEMENT from By-Laws. The Society shall not be responsible for statements or opinions advanced in papers or . . . printed in its publications (B7.1, Par. 3).

COPYRIGHT © 1996 by The American Society of Mechanical Engineers. Authorization to photocopy material for internal or personal use under circumstances not falling within the fair use provisions of the Copyright Act is granted by ASME to libraries and other users registered with the Copyright Clearance Center (CCC) Transactional Reporting Service provided that the base fee of $3.00 per article is paid directly to CCC, 27 Congress St., Salem, MA 01970. Request for special permission or bulk copying should be addressed to Reprints/Permission Department.

INDEXED by Applied Mechanics Reviews and Engineering Information, Inc. Canadian Goods & Services Tax Registration #126148048.

Downloaded 03 Jun 2010 to 171.66.16.159. Redistribution subject to ASME license or copyright; see http://www.asme.org/terms/Terms_Use.cfm

(Contents continued)

Technical Briefs

Announcements and Special Notices

Journal of Fluids Engineering

Editorial

This Editorial Board has strived not to lose sight of the fact that its purpose is to serve its readers, not its authors. The truth is that many members of our community view archival publications as a means to establish the quality and -alas- the quantity of their work. Moreover, the service actually offered to many readers is to communicate to them information needed to carry out more research that will result in more publications. This procedure does serve an important goal of archival publishing, namely the dissemination of original information in the areas covered by a journal. But an engineering journal should also reach the practitioners. This is not easy to do. Authors tend to address themselves to their peer researchers. In this way inner cells of author/readers develop which tend to leave out the rest of the community.

The Editorial Board of this Journal has been trying to reach a broader readership by various means. For this purpose, we established a new genre, the perspective article. Such articles present a body of work recently developed in a somewhat simplified way, starting from the fundamental concepts and emphasizing the practical aspects of the findings. Not all perspectives have this character but many such articles have aimed at reaching the practicing engineer. We have also attempted to reach a broader audience by launching the Technical Forum in which short articles, opinions and outlines of technical forums are presented. In these pages, we presented, for example, a sequence of columns dealing with the U.S. technical competitiveness, the transfer of technology and others.

This year, the JFE Editorial Board has decided to try another method to attract the attention of practicing engineers. Industrial experts are invited to write a few paragraphs assessing the relevance of accepted papers to the applied engineering world. Such discussions may also include ways in which the reported results can be utilized in applications and directions which continuing work can take. These discussions are published in the same issue with the relevant papers and thus serve as a highlight of the contributed papers. A few members of the Editorial Board (Ghoneim, Humphrey, Nelik and Sindir) have formulated the details of this procedure which are described in the editorial that appeared in the March issue of JFE. In the present issue we publish the first discussions prepared by industrial experts.

The efforts described above should not be perceived as changes in the aim and scope of the Journal. This Journal seeks to publish original material in fluid mechanics and its applications. The purpose of our most recent efforts is to make the material presented in the JFE pages more interesting and more accessible to the practicing engineers. Moreover, by promoting interaction between researchers and practitioners, we hope that we will motivate the research community to define and attack fundamental problems of interest to industry. Examples of such problems are described in the review articles that appear in this issue.

To emphasize our plans of reaching out to industry, we chose as a theme of this issue industrial fluid dynamics. Papers dealing with research directly related to industrial problems in fluid mechanics were collected and grouped together at the beginning of the issue. This Journal publishes routinely such papers but in this issue we have collected a few more than usually included in an issue and highlighted them by placing them ahead of the other contributions. We begin with a review of applications of computational fluid dynamics to a variety of fluids engineering problems encountered in automotive engineering. These are problems like the flow through exhaust manifolds, ventilation in the interior of an automobile, or underhood fluid flow for which so far we relied on simplified and crude models. This is followed by a perspective describing pump design experiences in the past few decades and defining the present needs and expectations for research and development in this area. The third article is a little more narrow in scope but goes deeper into the character of the flow and the operations of automotive torque converters.

Following the review articles we have three contributed papers on impeller characteristics and another discussing the flow through a pump guide vane. A paper dealing with hydraulic transients and vibrations and another on calculations of flow within the engine follow. Another problem of significance to industry is pipe flows. In this issue we include four papers dealing with crude oil transport, wavy-to-slug flow transition, buoyancy-driven air-water mixture and orifice flow characteristics in oil lines respectively. These papers are followed by three contributions on multi-phase flow. Two deal with cavitation and the third with airblast atomizers. Finally, we include here a paper on fish-tail curved diffusers and a paper on enclosure flows in torsionally-shaped geometries. The technical briefs at the end of the pages of this issue are led by three contributions of interest to industry. The first deals with a multiple-disk fan, the second describes a method to measure pressure gradients in capsule-liquid flows and the third is concerned with wind loads on low-rise structures. The technical forum also is dovoted to the theme of this issue. It contains a report on a serious effort to brong together researchers and practitioners of automotive engineering.

Discussions of the engineering significance to industry for some of the above papers are presented following the Technical Forum. We would like to thank here the following individuals who prepared discussions: Mark W. Johnson, Weir Pumps; Arthur Lefebvre, Pebworth; Glenn Cunningham, Williams Technologies, Inc.; Dr. W. J. Meiring, Shell International Oil Products, B. V.

D. P. Telionis
J. A. C. Humphrey
M. M. Sindir

Journal of Fluids Engineering

Technical Forum

By J. F. Foss[1]

A workshop: "Fluid Flows/Fundamental Automotive Issues" was held at Michigan State University in August 1995. The sponsors: four separate programs in 3 divisions of the NSF (including Fluid Mechanics and Hydraulics), the Big 3 Automakers and MSU, helped to achieve the objective conceived by Dr. R. Powell: to bring together the practitioners with NSF staff members and university faculty in the fluid mechanics, applied and computational mathematics, advanced scientific computing and the communications and computational systems areas for the purpose of clarifying the central problems faced by the former and the extant capabilities in the latter communities.

Substantial communication between the industrial, academic and NSF representatives was achieved at this first session. It was apparent to those present that the pre-competitive interests of the Big 3 representatives were commonly shared. For example, computer codes to support the design process, streamlined procedures for gridding complex geometries, and effectively dealing with grossly unsteady turbulent flows (inclusive of realistic "loss" effects) were common threads of the discussions in the four focus areas:

(i) automotive aerodynamics
(ii) climate control
(iii) induction and exhaust
(iv) underhood cooling.

The in-cylinder flows were acknowledged (in the organization phase) to be of common interest but ones that represented active areas of corporate, university and government lab research. The desire to bring attention to a smaller class of problems led to the four areas stated above. A report, available from the present author, Foss (1995), was prepared to document the outcomes of this workshop.

An evaluation of the August meeting led to the (Powell-Foss) realization that the general benefits of that first interaction could be beneficially enhanced by a follow-on, one-day session in which a smaller group of academics would meet with the Big 3 representatives (one each) in each of the four focus areas from which four "Research Challenge Problems" would be defined. These would represent the principal communication from the two sessions that would be made widely available. This follow-on session was held in April 1996.

It was also recognized that the one-day session could not deliver a refined problem statement and that four MSU faculty and graduate students should be charged with the responsibility to refine the outcome of the April deliberations, conduct a search of the relevant literature and prepare a concise statement of the challenge problem for each of the four focus areas.

The desired refinements have been accomplished and the four challenge problems have been defined; Foss (1996) provides the full text of these reports. The narrative text, as well as the collected literature references, that support these four problems are also available on the World Wide Web

//www.egr.msu.edu/ME/NSF_Big3_Wkshp

The following schematic representations and statements of the parameter ranges characterize the selected problems. The cognizant MSU faculty member and GRA are shown with the problem statement in order to recognize their contributions in the preparation of the problem statements. The report of the April session is also available from the General Chair; requests may be sent to foss@egr.msu.edu. The four challenge problems are briefly described below.

Automotive Aerodynamics (Prof. M. M. Koochesfahani, Mr. D. G. Bohl)

The flow in the "A Pillar" region was selected as a representative and an important region for the aerodynamics challenge problem. (The A Pillar is the structural member between the windshield and the side glass.) Aerodynamically, the lateral flow from the region of over-pressure at the windshield centerline to the low pressure of the side glass leads to a strong "A Pillar Vortex" motion. The intrinsic aerodynamic sound sources in this vortex are important contributors to the "wind noise" in the passenger compartment. Also, instabilities in the vortex core may lead to a "slapping sound" as the vortex moves laterally with respect to the side glass.

Studies that lead to better understanding of the vortex strength and the trajectory of its core for well documented conditions will contribute to the relevant knowledge base in this area. In addition, the Chrysler Corporation has established a generic model that defines the recommended challenge problem for this area. A side elevation of this model is shown in Fig. 1. Further details regarding this challenge problem are available in Foss (1996).

Acoustic studies require a Reynolds number (R_h) of order 1.3×10^6 ($= U_o h/\nu$) to provide realistic data. Studies concerned with the pressure/velocity/vorticity fields over this model can, perhaps, be viable at smaller R_h values but a turbulent boundary layer approaching the A Pillar (on the windshield) is required to establish an appropriate model study.

Climate Control (Prof. J. J. McGrath and Mr. G. Ambrose)

The interior windshield defrost/defog flow was selected as the basic challenge problem by the climate control focus group. (It is relevant to note that a strict government standard must be met in this regard before a vehicle may be sold in the US.) The geometry and operating conditions for this challenge problem are shown in Fig. 2.

The problem statement is readily altered to address behaviors that range from relatively basic (as shown) to increasing approximations to the prototype conditions. For the latter, an offset from the lip of the jet to the sloped impact plate (qua windshield) is one parameter and the slope angle is another. More

---

[1] Michigan State University, 133 Service Road, East Lansing, MI 48824.

GENERIC GREENHOUSE FULL SIDEGLASS PANEL
Normalized Dimensions Based Upon Height of Greenhouse

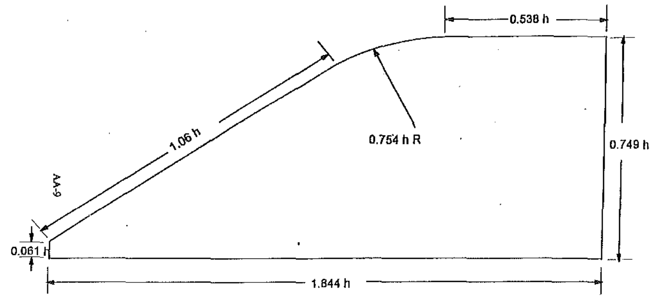

Note: Lower edge of panel is 0.123 h above the bottom surface of the model. The trailing edge of the panel is 0.908 h forward of the trailing edge of the model. The panel can be mounted flush with the exterior surface or with insets of 0.0205 h or 0.041 h.

Fig. 1 Elevation view of the side glass inset panel

substantial changes in the flow would occur if the confining side walls were removed; this would also make the model study closer to the three-dimensional defrost/defog flows in a vehicle.

Induction and Exhaust (Prof. G. Brereton and Mr. Erik Bertrand)

Transient flows in relatively short ($L/D < 20$) conduits with elbows, contractions, etc. characterize the important flows in this focus area. The selected challenge problem states a manageable, yet representative flow of this kind; see Fig. 3. The selected parameters ensure that this model problem contains the distinctive features of rapid transient effects such that quasi steady analyses/interpretations are not relevant. As noted in the Brereton/Bertrand description in Foss (1996), the Mach No., for induction/exhaust flows, can vary from 0–0.5 and the peak velocity Reynolds number ($U_o/D_o\nu$) can show excursions to 10^6 in 10's of milliseconds for typical IC engine operating conditions. These variations provide challenges for both the experimentalists and the numerical modelers.

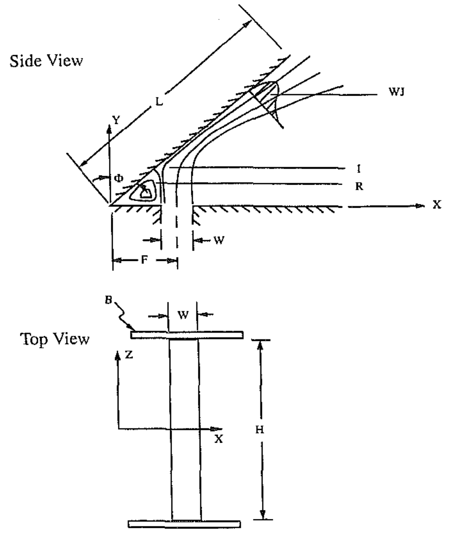

Characteristic Dimensions and Magnitudes of Parameters:

L ~ 1,000 mm	$30^o < \Phi < 60^o$
W ~ 30 mm (Range: 20 - 40 mm) H ~ 300 mm (Range: 200 - 400 mm) F ~100 mm (Range: 50 - 200 mm)	$-20^oC < T_a < 20^oC$
	$-20^oC < T_j < 65^oC$

Umax ~ 20 m/s; Unominal ~ 10 m/s; Volume flow rate ~ 50 - 150 cfm

Fig. 2 The climate control challenge problem

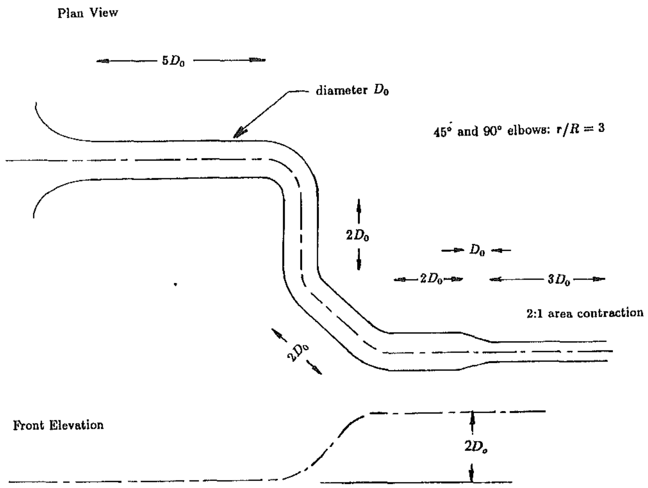

Fig. 3 The geometry for the induction/exhaust challange problem

Boundary Conditions for the Flow System of Fig. 3

1) Constant upstream stagnation pressure (e.g., p_{atm}).

2) The centerline velocity, at the exit plane, is designated as $U_2(t)$. A flow control value at the exit of the conduit (not shown) throttles the exiting flow such that $U_2(t)$ is described as

$$U_2(t) = \sin \Omega t \quad \text{for} \quad 0 \le t \le \pi/\Omega$$

$$U_2(t) = 0 \quad \text{for} \quad \pi/\Omega \le t \le 4\pi/\Omega$$

and $U_2(t)$ is periodic for each

$$T = 4\pi/\Omega\colon U_2(t) = U_2(t + T).$$

3) For Ω as an equivalent rotation rate, the relevant Ω values will be

$$1{,}000 \le \Omega \le 6{,}000 \text{ rpm}$$

A particular challenge in these flows, and one for which research contributions can and should be made, is the description of "loss coefficients" in this globally unsteady environment. To emphasize this matter, consider that the pressure drop—from the upstream to the conduit exit—in steady state conditions can be described as

(i) $p_{\mathrm{plenum}} - p_{\mathrm{exit}} = [KE$ flux at exit/mass flux$] + \Sigma\, gh_L$ where h_L is the conventional head loss, and

(ii) the integral sum of the local turbulence kinetic energy dissipation

$$\int_{\forall} \epsilon d\forall = \mu \int_{\forall} \overline{\frac{\partial u_i'}{\partial x_j}\left(\frac{\partial u_i'}{\partial x_j} + \frac{\partial u_j'}{\partial x_i}\right)}\, d\forall$$

plus the equivalent (and much smaller) term for the time mean velocity field:

$$\int E d\forall = \int \mu \frac{\partial \bar{u}_i}{\partial x_j}\left(\frac{\partial \bar{u}_i}{\partial x_j} + \frac{\partial \bar{u}_j}{\partial x_i}\right) d\forall.$$

It is recognized that the ϵ and E integrals are virtually impossible to evaluate at all points in the volume; however, the pressure difference does provide an easily applied integral check on these inaccessible integrals. In contrast, there is no equivalent instantaneous "balance" for the periodic challenge problem flow and, it is expected, that the integral over one cycle would lead to "loss effects" that are different from those that would exist if the pulsed flow rate were uniformly distributed in the time period "T."

Hence, unsteady "loss" effects are of principle interest in this focus area.

UNDERHOOD CHALLENGE PROBLEM -- AutoUHTM

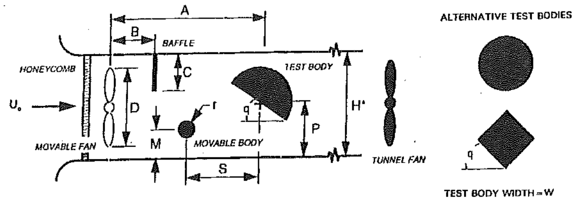

Dimension		Acceptable Range of Values
Test body downstream position	A	$0.00 < A/H < 2.00$
Baffle downstream position	B	$0.00 < B/H < 1.00$
Baffle height	C	$0.00 < C/H < 0.50$
Movable fan diameter	D	$0.00 < D/H < 0.90$
Blockage body vertical position	M	$0.00 < M/H < 0.50$
Test body vertical position	P	$0.00 < P/H < 0.50$
Test body rotation angle	q	$-90.0 < q < 90.0$
Test body dimension	R	$0.15 < R/H < 0.45$
Blockage body dimension	r	$0.10 < r/R < 1.00$
Movable fan vertical position	V	$0.00 < V/H < 0.50$
Test body width	W	$0.25 < W/H < 1.00$
Blockage body width	w	H

*Test section width = H

Fig. 4 The Underhood cooling challenge problem. Note: This statement was developed by Dr. G. Mandrusiak (G.M. Corp.) using the base information from Appendix B of Foss (1996). Notes: 1) Characteristic dimension (H) for automotive prototype is 1 m.; 2) Characteristic velocity in full-size underhood is (0.15)*(vehicle speed); 3) At idle, the characteristic Reynolds number will be $U_oH/\nu \approx 10^5$; 4) Characteristic fan speed in full-size underhood is 1200-1800 RPM.

Underhood Cooling (Prof. J. F. Foss and Mr. S. C. Morris)

The underhood flow field environment is one of considerable complexity. The technically challenging conditions are those for which strong thermal gradients exist and the cooling fan (and not "ram air") provides the motive force (i.e., idle or low speed operation). Accurate computational models for the isolated fan flow are not easily developed and the presence of condenser/radiator assemblies, non-axisymmetric shrouds, engine blockage, reverse flow leakage paths, and obstructions to the air flow that must return to the ambient make it quite difficult to compute the system behavior.

Such predictions are, however, quite important because of the required thermal protection for plastic and electronic components and the need to ensure adequately high temperatures at the catalytic converter.

The challenge problem in this focus area has been termed the "Auto UHTM" for "automotive underhood thermal management;" it is shown in Fig. 4. The indicated device is to provide a wide range of geometric parameters. It is expected that the cumulative results, reported for this generic model, will contribute to the development of enhanced computational capabilities that will support the design process.

References

Foss, J. F. 1995, Fluid Flows/Fundamental Automotive Issues Final Report: NSF Grant CTS-95-28866, 14 Dec.

Foss, J. F., 1996, Development of Challenge Problem Statements for the Workshop: Fluid Flows/Fundamental Automotive Issues.

Journal of Fluids Engineering

Industry Perspective

Experimental Measurements in a Centrifugal Pump Impeller[1]

P. A. Smith.[2] Environmental and commercial pressures to reduce energy consumption and maximize operational availability necessitate the supply of high-efficiency, low-loss equipment with a wide operational range and minimal noise emission. These requirements now are virtually universal and no longer dependent upon market sector or equipment function. The results presented depict a ''snapshot'' of the loss processes within a commercial centrifugal impeller, under a single forward flow condition and demonstrate the potential for their reduction, and therefore the scope for improvements to meet the emergent demands of the market.

To meet these needs, design methods require development and validation. The industry needs, simply to use, low labor intensive techniques which guarantee the optimum solution on a first time basis. Advances in computer codes for fluid analysis and advances in the ''size'' and speed of commercially available computers has made practical three dimensional computerised flow modeling possible.

The technique reported is one method of flow analysis which can be used to validate computerised flow analysis codings. While it is intrusive into the flow passage it does have the advantage of being simple, utilizing atmospheric air as the test medium and requiring only minimal power to drive the test rig. L.D.A. (Laser Doppler Anemometry) techniques may be favored as they offer measurements utilizing a more realistic test fluid i.e., water, without being intrusive into the flow passage. The rig complexity, however, is an order of magnitude greater and requires significant power to drive the test rig.

Interaction Between Sprays From Multiple Coaxial Airblast Atomizers[3]

A. Lefebvre.[4] The atomization literature is replete with reports of experimental studies carried out on atomisers of all types, including the coaxial airblast atomizer used in the present study. However, many practical combustion devices employ not just a single fuel nozzle but rather a cluster of nozzles, a notable example being the annular gas turbine combustor which normally features between 18 and 30 equispaced airblast fuel nozzles. Generally, it is found that placing these nozzles closer together enhances combustion performance but, if the spacing between nozzles is too small, the resulting spray interactions can have detrimental effects on both atomization quality and combustion performance. Surprisingly perhaps, these interactions between multiple sprays, which are clearly of great practical importance, appear to have received very little attention in the past, which makes this paper on the spray characteristics of multiple coaxial airblast atomizers of the type employed in space shuttle engines especially welcome.

The paper contains very detailed information on all the key spray characteristics of relevance to nozzle performance in the actual engine. It should therefore be of great interest and value to the combustion engineers whose job is to improve the performance of the space shuttle engine. Otherwise, it is a paper that will appeal mainly to other researchers in atomization. Most readers will find the detailed results a little overwhelming and will turn gratefully to the final sections which summarise the main findings on spray characteristics and their implications to combustion performance.

The main strength of the paper lies in its abundance of high quality experimental data, but such data tend to be indigestible in too large a helping. Authors' explanations of results are more interesting because they are often speculative and therefore open to question and debate. Some of the explanatory material provided in this paper is not entirely convincing. For example, it is suggested that the improved atomization resulting from a reduction in liquid flow rate increases droplet coalescence in the regions downstream from the nozzle. This explanation is difficult to accept, since small droplets are physically stronger and therefore less susceptible to coalescence than large droplets, despite their numerical superiority.

It is a little daunting to realize that the very large amount of information contained in this paper on the performance and spray characteristics of multiple coaxial airblast atomizers represents only the small tip of a very large iceberg. Only one variable has been examined—the effect of halving the liquid flow rate. Many other important parameters, such as atomizer dimensions, liquid and gas properties and, perhaps, the effect of air swirl, seem equally worthy of the authors' attention. Presumably, more extensive studies would provide answers to some of the interesting questions raised in this paper. What we have here is a valuable first step along the road to a better understanding of the modus operandi of multiple coaxial airblast atomizers. It might also serve to encourage similar experimental studies on the

---

[1] By A. C. Bwalya and M. W. Johnson published in this issue pp. 692–697.

[2] Rotating Machinery Division, Weir Pumps, Park Works, Manchester M402BA U.K.

[3] By Y. Hardalupas and J. H. Whitelaw, published in this issue pp. 762–771.

[4] Low Furrow, Pehworth, Stratford-upon-Avon, England CV378XW.

effects on spray properties of interactions between adjacent sprays of other, equally important, practical nozzle configurations.

A Novel Method to Measure Capsule Pressure Gradient in a Pipeline[5]

Glenn Cunningham.[6] Williams Technologies, Inc. (WTI) has been the principal consultant to the Coal Log Pipeline Program at the University of Missouri for the last five years. WTI is the operator of Black Mesa Pipeline, a 273 mile coal slurry pipeline in Arizona and Nevada and provides consulting services to the slurry and energy industry. The coal log pipeline technology may provide some unique advantages over coal transportation by slurry pipeline. Most important is that twice the amount of coal could be shipped with coal logs as compared to slurry in the same size pipeline with a dramatic decrease in the amount of water used. In addition, the coal would arrive at its destination in a form that could be handled with conventional coal conveyance and grinding systems, without the need for dewatering now required at the end of a coal slurry pipeline system.

The paper addresses a measurement problem not generally encountered in more conventional pipeline system design and operation. An accurate correlation for prediction of pipeline friction loss must be established prior to commercial application of coal log or capsule technology to enable sizing, location and cost estimating of major system components for determination of project feasibility.

The procedure described in the paper provides the basis for development of scale-up from laboratory data to larger scale applications. It is assumed that near term investigation of the coal log concept will include pumping tests of pilot plant scope. Utilization of the author's pressure gradient measurement method for these tests will be the first step in this development.

The authors also provide a more accurate method of researching the relative effects on pressure gradient of system parameters, such as capsule density and the diameter ratio of capsule to pipe. Correlations for full scale system design must also incorporate these considerations.

Transient Gas-Liquid Flow in Upward Sloping Pipes, Approaching the Wavy-to-Slug Flow Transition[7]

W. J. Meiring.[8] Multiphase flow technology is currently widely applied in the production and transportation of gas and oil. This has been made possible by the advent of reliable predictive methods for multiphase flow in pipelines. Since these models are mostly based on flow regimes, an accurate prediction of flow regime transitions is essential.

It is in this area that this paper makes some valuable contributions. It addresses two of the most important flow regime transitions, namely from stratified to slug flow and from stratified to annular flow. The mechanisms leading to the onset of slug flow are analysed in detail. The model used here is a refinement of the model introduced by Taitel et. al. It would be interesting to quantify the extent to which these refinements contribute to an improved prediction of the onset of slug flow. The paper also presents an improved model for the wetted wall fraction, θ, and thereby the transition to annular flow, which is defined by $\theta = 1$. This is important for predicting whether top-of-the-line corrosion will occur, and whether corrosion inhibitors will be effective.

The applicability of this work to industrial problems, however, has its limitations. The transient model presented is tuned to the specific conditions of the experimental set-up. Extrapolation to other conditions, in particular those relevant to industry, may not be reliable. The model for the wetted wall fraction is based on energy considerations for a specific liquid configuration. It is probably not applicable to large diameter pipelines, in which the wall wetting is dominated by other mechanisms, such as droplet deposition. Further work is needed in this area for a better understanding of the transition to annular flow.

---

[5] By J. Seaba and G. Xu, published in this issue pp. 867–870.

[6] Senior Consultant, William Technologies, Inc., 320 South Boston, Tulsa, OK 74103-3718.

[7] By E. Grolman and J. M. H. Fortuin published in this issue pp. 729–735.

[8] Research Physicist, Shell International Oil Products B.V., P.O. Box 38000, 1030 BN Amsterdam, The Netherlands.

Review: CFD Applications in the Automotive Industry

M. N. Dhaubhadel
Consultant,
Ford Motor Company,
Dearborn, MI
Senior Staff Engineer,
Automated Analysis Corporation,
Ann Arbor, MI

A general review of Computational Fluid Dynamics (CFD) applications in the automotive industry is presented. CFD has come a long way in influencing the design of automotive components due to continuing advances in computer hardware and software as well as advances in the numerical techniques to solve the equations of fluid flow. The automotive industry's interest in CFD applications stems from its ability to improve automotive design and to reduce product cost and cycle time. We are able to utilize CFD more and more in day-to-day automotive design, and we can expect better conditions for CFD applications in the coming years. CFD applications in the automotive industry are as numerous as are the codes available for the purpose. Applications range from system level (e.g., exterior aerodynamics) to component level (e.g., disk brake cooling). The physics involved cover a wide range of flow regimes (i.e., incompressible, compressible, laminar, turbulent, unsteady, steady, subsonic and transonic flows). Most of the applications fall in the incompressible range and most are turbulent flows. Although most of the flows encountered are unsteady in nature, a majority of them can be approximated as steady cases. The challenge today is to be able to simulate accurately some very complex thermo-fluids phenomena, and to be able to get CFD results fast, in order to effectively apply them in the "dynamic" design environment of frequent design changes. The key is to utilize CFD in the early design phases so that design changes and fix-ups later are minimized. Proper use of CFD early, helps to significantly reduce prototyping needs and consequently, reduce cost and cycle time.

Introduction

Applications of CFD in the automotive industry are numerous. Examples are exterior aerodynamics, engine cooling, and climate control. The objectives of the applications of CFD are to improve product design, reduce cost and cycle time and enhance understanding of the flow phenomena involved for better validation and testing. CFD is widely used by the automotive industry today. Unfortunately, a lot of information involved with the automotive applications can not be disclosed in greater detail, because of propietary reasons. Most of the big auto companies have their own CFD software but commercial codes are increasingly used because of high development costs involved in maintenance and up-keep of in-house codes.

In many cases of automotive components design, CFD has been used on a regular day-to-day basis to achieve reduction in cost and cycle time. In some cases, however, even with today's computers and softwares, the time taken for building the model and carrying out the analysis itself is still forbiddingly long. An example is unsteady flows in complicated geometries such as the underhood of a car where grid generation and CFD simulation both take too long to be able to cope with the frequent design changes that are prevalent in today's automotive design process. CFD also has difficulty when the flow physics involved are highly complicated, such as in massively separated flows and where surface quantities (e.g., heat transfer coefficients) are of interest. In most design applications, however, the degree of accuracy needed is not as rigorous as in research work and reasonable approximations can be employed. With continuing performance enhancements in CFD technology, things look a lot better today than they did just a few years ago.

CFD has come a long way in reducing prototype tests in many cases of automotive component design. A distinct advantage of being able to apply CFD in the design process is its ability to analyze several similar designs in a lot less time after the first model has been built. Also, the relative ease with which the effects of localized geometry changes can be ascertained with CFD is a big plus compared to prototype building and testing. However, in many instances design engineers are accustomed to prototype tests and are more confident with the test results than with CFD results. This is mostly because of inadequate exposure to CFD and many times because the CFD process takes too long to impact the design. For example, when complicated geometry is involved, the meshing part of the CFD design process takes a considerable amount of time, rendering it expensive. Similarly, the cpu time required for CFD solution in unsteady cases can be too long. Also, CFD has yet to mature in some areas with complicated physics and complicated geometries such as, combustion, sprays, underhood environment, and the underlying unsteady effects. For instance, the physical complications in combustion arise from chemical kinetics, turbulence and their interactions. These are not well defined in most cases. Underhood geometry is very complex and flow is characterized by massive separations and capturing the boundary layers accurately is a challenge. However, if appropriately used, CFD results can still be employed for comparative design information in many of these complicated cases. For example, with combustion, approximate reaction schemes can be used in many cases with turbulence-controlled eddy break-up model. Similarly, the underhood flow can be approximated as steady flow, except for the idle condition, and the temperature distributions crucial for component heat protection can be approximately predicted. Validation of CFD results in such cases is very important. The challenge is to come up with better and universally applicable physical modeling and faster CFD techniques in order to handle these complicated problems in a reasonable amount of time.

Fluid flow phenomena that are involved in the various automotive design processes cover a wide range of categories. Most of the flows involving air movement are incompressible and turbulent. A variety of turbulence models are available and the

---

Contributed by the Fluids Engineering Division for publication in the JOURNAL OF FLUIDS ENGINEERING. Manuscript received by the Fluids Engineering Division March 28, 1996; revised manuscript received July 18, 1996. Associate Technical Editor: D. P. Telionis.

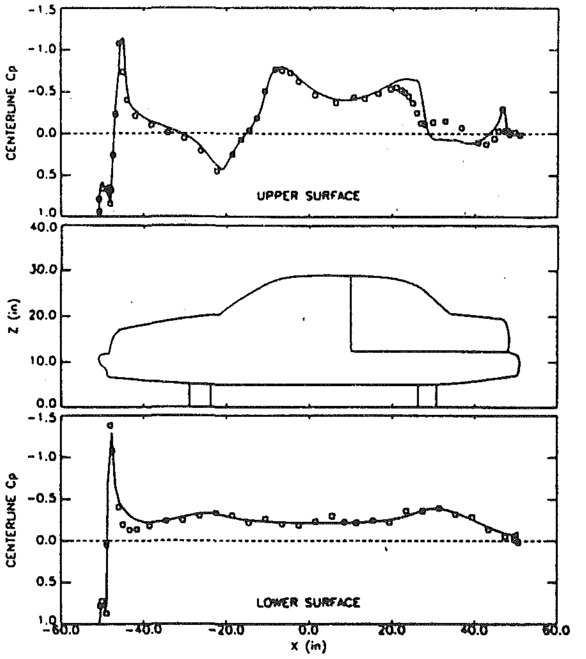

Fig. 1 A typical centerline pressure distribution for a Notchback (solid lines . . . CFD; squares . . . experiment)

standard k-ϵ model is the most widely used. The flow region of interest is represented by a finite computational domain such that the boundaries of the domain are well defined. The computational domain is discretized into finite elements or cells. The governing flow equations are cast into an algebraic system with dependent variables like velocity and pressure interior to the domain as unknowns by use of finite difference, finite volume or finite element technique. The algebraic system which is, in general, nonlinear and non-symmetric is solved by using matrix solvers which employ different numerical techniques such as Picard iteration, quasi-Newton and conjugate gradient. Segregated solvers which require less computer resources for large systems are gaining in popularity these days. Also iterative solvers are getting more and more popular for solving both linear and nonlinear, as well as symmetric and asymmetric algebraic systems. Recent developments in conjugate gradient based solvers e.g., Generalized Minimum Residual (GMRES) and BiConjugate Gradient (BCG) and multigrid solvers e.g. Full Approximation Scheme (FAS) are encouraging. Parallel implementation can significantly reduce turn around time when multiple processors are available. Adaptive mesh refinement and coarsening helps in reducing computer time required for obtaining grid independent solution. Continued developments in these techniques have made CFD computations faster and more attractive.

There are numerous commercial CFD codes available in the market. Selection of a code for a particular application is usually made after validation. First, the code is tested on bench mark problems such as flow past a circular cylinder, flow over a backward-facing step and cavity flow, for which a large amount of reliable test and/or numerical data are available. Data on CFD study of some benchmark problems can be found in the proceedings of the ASME Fluids Engineering Division Forums on Benchmark Problems in Fluid Mechanics (Freitas, 1995). Next, the code is tested on a simplified model of the problem at hand for which good test data is available. If the usefulness and accuracy of the code is verified by the previous steps, the code can be selected and applied on the actual prototype. The final design arrived at from CFD modeling and analysis is usually tested experimentally for validation.

Exterior Aerodynamics. A significant amount of CFD work in exterior aerodynamics can be found in the literature (Dhaubhadel, 1996; Himeno et al., 1990; Okumura and Kuriyama, 1995; Kobayashi, 1992; Williams et al., 1994; Hajiloo et al., 1996; Hucho and Sovran, 1993; Han et al., 1996; Ramnefors et al., 1996; Ahmed, 1992; Han, 1988; Nouzawa et al., 1992; Hutchings and Pien, 1988; Yamada and Ito, 1993; Himeno et al., 1990; Ono et al., 1992; Kawaguchi et al., 1989). The importance of CFD lies in its ability to predict drag accurately for use in efficient design of automotive body shapes. Aerodynamic forces and moments (C_d, C_L, C_{PM}, C_{YM}) and local vortical structures are of interest. Rear window, deck, and some sideview mirrors are known to influence drag substantially.

Williams et al. (1994) and Hajiloo et al. (1996) have made rigorous studies in validating CFD predicted aerodynamic forces (and moments) by direct comparison with experimental measurements for various automotive shapes. The CFD predictions of aerodynamic forces were reasonably accurate (within 5 percent except for C_L) for various configurations. Figure 1 (Williams et al., 1994) shows an example indicating good agreement between experimental fluid dynamics (EFD) and CFD. However, both of the CFD codes failed to match the experimentally observed separated flow region behind the back light as indicated in Fig. 2 (Williams et al., 1994). The CFD results do not show reattachment on the deck that the experimental results indicate. The experimental uncertainty data were not available but the repeatability of the test results were ascertained from tests at two different times. The discrepancy in the two CFD simulations could be due to the inadequacy of the k-ϵ turbulence model used. Drag forces computed in the various regions of the car indicate (Han et al., 1996 and Ramnefors et al., 1996) that design change decisions should not rely just

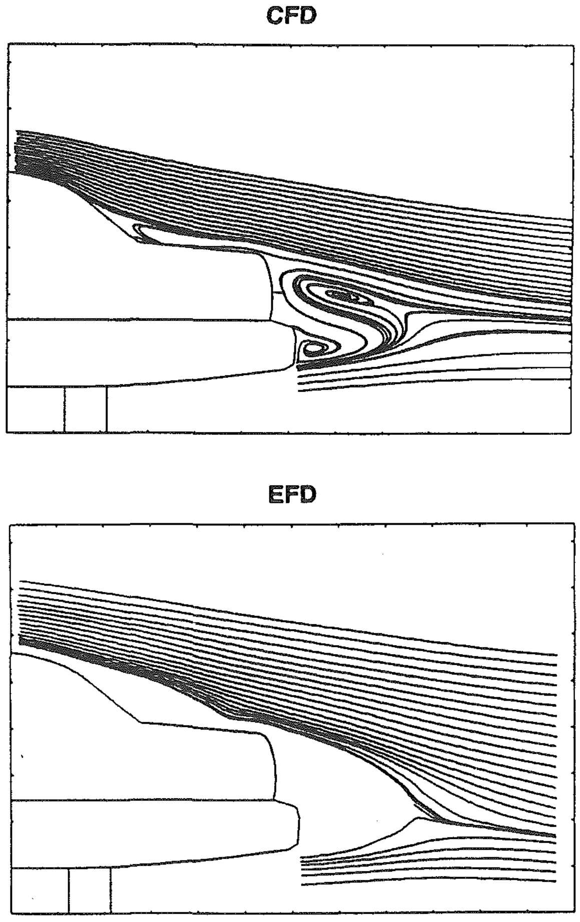

Fig. 2 Center plane streamlines for a Notchback

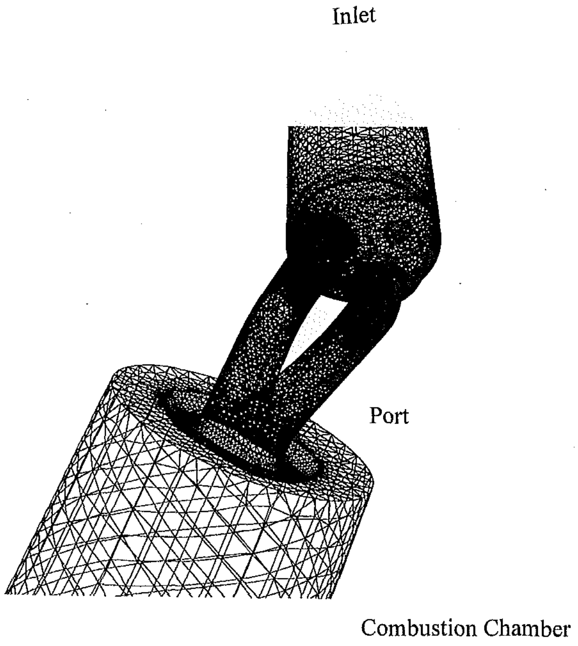

Fig. 3 Surface grid for a two valve per cylinder injection port

on the total drag and that local flow structures are important. Prediction of the local flow structures can, in general, be adequately made for design purposes. CFD simulation allows us to determine the effects of local geometry changes on the aerodynamic forces and provides a significant capability to directly compare two different designs. CFD provides a useful tool in ranking vehicle shapes in terms of their aerodynamic characteristics.

The influence of turbulence models in exterior aerodynamics has been studied by some researchers (Kobayashi, 1992; Han et al., 1996; and Ramnefors et al., 1996). The standard k-ϵ model appears to be the most widely used. There is no consensus on the suitability of any one model. Direct Numerical Simulations (DNS) of unsteady vehicle aerodynamics have started appearing in the literature (Nouzawa et al., 1992) but the computer resources required are too large to make the technique feasible in the day-to-day design process. Large Eddy Simulation (LES), Reynolds Stress Model (RSM), and Anisotropic Eddy Viscosity Model are still in the development stages and application to any realistic geometry is not viable today despite significant progress specially in LES (Tsubokura et al., 1995). Turbulence has always been a crucial issue and a universally applicable, reliable and economical way of solving real-world turbulent flows is still nonexisting. Realistic grids for exterior aerodynamics range in the order of a million elements. Mesh sensitivity appears to be tested with ''brute'' force mesh density increases in most aerodynamic simulations and there is a serious need for use of smart adaptive meshing in CFD of exterior automotive aerodynamics.

Climate Control. CFD applications in the climate control area (Lin et al., 1992; China and Yanagimoto, 1987; Shen et al., 1995; Besombes and Robin, 1996; Gronier and Gilotte, 1996; Currle, 1996; Toksoy et al., 1995; Fischer, 1995; Werner and Frik, 1995) include design of plenum, Heating, Ventilation and Air Conditioning (HVAC) module, Air Conditioning (A/C) duct, defroster duct, rear-heater duct and passenger compartment. Water entrainment, windshield de-icing, porous medium and solar radiation are some of the issues that are also resolved in the CFD computations. The objective is to obtain flow, thermal and acoustic distributions for maximum comfort with minimum pressure and energy loss through the ducting. Lin et al. (1992) studied the effects of A/C flow rate, A/C outlet location, body vent location and glass properties on passenger thermal comfort, which is defined by a complicated function of many factors including air velocity and temperature. They observed that the total flow rate and the A/C outlet location were the most important factors affecting passenger comfort. Shen et al. (1995) used CFD analysis for a plenum and observed that a number of guide vanes oriented in certain ways reduced the water droplets and improved the outlet velocity uniformity with only a slight (<5 percent) increase in the pressure drop. Werner and Frik (1995) presented results of CFD analysis of a HVAC module along with the A/C ducts for vent and heat-up mode. The computed velocity field at various cross sections in the heat-up mode and vent mode were shown. Although no validation of the results were presented, the potential use of this kind of analysis for design comparisons is obvious. CFD results allow design of various ductings, vanes and compartments to achieve optimized flow and thermal distributions with a minimum pressure drop and an acceptable noise level. Despite the general difficulty in addressing turbulence, droplet formation and break-up in water entrainment, CFD applications in the design of climate control components has been promising.

In-Cylinder Flows. The combustion process in internal combustion engines is strongly affected by fuel-air mixing. The mixing process between the injected fuel and the gas flow is complex and transient in nature. The mixing depends heavily on port and valve configurations, combustion chamber, injector tip location, injection timing, spray cone angle and droplet size. CFD is regarded in engine flows as a useful design and development tool. Because combustion depends on turbulence, use of an appropriate turbulence model is crucial. A droplet vaporization model is also important. There is a growing interest in CFD applications to engine flows and a significant amount of work can be found in the literature (Henriot et al., 1989; Haworth et al., 1990; Gosman et al., 1985; Franco et al., 1996; Varnavas and Assanis, 1996; Lebrere and Dillies, 1996; Shaw et al., 1993). Figure 3 shows a surface grid for an injection port for a two valve per cylinder engine. It is a common practice to obtain flow results for different valve lifts. A known pressure drop from inlet to exit is applied for the case considered. Figure 4 shows a typical velocity vector plot across a plane through the center of the valves. Jet-like flow is seen near the valve-openings, as expected. The recirculations seen indicate tumble effect, which is beneficial for mixing and lean combustion. Velocity vectors across the cylinder just below the valves also indicated swirl, which aided in the fuel-air mixing. Lebrere and Dillies (1996) carried out engine flow calculations using a Reynolds stress model. The highest velocity gradients were seen in the vicinity of the jets ensuing from the valve openings and turbulence production was large in this region. Both RSM and

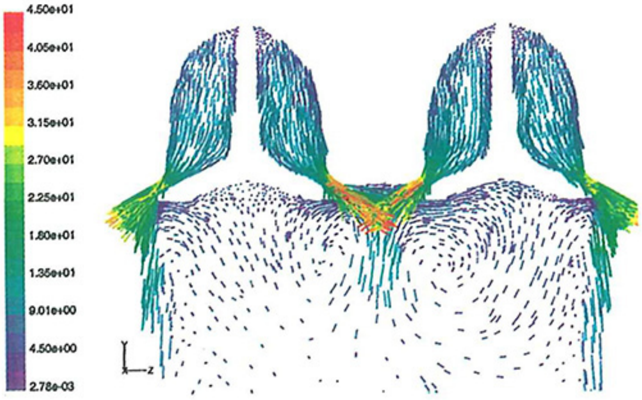

Fig. 4 Velocity vectors through the center of the port valves

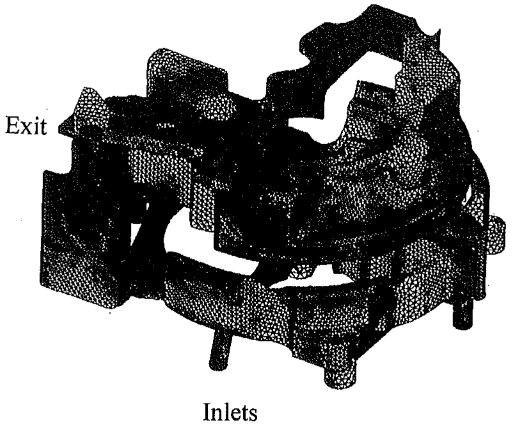

Fig. 5 A typical mesh for the cylinder head water jacket

k-ϵ models predicted the mean and turbulent flow fields matching their experimental results. Turbulence anisotropy was found to be strong at the spark plug location at the end of compression. CFD is increasingly used in anlyzing engine flows. However, the complex interaction between droplet formation, breakup, vaporization, chemical kinetics of combustion and turbulence is still a subject of research.

Engine Cooling. Control of engine coolant temperature is an essential part of modern engine design because of high performance and high durability requirements. Coolant passages of cylinder head and block are very complex and direct flow and thermal measurement or visualization is difficult and time consuming. CFD enables us to predict the peak and overall distributions of metal temperature in both the cylinder head and the block and the pressure drop associated with the coolant flow. Figure 5 shows the surface grid of the cylinder head (Birkett et al., 1996). Because of the complexity in the geometry, more time is spent in obtaining a mesh of the cylinder head water jacket than in obtaining the actual CFD solution. Figures 6 and 7 show the pressure distribution and the heat transfer coefficient distribution obtained from CFD solution. Most of the pressure drop occurs near the exit, indicating that geometry changes in this region could lead to reduced coolant pump capacity requirement. The heat transfer coefficients predicted indicate low cooling near the combustion face on the exhaust side (lower right of Fig. 7) indicating the need for geometry change for improved cooling. CFD results also provide information for changes in the coolant passage geometry in order to maintain the coolant temperatures within specified limits. The heat transfer coefficients can be used to check if the thermal stresses are within allowable limits. Lee and Cho (1995), Yuzo et al. (1988) and Sanford and Postlethwaite (1993) have conducted similar studies of engine coolant flow simulations. CFD provides a significant capability in engine coolant flow simulations and cylinder head water jacket design. Truly automatic mesh generators, when available, can be expected to reduce the turn around time significantly.

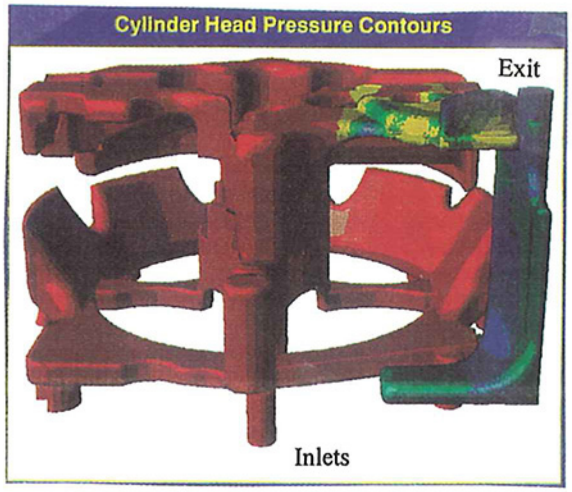

Fig. 6 Pressure distribution for the cylinder head

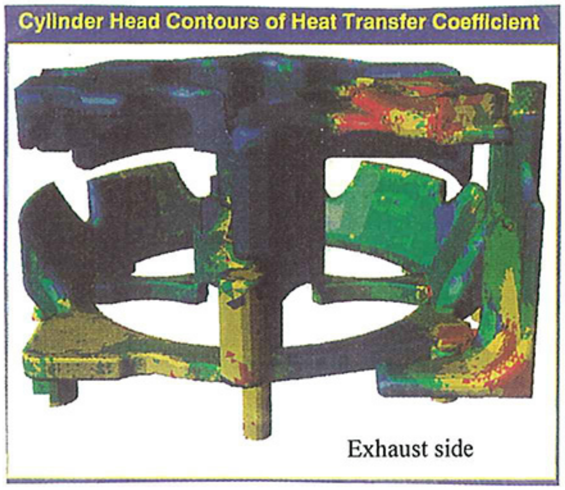

Fig. 7 Heat transfer coefficient distribution for the cylinder head

Exhaust Systems. Exhaust manifold, silencers and catalytic converters are some of the CFD application areas in exhaust systems. Figure 8 shows an example temperature distribution for an exhaust manifold. In actual cases, the maximum gas temperature could reach as high as 1200° K during high speed cruising. Temperature distributions and thermal stress levels are of interest in the design. The exhaust manifold itself is made of high heat resistant material and is designed to meet the fuel economy requirements at high cruising speed and the increasingly severe emission requirements. The high temperatures carried by exhaust gases affect other underhood and underbody components near the exhaust manifold. Lai et al. (1991) and Chen et al. (1988) presented results for dual monolith catalytic converters. The monolith brick resistance was modeled as a source term in the momentum equations. Isshiki et al. (1996) applied CFD to predict pressure losses and acoustic characteristics in silencers. The calculated pressure losses were found to

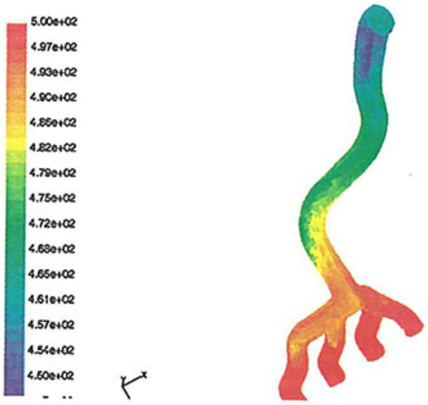

Fig. 8 Temperature distribution for the exhaust manifold

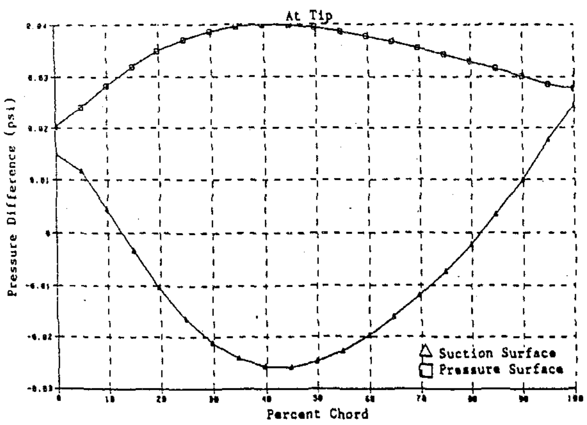

Fig. 9 Pressure side and suction side pressure distribution at the blade tip

agree well with the experimental measurements. CFD analysis allows prediction of important design factors, such as the exhaust component surface temperatures, the exhaust gas temperatures entering the muffler and the resonators, and flow uniformity and pressure drops in catalytic converters. A significant portion of the warranty involved in a car is heat related and CFD predictions allow modifications of cooling passages and heat-shielding to limit the temperatures within acceptable levels.

Rotating Machinery. Cooling fans, blowers, torque converters, oil pumps, disk brake cooling are some of the areas involving rotating machinery. Dhaubhadel et al. (1988) provided a CFD technique to aerodynamically design rotor blades of automotive cooling fans so that maximum flow rate and pressure rise across the fan were obtained for a given rpm. Figure 9 shows a typical pressure distribution predicted at the blade tip on the pressure side and the suction side. The area between the two curves indicate the extent of loading on the fan. Pressure distributions on the pressure surface and the suction surface indicate changes in the blade geometry for optimum loading or for the maximum flow rate for a given fan speed. Figure 10 shows the comparison of different blades with respect to pressure rise across the fan at different flow rates. Cyclic symmetry is usually exploited and a rotating frame of reference is used for the analysis. However, when the fan blades and the shroud are not oriented to provide cyclic symmetry, the whole fan and shroud assembly needs to be modeled. The isolated component analysis creates a practical difficulty, because the effect of other nearby components on the fan performance is not known. And a full vehicle model, because of size restrictions, does not allow fine enough mesh in the fan area to capture the fan effects. The general approach taken to alleviate the situation is to include a component model (in this case, a fan model coming out of the isolated component analysis, preferably with blockage considered and verified with experimental data) in the full vehicle simulation. Shen and Backer (1996) applied CFD to a dual fan alternator and found that the second fan reduced the component fluid temperature by roughly 20°C. Ecer et al. (1996) used CFD in the design of an alternator fan to improve air flow performance and were able to reduce the noise level by 4 db.

Toksoy et al. (1995) presented a method for HVAC blower design and concluded that the computational results provided a three-dimensional detailed picture of the flow allowing more knowledge and confidence in the CFD design process. Fischer (1995) conducted airflow simulation for automotive blowers and underscored the usefulness of CFD in predicting the relative effects of design changes.

Krusemann and Schmidt (1995) applied CFD for optimization of disk brake cooling. Distributions of temperature and heat transfer coefficient and flow rates through the disk provided a basis for design changes for cooling optimization.

Haworth et al. (1996) carried out transient calculations for gear pumps and vane pumps. Air bubbles in oil, leakage and non-aligned moving interfaces were accounted for. Transient CFD enhanced physical understanding of the pumping devices and allowed comparison between specific designs. Jian et al. (1996) analyzed a vane oil pump using sliding mesh interfaces. The solutions compared well with experimental results for low speeds. For speeds greater than 2500 revolutions per minute the deviation increased, possibly due to cavitation and leakage which were not modeled.

Rotating machinery pose additional complexity in CFD simulations owing to the unsteady interactions between rotating and non-rotating components. The effects of cavitation, leakage and inlet swirl are important considerations. Turbulence modeling is also an issue as with most other automotive CFD. Application of CFD to the design of rotating automotive components has continued to grow and in most cases it is used as an essential part of the design.

Underhood Cooling and Heat Protection. Underhood thermal protection is becoming more and more important in today's vehicle development due to higher output engines, tighter packaging and smaller engine compartments. Underhood geometry is the most complicated geometry in a vehicle CFD simulation. Also the flow under the hood is complex because of massive flow separations. An extensive amount of CFD simulation work can be found in the literature (Kuriyama, 1988; Aoki, 1990; Bauer et al., 1995; Shimonosono et al., 1993; Hara and Fujitani, 1988; Himeno et al., 1990; Dhaubhadel et al., 1995; Aoki et al., 1990; Katoh et al., 1991; Ashmawey et al., 1993; Dhaubhadel and Shih, 1996; Lyu and Ku, 1996). Meshing of the underhood geometry takes a considerable amount of time and obtaining grid independent solution is still a challenge because of the huge size of any realistic grid. The situation is more difficult when transient simulations are sought. Automatic solution adaptive mesh generators along with parallel processing can help reduce turn around time considerably. Fully automatic mesh generators with solution adaptive refining and coarsening capability are still not available and, as a result, most rely on one-shot one-mesh simulations. Also, because of the huge computer time and resources needed, underhood CFD simulation is rarely done with all three forms of heat transfer included. Instead, conduction through solid and radiation heat transfer are treated separately and the results are incorporated in the CFD simulation through modifications in the boundary conditions when needed.

Figure 11 shows the mesh distribution on an automobile surface including the underhood and underbody components. A

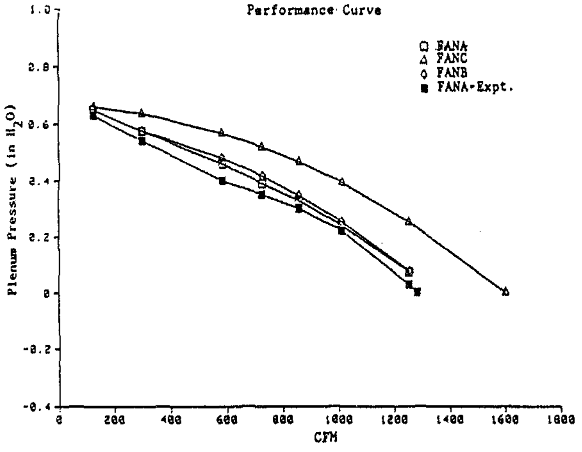

Fig. 10 Plenum pressure curves for different fans

typical plot of velocity vectors on a plane through the center of the car is shown in Fig. 12. The velocity distribution indicates the extent of convective cooling of the various underhood components. The flow and thermal distributions predicted provide information for any potentially beneficial design changes for optimized heat protection. Shimonosono et al. (1993) carried out CFD simulations and visualization experiments for an engine compartment and used the information to install flow control devices to optimize the thermal performance of the engine compartment. Kato et al. (1991) simulated 3-D flow in the engine compartment for vehicle speeds of 120 kmph (high speed), 35 kmph (low speed) and 0 kmph (idle condition) using a standard k-ϵ turbulence model. Mean velocity in front of the radiator matched well with the experimental values with a maximum of 10 percent deviation for the low vehicle speed case. Experimentally obtained heat rejection rates for the radiator and the condenser and surface temperatures and heat transmission rates for the engine were prescribed. CFD predicted temperatures matched well with the experimental values. Lyu and Ku (1996) studied the engine compartment flow and the effect of the frontal opening both numerically and experimentally. A high degree of nonuniformity in the mean flow velocity at the front of the radiator was observed. The cooling was found to be better for the lower radiator region than the upper one.

Meshing of underhood geometry in a reasonable design time frame is still a challenge today. The ''automatic'' mesh generators available today have difficulty handling the proximity of components. Because of the large size (a million or more elements) of the underhood mesh, unsteady flow simulation with all three forms of heat transfer is too time consuming and not feasible today with the available computers and CFD codes. Fully automatic mesh generators and highly efficient, solution adaptive, parallel CFD solvers, as well as better computers are needed before unsteady problems of this magnitude can be tackled for everyday design purposes. Steady state CFD solution of an underhood flow problem was unthinkable only a few years ago. With currently available CFD capability, a steady state solution on a 'coarse' mesh of about a million elements is obtainable in a few hours. This is indeed a breakthrough and the situation is expected to continue to improve over time.

Conclusions

CFD has emerged as a powerful tool for predicting flow and thermal distributions in vehicle systems. It is being accepted more and more in day-to-day design of automotive components. In cases where CFD solution is obtainable with sufficient accuracy, CFD simulation provides insight into the details of the flow features over the whole computational domain. Obtaining details throughout the domain may be difficult, if at all possible, with experimentation. CFD also provides flow data non-intrusively which may not be the case with some experiments. When applied properly, CFD can significantly reduce the need for prototype tests, as well as cost and design cycle time. Once a model has been created, it is usually very easy to determine the effects of geometry changes, flow parameter changes and material property changes. With continued developments in computer hardware and numerical techniques, CFD can be expected to be accepted like Finite Element Analysis (FEA) in the solid mechanics world.

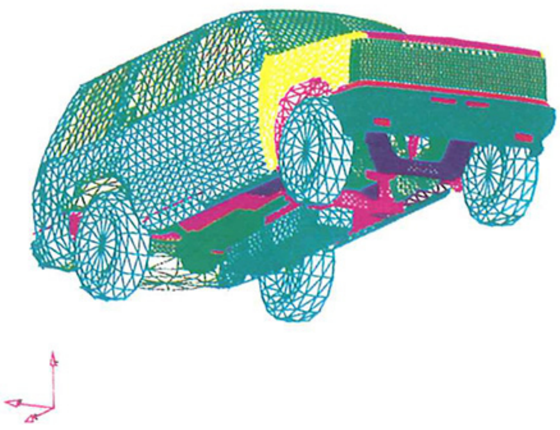

Fig. 11 Mesh distribution on the car surface

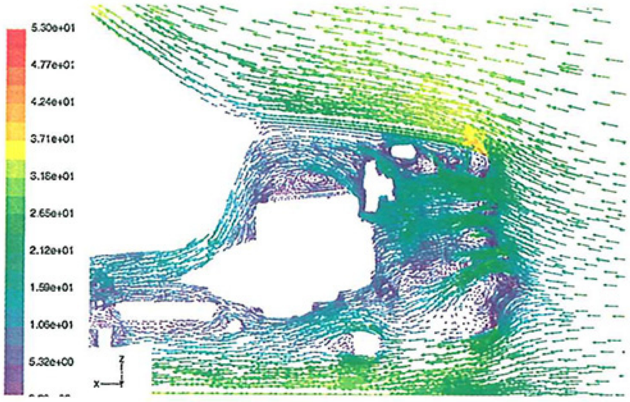

Fig. 12 Velocity vectors on the central plane

In some areas, CFD is not mature enough for direct application to design e.g. oil pumps, where cavitation and thin film bearing friction are not well understood. Adequacy of the turbulence models is always an issue. Interaction between droplet formation, break-up, vaporization, chemical kinetics of combustion and turbulence is complex and needs further research. And there is a serious need for automatic and solution adaptive mesh generators for complicated geometries. Segregated and iterative solvers and parallel algorithms have made CFD applications in automotive design more effective. Turn-around times for CFD solutions appear to go down by an order of magnitude or more in a year. With continued developments expected in computer hardware and CFD software, CFD should be able to satisfy the increasing demands expected of competitive automotive fluid dynamic design.

References

Ahmed, S. R., 1992, ''A Critical Review of the CFD-Methods Available to Compute Flow Around Automobiles,'' *Innovation and Reliability in Automotive Design and Testing,* Vol. 3, 1437–1456, Apr.

Aoki, K., Hanaoka, Y., and Hara, M., ''Numerical Simulation of Three Dimensional Engine Compartment Air Flow in FWD Vehicles,'' SAE 900086.

Ashmawey, M., Berneburg, H., Hartung, W., and Werner, F., ''A Numerical Evaluation of the Thermal Effects of the New V6 Engine on the Underhood Environment of the 1993 Opel Vectra,'' SAE 930295.

Bauer, W., Ehrenreich, H., and Reister, H., 1995, ''Design of Cooling Systems with Computer Simulation and Underhood Flow Analysis using CFD,'' C496/042/95, IMechE.

Besombes, G., and Robin, R., ''Car Passenger Environment CFD Simulation Integration into the Development of an Automotive HVAC,'' SAE 960813.

Birkett, C. A., Dhaubhadel, M. N., Daniel, S. I., and Balachander, R. S., 1996, ''Flow Analysis of a Diesel Engine Water Jacket Using Unstructured Tetrahedral Meshes,'' Proc. of the Forum on Automotive Applications of CFD, ASME, IMECE, Nov.

Chen, D. K. S., Bissett, E. J., Oh, S. H., and Ostrom, D. L. V., ''A Three Dimensional Model for the Analysis of Transient Thermal and Conversion Characteristics on Monolithic Catalytic Converters,'' SAE 880282.

China, H., and Yanagimoto, K., 1987, ''Prediction of Internal Flow of Passenger Car by Three-Dimensional Numerical Flow Analysis,'' *JSAE,* Vol. 41, No. 12, pp. 1376–1381.

Currle, J., ''Simulation of the Two-Phase Flow in the Waterbox of a HVAC System,'' SAE 960962.

Dhaubhadel, M. N., Akay, H. U., and Charles, H. N., ''Three Dimensional Finite Element Analysis for Aerodynamic Design of Fan Blades,'' AIAA 88-3641.

Dhaubhadel, M. N., Kumar, K., and Shih, T. S., 1995, "Evaluation of Commercial CFD Codes for Underhood Cooling," Ford VSCAE TMD Report, Feb.

Dhaubhadel, M. N., 1996, "CFD Applications in the Automotive Industry—Invited Keynote Presentation," ASME, FED-Vol. 238.

Dhaubhadel, M. N., and Shih, T. S., 1996, "Underhood Thermo-fluids Simulation for a Simplified Car Model," ASME, FED-Vol. 238.

Ecer, A., Toksoy, C., Didandeh, H., Zhivov, M., Hull, M., and Buening, D., "Computer Aided Design of Automotive Alternator Fans for Improved Cooling Performance and Noise," SAE 960274.

Fischer, D., "Airflow Simulation Through Automotive Blowers Using Computational Fluid Dynamics," SAE 950438.

Freitas, C. J., 1995, "Perspective: Selected Benchmarks From Commercial CFD Codes," ASME JOURNAL OF FLUIDS ENGINEERING, Vol. 117, No. 2, June.

Franco, A., Martorano, L., Stan, C., and Eichert, H., "Numerical Analysis of the Performances of a Small Two-Stroke Engine with Direct Injection," SAE 960362.

Gosman, A. D., Tsui, Y. Y., and Vafidis, C., "Flow in a Model Engine with a Shrouded Valve—A Combined Experimental and Computational Study," SAE 850498.

Gronier, P., and Gilotte, P., "Airflow Simulation of an Automotive Blower for HVAC Unit," SAE 960961.

Hajiloo, S., Williams, J., Hacket, J. E., and Thompson, S. A., "Limited Mesh Refinement Study of the Aerodynamic Flow Field Around a Car-Like Shape: Computational Versus Experimental Fluid Dynamics," SAE 960677.

Han, T., 1988, "A Navier-Stokes Analysis of Three Dimensional Turbulent Flows Around a Bluff Body in Ground Proximity, AIAA 88-3376, July.

Han, T., Sumantran, V., Harris, C., Kuzmanov, T., Huebler, M., and Zak, T., "Flow-Field Simulations of Three Simplified Vehicle Shapes and Comparisons with Experimental Measurements," SAE 960678.

Hanaoka, Y., and Aoki, K., "Numerical Simulation of Three Dimensional Engine Room Air Flow," *Proc. JSAE Autumn Convention 892.*

Hara, J., Fujitani, K., and Kuwahara, K. "Computer Simulation of Passenger Compartment Airflow," SAE 881749.

Haworth, D. C., El Tahry, S. H., Huebler, M. S., and Chang, S., "Multidimensional Port-and-Cylinder Flow Calculations for Two-and Four-Valve-Per-Cylinder Engines: Influence of Intake Configuration on Flow Structure," SAE 900257.

Haworth, D. C., Maguire, J. M., Mathes, W. R., Rhein, R., and El Tahry, S. H., "Dynamic Fluid Flow Analysis of Oil Pumps," SAE 960422.

Henriot, S., Lecoz, J. F., and Pinchon, P., "Three Dimensional Modelling of Flow and Turbulence in a Four-Valve Spark Ignition Engine—Comparison with LDV Measurements," SAE 890843.

Himeno, R., Tagaki, M., Fujitani, K., and Tanaka, H., "Numerical Analysis of the Airflow around Automobiles Using Multi-block Structured Grids," SAE 900319.

Himeno, R., Fujitani, K., and Tanaka, H., 1990, "A Study of Aerodynamic Characteristics of a Production Car Using a Finite Difference Analysis of Flows," Proc. JSAE Spring Convention 901.

Hutchings, B. J., and W. Pien, "Computation of Three Dimensional Vehicle Aerodynamics Using FLUENT/BFC, *Proc. 2nd International Conference on Supercomputing Applications in the Automotive Industry,* Seville, Cray Research, pp. 233–255.

Hucho, W., and Sovran, G., 1993, "Aerodynamics of Road Vehicles," *Annual Review of Fluid Mechanics,* 25, 485–537.

Isshiki, Y., Shimamoto, Y., and Wakisaka, T., "Simultaneous Prediction of Pressure Losses and Acoustic Characteristics in Silencers by Numerical Simulation," SAE 960637.

Jiang, Y., Przekwas, A., and Perng, C., "Computational Analysis of Oil Pumps with an Implicit Pressure Based Method Using Unstructured Mixed Element Grids," SAE 960423.

Katoh, N., Ogawa, T., and Kuriyama, T., "Numerical Simulation on the Three Dimensional Flow and Heat Transfer in the Engine Compartment," SAE. 910306.

Kawaguchi, K., Hashiguchi, M., Yamasaki, R., and Kuwahara, K., "Computational Study of Aerodynamic Behavior of a Three Dimensional Car Configuration," SAE 890598.

Kobayashi, K., "A Review of CFD Methods and Their Application to Aerodynamics," SAE 920338.

Lai, M. C., Kim, J. Y., Cheng, C. Y., Li, P., Chui, G., and Pakko, J. D., "Three Dimensional Simulations of Automotive Catalytic Converter Internal Flow," SAE 910200.

Krusemann, R., and Schmidt, G., "Analysis and Optimization of Disk Brake Cooling via Computational Fluid Dynamics," SAE 950791.

Kuriyama, T., 1988, "Numerical Simulation on Three Dimensional Flow and Heat Transfer in the Engine Compartment Using STREAM," *Proc. 2nd International Conference on Supercomputing Applications in the Automotive Industry,* Sevelle, Spain, Cray Research.

Lebrere, L., and Dillies, B., "Engine Flow Calculations Using a Reynolds Stress Model in the Kiva-II Code," SAE 960636.

Lee, J., and Cho, N., "Numerical Analysis of Gasoline Engine Coolant Flow," SAE 950274.

Lin, C. H., Han, T., and Koromilas, C. A., "Effect of HVAC Design Parameters on Passenger Thermal Comfort," SAE 920264.

Lyu, M., and Ku, Y., "Numerical and Experimental Study of Three Dimensional Flow in Engine Room," SAE 960270.

Nouzawa, T., Hiasa, K., Nakamura, T., Kawamoto, A., and Sato, H., "Unsteady—Wake Analysis of the Aerodynamic Drag of a Notchback Model with Critical Afterbody Geometry," SAE 920202.

Okumura, K., and Kuriyama, T., "Practical Aerodynamic Simulations (CD, CL, CYM) Using a Turbulence Model and 3rd-order Upwind Scheme," SAE 950629.

Ono, K., Himeno, R., Fujitani, K., and Uematsu, Y., "Simultaneous Computation of the External Flow Around a Car Body and the Internal Flow Through its Engine Compartment, SAE 920342.

Ramnefors, M., Bensryd, R., Holmberg, E., and Perzon, S., "Accuracy of Drag Prediction on Cars Using CFD—Effect of Grid Refinement and Turbulence Models," SAE 960681.

Sandford, M. H., and Postlethwaite, I., "Engine Coolant Flow Simulation—A Correlation Study," SAE 930068.

Shaw, C. T., Garysmith, J. L., and Richardson, S. H., "Influencing Engine Design Using Computational Fluid Dynamics," SAE 930877

Shen, F. Z., Backer, G. P., and Swanson, D., "HVAC Plenum Design Analysis," SAE 950113.

Shen, F. Z., and Backer, G. P., "Dual Fan Alternator Design Analysis," SAE 960272.

Shimonosono, H., Shibata, Y., and Fujitani, K., "Optimization of the Heat Flow Distribution in the Engine Compartment," SAE 930883.

Toksoy, C., Zhivov, M., Cutler, F., Ecer, A., Rayhill, M., Guzy, S., and Vasko, R., "Design of an Automotive HVAC Blower Wheel for Flow, Noise and Structural Integrity," SAE 950437.

Tsubokura, M., Kobayashi, T., Taniguchi, N., and Oshima, M., 1995, "Large Eddy Simulation of Turbulent Channel Flow Using an Unstructured Mesh," *Numerical Developments in CFD,* Dhaubhadel, M. N., Nakahashi, K., Habashi, W. G., Agarwal, K., and Oshima, K., eds., ASME FED-Vol. 215.

Varnavas, C., and Assanis, D. N., "A High Temperature and High Pressure Evaporation Model for the KIVA-3 Code," SAE 960629.

Werner, F., and Frik, S., "Optimization of an Automotive HVAC Module by Means of Computational Fluid Dynamics," SAE 950439.

Williams, J., Quinlan, W. J., Hacket, J. E., Thompson, S. A., Marinaccio, T., and Robertson, A., "A Calibration Study of CFD for Automotive Shapes and CD," SAE 940323.

Yamada, A., and Ito, S., "Computational Analysis of Flow Around a Simplified Vehicle-like Body, SAE 930293.

Yuzo, A., et al., "Numerical Simulation and Experimental Observation of Coolant Flow Around Cylinder Liners in V-8 Engine," SAE 880109.

Paul Cooper
Director, Advanced Technology,
Ingersoll-Dresser Pump Company,
Phillipsburg, NJ 08865
Fellow ASME

Perspective: The New Face of R&D—A Case Study of the Pump Industry

Introduction

In a recent issue of the *Technology Review,* President Emeritus Robert M. White (White, 1995) of the National Academy of Engineering says that other sectors of the economy are failing to pick up the slack as government research and development funds decline. Moreover, he goes on to say that in the past few years, six of the largest U. S. corporations have cut their R&D spending by 30 percent. In my own area of central New Jersey, Exxon's new R&D center has downsized so much that they have rented out some of the space to other companies. Over the past decade, many of those companies with two or three billion dollars in annual sales, who had corporate research centers, have simply closed them. An example is my own company, who conducted research in a handsome facility near Princeton for two decades prior to closing it in 1985. They built it on 200 acres near Princeton and staffed it with over 100 scientists, engineers, and support personnel. This year the still young building vanished, torn down to make way for real estate development.

Casualties of this kind appear to have occurred especially in those industries that I choose to identify as being "mechanical-engineering intensive." Perhaps the nature of mechanical engineering R&D is such that it is best done in closer proximity to the engineering of the product itself. In my own and other pump companies, such work is indeed now being done "onsite" at manufacturing facilities. However, in other industries, separate, offsite corporate R&D organizations are still essential to the business; for example, in pharmaceutical companies. They must regularly respond to market needs with new chemical formulations that have little relationship to their existing products.

This situation depresses many who have spent careers in R&D. Many of us have seen firsthand—even been a part of—the tremendous buildup of R&D organizations that occurred following World War II and continued through the sixties and seventies. Why did the closures and downsizing occur? Have they or will they destroy our ability to compete worldwide? Or are we now leaner and meaner? Perhaps the research centers became dinosaurs. Is there a better way? Or do they still exist in new forms and can these latter survive? Can, or should, R&D be done without the critical mass of research personnel that they supposedly provided?

Attempts to answer these questions easily lead to speculation. We might fare better by seeking the insight afforded by a case study. Let's take the pump industry, and particularly, the highly-engineered pump industry. This venerable enterprise stands squarely in the mainstream of ASME experience—being well represented over most of this century in the Transactions, including the *Journal of Fluids Engineering.* And this is only part of the vast literature at our disposal on the subject. Hopefully in this study we can see what has happened to R&D; i.e., the role it has played in our mechanical engineering industries, and where it is going.

Pump R&D

In the case of the pump industry, these developments can be viewed in the context of three distinct phases of R&D activity that have accompanied the growth of the pump business from the early years of this century; namely,

1. A *Professional Engineering phase,* in which a few outstanding technically motivated and commercially oriented individuals made significant and lasting contributions to the industry; then
2. A *Corporate Research Center phase,* characterized by the setting apart of dedicated offsite facilities, in which to pursue technical developments with that critical mass of professionals—unhindered by the day-to-day exigencies of the business; and finally
3. The present, *Focused, Applied R&D phase,* in which everything that is done is judged more in the light of whether it is imminently commercially relevant and viable.

The Professional Engineering Phase. The ASME Transactions introduce us to the first of these, namely, the Professional Engineering phase, which covers roughly the period up to the mid-fifties. There, one can find several reports on large pumps that were each a part of a major engineering project. From the referenced examples that follow, these articles reveal strong individuals who applied basic physics and engineering principles to the solution of technical problems of immediate commercial significance. These were professional engineers, who, without the benefit of modern technical support systems, distinguished themselves as having a strong grasp of a broad range of mechanical engineering disciplines and how these disciplines needed to be applied in order to achieve commercial success for their companies. Much of what they did is still used in one form or another in the pump industry today.

One example is J. P. Den Hartog's solution of an acoustics problem that occurred in the penstock of a large Francis hydraulic turbine. Figure 1 is taken from his 1929 ASME Transactions paper, in which he clearly describes the acoustic reinforcement that occurred in the penstock because of a poor vane combination (Den Hartog, 1929). He showed that the same phenomenon occurs in pumps. It came from the time when Den Hartog worked in industry, and it was written in the same style that he so illustriously applied later on as a professor at M.I.T. It is a very readable and practical paper, both in presentation and in significance for today's pump engineers (Makay et al., 1993). A recent paper by Bolleter on vane combinations for pump impellers and diffusers is a generalization of blade interaction theory and the attendant effects (Bolleter, 1988). Its appearance shows how relevant this work of Den Hartog still is.

Contributed by the Fluids Engineering Division of THE AMERICAN SOCIETY OF MECHANICAL ENGINEERS and presented at the 1995 International Mechanical Engineering Congress & Exposition, The Robert Henry Thurston Lecture, San Francisco, Ca., November 12–17, 1995. Manuscript received by the Fluids Engineering Division December 18, 1995; revised manuscript received September 4, 1996. Associate Technical Editor: D. P. Telionis.

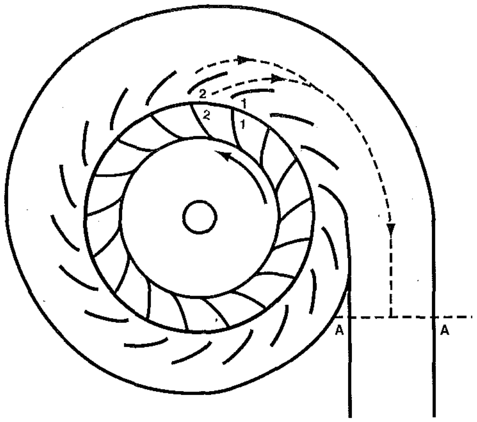

Fig. 1 Schematic representation of turbine scroll case and runner. Blade 2 of the runner has just interacted with Vane 2 of the row of inlet guide vanes that surround the runner, producing a pressure wave that travels at the speed of sound back to the penstock or scroll entrance at A-A. A short time later, Blade 1 interacts with Vane 1, creating another wave. If the time period between these interactions is such that the two pressure ***pulses arrive at A-A at the same time, the resulting reinforcement pro*****duces excessive pressure pulsations at A-A.**

Another example is Carl Blom's 1950 Transactions paper on the hydraulic design of the Grand Coulee pumps (Blom, 1950). Several geometries were considered, and work was done to optimize the design for performance and vibration-free operation. A $\frac{1}{13}$th scale model of this pump was tested in a loop at Caltech. There was then, and still is, a connection between the universities and industry. In this case, as for most others in those days, the university research was very specific and project oriented. Dr. Alan Acosta tells me that his first job as a graduate student was the polishing of the impeller in this model to provide hydraulic similarity to the 13-foot-diameter prototype impeller. This article is still a source of valuable data and experience that bears careful study by anyone aspiring to be a professional pump engineer.

Then there is the well-known work of Alexey J. Stepanoff. A prolific author and successful pump designer, he is best known for his book called *Centrifugal and Axial Flow Pumps* (Stepanoff, 1957). Those who knew him say that he was an intense individual who had a lot of pride in his capability and accomplishments. He was not a team player in the modern R&D program sense, but he had such a wide circle of acquaintances that his book is quite broad and covers all of the subject areas of interest to pump engineers today. Some of his explanations of the fluid dynamical phenomena occurring in pumps have rightly been questioned, but they do not invalidate his design recommendations. Yet, some of his *other* ideas were major contributions to the understanding of pump behavior. For example, he coauthored with Harold Stahl the first clear explanation of the thermodynamic effect of cavitating flow on pump performance; viz., why pumping hot water is easier (produces less internal vapor volume) than pumping cold water (Fig. 2) (Stahl et al., 1956). Stahl was another one of these professional pump engineers, and he distinguished himself as a hydraulic designer for many years—as did Stepanoff.

While my primary emphasis here is on industry, academic research helped to define this phase of pump R&D activity. The emphasis of university professors who worked in the pump field during this period was similar to that of their industrial counterparts. They became well known and respected in the industry, concentrating on commercially significant pump phenomena. An example is work on performance characteristics by Professor Kittredge, which can be found in the *Pump Handbook* (Karassik et al., 1986). Professor Knapp did pioneering work in this field, establishing the four-quadrant data that is still widely interpolated to geometries other than those he tested (Stepanoff, 1957). He is perhaps best known for his fundamental discovery that the rate of material removal due to cavitation is a sixth-power function of the velocity—at a constant cavitation number (Fig. 3) (Knapp, 1955). This was preceded by Fischer and Thoma's 1932 visualization of the flow within an impeller, still widely referenced. In Fig. 4 you see their portrayal of rotating stall at reduced flow rates (Fischer et al., 1932). Later came Ippen's Reynolds number corrections to hydraulic performance (Ippen, 1946). Even though he did this for a single pump geometry, Ippen's results have been used widely as the so-called viscosity correction for virtually all pump geometries. George Wislicenus (1965), like Carl Pfleiderer (1961) in Germany, founded design-oriented institutions and wrote the classic texts that many of us still use. All this work was done prior to the space race and the era of government funding for liquid rocket engine pump development and other aerospace pump hardware. Certainly there was government funding for university research in pump-related areas prior to this, particularly via the Navy, but this kind of support was soon to undergo a marked increase.

The Corporate Research Center Phase. The space challenge, beginning with Sputnik in 1957, intensified the demand for R&D to a point that not only did we see the great expansion of government laboratories but industry also responded by establishing formal research organizations, usually at the corporate level. So began the second phase of this case study, namely that of the Corporate Research Center. These centers were generally housed in campus-like facilities located away from the manufacturing plants. Pursuit of government contracts was undoubtedly a factor that drove this trend, and the pump industry was involved to a degree.

I now specialize this case study to the history of my own company's involvement in pump R&D beginning at their corporate research center and continuing down to the present day in one of their major factory locations. I believe this to be sufficiently representative of the pump industry to validate the conclusions that will emerge. Established in the sixties, this research center served over 30 divisions of the parent company, three of which built pumps. Thus the multidisciplined staff took on a host of projects that addressed the concerns of these divisions. Corporate support was supplemented by outside contracts that were selected on the basis of relevance to the company's business—both present and future.

Although the uninformed observer would say that pumps are an ubiquitous and mature product, they did command some attention as a worthy R&D subject at the center. One of the goals that was set for pumps was to "nurture an advanced hydraulics core competency," i.e., to develop and incorporate a working capability in this area as an integral part of the company's design procedures. A good deal of flow analysis capability had been developed for centrifugal compressors—particularly under NACA sponsorship—that could provide a rational fluid dynamical knowledge base for an otherwise empirical—albeit highly developed—science in the centrifugal pump field. Performance prediction codes were developed and coupled with quasi-three-dimensional flow analysis to form the basis of an advanced design procedure. Existing designs were analyzed with this system and investigated experimentally so as to be able to express in fluid dynamical terms the boundary conditions and inputs that would create near-optimum geometries. This formed a data base from which improvements could be made analytically. The experimental work included the study of flow in inlet passageways and volutes through flow visualization and pitot tube measurements. In frequent visits at the pump divisions, transfer of this technology was accomplished through reports, presentations, and application of the work to current jobs via onsite consultation by the researchers.

New product development was another goal of the pump work at the research center. New concepts were introduced at both the component level (i.e., impeller, diffuser, volute, etc.,) and that of the complete machine. One such project was a contract obtained by the center from the Department of Energy to improve slurry pumps for coal liquefaction service. Successful completion of the project could result in a new business for the company. Test rigs and loops were constructed, and hydraulic features were conceived and tested that would reduce erosion. For example, as shown in Fig. 5, a curved cutwater prevented erosion on the sidewalls by solid particles; whereas the horseshoe vortices generated by a straight cutwater drove these particles, causing sidewall wear (Kasztejna et al., 1986). While the results were gratifying, we all know that the coal liquefaction concept did not survive; so, no business resulted. Yes, it could develop at some undefined point in the future, but efficient use of R&D funds according to today's seemingly harsh commercial applicability standards would disqualify this effort—not only for industrial but also for government support.

An even more promising project was yet another DOE contract wherein large vertical pumps running in reverse were studied technically and economically for applicability to small hydropower installations (Cooper et al., 1981). The major pump division of the company furnished the hardware and did the demonstration testing in a facility that is illustrated in Fig. 6. Several orders resulted, and pumps were built, shipped, and installed in the field as fixed-geometry turbines. The power level of any one of these units did not exceed one megawatt and a flowrate of 10 cubic meters per second. Most of them were smaller. These were inexpensive compared to the classical variable-geometry machines that can accommodate a much larger range of flow rate. This business was driven by the Public Utility Regulatory Policies Act (1978) that provided tax relief for small electric generation projects and required utilities to buy the power. Later this law was changed, removing the tax incentive; and the construction of this kind of machinery reverted to the traditional hydroturbine companies. As exciting as this effort obviously became for some of us in the pump industry, we now have to admit that it gets low marks by today's standards. Yes, the company sold some of these machines, but the hoped-for core business never really developed.

Fortunately, though, there has been a small, steady stream of hydraulic power recovery turbine applications for hydrocracker and municipal water supply services. Research effort was expended here in order to optimize single and multistage pumps as pure turbines, thereby reducing the size and gaining several points of efficiency over what would be obtained if these were simply pumps running backwards as turbines (Nelik et al., 1984).

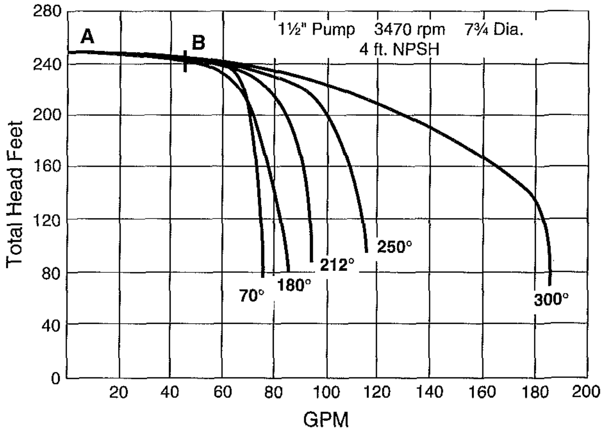

Fig. 2 Fluid vaporization effect on pump performance. Here are seen the head-versus-flowrate performance curves corresponding to different vapor volumes generated within the pump by local depressions below vapor pressure. The available NPSH is the same for all cases. With increasing water temperature, the critical point is approached, where the vapor has the same volume as the liquid, thereby producing liquid-only pump performance.

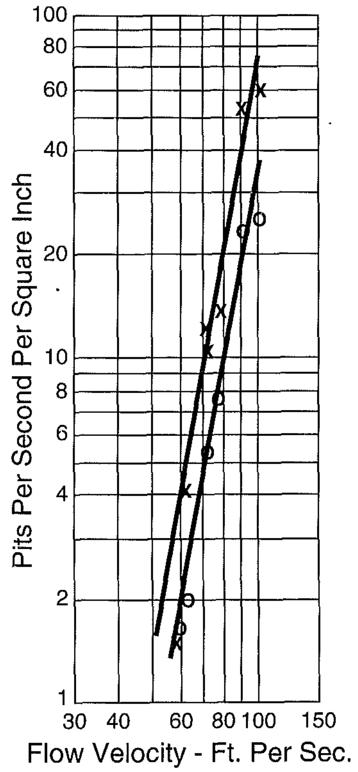

Fig. 3 Cavitation erosion in a venturi. The data show that the rate of material removal varies as the sixth power of velocity at a constant cavitation number. In a pump this would be the velocity relative to the impeller blade at the entrance. This velocity is often approximated by the impeller inlet tip speed.

Viewed objectively, the research center of this case study had its share of successes and failures so far as pumps were concerned. This is the kind of performance that is implied by the very word, "research." One should be expected to have a

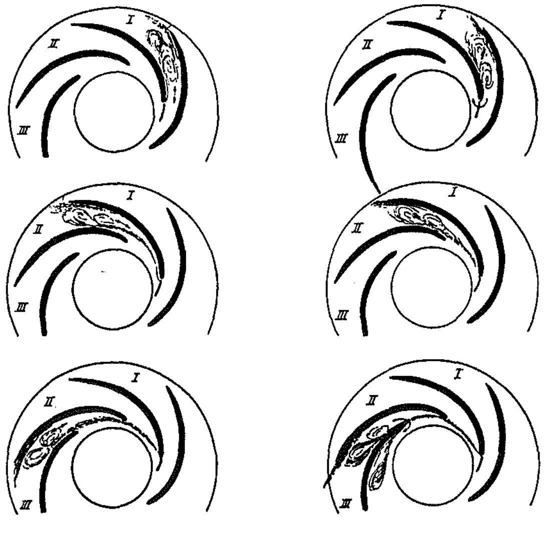

a) 20.6% of BEP

b) 2.5% of BEP

Fig. 4 Rotating stall in a pump impeller. For flowrates that are (*a*) 20.6 and (*b*) 2.5 percent of the best-efficiency flowrate. Sketched observations of injected dye patterns in Passages I, II, and III as time progresses. Note reversed flow around the leading edges for Case (*b*). Impeller rotation is clockwise.

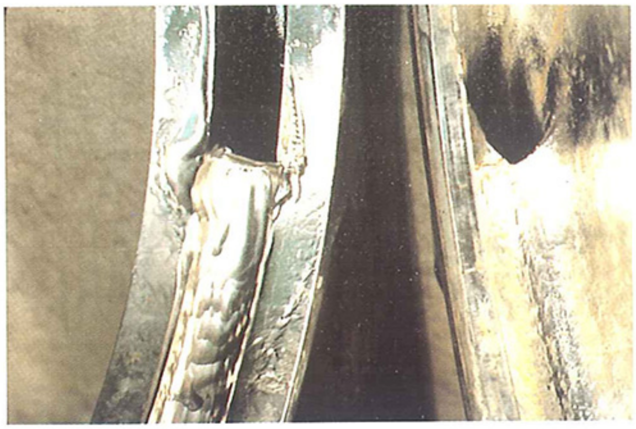

Fig. 5 Erosion of the cutwater (or tongue) region of a slurry pump. The sidewalls adjacent the straight cutwater show considerable wear associated with the horseshoe vortex system. This did not occur for the case of the curved cutwater.

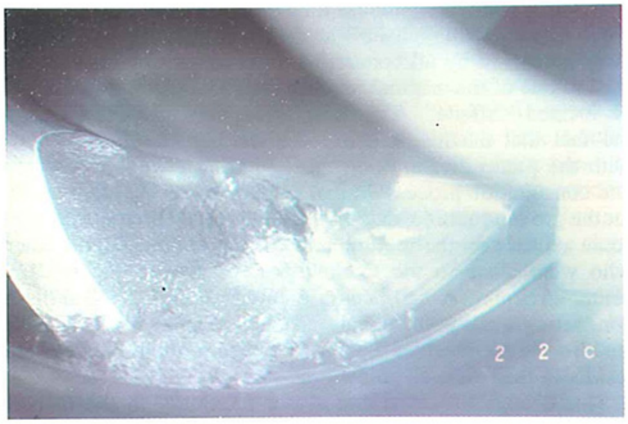

Fig. 7 Bubble cloud in a pump impeller. These bubbles and the larger associated cavity on the suction side of an experimental impeller blade were photographed with the aid of an Edgerton flash unit. The flowrate is about 75% of the design value, and the supplied NPSH is about twice the amount necessary to prevent significant loss of pump head generation due to two-phase activity within the pump. The blade is moving from right to left, and the leading edge of the next blade is at the upper right.

few dry holes, in oil exploration parlance. Nevertheless, after about twenty years of operation, a line of reasoning developed which was at least partly driven by increasing competitive pressure to reduce costs. R&D is sometimes an early casualty in such an atmosphere. Thus, much of the work done by this corporate research center—and presumably others of the same ilk—came to be regarded as costly, ineffective, and not always relevant to the technology needs of the company's business. When the inevitable cost squeeze developed, it was therefore not hard for the company to ''decentralize'' their R&D activities by closing the center.

Nevertheless, viewed in a gentler light, important research did get done—the results of which are still in use in the pump divisions or business units. Some argue that in a more favorable atmosphere—also accompanied by a longer term view on the part of corporate management, the closure might have been averted. However, the prevailing view is that these centers had to go, that effective R&D could not be conducted in them. We do not know what might have been. What actually happened instead was the transition to the third phase of the R&D activity in this case study, namely, the Focused, Applied R&D phase. This characterizes the era we are in today.

Focused, Applied R&D Phase. Yet not too long before the closure of the research center, work had commenced on what would later turn out to be an essential core technology for today's engineered pump business. This had to do with cavitation and pump life. A rig had been built for viewing cavitating flow. The cloud of bubbles appearing in Fig. 7 occurred on an experimental impeller in that rig. The photograph was made with the help of a one-microsecond-duration Edgerton Flash unit. This bubble cloud produced the erosion shown in Fig. 8, which shows a soft-aluminum impeller that ran in water at the same conditions for seven hours in the rig.

The general manager of the engineered pump division of the company had taken an interest in and had supported this as well as the other pump R&D projects at the center. Through his leadership and that of the outgoing director of research, the pump R&D effort of the center was salvaged. Upon closure, the general manager formed those who had been doing pump research into a new R&D group reporting to him and located at his manufacturing plant. All the equipment was transferred to a building in which he set aside about 10,000 square feet for this purpose. A new, larger version of what at the center had been called the Alexey J. Stepanoff Memorial Hydraulic Laboratory was laid out, and the equipment was transferred to this new location. Since that time, there have been additions and continuing upgrades of test loops, data acquisition computers, and other equipment, as projects conducted in these facilities have dictated. Indeed, the company had in this instance ''decentralized'' its research activities as stated.

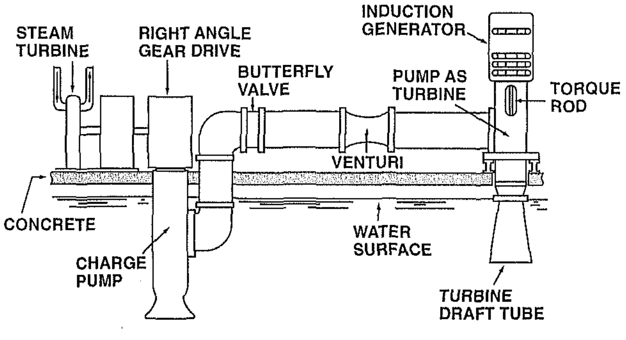

Fig. 6 Test loop for pumps operated in reverse as turbines. The test vehicle is the "pump as turbine" topped by an electric induction motor operated as a generator. A conical draft tube has been fitted to enhance the turbine performance of this unit. A steam-turbine-driven charge pump supplied the flow and head for the test vehicle.

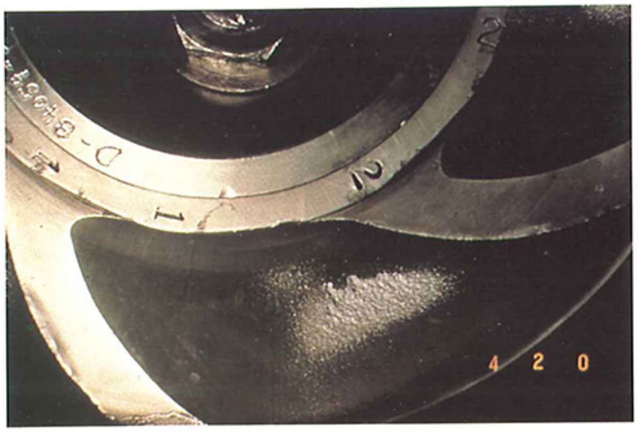

Fig. 8 Erosion caused by bubble cloud. The soft-aluminum impeller of Fig. 7 ran for seven hours at the conditions stated there. Impeller inlet tip speed was 27 m/s (89 ft/sec). Notice that the location of the erosion is that of the bubble cloud.

It was a relatively painless transition, and the location of the R&D organization "onsite" at the pump factory was immediately perceived by all concerned to be an advantage—in contrast to one of the original requirements that the research center be located "offsite." This new perception was due partly to the fact that the researchers were already closely associated with the pump division personnel via the technology transfer and consultation process. In that respect this R&D organization hit the ground running, having already focused their efforts with some success on the requirements of the engineers and others who were close to the marketplace. Moreover, the research center environment had been a training ground in the skills of conducting quality analytical and experimental work, and this enabled the members of the new organization to produce useful results in their new situation.

This change of venue and closer proximity to the marketplace—which also happened in other pump companies—helped to define a "new face of R&D." It was truly the beginning of a new era. The essential features of this new face soon emerged, beginning with a prioritization of the R&D effort that more directly addressed customer demands for better performance, reliability, and durability.

A sign of the times was an increasing emphasis on upgrades of existing products currently in the field, a trend that has continued, so that today's orders for new engineered pump equipment are hotly contested within the downsized community of manufacturers. Accordingly the R&D effort led the researchers more frequently into the field, where they could see, hear, and touch the pumps in operation. This in turn led to more informed analytical and experimental studies of design concepts that could be applied to both new and existing pumps.

Fitting appropriately into this environment were the cavitation studies that had begun at the research center. This, in fact, was a fundamental activity in what has become the raison d'être for modern pump R&D; namely, extending the life of high-energy pumps by reducing the vibrations, pressure fluctuations, and cavitation erosion that commonly occur in these machines. These were generally high-power multistage pumps used mainly in the utility industry. A new generation of boiler feed pumps, exemplified by that shown in Fig. 9, had appeared that ran faster and generated more head per stage. Shaft power levels had reached 50 MW (67,000 hp). To compound the challenge, power plants were beginning to cycle back on output at different points in the daily cycle. This implied a broader range of flow rate, flow coefficient, and angle of attack at the inlet to the already faster-running impellers. Because these machines were of traditional design and could not accommodate these new conditions, there appeared a rash of boiler feed pump failures—broken diffuser blades and impeller shrouds, bearing failures, and impellers severely eroded by cavitation. These were labeled loosely as "high-energy" phenomena that did not occur at lower pump power levels. A whole new retrofit market opened up that spawned new developments aimed at eliminating these problems.

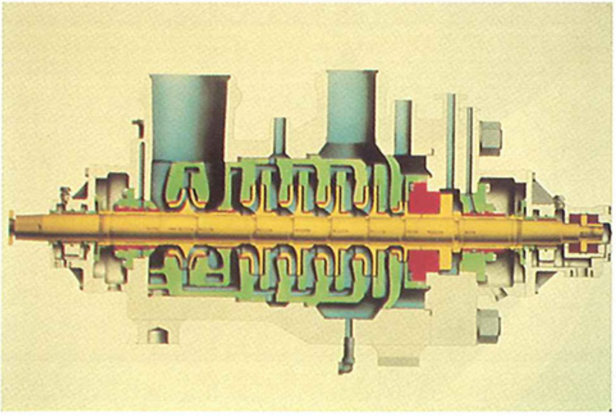

Fig. 9 High-energy boiler feed pump. Typical of the current generation of these machines, this 22 MW (29,500 hp) pump (encased in a barrel) supplies a 600 MW electric utility generating unit with 0.6 m^3/s (9,510 gpm) of 180C water at a pressure rise of 32 MPa (4,640 psi)

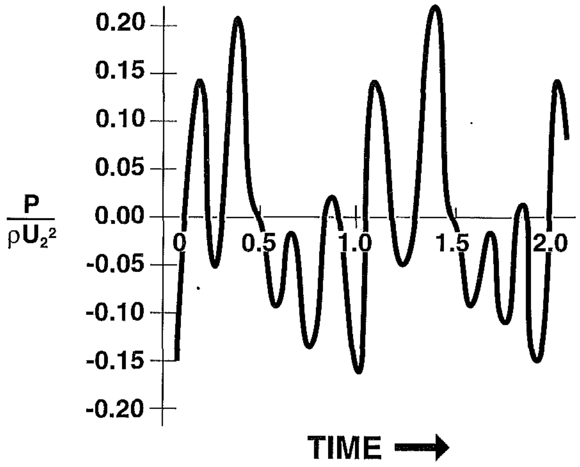

Fig. 10 Computed pressure fluctuations at the exit of a pump impeller. Iino (1981) produced this trace just within the impeller by unsteady potential flow analysis. The impeller was mounted in a vaned diffuser that was 3 percent larger in diameter than the impeller, and the flow rate was 70 percent of the design value. P is the static pressure above impeller inlet total pressure. One unit of time is how long it takes for a point on the impeller periphery to go from one diffuser vane to the next.

To put the problems in perspective and so define their limits, it became necessary to quantify what is meant by a "high-energy" pump (Cooper et al., 1988). Pressure fluctuations are a representative starting point, because they can give rise to damaging stresses. For example, Fig. 10 is a trace of the pressure at the exit of an impeller, as computed by Iino (1981) using potential flow methods. The amplitude of these fluctuations is on the order of the impeller pressure rise. A surrounding row of diffuser vanes cleared the blades of the neighboring impeller by three percent of the radius, and the flow rate was 70 percent of the best-efficiency value. Had the flow rate been 100 percent—and had the clearance been greater—the pressure fluctuations would have been lower. In fact, larger clearances are used in high-energy pumps for this reason. For a pressure difference δp—equal to the amplitude of these fluctuations—applied to the leading edge of the diffuser vane (having thickness t) as shown in Fig. 11, the stress s at the juncture of the vane with each

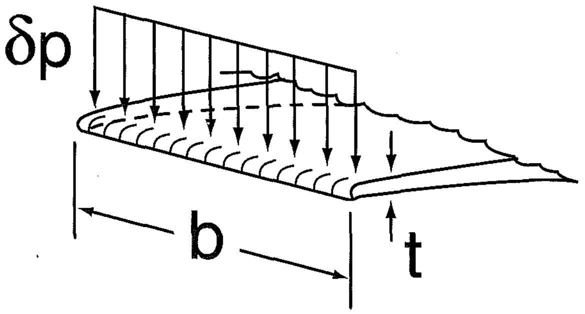

Fig. 11 Defining pump "energy level" in terms of stress on components. A typical highly stressed element in "high-energy" pumps is the diffuser, especially at the leading edges, where a strong fluid/structure interaction occurs. Stage pressure rise, depending on the velocity field as do pressure fluctuations, is therefore proportional to the pressure fluctuation amplitude δp.

sidewall is proportional to the square of the vane width or span b:

$$s = [(\delta p/2)(b/D)^2]/(t/D)^2 \qquad (1)$$

where D is the impeller diameter. The span, in turn, increases with the specific speed (Ω_s or N_s) of the pump stage; viz.,

$$b/D = \Omega_s^2\Psi^{3/2}/(4\pi\phi) \qquad (2)$$

where

$$\Omega_s = \Omega Q^{1/2}/(gH)^{3/4}\ (=N_s/2733) \qquad (3)$$

using consistent units, and

$$N_s = \mathrm{N(rpm)}[Q(\mathrm{USgpm})]^{1/2}/[H(\mathrm{ft\text{-}lbf/lbm})]^{3/4} \qquad (4)$$

with Ω as the rotative angular velocity, Q as the pump flowrate, and H as the generated head.

The relationship obtained by combining Eqs. (1) and (2) becomes

$$s = \delta p\Omega_s^2/[165\ (t/D)^2] \qquad (5)$$

and is found from the following curve fits to optimum head and flow coefficients (Ψ and ϕ, respectively):

$$\Psi = gH/U_2^2 \approx 0.383/\Omega_s^{1/3} \qquad (6)$$

$$\phi = (V_m/U)_2 \approx 0.1715\Omega_s^{1/2} \qquad (7)$$

where the subscript 2 denotes the exit of the impeller; V_m is the meridional component of the velocity; and U is the impeller blade speed. These particular fits were made to design data given in Stepanoff's book (1957). Now, since the pressure fluctuations δp for a given geometry are proportional to the stage pressure rise ($\Delta P_{\mathrm{stage}}$), the resulting stress can be expressed in terms of this rise:

$$\delta p \alpha \Delta P_{stage} = Ks(t/D)^2/\Omega_s^2 \qquad (8)$$

the constant K being found from experience. So, to limit the stress, one must limit the stage pressure rise—this limit decreasing with increasing specific speed.

Data on some representative high-energy pumps are given in Table 1. By the stage pressure-rise criterion, liquid rocket engine pumps have the highest energy level—and we all know they've had their share of operational difficulties. Fortunately, the life of these machines is a few hours at best. High-energy utility boiler feedwater pumps, on the other hand, must last for years; so, they have lower pressure-rise limits. Another way to characterize the energy level of a pump stage would be in terms of the torque per unit volume, which also is connected to and has the same dimensions as stress. This is indicated by the values of torque-over-impeller-radius-cubed given in the last column.

Figure 12 is a plot containing most of the pumps just given in Table 1. The curve results from an experience-based choice of the constant in the equation for limiting stage pressure rise, which varies inversely as the square of the specific speed as just developed. Pumps that fall below this curve have a sufficiently low energy level so that stresses arising from pressure fluctuations, cavitation bubble collapse, etc., are of no concern to the user. It would be interesting to know how well the Russian RD-170 pumps have fared, for they are off the top of the chart (Sutton, 1992).

The definition of high-energy pumps would not be complete without including cavitation, the phenomenon that was by this time commanding most of the attention in my own company's R&D program. The cavitation erosion rate has been empirically correlated by Guelich (1989) with an observable cavity length L_{cav} along the impeller blade. For the suction side of the blade, this can be expressed as follows:

$$dE/dt = F_{mat}C_lL_{cav}^{2.38}(\tau_A - \phi_e^2)U_e^6\rho_L^3A/(TS)^2 \qquad (9)$$

where

F_{mat} = constant of the material—typically 12-percent-chrome stainless steel
E = the erosion depth
C_l = constant peculiar to the side of the blade (greater for the pressure side)
τ_A = (available NPSH)/$(U_e^2/2g)$
ϕ_e = impeller inlet-eye flow coefficient, $(Q/A_e)/U_e$, where Q = volume flowrate, and A_e = impeller eye area normal to the axial component of velocity
NPSH = total pressure head in excess of the vapor pressure at the pump inlet
U_e = the impeller inlet tip speed
ρ_L = liquid density
A = constant of the liquid, related to vaporization; cf. Stahl et al. (1955)
TS = tensile strength of the impeller material

Laboratory observations of the cavity length L_{cav} versus NPSH together with impeller geometry-performance relationships, have led from Eq. (9) to another expression for the limiting stage pressure rise—this time in terms of admissible cavitation erosion (Sloteman et al., 1991):

$$\Delta P_{stg}/X = C_2/\{D_2^{0.61}N_s^{1.805}\mathrm{Life}^{1/3}(\tau_A - 0.04) \times [1 - (\tau_A - 0.15)^{1/3}]^{0.94333}\} \qquad (10)$$

where

C_2 = a constant containing C_l and others involved in deriving the above equation

Table 1 Data on high-energy pumps

Pump	No. of stages	Speed rpm	Flow USgpm	Head/stg ft-lbf/lbm	ΔP/stg. psi	Specific speed, N_s	Torque/r^3 psi
Rocket engine pumps							
F1 Oxygen	1	5,488	25,184	3,097	1,574	2,100	371
F1 RP1	1	5,488	15,234	5,167	1,812	1,112	160
SSME HP oxygen	1	31,000	7,265	9,639	4,795	2,715	1,283
SSME HP hydrogen	3	37,400	16,466	64,600	2,264	1,183	209
RD-170 oxygen	1	13,850	25,008	17,300	8,534	1,448	1,521
RD-170 RP1	1	13,850	14,485	20,000	7,100	992	698
Boiler feed pumps							
20 × 25 CA-4 (IDP)	4	4,160	21,620	3,000	1,169	1,509	128
12 × 18 CA-4 (IDP)	4	5,800	11,000	3,000	1,169	1,500	130
80CHTA-6 (IDP)	6	5,800	6,250	2,100	820	1,479	87
Advanced Class (Sulzer)	2	6,500	9,510	3,800	1,480	1,312	136

Notes to this table: RD-170 pump data derived from Sutton (1992); Advanced Class boiler feed pump data from Weldon (1970). Remaining data derived by Cooper (1992) from NASA (1975 and 1973) and internal company documents.

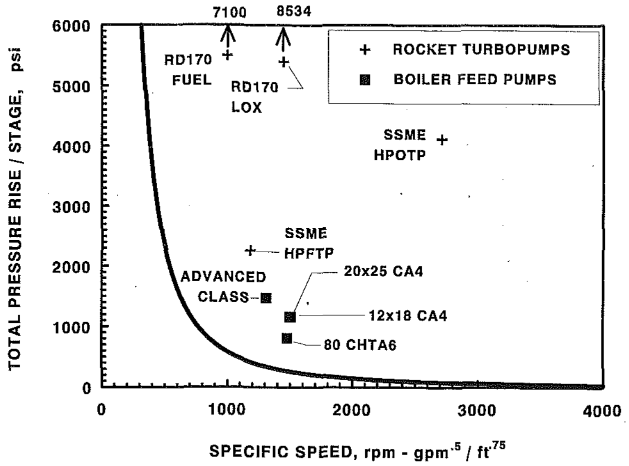

Fig. 12 High-energy pumps. Boiler feed pumps and rocket propellant turbopumps are compared in terms of the stage pressure-rise criterion formulated from Fig. 11. Compare this with the other stress quantity, namely torque/(impeller-outer-radius)^3 (last column in Table 1).

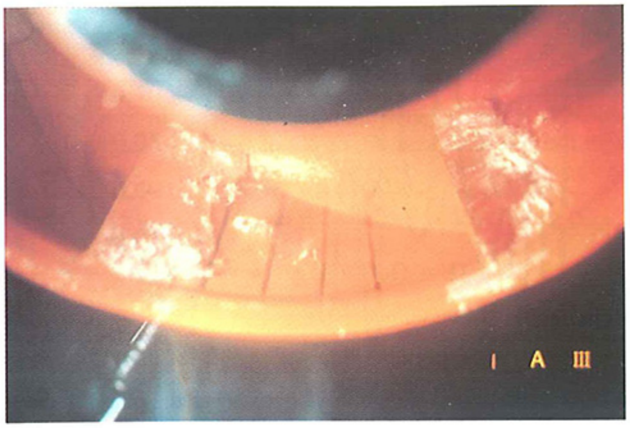

Fig. 14 Cavities in reference impeller (of conventional design). Half-scale model for cavitation minimization program for 18 MW (24,000 hp) crude oil pipeline pump. Stage specific speed Ω_s is 0.73 (= 2000 N_s in customary US units). τ_A = 0.54, which is nearly twice the value needed to maintain 97 percent of the noncavitating pressure rise-at full flowrate.

X = 1 for typical boiler feed pump impeller dimensions and blade angles

Life = the time for the erosion depth E to reach 75 percent of blade thickness

The important effect on the erosion rate dE/dt—true to Professor Knapp's discovery—is that it varies as the sixth power of the velocity, expressed here as the blade inlet tip speed U_e. And here again, for typical pumps at a constant cavitation number τ, a limiting stage pressure rise emerges, above which pump life is unsatisfactory.

Figure 13 is plot of Eq. (10). The curves reveal a trend for the stage pressure rise that is similar to that of the stress-related curve of Fig. 12. Pumps "A" and "B" noted above the curves are boiler feed pumps that were subjects of retrofit efforts. The challenge was to provide innovative blade shapes that would reduce the cavity length to zero. The first step in this process was to make a blade shape change that would raise the computed local minimum pressure (Sloteman et al., 1991). Then the resulting shape was optimized with the help of visual inspection of the cavitating flow in the inlet region of the impeller.

Soon, not only was this process being applied to retrofits but also to new pumps, where the energy level in the foregoing terms was significant and customer demands for long life in the face of the attendant cavitation were involved. The next four figures are a chronicle of how this was done on each of the two parallel entry stages on a 18 MW (24,000 hp) pipeline pump (Cooper et al., 1991). Two half-scale versions of the impeller were designed, built, and tested; the first "reference impeller" being of a conventional design, which, at the available NPSH supplied by the user, produced the cavities on the suction sides of the blades seen in Fig. 14. The second, improved, and final "model impeller" produced no cavities—as can be seen in the photograph of Fig. 15. Further, as Brennen (1994) has shown, cavitation is accompanied by pressure pulsations. And, for the reference impeller just presented, Fig. 16 is a plot of the amplitude and frequency of these pulsations measured in a test. For the improved design of the final model, except for inlet pressures or NPSH's below the available value, these pulsations disappeared, (Fig. 17).

As implied above, this technique has been successfully applied to several existing and new pumps. In fact, the acceptance of high-energy pump impellers sometimes requires the manufacturer to demonstrate the absence of cavities in a so-called "flow visualization" test, of which Figs. 14 and 15 are photographs. And high-energy pumps have other challenges—such as reducing the minimum flow rate—expressed as a fraction of the best-efficiency flow rate at which the pump can operate vibration free (Sloteman et al., 1995).

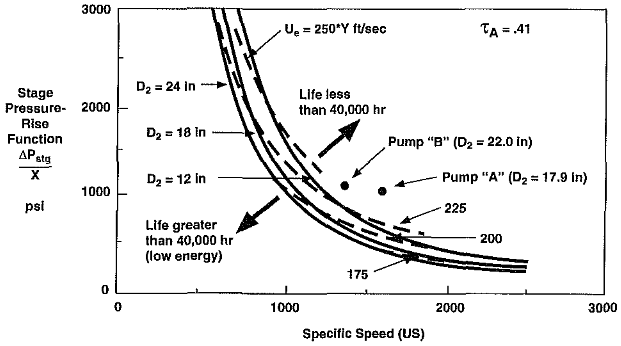

Fig. 13 Limiting stage pressure rise for resistance to cavitation erosion. Plots of Equation 10 for a life of 40,000 hours or about five years for conventional impeller designs. Pumps "A" and "B" are boiler feed pumps [25 and 50 MW (33,500, and 67,000 hp) shaft power, respectively] that originally had less than 40,000 hours' life and were retrofitted with advanced-design impellers producing fewer cavities and consequently much longer life. X and Y, both typically = 1, are defined in Sloteman et al. (1991).

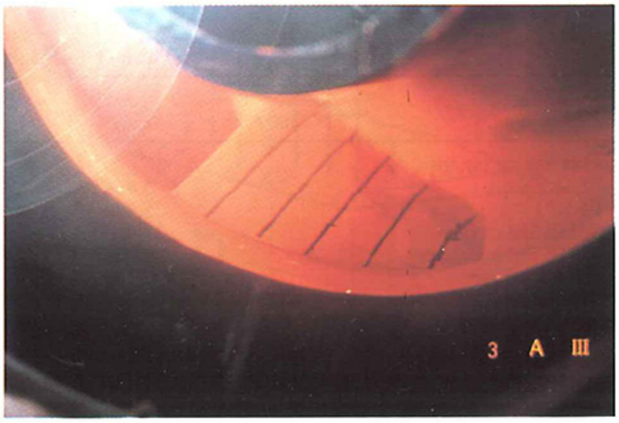

Fig. 15 Cavity-free final-design model impeller for the 18 MW pipeline pump

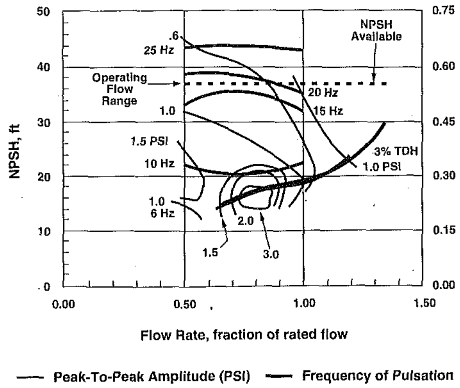

Fig. 16 Suction pressure pulsations for the reference impeller. (18 MW pipeline pump) Contours of constant amplitude and frequency cover a greater range of flow rate and NPSH than specified for actual operation by the user. The lower curve, labeled "3 percent TDH" is the locus of NPSH required to maintain the loss of pressure rise due to two-phase flow at 3 percent. This half-scale 2000-Ns impeller was tested at 1800 rpm.

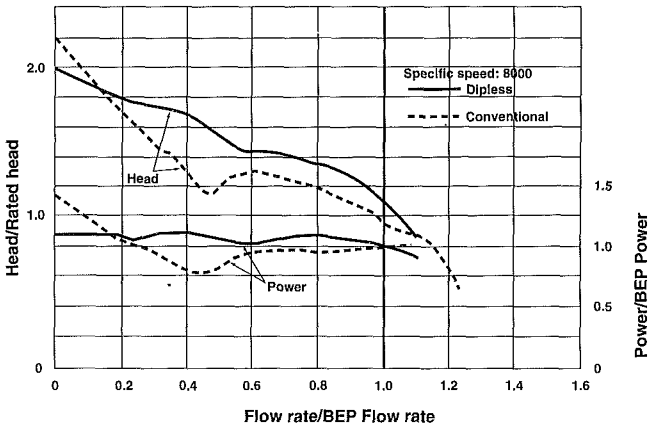

Fig. 18 Improving the performance curves of mixed-flow pumps. Fluid dynamical reasoning about the behavior of stalled flows led to changes that eliminated the "dip" commonly seen in high-flow-coefficient, high specific speed (3 or 8000-N_s) pumps. The power at zero flow allows for a smaller drive motor.

There are, of course, other challenges for today's focused, applied pump R&D engineers. One of these is the long-standing concern of pump users as to whether a high-specific-speed, mixed-flow pump can start up or run in parallel with other pumps without getting stuck in a low-pressure-rise stall zone near the minimum flow rate. These are large machines, which circulate cooling water through electric utility power plant condensers, each handling up to 25 m^3/s (400,000 USgpm). Eliminating the attendant "dip" in the conventional head-vs-flow performance curve for these pumps (Fig. 18) has historically eluded hydraulic designers, unless they chose to design larger, slower pumps. Yet, if it could be done; the small, fast, less costly pumps with a high flow coefficient could be offered without the dip. But, several tries would very likely be required if indeed the project could succeed at all. Therefore, R&D economics dictated a small model of the large pump. One was built to accommodate various impeller and diffuser designs and was run in a dedicated test loop. Shapes of these hydraulic elements were finally found that indeed removed the "dip"—also shown in Fig. 18. This was accomplished by introducing design schemes aimed at reducing the range of flow rate that is accompanied by stall and at maximizing the pressure rise produced within the actual stall zone. For example, a pump running against a closed valve is stalled; yet it produces a pressure rise that arises from solid-body rotation of the stalled fluid, as well as other factors that prevail in such a situation. As this is presently an inexact science, what could be called astute fluid dynamical reasoning was applied to get an improvement after each model test. A dividend from this effort was a reduction in the power consumed by the pump at zero flowrate (closed valve). The results had immediate commercial application.

A promising way to quantify the effects of the design improvements made in removing the dip would be to compute the flow field of each configuration with a CFD code (Graf, 1993). This was done for an impeller similar to the original one as shown in Fig. 19; the objective being to reproduce the dip analytically. This meant following up the flow field solution with an appropriate averaging procedure to obtain the resulting performance curve. This is the acid test for the applicability of CFD to the everyday challenges of R&D in the pump industry. These are steady-flow results—obtained on a workstation using a commercial code. Two separate solutions, one for the impeller and the other for the diffuser, were combined by matching circumferentially averaged boundary conditions in the space between these two elements. While the dip was computed, it was not close enough to the test results to be trusted in the foregoing development work (Fig. 20). Having said this, it is recognized that better computed results are possible; therefore, improved CFD solution techniques are being pursued in an

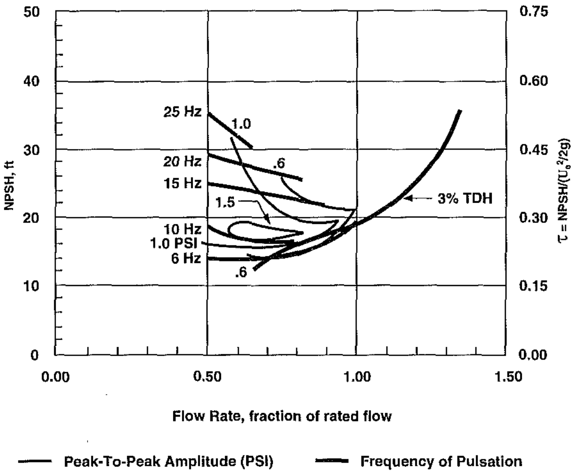

Fig. 17 Suction pressure pulsations in final-design model impeller (18 MW pump). No significant pressure pulsation activity is evident at the operating τ_A-value of 0.54. (Same size and speed as the impeller of Fig. 16.)

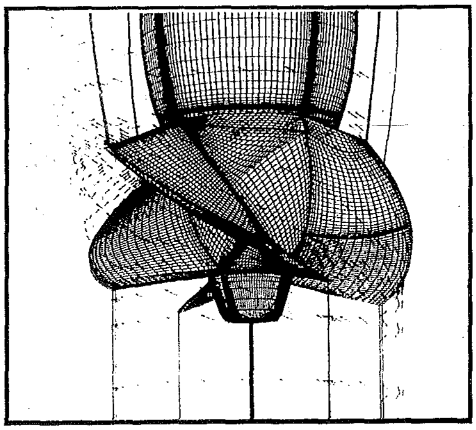

Fig. 19 CFD Solution of circulating-pump, mixed-flow-impeller flow field. The code used was TASCFLOW3D, which has been evaluated for pumps by Graf (1993).

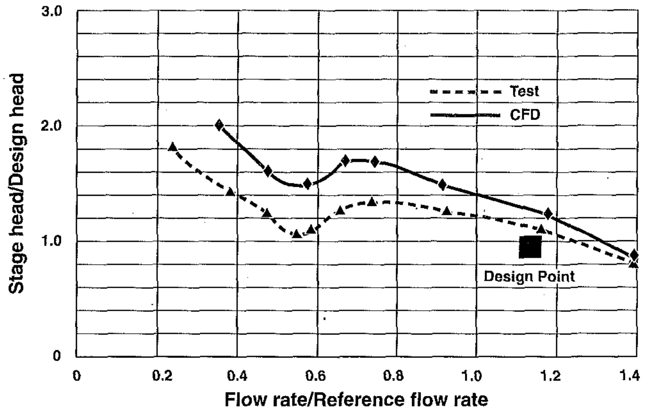

Fig. 20 Comparison of CFD-computed performance curve with test results. The TASCFLOW3D CFD calculation for the stage was obtained by combining two separate solutions—one each for the impeller and the diffuser.

R&D project as an enhancement of the hydraulic core competency of the company. Figure 21 is an example the reversed-flow patterns in stalled impellers have been computed via CFD, apparently for the first time (Graf, 1993; Cooper et al., 1994). And computing the distorted flow delivered by the typical radial-inflow inlet passage (Fig. 22) to a boiler feed pump first-stage impeller has provided insight into the fluid/structure interactions caused in high-energy pumps by such passageways.

CFD is being integrated into the fluid dynamic design process. The aim is to automate the use to such an extent that it can be included in the company's computerized knowledge-based system for the hydraulic design of the passages of impellers and the other flow elements. Blocked out in Fig. 23, this is essentially an expert system with which the geometry is created and optimized via interaction with an experienced pump hydraulic designer. Output is the finished design in the form of drawings and files of manufacturing information, including flow analysis and overall performance prediction, which are also embedded in the process. Developing, supporting, and enhancing this software is another R&D project.

Often, these R&D programs have been motivated by and conducted in conjunction with or in support of customer orders. Increased competition has created performance challenges that often require the expertise of the researchers to satisfy the demands of such orders. Consequently this ''high-technology support'' has taken its place alongside new product development and core-competency enhancement as a major activity of the R&D group.

The exigencies of this support work have led to new R&D programs and appropriate redirection for existing ones. The tools developed in the research center days became the forerunners of today's expanded, user-friendly systems which utilize the latest computer and laboratory measurements technology. When transferred to the product engineers around the company, the resulting technology has found more application. In this regard, concentration in the order-support rolé by some of the researchers has led to their transfer out of R&D and into product engineering groups, another method of transferring the technology and core competency so as to enhance the resulting product.

Commercial R&D

This, together with what might be regarded as standard new product development activity, would lead one to the conclusion that nothing unfavorable has happened to R&D in this case history. A small, focused group continues as in the earlier era. Ostensibly, only the venue has changed. But there is another subtle change that has undoubtedly contributed to the continuance of this pump R&D activity, in comparison to the reductions that have happened elsewhere. The R&D engineers—now a more multidisciplined group—have been taught to think both technically and commercially. New product development is done only when the whole product line has been laid out ahead of time and the production cost has been determined in consultation with the product and manufacturing engineering and the marketing people who must deal with the product on a day-to-day basis. And even then, every R&D activity is strategically evaluated by those carrying out the work.

This is necessitating a change in the character of the formal graduate engineering training required to perform industrial R&D. Rather than focus a large portion of one's effort in pursuit of an advanced degree on a particular problem, two of our people have taken courses in the management of technology and how to ''take technology to market,'' (Ford et al., 1981). The courses provide a broad knowledge of current and emerging technologies, including the business approach to exploiting them. Being able to innovate and sell what one has created are the hallmarks of the graduate. This would appear to augur *against* doing so much research and *more* for applying what exists. Rather than argue the merits of this approach, it has become necessary to face the fact that this is the essence of today's industrial R&D environment. Yet, one cannot escape the fact that an intellectual brain trust that has an in-depth command of the technology is essential to the success of a company that builds engineered products such as pumps. These people must look ahead and develop product concepts that will be needed several years hence.

- For example, it is reasonable to assume that complicated hydraulic systems for the bearings of multistage pumps—with the attendant hoses, reservoirs, filters, fittings and piping, etc.—will eventually disappear; being replaced by, say, magnetic bearings. Figure 24 shows a multistage

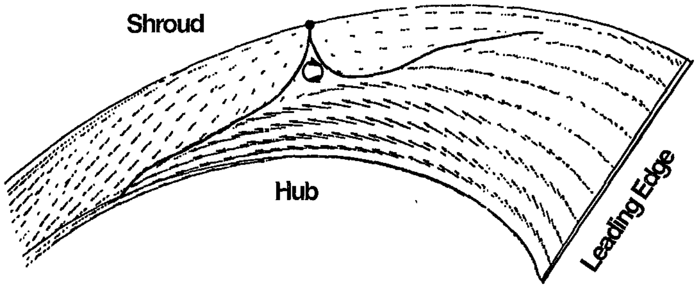

Fig. 21 Computation of the recirculating flow within a centrifugal impeller. This was computed for a flowrate slightly below 60 percent of the rated value (where stall usually exists) by TASCFLOW3D, (Graf, 1993). At still lower flowrates, the reversed flow region extends to the leading edge, with some of the fluid traveling upstream.

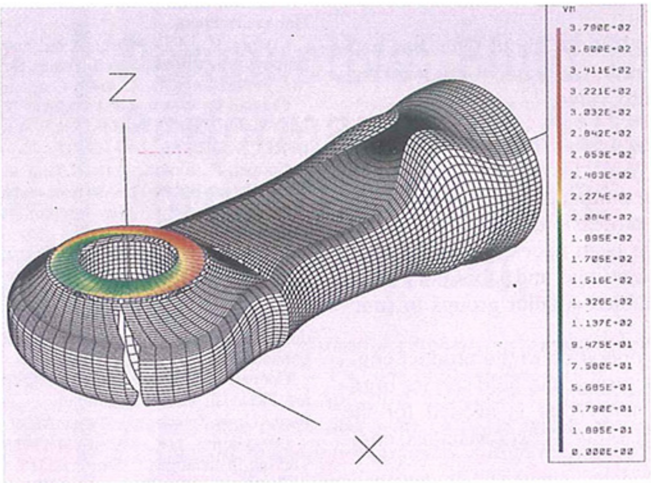

Fig. 22 Flow at the exit of a radial inlet passageway. Here, TASCFLOW3D simulated the distorted flow produced at the annular exit of this typical, "side-inlet" passage at the entrance to the first stage impeller of a boiler feed pump. The meridional velocity component is represented by color, the bottom of the color bar corresponding to zero. The maximum (red) is 1.75 times the average (yellow). Reduction of this distortion would also reduce the vibration arising from the consequent fluid/structure interaction.

pump fitted with such bearings. This concept is just beginning to be applied (Cooper et al., 1992). Lack of volume keeps the cost high; so, this approach is not yet widespread. Perhaps we have here a chicken-and-egg situation. If the vision is correct, the concept needs to be sold to enough users so that it will become cost effective. In today's cost-conscious atmosphere, this is an example of the selling that R&D persons now need to do to their own management, funding agencies and prospective users—if innovations are to come to fruition.

- Another example is the environmental attractiveness of pumps without seals, either those with magnetic couplings or close-coupled canned-motor pumps.
- And with the development of lower cost electronic components, variable speed could finally become an accomplished fact. It has been understood for a long time that power savings and greater pump life would accompany such a development. Computer technology would enable the users to control their processes through pump speed adjustment instead of by throttling valves.

The innovation process is also being aided by universities and entrepreneurial consulting firms who are associating some of their activities with the pump industry. Probably the best example among the universities is Texas A&M, who will sponsor the 14th consecutive annual pump users symposium in March, 1997. Income from this event is used to support their pump-related research activity. Another example is Caltech, with a long history of quality research focused on pumps. Industrial consortia involving pumps and other turbomachinery are in place at the University of Virginia, and Virginia Tech—as well as some consulting firms who have specialized in the various fluid and rotor dynamical aspects of these machines. In some respects, this is a throwback to the "professional engineering" era. In those days, we remember that the university researchers worked mostly in areas of immediate commercial significance. And in other respects, we see elements of the research center era in that the these universities have become multidisciplined centers for pump research, hopefully filling the gap left by the closures. In terms of training effective R&D engineers, this would appear to be an essential trend that must supplement the new commercial awareness if industrial companies are to be world technological leaders.

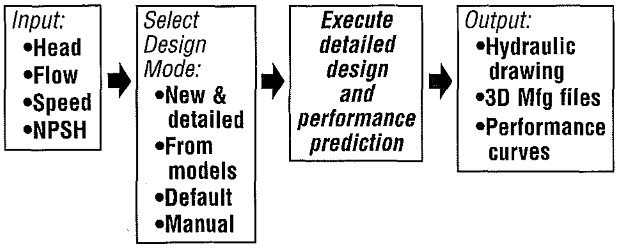

Fig. 23 Block diagram of hydraulic knowledge-based system for pumps. One- and two-dimensional performance prediction is combined with passage shape generators in a PC Windows Environment. CFD should eventually replace the present performance prediction schemes.

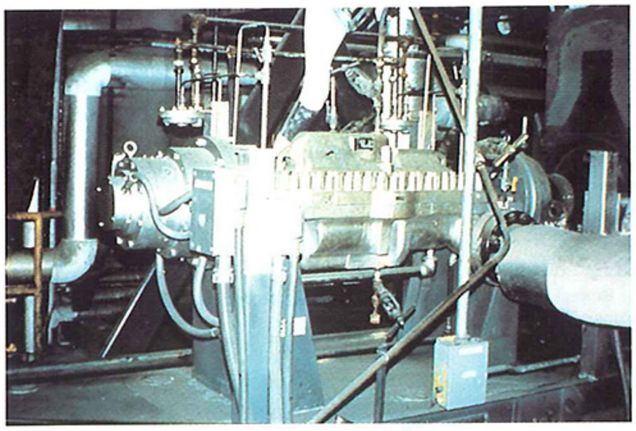

Fig. 24 Multistage pump fitted with magnetic bearings. This is an 8-stage, 450 kW (600 hp) pump in boiler feed service since 1990 that utilizes these new, noncontacting bearings. The shaft is kept positioned within 0.05 mm (0.002 in) via sensors and feedback circuitry that individually controls a multiplicity of electromagnetic coils positioned around the shaft (for radial loads) and adjacent to the thrust disc or runner (for axial loads) (Cooper et al., 1992).

Conclusions

In conclusion, answers to our questions about what has happened to research and development in mechanical-engineering-intensive industries have come into view:

- Upgraded R&D results of the past are being commercially applied, and the research "bin" is still being added to, with a clear view regarding potential application;
- The larger, critical mass of professionals that the research centers supported may have been necessary at the time, but developments in computational and laboratory hardware and software have enabled smaller groups to function effectively;
- The proximity of the R&D operation to the product engineering, marketing, manufacturing, and field service organizations has created a synergy that is needed for the survival of essential R&D in today's cost conscious, competitive environment.

Effective R&D can be carried out in today's environment, provided that

1. As in the past, essential research is conducted that will maintain and enhance the core technological competencies needed for our companies to stay in business;
2. Expert and knowledge-based systems are employed that utilize state-of-the-art computational hardware and continuously updated software, data acquisition equipment, together with capital improvements to laboratory facilities;
3. The work is continually reported upon and sold to customers and top management;
4. R&D personnel are knowledgeable about the commercial and competitive implications of their work, staying aware of them and regularly formulating the strategies needed for their technical developments to be exploited in the marketplace;
5. R&D expertise is applied to the support of the company's contractual obligations on technically challenging customer orders; and by this means, essential research is honed and redirected;
6. Innovations and new concepts with future commercial potential are part of the R&D effort; and
7. Corporate leadership maintains and promotes R&D that will strategically benefit the company.

Finally, all this seems to say that the R&D engineer must take on the leadership and business-oriented, field-seasoned approach of the "old timers" by

- learning all the technology, on the job, that is needed;
- applying this technology to solve problems;
- enhancing the standing and commercial accomplishment of the company; and, in the aggregate, enhancing the technical leadership and commercial leadership of our country relative to the rest of the world.

References

Blom, C., 1950, "Development of the Hydraulic Design for the Grand Coulee Pumps," *Trans. ASME,* Jan., pp. 53–70.

Bolleter, U., 1988, "Blade Passage Tones of Centrifugal Pumps," *Vibrations,* Vol. 4, No. 3, pp. 8–13.

Brennen, C. E., 1994, *Hydrodynamics of Pumps,* Concepts ETI and Oxford University Press.

Cooper, P., McCormick, W. M., and Worthen, R., 1981, "Feasibility of Using Large Vertical Pumps as Turbines for Small Scale Hydropower," *Waterpower '81, Proceedings,* U. S. Army Corps of Engineers, pp. 1584–1599.

Cooper, P., Wotring, T. L., Makay, E., and Corsi, L., 1988, "Minimum Continuous Stable Flow in Feed Pumps," *Symposium Proceedings: Power Plant Pumps,* EPRI CS-5857, pp. 2-97–2-132.

Cooper, P., Sloteman, D. P., Graf, E., and Vlaming, D. J., 1991, "Elimination of Cavitation-Related Instabilities and Damage in High-Energy Pump Impellers," *Proceedings of the Eighth International Pump Users Symposium,* Texas A&M University, pp. 3–19.

Cooper, P., and Jones, G., 1992, "Operating Experience, Including Transient Response, of a Magnetic-Bearing-Equipped Boiler Feed Pump," *Proceedings of MAG'92,* University of Virginia, pp. 19–28.

Cooper, P., 1992, "Living with Cavitation in Pumping Machinery," after-dinner presentation, Third International Conference on Cavitation, ImechE, unpublished.

Cooper, P., 1994, "Computational Fluid Dynamical Analysis of Complex Internal Flows in Centrifugal Pumps," *Proceedings of the Eleventh International Pump Users Symposium,* Texas A&M University, pp. 83–94.

Den Hartog, J. P., 1929, "Mechanical Vibrations in Penstocks of Hydraulic Turbine Installations," *Trans. ASME,* HYD-51-13.

Fischer, K., and Thoma, D., 1932, "Investigation of the Flow Conditions in a Centrifugal Pump," *Trans. ASME,* Vol. 54, pp. 143–155.

Ford, D., and Ryan, C., 1981, "Taking technology to market," *Harvard Business Review,* Mar./Apr. 1981, pp. 117–126.

Graf, E., 1993, "Analysis of Centrifugal Impeller BEP and Recirculating Flows: Comparison of Quasi-3D and Navier-Stokes Solutions," *Pumping Machinery—1993,* ASME, pp. 235–245.

Guelich, J. F., 1989, *Guidelines for Prevention of Cavitation in Centrifugal Feedpumps,* EPRI CS-6398. p. 2–14.

Iino, T., 1981, "Potential Interaction Between a Centrifugal Impeller and a Vaned Diffuser," *Fluid/Structure Interactions in Turbomachinery,* Wm. Thompson, ed., ASME, pp. 63–69.

Ippen, A. T., 1946, "The Influence of Viscosity on Centrifugal Pump Performance," *Trans. ASME,* Vol. 68, p. 823 et seq.

Karassik, I. J., Krutzsch, W. C., Fraser, W. H., and Messina, J. P., 1986, *Pump Handbook,* Second Edition, McGraw-Hill, pp. 2.194–2.265.

Kasztejna, P. J., and Cooper, P., 1986, "Hydraulic Development of Centrifugal Slurry Pumps for Coal Slurry Service," *Proceedings: Eighth International Symposium on Coal Slurry Fuels Preparation and Utilization,* U. S. Dept. of Energy, Pittsburgh Energy Technology Center, pp. 646–665.

Knapp, R. T., 1955, "Recent Investigations of the Mechanics of Cavitation and Cavitation Damage," *Trans. ASME,* October 1955, pp. 1045–1054.

Makay, E., Cooper, P., Sloteman, D., and Gibson, R., 1993, "Investigation of Pressure Pulsations Arising from Impeller/Diffuser Interaction in a Large Centrifugal Pump," *Proceedings: Rotating Machinery Conference and Exposition,* ASME, Vol. 1.

NASA, 1973, "Liquid Rocket Engine Centrifugal Flow Turbopumps," NASA SP-8109 of the series entitled NASA Space Vehicle Design Criteria (Chemical Propulsion.)

NASA, 1975, "Turbopump Systems for Liquid Rocket Engines," NASA SP-8107 of the series entitled NASA Space Vehicle Design Criteria (Chemical Propulsion.)

Nelik, L., and Cooper, P., 1984, "Performance of Multi-Stage Radial-Inflow Hydraulic Power Recovery Turbines," ASME Paper No. 84-WA/FM-4.

Pfleiderer, C., 1961, *Die Kreiselpumpen,* 5te Auflage, Springer Verlag.

Public Utility Regulatory Policies Act, 1978, PL 95-617, November 1978.

Sloteman, D. P., Cooper, P., and Graf, E., 1991, "Design of High-Energy Pump Impellers to Avoid Cavitation Instabilities and Damage," EPRI Power Plant Pumps Symposium.

Sloteman, D. P., Wotring, T. L., March, P., McBee, D., and Moody, L., 1995, "Experimental Evaluation of High Energy Pump Improvements Including Effects of Upstream Piping," *Proceedings of the Twelfth International Pump Users Symposium,* Texas A&M University, pp. 97–110.

Stahl, H. A., and Stepanoff, A. J., 1956, "Thermodynamic Aspects of Cavitation in Centrifugal Pumps," *Trans. ASME,* Vol. 78, pp. 1691–1693.

Stepanoff, A. J., 1957, *Centrifugal and Axial Flow Pumps,* 2nd Edition, Wiley.

Sutton, G. P., 1992, *Rocket Propulsion Elements, Sixth Edition,* Wiley. pp. 203, 215, 233–234, 328.

White, R. M., 1995, "Reshaping an R&D Jewel," *Technology Review,* Nov./Dec., p. 64.

Weldon, R., 1970, "Boiler Feed Pump Design for Maximum Availability," *Advanced Class Boiler Feed Pumps, I. Mech. E. Proceedings,* Vol. 184, Part 3N, pp. 18–35.

Wislicenus, G. F., 1965, *Fluid Mechanics of Turbomachinery,* in two volumes, Dover.

T. W. von Backström
Adjunct Senior Scientist, Aerospace
Engineering; Presently, Head of the
Department of Mechanical Engineering,
University of Stellenbosch, South Africa

B. Lakshminarayana
Evan Pugh Professor of Aerospace
Engineering and Director.

Center for Gas Turbine and Power,
Pennsylvania State University,
University Park, PA 16802

Perspective: Fluid Dynamics and Performance of Automotive Torque Converters: An Assessment

Experimental investigations by various groups over the past decade have uncovered the main features of the flow in hydraulic torque converters. Measurement techniques include laser and hot wire velocimetry, fast response and conventional five-hole probes, and blade and wall static pressure measurement. In both the pump and turbine, the through flow velocity is high near the pressure surface shell corner while the flow in the suction surface core corner is highly turbulent and may be separated and reversed. The position of the stator in a passage curved in the meridional plane leads to secondary flow and low velocities at the core near the pump inlet. Velocity gradients coupled with flow turning and rotor rotation lead to strong secondary flows. By using data from a combination of measurement techniques, torque converter torque, power and efficiency are calculated, and the effect of element efficiency on overall efficiency is demonstrated. It is concluded that design methods should be developed that allow for nonuniform velocity profiles, flow separation, secondary circulation and interaction effects between elements.

Introduction

The automotive torque converter is a complex turbomachine used to transfer power from an engine to a transmission. It has been used in automatic transmissions for numerous applications including passenger cars, trucks, buses, tractors and tanks. It has three important functions. First, it transfers power smoothly and efficiently from an engine to a transmission—the peak efficiency is in the range of 82 to 92 percent. Second, at low vehicle speeds, it has the ability to multiply engine torque for improved vehicle launching—the maximum torque multiplication is in the range of 1.6 to 3.5. Third, it is an effective damper to dampen engine torsional disturbances and shock loads. Maddock (1991), Jandasek (1962), By and Mahoney (1988) are three excellent references on the design and application of the automotive torque converter.

A typical automotive torque converter cross section is shown in Fig. 1, By (1993). It has the following components: 1) a mixed-flow pump connected to the engine crankshaft through the torque converter cover and the engine flexplate, 2) a mixed-flow turbine attached directly to the transmission shaft, 3) either a mixed-flow or an axial-flow stator attached to the transmission housing through a one-way clutch, and 4) a lock-up clutch, which transfers engine power directly to the transmission bypassing the torque converter. To minimize the effects of cavitation and to engage the lock-up clutch, the torque converter is fully filled and is pressurized with a charge pressure supplied by the transmission hydraulic system. Oil is pumped outward from the pump inlet and is discharged axially at the pump exit where it enters the turbine. It then flows inward from the turbine inlet to the turbine exit. The stator provides a reaction torque by directing the flow from the turbine exit back to the pump inlet. This closed-loop motion is repeated continuously. Under a constant input torque condition, maximum through flow velocity and maximum stator reaction torque occur when the turbine is stationary. As the turbine speed increases, the through-flow velocity and the reaction torque are reduced. As the turbine speed further increases, the reaction torque is eventually reduced to zero and the through-flow velocity is reduced to a minimum. This is referred to as the coupling point, where the torque converter ceases to multiply torque and starts to function as a fluid coupling. Beyond this point, the use of a one-way clutch allows the stator to rotate or free wheel in a forward direction.

Key performance parameters of the torque converter are speed ratio, efficiency, pump capacity coefficient, and K factor. Speed ratio, SR, is the ratio of turbine to pump speed. Torque ratio, TR, is the ratio of turbine to pump torque. Efficiency, η, is the ratio of turbine to pump power. It can be shown that efficiency is the product of speed ratio and torque ratio.

Recent interest in reducing automobile fuel consumption and air pollution has stimulated continued research into the fluid dynamics of the hydraulic torque converters. The basic flow field in a torque converter is toroidal and confined by an outer shell and inner core as shown in Figs. 1 and 2. In automotive torque converters, the stator blades are airfoil shaped but the pump and turbine blades are made of plate approximately 1 mm thick. In the torque converters under consideration, the blade inlet and outlet angles are typically 7 and 63 deg for the stator, -32 and 0 deg for the pump and $+52$ and -60 deg for the turbines. Torque converter flow fields are very complex. They are three-dimensional, viscous, and unsteady. Additional complexities arise due to the differential in rotor speed between the pump and the turbine and the associated wide variation in incidence angles. No other turbomachinery is subjected to such wide operating conditions. The turbine and the pump passages are narrow, long, and dominated by viscous effects, curvature, rotation, separation, secondary flow, and three-dimensional effects. Close coupling of the elements induce potential and viscous interactions at the rotor-rotor and rotor-stator interfaces resulting in large unsteadiness. Its nature and magnitude vary with the spacing between blade rows, the number of blades, the thickness of the trailing edges, the location of areas of flow separation, the characteristics of the blade wake profiles, the existence of secondary flows, and other geometrical and op-

---

Contributed by the Fluids Engineering Division for publication in the JOURNAL OF FLUIDS ENGINEERING. Manuscript received by the Fluids Engineering Division March 15, 1996; revised manuscript received September 6, 1996. Associate Technical Editor: D. P. Telionis.

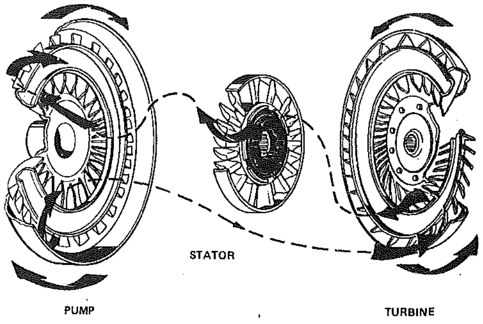

Fig. 1 Configuration and flow path of torque converter

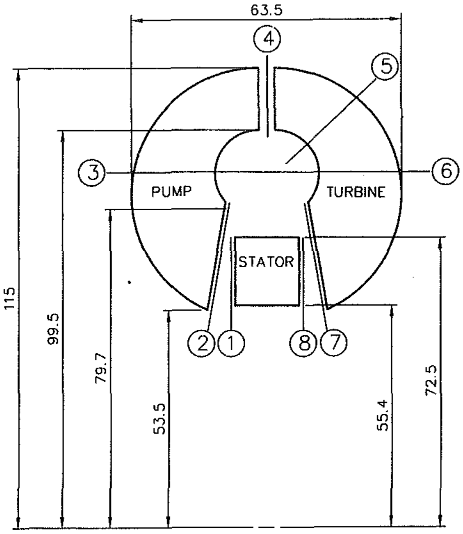

Fig. 2 Schematic of automotive torque converter showing measurement stations (dimensions are in mm)

erating parameters. A fundamental difference between the flow in torque converters and all other types of turbomachinery, except multi-spool gas turbines, is the presence of a least two rotors affecting the time-dependent flow. Further complications are the proximity of the elements to each other and the recirculating nature of the flow. These geometrical and flow characteristics present a challenge for experimentalists and computational fluid dynamicists.

Objectives and Scope

The original research was carried out with the ultimate objective of enabling designers to improve the performance, which can only be achieved if the fluid dynamics phenomena is well understood. Specific objectives present day designers have in mind are reducing the length of the torque converters for automobiles with transverse engines and secondly reducing fuel consumption in urban use. The objective seems to have been to understand the flow field which can be utilized in improving the design and performance. These data are valuable in validating computer codes, which can then be used in the design precess, thereby, reducing the design and development cycle. The objective of the research carried out by these (Bahr et al., 1990; By and Lakshminarayana, 1991; Browarzik, 1994; Marathe et al., 1996; Marathe and Lakshminarayana 1995) groups is to improve the performance and design of automotive torque converters through research and development. This is carried out through acquisition, analysis, correlation, and synthesis of the experimental data on the flow field (including pressure, velocity and turbulence field). An integrated experimental and CFD approach is used by some of these groups to develop codes for design, analysis, simulation, and improvements; thereby reducing the design and development cycle time.

The main objective of this paper is to examine the data available on flow in automotive-type torque converters and provide a coherent and critical assessment of the main characteristics

Nomenclature

$(C_{p_o})_{\mathrm{Abs}} = 2((P_o)_{\mathrm{Abs}} - p_{\mathrm{hub}})/\rho V^2_{\mathrm{ref}}$
C_{pb} = blade static pressure coefficient $2(p - p_{\mathrm{ref}})/\rho U^2_{\mathrm{tip}}$
C = chord length
$C_{p_s} = 2(p_s - p_{\mathrm{hub}})/\rho V^2_{\mathrm{ref}}$
FHP = five-hole probe
L = length
LDV = laser velocimetry
PSU = The Pennsylvania State University
P_s = power
P_o = stagnation pressure normalized by $\rho V^2_{\mathrm{ref}}/2$
P^*_f = nondimensional fluid power = $P_f/[(0.5\rho V^2_{\mathrm{ref}})(V_{\mathrm{ref}} R^2_P)]$
P^*_s = nondimensional shaft power = $P_s/[(0.5\rho V^2_{\mathrm{ref}})(V_{\mathrm{ref}} R^2_P)]$
PS, SS = pressure and suction surface
p, p_s = static pressure normalized by $0.5\rho V^2_{\mathrm{ref}}$
p_{ref} = reference pressure on hub
Q = volume flow normalized by $V_{\mathrm{ref}} R^2_P$
R = radius
RU = Ruhr-Universitat, Bochum, Germany
r = radial coordinate
SR = speed ratio (turbine/pump)
T = torque
TR = torque ratio (T_T/T_p)
U_{pt} = pump tip blade speed
UVA = University of Virginia
V = absolute velocity normalized by V_{ref}
V_r, V_θ, V_x = absolute radial, tangential and axial velocity
$V_{\mathrm{ref}} = U_{\mathrm{pt}}(1 - \mathrm{SR})^{0.5}$
V_{sec} = secondary velocity
W, W_θ = relative total and tangential velocity
x = coordinate normal to chosen radial line and to axis
y = coordinate parallel to chosen radial line
Z_n = number of blades
z = axial coordinate
β = blade exit angle measured from tangential direction
Δ = difference operator
η_{TC} = efficiency = $T_P\Omega_P/T_T\Omega_T$
θ = tangential coordinate
σ = slip factor
ρ = fluid density
Ω = angular velocity normalized by $(0.5V_{\mathrm{ref}}/R_P)$
ν = kinematic viscosity

Superscripts

$-$ = passaged averaged
$=$ = area averaged

Subscripts

Abs = absolute
f = fluid
h = hydraulic
our = exit
p = pump,
Pt = pump tip radius
ref = reference
S = stator
T = turbine
r, θ, z = components in r, θ, z directions
TC = torque converter
o = stagnation
x, y, z = components in x, y, z, directions

of the flow field and its impact on performance and design. While this paper is a review in the sense of integrating information and insights from various sources, the emphasis is on assembling a clear picture of the typical flow fields in automotive torque converters and their impact on performance and design. Much of the discussion will focus on the mean flow field, as its control will probably remain the main objective of the design and improvement process.

Background

Most of the insights in the present paper were based on the experimental investigations of groups at the Ruhr-Universitat in Bochum (RU), Germany, and at two universities in the USA: The Pennsylvania State University (PSU) and the University of Virginia (UVA). The group at the Ruhr-Universitat investigated the flow and performance of an industrial-type torque converter (Adrian, 1985 and Browarzik, 1994). It consisted of an unshrouded radial outflow (centrifugal) pump of conventional design. The torque converter had a stall torque ratio of 5.7 and a peak efficiency of 87 percent at a speed ratio SR = 0.55.

The discussion of the flow in automotive torque converters is primarily based on pump and turbine measurements at UVA by Brun et al. (1994, 1996a), Brun and Flack (1995a, b), and Gruver, et al. (1996); blade static measurements at General Motors by By and Lakshminarayana (1991, 1995a, b); stator, pump, and turbine exit measurements at PSU by Marathe and Lakshminarayana (1995), and Marathe et al. (1995a, b, 1996). Browarzik (1994), Brun and Flack (1995a, b), and Marathe et al. (1995a, b) have explained in detail how to acquire and analyze time dependent data in torque converters. The main flow visualization methods were the spark tracer method and the wall tracer method (Numazawa et al., 1983; Lee et al., 1994).

The groups at PSU and UVA carried out their research on models of the same automotive-type torque converter with 230 mm outer diameter as shown in Fig. 2. The blade numbers were typically 27, 29, and 19 in the pump, the turbine, and the stator respectively. The gaps between the elements were small and there was meridional flow curvature in all the elements including the nominally axial flow stators, due to the torus curvature. The stall torque ratio was 2.1. The facilities were operated typically at 1100 rpm. PSU used Shell Diala oil with $\nu = 4.8 \times 10^{-6}$ m^2/s, $\rho = 857$ Kg/m^3 at 60°C and UVA used Shell Flex 212 oil with $\nu = 2.2 \times 10^{-6}$ m^2/s. The main flow measurement techniques employed were laser anemometry (LDV) at UVA, hot-film anemometry at RU, and fast response five-hole probe (FHP) and wall static pressure measurements at PSU. The FHP measurements were acquired at station 1 (stator exit), station 4 (pump exit), station 8 (turbine exit or stator inlet) shown in Fig. 2. The LDV data was acquired at station 2 (pump inlet), station 3 (pump mid-chord), station 4 (pump exit), station 5 (turbine $\frac{1}{4}$ chord), station 6 (turbine mid-chord), and station 7 (turbine exit). These data are interpreted together to provide an integrated assessment of the flow field. In many instances, the data were reprocessed to examine critical flow features. Unpublished data from the groups at PSU an UVA are also reviewed. Furthermore, the flow field only at peak efficiency conditions (SR = 0.800) is examined in detail to assess the nature of flow field, even though a brief assessment at stall conditions is also included for completeness.

The computational effort is vigorously pursued by several groups (e.g., By et al., 1995c; Schulz et al., 1996; Kost et al., 1994; Marathe et al., 1996; and Tsujita et al., 1996). The computational effort is not reviewed in this paper due to limitations on the length of the paper and due to the fact that the torque converter flow field has not yet been computed satisfactorily. In addition to reviewing the experimental efforts at RU, PSU, and UVA, an attempt is made to list additional useful references (not quoted in the text) at the end of the paper. These are, however, not discussed as it was decided to concentrate on two torque converter geometries for the sake of brevity. These references also include earlier reviews, design methods, and computational efforts.

Accuracy of Measurements

Gruver et al. (1996) stated that he measured individual velocities to within four percent but that velocities along the suction surface might be contaminated. Bahr et al., 1990 reported agreement of mass flow to within 10 percent between inlet and exit flows of the stator, while Brun and Flack (1995a) reported measurement uncertainties for LDV measurement in a turbine of 0.1 m/s for a velocity of 3.5 m/s (three percent). They stated 95 percent confidence limits as ±0.05 m/s. Marathe and Lakshminarayana (1995) quote the accuracy of pressure measurements to be ±0.01 psi, with maximum cumulative error in velocity and pressure measurements to be about 2–3 percent. In our own correlations of data sets, including both PSU and UVA data, we found the standard deviation of the mean throughflow volume flow to be typically 3 percent of the mean.

Pump Flow Field

Flow at the Stator Exit and at the Pump Inlet. The assessment of the pump inlet field is based on the UVA data (station 2, Fig. 2) presented by Gruver et al. (1996) and the stator exit flow field (station 1, Fig. 2) is based on PSU data (Marathe et al., 1996). Interesting and undesirable flow features occurs as the flow progresses from the stator exit (data taken at 0.36 axial chord downstream of the stator) to the pump inlet (very near the leading edge). The absolute stagnation pressure contours at the exit of the stator, shown in Fig. 3, reveal the presence of a low pressure region near the shell and a distinct wake. The passage mass averaged values of $(C_{p_o})_{\mathrm{Abs}}$ shows a nearly uniform distribution from the core to the shell (Fig. 4). The axial velocity contours show lower axial velocities near the core region (Fig. 5). The passage averaged axial velocities shown in Fig. 6 indicate that the axial velocity near the core region is about 70 percent of that near the shell.

The axial velocity at the pump inlet (Fig. 7) shows some dramatic change occurring between the stator trailing edge and the pump inlet. The flow passage changes from axial to radial, with considerable torus curvature effects as the flow progresses from station 1 to 2, shown in Fig. 2. The velocity in the core region has decreased drastically (from a value of 0.335 to −0.013), resulting in reversed flow across the entire pitch within 20 percent of the spanwise distance from the core. The flow deceleration occurs due to the convex curvature near the

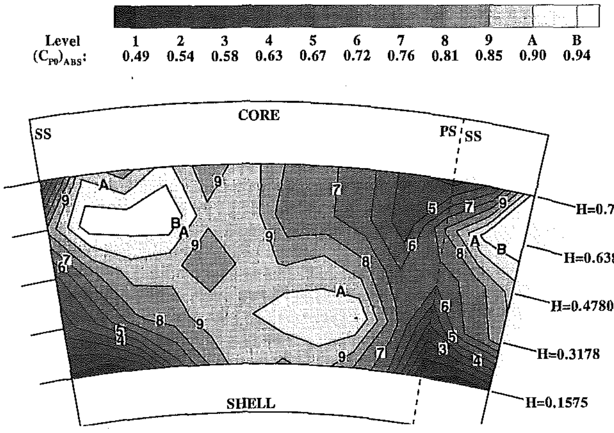

Fig. 3 Contours of absolute stagnation pressure coefficient $(C_{p_o})_{\mathrm{Abs}}$ at stator exit at SR = 0.800 (derived from PSU data in Marathe et al., 1996)

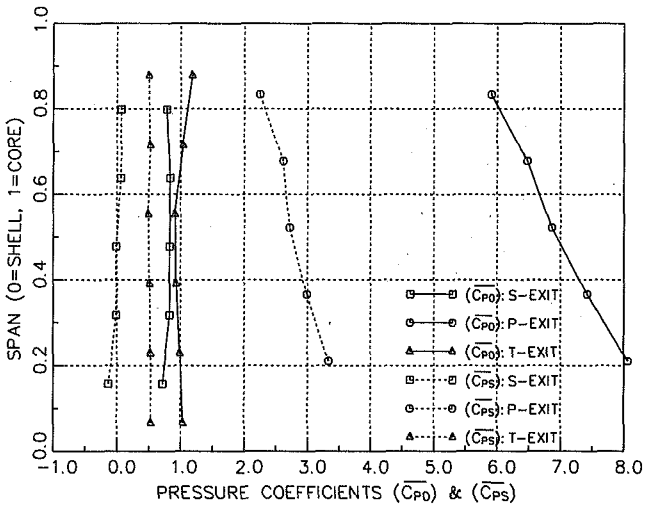

Fig. 4 Spanwise distribution of passage-mass averaged pressure coefficients $(\bar{C}_{p_0})_{Abs}$ and $(\bar{C}_{p_s})$ (PSU data)

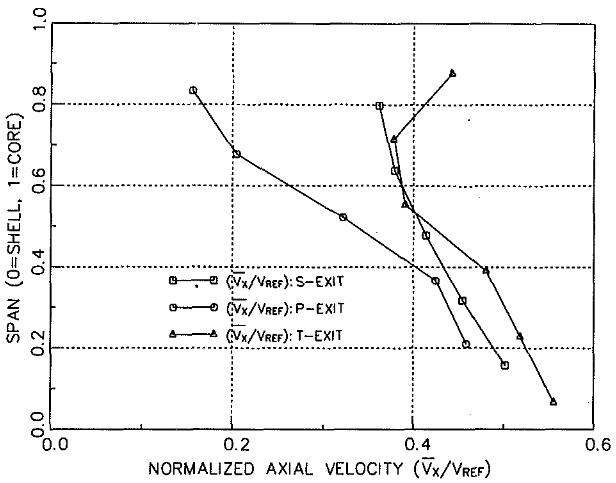

Fig. 6 Spanwise distribution of passage-mass averaged normalized axial velocity (V_x/V_{ref}) (PSU data)

core. It is clear from comparing the passage-averaged distribution of axial velocity (Figs. 6 and 8) that the axial velocity in the mid-span region has accelerated, while that near the core has decelerated substantially, resulting in back flow.

At the pump inlet (SR = 0.800), a strong tangential relative velocity component is directed at the pressure surface of the pump, with low energy flow along the suction surface. The relative tangential and relative total velocity near the core is nearly zero; and the absolute tangential and total velocity is highest in the core region at the pump inlet (Fig. 8). This is caused by pump dragging the separated flow along near the core region. The incidence to the pump blade row in the 20 percent span from the core is very high, resulting in flow separation near the leading edge of the pump. This is evident from the plot of secondary velocity vectors (not shown), where region of flow separation at the suction surface near the inlet is visible as a disturbed flow region. An incipient right-handed circulation pattern occurs near all surfaces, especially near the pressure surface where the flow with the increased angular momentum is flung outwards towards the core. The backflow at the pump inlet near the core is also evident in the pitch-averaged axial velocity profile (Fig. 8). It is caused by a combination of the sudden increase in flow area where the stator core shroud ends, the relatively large mean inlet incidence angle of 15.3 deg, and flow passage curvature.

At SR = 0.065 the contour plot of the axial velocity (not shown) indicates only small local regions of backflow concentrated in the suction and pressure corners in the spanwise range of about 10 percent from the core. The flow is more disturbed near the pressure surface at SR = 0.065 and less disturbed near the suction surface than at SR = 0.800. No backflow was evident in the pitch-averaged flow near the core, but the through flow velocity decreases continuously from mid section to core. The average relative flow angle is −3.1 deg. Since it implies that the flow enters the pump with virtually no relative whirl velocity, the backflow inducing diffusing action in the pump inducer is absent. As the angular momentum of this flow is reduced by impingement on the blade suction side, the radial pressure gradient forces it inwards. This mechanism contributes to setting up the circulatory secondary flow pattern.

It is clear from the discussion above that great care should be taken in designing the flow passage shape. Sudden increases in flow area should be avoided. The curvature of the flow field in the meridional plane is important; a small radius of curvature leads to velocity profile distortion, but a large radius leads to a longer flow path and a longer axial length torque converter. Potential flow methods often used in the design of turbomachinery will not be adequate because of the large stator wakes and secondary flows entering the stator. Leaning the rotor blades may help to suppress flows developing in the rotor inducer. A well-designed flow passage upstream of the pump and an

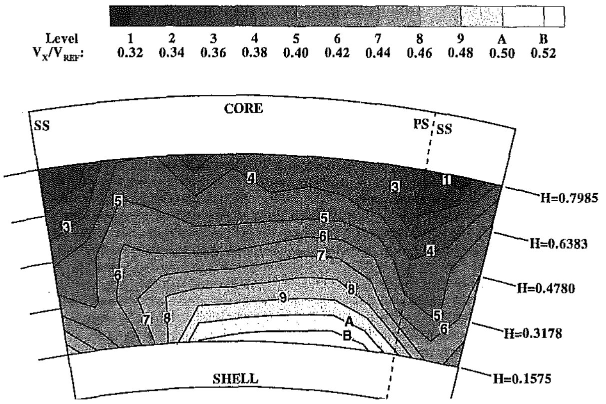

Fig. 5 Normalized axial velocity (V_x/V_{ref}) contours at stator exit at SR = 0.800 (PSU data)

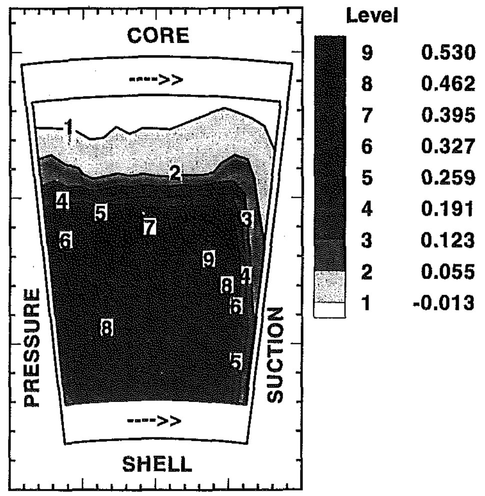

Fig. 7 Pump inlet axial velocity (V_x/V_{ref}) contours from LDV at SR = 0.800 (derived from UVA data in Gruver et al., 1996)

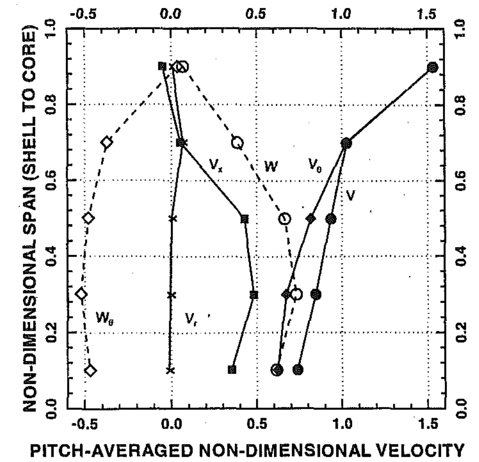

Fig. 8 Pump inlet velocity components from LDV at SR = 0.800 (derived from UVA data in Gruver et al., 1996)

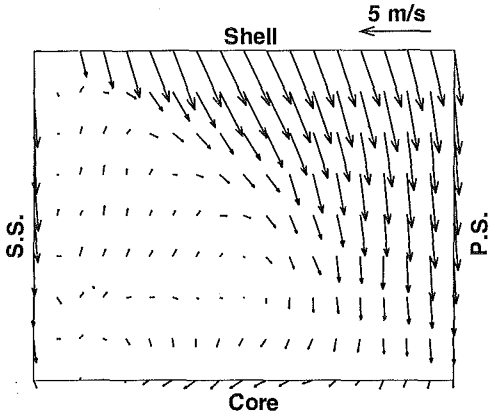

Fig. 10 Secondary velocity vector ($\underline{V}_{sec}$) at pump mid-chord from LDV data at SR = 0.800 (derived from UVA data in Gruver et al., 1996)

optimized pump inducer design may result in the elimination of flow separation in the pump inducer.

Flow at the Mid-Chord Plane of the Pump. The pump mid-chord plane is a plane perpendicular to the radial direction at a radial position between the centers of curvature of the core and the shell where the radius is 86.04 mm (station 3, Fig. 2). This plane would correspond approximately with the outlet plane of the pumps in the industrial torque converters of Adrian (1985) and Browarzik (1994). At a speed ratio of 0.065, the through flow velocity is fairly uniform, but at 0.800 there is a velocity gradient from the suction to the pressure surface, with a strong jet near the pressure side occupying nearly half the flow passage (Fig. 9).

At both SR = 0.800 and at SR = 0.065 there is a right-handed circulation centered near the suction surface core corner, as shown in Fig. 10. The secondary flow components are as large as the through-flow components. At a speed ratio of 0.800, the average through-flow secondary flow velocities and vorticity decreases with decreasing pump speed, but at a slower rate than the pump speed.

The through flow velocity contours, show in Fig. 9, clearly reveals major changes between the stations when compared with axial velocities at inlet (Fig. 7). The strong secondary flow that exists in this region (Fig. 10) has transported the high through flow velocity near the shell at inlet toward the pressure surface and the separation zone (up to 20 percent of span near the core, Fig. 7) has been transported toward the suction side spread across the entire core to shell region. This region of separation is not caused by an adverse pressure gradient on the suction surface as evidenced by the blade pressure data presented by By and Lakshminarayana (1995a), but by the secondary flow induced due to shear layers, rotation and curvature effects (Lakshminarayana, 1996, pp. 321–330). The secondary flow pattern shown in Fig. 10 has been captured reasonably well by a Navier-Stokes solver (By et al., 1995c).

Numazawa et al. (1983) found that the streamlines generally show a shell-to-core flow on the pump pressure surface at mid-chord, especially for SR = 0.800, indicating a circulation with the pump rotation, while at the exit there is a core-to-shell flow at a speed ratio of 0.800 and a converged flow towards the center of the surface at SR = 0.0. Lee et al. (1994) found that just before the mid-chord position the shell flow starts flowing up the pressure surface wall, more or less aligning itself with the exit meridional direction. This flow then migrates crosswise and downstream along the core surface toward the suction surface, but does not attach to it. The effect is the now familiar right-handed circulation at mid-chord shown in Fig. 10. In general, the data of Lee et al. (1994) tend to confirm those of Numazawa et al. (1983) and Gruver et al. (1996).

The flow circulation at the mid-chord of an automotive-type torque converter pump is much larger than that at the exit of the industrial type. The reasons are first, the presence of the stator blades immediately upstream of the former. They are conducive to velocity profiles that peak near the shell. Second, in the industrial-type pump the inducer blades lean forward from shell to core, inhibiting shell-to-core flow on the pressure surface.

Flow at the Exit of the Pump. The axial velocity and the secondary flow pattern at the exit of the pump (Station 4) are shown in Figs. 11, and 12, respectively. The secondary flow is

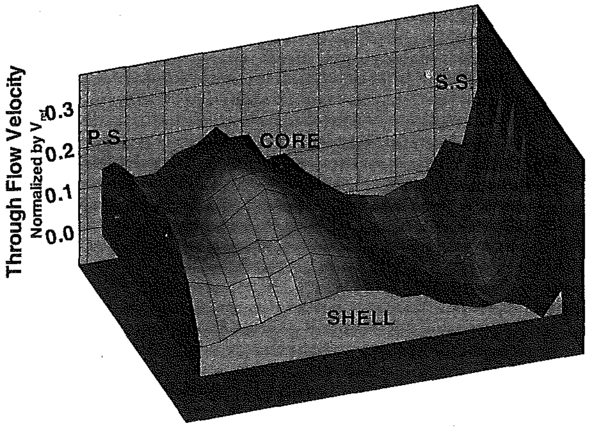

Fig. 9 Axial velocity at pump mid-chord from LDV at SR = 0.800 (derived from UVA data in Gruver et al., 1996)

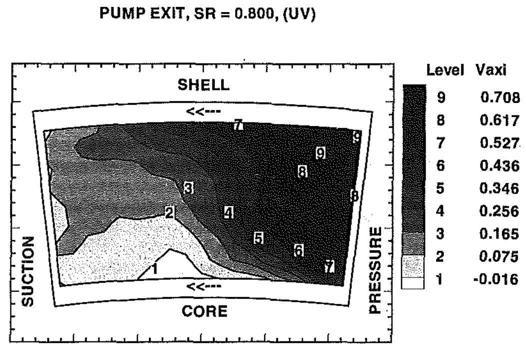

Fig. 11 Pump exit axial velocity contours from LDV at SR = 0.800 (derived from UVA data in Gruver et al., 1996)

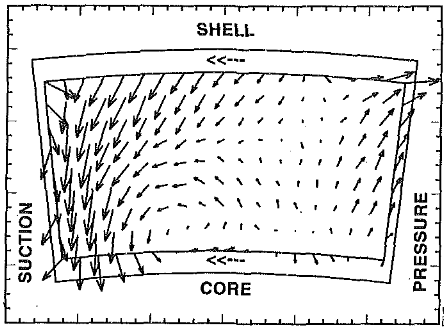

Fig. 12 Pump exit secondary velocity (V_{sec}) vector plot from LDV at SR = 0.800 (derived from UVA data in Gruver et al., 1996)

now left-handed, with a dominant ''jet'' flow pattern near the suction surface, moving from shell to core. It should be remarked that the magnitude and the direction of the Coriolis force ($2\Omega \times \mathbf{W}$) changes as the flow progresses, acting nearly in the blade-to-blade direction near the leading edge and core-to-shell at the pump exit. This indicates that the rotation induced secondary flow dominates the flow field in torque converter pumps. The left-handed circulation transports high energy mean flow from the pressure surface near the mid-chord location to the shell suction surface (Fig. 9). This is evident by comparing Figs. 9 and 11, and the corresponding secondary velocity vector in Figs. 10 and 12. The separated region now has moved to the corner formed by the core and suction surface. The flow at the exit of the pump resembles the ''jet-wake'' pattern observed in centrifugal compressors (Eckardt, 1980). It is interesting to note that the pitchwise center of the back flow (Fig. 11) is also the center of the vortex.

The passage-averaged mean stagnation pressure (Fig. 4) and the axial velocity (Fig. 6) clearly shows the effect of secondary flow on the spanwise mixing of the flow. The stagnation pressure and the axial velocity are both lower near the core region at the pump exit.

The pitch averaged velocity profiles for SR = 0.065 (not shown) are very similar to those at SR = 0.800. The axial velocity at SR = 0.065 varies more with pitch than with the span except near the core. No backflow region is evident at the core, but the axial velocity is low near the core. The secondary flow pattern (not shown) looks similar to that at SR = 0.800. The core-to-shell velocity gradient is smaller than at the mid-chord plane.

The relative exit flow angle and the slip factor at SR = 0.065 are found to be −7.0 deg and 0.897, for the LDV data. Wiesner (1967) gave the following equation for the slip factor of centrifugal impellers:

$$\sigma = 1 - (\cos \beta_{\text{out}})^{0.5}/Z_n^{0.7}$$

With $\beta_{\text{out}} = 0.0$ deg and $Z_n = 27$ the calculated slip factor is 0.900 which agrees well with the data. The Wiesner slip factor relationship was empirically derived for radial turbomachines but Strachan et al. (1992) have found that it predicted the pump torque and the overall performance of Jandasek's (1963) torque converter well for various pump exit blade angles.

In ordinary industrial pumps, nonuniform exit profiles and flow separation are to be avoided because these two phenomena generally inhibit pressure recovery in the diffuser or volute of the pump. These effects do not seem to be as serious in torque converters that are primarily momentum transfer devices and have no diffusers.

Blade Static Pressure Distributions for the Pump. By et al. (1995a) measured the blade static pressures near the mid-span, core and shell regions at speed ratios of 0.0, 0.6, 0.800. The data at SR = 0.800 is shown in Fig. 13. Their general observations are as follows. For the 0.0 speed ratio condition the static pressure distribution near the leading edge at the shell and mid-span is reversed, indicating negative incidence. The pump static pressure field changes drastically from shell to core, and the centrifugal and Coriolis force has dominant effects as analyzed in Lakshminarayana (1996, p. 277). A reversal of pressure distributions at the core over the last 25 percent indicates poor flow conditions at the suction surface core corner near the exit. The pressure distributions are better (this means that the pressure surface pressures are everywhere higher than the suction pressure and both vary fairly smoothly) for a speed ratio of 0.6, and slightly worse at 0.800 than at 0.6. At mid section a three-dimensional potential code can reasonably predict the static pressure distribution. A Navier Stokes code can be used to effectively predict the pump flow field (By et al. 1995c).

Discussion of Flow Fields in Pumps. As discussed before, the main features of the flow are the high through flow velocities near the pressure surface-shell corner and the large secondary circulation. Since the main flow in automotive-type mixed-flow pumps has a velocity gradient with the higher velocity near the shell, the blade curvature turns the near-core flow more than the near-shell flow thereby contributing to the right-handed secondary flow circulation. And since in the automotive-type mixed-flow pump, at a speed ratio of 0.800, the main flow has a gradient with a slightly higher velocity near the suction than near the pressure side, the curvature in the meridional plane deflects the flow on the pressure surface towards the core more than the flow near the suction side, also contributing to a secondary right-handed flow circulation. The effects mentioned so far act whether the pump rotates or not, but only when there is a velocity gradient at the inlet. This is one of the reasons why By (1993) found such large differences between the computed flow fields with uniform and non-uniform inlet velocity profiles. As the pump inlet flow has a profile with a higher velocity near the shell than near the core, the passage curvature in the meridional plane will keep the high momentum flow near the shell. As this flow moves outward beyond the quarter chord point it is forced in the direction of the pressure surface by the Coriolis force, while the low momentum fluid is turned more in the direction of rotation. Once the main flow has accumulated near the pressure surface, it will be kept there by the Coriolis force. These effects explain why the high velocity flow accumulates near the pressure surface-shell corner, and why there is typically a secondary flow circulation at the mid-chord plane in the same direction as the pump rotation. The accumulation of boundary-layer flow near the inside of the flow passage also explains the existence of the wake region near the core and why the flow there is highly turbulent.

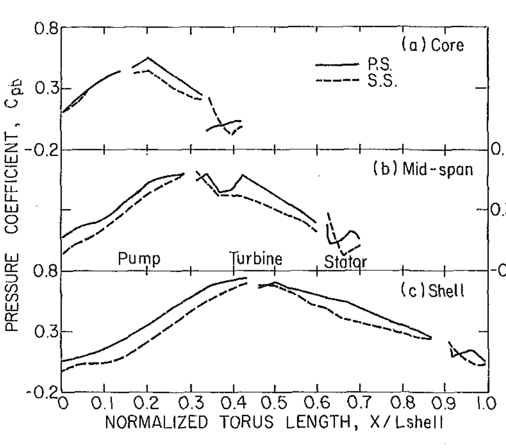

Fig. 13 Blade static pressure distribution at SR = 0.800 (adapted from By, 1993)

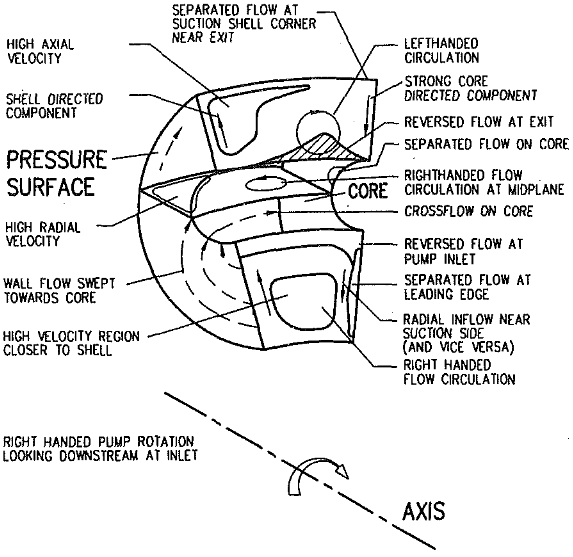

Fig. 14 Main flow features in a torque converter pump at SR = 0.800

A schematic of the flow features, based on the present knowledge of the torque converter flow field is shown in Fig. 14. The assessment of the data in an automotive mixed flow pump reveals the following:

1. The inlet velocity profile typically shows a small region of low velocity at the shell and separated flow at the core, depending on how much the pump shell to core span is larger than that of the stator. Strong secondary flows move this separation region to suction surface (shell-to-core) near mid-chord region and back to core region at the exit. A wake region exits near the core and the suction surface at the exit of pump. This indicates considerable spanwise and blade-to-blade mixing as the flow proceeds from the inlet to the exit.
2. The flow is smooth along the initial part of the pressure surface. At the mid-chord section, the high through flow velocity occurs near the pressure surface shell corner, with evidence of a wake in the suction surface core corner.
3. In a pump that rotates clockwise when looking downstream at the pump inlet, there is a strong right handed flow circulation at mid-chord, and in the opposite direction at the exit.
4. The inlet axial velocity profile is affected by whether the stator is positioned where there is curvature in the meridional plane or not.
5. At the pump exit, most of the flow is concentrated near the shell and pressure surface with little flow near the core, in both the radial and the mixed flow type of pump.
6. The agreement between the CFD predictions and measurements were reasonable, even with the present k-ϵ turbulence models.

Turbine Flow Field

The LDV measurement at inlet (station 4, Fig. 2), quarter chord (station 5), mid-chord location (station 6), (Brun and Flack, 1995a) and the five-hole probe measurements at the exit (station 8) of the turbine (Marathe and Lakshminarayana, 1995) are interpreted in this section to assess the flow features in the turbine.

Flow at the Inlet of an Automotive Torque Converter Turbine. The axial velocity profile shown at pump exit (Fig. 11) at SR = 0.800 (Brun et al., 1996a), undergoes substantial changes as it approaches the turbine inlet. The flow becomes more uniform in the blade-to-blade direction, with highest axial velocity occurring near the shell, and flow separation in the core region (about 10 percent of blade height) measured across the entire passage. The pump blade wake can be clearly seen at this location. It is the secondary velocities that undergo major change. The magnitudes of secondary velocities are substantially reduced at this location.

The main difference between the pump exit and the turbine inlet axial velocity profiles at SR = 0.800 is that at the turbine inlet, the velocities decrease more sharply near the core and shell compared to that at the pump exit. At SR = 0.800 the through flow component is only about a quarter of the absolute tangential component. A fractional adjustment in tangential velocity profile will then result in a noticeable adjustment in through flow profile. The turbine inlet blade angle changes from 55 deg at the core through 52 deg at mid span to 49 deg at the shell. Closer to the shell, however, the flow impinges with increasing angle on what is normally the suction side of the turbine blades. In these regions the turbine blades do work on the fluid, thereby increasing its energy. But the geometry of the flow and the blade passage is such that the flow relative to the turbine is turned farther away from the axial direction, and the relative total velocity increases. The through flow leaving the pump and entering the turbine near the shell is then accelerated and the flow is retarded near the core. This results in the flow lifting off the core, causing a velocity deficit at the core at the quarter and mid-chord sections.

At SR = 0.065, the outer half of the velocity profiles is almost uniform, but the inner half decreases towards the core. Relative flow angles are almost uniform, but the decrease in the pump exit through flow velocity results in an increased relative yaw angle into the turbine near the core. Consequently, the fluid does relatively more work near the core. The fluid energy is then reduced more near the core than elsewhere in the vicinity of the turbine inlet. Near the core, the turbine blades have to turn the flow through a greater angle towards the axial direction. Since this is a diffusing action, the already relatively energy deficient total relative flow near the core experiences a further reduction in velocity. The inlet pitch angle shows that the flow does not lift off the core at the inlet. However, since the inlet incidence angle is large (27 deg) and the turbine blades are thin plates (about 1 mm), the flow separates at the leading edge of the suction surface. Both the centrifugal and the meridional pressure gradient force the low momentum flow inwards toward the axis, causing separation at the core and preventing flow re-attachment to the core before mid-chord. The turbine inlet is a critical area and design methods incorporating all the major flow features are required to match the blade angle to the flow over a wide operating range.

Flow at the Quarter- and Mid-Chord Planes of a Turbine. At SR = 0.800 no flow separation is evident at the quarter chord plane, but there is a low velocity region at the suction surface-core corner. Minimum and maximum non-dimensional through flow velocities here are 0.08 and 0.59, and the circumferential component is 0.34. At mid-chord (Fig. 15), the velocity field shows no separation. Maximum velocity is 0.56 near the core and 0.12 near the pressure surface. A complex secondary flow pattern, which undergoes dramatic changes is observed as the flow progresses from turbine inlet to mid-chord (Fig. 16). The secondary flow pattern is from shell to core near suction surface quarter-chord as the flow approaches mid-chord. But, no vortex pattern is observed at these locations.

At the quarter-chord plane the flow is separated for SR = 0.065 over about 30 percent of the area. At the mid-chord plane the picture is similar except that the reversed flow now covers only about 15 percent of the flow area. A complex secondary flow pattern exists, consisting of two triangular flow regions. In the one, bounded by the core and suction surfaces, the sec-

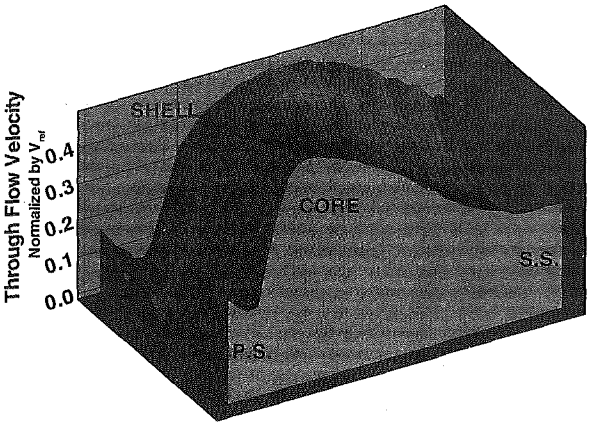

Fig. 15 Axial velocity contours at turbine mid-chord from LDV at SR = 0.800 (derived from UVA data in Brun and Flack, 1995a)

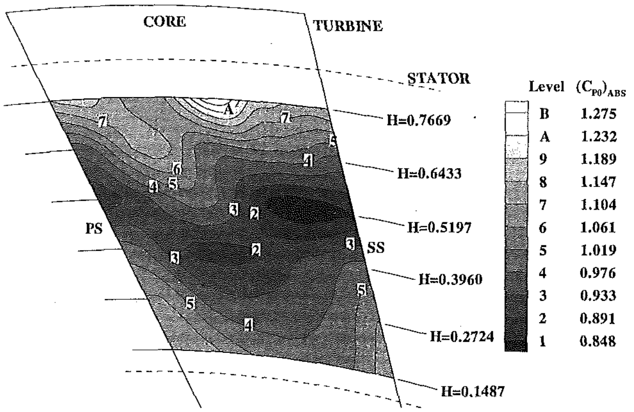

Fig. 17 Coefficient of absolute stagnation pressure $(C_{p_0})_{\text{Abs}}$ at turbine exit at SR = 0.800 (derived from PSU data in Marathe et al., 1995a)

ondary flow is directed to the suction surface-core corner feeding the reversed flow.

Lee et al. (1994) did flow visualization in automotive type torque converter turbines by means of a wall tracer method as a described earlier. At a speed ratio of 0.800 in the circular section torus torque converter, there is a flow separation on the suction surface near the turbine inlet. Where the flow reattaches, it more or less follows the blade passage in the meridional plane up to the quarter chord plane where it starts to deviate towards the core, eventually resulting in lift-off from the suction side and reversed flow at the three quarter point. On the pressure surface, there is an immediate flow deviation towards the core, which is strongest at about the quarter chord plane and then decreases again toward the exit.

Flow at the Exit of a Turbine. The stagnation pressure coefficient at the exit, plotted in Fig. 17, shows largest stagnation pressure drop (work done) near the shell and mid-span regions, and lowest work extracted and losses near the core region. The wake decays rapidly due to larger flow path as well as downstream potential effect due to stator blades. The flowfield is uniform for about 80 percent of span from the shell. The high absolute stagnation pressures and low relative stagnation pressures observed near the core is attributed to possible flow separation near the core inside the turbine passage caused by convex curvature of the torus. This is confirmed by the axial velocity distribution shown in Fig. 18, derived from a fast response five-hole probe. The low velocity region near the core region observed from the quarter-chord to the trailing edge region can be attributed to the curvature effects on the convex side. The flow decelerates (even in the absence of flow turning by the blades) in this region and accelerates near the shell region. Hence, the observed velocity profile increasing from the core to the shell is a attributed to curvature effects. The blade pressure distribution due to By and Lakshminarayana (1995b), shown in Fig. 13, does not indicate the presence of an adverse pressure gradient in this region. The low velocity regions observed near the core at quarter chord can be attributed to both adverse pressure gradient (Fig. 13) and curvature effect, while similar features near mid-chord and exit are attributed mainly to the curvature effect.

The passage and mass averaged distribution of absolute stagnation pressure coefficient, shown in Fig. 4, indicate that the stagnation pressure drop is highest near the shell and lowest near the core. This is consistent with axial velocity distribution. The radial distribution of the passage averaged axial velocity distribution (Fig. 6) shows a substantial reduction in axial velocity from shell to core, except at the last measuring point near the core.

The secondary flow pattern, derived from a fast response five-hole probe, plotted in Fig. 19, shows that substantial secondary flow occurs near the core region. A vortex pattern, with left-handed circulation, exists in the core region. The outward (towards the shell) secondary flow in the core region near the suction surface tends to move the low velocity and low pressure regions slightly outward as shown in Figs. 17 and 18.

General Discussion of Turbine Flow Field. A schematic of all the turbine flow features discussed in this section is shown in Fig. 20. By and Lakshminarayana (1995b) measured the wall static pressure distributions on the turbine blade along the mid-span and on the shell and core surfaces near the passage corners. They came to the following conclusions: Simple assumptions

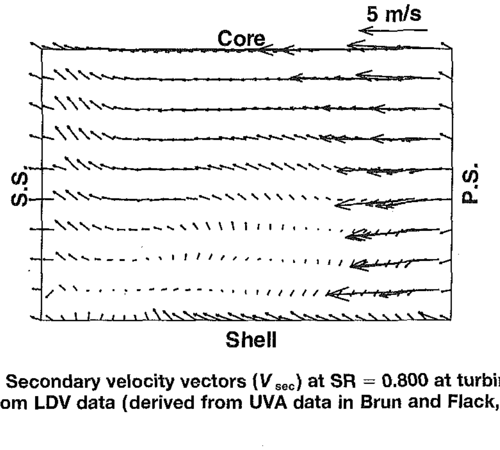

Fig. 16 Secondary velocity vectors (V_{sec}) at SR = 0.800 at turbine mid-chord from LDV data (derived from UVA data in Brun and Flack, 1995a)

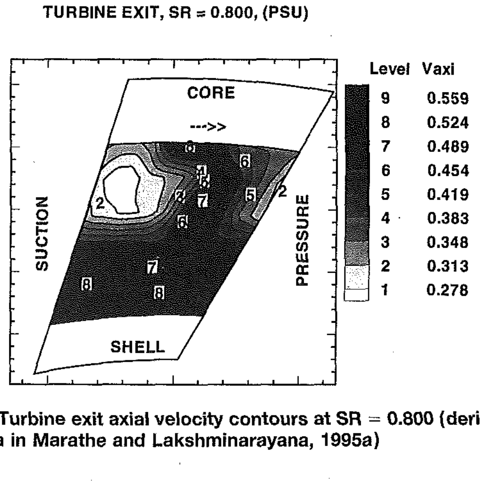

Fig. 18 Turbine exit axial velocity contours at SR = 0.800 (derived from PSU data in Marathe and Lakshminarayana, 1995a)

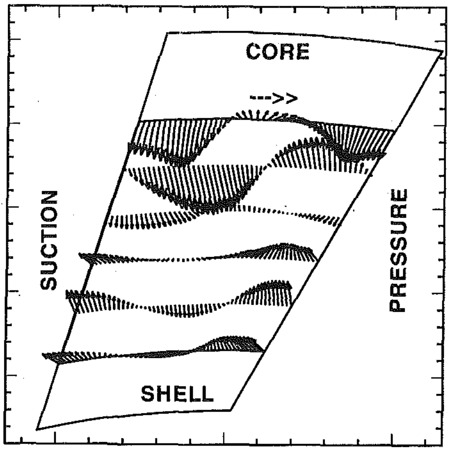

Fig. 19 Turbine exit secondary velocity (V_{sec}) vector plot at SR = 0.800 (derived from PSU data from Marathe and Lakshminarayana, 1995a)

like one-dimensional flow and simple radial equilibrium were not valid in the turbine. The pressure distribution was better at SR = 0.600 than at 0.800. A three-dimensional potential code could not accurately predict the static pressure distribution even at mid span under all speed ratio conditions, since the flow was not irrotational.

The blade pressure distribution at the mid-span, core, and shell regions, shown in Fig. 13, indicates that the flow in the initial part of the turbine (leading edge to about 10–15 percent chord) develops under an adverse pressure gradient. The blade static pressure actually increases, thus behaving like a pump. The pressure drop is continuous and well behaved beyond this location. Thus, it is clear that there is a mismatch between the pump exit flow and the turbine inlet flow. This is perhaps an area for improvement.

In an automotive-type torque converter with a mixed flow pump and turbine, the turbine operates under a much larger range of conditions than the pump, because under normal working conditions its speed changes much more than that of the pump. At low turbine speeds, the pressure gradient due to flow curvature in the meridional plane obviously has a much larger effect than that due to rotation, while in the pump, as at high speed ratios in the turbine, both effects play their parts.

At low speed ratios the mismatch between the direction of the flow in the turbine relative frame and the turbine inlet blade angle causes separation at the suction surface as reported by Brun and Flack (1995a), Lee et al. (1994), and By and Lakshminarayana (1995b). Because of its momentum, the main flow tends to accumulate in the pressure surface-shell corner, but the blade leaning angle is such that it tends to force the flow inwards, towards the torque converter axis, resulting in some shift in the main flow from the shell to the core, near the pressure surface. Because, at mid-chord the flow passage is deflected in two planes, with roughly the same radius of curvature, both curvatures affect the flow distribution. The turning in the meridional plane forces the main flow towards the shell, and the blade boundary layers towards the core, while the turning perpendicular to the meridional plane forces the main flow towards the pressure surface, and the core and shell boundary layers toward the suction surface (Fig. 20). These two effects result in the main flow migrating toward the pressure surface-shell corner, a process that is assisted by the forward lean of the blades at the mid-chord plane. The low momentum boundary layers are forced to the suction surface-core corner by the pressure gradients as reported by Brun and Flack (1995a). In the design of the torque converter under discussion there is little curvature in the turbine blades beyond mid-chord. Consequently, only the meridional curvature influences the flow beyond mid-chord at low speed ratios. The main flow is then found near the shell at the turbine exit, with the low momentum boundary layer fluid near the core. The disappearance of the blade-to-blade pressure gradient beyond the turbine exit causes a flow adjustment, resulting in a flow from pressure to suction surface at the exit.

Brun and Flack (1995a) found that the flow in the turbine at SR = 0.800 was not fundamentally different from that at SR = 0.065. Flow conditions at SR = 0.800 are generally better, however, because firstly the flow does not separate from the suction surface at the inlet, and secondly, there is a centrifugal pressure gradient component acting in the opposite direction to the meridional gradient near the exit, thereby reducing the nonuniformity of the exit profile and the concentration of low momentum fluid near the core.

Stator Flow Field

The only function of a stator in a torque converter is to impart additional angular momentum to the flow, beyond that imparted by the pump. The high torque ratio at the stall condition, when the turbine is stationary, requires a large flow deflection of about 120 deg, while the unity torque ratio requirement at a high speed ratio demands zero flow deflection. In the torque converter under consideration the stator blade inlet design angle is 7 deg, the outlet angle is 63 deg and the incidence angle varies between about plus and minus 50 deg. The dilemma of the designer is to design a blade row capable of a very high flow deflection, but with a low loss coefficient at a high negative incidence angle (Marathe et al., 1996).

To further complicate matters, it has been found that at off design conditions the stator flow field is highly three-dimensional (Bahr et al., 1990; By and Lakshminarayana, 1991; and Marathe et al., 1995a, 1996). The main flow approaching the stator from the turbine has a higher through flow velocity near the shell than near the casing, and the circumferential component near the core increases faster with speed ratio than that near the shell. Consequently, Bahr et al. (1990) found that the effect of the varying incidence angle with operating point was severe and that the one-dimensional theory was inaccurate: velocity profiles and torque distribution over the blade length were not uniform. The flow averaged turbulence intensity was high near the walls (approximately 20 percent compared to 10 percent near the mid-span).

Marathe et al. (1995a) measured the stator inlet flow field (turbine exit flow) with a five-hole probe coupled to five fast response transducers in an automotive type torque converter

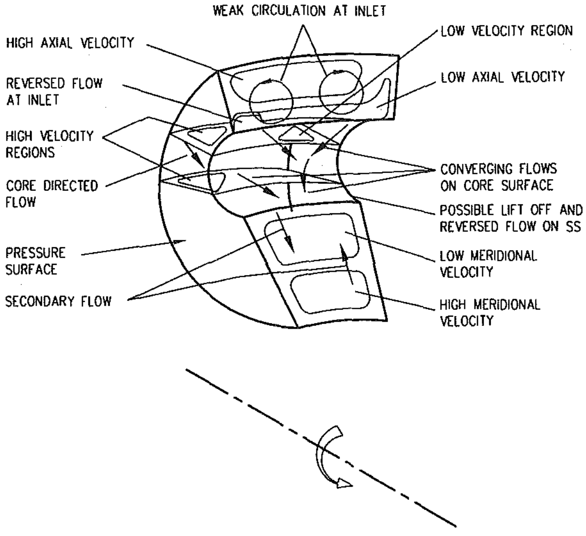

Fig. 20 Main flow features in a torque converter turbine at SR = 0.800

using oil as working fluid. The pressure signals were divided into five parts: the temporal average, the rotor-rotor interaction aperiodic component, the blade periodic component, the blade periodic component and the unresolved component. They found that pressure and velocity fluctuations were moderate but flow angle fluctuations were high. The turbine blade wakes were thin, and near the shell the wake decay was rapid. The secondary flow pattern in the turbine frame of reference showed overturning in the separation region near the core, underturning in the rest of the passage and a radial inflow in the entire passage (Fig. 19).

By and Lakshminarayana (1991) investigated the static pressure distribution over the axial flow stator blades of an automotive torque converter, measuring at the midspan and on the shell and core surfaces near the passage corners. They found that a panel method could predict the pressure distributions well only at mid-span. The blade pressure distribution (Fig. 13) indicates very large positive incidence (+57 deg) at SR = 0 and large negative incidence (−47 deg) at SR = 0.800. Most of the static pressure drop at SR = 0.800 occurs from the leading edge to 50 percent chord, while the static pressure drop at SR = 0 occurs aft of the mid-chord.

Marathe et al. (1995b) also measured the time dependent stator blade surface pressures at five points in the stator mid-chord plane. The location of transducers were at the leading edge and near the leading and trailing edges on the suction and pressure surfaces. The unsteady blade static pressures were found to be high near the leading edge and insignificant near the trailing edge. The source of unsteadiness is found to be the upstream wake as well as the upstream static pressure variation (potential effect).

The stator exit flow is presented in an earlier section (Figs. 3–6). At SR = 0.800 the pitch-averaged axial velocity profile at stator exit indicates large gradients from core-to-shell. The axial velocity is lower near the core. The deviation angle of 1.2 deg derived from FHP measurements at SR = 0.800 indicates that there is almost no flow deflection in the stator: the stator inflow angle is 54.6 deg and the outflow angle is 61.8 deg. The flow deflection at SR = 0.065 is found to be large. A deviation angle of 5.8 deg and turning angle of 95 deg is reported.

Discussion of Stator Flow Fields. One of the major features of the flow in the stator under consideration is large areas of separation found at SR = 0.800 when the flow deflection is small, and the absence of separation at SR = 0.065 when the flow deflection is large. A schematic of the flow field in the stator is shown in Fig. 21. The obvious solution to the flow separation at small defection (negative incidence) is to design the stator blades with almost flat pressure surfaces.

At SR = 0.800 there is separation on the pressure surface extending over the full span at mid-chord. It is caused by the combination of a large negative incidence angle and the concave shape of the stator blade profile. The separation over the full chord near the core is caused by the high incidence angle due to turbine rotation and flow overturning at the turbine exit near the core. The secondary flow at the exit consists of two weak circulation cells near the two blade walls. They induce core-to-shell flow near the walls, indicating a core pressure higher than the shell pressure, which is borne out by the static pressure distribution, although the gradient is very small. The low momentum boundary layer flow transported from core to shell along the suction surface eventually causes flow separation in the suction-shell corner near the exit.

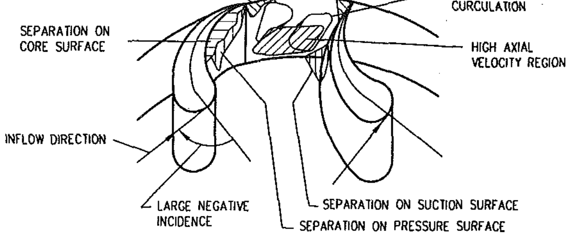

Fig. 21 Main flow features in a torque converter stator at SR = 0.800

At SR = 0.065 the high velocity exit flow is near the pressure shell corner, with a low velocity core near the suction shell corner, more or less coincident with a left handed vortex. The static pressure decreases from shell to core with a gradient that can be explained by a simple streamline curvature model that takes into consideration both the effect of the circumferential and the meridional velocity.

One of the major differences between the industrial and automotive types of torque converter lies in the stator exit meridional through flow velocity profile. In the industrial type, the higher velocity is near the core (Adrian, 1985), while in the automotive type it is near the shell as shown in Fig. 3 (Bahr et al., 1990; Marathe et al., 1996). This trend must be due to the presence of the stator blades near the torque converter axis of the automotive type. It is caused by the passage vortices associated with the curvature of the flow in the meridional plane between the turbine exit and the pump inlet. Consequently the pumps in the automobile type torque converters are exposed to less favorable meridional inlet velocity profiles than ordinary pumps and certain industrial torque converter pumps; the critical part of the flow passage, the core region where boundary layer flow accumulates, now starts with a low through flow velocity at inlet.

A schematic showing of all features discussed in this and earlier sections is shown in Fig. 21. This is based on an assessment of LDV data (UVA) and five-hole probe data (PSU).

Torque Converter Flow Field and Performance—An Integrated Assessment

The global features of the torque converter flow can be ascertained by examining Fig. 4, 6, 13, 14, 20, and 21. The stator inlet and exit stagnation pressure distribution is uniform from core to shell, with maximum losses occurring in the outer and inner third of the blade height. The stagnation pressure distribution at the exit of both turbine and pump is non-uniform, with lower values near the core. Low axial velocity near the core, and in some instances separated flow, in both of these components contribute to low pressure rise in the pump and low pressure drop in the turbine. This is also confirmed by passage average axial velocity distribution shown in Fig. 6.

The blade static pressure distribution (Fig. 13) shows that the stator provides a smooth entry to the pump (except in the core region as indicated earlier) at both SR = 0.800 and 0.065. The pump exit and the turbine inlet have not been matched well, with the initial part of the turbine behaving like a pump at SR = 0.800. The stator inlet and turbine exit matches well only at SR = 0.6, with large positive and negative angles at SR = 0.800 and 0. A two-stage stator with two separate clutches may be a solution here.

The area-mass averaged stagnation and static pressure distribution derived from five-hole probe data (Marathe, 1996) indicate that the stagnation pressure loss between the turbine exit and stator exit is lowest at SR = 0.6, and very high at both SR = 0.800 and 0.065.

The torque converter efficiency is the turbine power divided by the pump power. The efficiency is then essentially equal to the speed ratio multiplied by the torque ratio. The "lost" energy is dissipated in the working fluid, increasing its temperature. Zero efficiency at zero speed ratio in torque converters is unavoidable, as the output power is proportional to the turbine speed. Torque converter element and overall efficiencies were calculated from the experimental data.

Using area-mass averaged values of angular momentum at the inlet and exit of each of the components, a torque ratio (T_T/T_P) of 1.079 at SR = 0.800 was calculated yielding a torque converter efficiency of $\eta_{TC} = 0.863$. This is a fairly realistic internal efficiency for this torque converter, since from Bahr et al. (1990), $\eta_{TC} = 0.820$ at SR = 0.800 measured directly by a torque meter. The main reason for the resulting high values was that the cross-sectional areas over which the measurements were taken did not extend right to the walls where the lowest values of momentum and stagnation pressure occurred. The data (Fig. 13) based on blade static pressure (By, 1993) yields $\eta_{TC} =$ 0.828 and TR = 1.034.

If at SR = 0.065 the LDV pump exit and turbine inlet data are used in conjunction with the FHP stator exit and turbine exit data results in TR = 2.52, with $\eta_{TC} = 0.163$. The corresponding data from blade static measurements are TR = 2.09 and $\eta_{TC} = 0.136$ which includes drag torque on the pump. The direct measurement yields $\eta_{TC} = 0.13$, and TR = 2.0. Thus, it is clear that the flow measurements should provide detailed information on flow field as well as losses in each component.

Conclusions

Detailed conclusions for each component is given in the text and will not be repeated here. The following additional conclusions are drawn based on an integrated assessment of the flow field.

1. The stator inlet and exit stagnation pressure distribution are uniform from core to shell, with maximum losses occurring in the outer and inner third of the blade height.
2. The stagnation pressure distribution at the exit of both turbine and pump is nonuniform, with lower values near the core. Low axial velocity near the core, and in some instances separated flow, in both of these components contribute to low pressure rise in the pump and low pressure drop in the turbine. This is also confirmed by passage-averaged axial velocity distribution.
3. The blade static pressure distribution shows that the stator provides a smooth entry to the pump (except in the core region as indicated earlier) at both SR = 0.8 and 0.065.
4. The pump exit and the turbine inlet flow field have not been matched well, with the initial part of turbine behaving like a pump at SR = 0.8.
5. The stator inlet and turbine exit match well only at SR = 0.6, with large positive and negative incidence angles at SR = 0.8 and 0.
6. The stagnation pressure loss between the turbine exit and stator exit is lowest at SR = 0.6, and very high at both SR = 0.8 and 0.065.
7. The efficiencies and torque ratios derived from flow measurement agrees with those measured directly. The flow measurement provides detailed information as well as losses in each component.
8. The turbine efficiency is higher at design condition.

The flow in torque converters is extremely complex. Design methods accounting for all of the complexity must still be developed. They should at least be able to account for regions of flow separation and secondary flow circulation. Even though torque converters with peak efficiencies of 90 percent have been developed, the next generation would require design methods that allow for blade lean angles, the optimization of the shape of the flow passage and interaction effects between pump, turbine and stator. The development effort should concentrate on pump and stator and proper matching of components. CFD should be used to analyze existing and additional detailed measurements and to investigate the reasons why certain designs perform better than others.

Acknowledgments

This work was sponsored by the Powertrain Division of General Motors Corporation. The authors wish to express their appreciation to D. Maddock and R. By for technical discussions, R. Flack and K. Brun of the University of Virginia for making their data available, and B. Marathe and Y. Dong (PSU) for their assistance in the preparation of the paper. The first author's stay at PSU was funded by the University of Stellenbosch and the Foundation for Research Development of South Africa, and the Howden Group of South Africa.

References (Quoted)

Adrian, F. W., 1985, "Experimental and Analytical investigation of Flows in Hydrodyanmic Torque Converters," Ph.D. thesis (in German), The Ruhr University, Bochum, Germany.

Bahr, H. M. et al., 1990, "Laser Velocimeter Measurements in the Stator of a Torque Converter," SAE paper 901769

Browarzik, V., 1994, "Experimental Investigation of Rotor/Rotor Interaction in a Hydrodynamic Torque Converter Using Hot-Film Anemometry," ASME paper 94-GT-246.

Brun, K., Flack, R. D., and Gruver, J. K., 1996a, "Laser Velocimetry Measurements in the Pump of an Automotive Torque Converter: Part II Unsteady Measurement." *Journal Turbomachinery,* Vol. 118, No. 3, p. 570.

Brun, K., Flack, R. D., and Ainley, S. B., 1994, "Secondary Flow Measurement in a Mixed Flow Pump Using Laser Velocimetry," *Seventh International Symposium on Applications of Laser Techniques to Fluid Mechanics,* Lisbon, Portugal.

Brun, K., and Flack, R. D., 1995a, "Laser Velocimeter Measurements in the Turbine of an Automotive Torque Converter," Part I—Average Measurements, ASME paper 95-GT-292.

Brun, K., and Flack, R. D., 1995b, "Laser Velocimeter Measurements in the Turbine of an Automotive Torque Converter," Part II—Unsteady Measurements, ASME paper 95-GT-293.

By, R., 1993, "An Investigation of Three-Dimensional Flow Fields in the Automobile Torque Converter," Ph.D. thesis, Dept. of Aerospace Engineering, Pennsylvania State University.

By, R. and Lakshminarayana, B., 1991 "Static Pressure Measurement in a Torque Converter Stator," *Journal of Passenger Cars,* Vol. 100, pp. 1756–1764.

By, R., and Lakshminarayana, B., 1995a, "Measurement and Analysis of Static Pressure Field in a Torque Converter Pump," ASME JOURNAL OF FLUIDS ENGINEERING, Vol. 117, pp. 109–115.

By, R., and Lakshminarayana, B., 1995b, "Measurement and Analysis of Static Pressure Field in a Torque Converter Turbine," ASME JOURNAL OF FLUIDS ENGINEERING, Vol. 117, No. 2, pp. 473–478.

By, R., Kunz, R., and Lakshminarayana, B., 1995c, "Navier-Stokes Analysis of the Pump Flow Field of an Automotive Torque Converter," ASME JOURNAL OF FLUIDS ENGINEERING, Vol. 117, No. 1, pp. 116–122.

By, R. R., and Mahoney, J. E., 1988, "Technology Needs for the Automotive Torque Converter," Part I: Internal Flow, Blade Design and Performance, SAE paper 880482.

Eckardt, D., 1980, "Flow Field Analysis of Radial and Back Swept Centrifugal Impellers," *Performance Prediction of Compressors & Pumps, ASME.*

Fister, W., and Adrian, F.-W., 1983, "Experimental Researches of Flow in Hydrodyanmic Torque Converters," presented at the 7th Conference on Fluid Machinery, Hungary, Vol. 1.

Gruver, J. K., Flack, R. D., and Brun, K., 1996, "Laser Velocimeter Measurements in the Pump of a Torque Converter, Part I: Average Measurements," *Journal Turbomachinery,* Vol. 118, No. 3, p. 562.

Jandasek, V. J., 1963, "The Design of a Single Stage Three-Element Torque Converter. Passenger Car Automatic Transmissions," SAE Transmission Workshop Meeting, Second edition, *Advanced Engineering,* Vol. 5, p. 201.

Kost, A., Mitra, N. K., and Fiebig, M., 1994, "Computation of Unsteady 3D Flow and Torque Transmission in Hydrodynamic Couplings," ASME paper 94-GT-70.

Lakshminarayana, B., 1996, *Fluid Dynamics & Heat Transfer of Turbomachinery,* Wiley, New York, NY.

Lee, J.-S. et al., 1994, "Surface Flows Inside Automotive Torque Converters," *Proc. 5th Int. Symposium on Transport Phenomena and Dynamics of Rotating Machinery,* Vol. B, p. 887 (ISRO MAC), Maui, Hawaii.

Maddock, D. G., 1991, "Application and Design of Automotive Torque Converters," GM Powertrain Division, Class notes for an Automatic Transmission Course.

Marathe, B. V., 1996, "Experimental Investigation of Steady and Unsteady Flow Field in Automotive Torque Converters," Ph.D. thesis, Dept. of Aerospace Engineering, PSU, (in preparation).

Marathe, B. V., and Lakshminarayana, B., 1995, "Experimental Investigation of Steady and Unsteady Flow Field Downstream of an Automotive Torque Converter Turbine and Stator," *International Journal of Rotating Machinery,* Vol. 2, pp. 67–84.

Marathe, B. V., Lakshminarayana, B., and Dong, Y., 1996, "Experimental and Numerical Investigation of Stator Exit Flow Field of an Automotive Torque Converter," ASME paper 94-GT-32, to be published *ASME Journal of Turbomachinery,* Oct. 1996.

Marathe, B. V., Lakshminarayana, B., and Maddock, D. G., 1995a, "Investigation of Steady and Unsteady Flow Field Downstream of an Automotive Torque Converter Turbine and Inside the Stator, Part I—Flow at the Exit of the Turbine," ASME paper 95-GT-231.

Marathe, B. V., Lakshminarayana, B., and Maddock, D. G., 1995b, "Investigation of Steady and Unsteady Flow Field Downstream of an Automotive Torque Converter Turbine and Inside the Stator, Part II—Unsteady Pressure on the Stator Blade Surface," ASME paper 95-GT-232.

Numazawa, A. et al., 1983, "An Experimental Analysis of Fluid Flow in a Torque Converter," SAE paper, 830571.

Schulz, H., Greim, R., and Volgmann, W., 1996, "Calculation of Three-dimensional Viscous Flow in Hydrodynamic Torque Converters," ASME *Journal Turbomachinery,* Vol. 118, No. 3, p. 578.

Strachan, P. J., Reynaud, F. P., and von Backstrom, T. W., 1992, "The Hydrodynamic Modeling of Torque Converters," South African Inst. *Mech. E R&D Journal,* Vol. 8, No. 1.

Tsujita, H., Mizuki, S., and Ejiri, E., 1996, "Analysis of Flow Within Pump Impeller of Torque Converter," ASME paper 96-GT-444, presented at ASME IGTI meeting in Birmingham, England, June 1996.

Wiesner, F. J., 1967, "A Review of Slip Factors for Centrifugal Impellers," ASME *Journal of Engineering for Power,* Vol. 89, p. 558.

Additional References (Not Quoted)

Abe, K., and Kondoh, T., 1991, "Three-Dimensional Simulation of the Flow in a Torque Converter," SAE paper 910800.

Bai, L., Kost, A., Fiebig, M., and Mitra, N. K., 1994, "Numerical Investigation of Unsteady Incompressible 3D Turbulent Flow and Torque Transmission in Fluid Couplings," ASME paper 94-GT-69.

Ejiri, E., 1990, "A New Approach to Developing a More Efficient Torque Converter Stator," SAE paper 901765.

Folchert, U., Menne, A., and Waller, H., 1994, "Experimental Identification of the Dynamic Characteristic of Hydrodynamic Torque Converters and Couplings," ASME paper 94-GT-360.

Fujitani, K. R. R. Himeno, and Takagi, M., 1988, "Computational Study on Flow Through a Torque Converter," SAE paper 881746.

Hoshino, A. et al. 1990, "A Consideration on Performance improvement of Hydraulic Torque Converters," *Industrial Applications of Fluid Mechanics,* ASME FED Vol. 100, pp. 65–70.

Ishihara, T., 1955, "A Study of Hydraulic Torque Converters," Ph.D. thesis, University of Tokyo, AHO Report of the Institute of Industrial Science, Vol. 5, No. 7.

Ma, W., Luo, B. J., and Wu, S., 1991, "The Research on Quasi-Three-Dimensional Flow Design of Hydrodynamic Torque Converter Blades," SAE paper 912701.

Mercure, R. A., 1979, "Review of the Automotive torque Converter," SAE paper 790046.

Minato, K. et al., 1989, "A Performance Prediction of Hydrohynamic Torque Converter," SAE paper 900555.

Nagornaya, N. K., 1961, "Impact Losses and Coefficients in Hydraulic Torque Converter Blade Systems," *Russian Engineering Journal,* Vol. 6, pp. 21–24.

Sakamoto, H., Suyama, K., and Saka, T., 1992, "Study on Torque Converter Circuit Profile," SAE paper, 920765.

Wada, A. et al., 1995, "A PTV Analysis of Torque Converter Internal Flow," ASME paper, ASME FED Vol. 218.

Ziebart, E., 1953, "Investigations on a Foettinger Hydraulic Torque Converter," *Z-VDI,* Vol. 95, No, 30, pp. 1027–1036.

A. Khalid

J. Legrand
Laboratoire de Génie des
Procédés-C.R.T.T.,
BP 406-44602, Saint-Nazaire, Cedex,
France

J. M. Rosant
Laboratoire de Mécanique des
Fluides-URA CNRS 1217,
Ecole Centrale de Nantes, 44072, Nantes,
Cedex 03, France

Turbulent Flow Induced by an Impeller in a Closed Toroidal Loop

Swirl flow induced by an impeller was studied in a toroidal geometry. Both mean and root mean square axial velocities were measured using an electrochemical velocity probe. The effects on the flow of the rotational speed of the impeller and the circumferential position inside the torus reactor were investigated. The values of the mean axial velocity were compared with measurements obtained from residence time distribution method and from visualization experiments. The second part of this paper is devoted to the study of turbulent toroidal flow by determining power spectrum density of axial velocity fluctuations. The turbulent intensity in the torus reactor was shown to be homogeneous far downstream of the impeller; the turbulent intensity is strongly dependent on the radial coordinate near the agitator. The dissipation rate of energy, determined from the spectral analysis, is quasi-proportional to the Reynolds number. The dissipation rate of energy enabled the estimation of Kolmogorov's microscales in the different studied axial and radial locations. The results are consistent with the available literature.

Introduction

Agitation and mixing play a very important role throughout process industries. The effective control of the relevant processes requires the knowledge of the flow characteristics. The study of the torus reactor was undertaken to propose an alternative to the classical stirred tank (Belleville et al., 1992). By comparison with the latter, the main advantage of the torus reactor is an easier scale-up of its performance due to the absence of dead volume. The toroidal flow inside the reactor was induced by the rotation of an impeller placed in the pipe axis and can be ranged in the category of the swirling flows. With regard to the literature, there does not seem to be prior hydrodynamic information for the flow configuration investigated here. The works, which were interested in the toroidal geometry, mostly concern the thermosyphons (Lavine et al., 1986; Stern et al., 1988). They involve the three-dimensional analysis of natural convection in a toroidal loop. This geometry was also exploited for the study of suspension polymerization of styrene (Tanaka and O'Shima., 1988; Lee et al., 1990; Hosogai et al., 1992). The torus reactor belongs to the category of the loop reactors, which are characterized by a definitely directed circulation flow. They are especially appropriate for fluid systems requiring high dispersion effects and defined flow conditions throughout the whole reaction space, even for highly viscous chemical or biochemical systems (Blenke, 1979).

If turbulent swirling flows are of common occurrence in many engineering applications, few studies are devoted to turbulent swirling flows through curved pipes. Anwer and So (1993) analyzed the effect of swirl and bend curvature on secondary cells in turbulent curved pipe flows. They found that the secondary motion in the curved pipe is totally reorganized by swirl. In particular, they showed that the mean flow and turbulence distributions were more uniform across the curved pipe. So and Anwer (1993) studied the flow recovery from swirl and bend curvature and they found that the bend curvature accelerated the swirl decay and consequently, the recovery length was significantly shorter in curved pipe than in straight pipe.

The objective of this work is to analyze the axial velocity profile and to characterize the turbulent flow properties in a torus reactor. The axial velocity was determined by using an electrochemical velocity probe (Legrand et al., 1993). These measurements were compared with previous data obtained from residence time distribution and visualization experiments. The electrochemical probe was used to perform a spectral analysis of the axial velocity fluctuations. The power spectral density of the axial velocity fluctuations were calculated from the power spectral density of diffusional current measured with the velocity probe through the transfer function of the system. The radial evolution of the turbulence intensity and rate of dissipation were determined at two different axial positions. These parameters enable the estimation of Kolmogorov microscale values for different Reynolds numbers.

Experimental Apparatus and Procedure

The experimental test apparatus of toroidal geometry, made of transparent PVC, was composed of four bends at 90 deg, connected by four straight lengths (Fig. 1), and was placed horizontally. The internal tube diameter, d_t, was equal to 67 mm, the mean circumference of the torus was 2500 mm, which corresponds to a volume of 9.2 l. The fluid circulation inside the torus was generated by the rotation of a marine screw impeller (impeller diameter, $d_1 = 53$ mm; impeller axis diameter, $d_2 = 12$ mm; pitched angle of the blade, $\phi = 45$ deg). The rotation speed was varied between 100 and 1800 rpm. The hydrodynamic characteristics of the toroidal flow were investigated by using a velocity probe, the principle of which is based on the electrodiffusional determination of the mass transfer coefficients at a stagnation point. The electrochemical method was carried out by performing the cathodic reduction of potassium ferricyanide according to the reaction:

$$F_e(CN)_6^{3-} + e^- \rightarrow F_e(CN)_6^{4-}$$

This reaction has the advantage of being fast and not affecting the mass transfer surface. The electrolyte consisted of an equimolar ($2.0\ 10^{-3}$ M) solution of potassium ferri and ferrocyanide with sodium hydroxide (0.5 M). The physical properties of the electrolyte at 25°C are: $\nu = 9.33\ 10^{-7}\ m^2/s$; $\rho = 1020\ kg/m^3$; $D = 5.66\ 10^{-10}\ m^2/s$.

Contributed by the Fluids Engineering Division for publication in the JOURNAL OF FLUIDS ENGINEERING. Manuscript received by the Fluids Engineering Division February 14, 1996; revised manuscript received March 26, 1996. Associate Technical Editor: J. A. C. Humphrey.

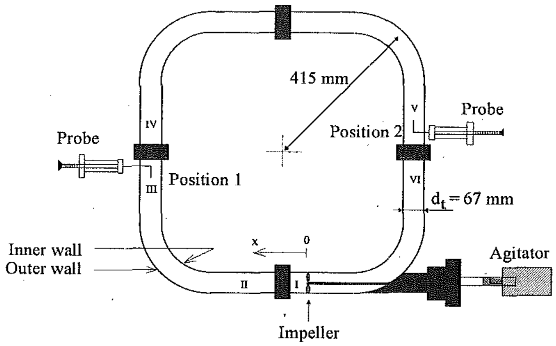

Fig. 1 Sketch of the experimental apparatus (the Roman numerals indicate the visualization sections)

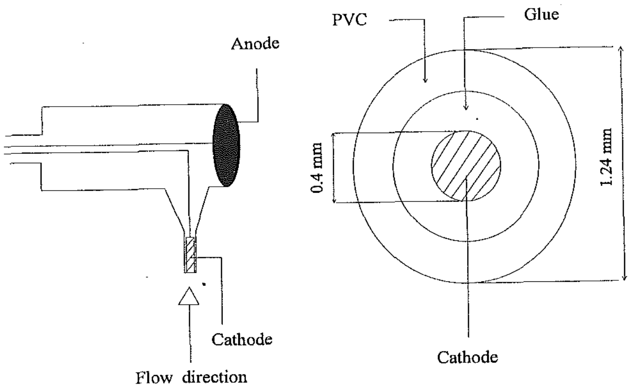

Fig. 2 Description of the electrochemical velocity probe

A two-electrode electric circuit was used. The cathode consisted of the cross-sectional area of a 0.4 mm diameter nickel wire, which was placed in a rigid tube. The external diameter of the probe was 1.24 mm. The anode consisted of a circular nickel disk of 10 mm in diameter. It was placed perpendicularly to the cathode (Fig. 2). Both anode and cathode were fixed in the same PVC support. This design made it possible the use of the probe without any modification of the experimental cell; moreover, the distance between anode and cathode was always the same. The potential between anode and cathode was fixed to 400 mV in order to ensure diffusional conditions on the cathode. The measured diffusional current was very low. It was converted to a tension and amplified with a gain equal to 10^4. The signal treatment was performed using a data acquisition system 3852A from Hewlett-Packard. The sampling frequency was equal to 500 Hz and the sample number equal to 2048 data points. The complete treatment included the calculation of the averaged value of the signal and the spectral characteristics by using Fast Fourier Transform.

The local turbulent properties were obtained by averaging eight records, corresponding to an acquisition time of about 32 seconds. So, taking into account the turbulence level in our experiments (Cousteix, 1989), the relative uncertainties in mean velocity and turbulence intensity were, respectively, equal to ±3 and ±5 percent.

The probe was calibrated in fully developed straight pipe flow (Legrand et al., 1993). The calibration curves were obtained when the velocity probe was located at the center of the tube. For the turbulent regime, the diffusional limiting current I_d is related to the velocity U in the following form:

$$I_d(\mu A) = 0.47U^{0.43}(\mathrm{cm/s}) \qquad (1)$$

Experimental Results and Discussion

Measurements of the Mean Axial Velocity in the Torus. The measurements of the axial velocity were performed at two selected positions in the torus reactor. They were located in straight lengths successively at 70 cm (position 1) and 195 cm (position 2), downstream from the impeller (Fig. 1). In each section the probe was moved through the radial distance. The construction of the probe restrained movement of the cathode between $r/R = -0.79$ to $+0.79$. In Fig. 3(*a*) the variation of the axial velocity in position 1 is plotted as a function of the nondimensional radial distance for various impeller speeds. It can be noticed that the velocity profile is relatively flat for low values of the rotation speed, N (rpm) ≤ 600. For high rotation speed values, $600 \leq N$ (rpm) ≤ 1800, we observe a minimum at the center of the tube. Contrary to the axial turbulent flow through a curved pipe (Azzola et al., 1986), the maximum velocity is located close to the inner wall. Visualization of the flow just downstream of the impeller showed a recirculation zone in the central part of the tube. The length of the recirculation zone is a function of the rotation speed of the impeller (Khalid, 1993). Therefore, the fluid particles located outside of this region are accelerated. In the same way, the secondary flow due to the centrifugal effect coupled with the helical motion due to the agitation disturbs the symmetrical profile that exists upstream of the impeller. Next, the trajectory of particles is oriented towards the inner wall of the torus. This causes a radial pressure gradient at the end of the bend, which accelerates the fluid particles near the inner wall. Figure 3(*b*) illustrates the axial velocity profile for different impeller speeds in position 2, located at about $\frac{3}{4}$ torus circumference from the impeller. It can be noticed that a relatively flat profile is obtained for all the studied values of the rotation speed. For high rotation speed we observe a slight deformation of the profile. The minimum velocity is located midway between the center and the inner wall, with an acceleration of the fluid elements near the inner wall.

Nomenclature

d_1 = impeller diameter
d_2 = impeller axis diameter
d_{ob} = probe diameter
d_t = tube diameter
D = diffusion coefficient
f = frequency
Fg = geometrical parameter, $Fg = (d_1^2 - d_2^2)/(d_t^2)\, tg\phi$
$H(f)$ = transfer function
i' = fluctuating current
I_d = diffusional limiting current
j = complex number
k = wave number, $k = (2\pi/\bar{U})f$
L = length of the torus reactor
N = rotation speed of the impeller
r = radial distance
R = internal radius of the tube, $R = d_t/2$
Re = Reynolds number, $\mathrm{Re} = U_c d_t/\nu$
Re_m = mixing Reynolds number, $\mathrm{Re}_m = Nd_1^2/\nu$
Sc = Schmidt number, $\mathrm{Sc} = \nu/D$
t_c = circulation time
u' = fluctuating velocity
$\bar{U}$ = time averaged axial velocity
U_c = circulation velocity
$W_{i'}(f)$ = diffusional power spectral density (PSD of the current fluctuations)
$W_{u'}(f)$ = hydrodynamic power spectral density (PSD of the axial velocity fluctuations)
ϕ = pitched angle of blades of the impeller
ϵ = dissipation rate of energy per unit mass
ν = kinematic viscosity
η = Kolmogorov's microscale
ω = pulsation, $\omega = 2\pi f$
ω_- = nondimensional pulsation, $\omega_- = (d_{ob}\omega/k_p\bar{U})\mathrm{Sc}^{1/3}$

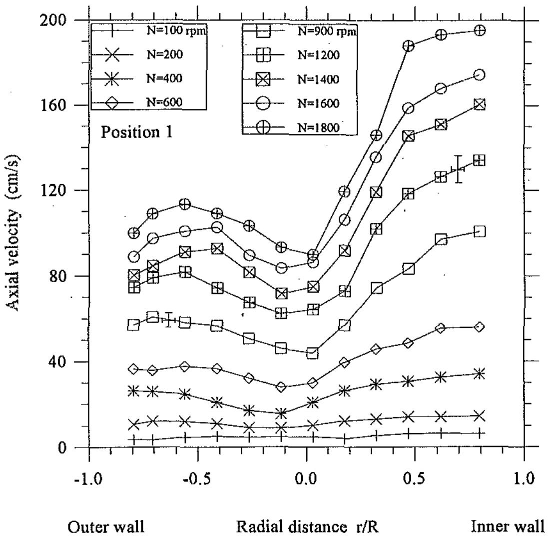

Fig. 3(*a*)

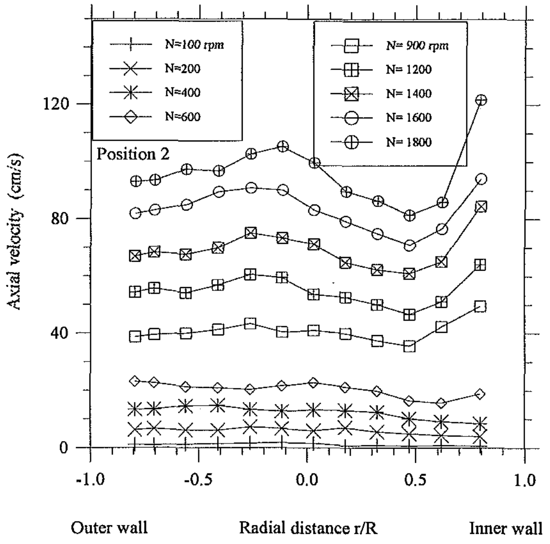

Fig. 3(*b*)

Fig. 3 Radial profile of the axial velocity in the torus: (*a*) position 1; (*b*) position 2; Uncertainty: ±3 percent

The results indicate that the flow in the torus is composed of the axial velocity, which ensures the circulation of the fluid through the longitudinal trajectory, the circumferential velocity, responsible for the helicoidal motion and the radial velocity generated by the radial pressure gradient due to the bend curvature. These constatations indicate that the velocity distribution presents a region where the maximum velocity follows the helicoidal motion. These results are consistent with those of Sato et al. (1979).

The mean axial velocity was obtained from the results of the velocity profile measured by the electrodiffusional method. The results are compared with the values determined by using the residence time distribution (RTD) method (Legrand et al., 1993) and those obtained by using a visualization technique. The experimental determination of RTD is based on the measurements of electrical conductivity variations of an electrolyte. A pulse of NaOH tracer was injected with a syringe into the torus. The conductivity of the fluid was detected by a platinum wire microprobe similar to those described by Torrest and Ranz (1969) and by Manning and Wilhelm (1963). The injection is located in the stirred zone of the impeller and the volume of tracer injected at each run is 0.5 cm^3 of NaOH. The RTD curves are independent of the radial position of the probe, which demonstrates that the radial mixing in the torus is very good. The analysis of RTD curves provides the average circulation time t_c. For a given impeller speed, t_c is the time necessary for a fluid particle to cover the torus circumference. It corresponds to the time between two successive peaks of concentration. Therefore, we can define a mean circulation velocity U_c as the ratio of torus length, L, to the circulation time:

$$U_c = \frac{L}{t_c} \tag{2}$$

The flow visualization was performed by using a laser tomography technique. The objective was to follow the motion of the particle-tracers with time. The particles were 0.3 mm diameter polystyrene spheres, the density of which is approximately equal to water at room temperature. The visualization results were obtained from negative photographs. Knowing the lighting frequency and the distance between two successive positions of one particle enables one to calculate the local velocity at different radial locations of the measure section. The local velocity was determined at six different positions (I to VI) in the torus (Fig. 1). In Fig. 4, the results of the different methods are compared with the empirical equation relating the fluid circulation and the rotation speed, expressed with nondimensional parameters as follows (Belleville et al., 1992):

$$\mathrm{Re} = 1.43 F_g \, \mathrm{Re}_m \tag{3}$$

where Re is the circulation Reynolds number, which characterizes the fluid circulation along the tube. This parameter is based on the inner tube diameter and the circulation velocity of the fluid. Re_m is the mixing Reynolds number, which characterizes the mixing inside the torus. It is based on the rotation speed of the agitator and the external diameter of the impeller. F_g is a geometrical parameter defined by:

$$F_g = \frac{d_1^2 - d_2^2}{d_t^2} \, tg\phi \tag{4}$$

In our experimental conditions F_g is equal to 0.575.

The discrepancy noticed between the axial velocities at positions 1 and 2 for the electrochemical method has two principal reasons. First, the velocity profile was integrated on the horizontal diameter and not on the whole cross-section. Then, due to the three-dimensional character of the flow, especially at

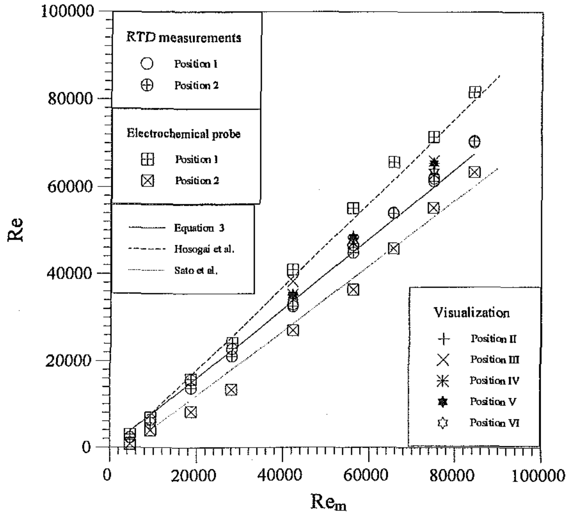

Fig. 4 Evolution of the circulation Reynolds number, Re, with the mixing Reynolds number, Re_m. Precision of ordinate: ±3.3 percent; precision of abscissa: ±1.5 percent.

position 1, the averaging procedure is not precise. Second, it is also due to the space required by the probe, in particular near the wall, indeed the nearest measures were carried out at 7 mm from the pipe walls, the average values of the axial velocity was calculated by using a polynomial function, which were representative of the velocity profile without consideration of the evolution of the velocity in the near-wall region. Thus for high rotation speed values the averaging procedure becomes inaccurate due to the lack of information near the walls. Nevertheless, the interest of the electrochemical measurement remains large by comparison with other techniques. It is distinguished by obtaining the local values of the instantaneous velocity along the radial distance, except near the wall. Then it allows to follow the evolution of the velocity profile in the transversal section and to characterize the turbulence inside the torus. According to the respective accuracy of the different experimental techniques, a good agreement is found between the present experimental data and Eq. (3), which was established with the residence time distribution data.

In Fig. 4 we have plotted the experimental results of Hosogai and Tanaka (1992), who were interested in the study of the flowing characteristics in a circular loop reactor. The performance of the torus have been performed by these authors in order to apply this configuration to the heterogeneous liquid-liquid reaction operation such as suspension polymerization of styrene. The circular loop reactor consists of two parts of the semicircular glass pipe. The marine screw and pitched blade paddle impellers were used as generators of the flow. They showed that the type and the pitch angle of the impellers deeply influence the level of the mean axial velocity inside the torus. In order to compare our results, we were particularly interested in the data of the flow generated by the marine screw impeller with 45 deg pitched angle. Due to the absence of the straight lengths the experimental results of Hosogai and Tanaka (1992) show higher values of the circulation Reynolds numbers as function of the mixing Reynolds numbers (Fig. 4).

Sato et al. (1979) have investigated the circulation flow through the elbowed loop reactor corresponding to the same configuration than the one studied in this paper. The axial velocity distribution was measured by using the conductivity method and compared with values obtained from a proposed discharge flow model. The range of Reynolds number investigated by Sato et al. (1979) was $2.3\ 10^3$–$2.0\ 10^5$.

They obtained lower values of the circulation velocities by comparison with Hosogai and Tanaka (1992). The differences between the results are not so large and remain acceptable by taking the size and different operating conditions into account. At least, in the turbulent flow regime, all the results show that the mean fluid velocity is proportional to the impeller speed. According to the experimental ascertainty (13 percent) by comparison with Eq. (3) our experimental results are in good accordance with the literature data.

Turbulent Rate Velocity in the Toroidal Loop. In the studied configuration, the values of the circulation Reynolds number, Re, were high and represented turbulent flow. The velocity fluctuations $u'(t)$ were transformed *to* current fluctuations $i'(t)$ on the electrochemical probe. In the frequency domain, it was shown (Nakoryakov et al., 1986) that the power spectral density (PSD) of the diffusional current fluctuations $W_{i'}$ is linked to the PSD of the velocity fluctuations $W_{u'}$ through the following expression:

$$W_{i'}(f) = |H(f)|^2 W_{u'}(f) \tag{5}$$

where $H(f)$ is the transfer function of the diffusional current response of a microelectrode to a sinusoidal modulation of a steady flow. The analytical expression of this function was given by Nakoryakov et al. (1986):

$$|H(j\omega)| = \left[1 + \frac{\omega_-^2}{15\ \mathrm{Sc}^{2/3}}\right]^{1/4} \times \left[\frac{1 + 2.32\ 10^{-3}\omega_-^2}{1 + 4.45\ 10^{-2}\omega_-^2 + 1.49\ 10^{-4}\omega_-^4}\right] \times |H(0)| \tag{6}$$

with

$$\omega_- = \left[\frac{d_{ob}\omega}{k_p \bar{U}}\right] \mathrm{Sc}^{1/3}$$

k_p is a numerical constant depending on the geometry of the probe, in our case $k_p = 2$. $H(0)$ is the value of the transfer function for $\omega = 0$. It was obtained from the calibration curve of the probe (eq. 1), then:

$$|H(0)| = 0.43\,\frac{\bar{I}}{\bar{U}} \tag{7}$$

in which $\bar{I}(\mu A)$ and $\bar{U}$(cm/s) are, respectively, the time-averaged value of the diffusional current and axial velocity.

In order to follow the evolution of diffusional and hydrodynamic spectral densities in the same order of magnitude, we have plotted in Fig. 5(a) the evolution of the ratio $W_{i'}(f)/|H(0)|^2$ and $W_{u'}(f)$ with the frequency. The graph shows the influence of the transfer function on the spectral density and the cut-off frequency corresponding to the transition between the low frequency plateau and the inertial subrange (Deslouis et al., 1993). The power spectral densities of the axial velocity fluctuations plotted in Fig. 5(a) correspond to an average of eight different runs performed in the same operating conditions. It can be noticed (Fig. 5(a)) that the hydrodynamic f_{ch} and diffusional f_{cd} cut-off frequencies are of the same order of magnitude for different Reynolds numbers. The location of these parameters in the spectrum densities curves shows that the order of magnitude of the wavelength of large structures, associated with the low frequency plateau, is about twice that of the tube diameter. These data show that the flow structures are stretched along the mean flow direction. This stretching was observed in the fully developed channel flow by Deslouis et al. (1993), who obtained a wavelength corresponding to the large structures equal to 2.75 times the height of the channel. The large eddies were also observed in a rectangular bend flow with axial entry, where the vortex stretching is caused by the curvature (Shiragami, 1989). The influence of the transfer function, which marked the difference between the hydrodynamic and diffusional PSD curves, was noted at the start of the inertial subrange. In this domain the energy spectrum is consistent with Kolmogorov's theory of isotropic turbulence, where the slope is equal to $\frac{-5}{3}$. For high frequencies (f greater than 130 Hz) the dissipation energy spectrum $f^2 W_{u'}(f)$ was approximated by a decreasing function proportional to f^{-5} (Fig. 5(b)), which corresponds to the viscous dissipation of energy (Wolff and Cognet, 1985).

The turbulence rate is given by the relative turbulence intensity, defined by the ratio $(\sqrt{\overline{u'^2}}/\bar{U})$. The fluctuating velocity is obtained by integration of the power spectral density (PSD) of the hydrodynamic fluctuations in the whole frequency range (Reynolds, 1974):

$$\overline{u'^2} = \int_0^\infty W_{u'}(f)\,df \tag{8}$$

In Figs. 6(a) and 6(b) we have plotted the variation of the turbulence intensity of the axial velocity versus the radial distance for positions 1 and 2. The turbulence intensity is quasi-independent of the rotation speed variation of the impeller. In position 1, it is equal to 18 percent between the outer wall and the center of the tube and decreases progressively to 8 percent near the inner wall at $r/R = 0.8$. We note that the turbulence

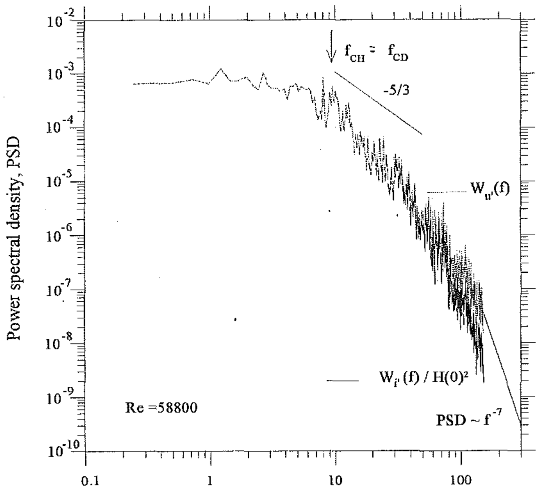

Fig. 5(*a*)

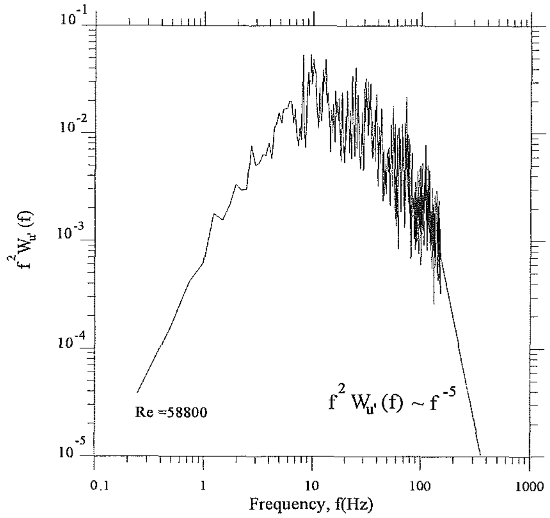

Fig. 5(*b*)

Fig. 5 Spectral analysis of axial velocity fluctuations in position 1 for Re = 58800 and $r/R = 0.03$: (*a*) power spectrum density of hydrodynamic ($W_{u'}$) and diffusional ($W_{i'}$) fluctuations; (*b*) variation of the dissipation energy spectrum, $f^2 W_{u'}(f)$

intensity in this region was practically the same for all rotation speed values between 600 and 1800 rpm and clearly lower than turbulence rate near the outer wall. In Fig. 6(*b*) we follow the evolution of the turbulence intensity in position 2 for the rotation speed values between 900 and 1800. The values vary between 9 and 16 percent through transversal distance. In this case, the influence of the impeller rotation speed was more important near the inner wall than near the outer one.

Our averaged experimental values of the turbulence intensities are reported in Figs. 6(*c*) and 6(*d*). The extreme values corresponding to Reynolds numbers between 23,000 and 70,000 are also indicated. With regard to the literature, the experimental results, which concern the turbulence characteristics of the flow configuration investigated here, were restricted. Thus, we have compared our results with similar types of turbulent flow in curved pipe or channel and in swirl flows. This study enables one to show the contribution to the mixing of the swirl flow, generated by the rotation of the impeller, by the comparison with the axial turbulent flow in a bend.

Because of their importance to many applications in engineering, the latter have been extensively investigated and the studies cover a wide range of Reynolds number and type of

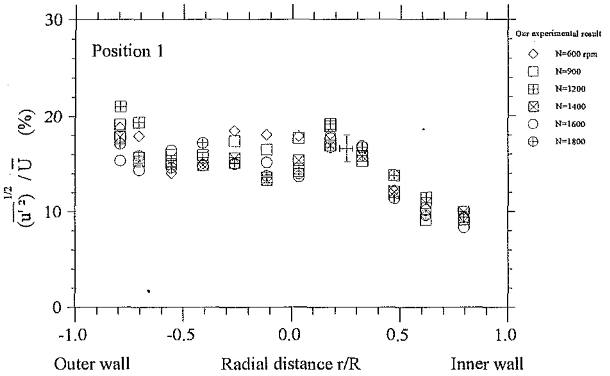

Fig. 6(*a*)

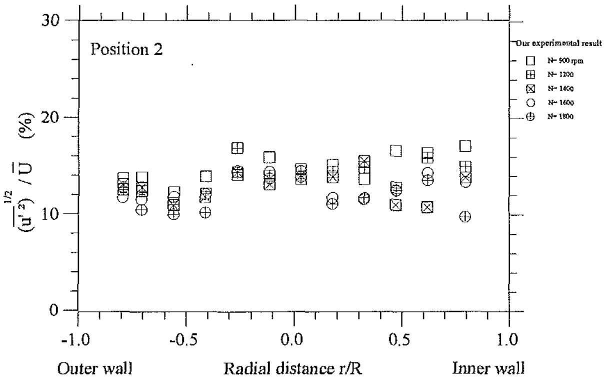

Fig. 6(*b*)

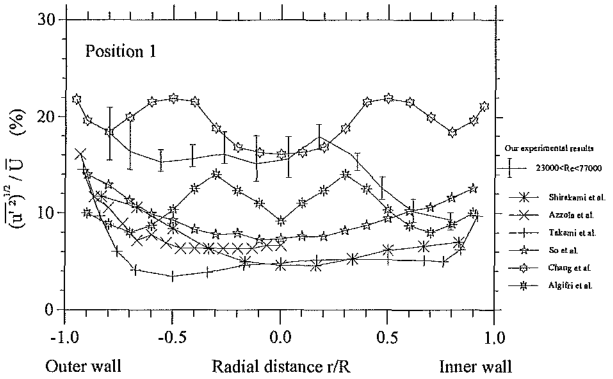

Fig. 6(*c*)

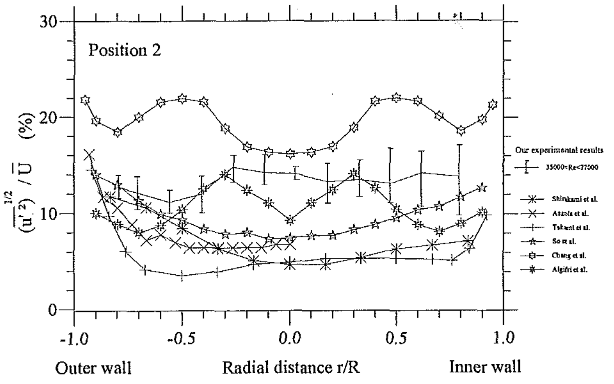

Fig. 6(*d*)

Fig. 6 Radial variation of the turbulence intensity: (*a*) position 1; (*b*) position 2. (*c* and *d*) Comparison with the literature available data Uncertainty: ±5 percent.

configurations such as the bends of 90 and 180 deg. Among these works, Shirakami et al. (1989) were interested in the study of the turbulent quantities in a rectangular bend at 90 deg by using the electrochemical method. The results of turbulence intensity of the axial velocity for this flow configuration at the exit of the bend for Re = 18000 are shown in Figs. 6(*c*) and 6(*d*). The values of $\sqrt{\overline{u'^2}}/\bar{U}$ were larger in the neighbourhood of the outer wall ($\sqrt{\overline{u'^2}}/\bar{U}$ = 10 percent) as compared with those in the neighbourhood of the inner wall, in which the turbulence intensity was equal to 8 percent. Otherwise this rate remains lower in the center of the tube with 5 percent as value of turbulence intensity. It can be considered that the turbulence intensity expressed the fact that the flow field has a stabilizing effect in the neighbourhood of the inner wall and a destabilizing effect in the neighbourhood in the outer wall. Takami et al. (1990) have studied the developing turbulent flow through a curved pipe at 180 deg for a Reynolds number equal to 19000 by using the Laser-Doppler velocimeter. These authors pointed out that the turbulence intensity is larger near the walls. It can be reached 20 percent close to the outer wall and was equal to 10 percent near the inner wall. In the core of the flow the turbulence level was slightly lower than 5 percent. Azzola et al. (1986) studied the evolution of the turbulent flow in a U-bend of circular cross-section. They showed that the axial turbulence distribution was larger near the pipe wall, in particular, the outside one and decreased at the center portion of the tube. In any case, the turbulence intensities measured in the bends with axial inlet of the flow remain lower than those of the torus with the swirl flow generated by the rotation of the impeller. The difference between the values was more important in the core region. Far from the mixing zone, the turbulence rate seems to have the same behavior on both walls.

Otherwise, we have given the experimental results of the swirl flow in a straight pipe, in order to analyze the effect of the swirl flow only without the curvature on the turbulence characteristics. Algifri et al. (1987, 1988) have studied the turbulent swirled flow in a cylindrical tube for different Reynolds numbers and for different swirl numbers. In these measurements, air was used as the working fluid and the swirling motion was given by means of the radial cascade with adjustable blades installed at the inlet of the test pipe. These authors show that the turbulent intensities are independent of the Reynolds number which confirms our observations. In a normal free swirl pipe flow, the components of the turbulent intensities are observed to have high values in the vicinity of the pipe wall. Their experimental data indicate that the swirl of the stream has a tendency to increase the turbulence intensities in the region close to the axis of the pipe at $r/R \sim 0.3$. As such with the swirl decay along the pipe axis, the turbulent intensities reduce at a faster rate in the direction of the flow within the core region than the vicinity of the pipe wall. Qualitatively these results are, in general, in agreement with the observations of Chang and Dhir (1995). The latter were interested in the study of turbulent swirl flows in a tube. The flow field was induced by injecting fluid tangentially through injectors, placed on the periphery. The Reynolds number in the tube was equal to 12,500 and the measurement section was situated at 10 diameters downstream of the entrance. A quantitative analysis shows that turbulence intensities are promoted by the swirl motion significantly and are about 15–20 percent of the bulk velocity. They show a local maximum near $r/R \sim 0.5$. The minimum was located in the middle of the core region. However the turbulent level in this configuration remains the highest by respect the other flow configurations. This was probably due to the mode of generation of the swirl flow, which provoked a great mixing in the entrance region due to the tangential fluid injection.

In Figs. 6(*c*) and 6(*d*), the experimental results of Anwer and So (1993) are also plotted. They have studied the swirling of the turbulent flow through a curved pipe. For these experiments two straight pipes were joined by a 180 deg bend, so that a fully developed turbulent pipe flow can be established at the entrance of the curved bend. A 6 diameters long rotating cylinder was installed at 6 diameters upstream of the curved bend entrance. Air flow through the pipe was provided by a centrifugal blower installed at the exit end of the test rig. Reynolds number, based on pipe diameter and mean velocity along the axial direction, was equal to 50,000. The mean and turbulent flow properties were provided by rotating hot wires. The radial distribution of the turbulence intensity for this configuration shows that the walls benefit of high values, more particularly the outer wall with a rate equal to 15 percent at $r/R = -0.1$. A progressive decrease was observed from the wall towards the center region of the tube. The core flow, which corresponding to $-0.3 \leq r/R \leq 0.3$ maintains a value of turbulence intensity equal to 8 percent. Because it was classified in the category of the swirling turbulent flow through a curved pipe, this configuration seemed to give the most similar type of the flow than the ours. Nevertheless, the discrepancy with our results are large particularly in the core of the flow. This is due to the difference between the mode of the generation of the swirl flow. The rotation of the marine screw impeller provokes higher turbulence level than the one induced by rotation of the cylinder installed upstream of the curved bend. In addition, our measurement positions with regard to the location of the swirl flow generators are different. This makes difficulties to compare our experimental results.

In order to apprehend the turbulence characteristics in the torus reactor, it was necessary to discuss the turbulent rate behaviour in the two different regions.

The first part concerns the region near the wall. It is noted the same behavior than that of the axial curved flow, with a turbulence intensity higher close to the outer wall than the inner one. In our experimental conditions, the rotation of the impeller speed up the secondary flow near the outer wall.

The second zone concerns the central portion of the tube, which benefits by a turbulence intensity higher than that observed through a bend at 90 or 180 deg with axial flow at the inlet. The turbulence level in this region was affected by the turbulent kinetic energy, communicated by the rotation of the impeller. The turbulence rate of the axial velocity is increased to attain 18 percent in position 1. This influence reduces far from the mixing zone with a rate equal to 14 percent in position 2.

Furthermore, the hydrodynamic power spectral density (PSD) can be used to estimate the values of the dissipation rate of energy by using the following relation, valid for isotropic turbulence (Cousteix, 1989):

$$\epsilon = 15\nu \int_0^\infty k^2 W_{u'}(k)dk \tag{9}$$

where k is the wavenumber given by Taylor's hypothesis:

$$k = \frac{2\pi}{\bar{U}} f \tag{10}$$

The variation of the dissipation rate of energy per unit mass against radial distance in positions 1 and 2 is shown in Figs. 7(*a*) and 7(*b*) for different rotation speed values. In position 1, it is noticed that the maximum dissipation is observed at the center of the tube, except for Re > 67000. The dissipation rate has an oscillating evolution between the center and outer wall. Otherwise, the minimum dissipation is located near the inner wall; its value remains, for different Reynolds numbers, lower than 0.01 m^2s^{-3} in this region, which corresponds to the large eddies dissipative of energy due to the shear flow. In fact, the mean wall shear stress is lower near the inner cylinder (Khalid, 1993). In position 2, the profile of dissipation rate of energy is relatively uniform in the section for all the Reynolds numbers. Figure 8 provides the dependence of the average dissipation

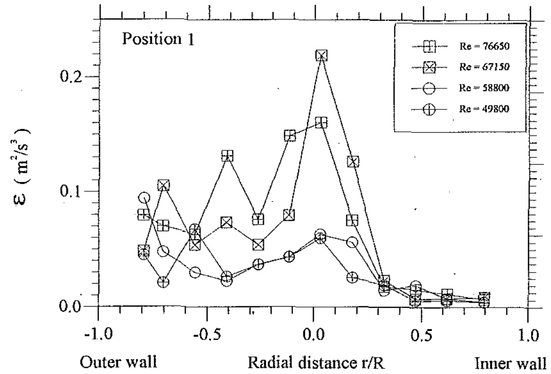

Fig. 7(*a*)

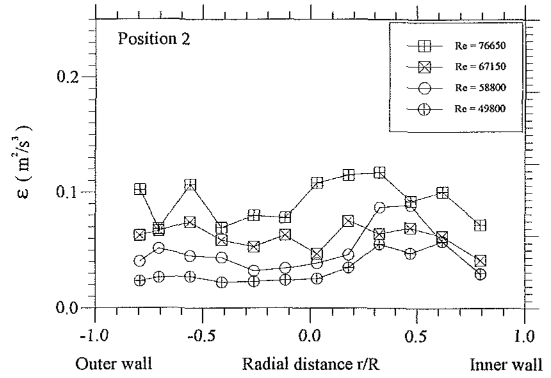

Fig. 7(*b*)

Fig. 7 Radial profile of dissipation rate of energy per unit mass: (*a*) position 1; (*b*) position 2; Uncertainty: ±14 percent

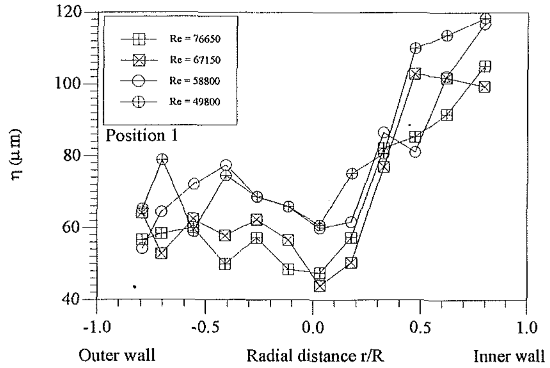

Fig. 9(*a*)

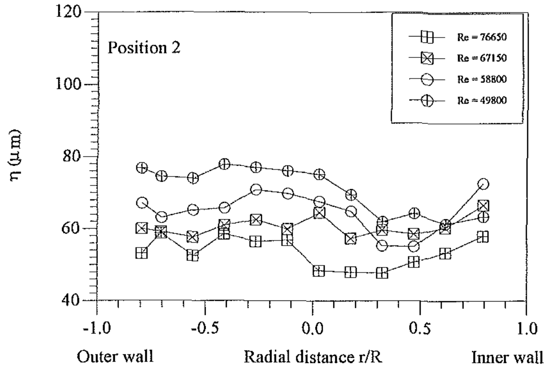

Fig. 9(*b*)

Fig. 9 Evolution of Kolmogorov's microscales with the radial distance: (*a*) position 1; *b*) position 2; Uncertainty: ±3.6 percent

rate with the circulation Reynolds number values. This rate was calculated from the values of different locations of the both positions 1 and 2. Hosogai and Tanaka (1992) proposed the following equation for the turbulent dissipation rate of energy in a toroidal geometry:

$$\epsilon = 8.8\ 10^{-2}\ \frac{\nu^3}{d_t^4}\ \mathrm{Re}^{2.75} \tag{11}$$

This equation enables one to relate the average of dissipation rate of energy per unit mass to the hydrodynamic characteristics of the flow and those of the rector such as the average circulation velocity and the tube diameter of the torus. Quantitatively, for high Reynolds numbers, our experimental results are in agreement with the values obtained by the last equation.

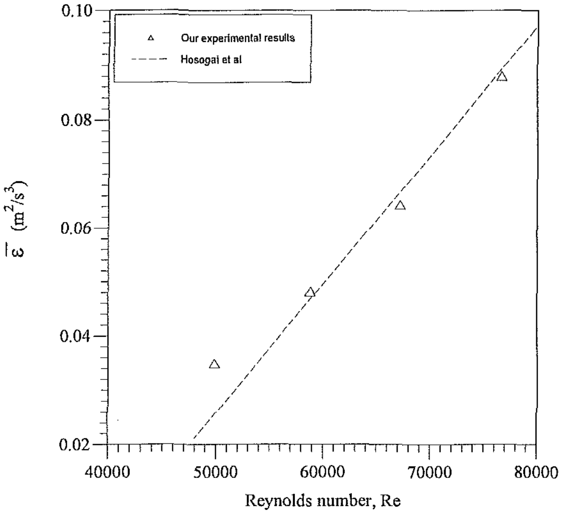

Fig. 8 Variation of the average rate of dissipation per unit mass with Reynolds number. Precision of ordinate: ±14 percent; precision of abscissa: ±3.3 percent.

The dissipation rate of energy can be used to estimate the Kolmogorov microscale η:

$$\eta = (\nu^3/\epsilon)^{1/4} \tag{12}$$

and by using Eq. (11), it is obtained:

$$\eta = 1.84 d_t\ \mathrm{Re}^{-11/16} \tag{13}$$

Due to its dimensions the electrochemical probe gives an order of magnitude of the microscale, which corresponds to the size of the smallest eddies, under which the viscous effect is very strong. In our experiments η varies between 50 μm and 80 μm in a range of Reynolds numbers between 49,000 and 77,000, except near the inner wall in position 1, where η increases progressively to reach 120 μm (Fig. 9). The increase of η near the inner cylinder in position 1 is related to the decrease of the dissipation rate; large eddies generate high turbulent kinetic energy and reduce the dissipation rate. Kolmogorov's microscales in our configuration have the same order of magnitude as those estimated in the center of the straight tube with fully turbulent flow by Davies (1972), who established the following correlation:

$$\eta = 4 d_t\ \mathrm{Re}^{-0.78} \tag{14}$$

Using this expression with our experimental conditions, the values of η are between 40 μm and 60 μm. The experimental measurements obtained by Robin (1987) in a fully developed flow in a square duct showed that the values of Kolmogorov's microscales varied between 70 μm and 48 μm when the Reynolds number increases from 11250 to 24500. It can be concluded that our experimental results are in good agreement with the values of η obtained in fully turbulent flow.

Conclusion

The fluid circulation induced in a toroidal geometry by an agitator is affected by a secondary motion due to the curvature. Therefore a perturbation can be seen in the axial velocity profile. After the first bend downstream of the impeller, the maximum velocity was shifted toward the inner wall. A recirculation zone is set up in the center of the tube. Far from the impeller, the degeneration of swirl flow was observed. The axial velocity profile is flat with slight deformation near the inner wall, which is due essentially to the curvature geometry.

The measurement of turbulence properties in two positions situated successively at 70 cm and 195 cm downstream of the impeller indicates that the variation of the rotation speed has no influence on the turbulence intensity of the axial velocity. In the zone of strong agitation, the maximum value of turbulence intensity is located between the outer wall and the center of the tube and varies between 17 and 20 percent. Toward the inner wall, the decrease of turbulence intensity of the velocity is continuous to attain a value equal to 8 percent. Finally, far from the zone of intense agitation, the radial distance has no influence on the longitudinal turbulence intensity.

References

Algifri, A. H., Bhardwaj, R. K., and Rao, Y. V. N., 1987, ''Prediction of the Decay Process in Turbulent Swirl Flow,'' *Proceedings of Institution of Mechanical Engineers,* Vol. 201, No. C4, pp. 279–283.

Algifri, A. H., Bhardwaj, R. K., and Rao, Y. V. N., 1988, ''Turbulent Measurements in Decaying Swirl Flow in a Pipe,'' *Applied Scientific Research,* Vol. 45, pp. 233–250.

Anwer, M., and So, R. M. C., 1993, ''Swirling Turbulent Flow Through a Curved Pipe. Part I: Effect of Swirl and Bend Curvature,'' *Experiments in Fluids,* Vol. 14, pp. 85–96.

Azzola, J., Humphrey, J. A. C., Iacovides, H., and Launder, B. E., 1986, ''Developing Turbulent Flow in U-Bend of Circular Cross-Section: Measurement and Computation,'' ASME JOURNAL OF FLUIDS ENGINEERING, Vol. 108, pp. 214–221.

Belleville, P., Nouri, L., and Legrand, J., 1992, ''Mixing Characteristics in the Torus Reactor,'' *Chemical Engineering of Technology,* Vol. 15, pp. 282–289.

Blenke, H., 1979, ''Loop Reactors,'' *Advances in Biochemical Engineers,* 13, Springer-Verlag, pp. 121–214.

Chang, F., and Dhir, V. K., 1995, ''Mechanisms of Heat Transfer Enhancement and Slow Decay of Swirl in Tubes Using Tangential Injection,'' *International Journal of Heat and Fluid Flow,* Vol. 16, pp. 78–87.

Cousteix, J., 1989, ''Turbulence et couche limite,'' Cepadues Edition, Toulouse, 114–163.

Davies, J. T., 1972, *Turbulence Phenomena,* Academic Press, INC, London, pp. 49–62.

Deslouis, C., Huet, F., Robin, S., and Tribollet, B., 1993, ''Spectral Analysis of Wall Turbulence with Photolithography Devised Electrochemical Probes,'' *International Journal of Heat and Mass Transfer,* Vol. 36, pp. 823–829.

Hosogai, K., and Tanaka, M., 1992, ''Study of Suspension Polymerization of Styrene with a Circular Loop Reactor,'' *Polymer Engineering and Science,* Vol. 32, pp. 431–437.

Khalid, A., 1993, ''Etude de l'écoulement généré par une hélice dans un réacteur de forme toroïdale,'' Thèse de Doctorat de l'Université de Nantes—Ecole Centrale de Nantes.

Lavine, A. S., Greif, R. and Humphrey, J. A. C., 1986, ''Three-Dimensional Analysis of Natural Convection in a Toroidal Loop: Effect of Tilt Angle,'' ASME *Journal of Heat Transfer,* Vol. 108, pp. 796–805.

Lee, D. Y., Kuo, J. F., Wang, J. H. and Chen, C. Y., 1990, ''Study on the Continuous Loop Tubular Reactor for Emulsion Polymerization of Styrene,'' *Polymer Engineering and Science,* Vol. 30, pp. 187–192.

Legrand, J., Khalid, A., Rey, C., and Belleville, P., 1993, ''Electrodiffusion Determination of Mass Transfer at the Stagnation Point and its Application to the Measurement of Axial Velocity in Toroidal Flow,'' *Soviet Electrochemistry,* Vol. 20, pp. 70–74.

Manning, F. S., and Wilhem, R. H., 1963, ''Concentration Fluctuations in Stirred Baffled Vessel,'' *American Institute of Chemical Engineering Journal,* Vol. 9, pp. 12–19.

Nakoryakov, V. E., Budukov, A. P., Kashinsky, O. N., and Geshev, P. I., 1986, ''Electrodiffusion Method of Investigation into the Local Structure of Turbulent Flows,'' Gasenko, V., G. and Novosibirsk, eds., Moscow, 42–59.

Reynolds, A. J., 1974, *Turbulence Flows in Engineering,* John Wiley, London, pp. 45–111.

Robin, S., 1987, ''Etude de la turbulence pariétale par la méthode électrochimique,'' Thèse de Doctorat de l'Université Pierre et Marie Curie, Paris VI.

Sato, Y., Murakami, Y., Hirose, T., Hashiguchi, Y., Ono, S., and Ichikawa, M., 1979, ''Flow Pattern, Circulation Velocity and Pressure Loss in Loop Reactor,'' *Journal of Chemical Engineering of Japan,* Vol. 12, pp. 448–453.

Shiragami, N., and Inoui, I., ''Turbulent Velocity Profile and Turbulent Statistical Quantities in a Rectangular Bend,'' *International Journal Engineering of Fluid Mechanics,* Vol. 2, No. 2, pp. 157–176.

So, R. M. C., and Anwer, M., 1993, ''Swirling Turbulent Flow Through a Curved Pipe. Part II: Recovery from Swirl and Bend Curvature,'' *Experiments in Fluids,* Vol. 14, pp. 169–177.

Stern, C. H., Greif, R., and Humphrey, J. A. C., 1988, ''An Experimental Study of Natural Convection in a Toroidal Loop,'' *Journal of Heat Transfer,* Vol. 110, pp. 877–883.

Takami, T., Sudou, K., and Tomita, Y., 1990, ''Flow of Non-Newtonian Fluids in Curved Pipes (Turbulent Flow),'' *Japan Society of Mechanics Engineering International Journal,* Vol. 33, No. 3, pp. 476–485.

Tanaka, M., and O'Shima, E., 1988, ''Dispersing Behaviour of Droplets in Suspension Polymerization of Styrene in a Loop Reactor,'' *The Canadian Journal of Chemical Engineering,* Vol. 66, pp. 29–35.

Torrest, R. S., and Ranz, W. E., 1969, ''Improved Conductivity System for Measurement of Turbulent Concentration Fluctuations,'' *Industrial and Engineering Chemistry Fundamentals,* Vol. 8, pp. 810–816.

Wolff, M., and Cognet, G., 1985, ''Etude locale du frottement pariétal dans un écoulement en conduite courbe,'' *Journal of Applied Mathematics and Physics,* Vol. 36, pp. 221–237.

A First Analysis of Flow Field Hysteresis in a Pump Impeller

K. A. Kaupert

P. Holbein[1]

T. Staubli

Turbomachinery Laboratory,
ETH Swiss Federal Institute of
Technology Zurich,
CH-8092 Zurich, Switzerland

The measured pump pressure discharge characteristic for a high specific speed radial pump ($\omega_s = 1.7$) reveals distinct discontinuities in part load operation. These pressure discontinuities occur at different threshold volume fluxes when increasing or decreasing the pump discharge and make up a hysteresis loop. The pump impeller characteristic was evaluated experimentally and numerically by taking the difference between the integrated impeller outlet and impeller inlet total pressure. The experimental and numerical characteristics agree well including the volume flux location and magnitude of the pressure discontinuities in the hysteresis loop. For volume fluxes within the hysteresis loop two stable well converged flows were calculated numerically. The numerical calculations were made on coarse and fine grids using commercially available software with and without the impeller clearance leakage flow. Further experimental and numerical comparisons are made at the impeller inlet/outlet with emphasis on the changing flow field in the hysteresis loop flow regime and its coupling to the onset of reverse flow zones. This combined application of numerical and experimental tools provides insight for the hysteresis flow field of a pump impeller characteristic.

1 Introduction

The prediction of the pump impeller characteristic with numerical computations is a valuable tool to pump manufacturers expediting design and modification processes. The designed impellers must later be proven on site over the operational domain and meet commercial customer guarantees. Pumps with large pressure discontinuities in part load operation are usually not accepted by clients because the discontinuities are often paired with positive slope characteristics which can lead to pump system instability.

The pressure discontinuity of a pump impeller pressure discharge characteristic is problematic to all parameters in part load operation, complex to predict both empirically and numerically. To our knowledge the data presented in this article are the first to give a numerical prediction of its occurrence.

In the literature explanations for the characteristic's pressure discontinuity range from a dependence on blade loading, changing incident flow angles, adverse pressure gradients in the pump impeller passages, impeller outlet flow volute tongue interaction, to a combination of the above which have been given ample attention in various surveys (Breugelmans and Sen, 1982; Fraser, 1982; Gülich, 1995; Hergt and Jaberg, 1989; Tanaka, 1980).

Investigated was a radial pump of high specific speed ($\omega_s = 1.7$, $n_q = 90$) which belongs to the category of pumps known to exhibit discontinuities in the pressure discharge characteristic (Hergt and Starke, 1985). The highly three-dimensional unsteady flow provides a complex test case for both numerics and experiments.

In the following, a detailed numerical analysis of the flow in this pump is presented coupled with experimental validation, together providing insight of the internal pump flow field within the hysteresis.

2 The Test Facility and Instrumentation

Under investigation was a single stage pump designed for the paper industry to transport slurry inhomogeneous substances. The impeller of outlet diameter $D_2 = 324$ mm ran within a double spiral volute to minimize radial forces. The impeller and meridional view with measurement traversal locations are depicted in Fig. 1, set at one circumferential position 90 deg from both volute tongues. Geometric specifications were,

- 7 blades, shrouded impeller,
- $D_1/D_2 = 0.83$ impeller inlet tip diameter,
- $B_2/D_2 = 0.27$ blade outlet height,
- $D_3/D_2 = 1.22$ volute tongues inlet diameter,
- 33 deg blade outlet back lean angle, 20 deg blade outlet rake,
- impeller material, gray mould steel 25.

The experiments were performed at a rotational speed of 750 rpm ($u_2 = 12.71$ m/s), having a best efficiency point (bep) volume flux of 0.196 m^3/s ($\phi = 0.174$) and a pump head of 5.8 m ($\psi = 0.704$).

Water at 18°C for the open pump circuit was drawn from an 80 m^3 reservoir into the pump through a flow straightener to provide uniform inlet flow at a Reynolds number of order 10^6 based on the blade chord. A booster pump increased the NPSH to avoid cavitation.

The test rig instrumentation consisted of devices for obtaining both global and local flow field pump data. Global pump data are the following quantities,

- volume flux, measured with a magnetic flow meter,
- head, measured differentially (ISO, 1987),
- shaft torque, measured with strain gages,
- rotational speed, measured optically (3600 pulses/rotation).

Errors associated with these measurements lie under ±0.5%.

Local flow field pump data were obtained as steady pressure and velocity distributions, measured with a 5 hole cylindrical probe. Errors associated with the 5 hole probe are ±2% in less disturbed flow, in complex flow zones the error rises substantially due to larger flow inertial, circulation, and secondary flow effects (Humm and Verdegaal, 1992). Unsteady flow field data was obtained using a fast response cylindrical one hole probe. Both probes were calibrated in an air free jet facility (Kupferschmied and Gossweiler, 1992) at the appropriate Reynolds number.

---

[1] Now at Sulzer Innotec Ltd., CH-8401 Winterthur, Switzerland.

Contributed by the Fluids Engineering Division for publication in the JOURNAL OF FLUIDS ENGINEERING. Manuscript received by the Fluids Engineering Division January 17, 1996; revised manuscript received September 6, 1996. Associate Technical Editor: B. Schiavello.

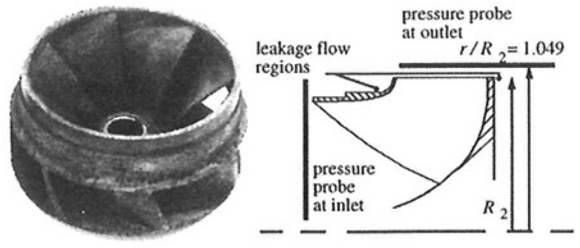

Fig. 1 The impeller and the pressure probe measuring positions

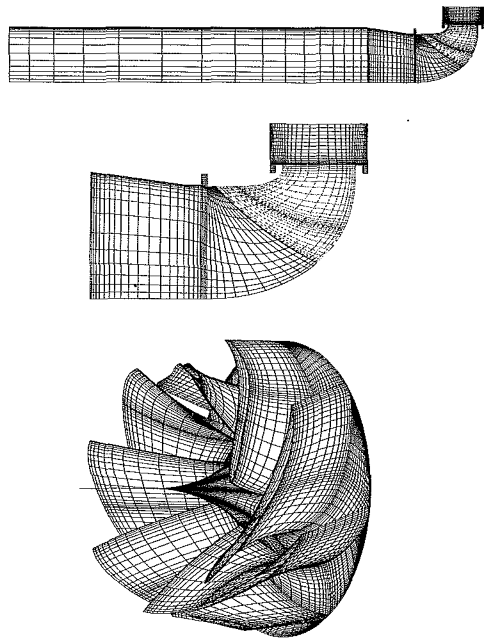

Fig. 2 The impeller and suction pipe numerical coarse grids. Impeller shroud is removed for viewing purposes.

3 Numerics

The numerical flow computations were performed for the same operating conditions as the experiments with the commercially available TASCflow code version 2.3. This code performs Reynolds averaging of the Navier Stokes equations in strong conservative form using a time marching procedure to obtain a steady state solution. A standard k-ϵ model was used for turbulence modeling (ASC, 1994). A coarse grid with 41,000 nodes was first implemented for the impeller, vaneless diffuser, and inlet suction pipe, shown in Fig. 2. No attempt was made to model the double spiral volute in which the experimental pump impeller operates. A fine grid was also used for computations containing 200,000 nodes but due to excessive computation times was put into limited use to evaluate grid refinement effects. The concept of flux analysis over flow cross sections was applied to check the physical consistency of the computed flow fields. Greater detail pertaining to the applied numerics has previously been expanded upon (Staubli et al., 1995).

The impeller clearance leakage flow was also included in the numerical calculations taken, however, as a boundary condition from experimental measurements.

4 The Experimental and Numerical Characteristics

In Fig. 3(a) the measured impeller and pump characteristics are shown. The pump characteristic was measured in accordance with ISO standards (ISO, 1987) while the impeller characteristic was evaluated by integrating the energy flux through flow cross sections (Staubli and Holbein, 1995) measured with the 5 hole pressure probe. The integrated total pressure was obtained from division of the energy flux at the impeller inlet and outlet, positions in Fig. 1, by the mass flow. This procedure was very time consuming requiring many high resolution (measurement step size was 4 percent of the volute inlet height) pressure probe traverses, thus only selected points along the impeller characteristic were determined. The measured impeller characteristic is larger than the global pump characteristic due to total pressure losses encountered in the double spiral volute of the pump. The depression in the pump characteristic for $\phi < 0.06$ (34% bep volume flux) is caused by prerotation in the suction pipe elevating the pressure in the suction pipe taps.

A zoom of the hysteresis loop found in the pump characteristic is shown in Fig. 3(b). Upon decreasing ϕ from $\phi > 0.123$ (70.7%) the top branch of the hysteresis loop is followed reaching a ψ-discontinuity at the stability limit of $\phi = 0.121$ (69.5%) where an abrupt ψ decrease occurs. Increasing ϕ from $\phi < 0.121$ (69.5%) the bottom branch of the hysteresis loop is followed reaching a discontinuity at $\phi = 0.123$ (70.7%) where an abrupt ψ increase occurs. These exact values were not measured in the impeller characteristic due to a lack of resolution in the selected pressure probe measurement points.

The numerically calculated impeller characteristic is also shown in Figs. 3(a) and 3(b) for the fine and coarse grid case without any impeller clearance leakage flow. The fine grid has been computed for fewer operating points and shows a definite upward shift from the coarse grid obtaining even better agreement with the measured impeller characteristic. Outside the two ψ-discontinuities on both the upper and lower branch of the hysteresis good numerical convergence was always obtained. At the transition between the two ψ-

Nomenclature

bep = best efficiency point
c = velocity, absolute system
c_m = absolute meridional velocity
c_r = absolute radial velocity
c_u = absolute circumferential velocity
C_p = pressure coefficient $[P(r, \theta, z) - P_{\text{stat inlet}}]/0.5\rho u_2^2$
d = probe traversal length
D = diameter
f = frequency [Hz]
g = gravitational constant [m/s^2]
H = pump head [m]
N = rotations per minute [rpm]
P_{tot} = total pressure
P = static pressure
Q = pump volume flux [m^3/s]
r = radial coordinate
R_1 = impeller inlet tip radius
R_2 = impeller outlet radius
S = control surface element
u_2 = impeller outlet circumferential velocity
u =
v = Cartesian coordinate velocities
w =
w = velocity, relative system
z = axial coordinate
n_q = pump specific speed (SI units) $NQ^{0.5}/H^{0.75}$
ω_s = pump dimensionless specific speed $\omega Q^{0.5}/(gH)^{0.75}$
ϕ = flow coefficient c_{m2}/u_2
ψ = total pressure coefficient $[P_{\text{tot outlet}} - P_{\text{tot inlet}}]/0.5\rho u_2^2$
ω = angular frequency [s^{-1}]
ρ = fluid density
θ = circumferential coordinate
$\Delta\phi = (Q_{\text{leakage}}/Q_{\text{pump}})\phi$

Subscripts

1 = pump impeller inlet
2 = pump impeller outlet
bp = blade passing
rms = root mean square quantities

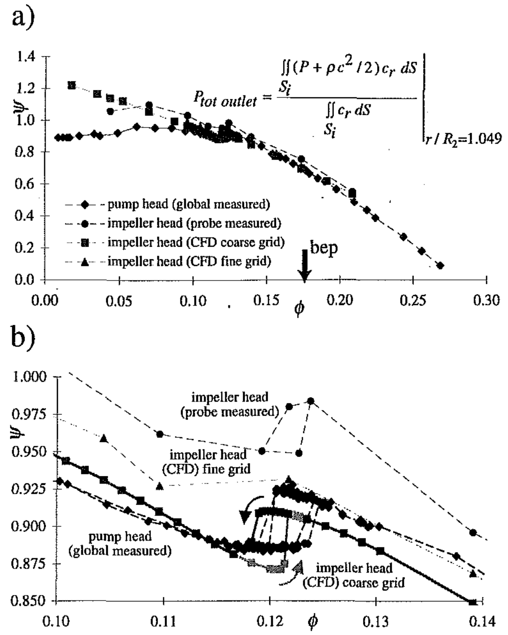

Fig. 3 The experimental and numerical characteristics. (*a*) The impeller characteristics evaluated according to the shown formula; (*b*) A zoom of the pressure discontinuity hysteresis loop.

branches numerical convergence was not obtained. A typical plot of the residual maximum pressure and three velocity components at the transition from the upper branch to the lower branch reveal the nonconvergence depicted in Fig. 4. This problem can be attributed to the code trying to numerically integrate the nonlinear differential equations in the rotating system with no mathematically stable solution, in agreement with the flow physics also having no stable solution at the ψ-discontinuity. The numerical points on the ψ-discontinuities of Fig. 3b are values taken after 200 iterations.

With the missing double spiral volute in the numerics only part of the pump flow is numerically solved. However, important statements may be made concerning the agreement of the measured pump characteristic and the calculated coarse grid impeller characteristic. First, the numerical volume fluxes at which the impeller characteristic hysteresis loop has its stability limits, where ψ-discontinuities occur, are in good agreement with those measured for the pump. Second, the magnitude of the ψ increase/decrease at the impeller characteristic hysteresis loop stability limits are in excellent agreement with those measured for the pump. This agreement permits the conclusion that the impeller internal flow must be responsible for this pump's hysteresis loop.

5 The Characteristic's Hysteresis Loop

Both experimental and numerical hysteresis loops in Fig. 3 provide a nonunique ψ versus ϕ relationship in which nonlinear transition between two branches occurs (Mayergouz, 1991). This hysteresis is nonstationary in that the ψ vs ϕ relationship may not be held indefinitely at all path states. Two stability limits exist where ψ-discontinuities occur.

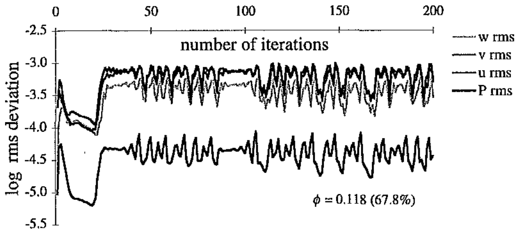

Fig. 4 The nonconvergence of four variables at the lower ψ-discontinuity for the entire computational grid

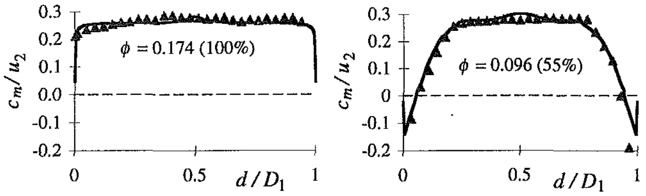

Fig. 5 Comparison of the meridional impeller inlet velocity at two flow coefficients

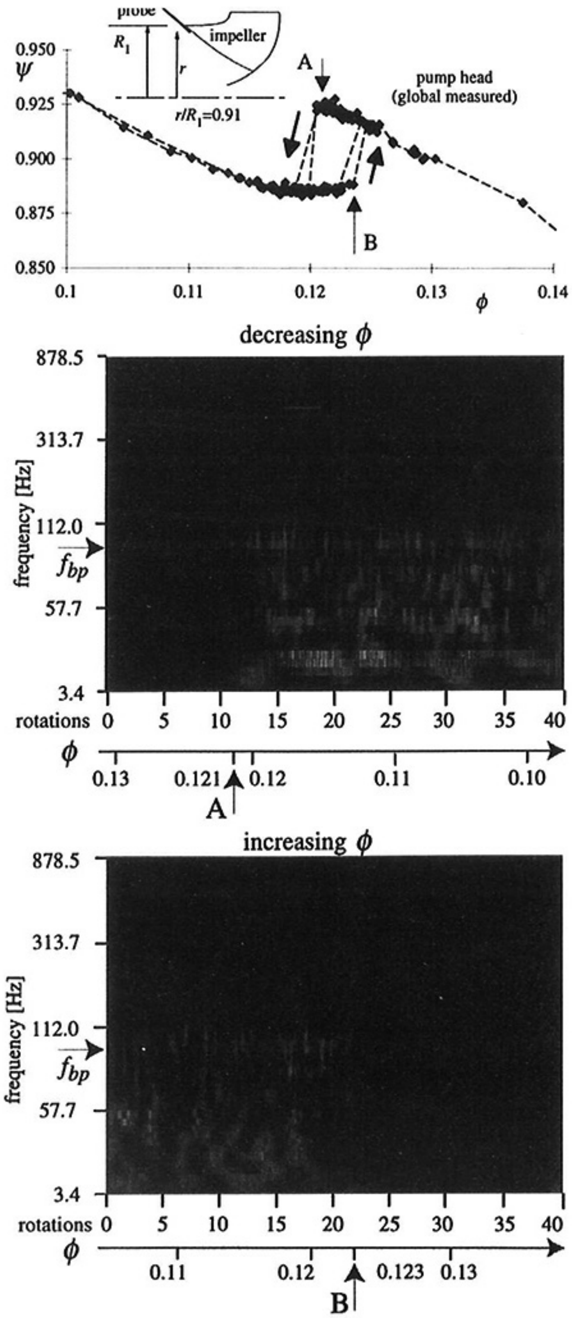

Fig. 6 The Haar wavelet transform magnitude of two probe measured unsteady pressure signals at the impeller inlet during slow throttling operation

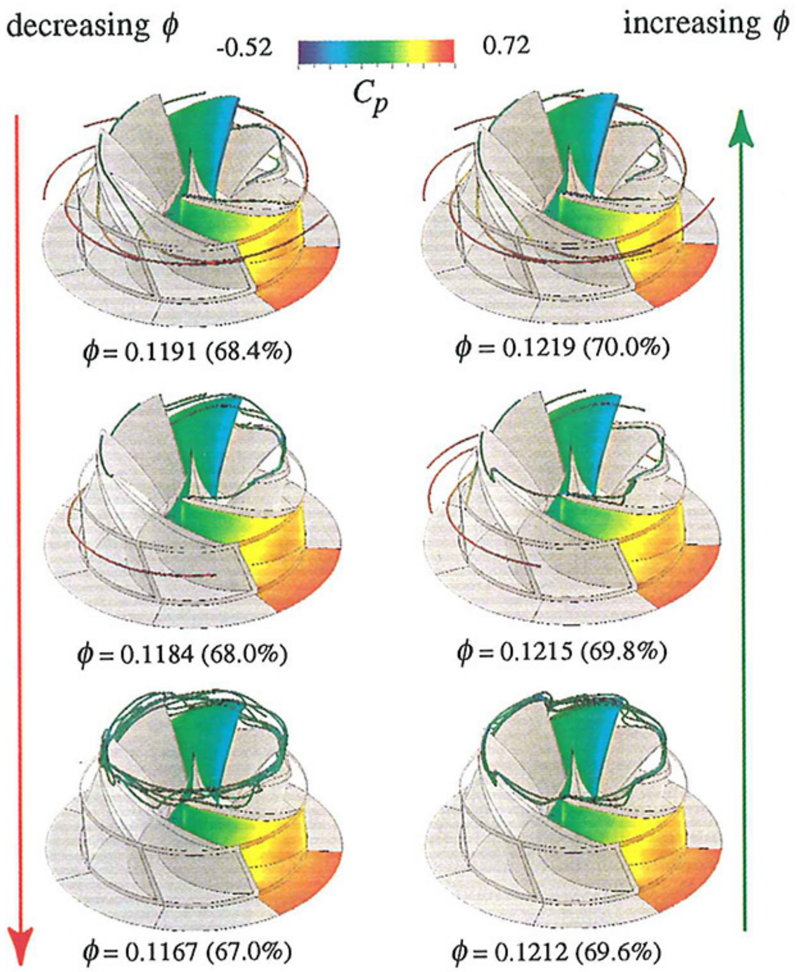

Fig. 7 The change in the impeller tip streamlines while increasing/decreasing ϕ within the hysteresis region. The shroud has been removed only for viewing purposes.

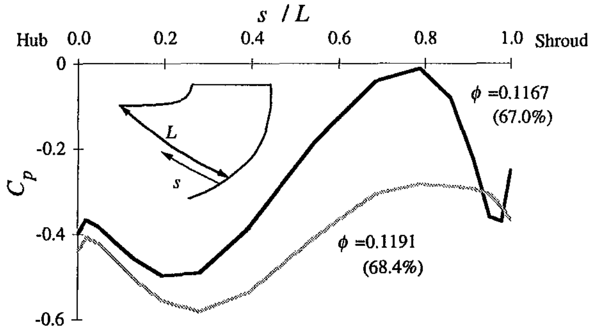

Fig. 8 The change in the blade suction surface pressure along the impeller leading edge while decreasing ϕ

A further characterization of ψ vs ϕ hysteresis lies in directional dependence, the location of branch transition from an increase/decrease in ϕ is influenced by the previous ϕ value meaning the hysteresis possesses local memory. In the experiments, data on the branches were taken from steady measurements. Additional tests confirmed quasi-steady and repeatable behaviour of the hysteresis loop for increasing/decreasing ϕ slowly ($|d\phi/dt| < 0.01\ \mathrm{s}^{-1}$).

The fundamental similarity between the experimental and numerical hysteresis loops are the ψ-discontinuities at two stability limits between two branches. Physically the ψ-discontinuities are an abrupt change in the specific energy transferred to the pressure head of the pump for a small perturbation in volume flux at the stability limits. This abrupt pressure change is often coupled with positive sloped characteristics leading to detrimental pump system instabilities (Guarga et al., 1991).

The ψ-discontinuities in the characteristics are caused by an abrupt change in flow properties within the pump. Exact reasons for this abrupt change lie in the complex interaction between coriolis, inertial, pressure and friction forces acting on the relative flow. The $\omega_s = 1.7$ pump with an impeller outlet tip solidity of 1.4 has relatively large blade passages and short blades for a radial pump implying lesser flow guidance, greater secondary flow development, and greater susceptibility to flow recirculation with characteristic discontinuities. Various studies (Gülich 1995; Hergt and Jaberg, 1989) dealing with pump characteristic discontinuities indicate a uniqueness for each case examined, the case studied here is not exemplary of all cases. However, in all cases reverse flow zones form at the impeller inlet and outlet at some ϕ. These zones have been postulated in a simplified manner (Gülich, 1995) to be a self healing of the flow field. Reverse flow zones form and act as blockage contracting the flow area forcing the remaining through flow to accelerate at the impeller inlet.

Impeller Inlet Flow. A quantitative comparison of the circumferentially averaged (pitch averaged) meridional velocity at the pump inlet is shown in Fig. 5 for the $\phi = 0.174$ and $\phi = 0.096$ (100 and 55% bep) operating points (Staubli et al., 1995). Both the numerically calculated distribution (line) and the probe measurements (triangles) fulfill the continuity of

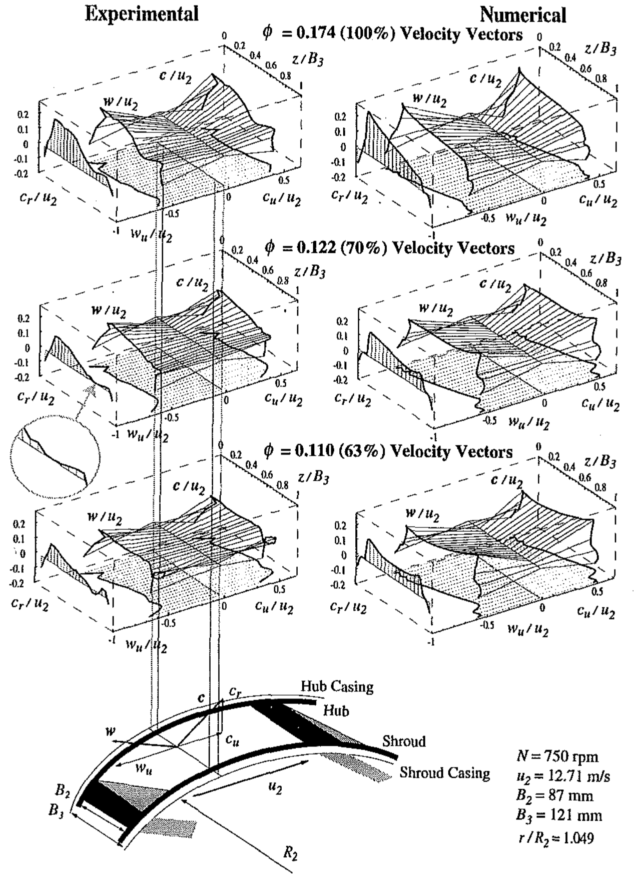

Fig. 9 Comparison of experimental and numerical impeller outlet velocity triangles. The circular magnifying glass indicates the region where impeller outlet reverse flow starts to occur for $\phi = 0.122$.

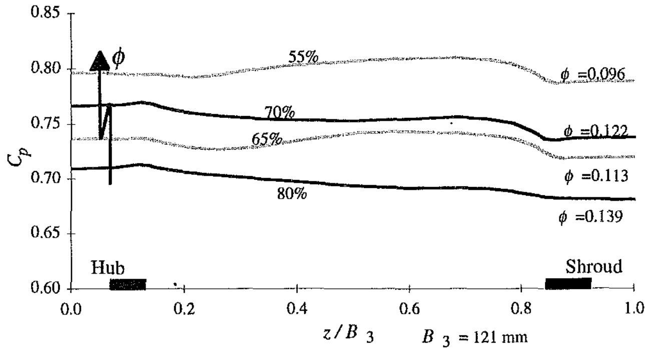

Fig. 11 The numerical impeller outlet static pressure distribution for a decreasing ϕ

mass, experiments to within an error of -1 and -2%, respectively. The computed profiles result from a rectangular upstream velocity profile. The inlet reverse flow at $\phi = 0.096$ (55%) has accurately been predicted. The circumferential averaged numerical inlet reverse flow has been determined to commence while decreasing ϕ at $\phi = 0.1180$ (67.8%) and cease while increasing ϕ at $\phi = 0.1213$ (69.7%), exactly the volume flux at the ψ-discontinuity stability point on the numerical hysteresis loop upper and lower branch. Experimentally the circumferential averaged inlet reverse flow was determined to occur/cease as inlet recirculation commenced/ceased, found with a fast response probe at the impeller inlet during a slow throttling ($|d\phi/dt| = 0.01\ \mathrm{s}^{-1}$) at $\phi = 0.121$ (69.5%) and $\phi = 0.123$ (70.7%) for decreasing/increasing ϕ respectively. These correspond to the stability points in the pump characteristic, localized in Fig. 6 with the aid of a Haar function wavelet transform in the time frequency plane (Kaupert, 1996) on a linear-log ordinate. During decreasing ϕ as the reverse flow commences (point A) the blade passing frequency becomes smeared and greater stochastic signal content exists due to a changing flow on the probe. During increasing ϕ as reverse flow ceases (point B) the stochastic signal content disappears to leave blade passing frequency. A clear explanation, however, to the three-dimensional flow changes occurring at the inlet to produce reverse flow is not provided.

Greater insight into the reverse flow mechanisms are obtained by viewing the numerical impeller flow streamlines about the hysteresis loop for points corresponding to an increase/decrease of ϕ, Fig. 7. For decreasing ϕ the flow streamlines at the impeller inlet tip undergo an abrupt change. At $\phi = 0.1191$ (68.4%) the impeller tip streamlines pass through the impeller, at $\phi = 0.1184$ (68.0%) they begin to deviate radially along the inlet blade suction side, and at $\phi = 0.1167$ (67.0%) they no longer have enough energy to traverse an adverse pressure gradient in the three-dimensional flow and do not pass through the impeller inlet tip. Upon exacter observation streamlines can be seen at the leading edge pressure side slightly entering the impeller and then be directed radially outward to reverse in flow direction and exit the impeller at a larger radius. This is the numerical flow recirculation zone at the impeller tip inlet. For increasing ϕ this process repeats itself in reverse order but at a larger volume flux.

For decreasing ϕ the numerical blade suction surface pressure along the leading edge, Fig. 8, reveals an abrupt change in the pressure gradient perpendicular to the healthy flow direction as the ψ-discontinuity in the impeller characteristic is reached. Excessive flow deceleration at the inlet lead to the formation of this pressure gradient parallel to the leading edge, acting outward near the impeller tip ($0.79 < s/L < 0.98$) along the leading edge. The pressure gradient change occurs abruptly during decreasing ϕ at the ψ-discontinuity stability point, while during increasing ϕ the pressure gradient disappears abruptly at the other ψ-discontinuity stability point. This effect is respon-

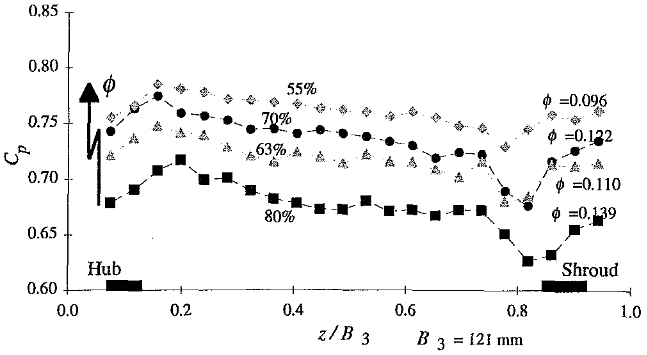

Fig. 10 The probe measured impeller outlet static pressure distribution for a decreasing ϕ

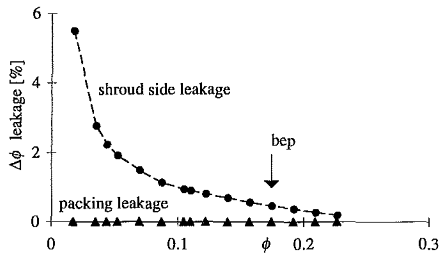

Fig. 12 Measured leakage flow as a percentage of through flow

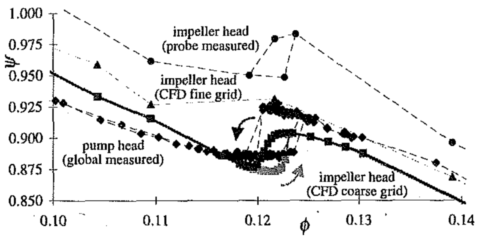

Fig. 13 Influence of adding impeller clearance leakage flows on the numerical coarse grid impeller characteristic

sible for the radial outward flow portion of the inlet recirculation occurring in the numerical impeller. A further manifestation hereto is the increase in pressure at the shroud ($s/L = 0.99$), a redirection of the streamlines occurs here.

Impeller Outlet Flow. A qualitative experimental and numerical comparison of the impeller outlet circumferentially averaged velocity triangles for $\phi = 0.174$, 0.122, and 0.110 (100, 70, and 63%) operating points is provided in Fig. 9, the axial velocity not being shown. Agreement between the velocity vectors is good, continuity of mass experimentally established at $\phi = 0.174$ (100%) to within −6% worsening as the operating point moves deeper into part load. Circumferential non uniformity in the impeller outlet flow is responsible for these increasing discrepancies at part load since these results are for only one circumferential probe measurement position.

Experimentally determined reverse flow (negative c_r) is seen to commence near the shroud side just below the $\phi = 0.122$ (70%) operating point (Note: negative c_r near the hub and shroud side clearance leakage flow regions occurs at all volume fluxes). This ϕ coincides with the commencement of inlet reverse flow however, it remains unclear if the two regions are physically linked together. The corresponding numerical frame in Fig. 9 does not show any impeller outlet reverse flow (c_r is always positive). There numerically exists a well defined reverse flow zone at the impeller inlet only not at the impeller outlet. This contradiction to experimental findings reveal the numerical models weakness in the impeller outlet shroud side predictions but inspite of this the pump impeller characteristic hysteresis loop occurs indicating the possibility of the hysteresis without any reverse flow formation at the impeller outlet.

To further enhance this point the probe measured circumferentially averaged static pressure at the impeller outlet is shown in Fig. 10 for 4 volume fluxes over the blade height. The effect of the abrupt total pressure drop manifested in the pump characteristic ψ-discontinuity occurs between $\phi = 0.122$ (70%) and $\phi = 0.110$ (63%). This C_p drop also occurs at the numerical impeller outlet, Fig. 11, but without any outlet reverse flow. Thus the outlet reverse flow and any volute tongue flow interaction are not a necessary condition for the ψ-discontinuity in this pump impeller characteristic.

6 Impeller Clearance Leakage Flow Effects

The leakage flow in the impeller clearance, Fig. 1, is a non-negligible quantity since it may be several percent of the total pump flow and is injected locally in a very sensitive flow region upstream of the impeller inlet. The measured leakage volume flux is shown in Fig. 12 as the percentage $\Delta\phi$ that the leakage flow represents vs ϕ. This was used as a numerical boundary condition at both the impeller shroud side inlet/outlet and the hub side to evaluate its influence on the impeller characteristic (Note: agreement between empirical predictions (Yamada et al., 1969) and measurements for 100% leakage volume flux reveal good accordance.) The numerical re-entering leakage flow at the impeller inlet notch was given a circumferential velocity equal to half the impeller tip velocity. Herewith the important outlet to inlet flow coupling was simulated, a labyrinth flow was not included in the numerical calculations.

The numerical pump impeller characteristic with leakage flow is shown in Fig. 13. The numerical hysteresis loop shifts to a slightly greater ϕ retaining however the magnitude of its ψ-discontinuity. No significant impeller outlet or inlet flow changes have been found to occur, the data previously presented remains virtually unchanged.

7 Conclusions

Agreement between numerical impeller with both experimental pump and impeller characteristics is excellent with respect to the two stability limits in ϕ, the local memory for ϕ in the hysteresis loop, and the magnitude of the two ψ-discontinuities.

Although experiments have shown simultaneous appearance of shroud side reverse flow at the impeller inlet and outlet, CFD results indicate that the presence of outlet recirculation is not a necessary condition for the ψ-discontinuities to occur. Agreement of measured and calculated inlet reverse flow is good inspite of the failure to predict numerical impeller outlet reverse flow.

The inclusion of impeller clearance leakage flow provides a more correct numerical impeller characteristic prediction but adds greatly to the numerical complexity. A good prediction of the impeller characteristic has been obtained for this pump without the leakage flow.

Numerically the impeller inlet tip streamlines reveal the formation/cessation of a recirculation zone occurring as the impeller characteristic stability limit is reached. A pressure gradient parallel to the blade leading edge near the impeller tip was found to abruptly form/cease as the inlet recirculation formed/ceased. Further investigation of the vorticity and unsteady flow field in this region is necessary.

Acknowledgments

This work was made possible by funding from Sulzer Pumps Ltd., Winterthur and the Swiss Commission for the Promotion of Applied Research.

References

ASC, (1994) TASCflow Documentation Version 2.3, Advanced Scientific Computing LDT, Waterloo, Canada.

Breugelmans, F. A. E., and Sen, M., 1982, "Prerotation and Fluid Recirculation in the Suction Pipe of Centrifugal Pumps," *Proceedings of the 11th Turbomachinery Symposium.*

Fraser, W. H., 1982, *Recirculation in Centrifugal Pumps, World Pumps,* pp. 227–235.

Guarga, R., Fanelli, M. A., and Nishi, M., 1991, "System Instability Caused by Hydraulic Machinery," *Vibration and Oscillation of Hydraulic Turbomachinery,* Ohashi, H., ed., Avebury Technical.

Gülich, J. F., 1995, "Untersuchung zur sattelförmigen Kennlinien-Instabilität von Kreiselpumpen," *Forschung im Ingenieurwesen,* Bd 61, Nr 4.

Hergt, P., and Jaberg, H., 1989, "Die Abströmung von Radiallaufrädern bei Teillast und ihr Zusammenhang mit Vollastinstabilität," KSB Technische Bericht 26, Frankental.

Hergt, P., and Starke, J., 1985, Flow Patterns Causing Instabilities in the Performance Curves of Centrifugal Pumps with Vanes Diffusers, Proceedings of the Second International Pump Symposium, Houston, p 67–75.

Humm, H. J., and Verdegaal, J. M., 1992, "Aerodynamic Design Criteria for Fast Response Probes," *XIth Symposium on Measurement Technology for Transonic and Supersonic Flows in Cascades and Turbomachines,* Munich.

ISO 5198, 1987, "International Organization for Standardization," Centrifugal, Mixed Flow and Axial Pumps, Code for Hydraulic Performance Test, Precision Grade, Edition 1.

Kaupert, K. A., 1996, "Quasi Joint Time Frequency Analysis in Turbomachinery," IMechE C500-004, 6th Conference on Vibrations in Rotating Machinery, Oxford.

Kupferschmied, P., and Gossweiler, C., 1992, "Calibration, Modelling and

Data Evaluation Procedures for Aerodynamic Multihole Pressure Probes,'' *XIth Symposium on Measurement Technology for Transonic and Supersonic Flows in Cascades and Turbomachines,* Munich.

Mayergouz, I. D., 1991, *Mathematical Models of Hysteresis,* Springer, New York.

Staubli, T., Holbein, P., and Kaupert, K. A., 1995, *Verification of Computed Flow Fields in a Pump of High Specific Speed,* ASME Fluids Engineering Division Summer Meeting, Hilton Head Island, USA, August.

Staubli, T., and Holbein, P., 1995, ''Analysis of Computed Pump Flows Based on Fluxes and Balance Equations,'' VDI Turbomachinery Conference, Report Nr. 1185, Erlangen Germany.

Tanaka, T., 1980, ''An Experimental Study of Backflow Phenomena in a High Specific Speed Propeller Pump,'' ASME 80-FE-60.

Yamada, Y., Nakabayashi, K., and Maeda, K., 1969, ''Pressure Drop Measurements of the Flow through Eccentric Cylinders with Rotating Inner Cylinders,'' *Bulletin of the JSME,* Vol. 12, pp. 1032–1040.

Experimental Measurements in a Centrifugal Pump Impeller

A. C. Bwalya

M. W. Johnson

Department of Mechanical Engineering,
The University of Liverpool,
P.O. Box 147, Liverpool L69 3BX, U.K.

Measurements of the 3-d velocities, total and static pressures have been made in a 0.89 m diameter commercial pump impeller, using air as the working fluid. Results at the peak efficiency operating point show separation of the flow near the shroud on the pressure side of the blade at the leading edge. This separation results in a low energy region which initially travels axially through the impeller to form a wake in the suction side shroud corner region. A region of reversed radial velocity is observed at the outlet, which is due to high blade sweep angle together with the poor guidance given to the flow by the blades in the mid-passage region.

Introduction

Detailed experimental research work in centrifugal turbomachinery has concentrated on compressors. This is primarily because of the significant efficiency improvement in small gas turbine engines and turbochargers which results if a reduction in losses within the compressor can be achieved. However, better understanding of centrifugal pump impeller flows can also lead to improved performance with associated reductions in operating costs.

The behavior of the flow in centrifugal compressors is now well documented. A wake region develops in the impeller (Eckardt, 1976), which is attributed to migration of low energy fluid from the boundary layers through the action of secondary flows (Johnson and Moore, 1983a). The position of the wake within the impeller discharge is close to the suction side shroud corner, although its exact position is influenced by flow rate (Johnson and Moore, 1983b; Farge and Johnson, 1990). The secondary flows within a compressor impeller are strong with flow angles of 40 or 50 degrees commonplace. It seems unlikely that such strong secondary flows can be expected in a pump where the passage length is shorter due to the lack of an inducer and the blade loading is less severe. Carey et al. (1985) found that at near design flow rates secondary flows were indeed weak. Off design, significant crossflows did develop, but are attributed to separation at the leading edge rather than secondary flow.

Experimental Rig

The impeller used in the current work is from a state-of-the-art commercial pump. Its principal geometrical and performance specifications are:

Geometry:

Blades = 6
Outside diameter = 890 mm
Inlet diameter = 650 mm
Hub diameter = 222 mm

Peak efficiency point at 742 rpm:

$\eta = 90\%$
Volumetric flow rate = 1.4 m^3/s
Head = 50 metres
Specific speed = 0.88

$$= 46.5 \left(\frac{\text{r.p.m.}\ (\text{m}^3/\text{s})^{1/2}}{\text{m}^{3/4}} \right)$$

In the current work, air is used as the working fluid and the impeller speed is 500 rpm, which gives an equivalent peak efficiency flow rate of 0.945 m^3/s. The Reynolds number is 22 times smaller when using air. The boundary layers are tripped at the impeller inlet to ensure that they are turbulent and hence the effect of smaller Reynolds number is minimised.

A schematic of the test rig is shown in Fig. 1. Air enters through an inlet duct which contains mesh screens and a honeycomb which remove any nonuniformities and swirl within the flow. The air then passes through the impeller and is discharged directly into the laboratory. Measurements are made using a 5 hole pressure probe which can be traversed in the hub to shroud direction at up to 30 different blade-to-blade locations on each of 6 measurement planes within the impeller passage. This is achieved by mounting the traverse gear on the rotating impeller as shown in Fig. 2. The locations of the six measurement planes are shown in Fig. 3. The 5 hole probe is connected to 4 differential pressure transducers mounted close to the axis of rotation on the back face of the impeller.

Results

The reduced static pressure ($p_r = p - \frac{1}{2}\rho\omega^2 r^2$) and rotary total pressure ($p^* = p_r + \frac{1}{2}\rho W^2$) are nondimensionalized using the maximum and minimum values of rotary total pressure ($p^*_{\max}$ and $p^*_{\min}$) observed within the impeller

$$P^*_{\max} = \frac{p^* - p^*_{\min}}{p^*_{\max} - p^*_{\min}} \quad (1)$$

$$P_r = \frac{p_r - p^*_{\min}}{p^*_{\max} - p^*_{\min}} \quad (2)$$

$p^*_{\max} = -245$ N/m^2 is equal to the rotary stagnation pressure at inlet to the impeller and hence P^* is unity within the potential core flow within the impeller. The minimum value of $p^* = -465$ N/m^2 is obtained at the wall in the region of lowest reduced static pressure. This region is found close to the inlet near the shroud suction side corner of the passage. The estimated accuracy for P^* and P_r is ± 0.05.

The electrical signals from the transducers are then amplified before passing through sliprings to a PC data logging system. The three mutually perpendicular velocity components and the reduced static and rotary total pressures at the measurement point are then determined from the probe calibration curves.

The velocity components perpendicular to the measurement plane are presented as a contour and the remaining component within the measurement plane as an arrow at each measurement point. The estimated accuracy is ±0.5 m/s for the flow velocity and ±5 degrees for the flow angle.

Contributed by the Fluids Engineering Division for publication in the JOURNAL OF FLUIDS ENGINEERING. Manuscript received by the Fluids Engineering Division March 24, 1995; revised manuscript received January 22, 1996. Associate Technical Editor: D. P. Telionis.

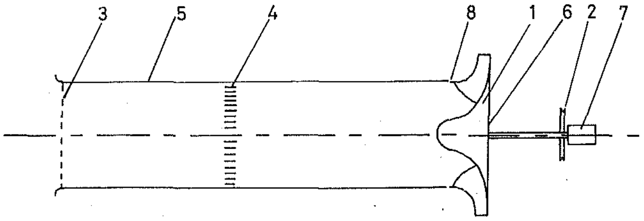

1 Impeller 2 Pulley driven by motor 3 Screens 4 Honeycomb
5 Inlet duct 6 Pressure transducers and amplifiers
7 Sliprings 8 Seal

Fig. 1 Schematic of test rig

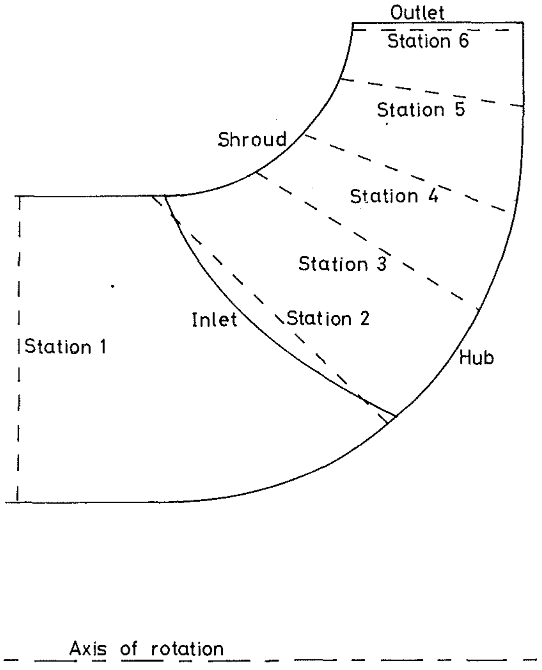

Fig. 3 Measurement planes

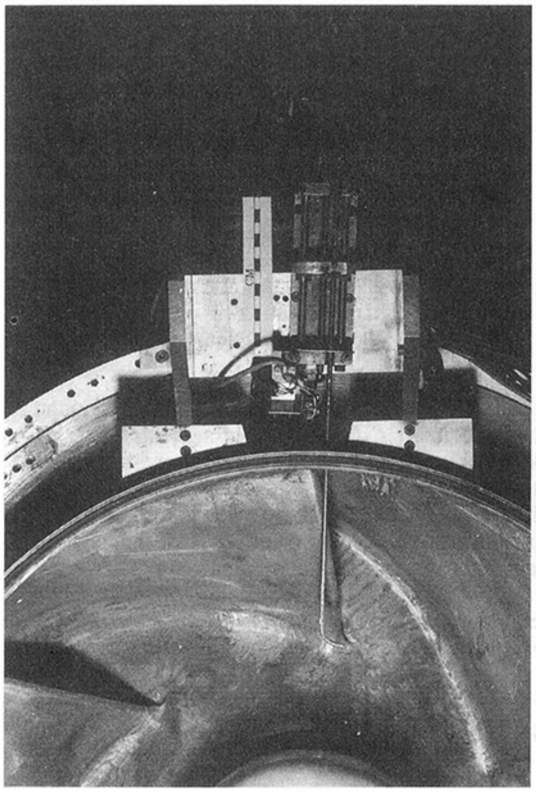

Fig. 2 Traverse gear mounted on the pump impeller

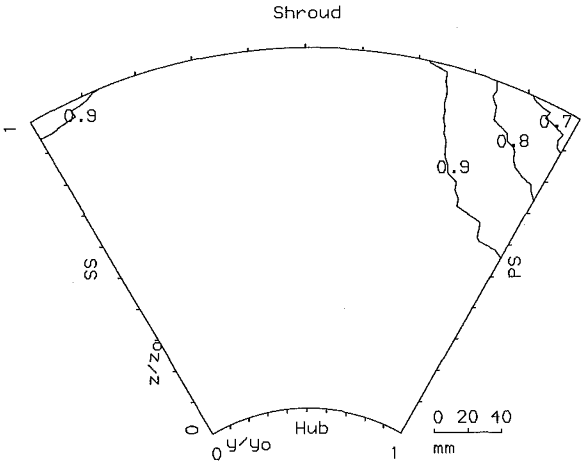

Fig. 4 Dimensionless rotary stagnation pressure P^* at Station 1 (Uncertainty ± 0.05)

Discussion

Station 1. The measurement plane at Station 1 is normal to the axis of rotation of the impeller and is upstream of the blade leading edge. Figure 4 shows that over the cross section little loss has occurred except in the shroud pressure side corner. This loss is probably an upstream effect of a local separation of the flow at the blade leading edge tip. If the flow near the shroud were uniform and reached the impeller with a zero absolute tangential velocity, the blade camber angle is such that the flow incidence would be close to zero and hence the flow would not separate. However, Fig. 5 shows that the flow near the shroud accelerates approaching the impeller due to the lower reduced static pressure (see Fig. 6) in this region. In addition, the shroud boundary layer will be skewed as it travels across the rotating shroud prior to reaching the blade leading edge. Both of these effects will tend to decrease the blade incidence angle significantly, which is believed to lead to the observed pressure side separation. The rise in axial velocity in the hub-to-shroud direction, due to the decrease in the reduced static pressure, is shown in Fig. 5. This decrease is primarily due to

Nomenclature

p = static pressure
p_r = $(= p - \frac{1}{2}\rho\omega^2 r^2)$ Reduced static pressure
p^* = $(= p_r + \frac{1}{2}\rho W^2)$ Rotary total pressure
P_r = dimensionless reduced static pressure (Eq. (1))
P^* = dimensionless rotary total pressure (Eq. (2))
r = radius
W = relative flow velocity
ρ = fluid density
ω = impeller rotational speed

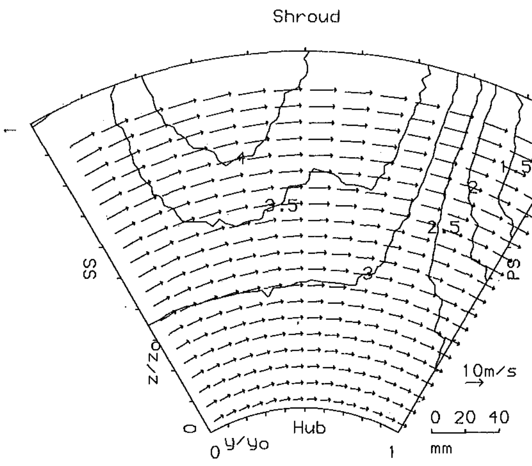

Fig. 5 Relative velocities at Station 1. Contours in m/s. (Uncertainty ± 0.5 m/s)

the centrifugal pressure gradient, which results from the axial to radial bend curvature.

Station 2. Station 2 is approximately 5 mm downstream of the blade leading edge and is at an angle of 44 deg to the rotational axis. Figure 7 shows that the low energy region observed at station 1 has moved across the shroud from the pressure side corner to $y/y_o \cong 0.3$. The reason for this movement is apparent when the relative velocities in Fig. 8 are considered. The tangential relative velocity within the low energy region is negligible in comparison with that elsewhere within the passage. The low energy region at $y/y_o \cong 0.9$ at station 1 has therefore moved more or less axially to $y/y_o \cong 0.3$ at station 2, but because the blade leading edge angle near the shroud is approximately 80 deg, the passage and the core flow have rotated through some 30 deg in the suction to pressure tangential direction, which accounts for the change in y/y_o value for the low energy region between the two stations.

Figure 7 shows two further areas of total pressure loss. The loss in the suction side shroud corner region is believed to be the result of migration of boundary layer fluid from the suction side and shroud surfaces due to secondary flows induced by the shroud curvature and the blade to blade Coriolis force, respectively. The region near the shroud pressure side is believed to be due to the adverse pressure gradient caused by the blades loading. A reduction of the axial relative velocity in this region (Fig. 8) is also further evidence of this boundary layer thickening process. Figure 9 shows that the centrifugal pressure gradient still dominates the reduced static pressure distribution and that the blade loading is higher near the hub than near the shroud.

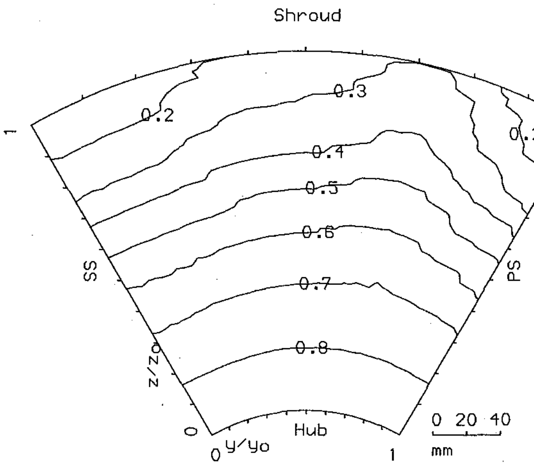

Fig. 6 Dimensionless reduced static pressure P_r at Station 1 (Uncertainty ± 0.05)

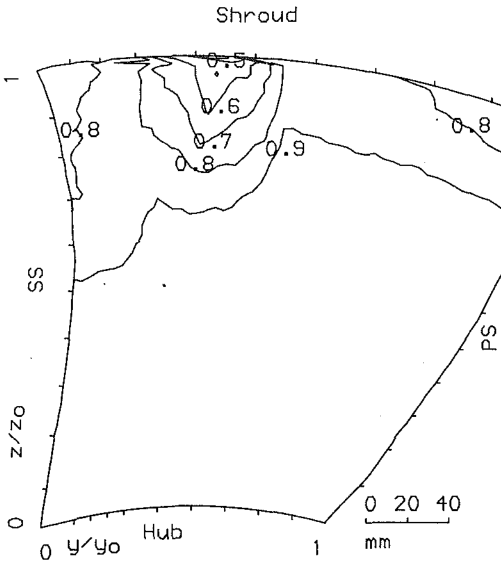

Fig. 7 Dimensionless rotary stagnation pressure P^* at Station 2 (Uncertainty ± 0.05)

Station 3. Station 3 is at an angle of 31.5 deg to the rotation axis and is a quarter of the way through the blade passage. It can be seen from Fig. 10 that the lowest energy fluid has accumulated in the suction side shroud corner region as it does in centrifugal compressor flows (Johnson and Moore, 1983a). The velocities within this region are also much reduced, and so this region can be regarded as a wake. Further losses are evident over the full width of the shroud and this is probably due to further boundary layer thickening in the pressure side corner due to further rises in reduced static pressure as shown in Fig. 11. Evidence of secondary flow in Fig. 12 is weak, but a reduction in tangential velocity, and hence a change in flow angle, is apparent as the shroud is approached. This suggests that a pressure to suction side Coriolis induced secondary flow is pres-

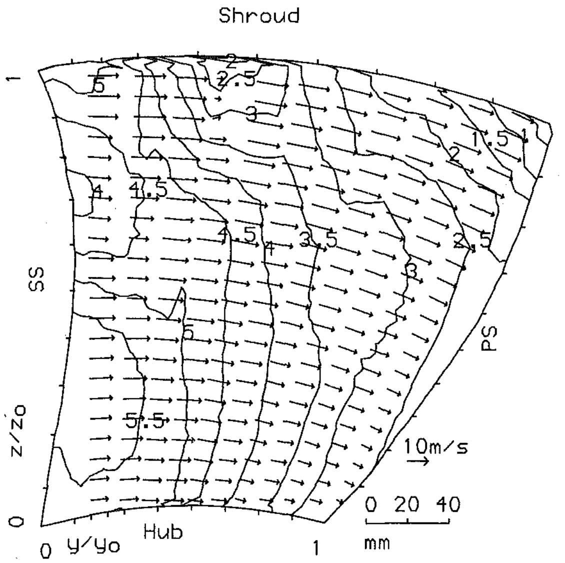

Fig. 8 Relative velocities at Station 2. Contours in m/s. (Uncertainty ± 0.05 m/s)

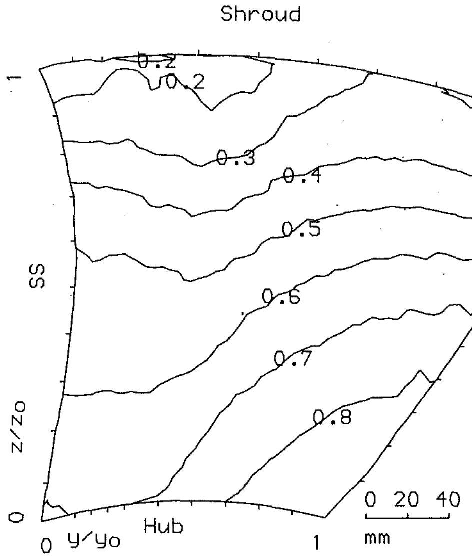

Fig. 9 Dimensionless reduced static pressure P_r at Station 2 (Uncertainty ± 0.05)

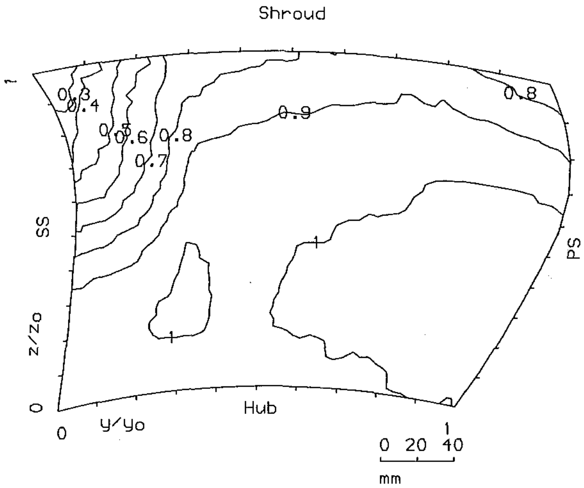

Fig. 10 Dimensionless rotary stagnation pressure P^* at Station 3 (Uncertainty ± 0.05)

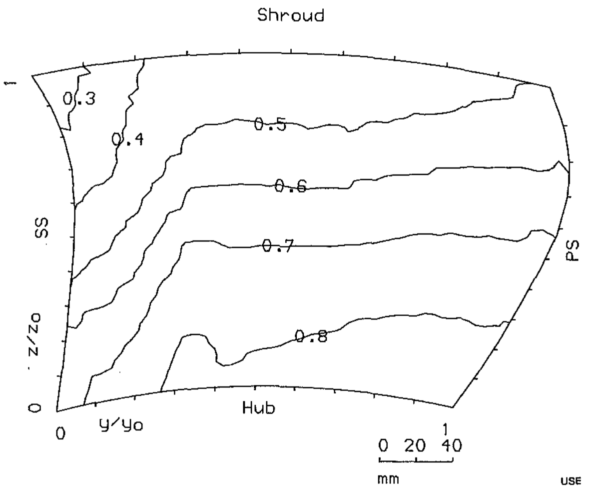

Fig. 11 Dimensionless reduced static pressure P_r at Station 3 (Uncertainty ± 0.05)

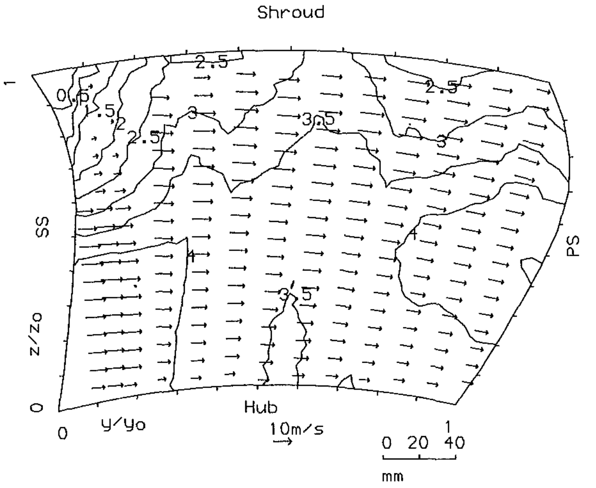

Fig. 12 Relative velocities at Station 3. Contours in m/s (Uncertainty ± 0.5 m/s)

ent carrying low p^* fluid toward the suction side corner. There is no evidence for secondary flow due to the axial to radial bend curvature on either the pressure or suction surfaces though. Secondary flow may exist though within the boundary layers on these surfaces, which were too thin at this station to be penetrated by the pressure probe.

Station 4. Station 4 is at an angle of 21.5 deg to the axis and is approximately halfway through the blade passage. Figure 13 depicts a low energy region in the suction side shroud corner region which has increased in size from Station 3. The minimum p^* within this region has increased, however, which suggests that substantial mixing must have occurred in this region. Much of the low energy fluid on the shroud at Station 3 has now moved toward the suction side corner and the increase in static pressure close to the pressure surface shroud corner (Fig. 14) has now slowed with a corresponding reduction in the boundary layer losses due to thickening. Secondary flow in the pressure to suction surface direction across the shroud is also apparent in Fig. 15 in that the magnitude of the tangential velocity component decreases markedly near the shroud, particularly between $y/y_o = 0$ and 0.6.

Station 5. The passage is essentially radial at station 5, which is three-quarters of the way through the blade passage. The wake region (Fig. 16) is now extensive and fills around 30 percent of the passage. The velocities (Fig. 17) are lower within this region, but a significant throughflow is still main-

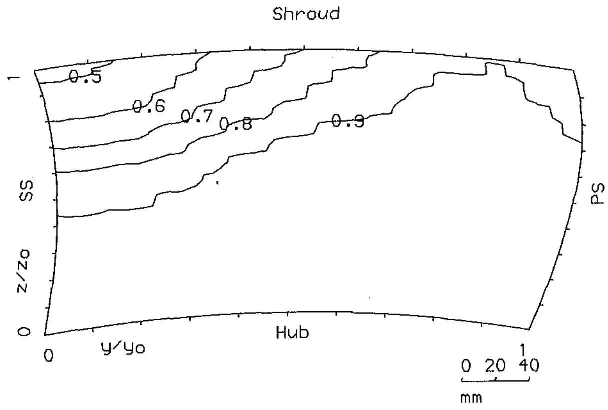

Fig. 13 Dimensionless rotary stagnation pressure P^* at Station 4 (Uncertainty ± 0.05)

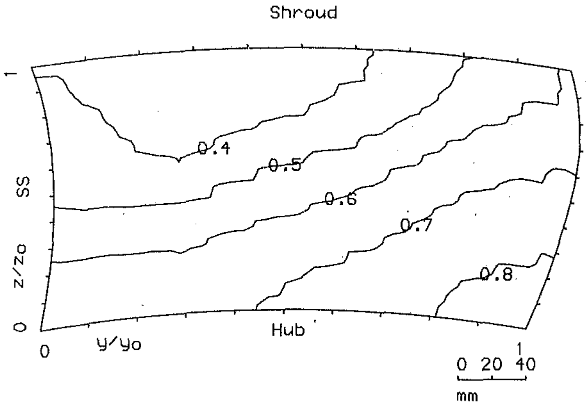

Fig. 14 Dimensionless reduced static pressure P_r at Station 4 (Uncertainty ± 0.05)

tained. The static pressure (Fig. 18) is now dominated by the blade-to-blade loading with a constant low pressure within the wake region.

Station 6. Station 6 is approximately 5 mm from the passage outlet. The stable location for the wake is now on the suction surface and hence the wake has started to move in this direction as shown by the secondary flow velocities in the shroud to hub direction on the suction surface in Fig. 19 and the total pressure contours (Fig. 20). An interesting feature of the flow at Station 6 is the stall region near the hub at $y/y_o \cong 0.5$ (Fig. 19) which is associated with a modest loss (see Fig. 20). The flow appears to accelerate in the tangential direction, as the static pressure drops between stations 5 and 6, but at the expense of the radial velocity component. The reason that the stall is most pronounced in the mid-passage region may be because the slip and hence the tangential velocity, is greatest in this region as the flow is not so well guided by the blading.

The static pressure contours (Fig. 21) show that the blades are essentially unloaded, but a significant hub-to-shroud pressure gradient is maintained.

Mass Averaged Pressures. The mass averaged reduced static pressure and rotary stagnation pressure, computed by numerical integration across the measurement planes, are pre-

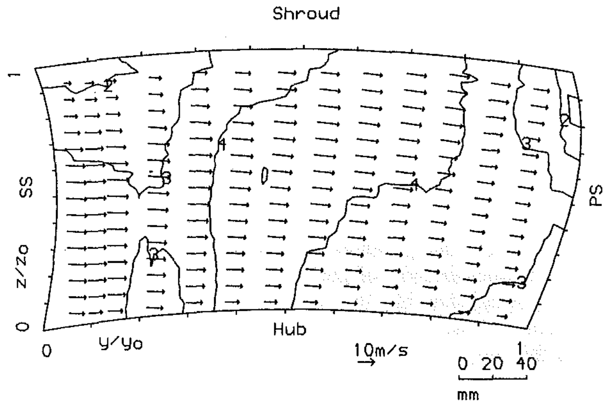

Fig. 15 Relative velocities at Station 4. Contours in m/s (Uncertainty ± 0.5 m/s)

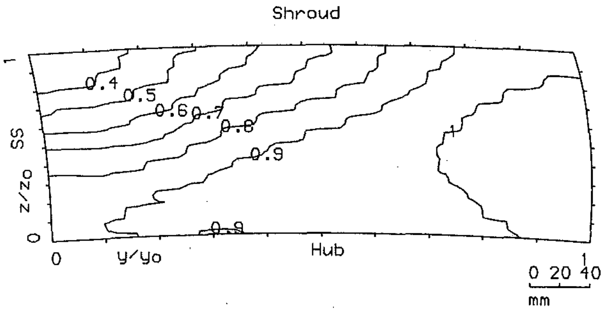

Fig. 16 Dimensionless rotary stagnation pressure P^* at Station 5 (Uncertainty ± 0.05)

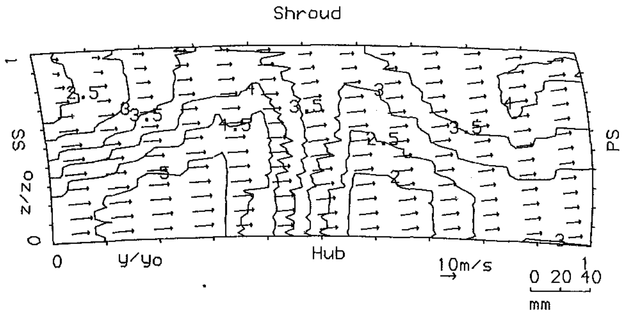

Fig. 17 Relative velocities at Station 5. Contours in m/s. (Uncertainty ± 0.5 m/s)

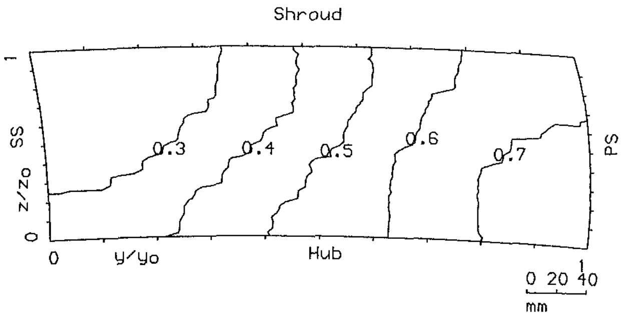

Fig. 18 Dimensionless reduced static pressure P_r at Station 5 (Uncertainty ± 0.05)

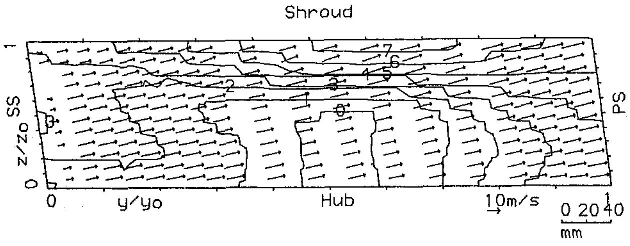

Fig. 19 Relative velocities at Station 6. Contours in m/s. (Uncertainty ± 0.5 m/s)

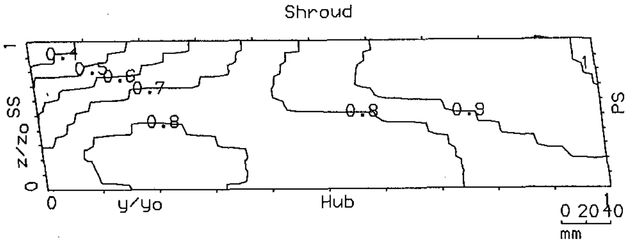

Fig. 20 Dimensionless rotary stagnation pressure P^* at Station 6 (Uncertainty ± 0.05)

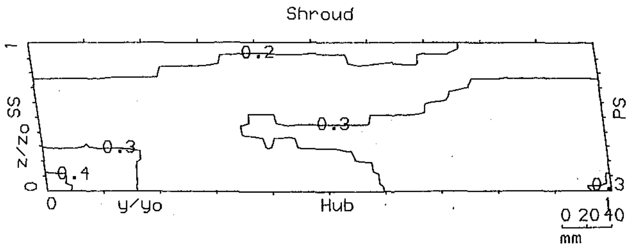

Fig. 21 Dimensionless reduced static pressure P_r at Station 6 (Uncertainty ± 0.05)

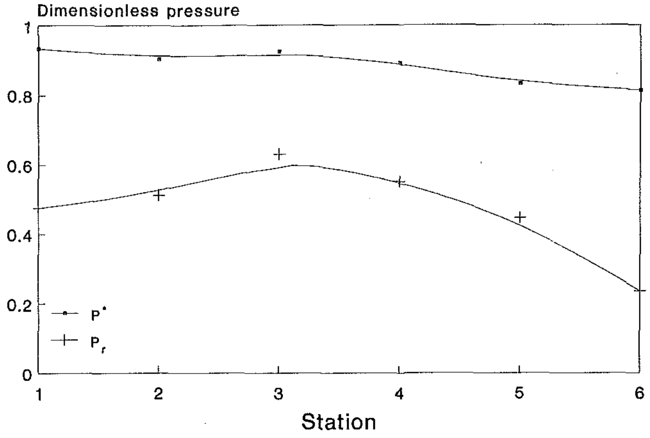

Fig. 22 Mass averaged dimensionless pressures (Uncertainty ± 0.05)

sented in Fig. 22. It can be seen that most of the losses occur between Stations 3 and 6 where most of the work is done on the fluid. The variation of the reduced static pressure depends not only on the losses, but also the variation in passage cross-sectional area. Figure 22 suggests that the impeller is not successful in diffusing the flow towards the outlet.

Conclusions

1. A significant leading edge loss, associated with separation of the boundary layer near the pressure side shroud corner, is observed. This separation is attributed to the increased axial velocity and a nonzero absolute tangential velocity within the shroud boundary layer, which results in negative incidence at the blade leading edge.
2. The low energy fluid from the leading edge separation region and the thickened shroud boundary layer are carried into a wake region which forms in the suction side shroud corner. Evidence of the Coriolis induced secondary flow responsible is seen in the cross velocity vectors, but curvature induced secondary flows up the blade surfaces are not observed.
3. The radial velocity component near the hub wall midway between the blades is negative over a significant region. This is believed to be due to the high blade sweep angle together with slip due to poor guidance of the flow by the blades in this region.

Acknowledgment

The authors thank Peter Smith and his colleagues at Weir Pumps and acknowledge the financial support of the Science and Engineering Research Council.

References

Carey, C., Fraser, S. M., Rachman, P., and Wilson, G., 1975, "Studies of the Flow of Air in a Model Mixed Flow Pump by Laser Doppler Anemometry. Part 2: Velocity Measurements Within the Impeller," NEL Report No. 699, Dept. of Trade and Industry.

Eckardt, D., 1975, "Detailed Flow Investigations Within a High Speed Centrifugal Impeller," ASME JOURNAL OF FLUIDS ENGINEERING, Vol. 98, pp. 390–402.

Farge, T. Z., Johnson, M. W., and Maksoud, T. M. A., 1989, "Tip Leakage in a Centrifugal Impeller," ASME *Journal of Turbomachinery,* Vol. *111,* pp. 244–249.

Farge, T. Z., and Johnson, M. W., 1990, "The Effect of Backswept Blading on the Flow in a Centrifugal Compressor Impeller," ASME Paper No. 90-GT-231.

Farge, T. Z., and Johnson, M. W., 1992, "Effect of Flow Rate on Loss Mechanisms in a Backswept Centrifugal Impeller," *International Journal of Heat and Fluid Flow,* Vol. *13,* No. 2, p. 189.

Johnson, M. W., and Moore, J., 1983a, "Secondary Flow and Mixing Losses in a Centrifugal Compressor Impeller," ASME *Journal of Engineering for Power,* Vol. 105, pp. 24–32.

Johnson, M. W., and Moore, J., 1983b, "Influence of Flow Rate on the Wake in a Centrifugal Impeller," ASME *Journal of Engineering for Power,* Vol. 105, pp. 33–39.

Krain, H., 1988, "Swirling Impeller Flow," ASME *Journal of Turbomachinery,* Vol. 110, pp. 122–128.

W. S. Yu
Graduate Student.

B. Lakshminarayana
Evan Pugh Professor of Aerospace
Engineering and Director.

Center for Gas Turbine and Power,
The Pennsylvania State University,
University Park, PA 16802

D. E. Thompson
Department Head,
Flow and Structural Acoustics,
Applied Research Laboratory,
The Pennsylvania State University,
University Park, PA 16802

Computation of Three-Dimensional Viscous Flow in High Reynolds Number Pump Guide Vane

A three-dimensional Navier-Stokes solver which utilizes a pressure based method is used to compute the incompressible flow field through the inlet guide vane (IGV) of a high Reynolds number pump. The solver has precise control of numerical dissipation through the second and fourth order artificial dissipation terms added to the momentum equations. A low-Reynolds-number form of two-equation turbulence model is used to account for the turbulence effects. Predicted blade surface static pressure distributions are in good agreement with the measurement. The tangential and radial components of the IGV wake velocity, as well as the IGV secondary flow, are predicted well. However, the predicted maximum defect in wake is larger than the measured data. Possible causes for this discrepancy are discussed. The defect in velocity in wakes at midspan is found to decay faster than the perturbation in velocity due to the secondary flow and wake in the tip region.

Introduction

Three-dimensional phenomena and viscous effects such as secondary flow, tip clearance flow, and wakes have appreciable effect on the fluid dynamic and acoustic performance of turbomachines. With the progress in high speed computing as well as Computational Fluid Dynamics (CFD), these viscous flows can be predicted reasonably well. Major advances have been made in predicting three-dimensional viscous flows in turbomachinery. A critical review of various techniques, assessment, and state-of-the-art is given in Lakshminarayana (1991). But the progress in predicting the flow field in pumps has been slow, especially in regard to capturing the viscous effects such as wakes and secondary flow. In a single stage pump, the interaction of the guide vane or stator wake with the rotor generates noise and forced vibration. The prediction of noise and vibration requires accurate simulation of wakes and secondary flow as well as the unsteady pressure field in the subsequent blade rows.

The overall objective of this research is to develop numerical techniques to predict the rotor-stator interaction effects and the noise generated. The approach is to use steady Navier-Stokes code for the upstream blade rows, and utilize the computed steady flow field to predict the unsteady flow field in the subsequent blade row. This paper presents results from the first step, the flow field in the guide vane of a pump. The inlet guide vane flow field has been computed accurately and presented in this paper. An existing code (Ho and Lakshminarayana, 1994) has been used to accomplish this goal. The code is validated against bench mark quality data in a high Reynolds number pump (HIREP) acquired by Zierke et al. (1993).

Governing Equations and Numerical Techniques

A steady-state, three-dimensional, incompressible Navier-Stokes solver, which utilizes a pressure based method, has been developed by Ho and Lakshminarayana (1996). Chien's Low-Reynolds-Number form of the two-equation model is used to capture the turbulence and transition effects. The momentum equations, two equation turbulence transport equations, and pressure equation are solved. These equations are all written in the same diffusion-convection manner in the generalized coordinate system (ξ, η, ζ) given by:

$$\frac{\partial(\rho JG_1\phi)}{\partial\xi}+\frac{\partial(\rho JG_2\phi)}{\partial\eta}+\frac{\partial(\rho JG_3\phi)}{\partial\zeta}$$
$$=\frac{\partial}{\partial\xi}\left(\Gamma\alpha J\frac{\partial\phi}{\partial\xi}+\Gamma\theta_1J\frac{\partial\phi}{\partial\eta}+\Gamma\theta_2J\frac{\partial\phi}{\partial\zeta}\right)$$
$$+\frac{\partial}{\partial\eta}\left(\Gamma\theta_1J\frac{\partial\phi}{\partial\xi}+\Gamma\beta J\frac{\partial\phi}{\partial\eta}+\Gamma\theta_3J\frac{\partial\phi}{\partial\zeta}\right)$$
$$+\frac{\partial}{\partial\zeta}\left(\Gamma\theta_2J\frac{\partial\phi}{\partial\xi}+\Gamma\theta_3J\frac{\partial\phi}{\partial\eta}+\Gamma\gamma J\frac{\partial\phi}{\partial\zeta}\right)+JS \quad (1)$$

The numerical scheme used is the PISO scheme due to Issa (1985). Second-order central difference schemes are used for the discretization of all the equations. In order to stabilize the solution, second and fourth-order central difference schemes are added to the momentum equations:

$$+\frac{1}{2}\epsilon_2\left[\frac{\partial}{\partial\xi}\left(|\rho JG_1|\frac{\partial\phi}{\partial\xi}\right)+\frac{\partial}{\partial\eta}\left(|\rho JG_2|\frac{\partial\phi}{\partial\eta}\right)\right.$$
$$\left.+\frac{\partial}{\partial\zeta}\left(|\rho JG_3|\frac{\partial\phi}{\partial\zeta}\right)\right]-\frac{1}{8}\epsilon_4\left[\frac{\partial}{\partial\xi}\left(|\rho JG_1|\frac{\partial^3\phi}{\partial\xi^3}\right)\right.$$
$$\left.+\frac{\partial}{\partial\eta}\left(|\rho JG_2|\frac{\partial^3\phi}{\partial\eta^3}\right)+\frac{\partial}{\partial\zeta}\left(|\rho JG_3|\frac{\partial^3\phi}{\partial\zeta^3}\right)\right] \quad (2)$$

Explicit addition of these terms makes it possible to accurately control the artificial dissipation. Since the second-order artificial dissipation term has strong effect on the accuracy of the solution, ϵ_2 is gradually reduced from 0.5 (initial) to 0.0 (final) in the iteration process.

Contributed by the Fluids Engineering Division for publication in the JOURNAL OF FLUIDS ENGINEERING. Manuscript received by the Fluids Engineering Division May 4, 1995; revised manuscript received February 20, 1996. Associate Technical Editor: L. Nelik.

The power-law schemes are used in the discretization of the k-ϵ equations, which require strong artificial dissipation. A pressure-correction equation is derived from the continuity equation and is used to update the pressure field. In the governing equations, the first derivative terms and the second derivative terms, which do not contain cross derivatives, are treated implicitly. The remaining terms are treated explicitly. The E-factor under-relaxation scheme due to Van Doormaal and Raithby (1984) is used in the formulation. The systems of algebraic equations are solved by an ADI method.

Periodic boundary condition is used for all the velocity components, pressure, k and ϵ at periodic surfaces. The no-slip condition is used on all the solid surfaces. Turbulence kinetic energy is set to zero at the solid surfaces. For Chien's (1982) model, the gradient in the turbulence dissipation rate is also set to zero on the solid surfaces. At the computational inlet plane, velocity vectors, free stream turbulence intensity, and length scale are prescribed using measured data. At the exit, static pressure is specified at mid-span and the following simplified radial equilibrium equation is used to derive the radial distribution of the static pressure:

$$\frac{\partial p}{\partial r} = \frac{\rho V_\theta^2}{r} \tag{3}$$

Validation Case

The case investigated here is the water flow through the IGV of the HIREP, which is measured by Zierke et al. (1993). HIREP consists of an inlet guide vane (IGV) with thirteen blades and a rotor with seven blades. This is a constant hub-tip radius stage (0.5) with a tip radius of 0.5334 m. The axial distance between the IGV and the rotor is about one IGV chord, which is 0.175 m. The IGV has a solidity of 1.36 at the hub and 0.68 at the tip. The IGV is lightly loaded, with axial inlet flow. Based on an inlet velocity of 10.5 m/s and the IGV chord, the Reynolds number is 2.6×10^6. At the inlet, the freestream turbulence intensity is 0.7 percent and the turbulence length scale is 8 mm (Zierke et al., 1993). At midspan, the blade stagger angle is 7.4 degrees, and the outlet flow angle is about 13 degrees. The variation of the blade turning angle in radial direction is very small. Measured static pressure on the IGV blade surface indicates that the blade has slightly lower loading near the endwalls than in the midspan. Detailed laser and five-hole probe data has been acquired (Zierke et al., 1993). At 49.7 percent axial chord downstream of the IGV, a miniature five-hole probe is used to measure the wake profiles at eleven radial locations.

Flow Field Inside the IGV Passage

Static Pressure Distribution on the Blade Surface. A $121 \times 51 \times 51$ (streamwise, tangential, and radial) grid is generated for the IGV and the grid is clustered near the blade surface and the hub and tip walls in order to accurately capture the boundary layers. No grid sensitivity study is carried out for this case. The value of y^+ for the first grid point away from the walls is less than 2.0. The computational inlet plane is located 78 percent axial chord upstream of the IGV leading edge. The endwall boundary layer thicknesses at the inlet are set to nearly zero. The exit plane is located one chord downstream of the trailing edge of the IGV.

Figure 1 shows the comparison between the predicted and measured blade surface static pressure coefficients K_p. The agreement between experiment and prediction is good. The distributions of the pressure coefficients at all the five radial locations are similar. On the pressure surface, the pressure decreases rapidly to about 10 percent chord, and is nearly constant beyond this point. On the suction surface, the pressure has a favorable gradient near the leading edge, and has a strong adverse pressure gradient near the trailing edge. This strong adverse pressure gradient causes the flow to separate on the suction surface near the trailing edge. The computation does capture the separation on the suction surface very near the trailing edge. Since the predicted pressure gradient is smaller than the measured values, the predicted separation length is also smaller. The predicted corner separation zone is also smaller than the measured one. The blade loading level is slightly lower for locations near the endwalls than the midspan location. The incidence angle near

Nomenclature

C = blade chord
C_f = skin friction coefficient, $= \tau_w/0.5\ \rho V_{\text{ref}}^2$
C_p = pressure coefficient, $C_p = (p - p_{\text{ref}})/0.5\ \rho V_{\text{ref}}^2$
C_{p0} = total pressure coefficient, $[(p_0 - p_{0,\text{ref}})/0.5\ \rho V_{\text{ref}}^2]$
C_x = axial chord
$\mathbf{e}$ = unit vector of coordinate system
G_1, G_2, G_3 = contravariant velocities
J = Jacobian of the coordinates transformation
K_p = pressure coefficient, $K_p = (p - p_{\text{ref}})/0.5\ \rho U_{\text{tip}}^2$
k = turbulence kinetic energy
l_t = turbulence length scale
p = static pressure
p_0 = total pressure
r, θ, x = radial, tangential, and axial coordinates
S = source term in Eq. (1)
T_u = freestream turbulence intensity
U_{tip} = rotation speed of the rotor tip
V = total velocity
V_c = total velocity at wake center
v_d = maximum velocity defect or gust amplitude
v_n = amplitude of the nth Fourier harmonic of the velocity
v_r, v_θ, v_x = velocity component in radial, tangential, and axial direction
$\mathbf{v}_s$ = secondary velocity vector (Eq. 7)
x, y, z = Cartesian coordinates, with x in axial direction ($x = 0$ at leading edge)
$y^+ = (\tau_w/\rho)^{1/2}\rho y/\mu$
$\alpha, \beta, \gamma = \nabla\xi\cdot\nabla\xi,\ \nabla\eta\cdot\nabla\eta,\ \nabla\zeta\cdot\nabla\zeta$
α = yaw angle
$\Delta\alpha_2$ = deviation angle ($=\alpha_2 - \alpha_{2,\text{avg}}$)
β = pitch angle
Γ = isotropic diffusion coefficient
ϵ = turbulence dissipation rate
ϵ_2, ϵ_4 = second and fourth-order artificial dissipation coefficients
ζ = loss coefficient, $\zeta = (p_0 - p_{01})/0.5\ \rho V_{\text{ref}}^2$
ζ_0 = averaged loss coefficient
θ = tangential coordinate, measured from suction surface to pressure surface in degree
θ = momentum thickness
$\theta_1, \theta_2, \theta_3 = \nabla\xi\cdot\nabla\eta,\ \nabla\xi\cdot\nabla\zeta,\ \nabla\eta\cdot\nabla\zeta$
μ = molecular viscosity
ξ, η, ζ = generalized coordinates
ρ = density
τ_w = wall shear stress, $= \mu(\partial u/\partial y)|_{y=0}$
ϕ = general scalar dependent variable (u, v, w, p, k, ϵ, or other variables)

Subscripts

avg = passage-averaged (Eq. 5)
d = defect at the centerline of wake or maximum variation
e = freestream value
le, te = leading and trailing edges
ref = reference value at inlet
1, 2 = inlet and exit

Superscript

$-$ = passage-averaged

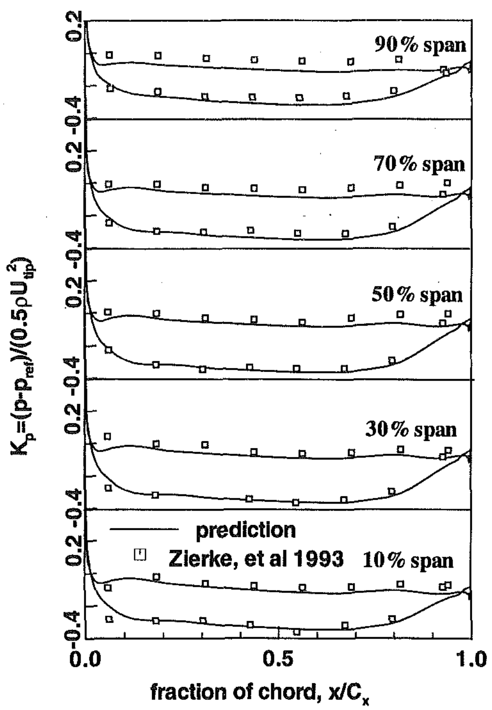

Fig. 1 Static pressure distribution on the blade surface of the IGV (90 percent span is near the tip)

the leading edge is found to decrease from the midspan to endwalls. This suggests three-dimensionality of the flow field as the flow approaches the blade.

Momentum Thickness and Loss Coefficient. Figure 2 shows the spanwise distribution of the momentum thickness on the suction surface of the IGV at three axial locations: 50, 75, and 95 percent chord. The momentum thickness increases with axial distance, and is more pronounced near the endwalls due to the interaction between the endwall boundary layer and the blade boundary layer on the suction surface. In addition to this, the corner separation at the hub wall and the casing wall and the blade trailing edge cause the momentum thickness to increase dramatically near the blade trailing edge. It should be noted that the calculation of the momentum thickness is not accurate very near the endwalls because the boundary is three-dimensional there and near the blade trailing edge. It is interesting to note that the momentum thickness near the trailing edge decreases as the wall is approached and increases dramatically very near the wall. This is due to the interaction between the corner separation, secondary flow, and the blade boundary layer. In the secondary flow region, the entrainment of the fluid by the secondary vortex has beneficial effect on the blade boundary layer in the immediate vicinity of the outer edge of the boundary layer. At the first two axial locations (50 and 75 percent chord), the momentum thickness is small and constant radially, except in the end wall regions. But near the trailing edge, the momentum thickness increases from hub to tip away from the wall.

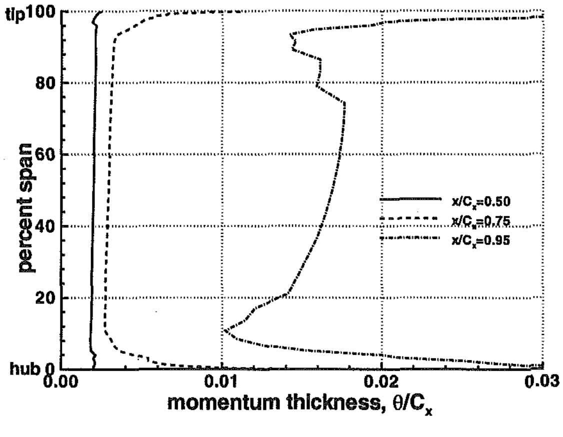

Fig. 2 Predicted momentum thickness distribution on the suction surface of the IGV

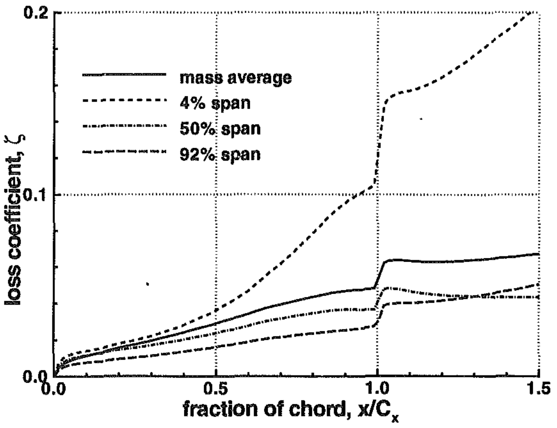

Fig. 3 Distribution of loss coefficient inside and downstream of the blade passage of the IGV

Experiment shows a transition occures at 15 percent chord at midspan. The present k-ϵ model has the inherent ability to capture the transition without any manual specification of the location of the transition. However, for the present case, a transition is predicted very near the leading edge. It is caused by the fact that this turbulence model usually gives high values of turbulent kinetic energy near the leading edge and thus predict the transition much earlier. Some modification has to be made during future study to predict the transition accurately.

Figure 3 shows the passage-averaged aerodynamic loss coefficient distribution inside the blade passage. The loss coefficient is defined as the loss of passage- and mass-averaged total pressure coefficient,

$$\zeta = C_{p0,\mathrm{avg}|\mathrm{le}} - C_{p0,\mathrm{avg}} \tag{4}$$

where the definition of the passage- and mass-averaging for a quantity ϕ is:

$$\phi_{\mathrm{avg}} = \frac{\int_s^p \rho v_x \phi d\theta}{\int_s^p \rho v_x d\theta} \tag{5}$$

The average loss coefficient is calculated by integrating the loss coefficient in the radial direction,

$$\zeta_0 = \frac{\int_{\mathrm{hub}}^{\mathrm{tip}} \rho (v_x \zeta)_{\mathrm{avg}} r dr}{\int_{\mathrm{hub}}^{\mathrm{tip}} \rho v_{x,\mathrm{avg}} r dr} \tag{6}$$

In Fig. 3, the $x/C_x = 0$ is the location of the blade leading edge. The trailing edge is at $x/C_x = 1$. At 4 percent span, the loss is much larger than the losses at other locations shown in the figure. This is due to the interaction between a large corner separation, which is observed experimentally, and the blade boundary layer. The casing wall corner separation is much smaller that the hub wall separation. The losses increase almost linearly from the leading edge to the trailing edge. The jump near the trailing edge is caused by the wake mixing. The increase in loss beyond this point is small, except for the 4 percent span.

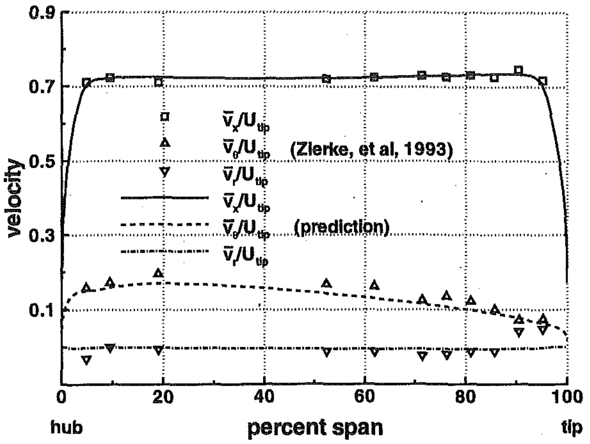

Fig. 4 Passage-averaged velocity distribution at 49.7 percent axial chord downstream of the IGV trailing edge

Flow at the Exit of the IGV

Radial Distribution of the Passage-Averaged Velocities and Flow Angles. The passage-averaged axial, tangential and radial velocity profiles at 49.7 percent chord axially downstream of the trailing edge of the IGV is compared with data in Fig. 4. The predictions are in excellent agreement with the data. The boundary layer thicknesses at the hub and the tip walls are also predicted very well. Because of the development of the endwall boundary layers, the axial velocity near the edges of the endwall boundary layers show slightly higher values than the axial velocity near the midspan section. Average radial velocity is very small in magnitude (Fig. 4). Measured radial velocity shows a higher value near the tip. This is possibly due to a measurement problem mentioned by Zierke et al. (1993). The lower radial velocity predicted near the hub is due to the lower predicted corner separation zone. The flow outlet angle ($\alpha_{2,\text{avg}}$) is about 13 degrees at midspan and is reduced several degrees towards the hub and the tip (Fig. 5). The flow turning decreases from midspan to endwalls. The agreement between the prediction and the data is good (both v_θ and α_2), considering the accuracy of the measurement with a five-hole probe is ±1°. The overturning very near the walls, caused by the secondary flow, is captured, even though there is no data available in this region. The underturning near the hub wall, from 5 to 20 percent of span, due to secondary flow and flow separation, is also captured reasonably well.

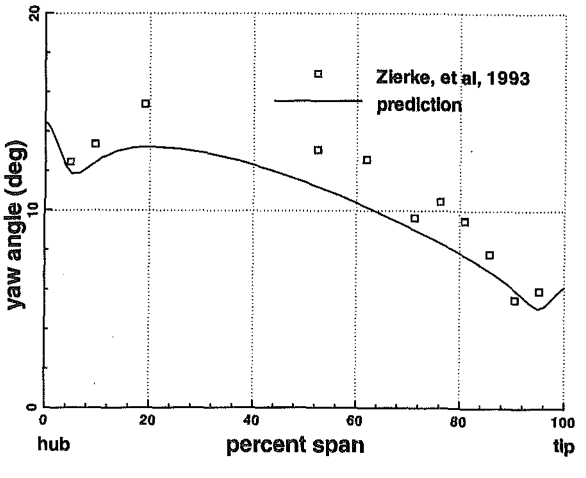

Fig. 5 Passage-averaged yaw angle distribution at 49.7 percent axial chord downstream of the IGV trailing edge

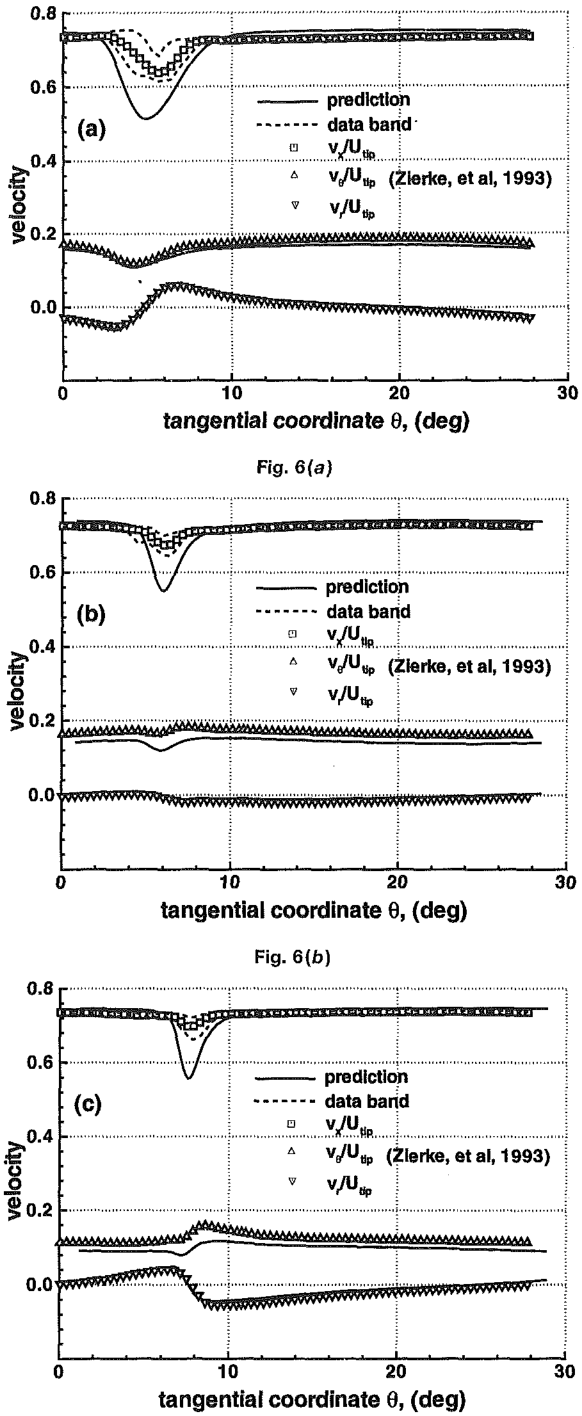

Fig. 6(*a*)

Fig. 6(*b*)

Fig. 6(*c*)

Fig. 6 Wake profiles at 49.7 percent axial chord downstream of the IGV trailing edge: (*a*) 9.5 percent span, (*b*) 52.4 percent span, (*c*) 81.0 percent span

Wake Characteristics and Effects of Turbulence Length Scale. Figure 6 shows the comparison between the predicted and the measured wake profile at three typical radial locations. The radial component of the velocity inside the wake is predicted very well, including the magnitude of the inward and outward radial velocity. The tangential velocity profiles are nearly identical to those of the measurement, but with a small and nearly constant shift. This is possibly due to the assumption that the inlet flow is axial.

The largest discrepancy between the prediction and the data is in the maximum velocity defect of the axial velocity profile. Zierke et al. (1993) measured the flow field in all the thirteen IGV passages and found considerable variation in the wake profiles across the circumference. The data band, shown in Fig. 6(*a*), (*b*), and (*c*), shows the scatter in the maximum defect in axial velocity in the wake is very large. Although the scatter in maximum velocity defect measured is quite large, the predicted values are still larger than the peak values of velocity defect measured. This is true for all spanwise locations. Also, the predicted wake width is slightly larger than the measurement.

The source of the discrepancy may be due to both the computational and the experimental inaccuracy. The experimental data was acquired with a five hole probe of diameter 1.67 mm. The spatial error due to the probe may account for some of the discrepancy. The other possibility in experimental inaccuracy is that the wakes may not be steady, they may oscillate due to the presence of the trailing vortex and the rotor downstream. Hence the probe may be averaging the wake resulting in lower axial velocity defects.

The computational inaccuracy may be due to the grid and the turbulence model used. In previous numerical investigations, Ho and Lakshminarayana (1996) found that freestream turbulent length scale and turbulent intensity can have appreciable influence on the wake prediction. In this calculation, a freestream turbulence intensity of 0.7 percent and a turbulence length scale of 8 mm are used (according to Zierke et al., 1993). An increase in turbulence length scale can reduce the maximum defect in the wake considerably. This is clear from the two-dimensional numerical simulation of the flow in the midspan section of the IGV carried out with three different turbulence length scale (Fig. 7). In the present three-dimensional computation, the values of T_u and length scale suggested by Zierke et al. (1993) are used. The predictions shown in Fig. 7 agree with the correlation suggested by Raj and Lakshminarayana (1973). The five hole probe, with a finite size, may be averaging the velocity near the wake center line, thus indicating lower velocity defect.

The two-dimensional profile loss coefficients predicted for these three cases are shown in Fig. 8. As expected, with an increase in the turbulence length scale, the profile loss at the exit increases due to faster decay of the wake. The loss coefficients at the exit for two-dimensional simulations ranges from 0.025 to 0.029, which is smaller than the three-dimensional prediction. It is possible that the radial velocity in the three-dimensional wake generates higher losses.

The IGV wake profiles are Fourier-decomposed to derive the harmonic contents. This is of interest to acousticians and designers in the prediction of the noise and vibration in the subsequent rotor blade row. The comparison between the predicted and measured harmonic content of the wake profiles shown in Fig. 9. Fourier coefficients with order of n which is not an integer multiple of 13 (No. of IGV blades) are very small and not shown in the figure. The measured background noise floor is of the order of 10^{-3} (v_n/U_{tip}). So Fourier harmonic with the order greater than 130 is not included in the figure either. The predicted tangential and radial components of the harmonics are in good agreement with the data. The predicted axial components of the harmonic are larger than the measured values. This is caused by the larger predicted maximum wake defect, shown in Fig. 6.

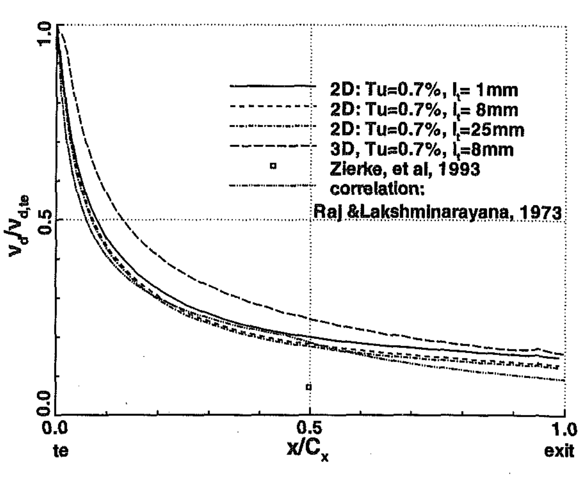

Fig. 7 Decay characteristics of the wake at mid-span predicted from 2-D simulation

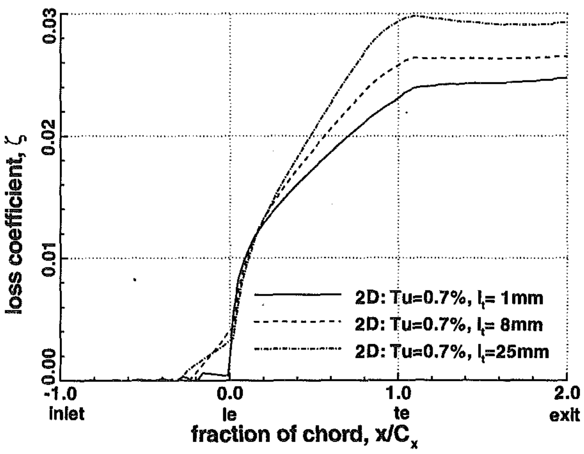

Fig. 8 Loss coefficient distribution at the mid-span predicted from 2-D simulation

Secondary Flow at the Exit. The measured and predicted secondary velocity vectors at 49.7 percent chord downstream of the IGV trailing edge are plotted in Figs. 10(*a*) and (*b*), respectively. The plotting plane is normal to the machine axis. The secondary velocity is derived by subtracting the circumferential-averaged tangential velocity at a given radius from the velocity vector,

$$\mathbf{v}_s = v_r \mathbf{e}_r + (v_\theta - v_{\theta,\text{avg}})\mathbf{e}_\theta \tag{7}$$

where $v_{\theta,\text{avg}}$ is the passage-averaged tangential velocity, $\mathbf{e}_r$ and $\mathbf{e}_\theta$ are unit vector in radial and tangential directions, respectively. The measured secondary velocities are derived from Zierke et al. (1993). The vectors are shown are viewed from downstream to upstream.

The location of the wake center and the trailing vortex sheet are clearly seen in both Fig. 10(*a*) and (*b*). Near the outer radius, the secondary vortex is clockwise, while it is counterclockwise near the hub. In the measurement, 42 percent span is found to have the maximum lift. In the computation, that section is closer to 45 percent span. The secondary flow near the casing is fairly strong and covers nearly 30 percent of the span near the suction surface corner. The predictions are in reasonably good agreement with the data. The location of the secondary vortex core, as well as extent, is captured well. The location and magnitude of the secondary flow in the hub region are also captured well.

The distribution of deviation angle $\Delta\alpha_2$ $(=\alpha_2 - \alpha_{2,\text{avg}})$ is plotted in Figs. 11(*a*) and (*b*). Excellent agreement between the prediction and the measurement is achieved. The discrepancy between the measurement and the prediction is at most one degree. The deviation angle (due to secondary flow) is one of the most important parameters sought by designers as these influence the flow field in subsequent blade rows. The Navier-Stokes code is able to capture both the local and the average

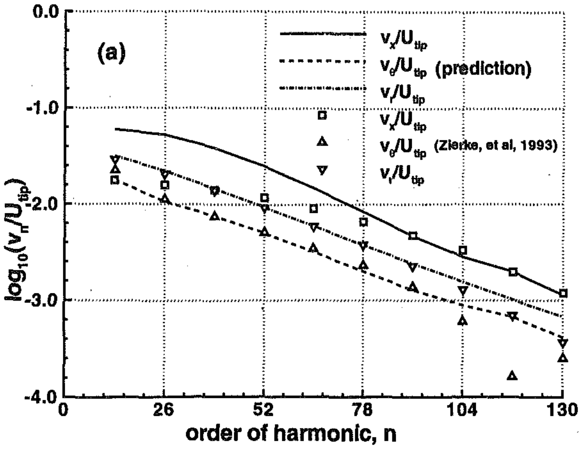

Fig. 9(*a*)

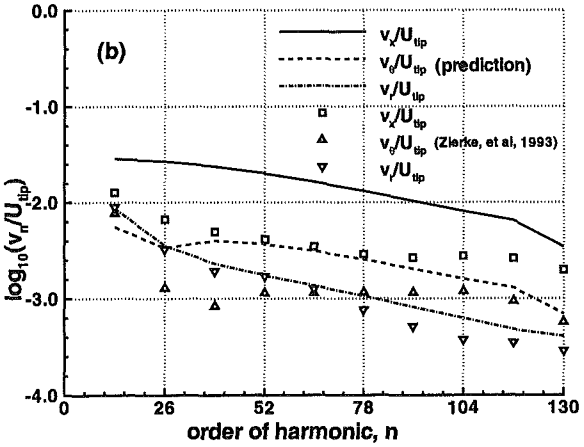

Fig. 9(*b*)

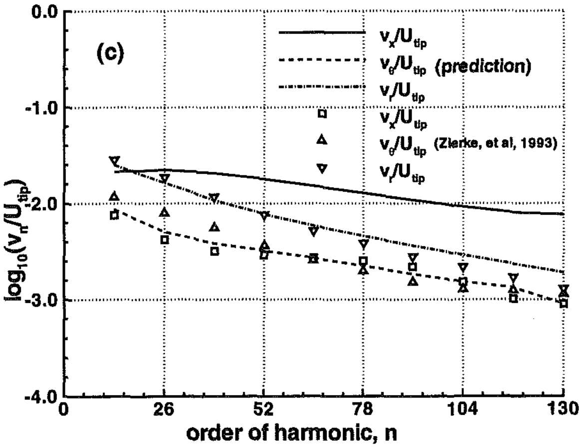

Fig. 9(*c*)

Fig. 9 Fourier content of the wake at 49.7 percent axial chord downstream of the IGV trailing edge, (*a*) 9.5 percent span, (*b*) 52.4 percent span, (*c*) 81.0 percent span

outlet angles shows its usefulness in the design and the performance analysis of pumps.

The Decay Characteristics of the Wake and the Secondary Flow. Both the wake and the secondary flow are major causes of unsteadiness, vibration, and noise generation in the subsequent rotor blade. The level of unsteadiness depends on the magnitude of the wake depth and the distortion caused by the secondary flow. The wake and the secondary flow both decay downstream of the trailing edge. It is interesting to know which of these sources decays faster and this should provide clue to the major sources of noise and vibration in pumps. The contour of the decay of the axial velocity defect in the wake ($v_{x,d}$) in the *x*-*r* plane is shown in Fig. 12. The decay rate of the wake in the axial direction is rapid near the trailing edge and slows down toward the exit computational plane. In the radial direction, the decay rate of the wake is almost constant over most of the span. The slowest decay rate occurs within a 10 percent span from the endwalls. A similar decay pattern is observed for the tangential component of the secondary flow as shown in Fig. 13. Here, the maximum variation of the tangential velocity in one pitch, $v_{\theta,d}$, is chosen as the represent of the secondary flow strength. It is clear from Figs. 12 and 13 that the decay of the secondary flow is much slower and the noise and vibration due to this source may dominate those due to the wake.

In order to compare the decay rate of the wake ($v_{x,d}$) and the secondary flow ($v_{\theta,d}$), the velocity defects or maximum variations are normalized by their respective values at the trailing edge (Fig. 14). Three spanwise locations are shown. Near the endwalls, where the wake and secondary flow are strong, the decay of the secondary flow is slower than the decay of the wake. The midspan wake has the fastest decay rate of all the distortions. It is thus clear that the distortions due to end wall flow persist longer than those due to the wakes away from the end walls. Hence the flows in these regions (both wakes and secondary flow) are major contributors to the unsteadiness, noise and vibration in turbomachinery.

Concluding Remarks

A three-dimensional Navier-Stokes solver which utilizes a pressure-based method is used to compute the incompressible flow field through the inlet guide vane of a high-Reynolds number pump. Accurate control of numerical dissipation is achieved

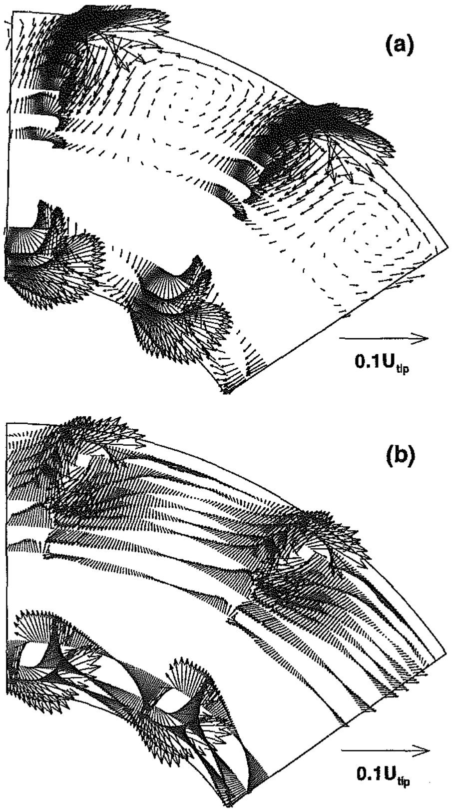

Fig. 10 Secondary velocity vectors (v_s) at 49.7 percent chord axially downstream of the IGV trailing edge, (*a*) prediction, (*b*) measurement

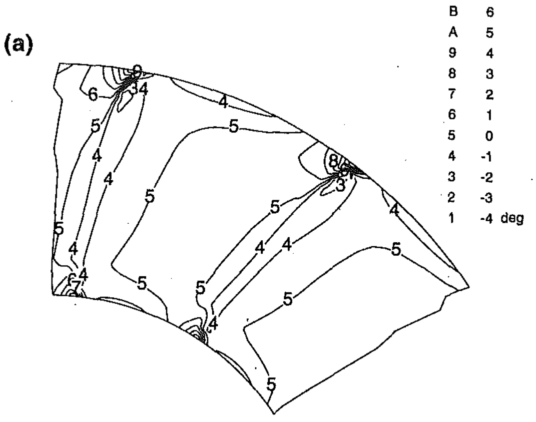

Fig. 11(*a*)

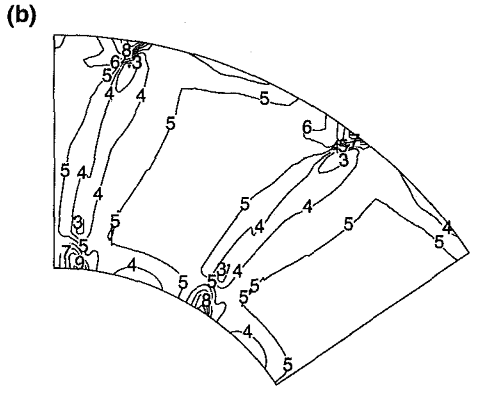

Fig. 11(*b*)

Fig. 11 Flow deviation angle ($\Delta\alpha_2$ in degrees) distribution at 49.7 percent axial chord downstream of the IGV trailing edge (*a*) prediction, (*b*) measurement

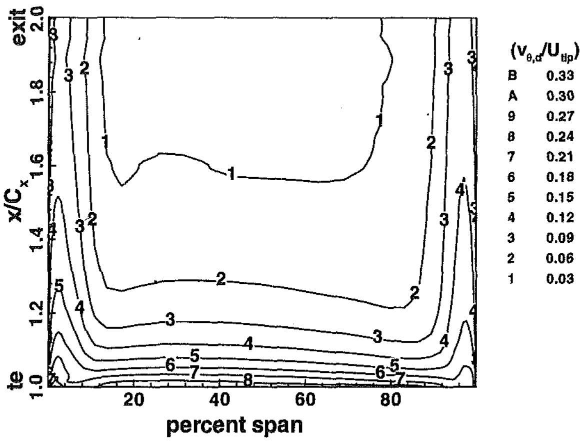

Fig. 13 Contour of the maximum variation in the tangential velocity ($v_{\theta,d}$) in *x-r* plane

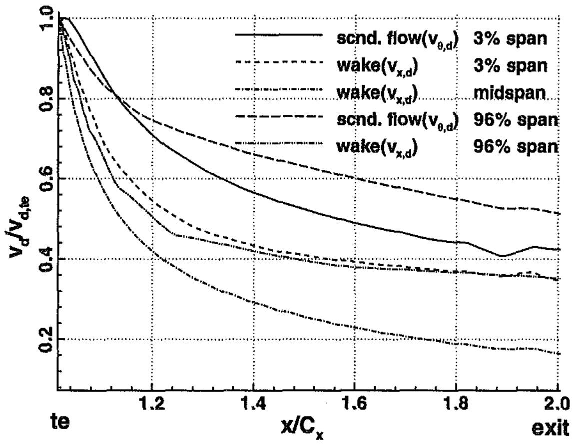

Fig. 14 Comparison of the decay of the wake and the secondary flow

through the use of explicit artificial dissipation terms. Based on the comparison between the computation and the measurement, the following conclusions can be drawn:

(1) The pressure distribution on the blade surface, and the flow inside the blade passage are predicted well.

(2) Tangential and radial components of the wake profiles are predicted very well. Discrepancy between the predicted and the measured maximum axial velocity defect of the wake is probably caused by numerical and experimental errors.

(3) Secondary velocity vectors and deviation angles at the exit of the IGV are in excellent agreement with the measurement. The Navier-Stokes procedure is thus very useful in the design and analysis of the pumps.

(4) The flow distortions in the end wall region (both wakes and secondary flow) decay slower than those due to the wake away from the end wall. Hence end wall flows may be major contributor to the unsteadiness, noise and vibration in pumps.

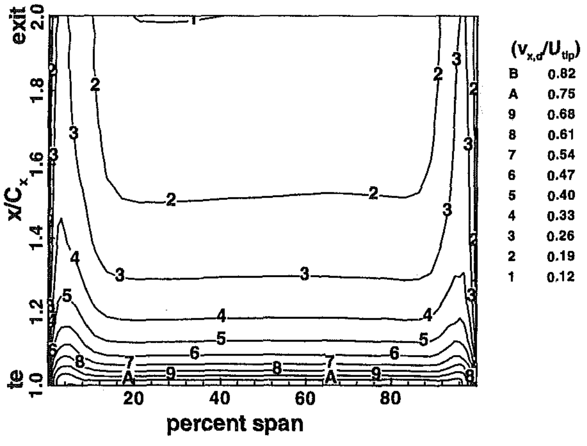

Fig. 12 Contour of the axial velocity defect ($v_{x,d}$) in *x-r* plane

Acknowledgment

This work is supported by the Office of Naval Research under the contract No. N00014-90-J1182 with J. Fein as the contract monitor. The authors are thankful to Dr. W. C. Zierke for providing the experimental data. Valuable suggestions by Dr. Y.-H. Ho in the use of the computational code and J. A. Mills, III in the preparation of this paper is acknowledged. The authors are also would like to acknowledge NASA for providing the supercomputing resources at the NAS Facility at NASA Ames Research Center.

References

Chien, K.-Y., 1982, "Predictions of Channel and Boundary-Layer Flows with a Low-Reynolds-Number Turbulence Model," *AIAA Journal*, Vol. 20, No. 1, pp. 33–38.

Ho, Y.-H. and Lakshminarayana, B., 1996, "Computational Modeling of Three-Dimensional Endwall Flow Through a Turbine Rotor Cascade with Strong Secondary Flows," *ASME Journal of Turbomachinery*, Vol. 118, pp. 250–260.

Issa, R. I., 1985, "Solution of the Implicitly Discretised Fluid Flow Equations by Operator-Splitting," *Journal of Computational Physics*, Vol. 62, pp. 40–65.

Lakshminarayana, B., 1991, "Assessment of Computational Techniques for Design and Analysis of Turbomachinery," ASME JOURNAL OF FLUIDS ENGINEERING, Vol. 13, pp. 315–352.

Raj, R., and Lakshminarayana, B., 1973, "Characteristics of the wake behind a cascade of airfoils," *Journal of Fluid Mechanics,* Vol. 61, Part 4, pp. 707–730.

Van Doormaal, J. P. and Raithby, G. D., 1984, "Enhancements of the SIMPLE Method for Predicting Incompressible Fluid Flows," *Numerical Heat Transfer,* Vol. 7, pp. 147–163.

Zierke, W. C., Straka, W. A., and Taylor, T. D., 1993, "The High Reynolds Number Flow Through an Axial-Flow Pump," The Pennsylvania State University/ARL Technical Report No. TR 93-12.

Air Influence on Similarity of Hydraulic Transients and Vibrations

T. S. Lee
Associate Professor.

S. Pejovic
Visiting Professor.

Mechanical and Production
Engineering Department,
National University of Singapore,
Singapore 119260

The effects of wave speed variation due to air content on the validity of similarity laws for model studies of hydraulic transients and hydraulic vibrations were investigated. Studies show that hydraulic similarities between geometrically similar model and prototype are reduced substantially for cases involving two- or three-phase flow. For flow with intensive cavitation, analysis shows that there is no hydraulic similarity between model and prototype. For pump discharge pipeline and turbine draft tube where two phase flow of air-water mixture occurs, analysis shows that the natural frequency and the response characteristics of the fluid system are a strong function of the local wave speed variation within the fluid system. This local wave speed variation is a function of the local transient air content and transient pressure.

Introduction

Hydraulic transients and hydraulic vibrations are common problems encountered in the operation of pumping stations, power plants, and hydraulic structures. Many model studies on the transient fluid flow and vibration problems have been carried out. Most of these studies are for cases with no air content in the fluid system (Pejovic, 1989–1990). However, in many applications, such as in turbine and pump operations, cavitation conditions are known to occur which resulted in two-phase flow at downstream of the fluid system. For cases with intensive cavitation in the fluid system, study on the similarity between model and prototype is few. With the present state-of-the-art, modelings of similarity for the time dependent hydraulic transient and vibration problems with air content were not satisfactory. Reliable data on air content and information on the characteristics of exciters are also difficult to obtain in prototype system (Jemcov et al., 1980). This add to the difficulties in trying to satisfactorily modelled similarity laws for the transient model studies with air content.

In model studies and analysis of prototype problems, similarity law for flow in hydraulic machine is generally valid for one-phase flow. Present guidelines and standards for equivalent model and prototype analysis accept that similarity of flow in model and prototype turbomachines exist before the critical cavitation coefficients are reached. In between the zone of incipient cavitation and critical cavitation (Fig. 1), similarity is considered to be satisfactory for the analyses of internal flow in machines. However, for flow in the downstream of the hydraulic machine and pipe system, a small quantity of gas bubbles will change system wave speed characteristics to the extend that similarity for the model study of hydraulic transient and hydraulic vibration problems may be difficult to satisfy. When hydraulic machines operate in the zone of cavitation (Fig. 2), air bubbles will flow through the machine resulting in two-phase flow in the downstream of the fluid system. Though deaeration devices may be used to minimize the air content, some air will still remain in the fluid system. Since it is almost impossible to predict the quantity of air getting through the machine and remain downstream of the system, systematic analysis has to be carried out with various assumed amount of air content (ϵ) in the model analysis of the transient fluid flow problem. The first study on the effects of air content on wave speed in a transient fluid system was conducted by Whiteman and Pearsall (1959). Detail survey on effects of air on wave speed in fluid systems was given by Lee (1991).

Modeling of Air Influence on Hydraulic Similarity

Two different types of air content models have been proposed in the literature in predicting the transient pressure behavior: the concentrated vaporous cavity model (Brown 1968; Provoost, 1976) and the discrete air release model (Lee, 1991–95; Wylie, 1993). The concentrated vaporous cavity model produces satisfactory results in slow transients, but produces unstable solutions for rapid transients, such as pump's stoppage with reflux valve closure. The discrete air release model produces satisfactory results in pump shut down cases, but is susceptible to long term numerical damping (Ewing, 1980; Jonsson, 1985). Typically, in the discrete air release model, the wave speed distribution along a pipeline (with node points $i = 0, 1, \ldots N$) is given by Lee (1991).

$$a_i^k = \sqrt{\rho_w(1 - \epsilon_i^k)\left(\frac{1}{K} + \frac{\epsilon_i^k}{np_i^k} + \frac{cD}{eE}\right)} \qquad (1)$$

The transient computation of the fraction of air content (ϵ_i) along the pipeline depends on the local pressure and local air volume:

$$\epsilon_T^{k+1} = \left(\frac{p_i^k}{p_i^{k+1}}\right)^{1/n} \epsilon_i^k \quad \text{and} \quad \epsilon_o^{k+1} = \left(\frac{p_o}{p_i^{k+1}}\right)^{1/n} \epsilon_o$$

$$\epsilon_i^{k+1} = \epsilon_T^{k+1} \quad \text{for} \quad p_i^{k+1} \geq p_g \quad \text{and} \quad \epsilon_T^{k+1} \leq \epsilon_o^{k+1} + \epsilon_g$$

$$\epsilon_i^{k+1} = \left(\frac{p_i^k}{p_i^{k+1}}\right)^{1/n} (\epsilon_i^k - \epsilon_g)$$

$$\text{for} \quad p_i^{k+1} \geq p_g \quad \text{and} \quad \epsilon_T^{k+1} > \epsilon_o^{k+1} + \epsilon_g$$

$$\epsilon_i^{k+1} = \left(\frac{p_i^k}{p_g}\right)^{1/n} (\epsilon_i^k + \epsilon_g) \quad \text{for} \quad p_i^{k+1} < p_g \qquad (2)$$

This air fraction content is then inserted into equation (1) to compute the wave speed along the pipeline for the various time level of transient computations through the characteristics equations:

Contributed by the Fluids Engineering Division for publication in the JOURNAL OF FLUIDS ENGINEERING. Manuscript received by the Fluids Engineering Division September 15, 1994; revised manuscript received February 20, 1996. Associate Technical Editor: L. Nelik.

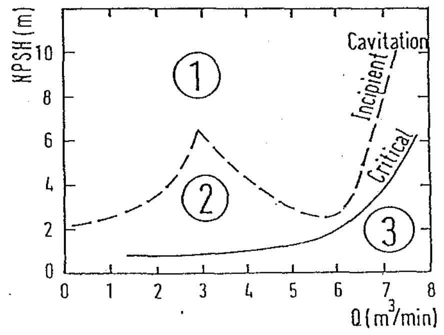

1 Similarity valid both for steady and transient flow (One-phase flow)

2 Similarity valid for steady internal flow. No similarity of transients and hydraulic vibrations (two-phase flow)

3 No Similarity

Fig. 1 Typical cavitation characteristics of cetrifugal pumps and domains for similarity

$$\pm \frac{g}{a}\frac{dh}{dt} + \frac{dc}{dt} + \frac{\lambda}{2D} c|c| \pm \frac{g}{a} c \sin \alpha = 0 \qquad (3)$$

The dynamic equation describing rotation of the pump during the run down stage is:

$$Idw/dt = M_e - M_h - M_f \qquad (4)$$

where M_e, M_h, M_f are the electric, hydraulic and bearing friction torque respectively.

The four quadrant characteristics of the run down pump is typically given by Fig. 2. Here, $h = H/H_o$, $\beta = M/M_o$, $v = Q/Q_o$, $\alpha = n/n_o$; $x = \pi + arctg(v/a)$ – speed – flow coefficient; $W_h = h/(\alpha^2 + v^2)$ – head coefficient and $W_M = \beta/(\alpha^2 + v^2)$ – torque coefficient. Subscript "o" relates to a reference point (usually point with highest efficiency).

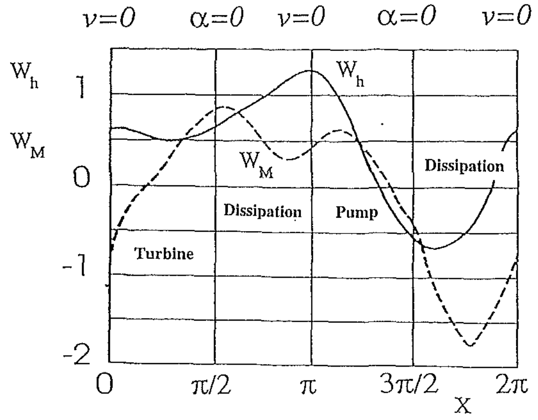

Fig. 2 Full centrifugal pump characteristics

Turbines, pumps, valves, air vessels, surge tanks, bifurcations, branches, dead-end pipes, loops, storage basins, etc, are represented by a general matrix equations of the form:

$$\begin{Bmatrix} H \\ Q \end{Bmatrix}_D = \begin{bmatrix} \cosh \gamma l & -Z_C \sinh \gamma l \\ -(\sinh \gamma l)/Z_C & \cosh \gamma l \end{bmatrix} \begin{Bmatrix} H \\ Q \end{Bmatrix}_U \qquad (5)$$

The hydraulic inertance $L = 1/(gA)$, hydraulic resistance $R = Q/(gdA^2)$ and hydraulic capacitance $C = gA/a^2$. The complex frequency $s = \sigma + i\omega$ (σ – coefficient of attenuation, ω – angular frequency). The characteristic impedance of the pipe is $Z_C = \gamma/Cs$ with $\gamma\sqrt{Cs(Ls + R)}$ = a complex propagation constant and l = pipe length.

From Eq. (5), the equations for hydraulic machines can be expressed in a simplified matrix form

Nomenclature

a = wave speed at a pipe section
A = cross-section area
c = flow velocity; parameter describing pipe constraint condition
C = hydraulic capacitance
D = diameter
e = pipe wall thickness
E = modulus of elasticity
f = frequency; dimensionless frequency, friction factor
F_r = Froude number
g = gravitational acceleration
h = piezometric pressure head; dimensionless pressure head
H = pressure head; amplitude of pressure head
H_p, H_c = represent the upstream and downstream pressure head at the penstock valve respectively
I = moment of inertia of rotating parts
K = bulk modulus; dimensionless parameters
l = length of pipe
L = hydraulic inertance; length of pipe section
M = slope of pump head-discharge curve; torque
N = speed of rotation, T time
NPSH = net positive suction head
n = speed of rotation; polytropic exponent
O = circumference of flow cross-section
p = pressure
p_g = gas release pressure
Q = amplitude of flow oscillation; volumetric flow
R = hydraulic resistance
R_h = hydraulic radius
s = complex frequency
t = time
T_a = unit starting time
T_f = closing time; period of oscillations
T_s = characteristic time; closing time of wicket gates or valves; period of oscillations
T_w = water starting time
u = peripheral speed of hydraulic machine runner
W_h = head coefficient
W_M = torque coefficient
x = distance along pipe; speed flow coefficient
Z_c = characteristic impedance of pipe
α = dimensionless speed of rotation (angular speed), pipe inclination
γ = propagation constant
ϵ = fraction of air or gas in liquid
ϵ_o = fraction of free gas in liquid at atmospheric pressure
ϵ_g = fraction of dissolved gas in liquid
λ = friction factor
ρ_w = mass density; water density
ω = angular frequency; angular speed
σ = coefficient of attention
σ_c = coefficient of cavitation, σ_c = NPSH/H
φ = slope of head-discharge curve

Subscripts

D = downstream end of pipe
i = denotes x-mesh
k = denotes time step
o = reference operating point (usually point with highest efficiency in pump operation)
U = upstream end of pipe
t = turbine

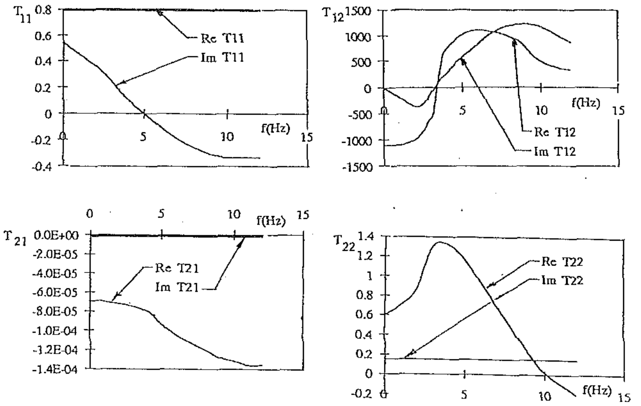

Fig. 3 Measured centrifugal pump matrix

$$\begin{Bmatrix} H \\ Q \end{Bmatrix}_D = \begin{bmatrix} 1 & -M \\ 0 & 1 \end{bmatrix} \begin{Bmatrix} H \\ Q \end{Bmatrix}_U + \begin{Bmatrix} H_p \\ Q_p \end{Bmatrix} \tag{6}$$

where $M = tg\varphi$ − slope of head-discharge curve; H_p and Q_p are the excitation pressure head and flow rate respectively. The value of M is usually assumed a real constant for pumps and turbines if the opening of wicket gates remains constant in the transient regime. For valve, $M = 2H/Q$ (H is the head loss, Q is the discharge through the valve).

However, the dynamic instability in many pumping systems with air content can not be analysed accurately by the above matrix model Jacob and Prenat (1990). An improved matrix model equation is proposed here:

$$[T] = \begin{bmatrix} T_{11} & T_{12} \\ T_{21} & T_{22} \end{bmatrix} \tag{7}$$

The four complex functions of frequency in Eq. (7) can be measured either in the laboratory or in the field. This is obtained through installation of four pressure transducers: two on the suction side and two on the discharge side of the straight section on both side of the machine. With three pressure transducers mounted on the downstream side of the fluid machinery, it is also possible to measure the wave speed for the downstream fluid system. For flow between incipient and critical cavitation conditions, it is noted that similarity law can be fulfilled with matrix equation (7). For cavitating and two-phase flows, the matrix can be obtained through experimental or field measurements. Figure 3 shows a measured pump matrix (Pejovic et al., 1993, 1994).

Results and Discussions

From the formulation through Eqs. (1)−(7), the transient characteristics of the prototype pumping system during pump run down were obtained and studied in this work. The pressure distribution of the pumping system obtained through the numerical models are similarly applied to the models of the prototype. For the similarity of flow in the geometrically similar systems, models of the prototype are defined by the dimensionless coefficients presented in Table 1, where $T_w = Q_o/(gH_o)\ \Sigma\ L(i)/A(i)$ is the water starting time; T_S is the characteristic time (such as closing time of wicket gates or valves T_f or their period of oscillations T_{fth}); $T_p = \Sigma\ L(i)/A(i)$ is the quarter period of pipes and $T_\alpha = I\omega_o/M_o$ is the unit starting time.

Table 1 Similarity conditions

1. Dimensionless water starting time	$K_u = T_w/T_s$
2. Dimensionless pipes quarter period	$K_n = T_s/T_p$
3. Dimensionless unit starting time	$K_a = T_a/T_s$
4. Froude's No related to axial speed	$F_{rc} = c_{zo}^2/(2gH)$
5. Froude's No related to runner speed	$F_{rc} = u^2/(2gH)$
6. Dimensionless mass density	$K_p = \rho/\rho_o$
7. Dimensionless cross-section area	$K_a = A(i)/A_o$
8. Friction factor	f
9. Dimensionless hydraulic radius	$K_r = R_h(i)/R_{ho}$
10. Dimensionless wave speed	$K_w = a(i)/a_o$
11. Fraction of free gas in liquid	ϵ_o

Table 2 Similarity of models to prototype

	Prototype	Model 1	Model 2
1. Length	$L(i)$	$L(i)/10$	$L(i)/10$
2. Head	H	H	$H/25$
3. Flow velocity	c	c	$c/5$
4. Volumetric flow	Q	$Q/100$	$Q/500$
5. Characteristic time	T_s	$T_s/10$	$T_s/2$
6. Wave speed	$a(i)$	$a(i)$	$a(i)/5$
7. Diameter	D	$D/10$	$D/10$
8. No of waves	N	N	N
9. Pipe thickness .	s	$s/10$	$s/4.86$
10. Modulus of elasticity	E	E	$E/100$
11. Speed rotation	n	$10n$	$2n$
12. Frequency	F	$10F$	$2F$
13. Pump/turbine diameter	D_t	$D_t/10$	$D_t/10$
14. Inertia of rotating parts	I	$I/100000$	$I/100000$
15. Dimensionless frequency $\bar{f} = nT_p$	f	f	f

Parameters presented in Table 2 shows that two different models can be formulated for a given prototype conditions: model 1 operates with the same pressure in all the homologous points of a system; and model 2 operates with reduced pressure according to the similarity law. Model 1 can be made from the same materials (steel pipes, concrete, and steel conduits, etc.) as the prototype, or with suitable materials to give the same wave speed in the homologous parts of the system for both the model and prototype. However, model 1 requires that some of the similarity parameters to be equal for both the model and the prototype, such as the pressure head H, flow velocities $c(i)$ and wave speeds $a(i)$. Model 2 can be made of plastic pipes. Hence, the modulus of elasticity is reduced by about 100 times and with the appropriate wall thickness, the wave speed can be reduced by 5 times (Perko, 1984). With all other the dimensions

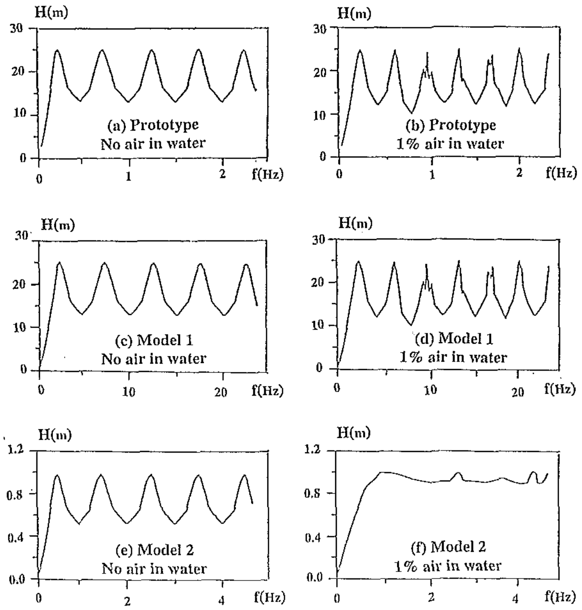

Fig. 4 Maximum pressure amplitudes in frequency domain

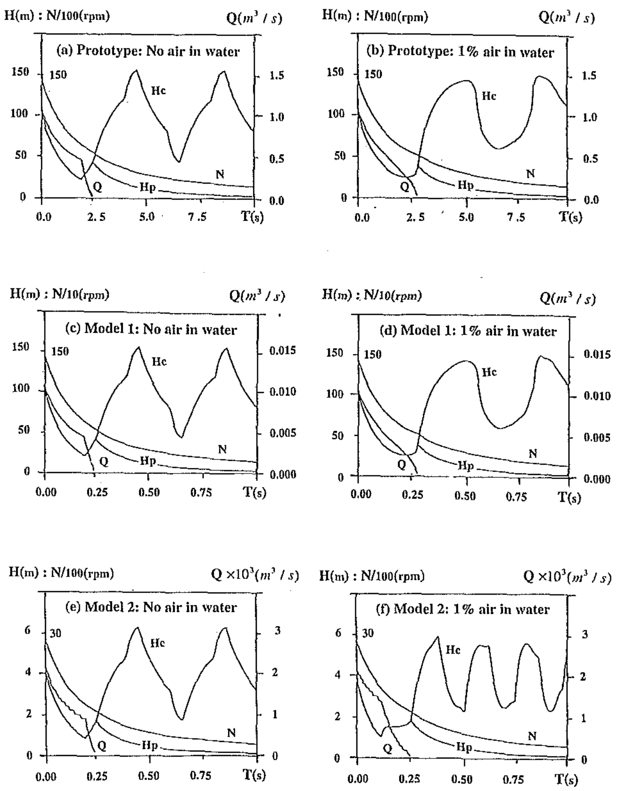

Fig. 5 Transient characteristics in time domain [*Hp*-pump head; *Q*-pump discharge; *N*-pump speed; *Hc*-pressure head downstream of check valve]

same as in model 1, the pressure head in model 2 is reduced by 25 times.

Numerical transient analysis were carried out for two different operating conditions: one-phase flow in a fluid system and two-phase flow of water and air bubbles mixture in the same system. The mathematical model for all the cases studied (prototype and the two models) include: two pumps in parallel operation each equipped with a nonreturn valve and a reservoir at the downstream end. The prototype system studied are: rated head of 100 m, discharge at 1.0 m^3/s and speed of rotation at 1450 rpm. The length of the pipe is 1000 m with a diameter of 1.0 m. Analysis was carried out for the rated operating point as the initial and boundary condition.

The homologous data for the models were calculated according to the similarity relations listed in the Table 2. The equality of the wave speeds $a(i)$ in all parts of model 1 can be fulfilled for the case of one-phase flow. For the case of two-phase flow, this equality can only be approximate, since the wave speeds are dependent on gas content and pressure. The wave speeds of $a(i)/5$ is difficult to achieve for the case of two-phase flow with model 2.

Results of the numerical computations for the prototype, model 1 (operating with the same pressure head) and model 2 (operating with a 25 times lower pressure head) for one-phase and two-phase flow conditions in the frequency domains are shown in Fig. 4. The corresponding cases in the time domain are shown in Fig. 5. Figures 4 and 5 show that, when the wave speed was reduced due to cavitation or air entrainment, the transient responses by model 1 and model 2 differ significantly. Some similarities were achieved for model 1 when compared with the results of the prototype. The results obtained from model 2 operating with the smaller pressure head was not satisfactory for system with 1 percent air. There is no similarity between the hydraulic transients of model 2 and the prototype, in spite of their geometrical similarity.

Conclusions

When models are geometrically similar to their prototypes in all aspects, similarity law when applied to hydraulic transients, hydraulic vibrations and pressure surges will generally be satisfied for all cases of one-phase liquid flow. For two-phase liquid flows, with geometrically similar models operating at the equivalent pressure head at the corresponding homologous point as the prototype, the similarity law may looked as though it is fulfilled. However, the variation of wave speed of the fluid system with respect to the gas content and transient pressure distorted the similarity characteristics the models of the gas-liquid system. For cases of incipient cavitation, study of the similarity of fluid flow through the physical models of prototype will be poor if the gas content in the fluid system is highly dependent on the transient pressure. For intensive cavitation and air entrainment in a fluid system, it is difficult to expect hydraulic similarity between the model and prototype flow.

Acknowledgment

Professor S. Pejovic wishes to acknowledge the National University of Singapore for providing a visiting professorship for his stay in Singapore.

References

Brown, F. T., 1968, "A Quasi Method of Characteristics with Application to Fluid Lines with Frequency Dependent Wall Shear and Heat Transfer," ASME *Journal of Basic Engineering*, pp. 217–227.

Ewing, D. J. F., 1980, "Allowing for Free Air in Waterhammer Analysis," *Proc. Third Int. Conf. Pressure Surges*, Canterbury, England, BHRA, pp. 80–91.

Jemcov, R., Krsmanovic, L., and Pejovic, S., 1980, "Excitations of Vibrations in Pumped Storage Power Plant 'Chaplaina,' (in Serbo-Croatian)," JUG EL, Ljubljana, pp. 443–495.

Jonsson, L., 1985, "Maximum Transient Pressures in a Conduit with Check Valve and Air Entertainment", Int Conf. on the Hydraulics of Pumping Stations, University of Manchester Inst of Sci and Tech (UMIST) & BHRA, England, pp. 55–76.

Lee, T. S., 1991, "Numerical Computation of Fluid Pressure Transients in Pumping Installations with Air Entrainment", *International Journal for Numerical Methods in Fluids*, Vol. 12, pp. 747–763.

Lee, T. S., 1994, "Numerical Modelling and Computation of Fluid Pressure Transients with Air Entrainment in Pumping Installations," *International Journal for Numerical Methods in Fluids*, Vol. 19, pp. 89–103.

Lee, T. S., 1995, "Numerical Studies on Effects of Check Valve Performance on Pressure Surges During Pump Trip in Pumping System with Air Entrainment," *International Journal for Numerical Methods in Fluids*, Vol. 21, pp. 337–348.

Pejovic, S., Boldy, A. P., and Obradovic, D., 1987, *Guidelines to Hydraulic Transient Analysis*, Technical Press, England.

Pejovic, S., 1989, "Similarity in Hydraulic Vibrations of Power Plants," Joint ASCE/ASME Int Conference on Fluids Machinery, San Diego, pp. 5–11.

Pejovic, S., 1990, "Similarity of Hydraulic Transients," *Pressure Surges—Proceedings of 6th Int Conf.*, BHAR, pp. 221–232.

Pejovic, S., and Boldy, A. P., 1992, *Guidelines to Hydraulic Transient Analysis of Pumping Systems*, P&B Press, Belgrade—Coventry, England.

Pejovic, S., Dunn, A., and Lai, C. K., 1993, "Machine Influence Stability and Response to Hydraulic Oscillations," *Proceedings, IAHR Working Group on the Hydraulic Machineries under Steady Oscillatory Conditions*, Lausane, pp. 30–36.

Pejovic, S., Dunn, A., and Lai, C. K., 1994, "Pump Influence on Hydraulic Vibrations and Stability in Laboratory and Reality," *Proc. IAHR 17th Symposium*, Beijing, Oct., pp. 1–6.

Perko, H. D., 1984, "Gasausscheidung in Instationarer Rohrstromung," Dissertation, University of Hannover, Institute for Fluid Mechanics.

Provoost, G. A., 1976, "Investigation into Cavitation in a Prototype Pipeline caused by Waterhammer," *Proc. 2nd Int Conf. on Pressures*, Bedford, England, BHRA, pp. 35–43.

Whiteman, K. J., and Pearsall, I. S., 1959, "Reflux Valve and Surge Tests at Kingston Pumping Station," Brit. Hydromech. Res. Asoc/National Engineering Laboratory Joint Report No 1.

Wylie, B. E., and Sweeter, L. V., 1993, *Fluid Transients*, Prentice-Hall, Englewood Cliffs, NJ.

L. Lebrère
Engineer, PSA Peugeot Citroën,
DRAS/RMP, Route de Gisy,
78140 Velizy-Villacoublay, France

M. Buffat
Professor of Université Claude Bernard,
Lyon I Laboratoire de Mécanique des
Fluides et Acoustique CNRS UMR 5509,
BP163, 69131 Ecully, France

L. Le Penven
Researcher, Laboratoire de Mécanique des
Fluides et Acoustique CNRS UMR 5509,
BP163, 69131 Ecully, France

B. Dillies
Engineer, PSA Peugeot Citroën,
DRAS/RMP, Route de Gisy,
78140 Velizy-Villacoublay, France

Application of Reynolds Stress Modeling to Engine Flow Calculations

To improve the prediction of turbulence inside internal combustion engines, a Reynolds stress turbulence model is implemented in the Kiva-II code. After a rapid description of the Launder-Reece-Rodi model (noted LRR), two validation test cases (the plane channel flow and the flow over a backward facing step) are presented. The advantages of a second order closure and the shortcomings of the LRR model are then analyzed. Finally, a simulation of an intake and compression stroke using both the standard $k - \epsilon$ model and the LRR model is described. As a precise knowledge of the velocity and turbulent fields near TDC is necessary for the prediction of the mixing and the combustion processes, we have analyzed the influence of the turbulence model on the flow field. Results are compared with experimental data and show a strong influence of the turbulence model even on the mean flow, especially at the end of the compression stroke (TDC).

1 Introduction

Numerical simulations of turbulent flows inside internal combustion engines have been used for many years (Gosman et al., 1984; El Tahry, 1985a; Watkins et al., 1991; Mao et al., 1994). Computational codes usually include many physical models to simulate all the phenomena involved in a combustion chamber (turbulence, combustion, spray). But, it is important to notice that, because the turbulence model describes the flow structure, it has a strong influence on the other physical models (combustion, spray, dispersion, . . .). The reliable predictive capabilities of a computational code for internal combustion flows partly lie on the potential of its turbulence model.

Today, all the industrial codes for engine flow simulations (FIRE, SPEED, STAR-CD, KIVA) use the $k - \epsilon$ model due to its robustness. However, turbulent flows in internal combustion engines have several characteristics that can not be described by a standard $k - \epsilon$ model. First, inside a combustion chamber, the anisotropy of the turbulence, due to the volume variation in the axial direction, cannot be taken into account by a $k - \epsilon$ model since this model is built on the hypothesis of a single velocity scale. Second, the $k - \epsilon$ model is inappropriate to simulate rotating flows (like swirl and tumble) which are extensively used inside IC engines to improve the combustion process in SI engines or the mixing process in diesel engines. To generate swirling or tumbling flows, new geometry configurations such as bowls in piston or roof-shaped combustion chambers have been devised for recent engines. Since the velocity and the turbulent fields are important parameters for mixing and combustion processes, it is necessary to characterize them precisely near TDC in order to improve the design of these new engines.

To improve the turbulence modeling and go beyond the Boussinesq hypothesis and the turbulent viscosity approach, we have adopted a second-moment closure model, which is called a Reynolds Stress Model (RSM). One of the first RSM models proposed in the literature is the Launder-Reece-Rodi model in 1975. At that time, computers were not powerful enough to allow the solution of the six additional transport equations for the Reynolds stresses $\widetilde{u_i u_j}$ and simplified versions such as Algebric Stress Models (ASM) have been developed (Rodi, 1976); but they lead to disappointing results for the flows where the diffusive or the convective transport plays an important role (Fu et al., 1988). Today, the growing power of computers allow us to consider the RSM models again. Many papers (El Tahry, 1985b; Jones et al., 1989; Watkins et al., 1990; Deschamps et al., 1994) have dealt with 2D axisymmetric steady or unsteady calculations using different turbulence models and RSM models usually prove to give better results, particularly in the case of swirling flows.

In this paper, we present a three-dimensional unsteady computation of an intake-compression stroke in a single cylinder engine using the LRR model. Our first objective is to demonstrate that such a 3D complex calculation can now be performed. Our second objective is to compare the results obtained with this second order closure model and those obtained using a standard $k - \epsilon$ model against some available experimental data. The first part of this paper describes the model of Launder-Reece-Rodi and its implementation in the Kiva-II code. The second part deals with two different two-dimensional incompressible steady test cases, the plane channel flow and the backward facing step flow, which were used to validate the implementation of the model. Other 3D test cases (the free round jet and the steady in-cylinder flow) have been used for the validation (Lebrère, 1995) but are not presented here. In the last part, we show the calculation of an intake-compression stroke inside a single cylinder engine. Results obtained with both turbulence models are compared with experimental data obtained by one point Laser Doppler Anemometry (LDA) measurements.

2 Mathematical Formulation

2.1 The Launder-Reece-Rodi Model. The equations for the Reynolds stresses $\widetilde{u_i u_j}$ may be written in cartesian tensor notation as:

Contributed by the Fluids Engineering Division for publication in the JOURNAL OF FLUIDS ENGINEERING. Manuscript received by the Fluids Engineering Division February 24, 1995; revised manuscript received September 12, 1996. Associate Technical Editor: F. Giralt.

$$\frac{\partial \overline{\rho}\widetilde{u_i u_j}}{\partial t} + \frac{\partial \overline{\rho}\widetilde{U}_k \widetilde{u_i u_j}}{\partial x_k} = \underbrace{P_{ij}}_{\text{Production}}$$

$$+ \underbrace{\Phi_{ij}}_{\text{Redistribution}} + \underbrace{D_{ij}}_{\text{Diffusion}} - \underbrace{\overline{\rho}\epsilon_{ij}}_{\text{Dissipation}} \quad (1)$$

In these equations, the symbol ($\bar{}$) is used for the conventional Reynolds average whereas the symbol ($\tilde{}$) denotes the Favre average, which is a density weighted average. We have used the "compressed turbulence" hypothesis (Wu et al., 1985) which assumes that the turbulent field is divergence free and the density fluctuations are negligible. This formulation may be used for low Mach number flows such as engine flows, where the mean flow is compressible. We will now describe the modelling used in the LRR model for the different terms in Eq. (1). The production term:

$$P_{ij} = -\overline{\rho}\left(\widetilde{u_i u_k} \frac{\partial \widetilde{U}_j}{\partial x_k} + \widetilde{u_j u_k} \frac{\partial \widetilde{U}_i}{\partial x_k} \right) \quad (2)$$

is treated exactly and doesn't require any modeling.

The redistribution term Φ_{ij}, which models the interaction between the turbulent pressure and the strain fluctuations, is divided into three contributions, namely:

1. the Rotta's linear term or "return to isotropy" term:

$$\Phi_{ij,1} = -C_1 \overline{\rho} \frac{\epsilon}{k} \left(\widetilde{u_i u_j} - \frac{2}{3} k \delta_{ij} \right) \quad (3)$$

2. the "isotropisation of production" term:

$$\Phi_{ij,2} = -C_2 \overline{\rho}(P_{ij} - \tfrac{1}{3} P_{kk}\delta_{ij}) \quad (4)$$

3. the "wall reflection" term:

$$\Phi_{ij,w} = C_{1w}\overline{\rho}\frac{\epsilon}{k}\left(\widetilde{u_k u_m} n_k n_m \delta_{ij} - \frac{3}{2}\widetilde{u_k u_i} n_k n_j - \frac{3}{2}\widetilde{u_k u_j} n_k n_i \right) f$$

$$+ C_{2w}\left(\Phi_{km,2} n_k n_m \delta_{ij} - \frac{3}{2}\Phi_{ik,2} n_k n_j - \frac{3}{2}\Phi_{jk,2} n_k n_i \right) f \quad (5)$$

where

$$f = \frac{L}{\xi} \quad \text{with} \quad L = \frac{C_\mu^{3/4}}{\kappa}\frac{k^{3/2}}{\epsilon}$$

is the wall distance function, κ the von Karman constant, n_i the ith component of the unit vector normal to the wall and ξ the distance of the nearest wall.

We have chosen a simpler isotropic form for the diffusion term (Lien et al., 1993; Debaty, 1994):

$$D_{ij} = \frac{\partial}{\partial x_k}\left(\frac{\mu_t}{\sigma_k} \frac{\partial \widetilde{u_i u_j}}{\partial x_k} \right) \quad (6)$$

instead of the usual Daly-Harlow expression:

$$D_{ij} = C_e \frac{\partial}{\partial x_k}\left(\widetilde{u_k u_l} \frac{k}{\epsilon} \frac{\partial \widetilde{u_i u_j}}{\partial x_l} \right) \quad (7)$$

The latter form gives rise to a number of cross-diffusion terms which turn out to be numerically destabilizing (Lien et al., 1994).

The dissipation tensor ϵ_{ij} is assumed to be locally isotropic, i.e., $\epsilon_{ij} = 2/3\epsilon\delta_{ij}$ where ϵ is the dissipation rate of the turbulent kinetic energy k. The dissipation rate ϵ is calculated using the following transport equation:

Table 1 Constants of the LRR model

C_1	C_2	C_{1w}	C_{2w}	$C_{\epsilon 1}$	$C_{\epsilon 2}$	$C_{\epsilon 3}$	σ_ϵ	σ_k
1.8	0.6	0.5	0.3	1.44	1.92	−1.	1.3	1

$$\frac{\partial \overline{\rho}\epsilon}{\partial t} + \frac{\partial \overline{\rho}\widetilde{U}_k \epsilon}{\partial x_k} = -C_{\epsilon_1}\frac{\epsilon}{k}\overline{\rho}\widetilde{u_i u_j}\frac{\partial \widetilde{U}_i}{\partial x_j} - C_{\epsilon_2}\overline{\rho}\frac{\epsilon^2}{k}$$

$$+ \frac{\partial}{\partial x_k}\left(\frac{\mu_t}{\sigma_\epsilon}\frac{\partial \epsilon}{\partial x_k} \right) + C_{\epsilon_3}\overline{\rho}\epsilon\frac{\partial \widetilde{U}_i}{\partial x_i} \quad (8)$$

Contrary to $k - \epsilon$ model, no equation is solved for the turbulent kinetic energy k which is equal to the half sum of the normal stresses. The constants of LRR model are given in Table 1.

As compared to the standard LRR model, the equation for dissipation rate contains an additional production term: $C_{\epsilon_3}\overline{\rho}\epsilon(\partial\widetilde{U}_i/\partial x_i)$. For the present simulations, the particular value $C_{\epsilon_3} = -1$, implemented in the standard Kiva-II code, was used. Different values for this constant have been proposed, ranging from +1 (Gosman et al., 1977) to −2/3 (Reynolds, 1980). The value −2/3 (associated with $C_{\epsilon_1} = 1$) proposed by Reynolds comes from an analysis of homogeneous isotropic compression with constant viscosity and makes the ϵ equation exact in the limit of rapid distorsion theory $((\partial\widetilde{U}_i/\partial x_i)(\epsilon/k) \gg 1)$. More recently, this proposal (or any choice of the constants such as: $-2/3C_{\epsilon_1} + C_{\epsilon_3} = -4/3$) has received a theoretical support in the general case, for non rapid and non isotropic compressed flow (Cambon et al., 1992a; Le Penven et al., 1993). These different values have not been tested in the present work since the main objective is to demonstrate the feasability of a 3D calculation for engine flows. Detailed analysis of turbulence models will be addressed in a future paper.

2.2 Numerical Implementation. The LRR model has been implemented in the Kiva-II code (Amsden et al., 1989). This code was originally developed at the Los Alamos Laboratory for engine flow simulations. It solves the unsteady equations for a three-dimensional turbulent flow using a finite volume method. The turbulence is tackled by a standard $k - \epsilon$ model. The computational grids are built with hexahedrons and the cartesian components of the velocity vector are stored at the cells vertices whereas the other variables are defined at cell centers. The transient solution is marched out in a sequence of cycles or timesteps. A computation cycle may be represented by the algorithm shown below:

- step 1: computation of the density ρ
- step 2: computation of the mean flow quantities velocity $\vec{U}$ *and pressure* p by the SIMPLE method
- step 3: computation of the turbulent quantities k and ϵ

The equations for ρ, k, and ϵ being weakly coupled to the mean flow field solution, these equations are not included in the SIMPLE iteration: each step is thus independently solved.

For boundary conditions at the wall, the usual logarithmic law is used to bridge the viscous sublayer region. For turbulent quantities, equilibrium between production and dissipation of the turbulent kinetic energy leads to the following boundary conditions for k and ϵ:

$$\begin{cases} \dfrac{\partial k}{\partial n} = 0 \\ \epsilon = \dfrac{C_\mu^{3/4}}{\kappa}\dfrac{k^{3/2}}{y} \end{cases}$$

where y is the distance from the first point cell to the wall.

To include the LRR model in the Kiva-II code, we have to choose the interpolation used for the Reynolds stresses. Some authors (Huang et al., 1985; Launder, 1989) recommend to stagger the stress locations on the faces of cells relative to the velocity locations in order to stabilize the computation. To preserve the structure of the code, we have used a staggered interpolation for the stresses but on the center of cells, as for all other thermodynamical variables in the Kiva-II code.

The second question is how to include the transport equations for the turbulence in the Kiva-II algorithm. We have used the same strategy as for the $k - \epsilon$ model, leading to the following algorithm:

- step 1: computation of the density ρ
- step 2: computation of the mean flow quantities velocity $\tilde{U}$ and pressure p by the SIMPLE method
- step 3: computation of the turbulent quantities $\widetilde{u_i u_j}$ and ϵ

This method results in considerable computational time savings, as solving turbulent equations in the second step would require to modify the SIMPLE algorithm and the structure of the code. Using this algorithm, the turbulence model can be considered as a ''black box'' and according to the required precision, one may choose between the $k - \epsilon$ or the LRR model.

To choose adequate boundary conditions for $\widetilde{u_i u_j}$ at the walls, two different methods have been implemented for 2D calculations where two of the six components of the Reynolds tensor are equal to zero. The first method, used by Lien et al. (1993), imposes Dirichlet conditions for the four non zero stresses. The imposed values were calculated using an asymptotic form of the transport equations and could be expressed as a fraction of the turbulent kinetic energy near the wall. This wall turbulent kinetic energy is obtained from the friction velocity U_f given by:

$$k = \frac{U_f^2}{C_\mu^{1/2}}$$

However, this method gives poor results in the case of the backward facing step flow and is difficult to extend for 3D flows. The second method, that we have adopted, uses a numerical condition which is an homogeneous Neuman boundary condition but it has no physical justification for the shear stresses. The ϵ equation of the LRR model keeps the same form as in the $k - \epsilon$ model and the same boundary condition is used at the walls. The boundary conditions for the LRR model are then:

$$\begin{cases} \dfrac{\partial \widetilde{u_i u_j}}{\partial n} = 0 \\ \epsilon = \dfrac{C_\mu^{3/4}}{\kappa} \dfrac{k^{3/2}}{y} \end{cases}$$

The numerical implementation of second order closure models are well known to be more unstable than eddy viscosity models which transform the stresses in stabilizing diffusion terms via the Boussinesq hypothesis. Some authors (Huang et al., 1985; Launder, 1989; and Farhanieh et al., 1993) recommend stabilization techniques such as adding an apparent viscosity in the momentum equations. For this study, no stabilization technique were necessary and the stresses are strictly treated as source terms. It is important to notice that the numerical diffusion was limited by using the second-order convection scheme QSOU (the most precise scheme in Kiva-II). Moreover, the meshes and the timesteps used in the different simulations are identical with the $k - \epsilon$ and the LRR model. For our implementation, the differences in computational time between the RSM model and the $k - \epsilon$ model is related to the number of transport equations to solve, that is a ratio of about 2.

3 Validations

The Kiva-II code with the LRR model is validated and assessed by comparing computations with experiments on two 2D steady incompressible test cases: the plane channel flow and the flow over a backward facing step. Comparisons with computations performed with the $k - \epsilon$ model are also included to show the advantages of a second order closure. For these two test cases, the streamwise (respectively the transverse) direction is denoted by the subscript 1 (respectively 3).

3.1 The Plane Channel Flow. The considered incompressible turbulent channel flow was studied by Comte-Bellot (1965) using a channel of half-width $R = 9$ cm and a maximum velocity at inlet $U_0 = 18.5$ m/s. This yields a Reynolds number of 57000 and the flow is fully turbulent. Instead of calculating the complete channel, we have simulated a portion of it with a length of 20 R. The walls are in the (1–2) planes.

Boundary conditions at inlet for streamwise velocity U_1, the turbulent kinetic energy k and the dissipation rate ϵ correspond to established profiles obtained with another code developed at Ecole Centrale Lyon (Brun, 1990). For the RSM simulation, we state at inlet:

$$\begin{cases} \widetilde{u_1^2} = \widetilde{u_2^2} = \widetilde{u_3^2} = \frac{2}{3} k \\ \widetilde{u_1 u_3} = -\nu_t \dfrac{\partial \widetilde{U_1}}{\partial x_3} \end{cases}$$

As outflow conditions, we impose zero gradient in the normal direction for all variables except for pressure which takes a prescribed value.

Three different computations were performed on a mesh with 92 × 41 grid points, one using the $k - \epsilon$ model, another using the LRR model and a last using the LRR model without the wall echo term $\Phi_{ij,w}$ (this model will be noted LRRNW for No Wall correction). Actually, the redistribution term and particularly the wall echo term is a major modeling problem and most efforts of researchers to improve the second order closure models are concerned with this term. The LRRNW calculation enables us to further investigate the influence of this term.

In Fig. 1, Reynolds stresses profiles across the channel are presented. These profiles are taken near the end of the computational domain ($x/R = 19$) where the flow is fully developed. The Reynolds stresses are divided by the friction velocity U_f calculated from the log law. Clearly, only a second-order closure model such as the LRR model and the LRRNW model is able to capture the anisotropy of this flow. These profiles show also that the modeling of the wall reflection term is not fully satisfying. Its role is to damp the component $\widetilde{u_3^2}$ normal to the wall and enhance the components $\widetilde{u_1^2}$ and $\widetilde{u_2^2}$ parallel to the wall. Whereas the second goal is reached, the damping of $\widetilde{u_3^2}$ is too strong, especially at the center of the channel. To avoid this difficulty, some authors (Launder, 1989) proposed to replace the linear wall distance function:

$$f = \frac{L}{\xi} \text{ with } L = \frac{C_\mu^{3/4}}{\kappa} \frac{k^{3/2}}{\epsilon}$$

by a quadratic function:

$$f = \left(\frac{L}{\xi}\right)^2$$

In our case, numerical results using this alternative form show that, if the wall effect decreases at the center of the channel, the Reynolds stresses model predictions remain poor in the near-wall region. This has motivated the choice of the linear function rather than the quadratic one. Finally, we can notice that the linearity of the shear stress $\widetilde{u_1 u_3}$ is not obtained with LRR model whereas it is with the LRRNW one. In conclusion, this wall-reflection term form doesn't seem very suitable, even

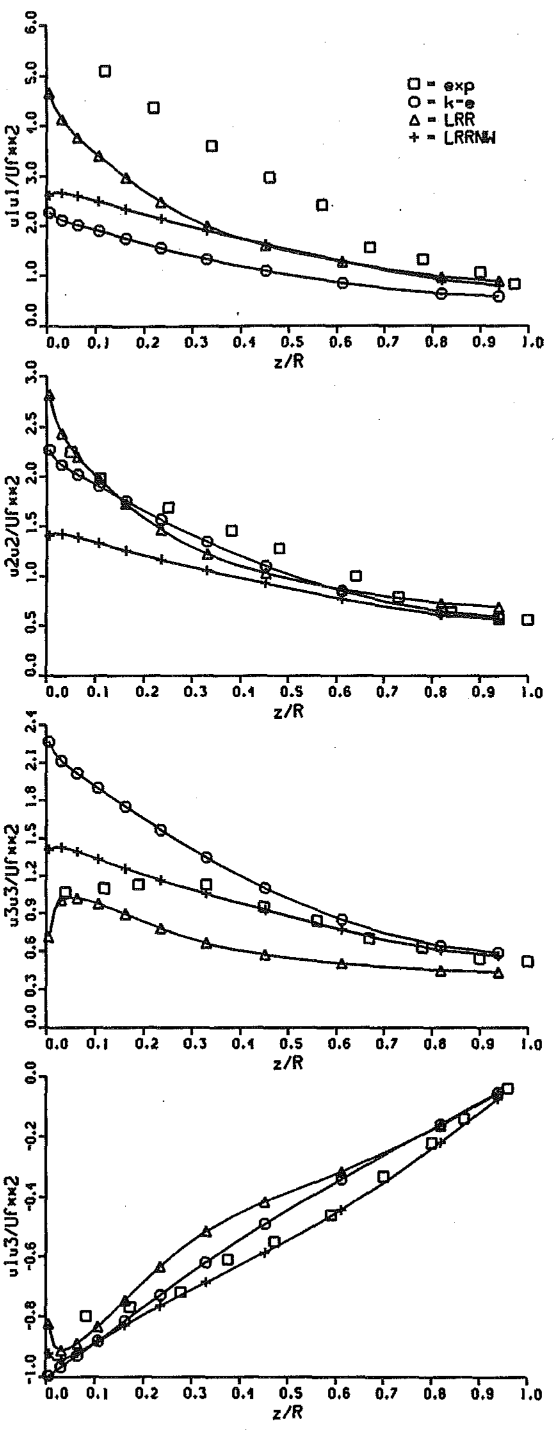

Fig. 1 Comparison of Reynolds stress profiles calculated with $k - \epsilon$, LRR and LRRNW models for the plane channel flow

in the simple test case of the plane channel flow, but today, there doesn't exist a better alternative.

In the LRR model, the presure-strain condition is expressed as a linear function of the anisotropy tensor $b_{ij} = \widetilde{u_i u_j} - \frac{2}{3} k\delta_{ij}$. In order to improve predictions for large levels of anisotropy observed, for example, in the vicinity of solid boundaries, some recent models include higher order terms in b_{ij}. As an illustration of this, we present the results obtained by the model due to Speziale et al. (1991) which includes quadratic terms in b_{ij}. This model is run without wall echo term. Figure 2 compares results obtained with this model noted SSG and those of the $k - \epsilon$ and the LRR models. The SSG model doesn't really improve the components parallel to the wall but the component normal to the wall u_3^2 is well predicted and the excessive damp near the channel center has disappeared. Moreover, the shear stress profile has a linear behavior as the LRRNW one. The SSG model was also used in the following test case but disappointing results were found (Lebrère, 1995). Consequently, only the LRR model is used in the next calculations.

3.2 The Backward Facing Step Flow. For this test case, a large number of numerical simulations using the $k - \epsilon$ model have shown that the position of the reattachment point is under-

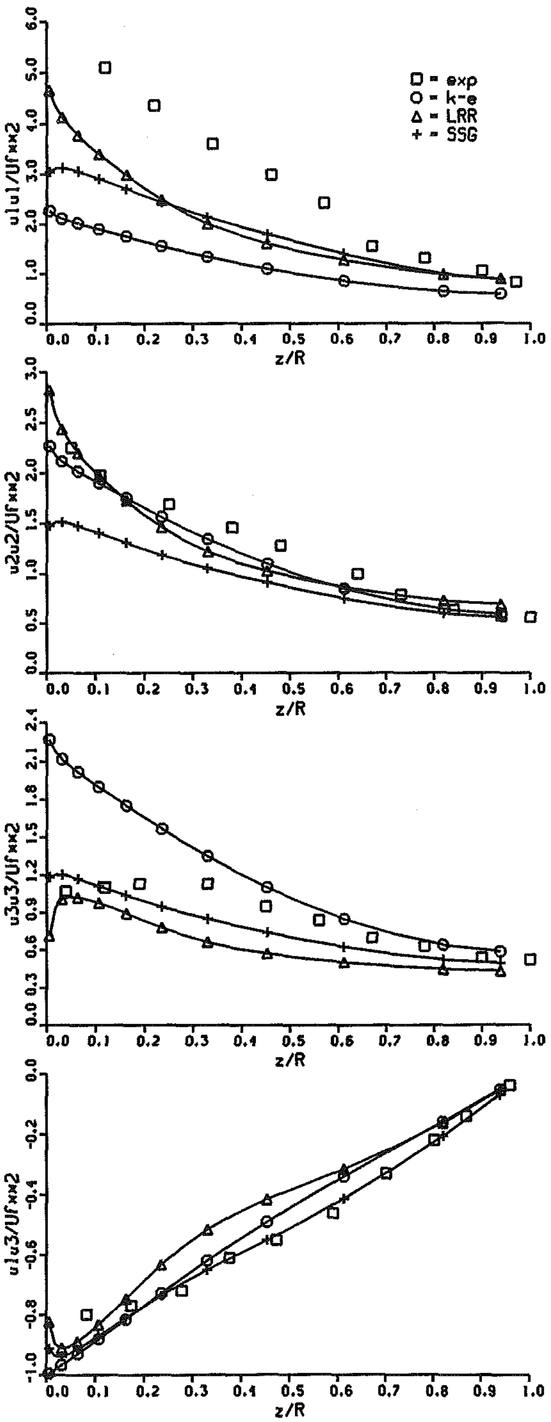

Fig. 2 Comparison of Reynolds stress profiles calculated with $k - \epsilon$, LRR and SSG models for the plane channel flow

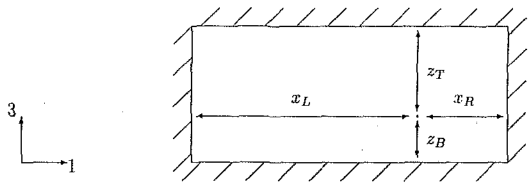

Fig. 3 Wall distances used in the LRR model wall-reflection term

predicted (Kline et al., 1981; Thangam, 1991). The experimental results are those of Kim et al. (1980).

At the inlet, the fully developed values of the primitives variables are imposed, namely U_1, k and ϵ profiles. For the normal stresses, the turbulent kinetic energy is distributed uniformly and for the shear stress, a Boussinesq formula is used:

$$\widetilde{u_1u_3} = -\nu_t \frac{\partial \tilde{U}_1}{\partial x_3}$$

At the outlet, the pressure is imposed and a zero normal gradient for the other variables is prescribed.

Computations were carried out using 252 × 45 grid points with both the $k - \epsilon$ and the LRR models. The two characteristic parameters of the problem are the step height ($h = 3.81$ cm) and the maximum velocity imposed at inlet ($U_0 = 18.2$ m/s). For this test case, the wall distance function was modified to take into account for all the walls and not only for the nearest one. More precisely, if we denote x_L, x_R, z_B, z_T distances along the axis to the surroundings walls and if we suppose the nearest wall of the point M is the lower wall as shown in Fig. 3, the classical wall distance function of the LRR model:

$$f(M) = \frac{L}{\xi} = \frac{L}{z_B}$$

is replaced by:

$$f(M) = L\left(\frac{1}{x_L} + \frac{1}{x_R} + \frac{1}{z_B} + \frac{1}{z_T}\right)$$

with the rule that the distance may become infinite if there is no wall in this direction.

In Fig. 4, contours of meanflow streamlines, using calculated trajectories, are plotted for both turbulence models. In each case, the dividing streamline is denoted by a black circle. The experimental value of the reattachment point is about $7h$. The computed near wall streamwise velocity gives a reattachment at $x/h = 6.2$ for the $k - \epsilon$ model and at $x/h = 7$ for the LRR model. This good result obtained using the LRR model may be explained by the fact that a second order closure model does account for streamline curvature, unlike the $k - \epsilon$ model. The LRR model also predicts the secondary corner eddy. However, as shown in Fig. 4, the LRR model produces unrealistic streamline pattern with dividing streamline curved backwards. Jakirlic et al. (1994) also indicate this anomalous behaviour and propose to include a new term in the ϵ equation to compensate for an excessive growth in the turbulence scale in the reattachment region. With this new model, the unrealistic flow pattern around the reattachment is eliminated.

Figure 5 presents streamwise velocity profiles predicted at several locations downstream of the step. The velocity is nondimensionalized by the maximum value $U_{\max}$ in the considered section and $z_{\max}$ represents the altitude where this maximum is reached. This method is chosen in order to compare numerical and experimental results but it is very sensitive to the maximum velocity location: this may explain the differences between experimental data and numerical predictions. It is interesting to notice that the LRR model gives better results than the $k - \epsilon$ model in the recirculation region and not as good outside. The good representation of the recovery region by the $k - \epsilon$ model is fortuitous and simply due to the premature reattachment (Lien et al., 1994).

As shown in Fig. 6, the computed turbulent kinetic energy profiles using the LRR model are in good agreement with experimental data. Its results are always better than those obtained with the $k - \epsilon$ model, particularly in the shear layer near the recirculation bubble: this feature may be attributed to the curvature induced attenuation of turbulence. Indeed, it is well known from experimental studies that the streamline curvature can either attenuate or amplify the normal stress perpendicular to the streamline as well as the shear stress depending on the sign of the radius of curvature relative to that of the mean strain. Streamline curvature creates anisotropy which may be captured only with a second order closure model.

4 Engine Flow Simulation

We have simulated an intake-compression stroke on a single cylinder engine. The specifications and the operating conditions of this engine are listed in Table 2.

Optical accesses in the cylinder allow to use one point Laser Doppler Anemometry (LDA) to measure the mean velocity components and the rms fluctuations. Experimental results are obtained using ensemble averaging without taking into account for cycle to cycle variations. More precisely, five measurement points have been explored, located on a cylinder diameter 12.6 mm below the cylinder head. These five points are depicted in Fig. 7. For each point, the axial and tangential velocities and the fluctuations have been measured. A complete description of the experimental apparatus can be found in Michard et al. (1993).

Calculations are performed using a mesh with 75000 nodes shown at BDC in Fig. 8. The intake pipe is taken into account in order to impose more precise boundary conditions. Actually, the mass flow rate was measured and this quantity was imposed in the inlet boundary. It is important to notice that the mesh used is a little different from the real geometry. The main difference with the real engine is the absence of optical accesses in the computational grid. This simplification is motivated by the difficulty to control the mesh motion when the piston moves in front of the optical accesses. This leads to a compression ratio of 6.05, greater than the experimental one (5.63). A little increase in the top clearance height would be a way to get the

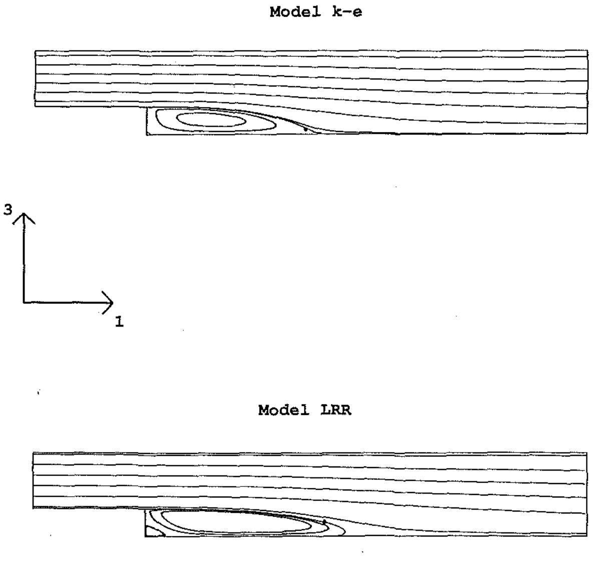

Fig. 4 Streamfunction contours using $k - \epsilon$ and LRR models for the backward facing step flow

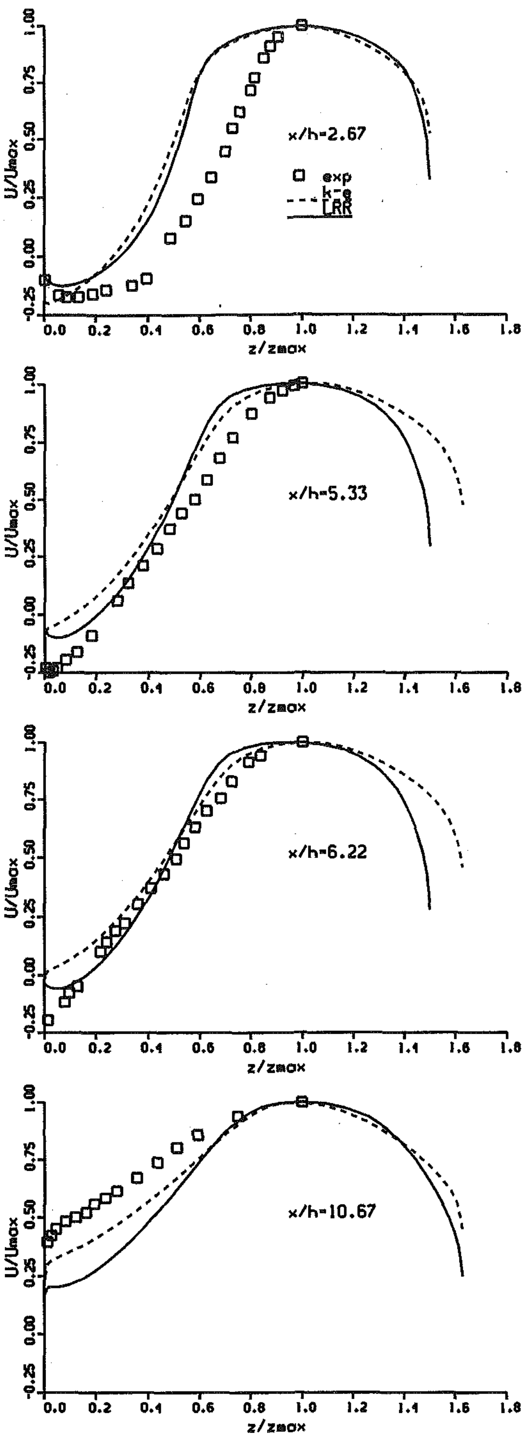

Fig. 5 Velocity profiles calculated with $k - \epsilon$ and LRR models for the backward facing step flow

experimental compression ratio and to avoid a priori discrepancies with the experimental case. But, the wall confinement is a very important parameter for mean flowfield and turbulence and we have preferred to keep the real top clearance height with a too high compression ratio. Experimentally, the compression ratio effect on the mean and turbulent flows could be partially studied: with the high compression ratio equal to 7.28, the piston moves on measurement points between 20° BTDC and 20° ATDC (Michard et al., 1993). Before this crank angle window, the compression ratio seems to have no effect on velocity fluctuations. Moreover, an homogeneous calculation of a compression stroke shows that a difference of 10 percent on the compression ratio only gives a difference of 3 percent on the turbulent kinetic energy level at TDC. Consequently, even though this compression ratio discrepancy slightly reduces the interest of the correlation between experiment and numerical simulation, the comparison between the $k - \epsilon$ model and the LRR model remains relevant.

In order not to take into account the exhaust valve closure, the calculations begin at 20° ATDC. At this crank angle, the intake valve lift is equal to 2.4 mm. In the same way, the valve is closed at 20° ABDC when the real lift is around 1 mm. These approximations are usual in engine simulations, though valve

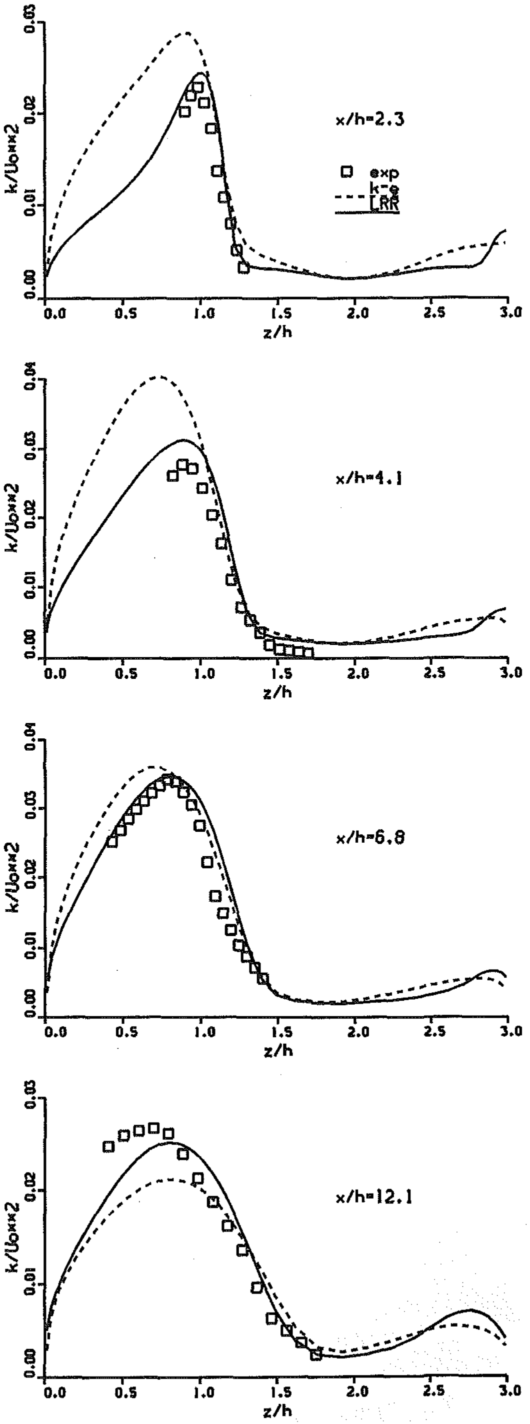

Fig. 6 Turbulent kinetic energy profiles calculated with $k - \epsilon$ and LRR models for the backward facing step flow

Table 2 Engine characteristics and operating conditions

Bore	86 mm
Stroke	89 mm
Displacement volume	0.5171
Top clearance	17.6 mm
Compression ratio	5.63
Connecting rod length	155 mm
Valve diameter	40.2 mm
Eccentricity	21.29 mm
Intake valve opening	14°BTDC
Intake valve closing	46°ABDC
Exhaust valve opening	55°BBDC
Exhaust valve closing	17°ATDC
Max valve lift	9.1 mm
Rpm	1000 rpm

lift values are often weaker (0.2 mm). The limiting constraint is here the curtain valve area cell distorsion which is associated with small timesteps and large numerical errors. The simulation stops at TDC.

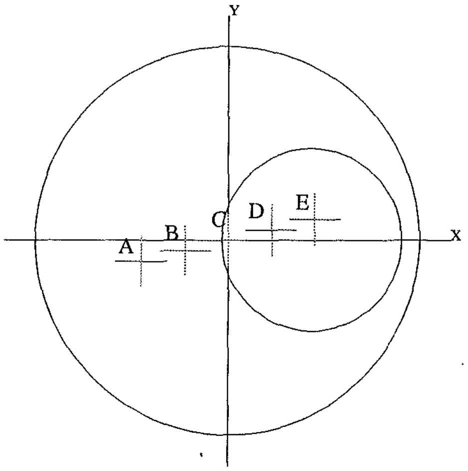

Fig. 7 Location of the five measurement points A, B, C, D and E

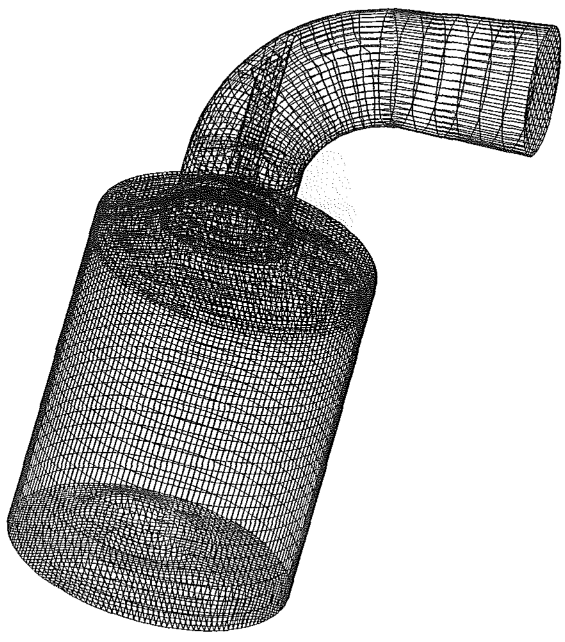

Fig. 8 Mesh at bottom dead center (BDC)

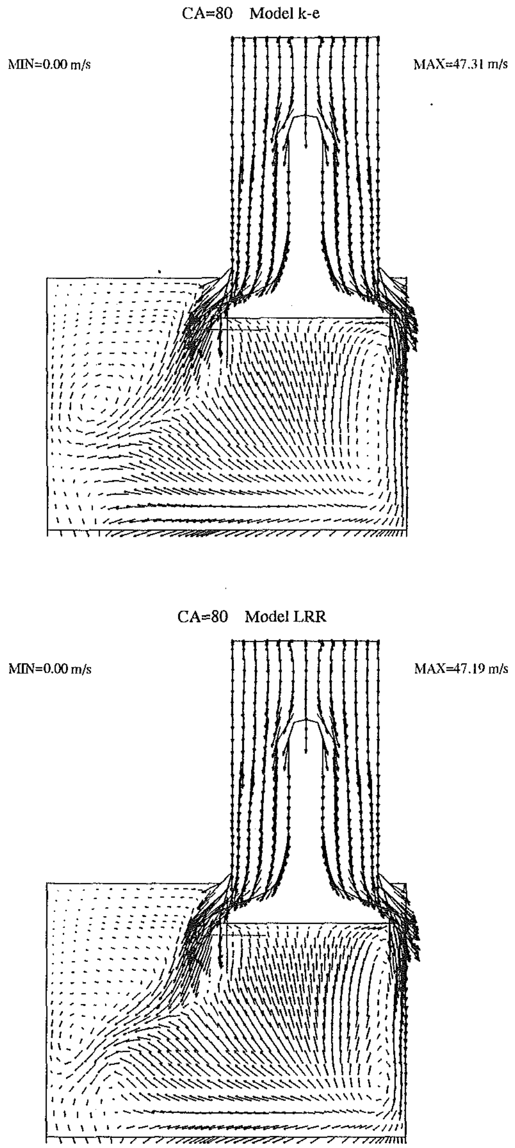

Fig. 9 Velocity field at CA = 80 in the symmetry plane of the cylinder calculated with the two turbulence models

The calculations are carried out using both $k - \epsilon$ and LRR models. In the LRR model, the wall distance function takes into account for the nearest wall and is calculated for each crank angle. Rigorously, this function should be calculated at each timestep but this would increase the computational time drastically (more of 90 percent of the whole simulation CPU time could be spent for the computation of this non-vectorized function). Nevertheless, the error corresponding to this approximation mainly affects the cells near the moving boundaries.

Figures 9 to 11 presents the velocity field in the symmetry plane of the cylinder (x plane) using the two turbulence models at three crank angles: 80, 340 and 360 degrees, i.e., nearly in the middle of the intake stroke, 20° BTDC and TDC. 20° BTDC correspond to a classical ignition crank angle and the structure of the aerodynamical field is very important at this moment. For these three crank angles, results obtained with the two turbulence models are quite different. Among the five measurement points, only the point C lies in the cutting plane and its position is represented by a cursor in each figure.

In Fig. 9, the main difference is located in the left part of the cut plane: the vortex above the valve jet is against the cylinder wall in the LRR simulation and seems to have a lower

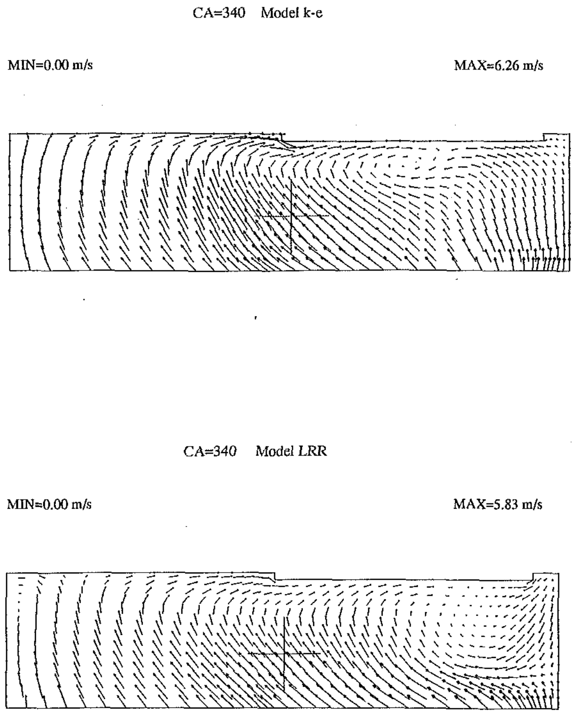

Fig. 10 *Velocity field at CA = 340 in the symmetry plane of the cylinder calculated with the two turbulence models*

intensity than in the $k - \epsilon$ computation. Below the valve jet, the LRR model predicts a small recirculation which is not simulated with the $k - \epsilon$ model. In Fig. 10, 20° BTDC, the LRR model predicts the existence of a large eddy in the right part of the cut plane. The $k - \epsilon$ model does not predict this eddy: on the other hand, we can see a small eddy under the valve that is not predicted with the LRR model. In the right part of the cut plane, the two turbulence models predict velocities with opposed sign. In the left upper corner, one can also note the more pronounced corner eddy in the LRR simulation than in the $k - \epsilon$ one. The maximum velocities (defined in the cut plane and not in the whole cylinder) calculated by both the $k - \epsilon$ and the LRR models differ from 7 percent at 340 deg and nearly 20 percent at 360 deg. In Fig. 11, eddies we could see in the previous figure have moved toward the cylinder axis. In the LRR simulation, the main eddy takes place in the middle of the top clearance volume, centered under the valve. In the $k - \epsilon$ one, the small eddy hasn't grown and the flow is globally parallel to the cylinder head. It is interesting to notice that the velocities in the right hand side of the cut plane have again the same sign in the two computations. Nevertheless, the flow structure near the left-hand side isn't identical: the LRR model predicts much larger secondary flows as in the backward facing step test case.

Other comparisons, at different crank angles and for other cut planes, show that the two turbulence models predict different velocity fields. Some characteristics of the velocity field are only present with one model. Even when both simulations predict the existence of an eddy, it has seldom the same form and the same location in the two cases. Of course, we cannot assess that the LRR model gives results closer to the reality than the $k - \epsilon$ model (PIV visualizations would be useful to assess the two turbulence models). Nevertheless, we expect that the LRR results are better since this model has a more physical background than the $k - \epsilon$ model.

Next figures (Figs. 12 to 16) compare the experimental and the predicted velocities and fluctuations at the five points shown above. In order to extract the computed values at the measurement points, an interpolation method was used to prevent discontinuities. Actually, a measurement point does not always coincide with a grid node and moreover, the mesh moves and cells are distorted. It is also important to notice that the five measurement points are at the same altitude and relatively near each other. The first interest of these figures is to compare the two turbulence model results. The comparison with experimental data is only partially relevant because:

1. Cycle to cycle variations are not taken into account in experimental data.
2. The numerical engine exhibits some differences such as the compression ratio from the experimental setup.
3. In-cylinder initial conditions are not fitted to experimental data. For example, the initial velocity field is uniformly set to zero in the cylinder. Experimentally, the five measurement point velocities are quite different at the start of the calculation and the velocity field is far from to be homogeneous. This may explain the poor agreement between numerical results and experimental data during the intake stroke.

For the mean axial velocity W, both turbulence models predicts the same behaviour. Qualitatively, the numerical predictions are in good agreement with experimental data for points D and E but not for points A, B and C. Experimentally, during the intake stroke, the point A is located in the jet since the axial velocity is positive i.e., oriented toward the piston. Numerically, this point does not belong to the valve jet but rather to one of eddies surrounding this jet. This explains why the calculated velocity is negative in the first part of the intake stroke. The mean tangential velocities V curves lead to the same remarks. Globally, at the five selected points, LRR model seems to have a little influence on the velocity components whereas we have noted many differences on the velocity field between the two turbulence models. This may perhaps be explained by the fact that the experimentally observed region is spatially limited and measurement points at a larger distance of the cylinder axis would certainly show more discrepancies between the two simulations.

As far as turbulent fluctuations are concerned, results obtained with the two turbulence models display greater departure

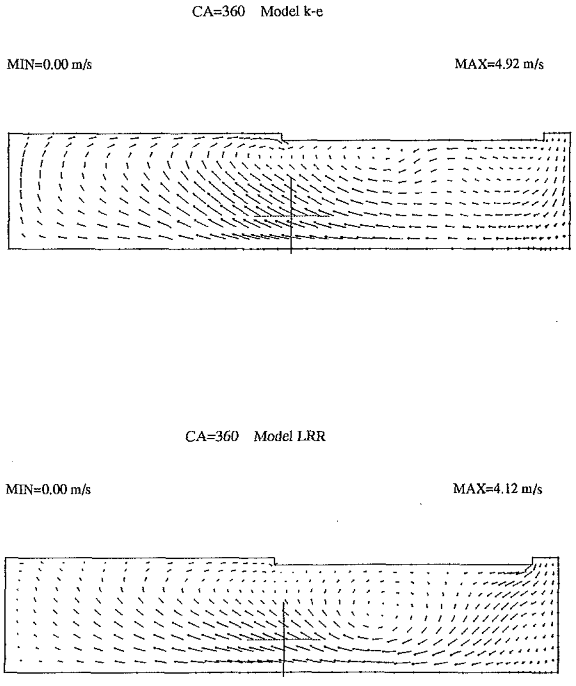

Fig. 11 *Velocity field at CA = 360 in the symmetry plane of the cylinder calculated with the two turbulence models*

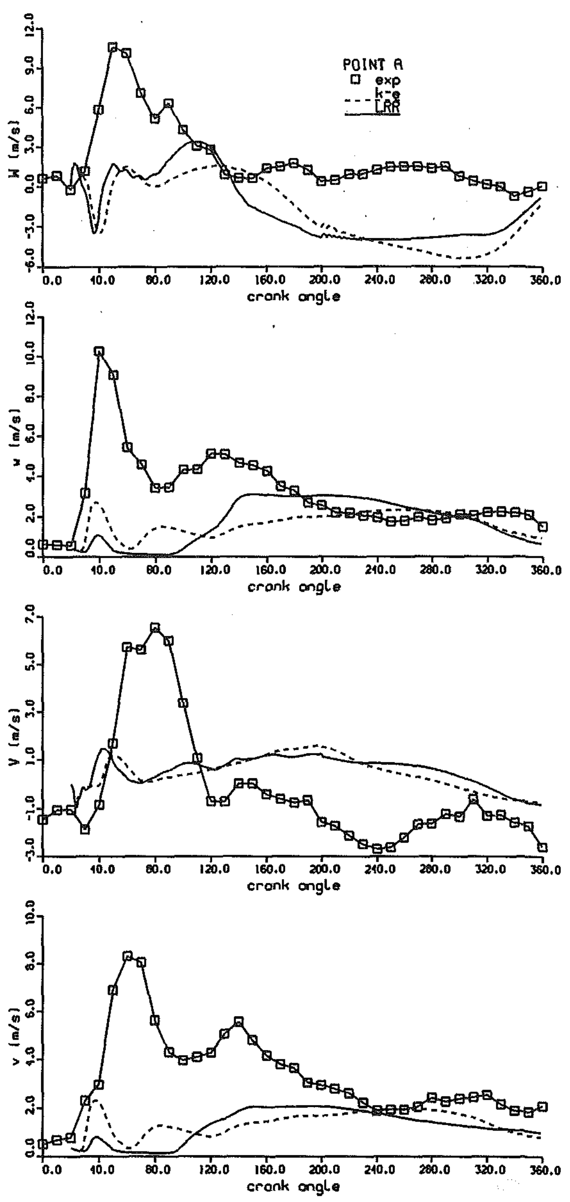

Fig. 12 Comparison of axial and tangential velocities and fluctuations at point A

than those on the mean velocity components. For a given fluctuation, the five experimental curves show that turbulence is strongly inhomogeneous during the intake stroke and the beginning of the compression one. For example, the axial fluctuation *w* reaches 14 m/s at point B during the first part of the intake stroke whereas this same fluctuation is lower than 4 m/s at points D and E. Toward the end of the compression stroke, the profiles tend to become homogeneous. Moreover, for a given point, the axial and tangential fluctuation profiles roughly follow the same trends even though the maximum values reached during the intake stroke are not the same. At the end of the compression stroke, turbulence seems to be isotropic, at least at the five measurement points i.e., in the cylinder core. Nevertheless, turbulence is anisotropic near walls and this feature justifies the use of a RSM model for engine flow calculations since this model takes into account anisotropy.

For the axial fluctuation *w*, results obtained with the $k - \epsilon$ model are quite surprising between 60 and 180 deg at points C, D, and E: the fluctuation *w* and the turbulent kinetic energy *k* reach its maximum value around 60 deg, decreases until 80 deg, remains constant then increases until 180 deg. On the other hand, the LRR predictions follow in a good manner the experimental data between these two crank angles. As production of turbulence is due to shear strains, we may assume that the $k - \epsilon$ model poorly predicts shear strains and thus velocity in this region. At point B, the LRR model underpredicts the axial fluctuation values during the intake stroke and the $k - \epsilon$ model predictions are closer to experimental values. Finally, we can notice that the axial fluctuation value at the end of the compression stroke is of the same order than the mean axial velocity component (i.e., around 2 m/s).

The ambiguous location of point A is confirmed on the fluctuation profiles: the peaks during the intake stroke are underpredicted by a factor between 4 and 10. For the tangential fluctuations *v*, we find the same characteristics than previously, namely a poor prediction of the $k - \epsilon$ model between 60 and 180 deg. But, looking at these profiles, it is difficult to say that the LRR results are better or at least more physical.

A new information which is not available with the $k - \epsilon$ model is given in Fig. 17. This figure presents the averaged

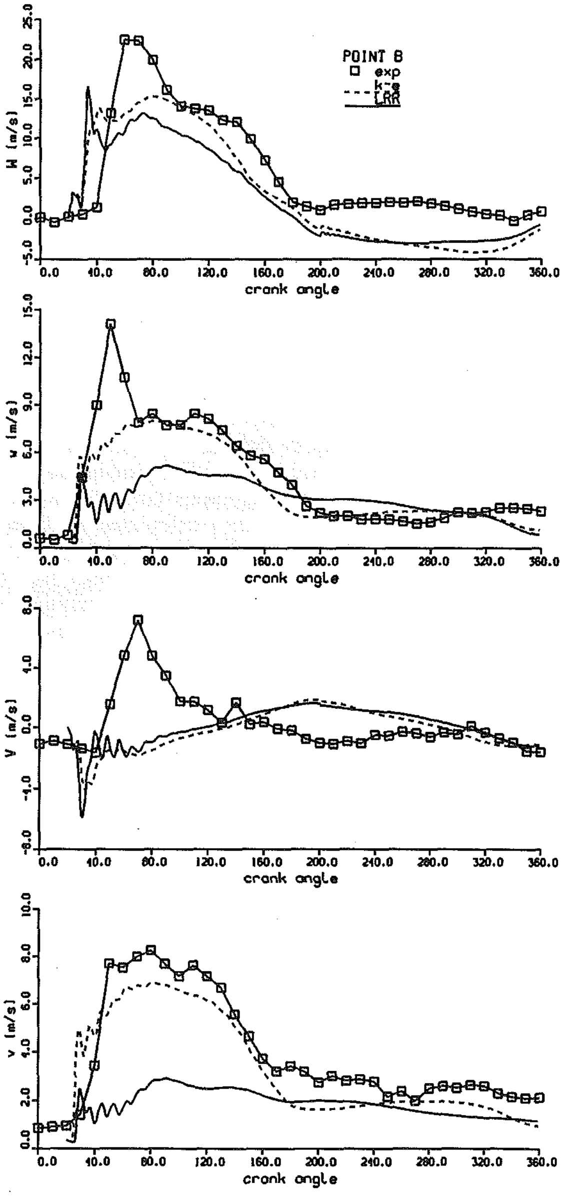

Fig. 13 Comparison of axial and tangential velocities and fluctuations at point B

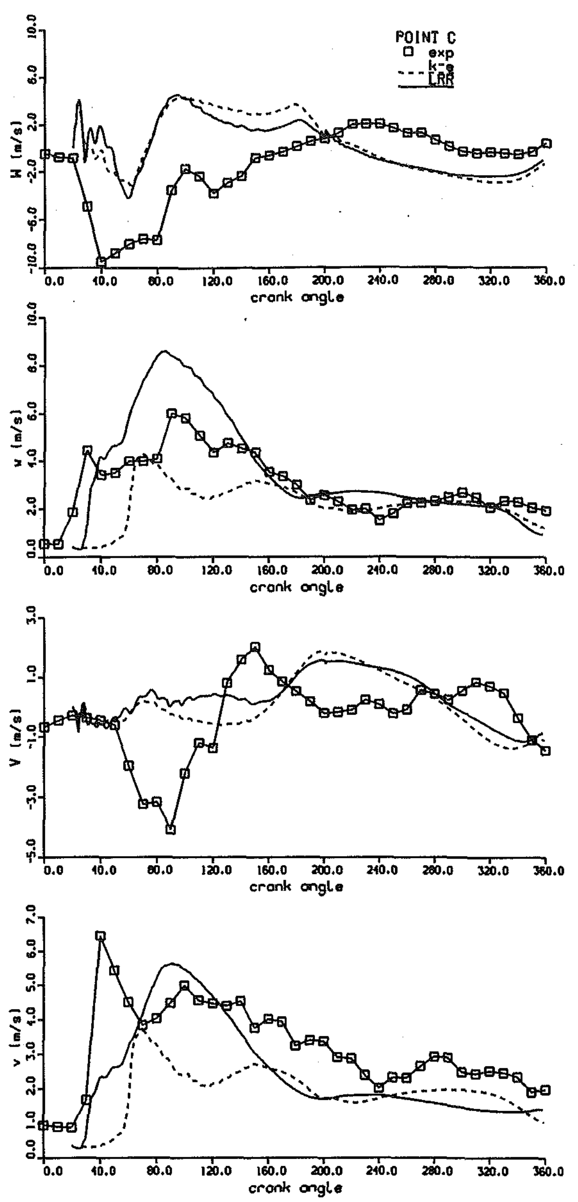

Fig. 14 Comparison of axial and tangential velocities and fluctuations at point C

fluctuation in the whole cylinder nondimensionalized by the velocity piston versus the crank angle. The four curves reach their maximum around 90 deg i.e., at the middle of the compression stroke. The u and v fluctuations are nearly equal during the whole engine cycle so we can say that the eccentricity of the valve does not create a strong anisotropy. It is interesting to notice that the averaged axial fluctuation is larger than u and v until 330 deg. At this crank angle, w strongly decreases down to 0.35 at TDC whereas the other fluctuations are of order of 0.5. This feature shows that the turbulence is strongly anisotropic near TDC, at the spark ignition crank angle for example. This conclusion which was drawn for averaged cylinder quantities is probably true for ignition zone quantities since turbulence is quasi-homogeneous at the end of the compression stroke as it can be seen on Figs. 12–16. The decrease of the axial fluctuation near TDC is probably due to the damping of the turbulence in the axial direction induced by the cylinder volume variation.

A first conclusion from this simulation is that the use of a second-order closure model is possible for an unsteady 3D computation. It is important to notice that the same mesh and the same timesteps have been used for the two turbulence models. As far as computational time is concerned, computations using the LRR model is only twice more expensive than with the $k - \epsilon$ model. This additional cost is quite acceptable since, as shown above, the LRR model provides new information.

Comparisons between experimental and numerical results at some points stay a difficult exercise even using a second order closure model. Globally, the LRR model gives results as good as the $k - \epsilon$ model on the five measurement points, but not better and quantitative reliable predictive capabilities are not yet reached. One can use two kinds of arguments to interpret these results. On the experimental side, it is necessary to take into account for cycle to cycle variations to get more precise measures and it was not investigated in our data. On the simulation side, it is obvious that a RSM model is not the wonder remedy in engine calculations even though it improves some results and brings new informations. We must keep in mind that the $k - \epsilon$ model has been employed for many years whereas it is one of the first unsteady three dimensional compressible simulation with the LRR model. The values of the constants or

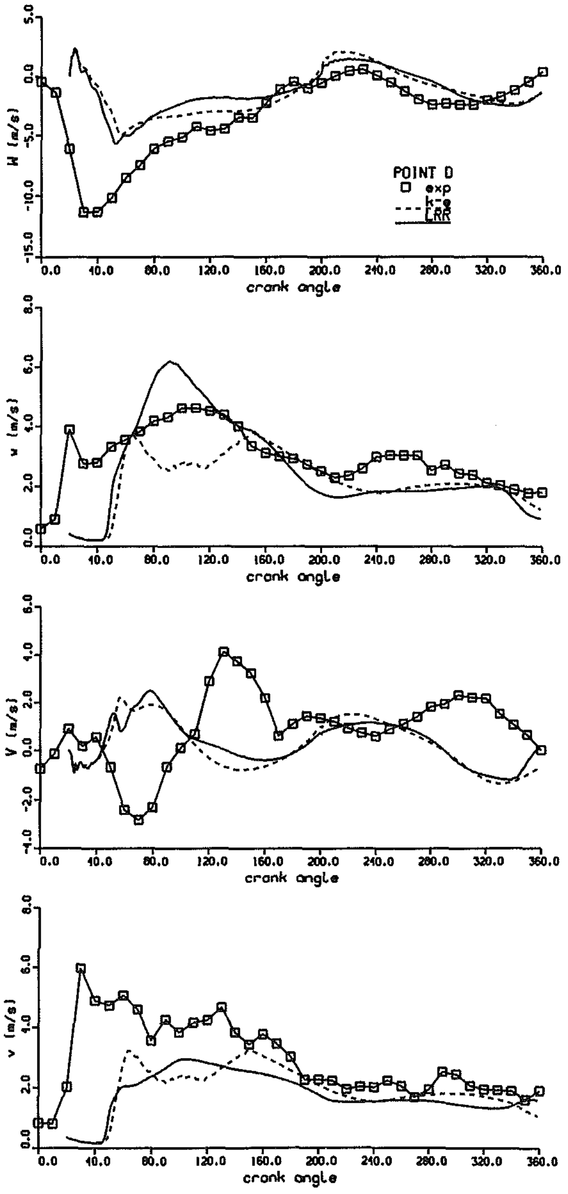

Fig. 15 Comparison of axial and tangential velocities and fluctuations at point D

the modelling of some terms in the Reynolds stress equations, which give good results in incompressible steady test cases, should perhaps be modified or improved for this kind of computation. Further numerical experiments on 3D unsteady flows will be necessary to improve and to analyze the results obtained with a RSM model.

5 Conclusion

Results obtained on incompressible steady test cases clearly prove that a Reynolds Stress Model gives better prediction than an eddy viscosity model. Whereas the second order models have appeared since 1975, it is only today that the increase of the computer power enables us to use a RSM model for industrial complex applications. In this paper, a three-dimensional unsteady compressible computation inside the combustion chamber of a reciprocating engine has been carried out using a second order closure model. The mean velocity fields predicted by a classical $k - \epsilon$ model and a more elaborate second order model are quite different and only the LRR model is able to capture the anisotropic character of the turbulence, especially at the end of the compression stroke.

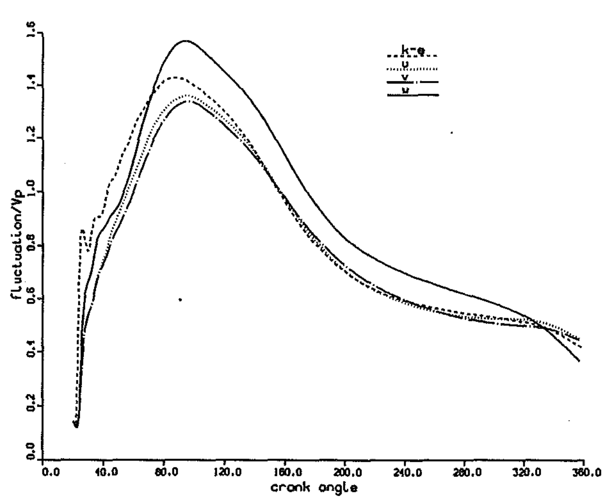

Fig. 17 Mean cylinder fluctuations computed by $k - \epsilon$ and LRR models: $k - e = (\frac{2}{3} k)^{1/2}$, $u = (\widetilde{u_1^2})^{1/2}$, $v = (\widetilde{u_2^2})^{1/2}$ and $w = (\widetilde{u_3^2})^{1/2}$

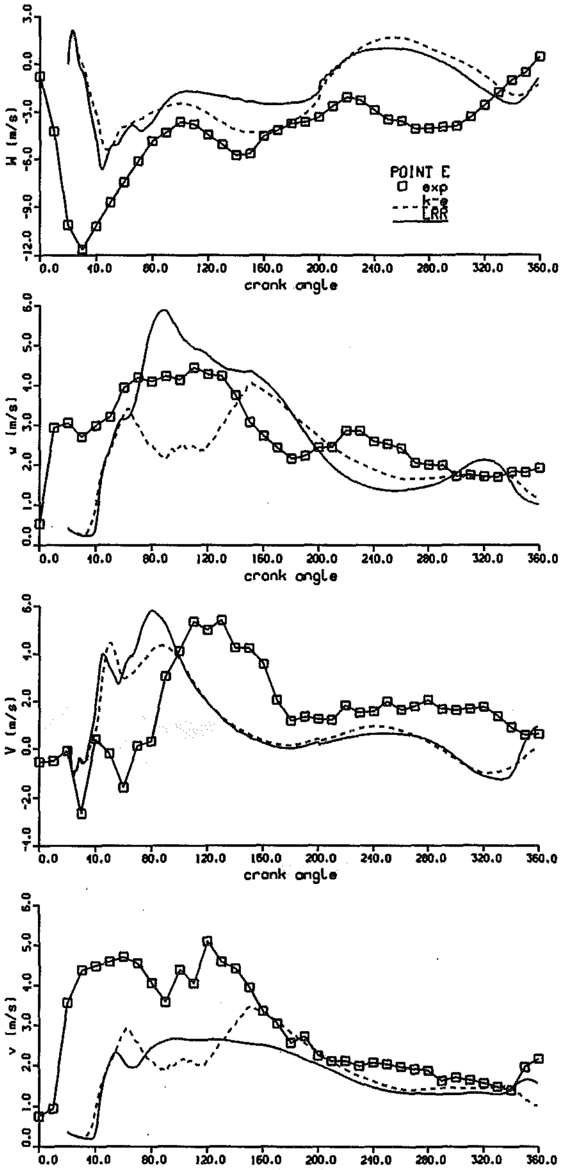

Fig. 16 Comparison of axial and tangential velocities and fluctuations at point E

Many developments of the LRR model have been proposed since 1975. Actually, the LRR model has some weakness, particularly the pressure-strain modelling and the wall echo modeling. Some of the new models keep the same number of equations but propose other modeling for pressure-strain or diffusion terms: this is the case of the SSG model used in the plane channel flow test case. Other models introduce new equations to take into account for the anisotropic character of the dissipation (Oberlack et al., 1992) or for the influence of the rotation on the turbulence (Cambon et al., 1992b). But, before including these recent progress in the modelling, it is necessary to go further with the LRR model and to compute other engine flows with different geometries and different initial conditions (swirling conditions for example). In conclusion, for engine flow calculations, the LRR model seems today one of the best compromise between an improvement of the predictive capabilities compared to the $k - \epsilon$ model and an increase of the computational cost. This model is not more difficult to use than the $k - \epsilon$ model and this criterion is very important for industrial applications.

Nevertheless, other approaches are possible to simulate a turbulent flow but their cost is inversely proportional to the modeling effort which is required to formulate them. Among these methods, Large Eddy Simulation (LES) technique appears to be one of the most attractive tools (Naitoh et al., 1990 is an illustration for engine flow calculation) but the mesh size necessary for this type of computations is still a limiting constraint for industrial applications.

Acknowledgment

The authors would like to thank PSA Peugeot Citroën (Velizy, France), the ANRT and the GSM.

References

Amsden, A. A., O'Rourke, P. J., and Butler, T. D., 1989, "KIVA-II: A Computer Program for Chemically Reactive Flows with Spray," LA-11560-MS, Los Alamos National Laboratory, Los Alamos, NM.

Brun, G., 1988, "Developpement et application d'une methode d'elements finis pour le calcul des ecoulements turbulents fortement chauffes," *Thèse de doctorat,* Ecole Centrale de Lyon.

Cambon, C., Mao, Y., and Jeandel, D., 1992a, "On the Application of Time Dependent Scaling to Modelling of Turbulence Undergoing Compression," *Eur. J. Mech. B/Fluids,* No. 6, pp. 683–703.

Cambon, C., Jacquin, L., and Lubrano, J. L., 1992b, "Toward a New Reynolds Stress Model for Rotating Turbulent Flows," *Physics of Fluids,* Vol. 4, pp. 812–824.

Comte-Bellot, G., 1965, "Ecoulement turbulent entre deux parois parallèles," *Publications Scientifiques et Techniques du Ministére de l'Air,* No. 419.

Deschamps, C. J., and Watkins, A. P., 1994, "Modeling of Turbulent Flow through Port/Valve Assemblies with an Algebraic Reynolds Stress Model," COMODIA 94, pp. 547–552.

Debaty, P., 1994, "Performances d'un modele du second ordre dans un code elements finis," *Thèse de doctorat,* Ecole Centrale de Lyon.

El Tahry, S. H., 1985a, "A Comparison of Three Turbulence Models in Engine-Like Geometries," *COMODIA,* Tokyo.

El Tahry, S. H., 1985b, "Application of a Reynolds Stress Model to Engine-Like Flow Calculations," ASME JOURNAL OF FLUIDS ENGINEERING, Vol. 107, pp. 444–450.

Farhanieh, B., Davidson, L., and Sundén, B., "Employment of Second-Moment Closure for Calculation of Turbulent Recirculating Flows in Complex Geometries with Collocated Variable Arrangement," *International Journal for Numerical Methods in Fluids,* Vol. 16, pp. 525–544.

Fu, S., Huang, P. G., Launder, B. E., and Leschziner, M. A., 1988, "A comparison of algebraic and differential second-moment closures for axisymmetric turbulent shear flows with and without swirl," ASME JOURNAL OF FLUIDS ENGINEERING, Vol. 110, pp. 216–221.

Gosman, A. D., and Watkins, A. P., 1977, "A Computer Prediction Method for Turbulent Flow and Heat Transfer in Piston/Cylinder Assemblies," *1st Symposium on Turbulent Shear Flow,* Penn. State Univ., Apr. 18–20 1977.

Gosman, A. D., Tsui, Y. Y., and Watkins, A. P., 1984, "Calculations of Three Dimensional Air Motion in Model Engine," SAE paper 840229.

Huang, P. G., and Leschziner, M. A., 1985, "Stabilization of Recirculating Flow Computations Performed with Second-Order Closures and Third-Order Discretization," *Proc. 5th Symp. on Turbulent Shear Flows,* Cornell University, Paper 20.7.

Jakirlic, S., and Hanjalic, K., 1994, "On the Performance of the Second-Moment High- and Low-Re-Number Closures in Reattaching Flows," *Proc. Int. Symp. on Turbulence, Heat and Mass Transfer,* Lisbon, Aug. 1994.

Jones, W. P., Pascau, A., 1989, "Calculation of Confined Swirling Flows With a Second Moment Closure," ASME JOURNAL OF FLUIDS ENGINEERING, Vol. 111, pp. 248–255.

Kim, J., Kline, S. J., and Johnston, J. P., 1980, "Investigation of a Reattaching Turbulent Shear Layer: Flow Over a Backward-Facing Step," ASME JOURNAL OF FLUIDS ENGINEERING, Vol. 102, pp. 302–308.

Kline, S. J., Cantwell, B. J., and Lilley, G. M., *1981,* Proceedings of the 1980–81 AFOSR-HTTM Stanford Conference on Complex Turbulent Flows, Stanford University Press, Stanford, CA.

Launder, B. E., Reece, G. J., and Rodi, W., 1975, "Progress in the Development of a Reynolds Stress Turbulence Closure," *Journal of Fluid Mechanics,* Vol. 68, pp. 537–566.

Launder, B. E., 1989, "Second Moment Closure and its Use in Modelling Turbulent Industrial Flows," *International Journal for Numerical Methods In Fluids,* Vol. 9, pp. 963–985.

Lebrère, L., 1995, "Modélisation de la turbulence au second ordre pour la simulation numérique d'écoulements dans les moteurs à pistons," Thèse de Doctorat, Ecole Centrale de Lyon.

Le Penven, L., and Serre, G., 1993, "Homogeneous Turbulence Submitted to Compression, Experimental Study and Modelling," *9th Symposium on Turbulent Shear Flow,* Kyoto (Japan), August 16–18, 1993.

Lien, F. S., and Leschziner, M. A., 1993, "Second-Moment Modelling of Recirculating Flow with a Non-Orthogonal Collocated Finite-Volume Algorithm," *Turbulent Shear Flows 8,* Springer-Verlag, Berlin, pp. 431.

Lien, F. S., and Leschziner, M. A., 1994, "Assessment of Turbulence-Transport Models Including Non-Linear RNG Eddy-Viscosity Formulation and Second-Moment Closure for Flow Over a Backward Facing Step," *Computers Fluids,* Vol. 23, pp. 983–1004.

Mao, Y., Buffat, M., and Jeandel, D., 1994, "Simulation of the Turbulent Flow Inside The Combustion Chamber of a Reciprocating Engine With a Finite Element Method," ASME JOURNAL OF FLUIDS ENGINEERING, Vol. 116, pp. 363–369.

Michard, M., Grosjean, N., Safsaf, D., and Lengyel, I., 1993: "Mesure d'échelles de turbulence dans un moteur alternatif," Rapport Final 1992, ME-TRAFLU.

Naitoh, K., Fujii, H., Takagi, Y., and Kuwahara, K., 1990, "Numerical Simulation of the Detailed Flow in Engines Ports and Cylinders," SAE paper No. 900256.

Oberlack, M., and Peters, N., 1992, "Closure of the Two-Point Correlation Equation as a Basis of Reynolds Stress Models," *Applied Scientific Research,* Vol. 51, pp. 533–538.

Reynolds, W. C., 1980, "Modelling of Fluid Motions in Engines—An Introductory Overview," *Symposium on Combustion Modeling in Reciprocating Engines,* eds., Plenum Press, 1980, pp. 41–66.

Rodi, W., 1976, "A New Algebraic Stress Relation for Calculating the Reynolds Stresses," *Z. Ang. Math. und. Mech.,* Vol. 56, p. 219.

Speziale, C. G., Sarkar, S., and Gatski, T. B., 1991, "Modelling the Pressure-Strain Correlation of Turbulence: An Invariant Dynamical Systems Approach," *Journal of Fluid Mechanics,* Vol. 227, pp. 245–272.

Thangam, S., 1991, "Analysis of Two-Equation Turbulence Models for Recirculating Flows," ICASE Report No. 91-61.

Watkins, A. P., Kanellakopoulos, P., and Lea, C. J., 1990, "An Assessment of Discretisation Schemes and Turbulence Models for In-Cylinder Flows," COMODIA 90, pp. 499–504.

Watkins, A. P., and Lea, C. J., 1991, "Development of Advanced Turbulence Models for the Calculation of Flows in Internal Combustion Engine Cylinders," IMechE *1991,* pp. 7–20.

Wu, C. T., Ferziger, J. H., and Chapman, D. R., 1985, report TF-21 NASA, Stanford.

Obstruction of Pipelines During the Flow of Waxy Crude Oils

Paulo R. Souza Mendes

Sergio L. Braga

Department of Mechanical Engineering,
Pontifícia Universidade Católica,
Rio de Janeiro, RJ 22453-900, Brazil

When a liquid solution is cooled as it flows laminarly through a tube, a radial concentration gradient is established, which causes mass transfer of the solute to occur toward the tube wall. The solute precipitates off the solution in the neighborhood of the wall, and adheres perfectly to it. The deposited mass gradually obstructs the conduit, affecting the pressure and flow fields. A simple model is presented that gives the thickness of the deposited layer as a function of axial position and time. The liquid solution is assumed to behave according to the Herschel-Bulkley rheological model. Results are presented in the form of time evolution of axial distributions of pressure, temperature, layer thickness, global heat transfer coefficient and Reynolds number.

Introduction

Heavy hydrocarbons tend to precipitate off waxy crude oils as they flow through tubes. The precipitated paraffin deposits on the tube inner wall, forming a solid layer that narrows the flow passage and eventually reduces drastically the rate of flow. This occurs when the tube wall is at a temperature lower than that of the oil, and also lower than the oil's cloud point.

The phenomena that govern this problem were not well understood until recently. In a pioneer study about this problem, Burger et al. (1981) worked with the hypothesis that the mechanisms of deposition are (i) molecular diffusion; (ii) brownian diffusion; and (iii) shear dispersion. Other researchers followed similar analyses (e.g., Addison, 1984; Kurban, 1991).

According to the literature on suspensions (e.g., Graham et al., 1991 and Mondy et al., 1994), shear dispersion would cause the paraffin crystals to migrate toward the opposite direction of the shear rate gradient, viz., from the region close to the wall toward the center of the tube. Thus, this mechanism cannot cause wax deposition. Brownian diffusion of the precipitated crystals also seems to be unimportant, because it is not directly related to heat transfer and there is experimental evidence that no deposition occurs when the walls are adiabatic or when the walls are hotter than the fluid (Burger et al., 1981).

Therefore, it is now believed that molecular diffusion governs wax deposition (Brown et al., 1993). Whenever there is a temperature difference between the wall and the oil, a radial temperature gradient is established in the flowing fluid. If the oil is rich in heavy hydrocarbons and enters the tube at a relatively high temperature, as it flows and its temperature decreases due to heat losses to the wall, it approaches the saturated state corresponding to the initial paraffin concentration. Because the paraffin solubility in the oil is a function of temperature, the radial temperature gradient causes a radial mass-concentration gradient, provided the oil temperature has already reached the cloud point corresponding to the initial concentration. The thus established concentration gradient promotes a radial mass transfer flux of paraffin toward the wall, where it precipitates off the oil and deposits.

The following analysis is an attempt to model in a relatively simple way this complicated process, which is of great importance in the oil industry. As far as the authors know, this is the first report in the open literature to present time evolutions of axial distributions of the layer thickness.

The Analysis

Calling δ the thickness of the deposited layer, we now present the system of equations whose solution includes the function $\delta(x, t)$, where x is the axial coordinate along the tube, measured from the tube inlet, and t the time variable. At $t = 0$ the tube wall is clean ($\delta(x, 0) = 0$, $\forall\ x$ between 0 and L, where L is the total tube length).

Some of the symbols employed in the present formulation are presented with the aid of Fig. 1. We employ a lumped formulation in the radial direction, to eliminate the dependence on the radial coordinate, r.

Two distinct regions of the flow are identified. The first starts at $x = 0$ and ends at x_d, where the petroleum's bulk temperature, T_b, reaches the cloud point, T_c (i.e., $T_b|_{x_d} = T_c$). The oil, which for the present purposes is seen as a solution of paraffins, is not yet at its saturated state, and then there is no precipitation or deposition.

The other flow region consists of the rest of the flow domain, i.e., $x_d \leq x \leq L$. We assume that in this region the oil is saturated everywhere, so that the existing temperature gradient corresponds to a solubility gradient which drives mass transfer toward the wall. This assumption has also been employed by Burger et al. (1981), and is based on experimental evidence (Addison, 1984).

We analyze here the situation in which the overall pressure differential at the tube extremities, Δp, is held constant. Due to wax deposition, the flow rate, Q, is expected to be a decreasing function of time. The bulk temperature is a function of position and time, $T_b = T_b(x, t)$. Consequently, the length of the clean-tube region, x_d, is a function of time. In other words, the size of the two above defined flow regions vary with time.

Momentum Balance. We employ the lubrication approximation in the present formulation, i.e., we assume that inertia terms in the momentum equation are negligible. This assumption is good provided δ is not a strong function of x or t, and leads to

$$\frac{dp}{dx} = -f\,\frac{\rho Q^2}{4\pi^2(R-\delta)^5} \qquad (1)$$

where $p = p(x, t)$ is the pressure, $f = f(x, t)$ the local friction factor, R the tube inner radius, and ρ the density of the flowing fluid, assumed to be constant.

Equation (1) may be seen as a definition of the friction factor, f, and can be integrated in x from 0 to L, yielding

$$\Delta p \equiv p_{\text{in}} - p_{\text{atm}} - \rho g H = \frac{\rho Q^2}{4\pi^2 R^4}\int_0^{L^*} \frac{f}{(1-\delta^*)^5}\,dx^* \qquad (2)$$

In this equation, p_{in} is the pressure at the tube inlet, p_{atm} at the tube exit (at $x = L$), g the acceleration due to gravity, H

Contributed by the Fluids Engineering Division for publication in the JOURNAL OF FLUIDS ENGINEERING. Manuscript received by the Fluids Engineering Division December 13, 1995; revised manuscript received September 5, 1996. Associate Technical Editor: H. Hashimoto.

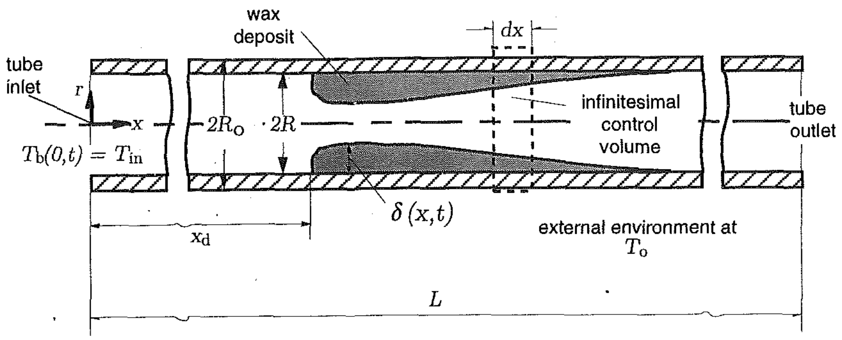

Fig. 1 Schematics of the problem

the height of the tube exit relative to the tube inlet, $L^* \equiv L/R$ the dimensionless tube length, $x^* \equiv x/R$ the dimensionless axial coordinate, and $\delta^* \equiv \delta/R$ the dimensionless thickness of the deposited layer.

The axial distribution of pressure is given by

$$P^* \equiv \frac{p - p_{\text{atm}} - \rho g H}{\Delta p} = \frac{\displaystyle\int_{x^*}^{L^*} \frac{f}{(1-\delta^*)^5}\, dx^{*\prime}}{\displaystyle\int_0^{L^*} \frac{f}{(1-\delta^*)^5}\, dx^*} \tag{3}$$

We can rewrite Eq. (2) in the form

$$Q(t) = 2\pi R^2 \sqrt{\frac{\Delta p}{\rho}}\, \frac{1}{\sqrt{\displaystyle\int_0^{L^*} \frac{f}{(1-\delta^*)^5}\, dx^*}} \tag{4}$$

Constitutive Law and Friction Factor. The generalized Newtonian fluid model is a good constitutive equation for shear flows in tubes when the main concern is the $Q \times \Delta p$ relation:

$$\boldsymbol{\tau} = \eta(\dot{\gamma})\dot{\boldsymbol{\gamma}} \tag{5}$$

where $\boldsymbol{\tau}$ is the extra-stress, $\dot{\boldsymbol{\gamma}} \equiv \text{grad}\, v + (\text{grad}\, \mathbf{v})^T$ the deformation rate, and $\dot{\gamma} \equiv \sqrt{\frac{1}{2}\,\text{tr}\, \dot{\boldsymbol{\gamma}}^2}$ its modulus.

The viscosity function $\eta(\dot{\gamma})$ should be selected such as to well represent experimental data. For suspensions, the Herschel-Bulkley viscosity function is often a representative choice:

$$\eta = \begin{cases} \dfrac{\tau_0}{\dot{\gamma}} + K\dot{\gamma}^{n-1}, & \text{if} \quad \tau > \tau_0; \\ \infty & \text{otherwise} \end{cases} \tag{6}$$

where $\tau \equiv \sqrt{\frac{1}{2}\,\text{tr}\, \boldsymbol{\tau}^2}$ is the modulus of the extra-stress, and τ_0, K, and n are rheological parameters. τ_0 is the yield stress (the stress level below which there is no flow), K the consistency index, and n the power-law index. Clearly, for Newtonian fluids $\tau_0 = 0$, $n = 1$, and K becomes the Newtonian viscosity. It is also worth mentioning that the power-law fluid ($\tau_0 = 0$, $n \neq$

Nomenclature

c = specific heat (J/kg K)
$\mathcal{D}$ = molecular diffusivity (m^2/s)
f = local friction factor (dimensionless)
g = acceleration due to gravity (m/s^2)
h_0 = external heat transfer coefficient (W/m^{2}K)
h_i = internal heat transfer coefficient (W/m^{2}K)
H = height of tube exit relative to tube inlet (m)
He = Hedstrom number
j_i = diffusion mass flux (kg/s m^2)
K = consistency index (Pa s^n)
L = tube length (m)
L^* = dimensionless tube length
m_d = mass of solid deposit (kg)
n = power-law or behavior index (dimensionless)
Nu$_0$ = external Nusselt number
Nu$_i$ = internal Nusselt number
p = pressure (Pa)
p_{atm} = pressure at tube exit (Pa)
p_{in} = pressure at tube inlet (Pa)
P^* = dimensionless pressure
Pe = Peclet number
Pe$_0$ = initial Peclet number
Q = flow rate (m^3/s)
Q_0 = initial flow rate (m^3/s)
r = radial coordinate (m)
R = tube inner radius (m)
R_0 = tube outer radius (m)
Re = Reynolds number
Re$_0$ = initial Reynolds number
x = axial coordinate (m)
x_d = length of clean tube (m)
x^* = dimensionless axial coordinate
x_d^* = dimensionless length of clean tube
S = solubility coefficient (kg/m^{3}K)
S^* = dimensionless solubility coefficient
t = time (s)
t^* = dimensionless time
T_b = oil bulk temperature (K)
T_c = cloud point (K)
T_i = temperature at solid-liquid interface (K)
T_{in} = oil inlet temperature (K)
T_0 = temperature of external environment (K)
U = overall heat transfer coefficient (W/m^{2}K)
U^* = dimensionless overall heat transfer coefficient
$\mathbf{v}$ = velocity vector field (m/s)
Z = auxiliary function (dimensionless)
$\dot{\gamma}$ = deformation rate, $\equiv \sqrt{\frac{1}{2}\,\text{tr}\, \dot{\boldsymbol{\gamma}}^2}$, (s^{-1})
$\dot{\boldsymbol{\gamma}}$ = rate-of-deformation tensor (s^{-1})
δ = thickness of deposited layer (m)
δ^* = dimensionless thickness of deposited layer
Δp = overall pressure differential (Pa)
η = viscosity function (kg/m s)
θ = dimensionless temperature
κ_d = thermal conductivity of deposited layer (W/m K)
κ_i = thermal conductivity of fluid (W/m K)
κ_w = wall thermal conductivity (W/m K)
ρ = mass density of fluid (kg/m^3)
ρ_d = mass density of deposited material (kg/m^3)
ρ_s = solubility (kg of solute per m^3)
τ = magnitude of the extra-stress tensor, $\equiv \sqrt{\frac{1}{2}\,\text{tr}\, \boldsymbol{\tau}^2}$ (Pa)
τ_0 = yield stress limit (Pa)
τ_i = shear stress at solid-liquid interface (Pa)
τ^* = dimensionless yield stress limit
$\boldsymbol{\tau}$ = extra-stress tensor (Pa)

1) and the Binghamian fluid ($\tau_0 > 0$, $n = 1$) are two other special cases of the Herschel-Bulkley fluid (Eq. (6)).

For a Herschel-Bulkley fluid, the friction factor, f, is a function of the Reynolds number, Re, the Hedstrom number, He, and the power-law index, n (Skelland, 1967). For the present purposes, the just mentioned dimensionless groups are defined as

$$\mathrm{Re} = \frac{8\rho\pi^{n-2}R^{3n-4}Q^{2-n}}{K\left[\frac{3n+1}{n}\right]^n}(1-\delta^*)^{3n-4} \tag{7}$$

and

$$\mathrm{He} = \frac{\pi^2 R^4\,\mathrm{Re}^2\tau_0}{\rho Q^2}(1-\delta^*)^4 \tag{8}$$

From Eq. (1) and a local force balance it is possible to show that

$$\tau^* \equiv \frac{\tau_0}{\tau_i} = \frac{8\,\mathrm{He}}{f\,\mathrm{Re}^2} \tag{9}$$

where τ_i is the local shear stress at the solid-liquid interface. It is now useful to define the following auxiliary function:

$$Z = (1-\tau^*)^3 + \frac{2(3n+1)}{2n+1}\tau^*(1-\tau^*)^2 + \frac{3n+1}{n+1}\tau^{*2}(1-\tau^*) \tag{10}$$

With the aid of the above definitions, the expression for the friction factor becomes, for laminar flow (Re < 3000):

$$f = \frac{8\,\mathrm{He}}{\mathrm{Re}^2} + \frac{64}{Z^n\,\mathrm{Re}} \tag{11}$$

From the above equations, it is clear that f is a known function of Q, and therefore if we knew $\delta^*(x^*, t)$, we would be able to solve (iteratively) Eqs. (4), (7), (8), (9), (10), and (11) to obtain $Q(t)$.

Energy Balance. As we discussed earlier, heat transfer plays a major role in the deposition process. If we apply the principle of conservation of energy to the control volume shown in Fig. 1, we readily get

$$\rho Q c\frac{dT_b}{dx} = 2\pi R U(T_o - T_b) \tag{12}$$

where c is the specific heat of the flowing fluid, $U(x, t)$ the overall heat transfer coefficient, and T_0 the temperature of the environment in which the tube is immersed. The overall heat transfer coefficient, U, is based on the inner (clean) surface.

We observe that U takes into account the convective inner and outer resistances, plus the conductive resistances of the tube wall and of the deposited layer:

$$U = \left[\frac{R}{R_0}\frac{1}{h_0} + \frac{R}{\kappa_w}\ln\left(\frac{R_0}{R}\right) + \frac{R}{\kappa_d}\ln\left(\frac{1}{1-\delta^*}\right) + \left(\frac{1}{1-\delta^*}\right)\frac{1}{h_i}\right]^{-1} \tag{13}$$

where R_0 is the external tube radius, h_0 and h_i the external and internal convective heat transfer coefficients (respectively), κ_w the wall thermal conductivity, and κ_d the thermal conductivity of the deposited layer. It is clear that U depends on δ^*, and that Eq. (13) can be rewritten in the following dimensionless form:

$$U^* \equiv \frac{UR}{\kappa_i} = \left[\frac{2\kappa_i/\kappa_0}{\mathrm{Nu}_0} + \frac{\kappa_i}{\kappa_w}\ln\left(\frac{R_0}{R}\right) + \frac{\kappa_i}{\kappa_d}\ln\left(\frac{1}{1-\delta^*}\right) + \frac{2}{\mathrm{Nu}_i}\right]^{-1} \tag{14}$$

In Eq. (14), κ_i is the thermal conductivity of the flowing fluid, and κ_0 the same transport property of the external fluid. Nu_0 and Nu_i are respectively the external and internal Nusselt numbers, defined as

$$\mathrm{Nu}_0 \equiv \frac{2R_0h_0}{\kappa_0};\quad \mathrm{Nu}_i \equiv \frac{2Rh_i}{\kappa_i}(1-\delta^*) \tag{15}$$

The external Nusselt number can be obtained with the aid of empirical correlations existing in the literature, which depend on the type of external flow. For the sake of simplicity, in this work we neglect both the external convective resistance ($\mathrm{Nu}_0 \to \infty$) and the wall conductive resistance ($\kappa_i \ll \kappa_w$).

A correlation for the internal Nusselt number is not available in the literature for the Herschel-Bulkley fluid, as far as we know. However, because the dependence on rheological parameters of the Nusselt number is due solely to the related dependence of the velocity profile, we believe that a reasonable approximation is to use the Nusselt number for the power-law fluid ($\tau_0 = 0$):

$$\mathrm{Nu}_i = \frac{3.66}{n^{0.12}} \tag{16}$$

The above expression is a curve fit to the solution given by Bird et al. (1987) for discrete values of n, and is expected to be valid for fully developed laminar flow in the range $0.33 \le n \le 1$. It is worth mentioning here that, in the situations where the lubrication approximation is not valid, this expression isn't either, because entrance effects also affect the Nusselt number.

Defining the dimensionless temperature $\theta \equiv (T_b - T_0)/(T_{\mathrm{in}} - T_0)$ and the Peclet number

$$\mathrm{Pe} \equiv (2\rho c Q)/(\pi R\kappa_i), \tag{17}$$

we can integrate Eq. (12) to obtain

$$\theta = \exp\left[-\frac{4}{\mathrm{Pe}}\int_0^{x^*} U^* dx^{*\prime}\right] \tag{18}$$

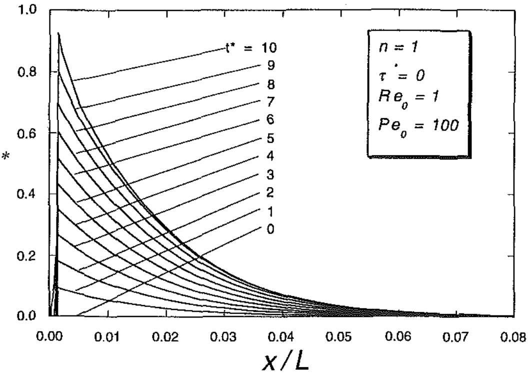

Fig. 2 Layer thickness distribution ($\mathrm{Pe}_0 = 100$)

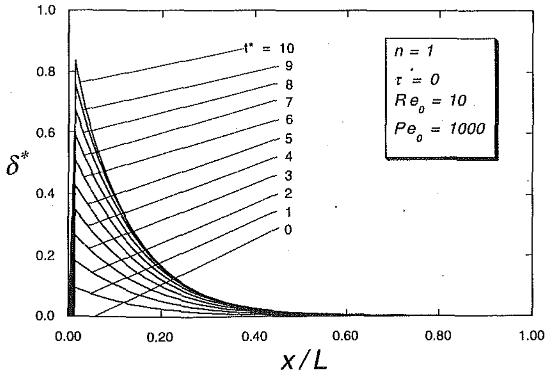

Fig. 3 Layer thickness distribution ($\mathrm{Pe}_0 = 1000$)

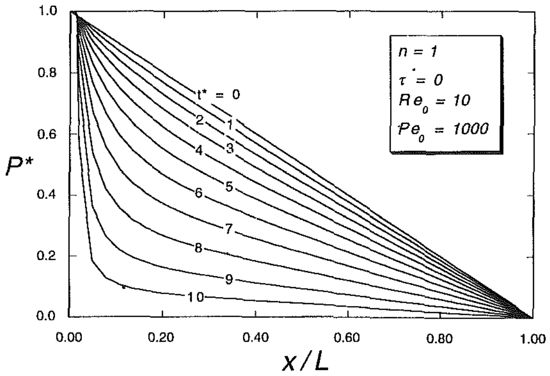

Fig. 5 Pressure distribution

Equation (18) also gives the length of clean tube, x_d^*, because, in the range $0 \le x^* \le x_d^*$, neither δ^* (which is zero in the clean-tube region) nor U^* depend on x^*, thus,

$$x_d^* = \frac{\ln\left(\dfrac{T_{\text{in}} - T_0}{T_c - T_0}\right)}{4U^*|_{\delta^*=0}}\,\mathrm{Pe} \qquad (19)$$

where $U^*|_{\delta^*=0}$ is given by Eq. (14) with $\delta^* = 0$.

We observe that x_d^* is also a function of δ^*, through Q. Because Q decreases with time, the same is expected to occur with x_d^*.

Layer Thickness. We need a governing equation for $\delta^*(x^*, t)$, to complete the problem formulation. The layer thickness is intimately related to the mass flux at the solid-liquid interface, j_i, which is defined by

$$j_i \equiv \frac{dm_d}{dt dA} \qquad (20)$$

where dm_d is the mass of solid deposited during the time interval dt on the surface of area dA. We can write that $dm_{dp} = \rho_d dV$, where ρ_d is the density of the deposited material. The infinitesimal volume dV is the volume of the mass that deposits on dA during dt, i.e., $dV = dAd\delta = dA(\partial\delta/\partial t)dt$. Therefore,

$$j_i = \rho_d \frac{\partial \delta}{\partial t} \qquad (21)$$

From Fick's law of molecular diffusion, we can also write another expression for the mass flux:

$$j_i = \begin{cases} 0, & \text{if } 0 \le x < x_d; \\ -\mathcal{D} \left.\dfrac{d\rho_s}{dT}\right|_i \left.\dfrac{\partial T}{\partial r}\right|_i, & \text{if } x_d \le x \le L. \end{cases} \qquad (22)$$

In this equation, $\mathcal{D}$ is the molecular diffusivity, ρ_s the solubility, and $d\rho_s/dT|_i$ the solubility coefficient, evaluated at the local solid-liquid interface temperature (T_i). For convenience we will call S this latter quantity ($S \equiv d\rho_s/dT|_i$).

The term $\partial T/\partial r|_i$ is the local temperature gradient at the solid-liquid interface, given by

$$\left.\frac{\partial T}{\partial r}\right|_i = -\frac{U^*}{1-\delta^*}\frac{T_{\text{in}} - T_0}{R}\,\theta \qquad (23)$$

Defining a dimensionless time $t^* \equiv \mathcal{D}t/R^2$, and combining Eqs. (21), (22), and (23), we get

$$\frac{\partial \delta^*}{\partial t^*} = \begin{cases} 0, & \text{if} \quad 0 \le x^* < x_d^*; \\ \dfrac{S^*U^*}{1-\delta^*}\,\theta & \text{if} \quad x_d^* \le x^* < L^*. \end{cases} \qquad (24)$$

where the dimensionless solubility coefficient, S^*, is defined by

$$S^* \equiv \frac{S(T_{\text{in}} - T_0)}{\rho_d} \qquad (25)$$

Equation (24), subject to the initial condition $\delta^*(x^*, 0) = 0$, completes the problem formulation. An iterative procedure has been employed to solve the system of equations presented in the above formulation. In this procedure, a fourth-order Runge-

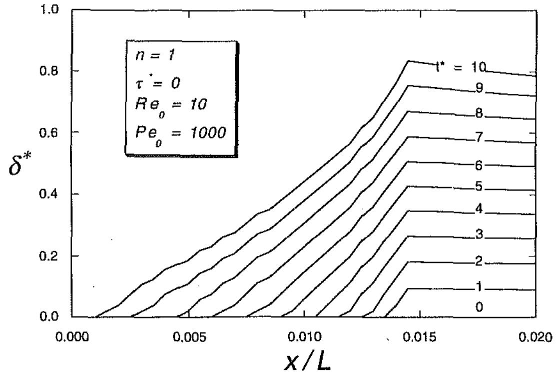

Fig. 4 Detail of the throat region

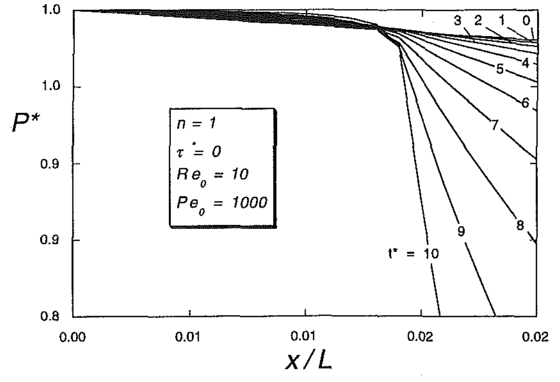

Fig. 6 Detail of pressure near throat

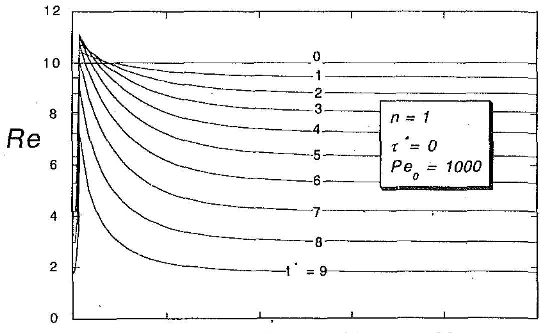

Fig. 7 Reynolds number distribution

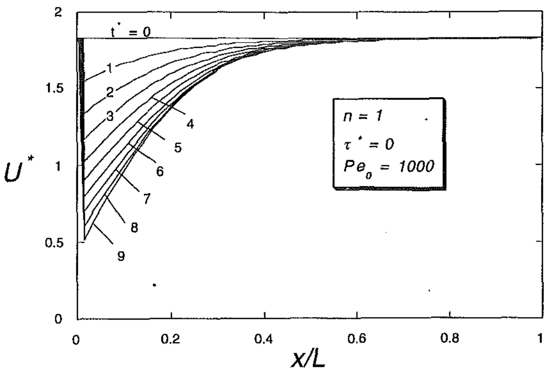

Fig. 9 Distribution of overall heat transfer coefficient

Kutta method with 100 uniformly spaced grid points has been employed to integrate Eq. (24) at each iteration. This grid was chosen after extensive testing with different combinations of the governing parameters, which showed that the results obtained are grid-independent.

Results and Discussion

The results presented here pertain to a length-to-radius ratio of $L/R = 1000$, a cloud point of $\theta_c \equiv (T_c - T_0)/(T_{\text{in}} - T_0) = 0.9$, a dimensionless solubility coefficient $S^* = 0.01$, and equal thermal conductivities of the fluid and deposited material ($\kappa_l/\kappa_d = 1$). The initial Reynolds number is kept at $\text{Re}_0 = 10$, except where otherwise stated. As we will discuss later, the influence of the initial Reynolds number is negligibly small for all cases investigated. The above parameter values are representative of real situations in the petroleum industry. First we present and discuss results pertaining to Newtonian fluids, and later we discuss the effects of non-Newtonian behavior.

Figures 2 and 3 present the axial distribution of the layer thickness for different (dimensionless) times. Figure 2 shows this result for an initial Peclet number of $\text{Pe}_0 = 100$, while Fig. 3 pertains to $\text{Pe}_0 = 1000$. These figures show that the location of maximum thickness (the throat) essentially doesn't vary with time, and corresponds to the initial boundary of the clean-tube region, i.e., $x = x_d$ at $t = 0$. This is true in the present cases because, since the wall temperature is uniform and the fluid temperature is a decreasing function of axial position, at this location the radial temperature gradient is quite high, especially for shorter times. This might not be the case if the thermal conductivity of the deposited material were poorer. As time elapsed and the layer thickened, a lower thermal conductivity would tend to displace downstream the position of highest radial temperature gradient, and a smoother thickness distribution would then be observed.

It is also seen that the deposited layer is concentrated in a quite narrow axial length for the lower initial Peclet number case ($\text{Pe}_0 = 100$, Fig. 2), while a more uniform layer of deposited material grows when the initial Peclet number is higher ($\text{Pe}_0 = 1000$, Fig. 3). In real situations, if the obstructed region is too narrow, the layer will not resist to drag forces and will be washed out by the flow before it has a chance to grow significantly. Therefore, the high Peclet number cases are the ones of concern if we are interested in avoiding obstruction, and for this reason most of the following results correspond to an initial Peclet number of $\text{Pe}_0 = 1000$.

Figure 4 shows the neighboring region of the throat in more detail. The thickness varies mildly with the axial position downstream the throat, and more sharply upstream of it. Along this short axial length of sharp thickness variation, inertia becomes more important, and the lubrication approximation is expected not to be as good as elsewhere in the tube. The validity of the lubrication approximation in this flow region is discussed later in this section.

Figures 5 and 6 show the pressure axial distribution. Initially the pressure falls linearly with the axial position, as it should do, but as the deposited layer grows this distribution changes significantly, the pressure losses tending to concentrate in the throat region as time elapses.

The local Reynolds number distribution is initially uniform (Fig. 7), but as the deposited layer builds up, it presents sharp peaks at the throat. We observe that overall Re decreases significantly due to obstruction, and for longer times even the Reynolds number values at the throat do not reach the initial value. The peak value can be up to three to four times the value away from the throat, for longer times.

The temperature distribution is shown in Fig. 8. First, we observe comparing Fig. 3 with Fig. 8, that for this case the fluid temperature reaches the wall temperature at an axial location about sixty percent of the tube length, beyond which there is

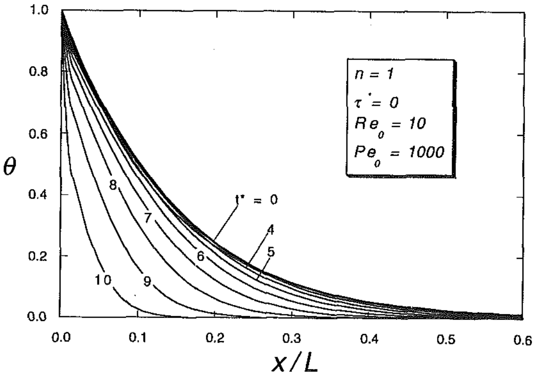

Fig. 8 Temperature distribution

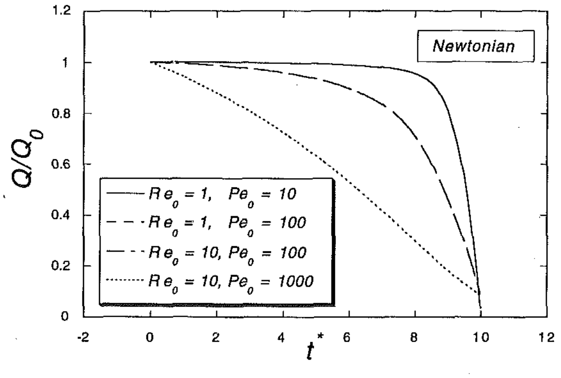

Fig. 10 Flow rate versus time (Newtonian cases)

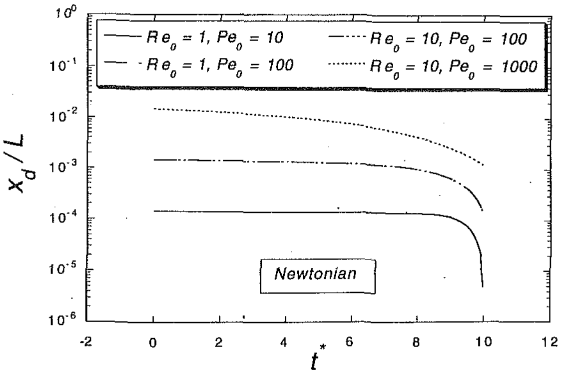

Fig. 11 Clean length versus time (Newtonian cases)

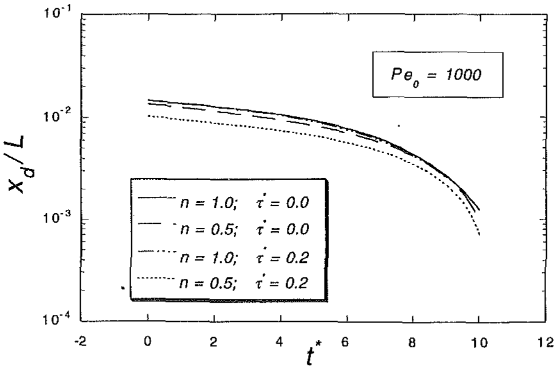

Fig. 13 Clean length versus time ($Pe_0 = 1000$)

no more deposition. This is a direct consequence of our physical model, and, as mentioned earlier, is in agreement with experimental observations. As the tube is obstructed, the fluid tends to reach thermal equilibrium with the tube wall at smaller values of the axial coordinate, because it flows more slowly and stays longer in contact with the cold wall. In other words, as time elapses the thermally active region where deposition occurs gets shorter. Figure 9 shows the distribution of local overall heat transfer coefficient along the tube. This figure illustrates that for the case examined the thermal resistance of the deposited layer dominates the overall resistance for relatively large thicknesses, which occurs near the throat if the time is not too short. Figure 10 shows the flow rate as a function of time, for different Reynolds and Peclet numbers. Firstly it is observed that the two curves for initial Peclet number $Pe_0 = 100$ are coincident. Because these two curves pertain to two different initial Reynolds numbers, it follows that in this range of parameters the effect of initial Reynolds number on the $Q(t)$ curve is negligible. The initial Peclet number, however, affects dramatically the flow rate curve. For low initial Peclet numbers, the flow rate remains invariant for a long period of time, but suddenly falls sharply. As the initial Peclet number is increased, the flow rate decreases more steadily with time. This behavior is readily understood upon examination of the thickness distributions shown in Figs. 2 and 3. Because the length of obstructed tube is short for low initial Peclet numbers, it causes negligible pressure losses except when the tube is nearly completely obstructed. For high initial Peclet numbers, the obstructed region is long, and even a thin deposited layer causes significant pressure loss and hence flow rate reduction. The behavior of the length of clean tube is obviously the same as the one observed for the flow rate (see Eq. (19)), as illustrated in Fig. 11.

So far we have discussed results for Newtonian fluids. For the other fluid behaviors examined, viz., power-law, Bingham and Herschel-Bulkley fluids, the qualitative trends of all the above discussed quantities is essentially the same as for the Newtonian fluid. Neither quantitatively the influence of non-Newtonian behavior is too striking, as illustrated in Figs. 12 and 13.

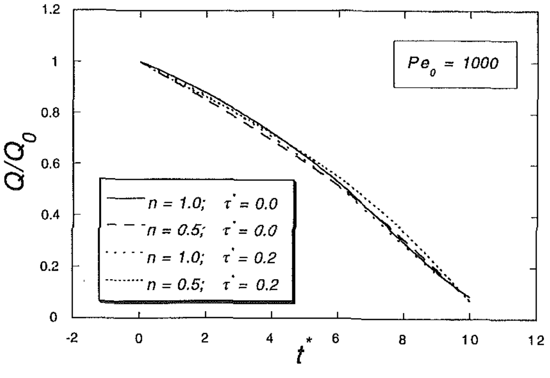

Fig. 12 Flow rate versus time ($Pe_0 = 1000$)

Finally, it is worth examining the effect of inertia in this flow. As we mentioned earlier, in the analysis we employed the lubrication approximation, which is valid if inertia term in the momentum balance is negligible. A simple order-of-magnitude analysis indicates that the ratio of inertia force to viscous force is, for the present problem, of the order of $\mathrm{Re}\,\partial\delta^*/\partial x^* = (R/L)\ \mathrm{Re}\,\partial\delta^*/\partial(x/L)$. From Fig. 4, the highest values of $\partial\delta^*/\partial(x/L)$ can be estimated to be about $0.74/0.011 = 67.3$. For $R = 3$ in, $L = 1$ km, and $\mathrm{Re} = 10/(1 - \delta^*) = 38.5$ at the throat, one gets 0.2 for the mentioned ratio. Therefore, for the cases presented in the manuscript, the lubrication approximation is reasonable. However, for other situations of practical interest this might not be the case, and this limitation of the analysis should be kept in mind.

Conclusions

The problem of tube obstruction during the flow of a liquid solution due to deposition of precipitated solvent on the wall is examined. Deposition occurs due to molecular diffusion. A mass flux of the solvent toward the wall is driven by a concentration gradient, which exists due to the presence of a temperature gradient.

It was shown that the Peclet number is the major governing parameter for this problem. Low Peclet numbers cause short obstructed lengths, which may not resist to drag forces and in this case real obstruction shouldn't occur. High Peclet number situations are more likely to cause obstruction in practical situations, because the tube length where deposition occurs is longer, and hence the deposited layer is not easily washed out by the flow.

Non-Newtonian fluid behavior has a small effect on the time evolution of the flow rate.

Acknowledgments

This research program has been executed with the financial support of Petrobras S. A. and CNPq (Brazilian Council for Scientific and Technological Development).

References

Addison, G. E., 1984, "Paraffin Control More Cost-Effective," AIME Society of Petroleum Engineers, Eastern Regional Meeting, SPE 13391, Charleston, W VA, Oct 31–Nov 2, pp. 203–210.

Bird, R. B., Armstrong, R. C., and Hassager, O., 1987, *Dynamics of Polymeric Liquids*, Wiley.

Brown, T. S., Niesen, V. G., and Erickson, D. D., 1993, "Measurement and Prediction of the Kinetics of Paraffin Deposition," SPE Report no. 26548, Oct., pp. 353–368.

Burger, E. D., Perkins, T. K., and Striegler, J. H., 1981, "Studies of Wax Deposition in the Trans Alaska Pipeline," *SPE Journal of Petroleum Technology,* June, pp. 1075–1086.

Graham, A. L., Altobelli, S. A., Fukushima, E., Mondy, L. A., and Stephens, T. S., 1991, "NMR imaging of Shear-Induced Diffusion and Structure in Concentrated Suspensions Undergoing Couette Flow," *J. of Rheology,* Vol. 35(1), pp. 191–201.

Kurban, A. P. A., 1991, "Deposition of organic residues during the flow of petroleums in ducts: Theory and Experiments (1st partial report)," Petrobras Internal Report no. 1165 (in Portuguese).

Mondy, L. A., H. Brenner, S. A. Altobelli, J. R. Abbott, and Graham, A. L., 1994, "Shear-Induced Particle Migration in Suspensions of Rods," *Journal of Rheology,* Vol. 38(2), pp. 444–452.

Skelland, A. H. P., 1967, *Non-Newtonian Flow and Heat Transfer,* Wiley.

Transient Gas-Liquid Flow in Upward Sloping Pipes, Approaching the Wavy-to-Slug Flow Transition

Eric Grolman[1]
Researcher.

Jan M. H. Fortuin
Professor.

Department of
Chemical Engineering,
University of Amsterdam,
Nieuwe Achtergracht 166,
1018 WV Amsterdam,
The Netherlands

A model is presented for transient, cocurrent gas-liquid pipe flow in the stratified-smooth and stratified-wavy flow regimes. It is based on the equations of continuity and motion in the direction of flow and results in two hyperbolic partial differential equations, which are solved numerically using the combined methods of lines (Schiesser, 1991) and characteristics (Stoker, 1957). In wavy gas-liquid pipe flow, three different interfacial areas and corresponding shear stresses are identified. Three friction-factor correlations were derived on the basis of an extensive set of 2500 steady-state measurements. The transient behavior of inclined gas-liquid pipe flow is successfully simulated and compares well with the results obtained from on-line measurements, right up to the onset of slug flow.

Introduction

The SW-I transition from stratified-wavy to intermittent (slug or semi-slug) flow is important in many industrial applications. In transportation pipelines the flow regime not only affects the pressure gradient (or rate of momentum transfer), but also determines the necessity for the installation of slug catchers and additional safety measures, to handle slugs and associated pressure oscillations. In many industrial pipelines, slugs are to be avoided.

Experiments were performed in our laboratory to study the SW-I transition in slightly inclined pipes ($0.1° \leq \beta \leq 6°$) during the cocurrent flow of gas and liquid. In inclined pipes, reducing the gas flow rate is sufficient to cause slugs, irrespective of the magnitude of the liquid flow rate, provided $\beta \geq \sin^{-1}(D/L)$. This is contrary to the more common studies in horizontal pipes, where the liquid flow rate must be increased to initiate slugging. While the ways in which the transitions are achieved are different, the mechanisms underlying the SW-I transition are generally assumed to be the same for both horizontal and slightly inclined pipes.

Several "Bernoulli-related" instability criteria have been proposed, where stability of waves is reduced by the higher gas velocity near the top of a wave, causing a local decrease in pressure, i.e., suction toward the channel roof. This local Kelvin-Helmholtz type of instability mechanism, which was proposed by Wallis and Dobson (1973) to cause slugs in rectangular channels and was adapted to a circular geometry by Taitel and Dukler (1976), has been used by many authors. In these models, an empirical factor close to one half is required to obtain agreement between theory and experiments. The origin of this factor has not been resolved.

Wallis (1969) used linearized, one-dimensional wave equations to predict instabilities in various types of gas-liquid flow. This linear theory, which forecasts the onset of slug flow when the viscous and inviscid wave velocities are equal, is presented elegantly by Barnea and Taitel (1993).

Taitel et al. (1978) introduced a model for *transient* gas-liquid flow, which is based on similar linearized equations and is evaluated numerically. Their analysis shows that instabilities can be caused prematurely during transient events. The model for transient flow was adopted by Crowley et al. (1992) to predict the onset of slug flow in horizontal pipes. However, in their simulations the gas-phase Bernoulli effect is neglected. Furthermore, the numerical technique for integration with respect to time has been improved in the present paper, since the earlier finite-differences approach was found to lead to accumulating rounding errors on larger time scales.

Recently, Minami and Shoham (1994) engaged semi-implicit numerical techniques and presented measured and simulated transient data from a *horizontal,* 77.9 mm diameter pipeline. The shear stresses used in these simulations were obtained directly from measurements, not from general friction factor models.

The disclosure of the mechanisms of flow pattern transition requires a detailed analysis of stratified-wavy flow, with the inclusion of waves of non-zero amplitude and Bernoulli effects. This leads to equations that can only be solved numerically. The MARS (Modified Apparent Rough Surface) model presented in this paper correctly predicts the transient behavior of stratified-wavy gas-liquid pipe flow, up to the transition to slug flow and is sustained by continuous, axially-averaged, on-line liquid-holdup measurements. Furthermore, it allows reconstruction of the local time dependent behavior of inclined gas-liquid flow and hence facilitates a detailed analysis of the mechanisms leading to the onset of slug flow.

Experiments

Over 2500 experiments were performed in two glass pipes (D = 26 mm, L = 10.7 m; D = 51 mm, L = 15 m), with air/water ($\rho_G = 1.2$ kg m^{-3}; $\eta_G = 1.8\ 10^{-5}$ Pa s; $\rho_L = 998$ kg m^{-3}; $\eta_L = 10^{-3}$ Pa s; $\sigma = 72\ 10^{-3}$ Pa m) and air/tetradecane (n-$C_{14}H_{30}$; $\rho_L = 762$ kg m^{-3}; $\eta_L = 2.1\ 10^{-3}$ Pa s; $\sigma = 28\ 10^{-3}$ Pa m) systems, at fourteen angles of inclination β, ranging from $-3°$ to $+6.0°$ ($\pm 0.005°$). The gas and liquid flow rates, average liquid holdup and several temperatures were recorded on-line, as shown schematically in Fig. 1. The gas and liquid flow rates studied and the values of the liquid holdup thus obtained range from: $1.5 \leq u_{GS}/(\text{m s}^{-1}) \leq 30.2$; $1.7\ 10^{-4} \leq u_{LS}/(\text{m s}^{-1}) \leq 0.056$; $0 < \epsilon_L \leq 0.42$, respectively. The low range of gas flow

---

[1] Current address: Delft University of Technology, Faculty of Chemical Technology and Materials Science, Section Industrial Catalysis, Julianalaan 136, 2628 BL Delft, The Netherlands.

Contributed by the Fluids Engineering Division for publication in the JOURNAL OF FLUIDS ENGINEERING. Manuscript received by the Fluids Engineering Division November 4, 1995; revised manuscript received May 23, 1996. Associate Technical Editor: Jong H. Kim.

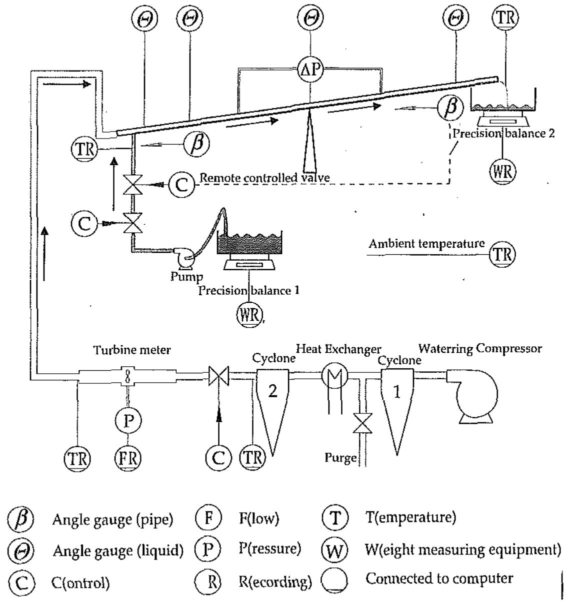

Fig. 1 Schematic diagram of the experimental apparatus

rates has received special attention because here, the effects of small inclination angles are severe. The superficial gas velocity was calculated from a turbine-meter signal (±0.5 percent). The superficial liquid velocity (in and out) was calculated from continuous weight measurements (±0.5 g), both at the entrance to and the exit from the pipe, using a pair of precision balances sampled at 5 Hz. The average liquid holdup in the pipe is calculated from the total liquid mass balance (±1.0 g). A small correction is applied for evaporation of liquid during experiments. The average axial pressure gradient is measured with precision alcohol manometers (±1 percent), across the gas phase. To determine the conditions of flow pattern transition in inclined pipes, the gas flow rate is gradually decreased at constant liquid flow rate and temperature, until the occurrence of a slug terminates the experiment. Because the flow pattern boundary is approached from within the wavy flow regime and all the signals are recorded on-line, the conditions of unstable wavy flow can be determined precisely. These measurements are reproducible within approximately 1 percent of both the gas flow rate and liquid holdup, at constant u_{LS}.

Some entrainment of liquid in the gas phase was observed at the higher range of gas flow rates ($u_{GS} > 15$ m s^{-1}). However, due to the relatively small liquid flow rates of $u_{LS} \leq 0.056$ m s^{-1} and due to the focus on the lower range of gas flow rates, entrainment was very limited in all experiments. Finally, neglecting entrainment in the MARS model was justified by the quality in the prediction of total liquid holdup and overall pressure gradient.

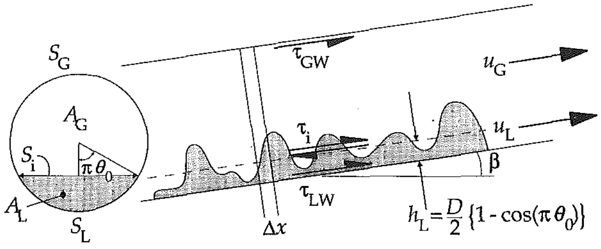

Fig. 2 Schematic view of gas-liquid pipe flow

Model

Assumptions. The model presented here largely follows the procedure and terminology introduced by Taitel et al. (1978). The main differences between the latter and the present analysis are:

The inclusion of the effects of changes in the gas-phase dynamic pressure, i.e., Bernoulli effects;
the incorporation of a liquid-phase velocity profile factor χ ($\chi \equiv \langle v_L^3 \rangle / \langle v_L \rangle^3$);
the equations used for the frictional contributions to the loss of momentum;
the numerical procedure used to integrate the resulting hyperbolic partial differential equations.

Furthermore, first-order approximations are used, with the additional assumptions of incompressible fluids, quasi-steady flow of gas, a flat gas-phase velocity profile and negligible effects of surface tension σ (i.e., the long wavelength approximation).

Equations of Continuity and Motion. Figure 2 is a schematic view of inclined gas-liquid pipe flow and contains the symbols and conventions used in the following derivations. Equations (1) to (4) constitute the basis of the model for transient, inclined gas-liquid pipe flow:

the liquid-phase continuity equation:

Nomenclature

A = cross-sectional area; Fig. 2, m^2
A'_G = = $\partial A_G/\partial h_L = -\partial A_L/\partial h_L$, m
A'_L = = $\partial A_L/\partial h_L$; Eq. (7), m
a_2 = acceleration; Eq. (8), m s^{-2}
D = pipe diameter, m
E = friction and gravity; Eq. (9), m s^{-2}
Fn = friction number; Eq. (18), 1
f = Fanning friction factor, 1
g = gravitational acceleration, m s^{-2}
H = averaged height; Eq. (7), m
h_L = local liquid level in pipe, m
k = equivalent sand roughness, m
L = length of pipe, m
N = number of grid points, 1
P = pressure, Pa
Re = Reynolds number; Eq. (14), 1
S = perimeter; Eq. (13) and Fig. 2, m
t = time, s
s_i = dimensionless interfacial perimeter; Eq. (12), 1
u = gas or liquid velocity, m s^{-1}
v = velocity on a streamline, m s^{-1}
x = axial coordinate, m
β = angle of inclination, deg
ϵ_L = liquid holdup; vol. fraction, 1
η = dynamic viscosity, Pa s
θ = wetted wall fraction, 1
θ_0 = min. wetted wall fraction, 1
ρ = density, kg m^{-3}
σ = surface tension, N m^{-1}
τ = shear stress, Pa
φ = frequency; Eq. (24), s^{-1}
χ = liquid velocity profile factor; $\chi \equiv \langle v_L^3 \rangle / \langle v_L \rangle^3$, 1

Subscripts

exp. = measured
G = gas
h = hydraulic ($D_h = 4A/S$)
i = interfacial (gas-liquid)
L = liquid
MARS = Modified Apparent Rough Surface model (Grolman, 1994)
S = superficial
SW-I = at the SW-I transition
W = (at the pipe) wall

$$\frac{\partial \rho_L A_L}{\partial t} + \frac{\partial \rho_L A_L u_L}{\partial x} = 0 \tag{1}$$

the liquid-phase momentum equation:

$$\frac{\partial \rho_L A_L u_L}{\partial t} = -\chi \frac{\partial \rho_L A_L u_L^2}{\partial x} - A_L \left[\frac{\partial P}{\partial x}\right]_L - A_L \rho_L g \frac{\partial h_L}{\partial x} - \tau_{LW} S_L + \tau_i S_i - A_L \rho_L g \sin(\beta) \tag{2}$$

On physical grounds, the gravitational acceleration g preceding the liquid level gradient $\partial h_L/\partial x$ in Eq. (2), does not contain a factor cos (β). This is due to the fact that, in inclined pipes, the pressure at a certain axial position *x on the pipe wall,* is affected by the static head above, hence a little downstream of point x, while the pressure *at the gas-liquid interface* is not. Averaged across all liquid depths, for inclination angles $\beta \leq 30$ deg and in first-order approximation, the factor cos (β) was shown to vanish (Grolman, 1994).

the gas-phase continuity equation:

$$\frac{\partial \rho_G A_G}{\partial t} + \frac{\partial \rho_G A_G u_G}{\partial x} = 0 \tag{3}$$

the gas-phase momentum equation:

$$\frac{\partial \rho_G A_G u_G}{\partial t} = -\frac{\partial \rho_G A_G u_G^2}{\partial x} - A_G \left[\frac{\partial P}{\partial x}\right]_G + A_G \rho_G g \frac{\partial h_G}{\partial x} - \tau_{GW} S_G - \tau_i S_i - \rho_G A_G g \sin(\beta) \tag{4a}$$

Using $\partial h_G = -\partial h_L$, $\partial A_G = -\partial A_L$ and $\rho_G u_G A_G =$ constant; i.e. quasi-steady flow of gas, Eq. (4*a*) is rearranged to:

$$\left[\frac{\partial P}{\partial x}\right]_G = -\left\{\rho_G g + \rho_G u_G^2 \frac{A_L'}{A_G}\right\} \frac{\partial h_L}{\partial x} - \tau_{GW} \frac{S_G}{A_G} - \tau_i \frac{S_i}{A_G} - \rho_G g \sin(\beta) \tag{4b}$$

Combining Eqs. (1)–(3) and (4*b*), the following set of hyperbolic differential equations is obtained (Grolman, 1994):

$$\frac{\partial h_L}{\partial t} = -u_L \frac{\partial h_L}{\partial x} - H \frac{\partial u_L}{\partial x} \tag{5}$$

$$\frac{\partial u_L}{\partial t} = -a_2 \frac{\partial h_L}{\partial x} - (2\chi - 1) u_L \frac{\partial u_L}{\partial x} - E \tag{6}$$

The parameter H in Eq. (5), which can be shown to approximate the average liquid height in a partially filled circular pipe, is defined as:

$$H \equiv \frac{A_L}{A_L'}; \quad \text{with} \quad A_L' \equiv \frac{\partial A_L}{\partial h_L} \tag{7}$$

The acceleration a_2 contains the effects of gravitation, liquid-phase velocity-profile factor χ and the gas-phase Bernoulli effect, respectively, and is defined as:

$$a_2 \equiv \frac{\rho_L - \rho_G}{\rho_L} g + (\chi - 1) u_L^2 \frac{A_L'}{A_L} - \frac{\rho_G}{\rho_L} u_G^2 \frac{A_L'}{A_G} \tag{8}$$

The term E in Eq. (6) contains gravitational and all frictional contributions to the loss of momentum:

$$-E \equiv -\frac{\tau_{LW} S_L}{\rho_L A_L} + \left\{\frac{1}{A_L} + \frac{1}{A_G}\right\} \frac{\tau_i S_i}{\rho_L} + \frac{\tau_{GW} S_G}{\rho_L A_G} - \left\{1 - \frac{\rho_G}{\rho_L}\right\} g \sin(\beta) \tag{9}$$

Equations (5) and (6) are the overall equations, which are to be integrated with respect to time at every axial position x in the pipe. Successful simulation requires correct numerical techniques for integration and an accurate model for the frictional terms in Eq. (9).

The Frictional Contributions to the Loss of Momentum. The terms in Eq. (9) dictate the steady-state value of the liquid holdup and the initial and final states of transient events. The marginally stable conditions close to the SW-I transition require the relative magnitude of each of the terms in Eq. (9) to be precisely modeled. Over 2500 experiments were performed, in pipes of 15, 26, and 51 mm diameter, at 14 angles of inclination ($-3° \leq \beta \leq 6°$) and using two gas-liquid systems. The results of these efforts were condensed in the Modified Apparent Rough Surface (MARS) model, which is used to predict each of the frictional terms in Eq. (9).

Perimeters. An important phenomenon to take into account in modeling gas-liquid pipe flow is that the liquid gradually creeps up the inner sides of the pipe with increasing gas and liquid flow rates. This may give rise to significantly increased values of the interfacial (S_i) and liquid-to-wall (S_L) perimeters and affects each of the corresponding shear stresses. The current correlation for the wetted wall fraction θ ($\theta \equiv S_L/\{\pi D\}$) extends the model of Hamersma and Hart (1987) to include inclined flow (Grolman, 1994), whereby θ_0 is defined as the minimum value of the wetted wall fraction at the current value of the liquid holdup:

$$\theta = \theta_0 \left(\frac{\sigma_{water}}{\sigma}\right)^{0.15} + \frac{\rho_G \left\{\frac{\rho_L u_{LS}^2 D}{\sigma}\right\}^{0.25} \left\{\frac{u_{GS}^2}{(1 - \epsilon_L)^2 g D}\right\}^{0.8}}{(\rho_L - \rho_G) \cos(\beta)} \tag{10}$$

The liquid holdup ϵ_L is calculated from the liquid level h_L and vice versa, using the following equations

$$\pi\theta_0 = \arccos(1 - 2h_L/D); \quad \epsilon_L = \theta_0 - \sin(2\pi\theta_0)/(2\pi) \tag{11}$$

The dimensionless interfacial perimeter s_i is estimated by the following linear combination of θ and θ_0 (Eqs. (10) and (11)):

$$s_i \equiv \frac{S_i}{\pi D} = \frac{\theta - \theta_0}{1 - \theta_0} (1 - \epsilon_L)^{0.5} + \frac{1 - \theta}{1 - \theta_0} \frac{\sin(\pi\theta_0)}{\pi} \tag{12}$$

The following set of interfacial perimeters is obtained:

$$S_i = s_i \pi D; \quad S_L = \theta\pi D; \quad S_G = (1 - \theta)\pi D \tag{13}$$

These perimeters are also used to calculate the hydraulic diameters ($D_{hG} = 4A_G/S_G$, $D_{hL} = 4A_L/S_L$), and the gas and liquid-phase Reynolds numbers:

$$\mathrm{Re}_G = \rho_G u_G D_{hG}/\eta_G = \mathrm{Re}_{GS}/\{(1 - \theta + s_i)\};$$
$$\mathrm{Re}_L = \rho_L u_L D_{hL}/\eta_L = \mathrm{Re}_{LS}/\theta \tag{14}$$

Shear Stresses. The three shear stresses are calculated using Fanning friction factors:

$$\tau_{GW} = \frac{f_G \rho_G u_{GS}^2}{2(1 - \epsilon_L)^2}; \quad \tau_{LW} = \frac{f_L \rho_L u_{LS}^2}{2\epsilon_L^2};$$
$$\tau_i = \frac{f_i \rho_G}{2} \{u_G - u_i\}^2 \tag{15}$$

The average interfacial velocity u_i in Eq. (15) is estimated, on the basis of wave velocity measurements and various integrated laminar velocity profiles (Grolman, 1994), by:

$$u_i = 1.8 u_{LS}/\epsilon_L \quad \text{when} \quad \mathrm{Re}_L < 2100;$$

$$u_i = u_{LS}/\epsilon_L \quad \text{when} \quad \mathrm{Re}_L \geq 2100 \qquad (16)$$

The (smooth-pipe) gas-phase friction factor is calculated according to Eck (1973):

$$f_G = \frac{0.07725}{\{\log_{10}[\mathrm{Re}_G/7]\}^2} \qquad (17)$$

The interfacial friction factor is the crucial, most difficult to model parameter. Based on steady-state measurements, f_i is calculated iteratively, according to the following empirical algorithm:
calculate the friction number Fn, initially using an estimate for f_i (e.g., $f_i = f_G$):

$$\mathrm{Fn} = \frac{f_i\left(\frac{u_{GS}}{\sqrt{gD}}\right)\left(\frac{\sigma}{\eta_L\sqrt{gD}}\right)^{0.04}\left(\frac{\rho_L g D^2}{\sigma}\right)^{0.22}}{(0.05 + f_i)(1 - \epsilon_L)^{1.5}} \qquad (18)$$

calculate the frictional relative roughness k/D:

$$\frac{k}{D} = \frac{0.5145\,\epsilon_L}{s_i^{1.5}}\{\tanh[0.05762(\mathrm{Fn} - 33.74)] + 0.9450\} \qquad (19)$$

calculate the interfacial friction factor, using the (rough-pipe) equation of Eck (1973):

$$f_i = \frac{0.0625}{\left\{\log_{10}\left(\frac{15}{\mathrm{Re}_G} + \frac{k}{3.715D}\right)\right\}^2} \qquad (20)$$

repeatedly apply Eqs. (18) to (20), until convergence is reached, e.g. until the change in f_i between two consecutive iterations is smaller that 0.01 percent.

Finally, for turbulent liquid layers ($\mathrm{Re}_L \geq 2100$) the liquid-phase friction factor f_L is calculated relative to f_i, using the equation of Hart et al. (1989). For laminar liquid layers some improvement was obtained with a modification of the Hart et al. correlation:

$$f_L = f_i\, 202\left(\frac{\eta_{water}}{\eta_L}\right)^{0.274}\theta_0\, \mathrm{Re}_{LS}^{-1}\, \mathrm{Re}_G^{0.25}; \quad \mathrm{Re}_L < 2100$$

$$f_L = f_i\, 108\, \mathrm{Re}_{LS}^{-0.726}; \quad \mathrm{Re}_L \geq 2100 \qquad (21)$$

Note that the shear stresses, perimeters, and Reynolds numbers are recalculated at every grid point during the simulations, using the local values of u_L, u_G, and ϵ_L.

Numerical Solution of the Hyperbolic PDE's. Equations (5) and (6) are rewritten in operator form, using a procedure similar to that of Taitel et al. (1978):

$$\frac{\partial}{\partial t}h_L = \frac{-1}{2\varphi}\left\{[(2\chi - 1)u_L + v_1]\frac{\partial}{\partial x_A} - [(2\chi - 1)u_L - v_1]\frac{\partial}{\partial x_B}\right\}u_L - \frac{1}{2}\left\{(u_L + v_2)\frac{\partial}{\partial x_Y} + (u_L - v_2)\frac{\partial}{\partial x_Z}\right\}h_L \qquad (22)$$

$$\frac{\partial}{\partial t}u_L = -E - \frac{1}{2}\left\{[(2\chi - 1)u_L + v_1]\frac{\partial}{\partial x_A} + [(2\chi - 1)u_L - v_1]\frac{\partial}{\partial x_B}\right\}u_L - \frac{1}{2}\varphi\left\{(u_L + v_2)\frac{\partial}{\partial x_Y} - (u_L - v_2)\frac{\partial}{\partial x_Z}\right\}h_L \qquad (23)$$

where

$$\varphi \equiv \sqrt{\frac{|a_2|}{H}}; \quad v_2 = \frac{a_2}{\varphi} \quad \text{and} \quad v_1 = |v_2| = H\varphi \qquad (24)$$

and for stability, $a_2 > 0$ and $v_2 = v_1$.

In addition, each axial derivative has acquired an index A, B, Y, or Z. If these derivatives were identical, it is easily verified that Eqs. (22) and (23) reduce to Eqs. (5) and (6). However, each of the axial derivatives in Eqs. (22) and (23) is preceded by a factor that constitutes a characteristic velocity. Contrary to Taitel et al. (1978) and due to inclusion of the liquid-phase shape factor χ, four, instead of two characteristic velocities are obtained:

$$\partial/\partial x_A\text{: } \{(2\chi - 1)u_L + v_1\}; \quad \partial/\partial x_B\text{: } \{(2\chi - 1)u_L - v_1\};$$

$$\partial/\partial x_Y\text{: } (u_L + v_2); \quad \partial/\partial x_Z\text{: } (u_L - v_2). \qquad (25)$$

The common rules for calculating the axial derivatives are used: an upstream derivative (i.e., calculated on the upstream side of point x) when the characteristic velocity is positive and a downstream derivative when the characteristic velocity is negative. This ensures that the evolution of a disturbance travelling downstream is predicted using upstream properties and vice versa, thus providing numerical stability. Finally, the axial gradients in Eqs. (22) and (23) are calculated using three-point biased derivatives, instead of their two-point equivalents.

At grid point No. 2, three points are available for calculating the downstream derivative, but only two points are available on the upstream side (the third being positioned before the entrance to the pipe). Commonly, a three-point centered derivative is inserted. However, we occasionally obtained numerical oscillations using the centered approach. Instead, oscillations are avoided by using a two-point forward derivative at this grid point. To the downstream derivative at grid point No. $(N - 1)$, a similar argument applies. The derivatives at the end points (Nos. 1 and N) never pose this problem, due to the boundary conditions.

Initial Conditions. The simulations are started from a uniform, steady-state situation, where the liquid holdup matches the solution of the implicit steady-state liquid holdup equation $E = 0$, with E from Eq. (9), while h_L is calculated iteratively from ϵ_L using Eq. (11).

The Boundary Conditions at $x = 0$ and $x = L$. The boundary conditions require the liquid levels at $x = 0$ and $x = L$ to be affected by liquid level and velocity gradients within the pipe only, since $\partial h_L/\partial x$ and $\partial u_L/\partial x$ are undefined for $x < 0$ and $x > L$. Therefore, only backward characteristics (three-point downstream derivatives) are used at $x = 0$, and only forward characteristics (three-point upstream derivatives) are used at $x = L$, irrespective of the characteristic velocities of Eq. (25), at these points.

At point $x = 0$, there exist two types of boundary condition, depending on the local characteristic velocities. When one or more are negative, waves are capable of travelling upstream and either the liquid velocity or the liquid height can be specified as a function of time. This is called subcritical flow. When all the local characteristic velocities are positive, no wave can travel

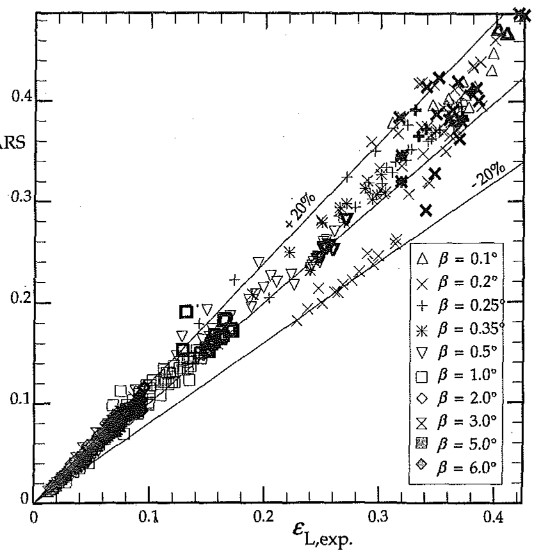

Fig. 3 The steady-state liquid holdup approaching the wavy-to-intermittent transition, modeled (MARS) versus measured (exp.) values. 503 experiments, system = air/water, D = 26 mm. Bold markers: Unstable wavy flow at the SW-I transition.

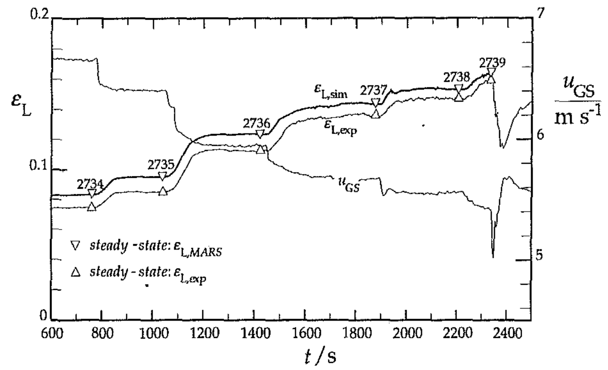

Fig. 4 Subcritical gas-feed transient. $\epsilon_{L,sim}$, the simulated and $\epsilon_{L,exp}$, the measured liquid holdup and u_{GS} the superficial gas velocity, as a function of time; β = 1.0 deg, D = 26 mm, L = 10.7 m, system = air/water. Bold line is simulated, thin line is measured.

upstream and both the liquid height and the liquid velocity must be specified. The latter is called supercritical flow (at $x = 0$).

The Method of Lines. In literature, it is common to use finite differences to integrate Eqs. (5) and (6). This implies calculating a rate of change at an instant t (with Eqs. (22) and (23)) and calculating the situation at $t + \Delta t$ by adding a product of the form (Δt.rate_of_change) to the original liquid velocity and height. This Eulerian type of integration is generally known to lead to accumulating errors, and much better results were obtained using the method of Lines (Schiesser, 1991). The two integration methods were evaluated by comparing the liquid holdup obtained from a total liquid mass balance to the value obtained from averaging the liquid holdup values across all grid points. The finite difference scheme appears to 'lose' liquid at an unacceptable rate, while the method of lines gives consistent results.

Results and Discussion

Figure 3 shows the steady-state liquid holdup according to the MARS model, as a function of the measured values, for air/water flow in a 26 mm diameter pipe, for many small angles of inclination and up to the transition to intermittent (slug or semi-slug) flow. Measurements with an air/tetradecane system and in a 51 mm diameter pipe, show equally good results and are not reproduced here. A criterion for the transition from wavy to intermittent flow for steady-state flow is provided in Grolman et al. (1996).

Figure 4 shows both simulated (bold line) and measured (thin line) values of the axially averaged liquid holdup ϵ_L (left-hand axis) as a function of time t, for air/water flow in a glass pipe of diameter D = 26 mm, at an angle of inclination β = 1.0 deg. In addition, the superficial gas velocity u_{GS} is shown (right-hand axis), which was decreased step-wise during the experiment.

The sharp decrease in u_{GS} at $t \approx 2340$ s, reflects the occurrence of a liquid slug. It is accompanied by a decrease in the measured, average liquid holdup, because the slug traverses the system at high velocity and causes a significant reduction in the average liquid holdup as soon as it leaves the pipe. The simulated liquid holdup follows the measured values quite closely up to this point. After t = 2340 s, the simulated liquid level locally exceeds one pipe diameter, reflecting the onset of slug flow in the simulated system, which is caused by the sudden decrease in the input gas flow rate at this point. Since the equations used are invalid for slug flow, this is where the simulation ends.

Figure 5 shows the simulated and measured liquid holdup up to the transition to slug flow, for air/water flow at the smaller inclination angle of 0.5 deg. In Fig. 5, a series of three slugs (small, large, and small again) can be identified from successive decrements in the liquid holdup signal around $t \approx 3420$ s. The individual slugs in Fig. 4 are smaller and therefore are harder to identify.

The measured steady-state values of liquid holdup and pressure gradient that correspond to the marked events shown in Figs. 4 and 5 are summarized in Table 1. Furthermore, the values calculated with the steady-state MARS-model are given, together with the transport properties required for these calculations.

The agreement between measured and simulated signals in Figs. 4 and 5 is good, considering the length of the time records and the marginally stable conditions encountered close to the wavy-to-slug flow transition. The calculated transient liquid holdup passes exactly through the points calculated with the steady-state MARS model, i.e., solving Eq. (9) for E = 0. It shows that the numerical scheme is stable and fully consistent with the steady-state equations, which are based on identical friction factor equations, but were calculated separately from the time-dependent model. Since the calculated transient liquid holdup passes through the steady-state values, discrepancies (up to 12 percent in Fig. 4), are explained by imperfections in the (steady-state) friction factor equations presented. These imperfections are also evident by comparison of the modeled and

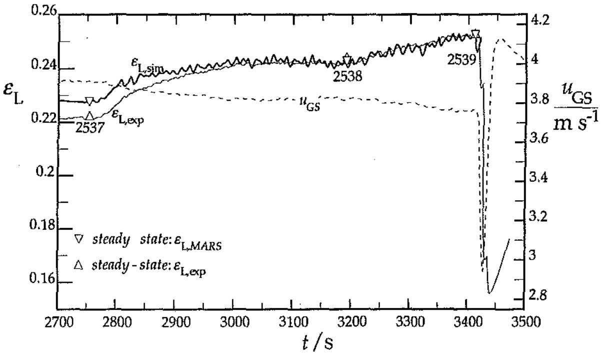

Fig. 5 Subcritical gas-feed transient. $\epsilon_{L,sim}$, the simulated and $\epsilon_{L,exp}$ the measured liquid holdup and u_{GS} the superficial gas velocity, as a function of time; β = 0.5 deg, D = 26 mm, L = 10.7 m, system = air/water. Bold line is simulated, thin line is measured.

Table 1 Experimental and modeled physical quantities (steady-state, except No. 2739)

No. unit →	u_{GS} m s^{-1}	u_{LS} 10^{-3} m s^{-1}	$\epsilon_{L,\mathrm{exp}}$ —	β degrees	$-(dP/dL)_{\mathrm{exp}}$ Pa m^{-1}	$\epsilon_{L,\mathrm{MARS}}$ —	$-(dP/dL)_{\mathrm{MARS}}$ Pa m^{-1}
2537	3.91	5.745	0.222	0.5°	36.9	0.228	33.5
2538	3.82	7.546	0.244	0.5°	38.9	0.243	35.0
2539	3.76	8.641	0.253	0.5°	41.6	0.253	36.0
2734	6.66	8.201	0.075	1.0°	55.6	0.084	48.0
2735	6.41	8.203	0.086	1.0°	54.5	0.096	47.6
2736	5.93	8.128	0.113	1.0°	54.3	0.124	48.6
2737	5.65	8.076	0.137	1.0°	56.1	0.145	50.2
2738	5.53	8.069	0.148	1.0°	56.7	0.154	51.0
2739	5.39	8.063	0.161	1.0°	—	0.164	51.8

$\rho_L \approx 998$ kg m^{-3}; $\rho_G \approx 1.22$ kg m^{-3}; $\eta_L \approx 1.01\ 10^{-3}$ Pa s; $\eta_G \approx 1.8\ 10^{-5}$ Pa s; $\sigma \approx 72\ 10^{-3}$ Pa m

measured values of steady-state liquid holdup printed in Table 1 and plotted in Fig. 3. Nevertheless, the steady-state predictions in Fig. 3 are state of the art, because they cover a range of ten angles of inclination under marginally stable, low velocity conditions. Figures 4 and 5 illustrate just how sensitive the liquid holdup is to small changes in gas flow rate, under these demanding circumstances.

The transition from wavy to slug flow itself is not (yet) obtained directly from the transient simulations, even though the gas-phase Bernoulli effect (the last term in Eq. (8)), was included directly into the simulations. This term renders the equations ill-posed when a_2 from Eq. (8) becomes negative. For the low gas velocities presently investigated, this is not the case. Furthermore, the liquid-phase profile factor χ is stabilizing, when its value exceeds one (see the second term in Eq. (8)). In fact, the incentive to include χ in the equations, is that it follows naturally from the derivations and that it appears in the part of the equations that determines the stability of the stratified-wavy flow. Furthermore, χ affects (increases) the velocity of the simulated interfacial waves, which are systematically below the velocity of interfacial waves observed, especially close to the slug flow transition (Kordyban, 1977; Grolman, 1994). Analytically derived linear theory (Barnea and Taitel, 1993) suffers from the same discrepancies in the wave velocity. Analytical integration of various fully developed laminar liquid velocity profiles results in the range $1.54 \leq \chi \leq 2.38$, depending on liquid holdup and distribution of the liquid phase across the interior of the pipe (Grolman, 1994). To test for the effects of χ, the liquid holdup in Figs. 4 and 5 was simulated with both $\chi = 1.0$ and $\chi = 2.38$, without discernible changes in these graphs. On a smaller, local scale, some effects of increased disturbance-wave velocity were observed, but could not be verified with measured data, since no video recordings of the liquid level were available. Evidently, at higher liquid velocities u_L, the effect of χ in Eq. (8) is more pronounced and would be more noticeable.

Finally, waves may cause oscillations in the liquid layer velocity profile that do no extend across the complete liquid layer depth. When the velocity profile is not fully developed, χ values in excess of 2.38 may occur. Presently, there is no way to select the "correct" value for χ to use in a direct simulation of interfacial wave growth and the resulting transition to slug flow.

Conclusions

On-line measurements of the liquid holdup and the superficial gas and liquid velocities have revealed the transient behaviour of inclined gas-liquid pipe flow, up to the point of the onset of slug flow, for 1270 sets of measurements. The numerical implementation of the MARS model, using a combination of the Method of Lines and the Method of Characteristics, results in a stable numerical scheme that is both consistent with the steady-state model and with the steady-state and transient measured liquid holdup values. Since the simulated liquid holdup is the integrated result of the in and outgoing liquid flow rates, and since it is still consistent with the steady-state holdup value after 1600 simulated seconds (Fig. 4), numerical round-off errors are negligible. The measurement errors introduced by the measuring equipment are listed in the Experiments section and are but a small fraction of the scatter in the results. Since the liquid holdup is a very complicated function of the measured physical quantities, a direct analysis of accumulated errors is not feasible, especially because the sensitivity to errors varies widely with gas flow rate and angle of inclination. From the reproducibility of the data, the experimental uncertainty is still an order of magnitude below the errors introduced by the friction factor equations and justifies further efforts to improve the MARS model. Nevertheless, the discrepancies that remain are small compared to the errors obtained when other friction factor equations presently available are used to model the data presented.

The value of the models presented lies in the fact that, for the first time, inclined gas-liquid pipe flow at marginally stable conditions, can be simulated directly, giving liquid holdup and pressure gradient values that closely adhere to the values observed in the experiments. Since the occurrence of the first slug is a local transient phenomenon, the next step is to locally analyse the stability of the simulated gas-liquid flow, while maintaining the gas-phase Bernoulli effect and liquid-phase shape factor χ in the equations. For laminar liquid flow, the liquid-phase shape factor appears naturally in the momentum Eq. (2) and affects both the stability of the stratified-wavy flow and the growth and velocity of interfacial waves. Since the correct value for χ is not obvious, and depends on the local instantaneous liquid velocity profile, it deserves further attention. In this respect extension of the one-dimensional grid in other directions, although complicated, could also be considered.

References

Barnea, D., and Taitel, Y., 1993, "Kelvin-Helmholtz Stability Criteria for Stratified Flow: Viscous Versus Non-Viscous (Inviscid) Approaches," *International Journal of Multiphase Flow*, Vol. 19, pp. 639–649.

Crowley, C. J., Wallis, G. B., and Barry, J. J., 1992, "Validation of a One Dimensional Wave Model for the Stratified-to-Slug Flow Regime Transition, With Consequences for Wave Growth and Slug Frequency," *International Journal of Multiphase Flow*, Vol. 18, pp. 249–271.

Eck, B., 1973, *Technische Strömungslehre*, Springer-Verlag, New York.

Grolman, E., 1994, "Gas-Liquid Flow With Low Liquid Loading in Slightly Inclined Pipes," Ph.D. thesis, University of Amsterdam, The Netherlands, ISBN 90-9007470-8.

Grolman, E., Commandeur, C. J., de Baat E. C., and Fortuin, J. M. H., 1996, "The Wavy-to-Slug Flow Transition in Inclined Gas-Liquid Pipe Flow," *AIChE Journal*, Vol. 42, pp. 901–909.

Hamersma, P. J., and Hart, J., 1987, "A Pressure Drop Correlation for Gas-Liquid Pipe Flow with a Small Liquid Holdup," *Chemical Engineering Science*, Vol. 42, pp. 1187–1196.

Hart, J., Hamersma, P. J., Fortuin, J. M. H., 1989, "Correlations Predicting Frictional Pressure Drop and Liquid-Holdup During Horizontal Gas-Liquid Pipe Flow With a Small Liquid Holdup." *International Journal of Multiphase Flow*, Vol. 15, pp. 947–964.

Kordyban, E., 1977, "Some Characteristics of High Waves in Closed Channels Approaching Kelvin-Helmholtz Instability," ASME JOURNAL OF FLUIDS ENGINEERING, Vol. 99, pp. 339–345.

Schiesser, W. E., 1991, *The Numerical Method of Lines: Integration of PDE's* Academic Press, San Diego.

Stoker, J. J., 1957, *Water Waves: The Mathematical Theory with Applications,* Interscience Publish. Inc., N.Y.

Minami, K., and Shoham, O., 1994, "Transient Two-Phase Behavior in Pipelines—Experiment and Modeling," *International Journal of Multiphase Flow,* Vol. 20, pp. 739–752.

Taitel, Y., and Dukler, A. E., 1976, "A Model for Predicting Flow Regime Transitions in Horizontal and Near Horizontal Gas-Liquid Flow." *AIChE Journal,* Vol. 22, pp. 47–55.

Taitel, Y., N. Lee, and A. E. Dukler, 1978, "Transient Gas-Liquid Flow in Horizontal Pipes: Modelling the Flow Pattern Transitions." *AIChE Journal,* Vol. 24, pp. 920–933.

Wallis, G. B., 1969, *One-Dimensional Two-Phase Flow.* McGraw Hill, New York.

Wallis, G. B., and Dobson, J. E., 1973, "The Onset of Slugging in Horizontal Stratified Air-Water Flow," *International Journal of Multiphase Flow,* Vol. 1, pp. 173–193.

V. Ramanathan
Civil Engineer, Wenck Associates Inc.,
1800 Pioneer Creek Center, P.O. Box 428,
Maple Plain, MN 55359-0428,
Formerly, Research Associate,
St. Anthony Falls Laboratory

Roger E. A. Arndt
Professor, St. Anthony Falls Laboratory,
University of Minnesota, Minneapolis, MN
55414

Fluid Mechanical Considerations in the Design of an Improved Aerator

An efficient diffused aeration device was developed using the "air lift" principle. With the aid of theoretical analysis and experimentation over a wide range of geometrical parameters, simple empirical correlations were developed that accurately predict water velocity and void fraction.

Introduction

This paper describes the fluid mechanical considerations associated with the design of an improved diffused aeration device (herein called the SAF Diffuser). Diffused aeration means the injection of air under pressure below a liquid surface to form bubbles. Oxygen diffuses across the bubble surfaces as they move toward the free surface.

The energy requirement for aeration in sewage treatment, aquaculture, and various chemical processes is significant. For example, the Pigs Eye Sewage Treatment Facility in St. Paul, MN consumes eight million dollars worth of electricity for aeration annually. Considering the number of sewage treatment facilities nationwide, it is easily seen that even a minor improvement in efficiency would be a significant benefit. The objective of this study was to develop a device with improved aeration efficiency (defined as the mass of oxygen transferred per unit power).

Bubble size is an important parameter affecting the oxygen transfer efficiency. Barnhart (1969) has shown that bubbles roughly 2 mm in diameter are required for maximum efficiency in an air-water system. Bubbles in this size range are usually produced by injecting air through devices having very small pore sizes (<40 microns) (Ashley et al., 1990). In these devices, bubble formation is controlled by gravitational forces and surface tension:

$$d_b \cong 1.8\left[\frac{\sigma d_o}{\rho g}\right]^{1/3}$$

Because of the very small pore sizes involved, such devices are often subject to clogging, resulting in deterioration of mass transfer efficiency and escalation of already significant power requirements. The aeration device being developed by the authors addresses this problem by producing small bubbles with much larger holes. The basic principle of the device involves the control of the bubble size and the bubble rise velocities in a plume. This is accomplished by generating bubbles in the buoyancy induced flow field inside a vertical "composite" draft tube. The shearing action created by the induced flow is the major factor in creating smaller bubbles. Here, the bubble size is roughly *independent* of orifice size:

$$d_b \cong \left\{\frac{1}{1/F_{rb}^2 + 0.38}\right\}^{1/4}\left[\frac{Q_{ao}}{V_o}\right]^{1/2}$$

This equation is discussed in Ramanathan and Arndt (1994) who found that it is in good agreement with the empirical work of Sada et al. (1978).

Utilizing the principal of bubble formation in a buoyantly induced shear flow, we have been able to develop a new device that shows promise for significant reduction in the power required for aeration. Laboratory studies show that improvements in aeration efficiency of about 30% are possible. Farmer and Arndt (1995) were also able to demonstrate the feasibility of using the device in aquaculture applications in a recent field study.

Figure 1 shows the geometric configuration of the device. Air is injected through the peripheral orifices located near the inlet end of the tube to create a buoyancy induced flow. The induced water velocity exerts a drag on the bubbles that are being formed at the peripheral orifices. This drag force causes the bubbles to detach from the orifices much before they grow to the normal size that they would have otherwise attained in a stagnant water body. For a given air flowrate, the induced water velocity and therefore the bubble size depends upon the tube dimensions.

The air lift principle used in the SAF Diffuser involves the induction of liquid flow by buoyancy of coflowing air. The principle has many applications besides aeration, such as air lift pumps and air lift reactors. The term "composite draft tube" is used to denote a tube whose cross sectional area varies along its length in a prescribed manner. Ramanathan and Arndt (1994) found that a composite draft tube (i.e., a tube diameter that is larger than the inlet diameter) has a higher oxygen transfer efficiency. By having a draft tube diameter that is larger than the throat diameter, retention time is increased while maintaining high velocities (V_o) in the throat for efficient bubble formation. Observations also show that a ring vortex is stabilized at the sudden enlargement between the draft tube and the throat. This vortex apparently enhances mixing and thereby enhances oxygen transfer within the draft tube.

The Experimental Facility

Figure 2 shows the details of the experimental facility. The facility consists of a large tank filled with water at the center of which the tube under study was mounted. Air was injected into the tube through peripheral orifices located near the inlet end. The air was drawn from the laboratory air supply through a piping system consisting of an air filter, pressure regulator, surge chamber, rotameter, pressure and temperature indicators and needle valve.

The studies were carried out with tubes of different diameters and lengths as shown in Table 1. The diameter of the peripheral orifices was 1 mm. The draft tube diameters varied from 1.1 cm to 5.79 cm, and the tube lengths varied from 18.49 cm to 36.2 cm. This corresponded to diameter ratios between 1.0 and 1.46 and length ratios between 4.31 and 24.13. The tubes of diameters up to 1.6 cm were studied in a tank of size 0.45 m

---

Contributed by the Fluids Engineering Division for publication in the JOURNAL OF FLUIDS ENGINEERING. Manuscript received by the Fluids Engineering Division August 10, 1995; revised manuscript received September 6, 1996. Associate Technical Editor: J. Katz.

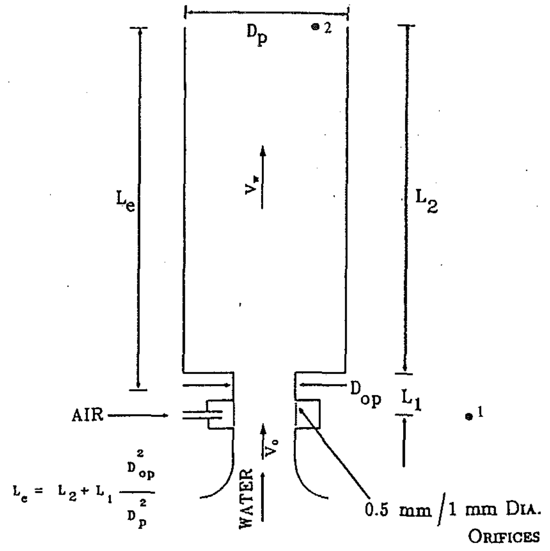

Fig. 1 Geometric configuration of the tube

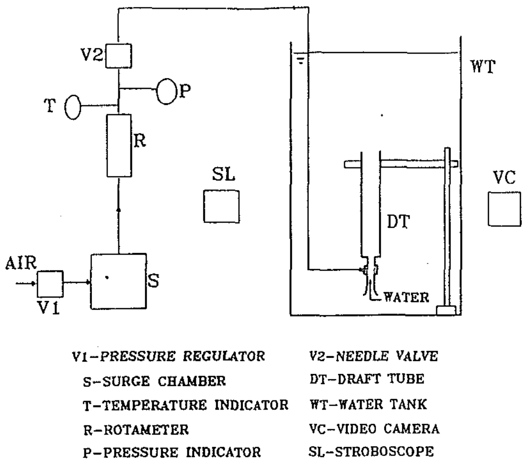

Fig. 2 Schematic of experimental facility

× 0.45 m × 0.65 m (height). The larger tubes were studied in a tank of size 1.2 m × 1.2 m × 1.4 m (height).

The experimental procedure consisted of first adjusting the air flowrate through the device using the rotameter and the needle valve and then measuring the mean water flowrate and the mean void fraction of the induced flow through the device. The water depth up to the air inlet into the tube was kept at 0.5 m for all the tubes. Each tube was tested up to a maximum air flowrate which corresponded to about 1.4 to 3.6 cc/s per orifice, depending upon the design. The water temperature was maintained at 20°C (±2°C). The temperature of air in the supply tube varied between 18°C and 22°C.

Figure 3 shows the arrangement for the measurement of the induced water flowrate through the tube. The arrangement consisted of an inner tank and an outer tank. The tube under study was mounted at the bottom of the inner tank. The air water mixture from the tube would discharge into the inner tank. Water from the inner tank would be pumped back into the main (outer) tank through a circulating pipe containing a flowmeter for measurement of the induced water flowrate. For each experimental condition, the valve in the circulating pipe would be throttled to maintain the same water level in the inner and the outer tanks. Thus the corresponding water flowrate would be equal to the mean water flowrate through the tube.

The volumetric mean void fraction in the tube was measured by rapidly and simultaneously shutting off the inlet air and the air-water discharge. The volume of entrapped air in the tube could then be simply measured. A specially designed quick shut-off valve was used for this purpose as shown in Fig. 4. The valve consisted of a spring actuated rotating arm mounted over a fixed base. The rotating arm was supported by a trigger. The outlet end of the tube under study was connected air tight to a matching opening provided in the body of the fixed base. The air supply tube also passed through a hole provided in the body of the fixed base. With the rotating arm supported by the trigger, part of the air supply tube (in the immediate upstream vicinity of the location where it passed through the fixed base) is juxtaposed in the clearance between the rotating arm and a fixed solid block. The rotating arm was mounted so that upon releasing the trigger, the arm would swing over the outlet end of the tube and close the tube and simultaneously shut off the air supply. The void fraction is equal to the fraction by volume of air entrapped inside the tube upon closure of the valve.

Nomenclature

A_{op} = cross-sectional area of the tube inlet
A_p = cross-sectional area of the tube
d_b = bubble diameter
d_o = orifice diameter
D_{op} = diameter of the tube inlet
D_p = diameter of the tube
D_r = diameter ratio = (D_p/D_{op})
F_{ra} = air flow Froude number = $J_a/\sqrt{L_e g}$
F_{rb} = Froude number based on bubble size and inlet flow velocity = $V_o/\sqrt{g d_b}$
F_{rw} = water flow Froude number = $V_w/\sqrt{L_e g}$
f = friction factor for developing air-water bubbly flow
g = gravitational acceleration
H = depth of water
J_a = superficial air velocity = (Q_a/A_p)
J_w = superficial water velocity = (Q_w/A_p)
K = overall loss term
K_b = term representing the losses due to the lateral entry of air bubbles into the tube at the air inlet
k_c = appropriate contraction loss coefficient at the bubble entrance region
K_e = entrance loss term
K_{ex} = expansion loss term
K_f = friction loss term
K_s = secondary loss term
L_e = effective tube length = $(L_2 + (L_1(A_{op}/A_p))$
L_r = length ratio = (L_e/D_p)
L_1 = inlet tube length in the entrance region above the air inlet
L_2 = tube length
p_1 = pressure at 1
p_2 = pressure at 2
Q_{ao} = air flow rate in one orifice
Q_a = air flowrate corresponding to the pressure at the tube center
V_a = mean air velocity in the tube = (J_a/α)
V_{ao} = air velocity through one orifice
V_m = mean velocity of air—water mixture in the tube
V_o = water velocity in the tube inlet, upstream of the orifices
V_w = mean water velocity in the tube = $(J_w/(1-\alpha))$
α = mean void fraction of air in the tube
ν_w = kinematic viscosity of water
ρ_a = density of air
ρ_m = density of air-water mixture in the tube
ρ_w = density of water
σ = surface tension

Table 1 Details of configurations studied

Design	D_{op} cm	D_p cm	L_e cm	D_r	L_r	No_p	Q_{am}/No_p cc/s
A	1.10	1.10	18.92	1.00	17.20	32	1.44
B	1.10	1.10	26.54	1.00	24.13	32	1.63
C	1.10	1.27	19.05	1.15	15.06	32	1.65
D	1.10	1.27	26.58	1.15	21.01	32	1.65
E	1.10	1.61	18.49	1.46	11.50	32	1.65
F	1.10	1.61	26.10	1.46	16.26	32	1.65
G	5.17	5.17	29.82	1.00	5.76	108	3.62
H	5.79	5.79	25.00	1.12	4.31	108	3.62
I	5.79	5.79	36.20	1.12	6.25	108	3.06

Note: Q_{am} = Maximum air flow rate, cc/s; No_p = Number of peripheral orifices; Orifice diameter = 1 mm; Orifice spacing = 4.5 mm ± 0.5 mm.

From the measured values of the mean water flowrate Q_w and the mean void fraction α, the mean water and air velocities were calculated using the relationships given below:

$$J_w = Q_w/A_p \tag{1}$$

$$V_w = J_w/(1-\alpha) \tag{2}$$

$$V_o = Q_w/A_{op} \tag{3}$$

$$J_a = Q_a/A_p \tag{4}$$

$$V_a = J_a/\alpha \tag{5}$$

Theoretical Considerations

When the device is submerged in a homogeneous body of water without any air being injected into it, the weight of the water inside the tube is exactly balanced by the pressure exerted on it by the neighboring fluid outside the tube. Introduction of air modifies the hydrostatic pressure distribution inside the tube because of the reduction in the density of the air-water mixture in the tube as compared to the water outside. Because of this pressure difference, the fluid inside the tube gains kinetic energy.

Considering the fluid as ideal, application of the Bernoulli equation yields the following chimney equation (see Appendix A):

$$F_{rw} = \frac{V_w}{\sqrt{L_e g}} = \left[\frac{2\alpha}{(1-\alpha)}\right]^{0.5} \tag{6}$$

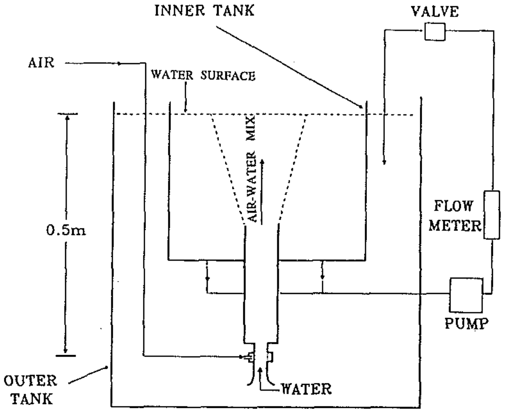

Fig. 3 Arrangement for measurement of water flowrate

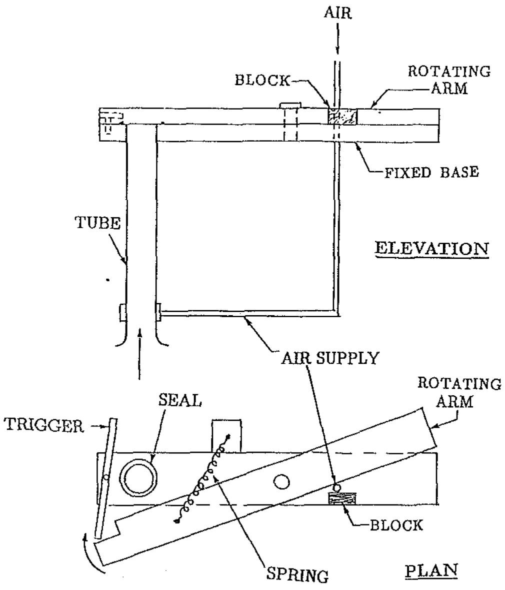

Fig. 4 Valve for measurement of void fraction

Major energy losses were accounted for by modifying standard loss coefficients that are readily accessible in the literature. In this analysis the effects of void fraction on density and cross sectional area were accounted for. The details can be found in Ramanathan and Arndt, 1994. Equation (6) is modified to read:

$$F_{rw} = \frac{V_w}{\sqrt{L_e g}} = \left[\frac{2\alpha}{(1-\alpha)K}\right]^{0.5} \tag{7}$$

where

$$K = 1 + K_e + K_{ex} + K_f + K_b + K_s \tag{8}$$

$$K_e = k_e D_r^4(1-\alpha) \tag{9}$$

$$K_{ex} = (D_r^2 - 1)^2 \tag{10}$$

$$K_f = f(L_e/D_p)(1-\alpha) = fL_r(1-\alpha) \tag{11}$$

$$K_b = k_c D_r^4/(1-\alpha) \tag{12}$$

There are terms in Eqs. (7)–(12) that are not well known. First, the frictional pressure drop (represented by K_f) in bubbly flow through vertical pipes shows considerable departure from the commonly used models of Lockhart and Martinelli (1949) and Armand (1950). For small liquid velocities and air volumetric quality, the frictional pressure drops in bubbly flow have been reported to be roughly 10–20 times the corresponding single phase flow values (Aoki and Inoue, 1965; Nakoryakov et al., 1981; Kytomaa and Brennen, 1986). Experimental studies of Nakoryakov et al. (1981) show that in the bubbly flow regime, the wall shear stress is significantly affected by the void fraction distribution within the tube and that the high values of friction factors result from the high void fraction peaks near the wall.

Second, one effect of the lateral entry of the bubbles from the peripheral orifices into the tube is to cause a contraction of the water flow and an associated energy loss. The loss coefficient k_c given in Eq. (12) would then depend on the void fraction and the void fraction distribution downstream of the peripheral orifices.

In addition, there are other energy terms to be considered such as the surface tension energy of the bubbles, the energy associated with the expansion and oscillation of the bubbles during formation and while ascending. These terms are grouped into a single term K_s. In trying to develop a simplified expression for the three aforementioned losses, these losses are combined into a single loss and a combined loss term K_{fb} is defined as:

$$K_{fb} = K_f + K_b + K_s \tag{13}$$

K_f and K_b are given by Eqs. (11) and (12), respectively. Both f(Eq. (11)) and k_c (Eq. (12)) depend on the void fraction and the lateral void fraction distribution, i.e. the void fraction distribution across the pipe. Though it is recognized that Reynold's stresses and the lift forces experienced by the bubbles are the significant mechanisms governing the lateral void fraction distribution, this phenomenon is as yet poorly understood (Kytomaa and Brennen, 1986; Bertodano et al., 1990). Experimental results of Nakoryakov et al. (1981) show that the lateral void fraction distribution depends on the mean void fraction and the water velocity. Equation (6) already suggests a dependence of the water velocity on the mean void fraction. Considering this dependence and the parameters affecting K_f and K_b as shown in Eqs. (11) and (12) and also assuming that the secondary losses would depend on the void fraction and the tube geometry, it is postulated that K_{fb} could be approximated by a functional relationship of the following form:

$$K_{fb} = K_{fb}(\alpha, D_r, L_r) \tag{14}$$

This functional relationship was established experimentally.

To determine the water velocity using Eq. (7), an additional expression for the mean void fraction in the tube is required. The void fraction can be expressed as

$$\alpha = \frac{J_a}{V_a} = \frac{J_a}{V_w + V_r} \tag{15}$$

In the above expression for the void fraction, J_a depends on the air flowrate and the tube diameter. Considering an air water system, the independent parameters that conceivably affect the term $(V_w + V_r)$ are the superficial air velocity J_a, the tube dimensions, densities of air and water, and the gravitational acceleration. Dimensional considerations lead to a functional relationship of the following form:

$$\alpha = \alpha\left(\frac{J_a}{\sqrt{L_e g}}, D_r, L_r, \frac{\rho_w - \rho_a}{\rho_w}\right) \tag{16}$$

Since $\rho_a \ll \rho_w$, the term $(\rho_w - \rho_a)/\rho_w$ is, for practical purposes, a constant. Therefore Equation (16) can be written as

$$\alpha = \alpha\left(\frac{J_a}{\sqrt{L_e g}}, D_r, L_r\right) = \alpha(F_{ra}, D_r, L_r) \tag{17}$$

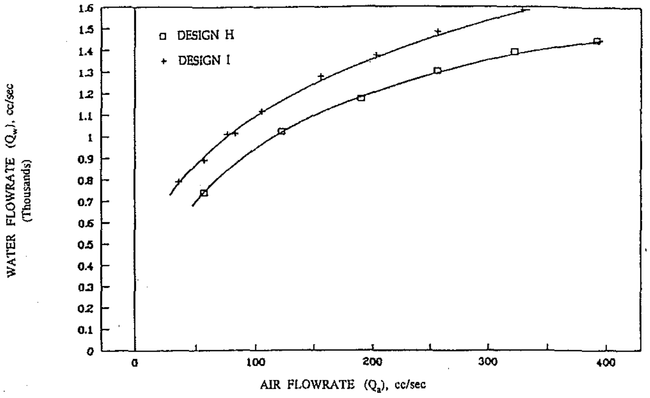

Fig. 5 Water flowrate versus air flowrate (Designs H and I) Measurement errors: Water flowrate, 2 percent; air flowrate, 2 percent

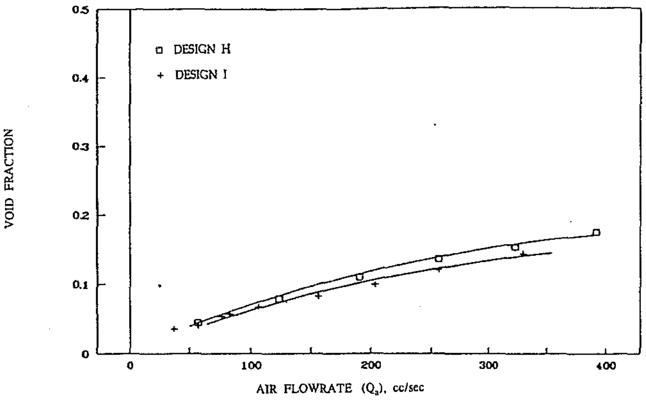

Fig. 6 Void fraction versus air flowrate (Designs H and I) Measurement errors: Void fraction, 3.8 percent; air flowrate, 2 percent

where

$$F_{ra} = \frac{J_a}{\sqrt{L_e g}}$$

In considering such a relationship for the case of homogeneous equilibrium flow within the tube, it is recognized that the actual flow within the tube would not be in homogeneous equilibrium. However, homogeneous equilibrium flow is assumed in order to examine the existence of the relationship of the form given by Eq. (17) for such flow. This approximation would mean zero slip velocity between water and air. Then we have $V_r = 0$ or $V_w = V_a$.

The void fraction in the tube would then be given by

$$\alpha = \frac{J_a}{V_w} \tag{18}$$

Substituting for α from Eq. (18) in Eq. (7), we get,

$$\frac{J_a}{\alpha\sqrt{L_e g}} = \left[\frac{2\alpha}{(1-\alpha)K}\right]^{0.5} \tag{19}$$

On rearranging,

$$\alpha = \left(\frac{1}{2}\right)^{1/3}\left[\frac{J_a}{\sqrt{L_e g}}\right]^{2/3} K^{1/3}(1-\alpha)^{1/3} \tag{20}$$

For low void fractions, the term $(1-\alpha)^{1/3}$ is very nearly equal to unity. Neglecting this term, Eq. (20) reduces to the following form:

$$\alpha = 0.794\left[\frac{J_a}{\sqrt{L_e g}}\right]^{2/3} K^{1/3} \tag{21}$$

This idealized result compares favorably with the experimental results of Merchuk (1986). He has shown that the void fraction in a two dimensional air lift reactor can be expressed in terms of the superficial air velocity by the following expression:

$$\alpha = 0.047 J_a^{0.59} \tag{22}$$

Merchuk (1981) has also observed that the correlation for void fraction is affected by the system geometry. Merchuk's experimental correlation was obtained under conditions with slip velocities between the water and the air phases. These findings show that the functional relationship of the form given by Eq. (21) for the void fraction could exist even with slip velocities between the water and the air. As shown by Eqs. (7) through (12), the term K, representing the losses in the tube,

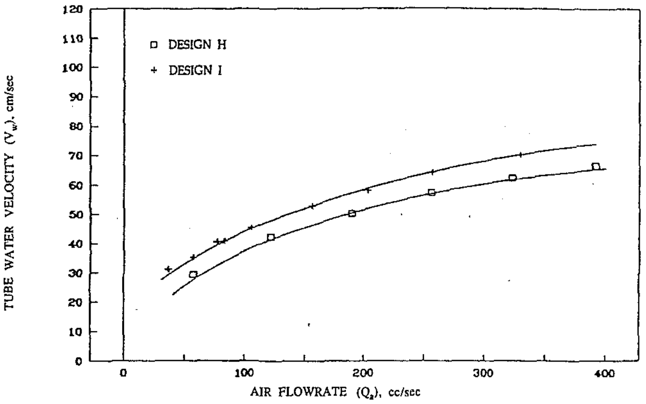

Fig. 7 Tube water velocity versus air flowrate (Designs H and I) Experimental errors: Water velocity, 4.3 percent; Air flowrate, 2 percent

depends on the tube geometry and the void fraction. Introducing this dependence into Eq. (21), we get

$$\alpha = \alpha\left(\frac{J_a}{\sqrt{L_e g}}, D_r, L_r\right) \tag{23}$$

Such a correlation would enable the determination of the mean void fraction in the tube from known values of the air flowrate and the parameters describing the tube geometry, i.e., the length ratio, L_r and the diameter ratio, D_r.

Experimental Results

No attempt was made to document the details of the flow within the draft tube. However, limited video observations show that the bubble size in the tube is between 2 mm and 3 mm. The flow was also observed to be in the bubbly flow regime for all experimental conditions.

Figure 5 contains a typical plot of water flowrate versus air injection rate. As the air flowrate is increased, the water flowrate increases. The rate of increase of the water flowrate diminishes with increasing air flowrate until the water flowrate reaches an asymptotic maximum. For all cases, tubes with larger diameter ratios were found to have a larger water flowrate for a given air flowrate. Also the water flowrate was higher for the longer tubes.

By comparison, the dependence of void fraction on air flowrate displays a different trend as shown in Fig. 6 for a typical case. In all cases the void fraction increases with an increase in air flowrate and decreases with an increase in diameter ratio. The void fraction also decreases as the length of the tube is increased.

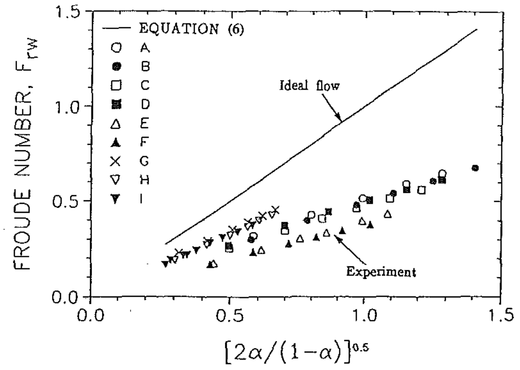

Fig. 8 Comparison of ideal flow Froude number and experimental values. A through I refer to tube designs shown in Table 1.

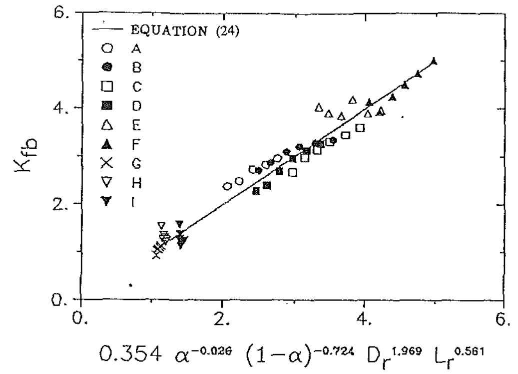

Fig. 9 Experimental correlation for K_{fb}. Coefficient of determination = 0.964, Standard error = 0.22. A through I refer to tube designs shown in Table 1.

The water velocities in the tube V_w were calculated from the measured water flowrates and void fractions using Eqs. (1) and (2). A typical correlation is shown in Fig. 7. The water velocity increases with an increase in the air flowrate or the tube length. For a given air flowrate, the water velocity decreases as the diameter ratio increases.

Using the values of V_w, the Froude number defined by Eq. (7) was calculated for each experimental point. The ideal flow Froude number for each experimental point was also calculated from the experimental values of the void fraction using the ideal chimney equation (Eq. (6)). Figure 8 contains a comparison of the ideal flow Froude number with the real flow values. The difference between the ideal chimney equation and the experimental values arises out of the energy losses in the tube as discussed previously.

In order to incorporate the losses in the Eq. (7), an expression for the loss term K_{fb} was required. The experimental data were used to calculate the loss term K_{fb} using Eqs. (7) through (10) and Eq. (13) and an empirical functional relationship of the form (17) was established through multiple regression:

$$K_{fb} = 0.354\alpha^{-0.026}(1-\alpha)^{-0.724}D_r^{1.969}L_r^{0.561} \tag{24}$$

The coefficient of determination (r^2) was 0.964 and the standard error was 0.22 (number of observations = 56; degrees of freedom = 51) (see Fig. 9).

Substituting for K_{fb} from Eq. (24) into Eq. (8), the following relation for the tube Froude number F_{rw} is obtained:

$$\mathrm{F}_{rw} = \frac{V_w}{\sqrt{L_e g}} = \left[\frac{2\alpha}{(1-\alpha)(1+K_e+K_{ex}+K_{fb})}\right]^{0.5} \tag{25}$$

Equation (25) expresses the empirical relationship between the water velocity in the tube, and the void fraction and the tube geometry. This is shown in Fig. 10.

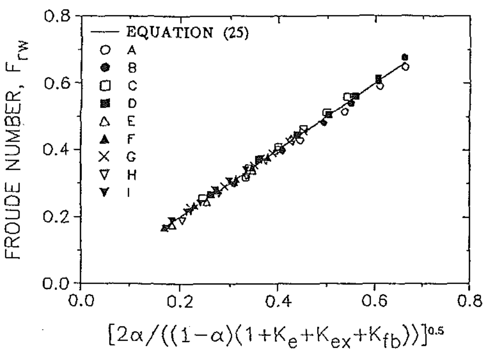

Fig. 10 Correlation for Froude number using experimental loss coefficients. A through I refer to tube designs shown in Table 1.

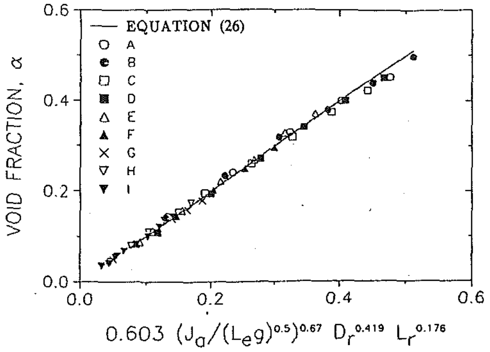

Fig. 11 Experimental correlation for void fraction. Coefficient of determination = 0.997; Standard error = 0.008. A through I refer to tube designs shown in Table 1.

The experimental void fraction data were also used to develop an empirical relationship suggested by Eq. (23):

$$\alpha = 0.603\left[\frac{J_a}{\sqrt{L_e g}}\right]^{0.67} D_r^{0.419} L_r^{0.176} \tag{26}$$

The coefficient of determination r^2 was 0.997 and the standard error was 0.008 (number of observations = 56; degree of freedom = 52).

Equation (26) and the experimental data are plotted in Figure 11. Using Eqs. (25) and (26), the mean water velocities and void fractions in the tube for given air flowrate and tube dimensions can be determined.

Conclusions

A combination of analysis and extensive experimentation has led to simple empirical correlations to predict the phase velocities and void fractions associated with the complex air-water flow through vertical draft tubes in the bubbly flow regime. The results of these studies indicate the following:

(i) The tube Froude number based on the induced water velocity and the tube length is a function of the mean void fraction and the energy losses in the tube. The energy losses depend on the tube geometry and the mean void fraction. Hence the tube Froude number can be expressed as a function of the mean void fraction and the parameters defining the tube geometry namely, the length ratio and the diameter ratio. This functional relationship is given by Equation (25).

(ii) The void fraction in the tube depends on the tube Froude number based on the superficial air velocity and the geometry of the tube. Equation (26) expresses this relationship.

(iii) Using Eqs. (25) and (26), the induced water velocities and void fractions associated with the bubbly flow of air-water mixture in the tube can be predicted for a wide range of air flowrates and tube geometries.

References

American Society of Mechanical Engineers, 1961, *Flowmeters Computation Handbook.*

Aoki, S., Inoue, S., 1965, "Fundamental Studies in Pressure in an Air Water Two Phase Flow in Vertical Pipes," *Proceedings 2nd Japan Heat Transfer Symposium.*

Armand, A. A., 1950, "Pressure Drop in Two Phase Mixture in Horizontal Pipes," *Izv. VTI I.*

Ashley, K. L., Mavinic, D. S., and Hall, K. J., 1990, "Effects of Orifice Size and Surface Conditions on Oxygen Transfer in a Bench Scale Diffused Aeration System," *Environmental Technology,* Vol. 11.

Barnhart, E. L., 1969, "Transfer of Oxygen in Aqueous Solutions," *ASCE J. Sanitary Eng. Div.,* June.

Bertodano, M. L., Lee, S. J., Lahey Jr., R. T., and Drew, D. A., 1990, "The Prediction of Two Phase Turbulence and Phase distribution phenomenon using a Reynolds stress model," ASME JOURNAL OF FLUIDS ENGINEERING, Vol. 118, Mar.

Farmer, R., and Arndt, R. E. A., 1995, "Development of an Efficient Aeration System for Aquaculture," *St. Anthony Falls Hydraulic Laboratory,* Project Report No. 373, June.

Kytomaa, H. K., and Brennen, C. E., 1986, "Measurements of Friction Pressure Drops in Vertical Slurry and Bubbly Flows," *ASME Cav. and Multiphase Flow Forum,* FED—Vol. 36.

Lockhart, P. W., and Martinelli, R. C., 1949, "Proposed Correlation of Data for Isothermal Two Phase Two Component Flows in Pipes," *Chemical Engineering Progress,* Vol. 45.

Merchuk, J. C., 1986, "Gas Hold-Up and Liquid Velocity in a Two Dimensional Air Lift Reactor," *Chemical Engineering Science,* Vol. 41.

Merchuk, J. C., 1981, "Local Hold-Up and Liquid Velocity in Air Lift Reactors," *AIChE Journal,* May.

Nakoryakov, V. E., Kashinsky, O. N., Burdukov, A. P., and Odnoral, V. P., 1981, "Local Characteristics of Upward Gas Liquid Flows," *International Journal of Multiphase Flow,* Vol. 7.

Ramanathan, V., and Arndt, R. E. A., 1994, "Experimental Development of a Novel Aeration Device," *St. Anthony Falls Hydraulic Laboratory,* Project Report No. 350, University of Minnesota, Apr.

Sada, E. et al., 1978, "Bubble Formation in Flowing Liquid," *The Canadian Jour. of Chem. Eng.,* Dec.

Takeli, S., and Maxwell, W. H. C., (1978), "Behavior of bubble screens," *University of Illinois at Urbana-Champaign,* Report No. UILU-ENG-79-2019, September.

APPENDIX A

The Chimney Equation

Consider the tube shown in Fig. 1. Applying Bernoulli equation between points 1 and 2, we get

$$p_1 = p_2 + \rho_m \frac{V_m^2}{2} + g\rho_m L_e \tag{A.1}$$

or

$$\rho_m \frac{V_m^2}{2} = (p_1 - p_2) - g\rho_m L_e \tag{A.2}$$

Assuming that the pressure outside the plume is hydrostatic and its variations in the plume are small (Takeli and Maxwell, 1978), the pressure at the point 2 would be equal to the hydrostatic pressure. With this assumption, we get

$$(p_1 - p_2) = \rho_w g L_e \tag{A.3}$$

Substituting for $(p_1 - p_2)$ from Eq. (A.3) into Eq. (A.2),

$$\rho_m \frac{V_m^2}{2} = L_e g(\rho_w - \rho_m) \tag{A.4}$$

To express the mixture velocity V_m in terms of the water velocity V_w and the air velocity V_a, consider the mass flux of the mixture at any cross section of the tube:

$$\rho_m V_m = \rho_w V_w (1 - \alpha) + \rho_a V_a \alpha \tag{A.5}$$

Equation (A.5) can be written as

$$V_m = \frac{\rho_w V_w (1 - \alpha)}{\rho_m} + \frac{\rho_a V_a \alpha}{\rho_m} \tag{A.6}$$

The density of the mixture can be expressed in terms of the void fraction (Takeli and Maxwell, 1978):

$$\rho_m = (1 - \alpha)\rho_w + \alpha\rho_a \tag{A.7}$$

Since $\rho_a \ll \rho_w$, the above equation can be written as

$$\rho_m = (1 - \alpha)\rho_w \tag{A.8}$$

Substituting for ρ_m from Eq. (A.8) into Eq. (A.6),

$$V_m = V_w + \frac{\rho_a V_a \alpha}{\rho_m} \tag{A.9}$$

where $\rho_m \approx \rho_w$.

Again, since $\rho_a \ll \rho_w$, the above equation can be approximated as

$$V_m = V_w \tag{A.10}$$

Substituting for V_m from Eq. (A.10), Eq. (A.4) becomes

$$(1-\alpha)\rho_w \frac{V_w^2}{2} = gL_e(\rho_w - \rho_m) = \rho_w g L_e \alpha \tag{A.11}$$

or

$$F_{rw} = \frac{V_w}{\sqrt{L_e g}} = \left[\frac{2\alpha}{(1-\alpha)}\right]^{1/2} \text{[Chimney Equation]} \tag{A.12}$$

APPENDIX B

Measurement Errors

Water Flowrate. The water flowrate through the larger tubes were measured with an orifice plate conforming to the ASME standards and the water flowrates through the smaller tubes were measured with a rotameter. The errors associated with these measurements are estimated below separately.

Orifice Plate. The water flowrate through the orifice plate is given by the following equation (ASME, 1961):

$$Q_w = (D^2 I h_w^{1/2})/\gamma_w^{1/2} \tag{B.1}$$

The diameter of the pipe was measured with a vernier having a least count of 1/1000 th of an inch and rounded off to the nearest 1/100th of an inch. The error arising out of this rounding would be 0.25 per cent. The value of the specific weight of the water was taken from the standard tables and the associated error is not considered here.

The error (95 percent confidence limit) associated with the value of the Meter Constant I is 0.5 percent (ASME, 1961).

In order to estimate the error of the differential pressure measurements, these measurements were repeated six times for one of the experimental conditions. The standard deviation observed was 0.62 per cent of the mean. To get the 95 percent confidence interval value, the standard deviation was multiplied by the corresponding student t value of 2.571 (degree of freedom = 5). This gave an error value of 1.59 percent.

From the above error estimates, the error associated with the flowrate was estimated as below assuming that all the errors estimated above pertain to the 95-degree confidence level.

$$\frac{dQ_w}{Q_w} = \left[\left[\frac{2dD}{D}\right]^2 + \left[\frac{1}{2}\frac{dh_w}{h_w}\right]^2 + \left[\frac{dI}{I}\right]^2\right]^{1/2} = 0.014 \text{ (1.4 percent)}$$

Rotameter. From information supplied by the manufacturer,

$$\frac{dQ_w}{Q_w} = 0.02$$

Air Flowrate. From information supplied by the manufacturer,

$$\frac{dQ_a}{Q_a} = 0.02$$

Void Fraction. The void fraction was calculated from the measured values of the length of the entrapped air column inside the tube upon the closure of the valve using the following equation

$$\alpha = L_a/L_e \tag{B.3}$$

The length of the air column was measured using a cathetometer having a least count of 0.1 mm. Assuming 0.05 mm as the error associated with this measurement, for the shortest length of the air column, the error works out to 0.55 per cent. Along similar lines, the error in the determination of the effective tube length works out to 0.26 percent.

In addition to the errors associated with the measurement of the lengths of the air column and the tube, there are errors arising from the non-uniformity in the closing time of the quick shut-off valve. To assess this error, the void fraction measurement was repeated seven times under the same experimental condition and the standard deviation was calculated. The value of the standard deviation obtained was 1.37 percent of the mean. The value of the standard deviation observed was multiplied by the value of Student t corresponding to a degree of freedom of 6 to obtain the error corresponding to the 95 percent confidence level. This gave an error estimate of 3.3 percent.

It is also possible that there might be a difference between the actual closing times of the air inlet and the water outlet of the tube by the rotating arm of the valve. This time delay would cause an error in the determination of the accumulated air volume. To estimate this error, it was assumed that the time delay would be 25 percent of the valve closure time. With this assumption, for the smallest tube, with the largest air flowrate for which it was tested, the error was calculated as 1.86 percent.

Combining all the above errors and assuming that each of the errors has a confidence limit of 95 percent, the error in the void fraction is calculated as

$$\frac{d\alpha}{\alpha} = [0.55^2 + 0.26^2 + 3.3^2 + 1.86^2]^{1/2} = 0.038$$

Study of Unsteady Orifice Flow Characteristics in Hydraulic Oil Lines

Seiichi Washio
Professor,
Faculty of Engineering.

Satoshi Takahashi
Research Associate,
Faculty of Engineering.

Yonguang Yu
Graduate Student (Doctoral Course).
Graduate School of Natural Science
and Technology.

Okayama University, 3-1-1 Tsushimanaka
Okayama, Japan 700

Satoshi Yamaguchi
Engineer,
Toyoda Machine Works, Ltd.,
1-1 Asahimachi, Kariya, Aichi, 448 Japan

A technique to measure fluctuating differential pressures with high fidelity has been developed first. When applied to detecting differential pressures generated by an accelerated or decelerated liquid column, the technique turned out to be effective in finding unsteady flow rates. An experimental study has been carried out on periodically changing hydraulic oil flows through an orifice. The results support the validity of the traditional standpoint that characteristics of an unsteady orifice flow can be approximately represented by those of a steady-state one. When inspected in detail, however, a net pressure loss across an orifice in a periodical flow is delayed against a change of the flow rate. The resulting relation between the pressure loss and the flow rate describes a loop with a counter-clockwise hysteresis and a nonlinear twist along the steady-state one. Pressure recovery in a pulsating orifice flow varies with the flow rate almost along the steady-state relation, which is confirmed when the change is not fast.

1 Introduction

An orifice, which is an essential component used as a nonlinear resistance in a fluid system, gives a pressure loss to the flow through it and also produces a small pressure recovery downstream. It is empirically known that the recovery, as well as the loss, is proportional to the square of the flow rate when the flow is steady.

When it is required to know the characteristics of an unsteady orifice flow for system analysis, it is common to assume that they are basically the same as those of a steady-state one. In an attempt to verify this assumption, D'Souza and Oldenburger (1964) have qualitatively confirmed that an orifice impedance in a pulsating hydraulic oil flow is given by a tangent to the orifice's steady-state relation between the pressure loss and flow rate. From a more precise viewpoint, however, there should be some physical differences between unsteady orifice flows and steady-state ones.

In acoustics where orifices have long been a major subject of study, attention has been exclusively paid to evaluating their acoustical impedances including end corrections. Among many works so far conducted to measure orifice impedances, Bolt et al. (1949) and Thurston and Martin Jr. (1953) have discovered that as the amplitude of oscillation increases, the resistance of an impedance increases while the inertance decreases.[1] Although those results clearly demonstrate nonlinearity, the authors have not succeeded in physically explaining the behavior of inertance.

Washio et al. (1982) have found in their experimental studies of periodic hydraulic oil orifice flows the phenomenon that might be related with this peculiar behavior of inertance; an oscillatory change of a net pressure loss across an orifice has a delay against that of the flow rate. Since the method used there to measure unsteady flow rates was the so-called impedance tube which was based on the theory of wave transmission in a pipe, though, the accuracy of the results was affected by the inevitable discrepancy between the experimentally used pipe end and the theoretically assumed one.

The present paper reviews the same subject with the intention of clarifying the true characteristics of an unsteady orifice flow, using a more reliable method which can measure fluctuating flow rates without being affected by the experimental conditions at pipe ends. As a preparatory work, an idea to accurately measure fluctuating differential pressures has been put into practice. The technique is applied to detecting pressure differences kinetically induced by the motion of a liquid column to find unsteady flow rates.

2 Theoretical Foundation

The wave equation for a viscous liquid in a pipe provides a theoretical tool for the present study. When the Navier-Stokes equations of motion, the continuity equation and the equation of state are solved in the Laplace domain under an assumption of axisymmetry (D'Souza and Oldenburger, 1964), a relation between pressures and flow rates at two separate sections I and II (Fig. 1) is given as follows:

$$\begin{pmatrix} P_2 \\ Q_2 \end{pmatrix} = \begin{pmatrix} \cosh sF_i(z)T_l & -Z_iF_i(z)\sinh sF_i(z)T_l \\ \dfrac{-\sinh sF_i(z)T_l}{Z_iF_i(z)} & \cosh sF_i(z)T_l \end{pmatrix} \begin{pmatrix} P_1 \\ Q_1 \end{pmatrix} \tag{1}$$

where

$$F_i(z) = \left[\frac{I_0(z)}{I_2(z)}\right]^{1/2}, \quad z = \sqrt{\chi_0 s}, \quad \chi_0 = \frac{a^2}{\nu} \tag{2}$$

$$T_l = \frac{l}{c}, \quad Z_i = \frac{\rho c}{\pi a^2} \tag{3}$$

Theoretical discussions in the following sections are conducted with these equations.

3 Measurements of Unsteady Differential Pressures

3.1 Basic Concept. Conventional differential pressure transducers, which usually require long conduits leading to the

---

[1] The acoustic resistance is defined as the real part of the acoustic impedance and the acoustic inductance is defined as the reactive part divided by the radian frequency. The reactive part is also known as the acoustic inertance or the acoustic mass.

Contributed by the Fluids Engineering Division for publication in the JOURNAL OF FLUIDS ENGINEERING. Manuscript received by the Fluids Engineering Division December 13, 1995; revised manuscript received June 26, 1996. Associate Technical Editor: P. W. Bearman.

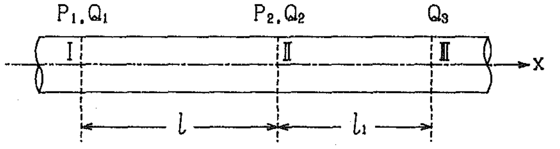

Fig. 1 Wave transmission line

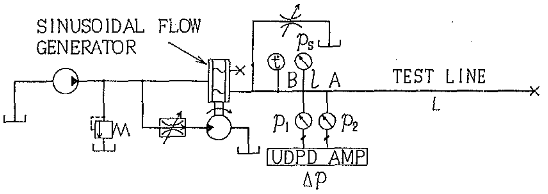

Fig. 2 Hydraulic oil line to examine UDPD system

measuring points, cannot respond to quick changes of a pressure difference. The idea adopted here to overcome this shortcoming is applying two individual pressure transducers to each measuring point and subtracting between the two outputs. Errors in this method are mainly caused by a disagreement of amplification gains between the two transducers. In order to minimize the errors, the two gains have been adjusted to become as equal as possible. Electrical frequency characteristics and common mode rejection (CMR) of the thus tuned amplifier turned out to be constant up to 3 kHz (uncertainty in gain = ±0.3 percent, phase lag = 2 degrees at 2 kHz, 8 degrees at 3 kHz) and less than −40 dB up to 1 kHz, respectively.

3.2 Examination of Accuracy. Semi-conductor pressure transducers, having a natural frequency of 60 kHz, a linearity within ±1 percent and a rated pressure of 3 MPa, are used with pressure taps of 1 mm in diameter and 1 mm in length. The overall accuracy of the unsteady differential pressure detecting system (UDPD system in abbreviation), which includes not only the electrical circuit but the pressure transducers and taps as well, has been examined with the hydraulic oil line (VG46 mineral oil, $\nu = 1.28$ cm^2/s @ 20°C) illustrated in Fig. 2. A sinusoidal flow generator (Washio and Konishi, 1978) creates harmonic waves in a test pipe ($L = 2.98$ m in length, $a = 8.2$ mm in radius) which has a closed end and two pressure taps axially separated by $l = 100$ mm at the entrance. During the measurement a thermistor monitors the oil temperature. (uncertainty = ±0.1°C)

The frequency response of the transfer function, defined as

$$G_{PD}(s) = \frac{\Delta P(s)}{P_1(s)} = \frac{\cosh sF_i(z)T_L}{\cosh sF_i(z)T_{L+l}} - 1$$

$$\Delta P = P_2 - P_1 \qquad (4)$$

has been measured to examine the UDPD system. Circles and solid curves in Fig. 3 show experimental results and theoretical predictions by Eq. (4) (Washio and Konishi, 1978), respectively, which agree well with each other.

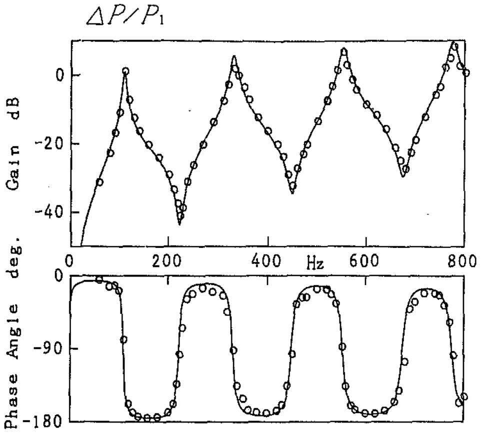

Fig. 3 Frequency response of UDPD system. (Uncertainty in gain is ±0.5 dB and that in phase angle is ±8 degrees.)

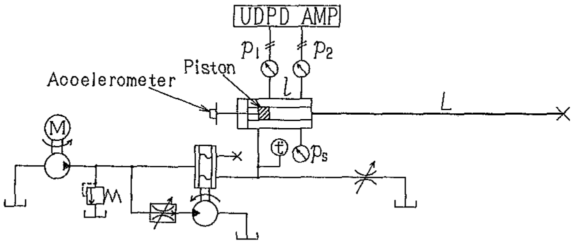

Fig. 4 Experimental setup to examine the present method of measuring unsteady flow rates

In order to check the CMR of the UDPD system, frequency responses of the same transfer function $\Delta P/P_1$ have been conducted with two pressure taps located at the same section of pipe. The results show that the overall CMR is less than −40 dB over the range up to 800 Hz.

4 Measurements of Unsteady Flow Rates

4.1 Principle. The following relations are derived from Eq. (1).

$$Q_3 = Q_2 \cosh sF_i(z)T_{l_1} - \frac{1}{Z_i F_i(z)} P_2 \sinh sF_i(z)T_{l_1}$$

$$P_1 = P_2 \cosh sF_i(z)T_l + Z_i F_i(z) Q_2 \sinh sF_i(z)T_l$$

Nomenclature

$F_i(z)$ = propagation operator
$G_{PD}(s)$ = transfer function relating differential pressure with a pressure
$I_n(z)$ = nth order modified Bessel function of 1st kind
P = Laplace transform of pressure
Q = Laplace transform of flow rate
a = pipe radius
a_c = acceleration
a_o = orifice radius
c = velocity of sound
f = fundamental frequency of pulsation
l = distance between pressure taps
l_o = orifice thickness
p = pressure
q = flow rate
s = Laplace operator
t = time
T_l = transmission time over distance l
Z_i = characteristic impedance of pipe
ΔP = Laplace transform of differential pressure
Δp = differential pressure
ϵ = correction factor for unsteady extending flow
ν = kinematic viscosity
ρ = density
ω = angular frequency of pulsation, $2\pi f$

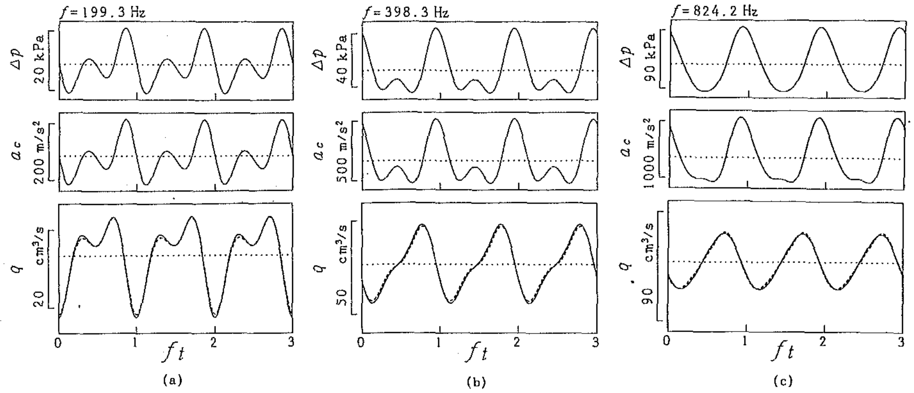

Fig. 5 Flow rate waveforms differently obtained from kinetic differential pressures (uncertainty = ±5 percent) and accelerations (uncertainty = ±2 percent)

Eliminating Q_2 and P_1 from the above equations yields

$$Q_3 = -\frac{\cosh sF_i(z)T_{l_1}}{Z_iF_i(z)\sinh sF_i(z)T_l}\Delta P + \frac{\cosh sF_i(z)T_{l_1} - \cosh sF_i(z)T_{l+l_1}}{Z_iF_i(z)\sinh sF_i(z)T_l}P_2 \quad (5)$$

On the basis of this relation, flow rates can be determined exclusively from Δp and p_2, which means the present method has an advantage that terminal conditions of a test line have no influence on the accuracy of obtained flow rates.

4.2 Availability. The availability of the method is examined with an experimental setup shown in Fig. 4. Pulsation produced by the sinusoidal flow generator excites a light piston placed at the entrance of a pipe with its end closed. An accelerometer (linearity: 1/250%/g, responsive frequency: 4 to 6000 Hz) connected to the piston by a rod detects the motions, while the UDPD system measures differential pressures between two taps located close to the piston and l = 100 mm downstream from it, respectively. It has been confirmed that original waveforms are satisfactorily reproduced with the first three harmonics obtained by Fourier analysis of experimental data.

Waveforms of the flow rate (q) at the piston, separately determined from kinetic differential pressures (Δp) and accelerations (a_c), are plotted for three different kinds of frequencies in Fig. 5 by the solid and dotted lines, respectively, with the non-dimensional time ft taken on the abscissa. Reproduced wave-forms of the differential pressures Δp and accelerations a_c are also displayed in Fig. 5 for reference. Flow rates obtained from the kinetic differential pressures are in good agreement with those measured by the accelerometer, which proves the availability and accuracy of the present method to measure unsteady flow rates.

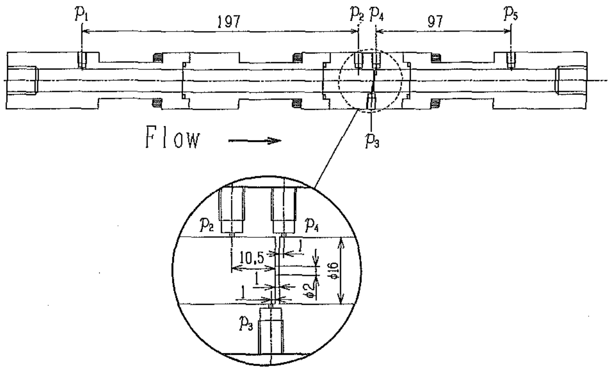

Fig. 6 Test channel with an orifice and pressure taps

5 Investigations of Unsteady Orifice Flows

5.1 Experimental Setup. Four different blocks are jointed to construct a test channel (16 mm ID) with an orifice (2 mm in diameter, 1 mm in thickness), as is illustrated in Fig. 6. Along the channel wall 3 (p_1 to p_3) and 2 (p_4, p_5) pressure taps (ϕ1 mm) are bored upstream and downstream of the orifice,

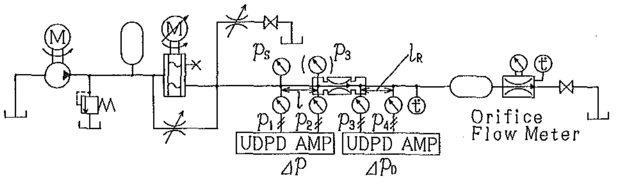

Fig. 7 Hydraulic oil circuit to measure unsteady orifice characteristics

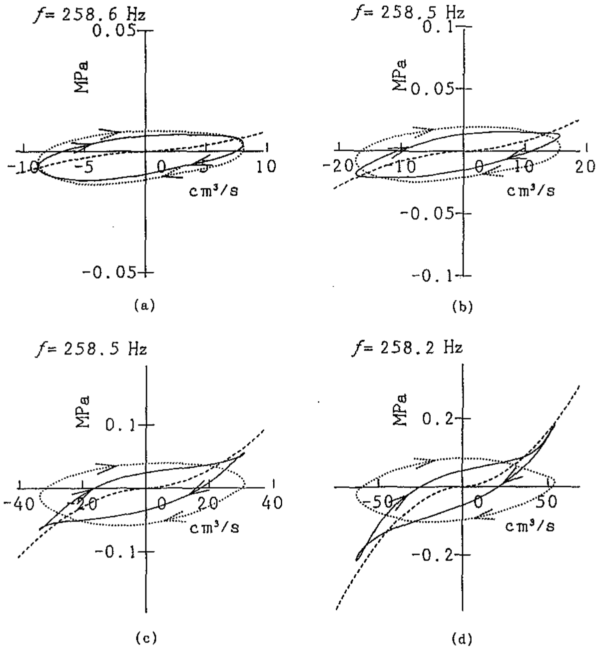

Fig. 8 Relations between overall pressure drop and flow rate in an oscillatory orifice flow. The experimental uncertainties in both the flow rate and pressure drop are within ±5 percent.

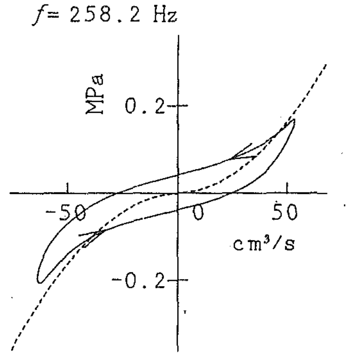

Fig. 9 Net pressure loss in an oscillatory orifice flow

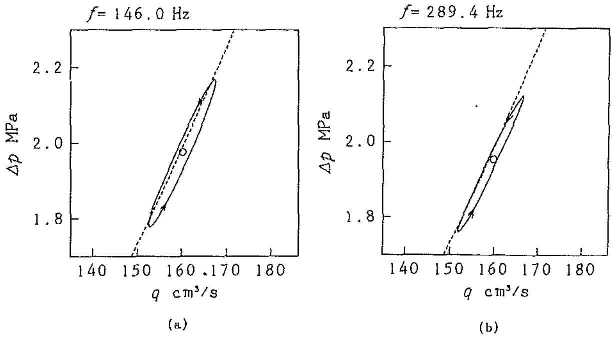

Fig. 11 Relations between net pressure loss and flow rate in a pulsating orifice flow (large q_{AVE})

respectively. The two taps p_1 and p_2 in the upstream channel are used for measuring unsteady flow rates. The distance l between them is chosen to be either 197 mm or 600 mm according to whether the change is fast ($f > 100$ Hz) or slow ($f < 100$ Hz), while the tap p_2 is $l_1 = 10.5$ mm away from the orifice. The other two taps p_4 and p_5 in the downstream channel are separated by 97 mm and assigned to measure pressure recoveries. Taps p_3 and p_4 are placed right before and after the orifice plate, respectively, to detect pressure drops across the orifice. Semi-conductor pressure transducers of the same kind as used above are mounted on each tap.

A hydraulic oil circuit used for the test is shown in Fig. 7. In a pulsating flow created by the sinusoidal flow generator, either pressure drops $p_3 - p_4$ or pressure recoveries $p_5 - p_4$ are directly measured, while flow rates at the orifice are obtained by Eq. (5) from the data of $p_2 - p_1$ and p_2. An average flow rate q_{AVE} is also measured with the uncertainty of ±1 percent by an orifice-type flow meter placed downstream of the test line after pulsation is absorbed by an accumulator.

5.2 Unsteady Pressure Loss

(1) Oscillating Flow With Zero Average. Measurements are first carried out for flows reciprocating through the orifice with the amplitude being varied. Taking the pressure drop and flow rate on orthogonal axes, respectively, and plotting experimental data over one period of oscillation yields closed curves shown by the solid lines in Fig. 8. Arrows on the curves indicate a direction of transition, and the broken lines give the steady-state relation of the orifice empirically determined in advance.

In an unsteady flow, a pressure drop across an orifice is considered to comprise of two different kinds of pressure differences. One is a kinetic pressure difference caused by accelerating or decelerating fluid through the orifice and accordingly is related linearly with the flow rate. The other is a net pressure loss which is brought about by energy dissipation in a turbulent jet flow downstream of the orifice and changes nonlinearly with the flow rate. The traditional standpoint claims that the latter is no different from the steady-state pressure loss.

The dotted lines in Fig. 8 show the kinetic pressure difference theoretically evaluated by the following equation which Washio and Konishi (1982) have previously given in their unsteady extending viscous flow model:

$$\Delta p_E = j\rho\omega Q_{\mathrm{orif}}\left[2\epsilon\tilde{G}(a_0, a, j\omega) + \frac{l_0}{\pi a_0^2}\{F_i(z_0)\}^2\right]$$

$$\tilde{G}(a_0, a, j\omega) = \frac{1}{2\pi}\left(\frac{1}{a_0} - \frac{1}{a}\right) \times \left\{1 + \frac{1}{2}\left(\frac{1}{a_0} + \frac{1}{a}\right)\sqrt{\frac{\nu}{j\omega}} + \frac{1}{3}\frac{\nu}{j\omega}\left(\frac{1}{a_0^2} + \frac{1}{a_0 a} + \frac{1}{a^2}\right)\right\} \quad (6)$$

In Fig. 8(*a*), the measured overall pressure drop (solid line) describes an elliptical loop with a clockwise hysteresis which coincides well with the theoretical prediction of kinetic pressure difference (dotted line). This result clearly demonstrates that in an oscillating orifice flow with a small amplitude, a nonlinear loss is negligible compared to a linear pressure difference kinetically induced by the fluid motion. As the amplitude increases (Fig. 8(*b*)–(*d*)), however, the solid line loops tend to stretch along the steady-state curve, accompanied by a twist and even self-crossings at both tips and deviating from the dotted line loops (kinetic differential pressure).

In order to find the true meaning of this peculiar behavior, the kinetic pressure difference calculated by Eq. (6) is sub-

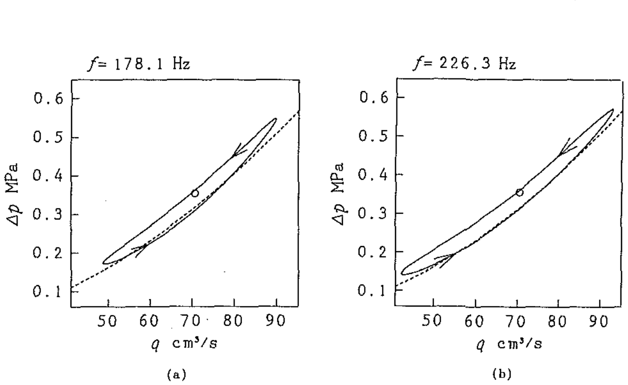

Fig. 10 Relations between net pressure loss and flow rate in a pulsating orifice flow (small q_{AVE})

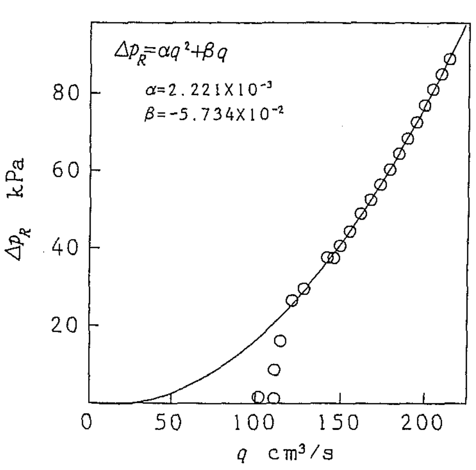

Fig. 12 Steady-state relation between pressure recovery and flow rate. (Uncertainties in both pressure recovery and flow rate are within ±1 percent.)

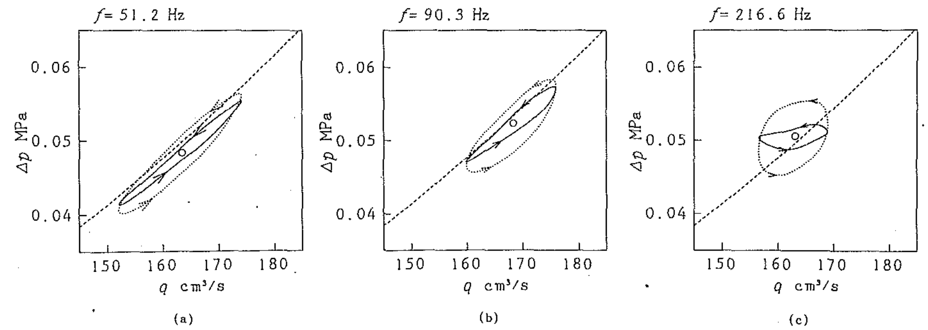

Fig. 13 Relations between pressure recovery and flow rate in a pulsating orifice flow

tracted from the overall pressure drop, and the remainder, which can be regarded as the net pressure loss, is similarly plotted against the flow rate. The result thus obtained from the data in Fig. 8(*d*) is shown by the solid line in Fig. 9. This time the closed loop, which gives the unsteady relation between the net pressure loss and the flow rate, turns out to have a counterclockwise hysteresis as well as a nonlinear twist along the steady-state curve. Since a counterclockwise hysteresis indicates the existence of a delay pressure loss has against the flow rate, it can be presumed that turbulent energy dissipation in an orifice jet flow, or a mechanism to generate a nonlinear pressure loss has "inertia" against a change of the flow rate.

(2) *Pulsating Flow with Nonzero Average.* Measurements are conducted next in pulsating flows through the orifice when amplitudes of pulsation are large or small compared to the average flow rate. This time the UDPD system to detect the pressure drop $p_3 - p_4$ is adjusted to offset their DC components to avoid saturation of the amplifier. The offset voltages are recorded to find the average pressure drop Δp_{AVE}.

Just in the same way as Fig. 9, remainders after kinetic pressure differences are subtracted from experimental pressure drops are plotted against flow rates in Figs. 10 and 11, where additional circles indicate the average points determined by $(q_{\mathrm{AVE}}, \Delta p_{\mathrm{AVE}})$. The results turn out loops with counter-clockwise hysteresis, extending along the steady-state curve with a warp when q_{AVE} is small (Fig. 10) and tangential to it when q_{AVE} is large (Fig. 11). It is acknowledged again from the counter-clock-wise hysteresis that the energy dissipation mechanism in an orifice jet flow has a delay against a flow change. Moreover, Figs. 10 and 11 have given definite evidence to the traditional assertion that characteristics of an unsteady orifice flow can be approximately represented by the steady-state ones.

5.3 Unsteady Pressure Recovery

(1) *Steady-State Characteristics.* With a conventional strain-gauge-type differential pressure transducer (rated at 100 kPa) connected to the pressure taps p_4 and p_5, pressure recoveries $\Delta p_R = p_5 - p_4$ are measured together with flow rates for a steady flow. The results are plotted by circles in Fig. 12, where the solid line gives a quadratic curve $\Delta p_R = \alpha q^2 + \beta q$ determined by the least square approximation of the experimental data except ones with substantial deviations. The deviations of data from the curve show that transition of the pressure recovery point, which Washio et al. (1986) have discovered is a phenomenon peculiar to hydraulic oil orifice flows, has occurred.

(2) *Unsteady Characteristics.* The pressure difference $\Delta p_D = p_5 - p_4$ detected in an unsteady flow naturally contains not only a pressure recovery but also a kinetic pressure difference induced by the motion of an oil column between the two pressure taps. Here the latter is evaluated from its upstream equivalent $\Delta p = p_2 - p_1$ as $\Delta p l_R / l$, where l_R is the distance between the two taps p_4 and p_5. Then the net pressure recovery Δp_R is separated from the overall pressure difference Δp_D as follows:

$$\Delta p_R = \Delta p_D - \Delta p \frac{l_R}{l} \qquad (7)$$

Measurements are conducted in orifice flows pulsating at different frequencies. The net pressure recoveries obtained by Eq. (7) are plotted against the flow rates by the solid lines in Fig. 13. The dotted lines show the overall pressure differences Δp_D for reference and the broken lines indicate the steady-state relation. When the frequency of pulsation is relatively low (Fig. 13(*a*), (*b*)), the loops of the net pressure recovery (solid lines) stretch tangential to the steady-state curve. When the frequency is large (Fig. 13(*c*)), however, the loop does not fit the steady-state curve anymore.

As the frequency of pulsation increases, increasing kinetic pressure differences occupy a bigger part of measured pressure differences Δp_D. Therefore the accuracy of the net pressure recoveries calculated by subtraction in Eq. (7) can easily deteriorate with an increasing frequency.

6 Conclusions

Methods to accurately measure unsteady differential pressures and also unsteady flow rates have been proposed. Measurements of periodically changing orifice flows by the methods proposed revealed that the net pressure loss across an orifice describes a closed loop with a counter-clockwise hysteresis against the flow rate. This fact indicates that in an unsteady orifice flow, the downstream jet with turbulent eddies, in which a nonlinear pressure loss is generated through dissipation of kinetic energy, changes its structure with a delay after the flow rate changes. Such a behavior can be called "eddy inertia" in an orifice jet flow. Moreover, the well-established fact that a steady-state pressure drop—flow rate relation of an orifice can be the first approximation to the characteristics of an unsteady orifice flow has been proved valid.

References

Bolt, R. H., Labate, S., and Ingard, U., 1949, "The Acoustic Reactance of Small Circular Orifices," *The Journal of the Acoustical Society of America*, Vol. 21, No. 2, pp. 94–97.

D'Souza, A. F., and Oldenburger, R., 1964, "Dynamic Response of Fluid Lines," ASME *Journal of Basic Engineering*, Vol. 86, pp. 589–597.

Thurston, G. B., and Martin Jr., C. E., 1953, "Periodic Fluid Flow through Circular Orifices," *The Journal of the Acoustical Society of America*, Vol. 25, No. 1, pp. 26–31.

Washio, S., and Konishi, T., 1978, "Research on Wave Phenomena in Hydraulic Lines, 3rd Report, Frequency Characteristics between Pressure and Flow Rate," *Bulletin of the JSME*, Vol. 21, pp. 1277–1283.

Washio, S., and Konishi, T., 1982, ''Research on Wave Phenomena in Hydraulic Lines, 8th Report, Theoretical Investigation on End Correction Problem—Part 2, Estimation of Viscous Resistance,'' *Bulletin of the JSME,* Vol. 25, pp. 789–796.

Washio, S., Konishi, T., Nishii, K., and Tanaka, A., 1982, ''Research on Wave Phenomena in Hydraulic Lines, 9th Report, Experimental Investigation of Oscillatory Orifice Flows,'' *Bulletin of the JSME,* Vol. 25, pp. 1906–1913.

Washio, S., Konishi, T., Nishii, K., and Tanaka, A., ''Research on Wave Phenomena in Hydraulic Lines, 10th Report, Experimental Discussion on Unsteady Nonlinearity of Orifice Flows,'' *Bulletin of the JSME,* Vol. 25, pp. 1914–1920.

Washio, S., Konishi, T., Okamura, T., Kakutani, S., Iida, K., and Yamamoto, H., 1986, ''Experimental Studies on Pressure Distribution in Orifice Jet Flows of Low Reynolds Numbers,'' *Bulletin of the JSME,* Vol. 29, pp. 781–786.

Si Huang
Invited Researcher,
Institute of Fluid Science,
Tohoku University,
1-1, Katahira 2-chome, Aoba-ku,
Sendai 980-77, Japan

Akio Ihara
Professor,
Yamaguchi University,
1677-1, O-aza Yoshida,
Yamaguchi 753, Japan

Hideo Watanabe
Research Associate,
Institute of Fluid Science,
Tohoku University,
1-1, Katahira 2-chome, Aoba-ku,
Sendai 980-77, Japan

Hiroyuki Hashimoto
Senior Advisor,
Ebara Research Co.,
2-1, Honfujusawa 4-chome,
Fujisawa-shi 251, Japan,
Mem. ASME

Effects of Solid Particle Properties on Cavitation Erosion in Solid-Water Mixtures

A systematic investigation has been carried out on cavitation erosion in solid-water mixtures using vibratory test facilities and some analytical devices. A mixture of distilled water and heterogeneous solid particles is used. It is shown in this work that solid particles play significant roles on acoustic cavitation erosion through two ways when present in liquids. They aggravate the abrasive wear of materials owing to the effects of particle size, concentration, and hardness. In addition, they relieve the damage produced by the reduction of the collapse pressure of cavitation bubble because of the variation of the physical properties in mixtures. Total erosion is dependent on this governing factor.

1 Introduction

Cavitation and erosion in solid-liquid flows are encountered in nature and a large variety of industrial fields such as mechanical, chemical, and metallurgical engineering. Cavitation erosion of hydraulic machinery in the high sediment rivers, results in frequent replacement of components and assemblies. Recent research concerning industrial applications of acoustic cavitation in solid-liquid media may lead to the synthesis of solid phases or the interaction of energy and matter difficult to fulfill in other ways.

Cavitation erosion in solid-liquid flows involves the interaction of liquid cavitation and the effects of solid phase, which constitutes a complex but fascinating phenomenon. In this area, however, comparatively few investigations have been published. Duan (1981) studied the damage of cylindrical bronze body in a sand-water flow ($x = 5$ percent, $D = 100$ μm) in a water tunnel. His results indicated that the erosion intensity with cavitation was 2–4 times of that without cavitation. Guo et al. (1983) investigated the comparative damage of a 250-mm-diameter water turbines in natural river silt condition ($x = 4 \sim 5$ percent) and showed that the relation of weight losses by cavitation in pure water, sand abrasion singly and the combined damage was about 1:5:15. From these works, it has been concluded that the cavitation erosion in a flow containing sand is more severe than that in clean water. The sand abrasion and the cavitation nuclei entrained by particles both yield extra damage. There were also the opposite results obtained by other researchers. Huang et al. (1983) used a venturi tube device ($V = 26$ m/s, $\sigma = 0.84 \sim 0.87$) with sand-water mixtures ($x = 0 \sim 5$ percent, $D = 20$ μm) and carried out an experiment on cavitation resistance of several metal materials such as bronze, aluminum and stainless steel. There was no marked variation of erosion by additives of sand particles from the experiment. Zheng (1984) performed an erosion test of bronze specimen in sand-water mixtures ($x = 0 \sim 15$ percent, D is about 10 μm) using a 30 μm-amplitude vibratory facility. Zheng's result indicated that weight loss of specimen slightly increased with sand content within a smaller range ($x < 1$ percent), but decreased with the further increase of sand content and reached half of that in pure water. It was summarized from these studies that the reduction of erosion was attributed to that sand particles affected the generation of cavitation pits as the eroded surface was polished by particles. Abrasive wear of sand had more influence on damage than cavitation while sand content becomed large.

Systematic knowledge of cavitation erosion in solid-liquid flows is obviously far from clear. In this work, the experimental research is carried out using a vibratory facility and some analytical devices, with the aim for understanding the general trends and the mechanisms of cavitation erosion in solid-water mixtures; as well as the variation of cavitation erosion in solid-water mixtures when the external acoustic pressure field is varied.

2 Experimental Apparatus and Procedures

For present measurement of cavitation erosion, two sets of piezoelectric drive units with the same frequency ($f = 19.5 \pm 0.5$ kHz) but different horn diameters ($d = 12, 20$ mm) were employed. As shown in Fig. 1, the test apparatus was instrumented to measure as well as control various test conditions such as temperature of test liquid and the amplitude of vibratory horn. The amplitude of vibration could be altered by adjusting an output voltage of the frequency generator, according to their relation that was preliminarily measured using a calibrated-scale microscope. The temperature of the cooling water was set at 293 K.

The test mixtures were mixed in a special bath within the concentration region, in which all particles were well excited by vibrating horn to achieve a homogeneous solid-water mixture. To check the homogeneity of solid-liquid mixtures, the samples of mixtures beneath the vibrating specimen were

---

Contributed by the Fluids Engineering Division for publication in the JOURNAL OF FLUIDS ENGINEERING. Manuscript received by the Fluids Engineering Division September 19, 1995; revised manuscript received May 13, 1996. Associate Technical Editor: Joseph Katz.

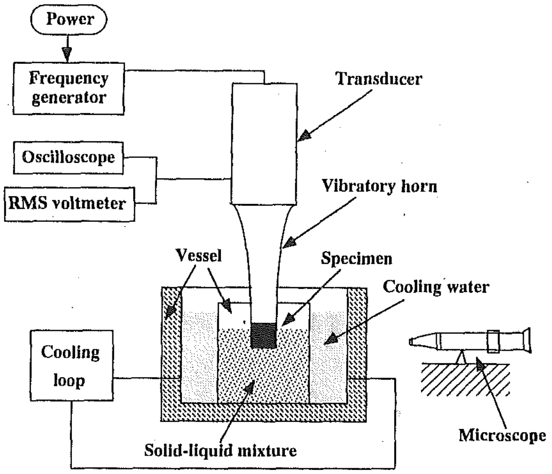

Fig. 1 Schematic drawing of test facility

Table 1 Physical properties of test materials at 293 K

Material	Density (kg/m^3)	Hardness (N/m^2)	Young's modulus (N/m^2)	Sonic speed (m/s)
Specimen:	$\times 10^3$	$\times 10^8$	$\times 10^{10}$	$\times 10^3$
Copper	8.96	7.5	12.3	3.71
Abrasive:				
Aluminum	2.70	2.50	6.85	5.04
Molybdenum	10.2	27.5	35.0	5.85
Nickel	8.90	12.5	20.1	4.79
Quartz	2.67	115	13.0	6.10

spooned during exposure. The suspended particles were separated from the samples and the actual particle concentrations were measured. For the quartz particles with $D = 50$ μm, the biggest size among all test particles, the actual concentrations were 9.7 and 14.3 percent, respectively, corresponding to the setting concentration $x = 10$ and 15 percent. This result showed that solid-liquid mixtures have a sufficient homogeneity for experiment.

All quantitative tests and measurements of damage were conducted under the standard method of vibratory cavitation erosion test guided by ASTM (1977).

3 Physical Properties of Test Materials

The copper with 99.9 percent in purity, subject to erosion, was used for the test material. Four kinds of the solid-water mixtures were made up using distilled water with quartz, aluminum, nickel, and molybdenum particles. Some physical properties of the test materials are given in Table 1. We used three mesh sizes of quartz particles, i.e., $D = 0.8$, 4 and 50 μm, as well as one mesh size ($D = 4$ μm) of aluminum, nickel, and molybdenum particles.

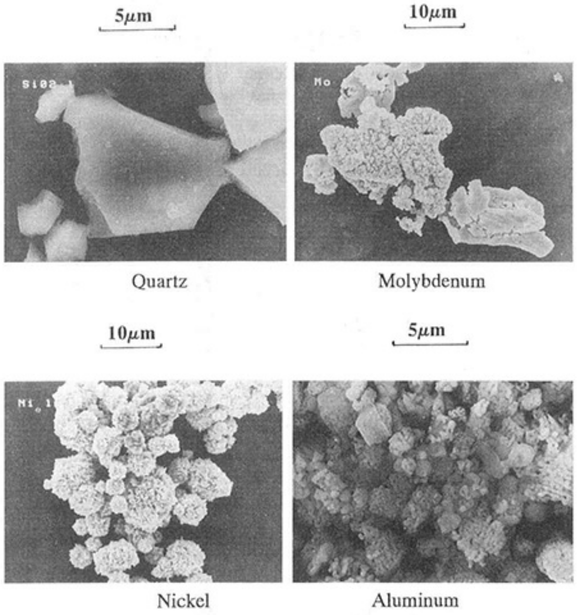

Quartz Molybdenum

Nickel Aluminum

Fig. 2 SEM photographs of test particles ($D = 4$ μm)

The quartz particles are of interest in this study because they are the main ingredient of silt harmful to fluid machinery in high sediment rivers (Watson and Liu, 1992; Mei, 1992). From Table 1, the quartz particles have the lowest density and highest hardness and sonic speed in the test particle group. The nickel particles have a density approximate to that of molybdenum, and their hardness is near that of the eroded material, i.e., the copper specimen. The molybdenum particles have greatest density but are of intermediate hardness compared with the other materials. Among these additives, the aluminum particles have the lower hardness even lower than the eroded material, copper. The appearances of the four kinds of particles were observed using a scanning electronic micrometer (SEM, Hitachi S-4100L). As seen in their SEM photographs (Fig. 2), the quartz particles have irregular shapes with sharp edges. The aluminum and molybdenum particles have irregular shapes but do not have sharp edges, while the shapes of the nickel particles are nearly spherical.

4 Experimental Results and Discussion

4.1 Damaged Patterns of Specimen Surfaces. Like the results revealed in other studies (Plesset, 1960; Tichler, et al.,

Nomenclature

A = amplitude of vibratory horn
c = sonic speed
D = mesh diameter of solid particle
D_e = equivalent diameter of solid particle
$\bar{D}_{10}$ = arithmetric mean particle diameter ($= \sum_i^N D_{ei} f(D_{ei})$)
d = diameter of test specimen
f = frequency of vibratory facility
$f(D_e)$ = percent sample composition
H_a = hardness of solid particle
H_m = hardness of eroded material
H^* = nondimensional hardness ($= H_a/H_m$)
k = number of phases
m = amplitude exponent as to cavitation erosion
N = number of particle sample recorded in image processor-analyzer
n_d = exponent of specimen size as to cavitation erosion
n_p = exponent of particle size as to cavitation erosion
R = radius of bubble
R_w = weight loss rate of specimen ($= dW/dt$)
t = time
U = velocity of bubble wall
W = weight loss of specimen
x = weight ratio of solid particles in solid-water mixtures
α = volume ratio
ρ = density of medium
σ = cavitation parameter

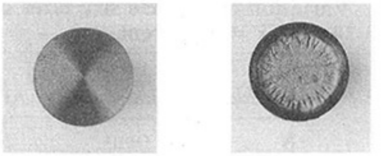

(a) Uneroded surface (b) Distilled water

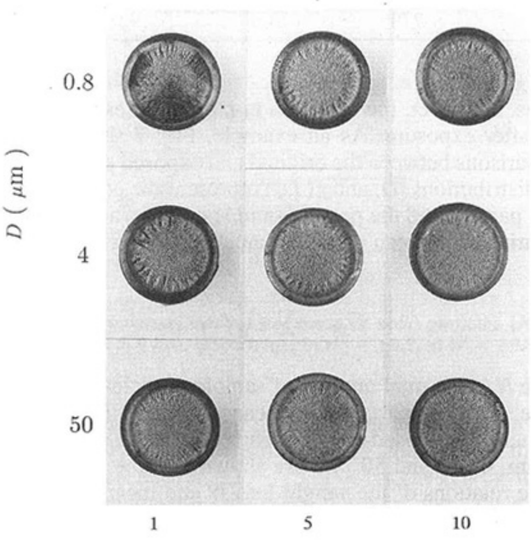

(c) Quartz-water mixture

Fig. 3 Photographs of uneroded and eroded specimen surfaces (A = 25 μm, d = 12 mm, t = 30 min)

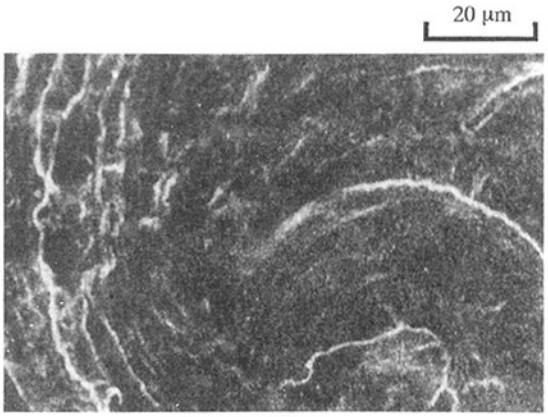

(a) Distilled water.

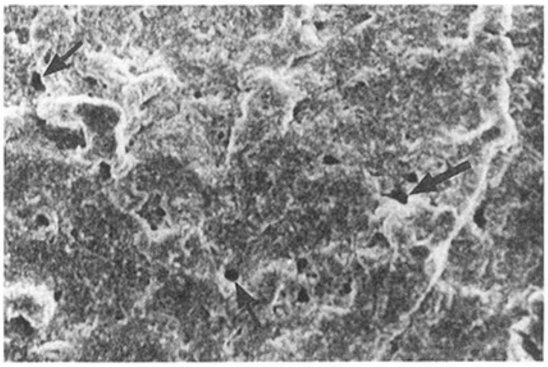

(b) Quartz-water (D=50 μm, x=5%).

Fig. 4 SEM Photographs of eroded specimen surfaces (A = 25 μm, d = 12 mm, t = 3 min)

1970), several deep grooves appeared and distributed symmetrically on the eroded specimen surface exposed in distilled water (shown in Fig. 3). The analysis of Taylor (1950), Plesset (1960) pointed out that such grooves could be generated by a radial surface flow beneath the vibrating specimen. In the mixture tests, the increase of weight concentration x and size D of solid particle in the solid-water mixtures, resulted in reduction of these grooves. The corresponding damage appearance became finer and more uniform. The present result indicates that the movement of the suspended solid particle can wear away the grooves or suppress the generation of the radial flow mentioned by Plesset. The abrasive wear seems to play more roles because the effect became intensified when using harder solid particles. The damaged surfaces of the specimens were observed using SEM (Fig. 4). In contrast to the specimen surface tested in pure water, where only large scale deformations arose, the specimen surface exposed in the quartz-water mixture had meticulous deformations in every local part. Some pits were discovered successively with an exposure time as pointed with arrows in Fig. 4, and they developed in size and depth simultaneously. Accordingly, it was inferred that such pits were caused by the collision of the solid particles so that erosion was aggravated.

4.2 Time Histories of Weight Loss and Weight Loss Rate. Figures 5 and 6 show typical results of the weight loss and weight loss rate with exposure time. These figures compose the results for distilled water, the quartz-water, the aluminum-water (A-W), the nickel-water (N-W) and the molybdenum-water (M-W) mixture tests. Generally, the weight loss in the quartz-water mixture is more and the weight loss in the nickel-water mixture is less compared with in other solid-water mixtures (Fig. 5). For all cases, as seen in Fig. 6, the weight losses accelerate fast after an incubation period (about 5 minutes), then the loss rate enters a steady state after the acceleration period (about 10 minutes).

4.3 Effect of Solid Particle Size. Early measurement (Huang et al., 1993) discovered that the quartz particles tended to lose their size influences on the cavitation erosion of the specimen in quartz-water mixtures with exposure time. This implies that the solid particles as well as the test specimen are all worn out when they are exposed to an acoustic pressure field. To ascertain this, the original and exposed samples of heterogeneous particles (quartz, aluminum, nickel and molybdenum) were observed for appearance using SEM. Also, the

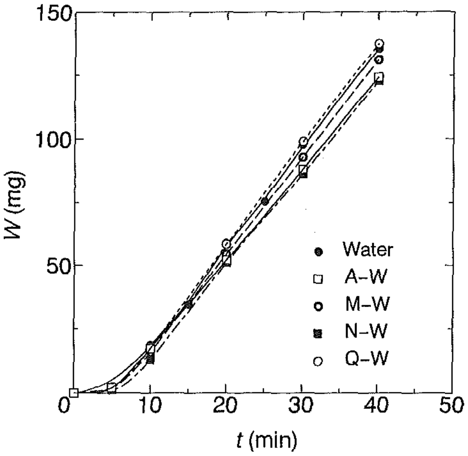

Fig. 5 Weight loss versus exposure time (A = 25 μm, d = 20 mm, D = 4 μm, x = 5 percent. Uncertainty in t = ±0.05 min, in W = ±0.5 mg.)

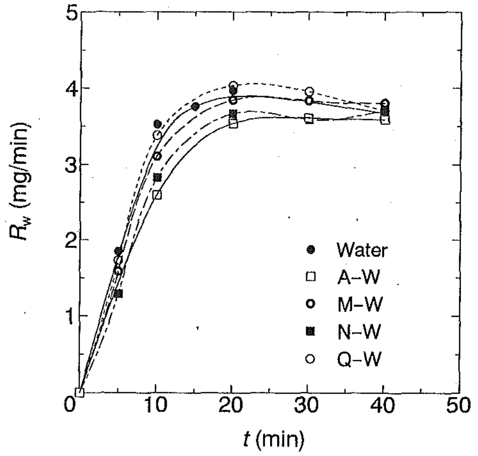

Fig. 6 Weight loss rate versus exposure time (A = 25 μm, d = 20 mm, D = 4 μm, x = 5 percent. Uncertainty in t = ±0.05 min, in W = ±0.5 mg.)

Table 2 Variation of particle size after exposure (A = 25 μm, d = 20 mm, x = 5 percent

Particle type	Before exposure		After 30-min exposure	
D (μm)	N	$\bar{D}_{10}$ (μm)	N	$\bar{D}_{10}$ (μm)
0.8	2030	1.7	3580	0.97
4	952	4.1	1580	1.9
50	779	14.6	928	7.7

size distributions of quartz particles were measured by an image processor-analyzer (Nireco Co. Ltd., Luzex III) before and after the exposure. It was hard to distinguish the appearance of the exposed particles from the original ones in the SEM photographs. However, the variation in particle sizes is quite significant after exposure. As an example, Fig. 7 shows one of the comparisons between the original and exposed particle (30 min) size distributions. D_e and $f(D_e)$ represent the equivalent diameter of particle and the percent sample composition, respectively. The arithmetic mean particle diameters $\bar{D}_{10}$ are obtained as follows:

$$\bar{D}_{10} = \sum_{i=1}^{N} D_{ei} f(D_{ei}), \tag{1}$$

where N is the total number of sample particles recorded in the image. The comparisons of mean diameters $\bar{D}_{10}$ between the original and exposed quartz particles for three mesh sizes, D = 0.8 μm, 4 μm and 50 μm, are shown in Table 2.

The relations of the weight loss W and mean particle diameters $\bar{D}_{10}$ in the quartz-water mixture are correlated in logarithmic charts (Fig. 8). The particle size exponents n_p relation with cavitation erosion can be obtained in the chart for the quartz-water mixture. In this chart, the value n_p = 0.55 may represent the general trend as to the influence of particle size on cavitation erosion although data scatter in a quite large range.

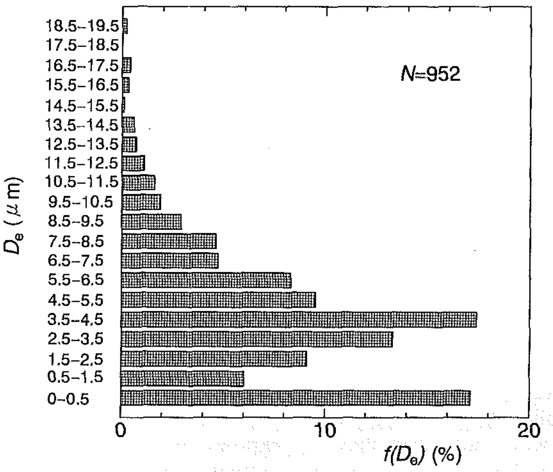

Fig. 7(a) Original particles

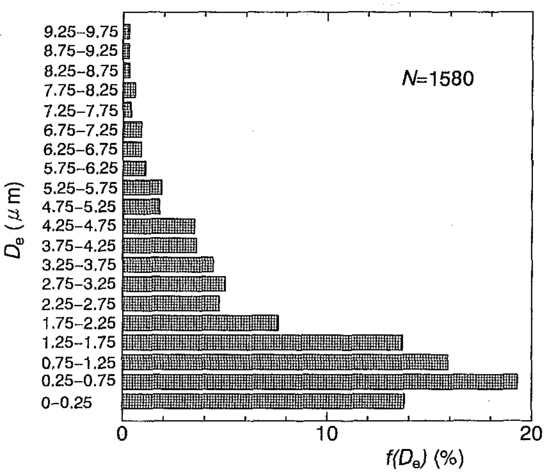

Fig. 7(b) Exposed particles (A = 25 μm, d = 20 mm, t = 30 min, x = 5 percent)

Fig. 7 Size distributions of quartz particles measured by image processor-analyzer (D = 4 μm. Uncertainty in D_e = ±0.1 μm).

4.4 Effect of Particle Hardness. Figure 9 shows the weight loss of the copper specimen as the function of the relative hardness of solid particle (abrasive), where the relative hardness H^* means the ratio of the hardness H_a of the abrasive to the hardness H_m of the eroded material. The weight loss rises with increasing an abrasive hardness for all particle proportions are as expected. With an increase of particle proportion, the relation of weight loss and the abrasive hardness has a similar tendency to that in the case of the abrasive wear (Khrushov, 1957, 1974), i.e., there are three regions of abrasion concerning abrasive hardness: low abrasion (region I, $H^* < K_2$), accelerated abrasion (region II, $K_2 < H^* < K_1$) and high abrasion (region III, $H^* > K_1$). Very little wear takes place in region I, then the material loss remarkably increases in region II until entering region III, where the wear is relatively constant regard-

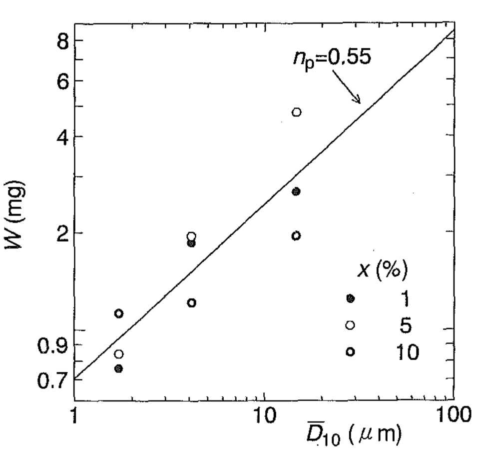

Fig. 8 Effect of particle size in quartz-water mixtures (A = 25 μm, d = 20 mm, t = 5 min, $W \propto \bar{D}_{10}^{n_p}$. Uncertainty in $\bar{D}_{10}$ = ±0.1 μm, in W = ±0.5 mg.)

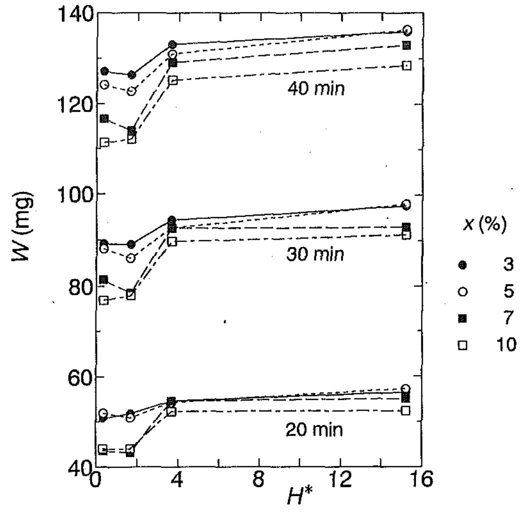

Fig. 9 Weight loss versus relative hardness of solid particles (A = 25 μm, d = 20 mm, D = 4 μm. Uncertainty in H^* = ±0.2, in W = ±0.5 mg.)

less of an increase of abrasive hardness. On the basis of a large number of abrasive wear tests Khrushov (1974) found that K_1 was 1.3 ~ 1.7 and K_2 was 0.7 ~ 1.1. For the present cavitation erosion tests in solid-liquid mixtures, however, the values of K_1 and K_2 in Fig. 9 move to 4 and 2, respectively. The increases of values can be attributed to the difference of two kinds of erosion methods. Khrushov's values came from the wear test in which specimen was rubbed directly against fixed abrasive grains, while the present damage test was cavitation erosion in solid-water mixtures with the lower particle concentration.

4.5 Effect of Solid Particle Concentration. Figures 10 and 11 show the weight loss in the steady period in four kinds of the solid-water mixtures (quartz-water, aluminum-water, nickel-water, molybdenum-water) for various concentrations of particles. It can be seen in Fig. 10 that the damage decreases monotonically as one goes from the pure distilled water to high proportions of the nickel particles, the aluminum particles or the molybdenum particles. The behavior in the quartz-water mixture, however, is quite different (Fig. 11). As solid-water mixtures become concentrated, the specimens undergo a damage course with a peak value. Usually, the peak weight loss takes place around $x = 5$ percent in particle concentration. These results may be understood from two factors. On one hand, the wear due to the solid particle aggravates damage to the material with the increase of particle concentration, size, and hardness. On the other hand, Huang et al. (1995) theoretically analyzed bubble behaviors and developed a following bubble wall equation of a single spherical bubble in solid-liquid and liquid-liquid mixtures with the assumption that the mixtures are homogeneous.

$$\left(1-\frac{U}{c_m}\right)R\frac{dU}{dt}+\frac{3}{2}\left(1-\frac{U}{3c_m}\right)U^2 = \left(1+\frac{U}{c_m}+\frac{R}{c_m}\frac{d}{dt}\right)\frac{p_B-p_A}{\rho_m}, \qquad (2)$$

where p_A and p_B are the ambient pressure and the pressure at the bubble wall. Density and sonic speed in a mixture are $\rho_m = \sum_{k=1}^{K} \rho_k\alpha_k$ and $c_m = (\sum_{k=1}^{K} \rho_k\alpha_k \sum_{k=1}^{K} (\alpha_k/\rho_k c_k^2))^{-1/2}$. The numerical result of Eq. (2) indicates that the bubble collapse pressure declines owing to the variation of physical properties (viscosity, density, surface tension, and sonic speed) of medium with the additives of solid particles, suggesting a reduction of

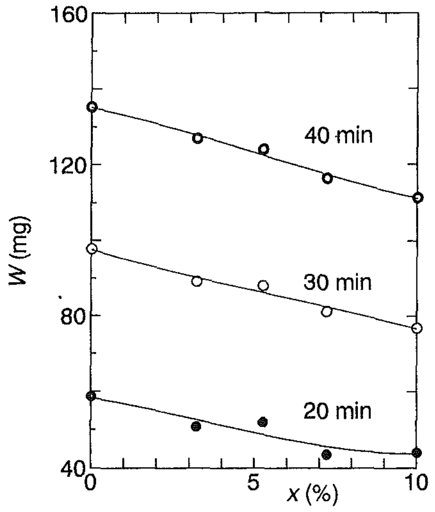

Fig. 10(*a*) Aluminum-water

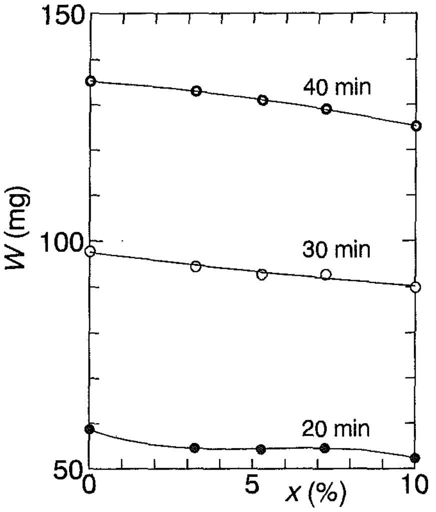

Fig. 10(*b*) Molybdenum-water

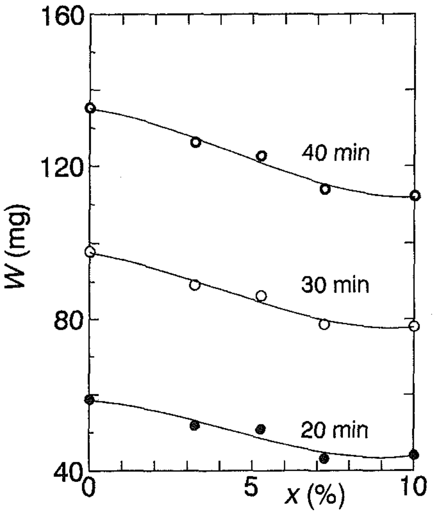

Fig. 10(*c*) Nickel-water

Fig. 10 Weight loss versus particle concentration in the solid-liquid mixtures (A = 25 μm, d = 20 mm, D = 4 μm. Uncertainty in x = ±0.5 percent, in W = ±0.5 mg.)

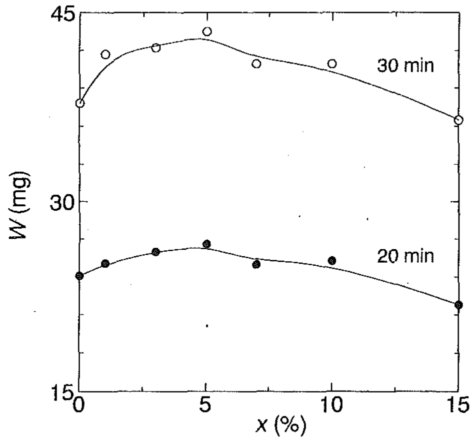

Fig. 11(*a*) $D = 0.8$ µm

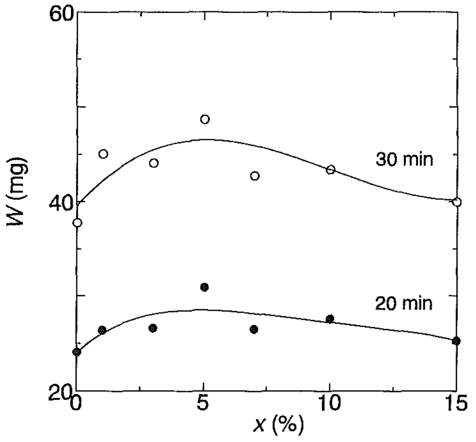

Fig. 11(*b*) $D = 4$ µm

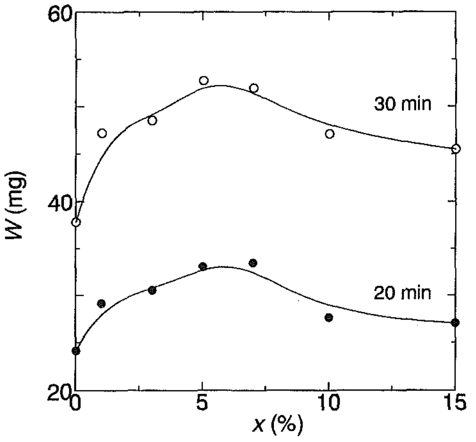

Fig. 11(*c*) $D = 50$ µm

Fig. 11 Weight loss versus particle concentration in the quartz-water mixtures ($A = 25$ µm, $d = 12$ mm. Uncertainty in $x = \pm 0.5$ percent, in $W = \pm 0.5$ mg.)

cavitation damage. The increase or decrease of the total erosion damage depends on which factor is predominant corresponding to different kinds of mixtures. For instance, the abrasion of the nickel particle is small because of its lower hardness and spherical configuration, but its density is so large that the cavitation damage of specimen considerably alleviates in the nickel-water mixture. Therefore the total loss in the nickel-water mixture is mainly occupied by the cavitation proportion (Fig. 10). In the quartz-water mixture, however, the quartz particle has a lower density, a higher hardness and a sharper shape compared with other kinds of particles. It is inferred that the quartz particle plays same order roles both on cavitation and abrasion in the quartz-water mixture, leading to a peak value arising in the distribution of total weight loss (Fig. 11).

4.6 Effect of Vibrating Conditions. Vibratory cavitation in liquids is notably affected by the external conditions including the amplitude and size of vibratory horn, which control the intensity and the distribution of acoustic pressure.

In the quartz-water mixtures, we performed the experiments to examine the relations of the cavitation erosion with the amplitude and the diameter of vibratory horn. Figure 12 shows the cavitation erosion of copper specimens correlated to three amplitudes measured in the quartz-water mixtures. In Fig. 12, the experimental data are plotted in the logarithmic charts so that the amplitude exponents can be obtained. There is no considerable difference of amplitude exponent between in the distilled water ($x = 0$ percent) and in the quartz-water mixtures. The weight lose of specimen approximately has a linear relation with vibratory amplitude, coincident with the measured results in water by other researchers (Hobbs, 1966, 1969; Thiruvengadam, 1966).

Figure 13 gives the cavitation erosion correlated to two specimen sizes measured in the quartz-water mixtures. As seen in Fig. 13, the weight loss in the pure water has higher scale exponents, which are near $n_d = 2$. In the quartz-water mixtures, however, the scale exponents seem to slightly decline due to the acoustic energy loss as the mixture becomes concentrated.

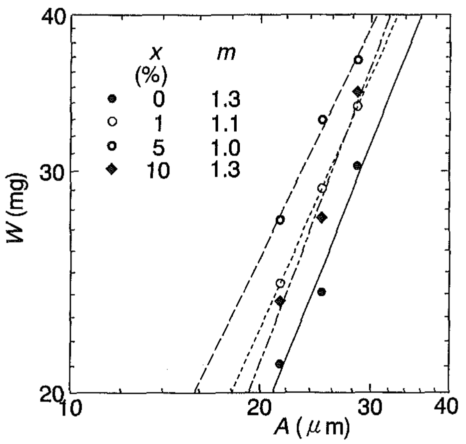

Fig. 12(*a*) $t = 20$ min

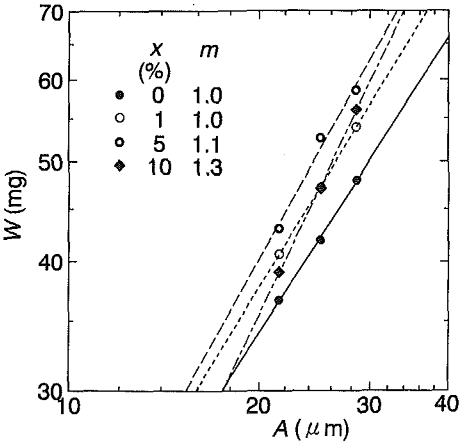

Fig. 12(*b*) $t = 30$ min

Fig. 12 Relation between weight loss and amplitude in the quartz-water mixtures ($d = 12$ mm, $D = 50$ µm, $W \propto A^m$. Uncertainty in $A = \pm 0.3$ µm, in $W = \pm 0.5$ mg.)

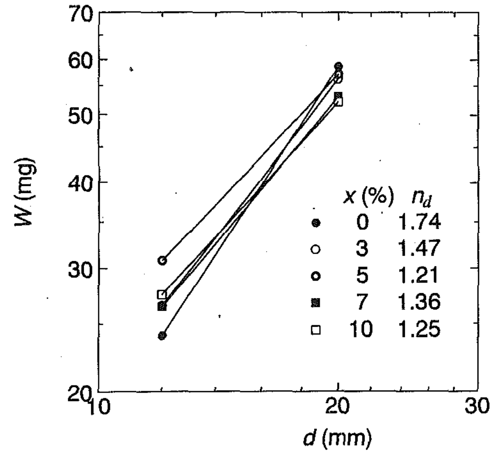

Fig. 13(*a*) $t = 20$ min

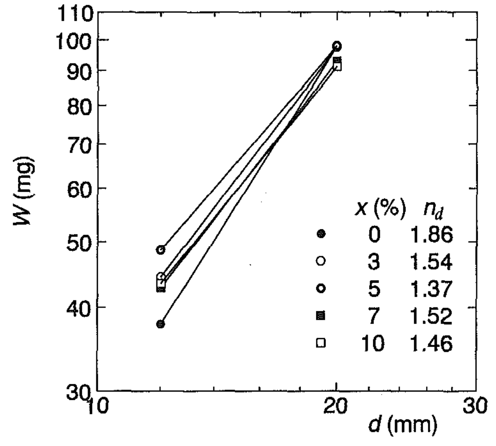

Fig. 13(*b*) $t = 30$ min

Fig. 13 Effect of specimen size on damage in the quartz-water mixtures ($A = 25$ μm, $D = 4$ μm, $W \propto d^{n_d}$. Uncertainty in $d = \pm 0.1$ mm, in $W = \pm 0.5$ mg.)

Anyway, all values of scale exponents are in the range $n_d = 1 \sim 2$, which are coincident with the results with the flowing or jet impact methods (Canavelis, 1968; Ito et al., 1988).

5 Conclusion

Attempts have been made experimentally to study the cavitation erosion in solid-water mixtures using vibratory facilities and some analytical devices. The following conclusions are noteworthy:

In solid-water mixtures, damage pattern on the eroded surface of specimen develops uniformly. The grooves arising on the eroded surface of specimen in water gradually disappear with the increase of solid concentration and particle size. By SEM, it is found that some pits due to particle collisions occur on the specimen surface, and develop in size and depth with exposure time.

Solid particles are worn out under the acoustic cavitation so that the influence of particle size on the erosion of specimen disappears with exposure time.

Solid particles play significant roles on cavitation erosion when added to liquids by means of two ways, namely aggravating abrasive wear of materials by the effects of particle size, concentration and hardness; relieving the damage of collapse bubble pressure because of the variation of the physical properties in mixtures. The total damage distribution relies on properties of particles. In the quartz-water mixtures, there is a maximum weight loss occurring at a certain solid concentration. However, weight losses have a decline tendency with particle concentration at the various degrees, in the mixtures of aluminum-water, nickel-water and molybdenum-water.

Cavitation erosion is measured by altering the acoustic conditions in two vibratory facilities, including the vibration amplitude and the vibratory specimen diameter. The exponents of an amplitude and a specimen scale in solid-water mixtures are obtained respectively by correlating to the weight losses of copper specimens. In brief, the exponent value of either amplitude or specimen scale in solid-water mixtures is quite close to that in water.

Acknowledgment

The authors wish to express their thanks to Mr. T. Sato, Technician of the Institute of Materials, Tohoku University; Mr. K. Katagiri and Mr. K. Asano, Technicians of the Institute of Fluid Science, Tohoku University for their cooperation with the research. This research was partly supported by the grant from the Mitsubishi Foundation.

References

ASTM, D32-77, 1977, *Standard Method of Vibratory Cavitation Erosion Test.*

Canavelis, R., 1968, "Jet Impact and Cavitation Damage," ASME *Journal of Basic Engineering*, Vol. 90, pp. 355–366.

Duan, C. G., 1981, *Silt Abrasive Erosion of Hydraulic Turbine*, Tsinghua University Press, pp. 107–112 (in Chinese).

Guo, Z. X., Zhang, L. X., and Wang, Z. G., 1983, "Experimental Investigation into Sand Erosion of hydraulic Machines in China," *Abrasion and Cavitation in Hydraulic Machinery*, pp. 13–32 (in Chinese).

Hobbs, J. M., 1966, "Experience with a 20-kc Cavitation Erosion Test," ASTM *Symposium on Erosion by Cavitation or Impingement*, pp. 159–185.

Hobbs, J. M., and Rachman, D., 1969, "Environmentally Controlled Cavitation Test (Improvements in a Cavitating Film Erosion Test)", ASTM *Symposium on Characterization and Determination of Erosion Resistance*, pp. 29–47.

Huang, J. T., et al, 1983, "Experimental Study of Cavitation Resistance of Concrete, Brittle Cementing Materials and Some Metals in Sediment Flow," *Proceedings of 2nd Asian Congress of Fluid Mechanics*, pp. 50–57.

Huang, S., Ihara, A., Hashimoto, H., and Watanabe, H., 1993, "Experimental Study on Cavitation Erosion in Solid-Liquid Mixture by Vibratory Method," *Proceedings of 4th Asian International Conference on Fluid Machinery*, Suzhou, pp. 600–606.

Huang, S., Ihara, A., Hashimoto, H., and Watanabe, H., 1995, "Bubble Behaviors in Solid-Liquid and Liquid-Liquid Mixtures," *Japanese Journal of Multiphase Flow*, Vol. 9, pp. 301–307 (in Japanese).

Ito, Y., et al, 1988, "A Study on Cavitation Scale Effects Especially with Respect to Cavitation-Induced High-Pressure Pulses," *Trans. JSME* (B), Vol. 54, pp. 2727–2733 (in Japanese).

Khrushov, M. M., 1957, "Resistance of Metals to Wear by Abrasion; Related to Hardness," *Proceedings of Conference on Lubrication and Wear*, London, pp. 655–664.

Khrushov, M. M., 1974, "Principles of Abrasive Wear," *Wear*, Vol. 28, pp. 69–88.

Mei, Z. Y., 1992, "A Survey of Research and Development of Slurry Pumps in China," *Proceedings of International Conference on Pumps and Systems*, Beijing, pp. 7–20.

Plesset, M. S., 1960, "On Catholic Protection in Cavitation Damage," ASME *Journal of Basic Engineering*, Vol. 82, pp. 808–816.

Taylor, G. I., 1950, "The instability of Liquid Surface When Accelerated in Direction Perpendicular to Their Plane I," *Proceedings of Royal Society*, Series A, Vol. 201, pp. 192–198.

Thiruvengadam, A., 1966, "The Concept of Erosion Strength," ASTM *Symposium on Erosion by Cavitation or Impingement*, pp. 22–41.

Tichler, J. W., et al, 1970, "Resistance Against Cavitation Erosion of 14 Chromium Steels," ASME *Journal of Lubrication Technology*, Vol. 92, pp. 220–229.

Watson, M. A. and Liu, Y., 1992, "Yellow River Dams: Development of Erosion-Resistant Materials for Gates," *Proceedings of International Symposium on Cavitation and Erosion in Hydraulic Structures and Machinery*, Nanjing, pp. 206–211.

Zheng, D. Q., 1984, "An Exploration of Effects of Concentration of Suspending Sands in Water on Cavitation Erosion," *Proceedings of First National Symposium on Cavitation*, pp. 71–85 (in Chinese).

Branko Bajić
Head of Signal Processing and
Hydrodynamical Acoustics Group,
Brodarski Institute,
Marine Research & Special Technologies,
Zagreb, Croatia

Andreas Keller
Academic Director,
Obernach Hydraulic Research Laboratory,
Munich University of Technology,
Obernach, Germany

Spectrum Normalization Method in Vibro-Acoustical Diagnostic Measurements of Hydroturbine Cavitation[1]

Full-scale vibro-acoustical diagnostic measurements of cavitation in four Francis 6 MW double runner turbines were performed. Two types of sensors were used—a hydrophone sensing waterborne noise at the pressure side of a runner and an accelerometer mounted at various points at the outer turbine casing, facing the runner's pressure side. The correlation of noise and acceleration intensity with suction-side pressure fluctuations and runner position was checked. A simple but efficient method of spectrum normalization, which rejects the influence of the measurement set characteristics and vibro-acoustical characteristics of a turbine, was developed. The resulting spectra reveal the dependence of cavitation source strength on the turbine power as a function of noise or acceleration frequency.

Introduction

Vibro-acoustical methods of diagnosing and monitoring cavitation in hydraulic machinery are nondestructive and easy to perform. This explains a steady interest in cavitation-generated noise and vibration by numerous engineers and scientists dealing with cavitation erosion in turbines, pumps etc. Although the related research has been carried out for decades (see the early papers by Pearsall, 1966 and Varga et al., 1969), and although the crucial results concerning the correlation of cavitation erosion with vibro-acoustical signatures of cavitation seem to have been achieved (Abbot, 1989 and Bourdon et al., 1989), no standardized method for vibro-acoustical diagnosis of cavitation or cavitation erosion in hydraulic machinery is yet available. Thus, further data from well-controlled experiments and better methods for analysis of their results are needed.

The aim of this paper on full-scale measurements on four Francis 6 MW double runner turbines, in which erosion has been encountered, is to contribute along these lines. The problems of vibro-acoustical field sampling, and signal and data processing are dealt with. A useful data processing technique, spectrum normalization, is defined and checked.

Measurement Set

As sensors, a Brüel & Kjaer accelerometer 4371, having a mounted resonance at 40–50 kHz, and a Brüel & Kjaer hydrophone 8103, with a resonance outside the working frequency range, were used. They were mounted symmetrically at the two sides of each of the turbines (arrows in Fig. 1), at the outer casing, facing the pressure side of runners (Fig. 2). Three locations of the sensors were tested:

I— as close to the runner as possible, but in a position where the metallic parts between the sensor and cavitation noise sources are the thinnest,
O— rather far from the runner, with the whole wicket gate between the runner and the sensor, and
M— a mid-position.

The hydrophone was mounted in the O-location, in a hole in the turbine casing. It was isolated from structure-born noise, and was positioned outside the flow. The accelerometer was fixed onto the outer surface of the casing; it was tested in all the three locations.

A suitable analog-digital electronic system was used. It enabled appropriate signal conditioning, band-pass filtering, modulation analysis by linear detection with low-pass filtering, periodic signal extraction, correlation analysis, and two types of spectrum analysis—power spectrum density and amplitude spectrum estimation, all with averaging either fixed in time or synchronized with the shaft rotation, and with averaging in the frequency domain resulting either in a fixed narrow-band or fixed relative-band resolution. For the synchronization, an angle encoder coupled with the turbine shaft was used.

At various turbine power values, the system was checked with regard to the reproducibility of the measurement results. Stable deterministic functions, reproducible within the limits of random errors due to a finite averaging time, were found. As to the background noise coming from the electronics, from the non-vibro-acoustical sources in a turbine, and from the other turbines, the situation was also found acceptable. At the power net frequency and its lower harmonics, the disturbances are domineering. At the other frequencies, especially those above 1 or 10 kHz, the contribution of what is considered to be cavitation is dominant. Here, the circumstances depend on the turbine power: at high power values the useful high-frequency components are fully free of disturbances, but their spectra gradually converge to flow noise spectra when the turbine power is decreased. The usable frequency/power range was found to be sensor-dependent.

Measurement and Analysis

Measurement Results. Mean narrow-band noise spectra measured in turbines are illustrated in Figs. 3 and 4, and modulation waveforms of the high-frequency noise in Fig. 5. Two sensors are presented—the accelerometer in the internal location and the hydrophone in the outermost one. The modulation was derived from the accelerometer signals at $P = 6$ MW,

---

[1] The work was done within the project KRO ENG 1 supported by the German Ministry of Research and Technology and administered by the GKSS-Forschungszentrum Geesthacht and the KFA-Forschungszentrum Jülich, and the project 2-05-408 supported by the Croatian Ministry of Science and Technology. The paper was presented at the International Symposium on Cavitation CAV'95, Deauville, France, May 1995.

Contributed by the Fluids Engineering Division for publication in the JOURNAL OF FLUIDS ENGINEERING. Manuscript received by the Fluids Engineering Division July 20, 1995; revised manuscript received January 2, 1996. Associate Technical Editor: L. Nelik.

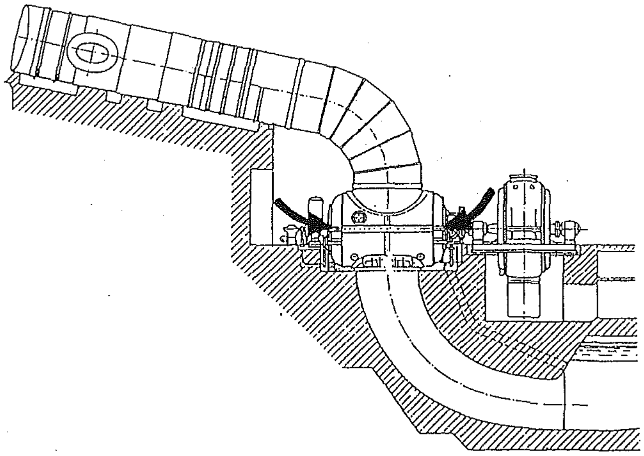

Fig. 1 Machinery outlook

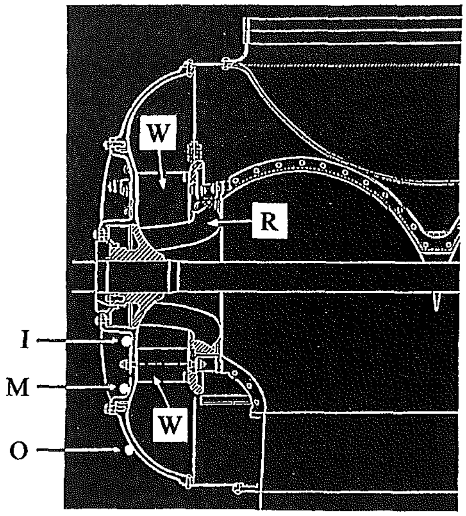

Fig. 2 Cross-section of a turbine: W—wicket gate, R—runner; I, M, O—locations of the sensors

in the frequency range 30–70 kHz (denoted in Fig. 3). The modulation spectra derived from these high-frequency signals are given in Figs. 6 and 7. Some results of suction-side pressure measurements are given in Fig. 8, and some data related to the influence of the sensor position in Fig. 9.

As it is seen in Figs. 3 and 4, the noise spectra have a highly pronounced resonant structure in the frequency band above 1 kHz. (The lines at lower frequencies in Fig. 3 are due to disturbances.) Although the resonances are sharper and stronger in the acceleration signals, they are present also in the pressure signals picked up by means of the hydrophone. Only one of all these lines can be attributed to the sensor characteristics—the one lying at the resonant frequency of the accelerometer. Since no narrow-band vibro-acoustical sources exist in turbines at such high frequencies, the resonances have to be attributed to the transfer functions between the source and the sensor. The same holds for a part of the monotonous trend of the noise spectra form.

The broad-band character of the input high-frequency signals is proved also by the pulse form of the amplitude modulation waveform in Fig. 5(a). Moreover, such randomly appearing short pulses are characteristic of cavitation. Thus, the high-frequency components of the spectra in Figs. 3 and 4, above 1

Nomenclature

$a(t)$ = signal picked up by the accelerometer
$C(P) = C(P, P_o, f)$
$= 10 \log (\Gamma(f, P)/(\Gamma(f, P_o))$
= normalized cavitation source level
f = signal frequency, modulation frequency
f_o = runner revolution frequency
$G_x = G_x(f, P)$
= power spectrum density of $x(t)$
G_o = reference in power spectrum level: 1 μPa^2/Hz, 1 (m/s^2)^2/Hz, 1 for $x(t) = p(t)$ or $s(t)$, $a(t)$, $m_a(t)$, respectively
I = internal location of a sensor (Fig. 2)
k = harmonic order (k: k times per revolution)
$l_x = l_x(k) = 20 \log (\mathcal{M}_x(k))$
= amplitude order-spectrum level of $M_x(\theta)$
$L_x = L_x(f, P)$
$= 10 \log (G_x(f, P)/G_o)$
= power spectrum level of $x(t)$
$\mathcal{L}_x = \mathcal{L}_x(f, P, P_o)$
$= 10 \log (G_x(f, P)/G_x(f, P_o))$
= normalized power spectrum level of $x(t)$
$\mathcal{L}_{xb} = \mathcal{L}_{xb}(f, P_o)$
= background noise component of $\mathcal{L}_x(f, P, P_o)$
$\mathcal{L}_{xl} = \mathcal{L}_{xl}(f, P_o)$
= lower level limit of direct applicability of $\mathcal{L}_x(f, P, P_o)$
$m_x(t)$ = amplitude of $x(t)$ normalized to a mean value 1
M = mid-location of a sensor (Fig. 2)
$M_x(\theta)$ = periodic component of $m_x(t)$ $= m_x(\theta/(2\pi f_o))$
$\mathcal{M}_x(k)$ = amplitude order-spectrum of $M_x(\theta)$
O = outermost location of a sensor (Fig. 2)
$p(t)$ = signal picked up by the hydrophone
P = turbine power
P_o = reference P-value
r = number of runner blades
$s(t)$ = suction-side pressure fluctuations
t = time variable
T = runner revolution period
$T_x(f, P)$ = source-to-sensor transfer function related to $x(t)$
w = number of wicket-gate blades
$\Gamma(f, P)$ = cavitation source strength: free-field unit-distance power spectrum density of the hydro-acoustic pressure generated by cavitation
θ = angular position of the runner

Turbine Data

Powerplant (Fig. 1) = Kraftwerk III of SKW-Trostberg, Germany-four turbines
Type (Figs. 2) = double runner Francis
Maximum turbine power = 6.75 MW
Maximum efficiency power = 5.5–6.0 MW
Discharge = 23 m^3/s
Net head = 38 m
Suction head = 5.1 m
Runner diameter = 1.36 m
Revolution frequency, f_o = 500 min^{-1}
Number of wicket-gate blades, w = 20
Number of runner blades, r = 15

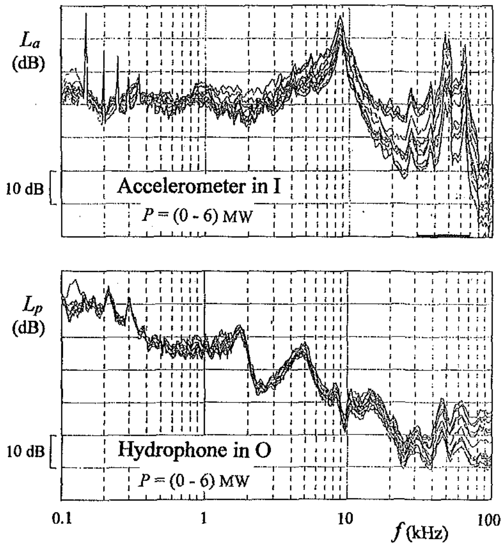

Fig. 3 Noise power spectra recorded at a turbine at different power values

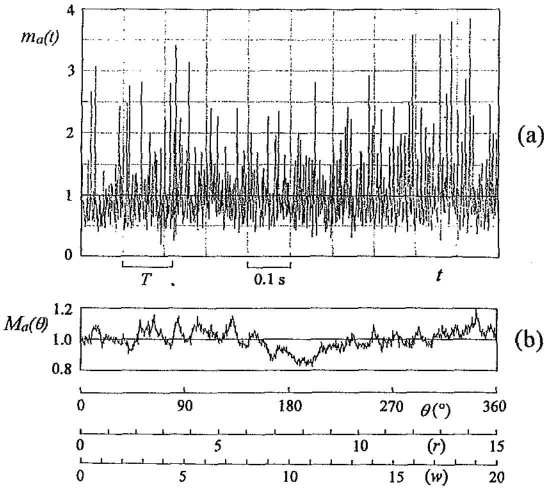

Fig. 5 Illustration of amplitude modulation waveforms of high-frequency noise: (*a*) total waveform, (*b*) periodic modulation

kHz when measured by means of the accelerometer and above 10 kHz by the hydrophone, where the influence of the turbine power change is felt, may be, at least partly, attributed to cavitation.

Modulation. The idea that the measured high-frequency signals are originating from cavitation is supported by the modulation spectra too. Indeed, as is seen in Fig. 5, there is periodicity in the time/angle dependence of the noise intensity, and it follows the rhythms characteristic of cavitation:

1—once per revolution period, one or a group of exceptional runner blades react to the up/down inflow unsymmetry,

r and harmonics, all the r blades of the runner react to this unsymmetry,

w and harmonics, the exceptional runner blade reacts to the inflow disturbances produced by the blades of the wicket gate.

A further possible rhythm, $k = rw$, which comes at 2.5 kHz, was not detected in the present case. Even if observable, it was suppressed by the low-pass filter in the detector; the limit frequency of this filter was set at 1 kHz.

Therefore, the characteristic modulation rhythms which reproduce the influence of the inflow irregularities and the irregularities of the runner and the wicket gate are detected: although hardly readable in the modulation waveform (see the two lower scales in Fig. 5(*b*)), they are rather clearly observable in the spectrum of the periodic modulation component (Fig. 6). However, as can be seen in the power spectrum of the total modulation signal presented in Fig. 7, the related spectrum lines are relatively weak. This does not seem to be in accordance with the idea of using the unsteadiness of the acoustic power generated by the turbine as an indicator of the cavitation erosion rate (Abbot, 1989).

In the total modulation spectrum there is an additional line at 1 Hz. The origin of this line is explained by the results of suction-pressure measurements. Some of these are given in Fig. 8. The upper spectrum in this figure is related to the same situation as in Figs. 5–7. The arrows in Figs. 7 and 8 denote the same process: the modulation of high-frequency noise in the rhythm of 1 Hz has its origin in the fluctuations of the suction-side pressure. To put it formally: the pressure fluctuations result in the changes of the cavitation number.

As expected, the periodic instability of the suction-side pressure is flow-rate dependent. This can be seen in Fig. 8: the hump at 1 Hz at the power of 6 MW is shifted to ca 0.4 Hz at 2 MW. As to the other possible rhythms of this process, only a weak trace of the once-per-revolution period of the up/down in-flow inhomogeneity was detected.

Sensor Position Influence. The results obtained by the accelerometer in different locations, which are, in a version with strong averaging in the frequency domain, illustrated in Fig. 9, also proved useful concerning the cavitation identification. The related narrow-band spectra were found similar to those in Figs.

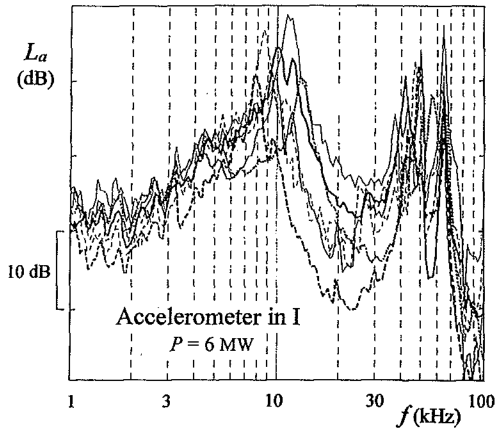

Fig. 4 Turbines/runners comparison at the same power

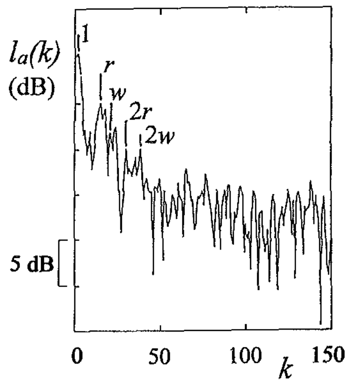

Fig. 6 Spectrum of the periodic modulation waveform of Fig. 5(*b*)

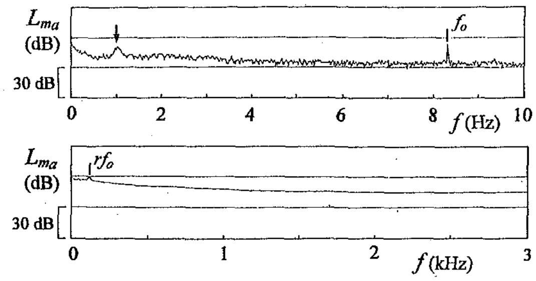

Fig. 7 Spectrum of the total amplitude waveform of Fig. 5(*a*)

3 and 4. The resonances were pronounced, but the details of the spectrum form were different. While these differences can be attributed to the differences in the energy paths, the general trend of spectra, with stronger power influence at higher frequencies, shows that the noise components in this frequency range are, in all the sensor locations, generated by cavitation. The mean trend of the amplitude dynamic range, denoted by the arrows in Fig. 9, enables a rough estimation of the location of the cavitation noise sources. Indeed, as the sensor approaches the turbine shaft, i.e., the runner, the contribution of the power-dependent component of noise becomes more pronounced. Thus, as expected, in the considered turbine the cavitation was located at the runner or in its vicinity.

Spectrum Normalization

Concept. As demonstrated above, at high enough values of the turbine power, P, high-frequency portions of the measured spectra, $G_a(f, P)$ and $G_p(f, P)$, of the turbine casing acceleration, $a(t)$, and the acoustic pressure in water at the runner's pressure side, $p(t)$, can be rather safely attributed to a broadband source describing the cavitation at the runner or in its vicinity. This implies that the resonant character of the spectra is due to sensor characteristics and vibro-acoustical characteristics of the turbine structure, i.e., of the (acoustically) closed water volumes, the metallic structure itself, and the hydroelastic interplay of water and the structure. Thus, both measured spectra can be derived from the same source strength spectrum, $\Gamma(f, P)$,

$$G_a(f, P) = |T_a(f, P)|^2\Gamma(f, P),$$
$$G_p(f, P) = |T_p(f, P)|^2\Gamma(f, P), \qquad (1)$$

by means of the appropriate transfer functions, $T_a(f, P)$ and $T_p(f, P)$, which include both measurement set and turbine characteristics. In order to incorporate the influence of the variable opening of the wicket gate, these functions have to be understood as dependent on the turbine power. However, if this dependence is neglected,

$$T_a(f, P) \approx T_a(f, P_o),$$
$$T_p(f, P) \approx T_p(f, P_o), \quad P_o = \text{const.}, \qquad (2)$$

one obtains a simple model of the process, which results in

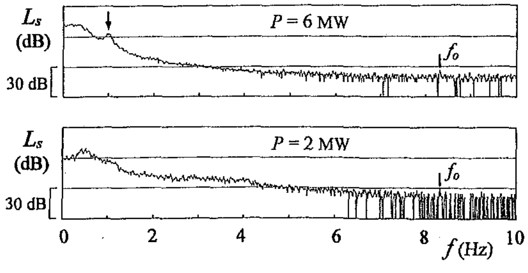

Fig. 8 Spectra of the suction-side pressure fluctuations

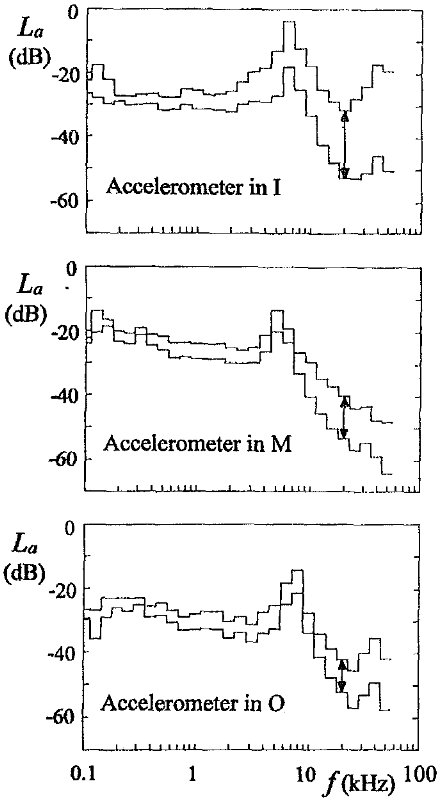

Fig. 9 Maxima and minima of the noise spectra ($\frac{1}{3}$-octave resolution) recorded by means of the accelerometer in the three locations at turbine power between 0 and 6 MW

$$C(P, P_o, f) \approx \mathcal{L}_a(f, P, P_o) \approx \mathcal{L}_p(f, P, P_o), \qquad (3)$$

for

$$C(P, P_o, f) = 10 \log (\Gamma(f, P)/\Gamma(f, P_o)),$$

where

$$\mathcal{L}_a(f, P, P_o) = 10 \log (G_a(f, P)/G_a(f, P_o))$$

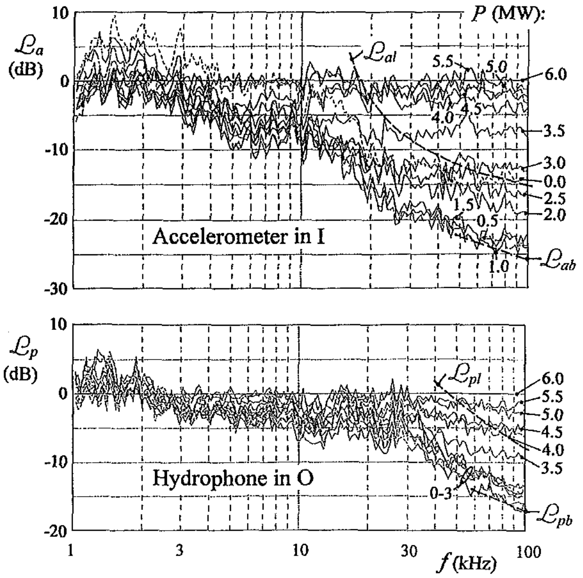

Fig. 10 Normalized spectra (reference power 6 MW)

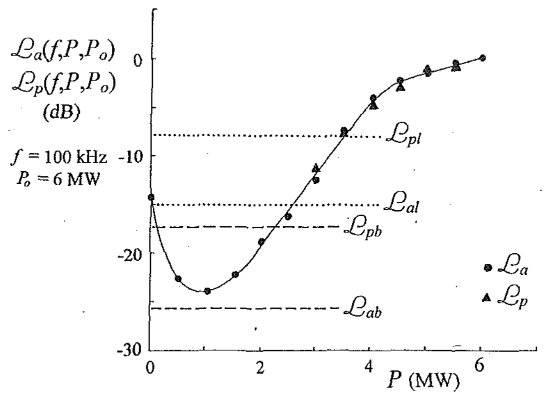

Fig. 11 Power dependence of the high-frequency components of the normalized spectra collected by means of two sensors

and

$$\mathcal{L}_p(f, P, P_o) = 10 \log (G_p(f, P)/G_p(f, P_o))$$

are normalized spectra derived from the measured ones, P_o is the reference power value, and $C(P) = C(P, P_o, f)$ is the normalized cavitation source level.

The natural way to define the cavitation source strength $\Gamma(f, P)$ is to relate it to the hydroacoustic pressure generated by the cavitation and to calibrate it as the power spectrum density of the hydroacoustic pressure which would be measured at a unit distance from the source in an acoustically free field.

If justified, the model (3) may be quite useful: by rejecting the transfer function influence, it suppresses the irrelevant data on the measurement method and, through the normalized spectra, reveals in $C(P, P_o, f)$ free data on the cavitation. Here, however, the form of the cavitation noise spectrum is lost, and only the frequency distribution of its dependence on the turbine power is preserved. Although limited in their content, such data may prove useful or even sufficient in a process of diagnosing the cavitation in a turbine.

The spectrum normalization procedure (1)–(3) is justified only for a source to which the transfer function implicitly built in the reference spectrum is related. The spectrum measured at the maximum achieved turbine power is a good choice for such a reference, since in that spectrum cavitation noise can be expected to dominate in the broadest frequency band, ensuring the proper transfer function to be relevant. As to the results obtained at lower power values, only those derived from spectra or parts of spectra in which background noise contribution is negligible may be considered correct. However, if an estimate of the background-noise contribution to the measured or normalized spectra is available, the range of results applicability can be broadened: instead of using the direct estimates (3), one can derive the normalized cavitation source level according to

$$C(P, P_o, f) \approx 10 \log (10^{\mathcal{L}_a(f,P,P_o)/10} - 10^{\mathcal{L}_{ab}(f,P_o)/10}),$$

$$C(P, P_o, f) \approx 10 \log (10^{\mathcal{L}_p(f,P,P_o)/10} - 10^{\mathcal{L}_{pb}(f,P_o)/10}), \quad (4)$$

where the background components, $\mathcal{L}_{ab}(f, P_o)$ of $\mathcal{L}_a(f, P, P_o)$ and $\mathcal{L}_{pb}(f, P_o)$ of $\mathcal{L}_p(f, P, P_o)$, are assumed uncorrelated with cavitation components, and are rejected.

Check. The normalized spectra derived from the measured spectra of Fig. 3 are shown in Fig. 10. The lower dashed curves in both groups of spectra in Fig. 10 denote the estimates of the background noise, $\mathcal{L}_{ab}(f, P_o)$ and $\mathcal{L}_{pb}(f, P_o)$, and the upper ones, $\mathcal{L}_{al}(f, P_o)$ and $\mathcal{L}_{pl}(f, P_o)$, the limits above which the background-noise contributions may be considered negligible and thus the data may be used directly. It is obvious that the data collected by means of the accelerometer in the I-position are wider in scope than those obtained by means of the hydrophone in O, that at both sensors the results at and about 100 kHz are the best choice for further considerations, and that signals at frequencies above 100 kHz would render even more stable results.

A comparison of the raw spectra (Fig. 3) and the normalized ones (Fig. 10) shows that the resonant structure of the former is efficiently eliminated by the normalization, and that even the components in the 80–100 kHz band, which lie outside the nominal working range of the accelerometer and are highly suppressed in the raw form, comply in a smooth way with a general trend of the normalized spectra. As to this trend, the power dependence of the cavitation source strength appears to be quite uniform in a given frequency range. Indeed, within the range of applicability of the results, the values of $\mathcal{L}_a(f, P, P_o)$ and $\mathcal{L}_p(f, P, P_o)$ are almost constant in f; the remaining fluctuations are mostly due to the finite averaging. Also the regularity expressed by (3) or (4), that both sensors must yield the same normalized result, is verified within the limits of the accuracy imposed by random errors. This is shown in Fig. 11, where the two sensors are compared. (Here, a systematic error of 2 dB in the spectrum level recorded by means of the hydrophone at 6 MW was corrected.)

As to the three locations of the accelerometer, the I-location, shown in Fig. 10, was the best. In the O-location similar normalized data were obtained by means of both the accelerometer and the hydrophone. The M-location proved unsuitable for the spectrum normalization processing: at some values of the turbine power, the wicket gate, which lay too close to the sensor, distorted the transfer function too strongly for the assumption (2) to be justified.

Application. An example of the final form of data, prepared for interpretation, is given in Fig. 12. Here, the background-noise estimates, denoted by the dashed-line curves in Fig. 11, together with the raw normalized spectra of Fig. 10, are used in (4) in order to produce the normalized source level of the turbine cavitation, $C(P, P_o, f)$. The values resulting from the measurements, presented by dots, are thus referenced to P_o = 6 MW, and are read at f = 100 kHz. The choice of P_o determines only the position of the zero-decibel point and is thus irrelevant, and the nominal f-value also introduces only a formal limitation. Indeed, as can be seen in Fig. 10, the physical mechanism which governs the process functions so that, at least within the frequency range covered by the stable results, there is apparently no frequency dependence. Thus, $C(P, P_o, f)$ may be interpreted as a simple function of the turbine power, $C(P)$.

The empirical interpolation presented by the solid-line curves in Fig. 12 shows that in a turbine considered, three cavitation-related ranges of the turbine power can be identified, transition

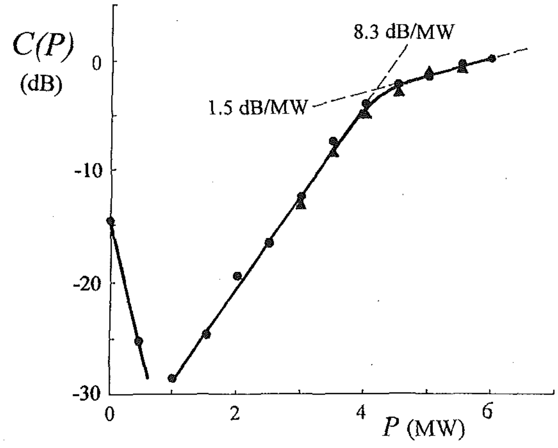

Fig. 12 Final result: Power dependence of cavitation source strength estimated by the spectrum-normalization method

between them falling at ca 0.8 MW and ca 4.1 MW. It seems plausible to relate them to three types of cavitation.

The peculiar effect at the low-power values may be explained by the cavitation provoked by a dramatical rise of the angle-of-attack resulting from the unfavorable form of the flow through the almost closed wicket gate or, possibly, by the cavitation at the wicket gate itself. Here, certainly, the most pronounced distortion of the vibro-acoustical transfer functions my also be expected; this would make the normalized results unusable. However, the acoustical consequences of the gate closure would result in a decrease of the vibro-acoustical intensity and not in its increase. Thus, even if not correctly estimated quantitatively, the rise of the intensity below 0.8 MW has to be attributed to the cavitation.

While these low-power effects have a minor practical importance since such low power values are rarely used, the effects described by the other two lines with different slopes, may have to do with erosion. Here a maximum of applicability of the present method is reached: two cavitation forms seem to be identified at higher powers, and the power value at which they replace one another is determined. If this conclusion is accompanied by the fact presented by Fig. 4, that different turbines and runners, although nominally identical, have strongly different vibro-acoustical signatures, the full potential of the method can be evaluated. In the present case the results of the vibro-acoustical survey were used to conceive the working plan of the powerplant, optimized with respect to the risk of cavitation erosion.

Conclusions

The proposed and successfully checked simple method of processing data collected in vibro-acoustical diagnostic measurements of hydroturbine cavitation - spectrum normalization, efficiently suppresses the influence of sensor characteristics or turbine vibro-acoustical characteristics and yields an estimate of the dependence of the cavitation intensity on the turbine power as a function of the frequency of vibroacoustical energy. The sensor type, its characteristics and its location influence only the width of the range in the turbine power-frequency-cavitation intensity diagram in which results are directly interpretable. It is recommendable to use such a measurement configuration which enables the efficient noise transmission from the cavitating water volume to the sensor, and suppresses the transmission changes due to variable turbine elements like the wicket gate.

The presented measurement procedure based on an accelerometer mounted at the turbine casing and a combined signal analysis, which comprises modulation analysis and analysis of hydrodynamic pressure fluctuations, proved useful for the identification of cavitation components of the vibro-acoustical signature of the turbine. The signal components above 10 or even 100 kHz were found optimal for cavitation diagnostics; the spectrum normalization technique makes useful also the spectrum components which fall outside the nominal working range of the sensor.

No evidence was found which would support the assumption that the unsteadiness of the cavitation vibro-acoustical field intensity could be used as an indicator of the cavitation erosion intensity. In the considered case, although erosive, cavitation was not accompanied by strong modulation.

Acknowledgment

The measurements in the powerplant were generously enabled by the SKW Trostberg AG. The authors acknowledge this support, and are especially grateful to the team of the SKW Kraftwerk III for the help during the measurements. The authors are grateful to Mr. P. Bourdon of IREQ for a critical remark related to the interpretation of modulation results.

The first author is grateful to Dr. A. Keller and Professors Th. Strobl and J. Knauss, and to other members of the staff of the Obernach Laboratory for their hospitality. The authors acknowledge the help of Miss H. Kriner in producing the final form of the paper.

References

Abbot, P. A., 1989, "Cavitation Detection Measurements on Francis and Kaplan Hydroturbines," *Proceedings of the International Symposium on Cavitation Noise and Erosion in Fluid Systems,* San Francisco, CA, American Society of Mechanical Engineers FED-Vol. 88, pp. 55–61.

Bourdon, P., Simoneau, R., Lavagne, P., 1989, "A Vibratory Approach to the Detection of Erosive Cavitation," *Proceedings of the International Symposium on Cavitation Noise and Erosion in Fluid Systems,* San Francisco, CA, American Society of Mechanical Engineers, FED-Vol. 88, pp. 103–109.

Pearsall, I. S., 1966, "Acoustic Detection of Cavitation," *Symposium on Vibrations in Hydraulic Pumps and Turbines,* Manchester, England, *Proceedings of Institute of Mechanical Engineers,* 1966–67, Vol. 181, Pt 3A, pp. 1–8.

Varga, J. J., Sebestyen, G., and Fay, A., 1969, "Detection of Cavitation by Acoustic and Vibration-Measurement Methods," *La Houille Blanche,* Vol. 24, No. 2, pp. 137–149.

Interaction Between Sprays From Multiple Coaxial Airblast Atomizers

Y. Hardalupas
Engineering, Physical Sciences Research
Council Advanced Research Fellow.

J. H. Whitelaw
Professor.

Imperial College of Science, Technology
and Medicine,
Mechanical Engineering Department,
London SW7 2BX, United Kingdom

Phase Doppler measurements of size, velocity, liquid flux, and average mass fractions were obtained in sprays produced by three identical coaxial airblast atomizers, with their axes placed in a triangular arrangement at distances of two air jet diameters from each other; the arrangement simulates the spray interaction in the preburner of the space shuttle main engine with water and air respectively replacing the liquid oxygen and hydrogen of the preburner sprays. Each nozzle comprised a liquid jet with exit diameter of 2.3 mm centred in a 8.95 mm diameter air stream. Two liquid flowrates were examined, while the air flowrate was kept constant, resulting in Weber number at the exit of the nozzle around 1100, air-to-liquid momentum ratio 8.6 and 38, velocity ratio 24 and 51, mass flowrate ratio 0.35 and 0.75, liquid jet Reynolds number 10,000 and 21,000 and air jet Reynolds number around 108,000. The air flow characteristics were compared to the flow without liquid injection. Up to 10 air jet diameters from the nozzle exit, individual spray characteristics dominated and maximum Sauter mean diameters, typically around 150 μm, and liquid flux were observed on the geometrical axes of the nozzles. Spray merging was strong in the region between the nozzle axes, where the Sauter mean diameter reduced and the liquid flux and the mean and rms of the fluctuations of the axial velocity of the droplets and the air flow increased relative to the single spray. Downstream of 25 air jet diameters from the nozzle exit, the multiple sprays merged to a single spray-like flow produced by a nozzle located at the centre of the triangular region between the nozzle axes. Reduction of the liquid flowrate by 50 percent, improved atomization by 25 percent, shortened the axial distance from the nozzles where the individual spray characteristics disappeared by 30 percent and increased the air flow turbulence by 20 percent. Droplet coalescence was negligible for high liquid flowrates, but for reduced liquid flowrates coalescence became important and the Sauter mean diameter increased with the axial distance from the exit by around 15 percent. Spray merging increased the air flow turbulence and the local mass fraction distribution of the air in the region between the nozzle axes by around 50 and 40 percent respectively relative to the single sprays, resulting in a fuel rich region with increased gas flow turbulence which may influence the ignition process in the preburner of the space shuttle main engine.

1 Introduction

The atomization of liquid oxygen by a high velocity coaxial hydrogen stream is required in the preburner of the main engine of the space shuttle (SSME). The combustion stability of rocket engines has been shown to depend on the geometry of the coaxial injectors and on the gaseous and liquid injection velocity (Wanhainen et al., 1966) and the combustion efficiency is affected by the size characteristics and the spray width (Priem and Heidman, 1959), since both parameters affect the evaporation of the oxidizer and its mixing with the fuel. The characteristics of the sprays produced by single coaxial injectors have been studied extensively and the findings of early studies, based on spray angle and mean droplet size averaged over the spray rather than local values, have been reviewed by Ferrenberg et al. (1985) and Lefebvre (1989) and empirical correlations between droplet mean diameters and nozzle operating conditions have been suggested, for example Kim and Marshall (1971), Lorenzetto and Lefebvre (1977), although their ability to predict the spray characteristics of different nozzle geometries and over a wide range of conditions is limited, Ferrenberg et al. (1985). The parameters affecting atomization such as the velocity, density, viscosity and surface tension of the gas and the liquid and the geometry of the nozzle, are commonly expressed as nondimensional numbers, e.g., exit Weber number, gas-to-liquid ratios of velocities, mass flowrates and the momentum fluxes and Reynolds numbers of the gas and the liquid jet. The exit Weber number is defined:

$$\mathrm{We}_{exit} = \frac{\rho_g (U_{gas} - U_l)^2 D_l}{\sigma} \tag{1}$$

where ρ_g is the gas density, $U_{gas} - U_l$ is the relative velocity between the gaseous and the liquid jets at the exit, D_l is the diameter of the liquid jet exit, and σ is the surface tension. The gas-to-liquid mass flowrate, momentum and velocity ratios are:

$$\mathrm{MFR} = \frac{\rho_g U_{gas} (D_{gas}^2 - D_{le}^2)}{\rho_l U_l D_l^2} \tag{2}$$

$$\mathrm{MR} = \frac{\rho_g U_{gas}^2 (D_{gas}^2 - D_{le}^2)}{\rho_l U_l^2 D_l^2} \tag{3}$$

$$\mathrm{VR} = \frac{U_{gas}}{U_l} \tag{4}$$

Contributed by the Fluids Engineering Division for publication in the JOURNAL OF FLUIDS ENGINEERING. Manuscript received by the Fluids Engineering Division, November 15, 1994; revised manuscript received August 22, 1996. Associate Technical Editor: M. W. Reeks.

where D_{le} is the external diameter of the liquid tube and D_{gas} is the gaseous jet diameter. The Reynolds numbers of the gaseous and liquid jets are based on the corresponding diameters and the average velocities U_{gas} and U_l at the nozzle exit.

Early work on sprays made use of droplet capture and imaging techniques (Weiss and Worsham, 1959) and hot wax freezing (Burick, 1972; Falk, 1975), but accuracy was limited. Optical nonintrusive techniques, such as laser diffraction (Caré and Ledoux, 1991) and the combined visibility and intensity based interferometric technique (Ferrenberg et al., 1985) have allowed more accurate and detailed size measurements, but with inaccuracies due to attenuation of the incident laser beams and the scattered light (Kliafas et al., 1990) in the dense regions of the sprays. Recently, the phase Doppler anemometer has been used successfully to provide local spray characteristics of single coaxial injector elements (e.g., Eroglu and Chigier, 1991; Sankar et al., 1991, 1992; Zaller and Klem, 1991; Hardalupas and Whitelaw, 1994; and Engelbert et al., 1995) with high spatial resolution and better accuracy than previous nonintrusive techniques. Engelbert et al. (1995) correlated the near and far field spray characteristics in an effort to improve the understanding of break-up phenomena and correlated the droplet diameters in the sprays from single atomizers with the air-to-liquid momentum ratio. However, the preburner of the SSME has 260 coaxial injector elements on the faceplate of the combustion chamber at distances of the order of a few nozzle diameters from each other and, although it is expected that the interaction between the sprays may modify their spray characteristics (Ferrenberg et al., 1985), this has not been quantified.

Spray interaction may modify the droplet sizes and velocities and the spatial distribution of the air and the liquid in the sprays relative to the single nozzle spray for the following reasons. The air flow within around 20 liquid jet diameters from the exit of each nozzle may be influenced by the presence of the surrounding flows, resulting in different atomisation characteristics for each nozzle. The merging of the sprays may lead to droplet coalescence and, as a result, increase of droplet diameters with the axial distance from the nozzle exit and in comparison to the single spray. Spray merging may also modify the air flow turbulence and the spatial distribution of the air and the droplets, leading to equivalent modification of the local air-to-fuel ratio relative to the single atomizer.

The purpose of this paper is to quantify spray interaction by reporting measurements of droplet size, air and droplet velocities, liquid flux and local mass fractions in sprays produced by three identical coaxial airblast atomizers with their axes placed at distances of a few nozzle diameters from each other. These measurements quantify atomization and droplet coalescence, air and droplet flow distributions and local air-to-fuel ratio and air flow turbulence. The spray characteristics from a multiple nozzle arrangement are compared with those of the single sprays. The influences of liquid flowrate and axial distance from the nozzle exit on spray characteristics and of the injection of liquid on the mean and turbulent air flow of the multiple nozzles are quantified. The flow configurations, instrumentation, and measurement accuracy are considered in Section 2, which is followed by the presentation and discussion of the results in Section 3. The paper ends with a summary of the more important conclusions.

2 Experimental Arrangement and Instrumentation

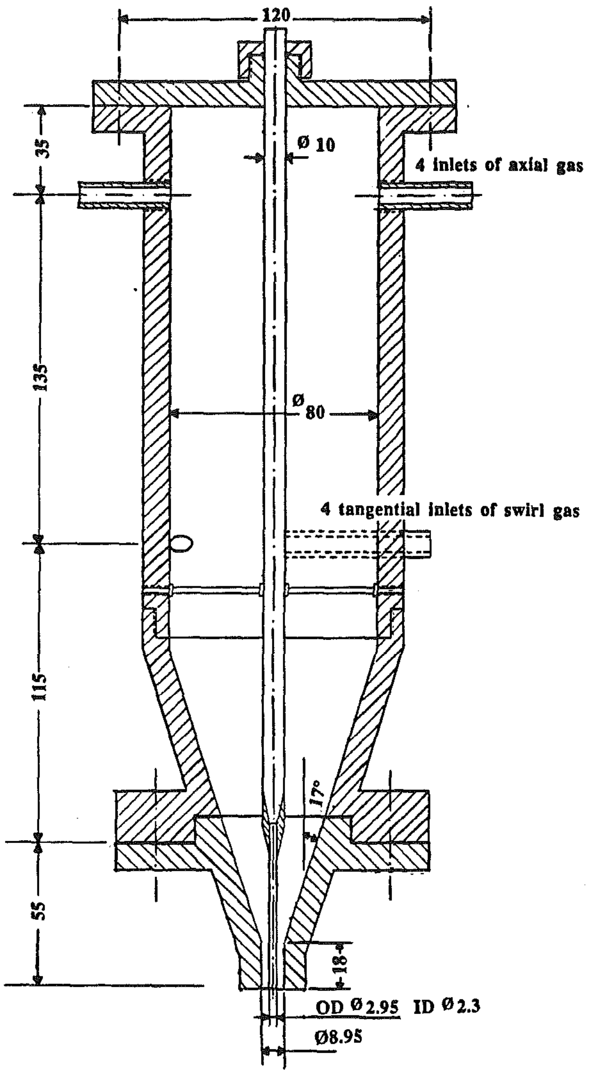

Fig. 1 Geometry and main dimensions of the single coaxial atomizer with 8.95 mm diameter of the air jet

The airblast atomizer of Fig. 1 is geometrically similar to that used in the SSME and with air replacing the hydrogen and water the liquid oxygen of the engine. A central tube, which carried the liquid to the nozzle, had an external diameter of 10 mm with a taper to 2.95 mm with internal diameter D_l of 2.3 mm (0.090 in.) and length to diameter ratio of 22. The air flowrate was supplied by four air inlets with their axes normal to that of the nozzle as shown in Fig. 1. The air flow was accelerated by a conical shape contraction to reduce possible flow asymmetries before the exit. Experiments were carried out with a single nozzle of 8.95 mm diameter, attached at the exit of the air jet and resulting in an annular width of 3 mm. Three nozzles identical to that of the single injector were arranged as in Fig. 2, in a triangle with 18 mm distance between their axes of symmetry. The coordinate system used for the presentation of the results is also shown in Fig. 2. Differences between the air and water flowrates supplied to each of the three nozzles were less than 5% during the tests. The experiment investigated sprays produced by injectors with constant air flowrate corresponding to a velocity, $U_{gas} = 182$ m/s, averaged over the area of the annulus at the exit, and two liquid flowrates resulting in velocity averaged over the area of the liquid jet exit, U_l, of 7.6 and 3.6 m/s, respectively, for cases 1 and 2 of Table 1, where the operating conditions of the sprays and the corresponding non-dimensional numbers are given. In all cases, the exits of the liquid and the air jet were in the same plane. The mean axial velocity profiles in the annulus at the nozzle exit were flat and the boundary layer thickness at the outer edge of the air jet was around 0.7 mm. The corresponding rms of the fluctuations of the axial velocity in the central region of the annulus was around $0.04U_{gas}$ and in the shear layer around $0.3U_{gas}$. The geometry and the operating conditions of the sprays in the SSME are also shown in Table 1 and confirm that the flow

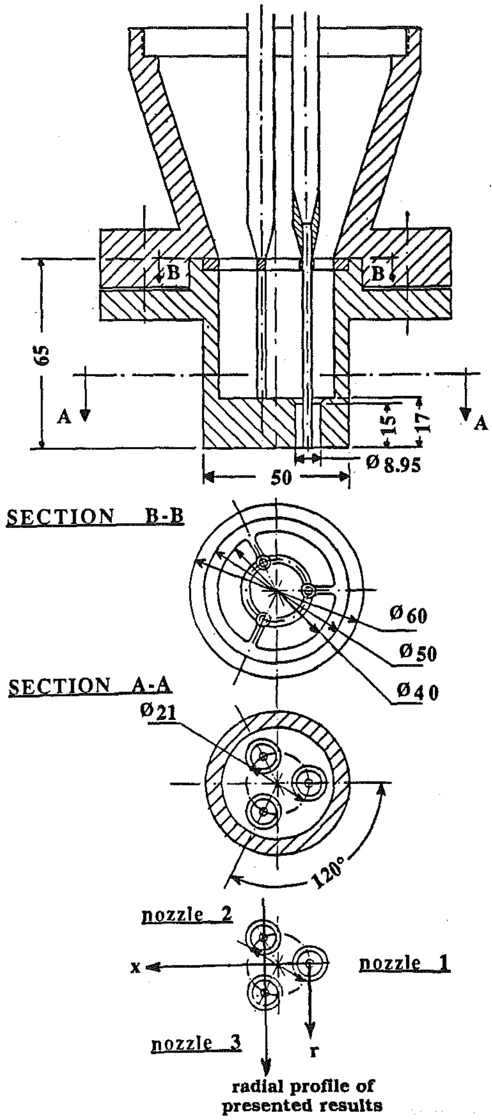

Fig. 2 Geometry of the three identical nozzles attached at the exit of the atomizer of Fig. 1 and the coordinate system used for the study of the multiple spray interaction

conditions were similar, apart from the exit Weber number, which was around one order of magnitude lower in the current experiment. However, this shortcoming is not expected to influence the conclusions from the current work, since the spray characteristics are mainly affected by the air-to-liquid momentum ratio and the nozzle geometry (Engelbert et al., 1995).

Air was supplied to the nozzle by a compressor and metered by a rotameter before passing to a settling chamber from which four tubes led to the axial inlets of the experimental arrangement of Fig. 1. The water was pumped from a tank and the flowrate was adjusted by a valve in the return line of excess liquid to the tank and was filtered to remove inclusions of particles larger than 10 μm. It was, subsequently, metered by a rotameter, which operated at a gauge pressure between 10 and 50 KPa. The atomizer was positioned so that the spray exhausted vertically downwards towards a tank, which collected most of the liquid content of the spray. An exhaust system attached at the side of the collection tank removed the air with the mist of the small droplets generated by the spray. Flow straighteners were positioned at the entrance of the collection tank to ensure that the spray remained undisturbed by the exhaust system. The air rotameters operated at a gauge pressure of 200 KPa and the flow rates were corrected to N.T.P. from calibration charts provided by the manufacturer. The air and water flowrates supplied to the nozzle during the measurements were kept constant within 5 percent. The air flow was occasionally seeded with TiO_2 powder, nominally micron-sized and small enough to trace the air flow, when the velocity characteristics of the air jets were measured without the liquid jets. The refractory powder was dispensed by two reverse cyclone feeders (Glass and Kennedy, 1977), connected at two of the axial inlets of the atomizer.

The velocity, diameter and flux of the liquid droplets were measured by a phase-Doppler velocimeter (Hardalupas, 1989 and 1990), which comprised transmitting optics based on a rotating grating as beam splitter and frequency shifter and integrated receiving optics which collected the light scattered from the measuring volume in the forward direction at an off-axis scattering angle of 30 deg on the bisector plane of the two laser beams to ensure that refraction through the droplets dominated the scattered light. The collected light was focused to the centre of a 100 μm slit and passed through a mask with three evenly spaced rectangular apertures before reaching the three photodetectors. The beam intersection angle of the anemometer was adjusted to allow the measurement of droplet diameters up to 360 μm and the optical characteristics of the instrument are given in Table 2.

The measured size distributions and the mean diameters at each point were based on 20,000 measurements resulting in statistical uncertainties of less than 2 percent (Tate, 1982) and the sizing accuracy was better than 2 μm for droplets larger than 20 μm. The uncertainty is larger for the smaller droplets due to the tolerance of the phase-measuring electronic circuit and the oscillations of the phase shift remaining on the calibration curve of the instrument (Hardalupas, 1989). Droplet velocities were obtained in 60 size ranges of 6 μm with uncertainties of less than 1 and 4 percent for the mean and rms values respectively, based on the average sample size of at least 1000 in each class for the smaller sizes and around 2 and 6 percent for the

Table 1 Dimensions and operating conditions of coaxial atomizers

Operating parameters	Case 1	Case 2	Air only	Preburner sprays of the SSME
Liquid jet diameter OD/ID (mm)	2.95/2.3	2.95/2.3	2.95/2.3	3.76/2.26
Air jet diameter (mm)	8.95	8.95	8.95	4.93
Annular width (mm)	3	3	3	0.585
Distance between spray axes (mm)	18	18	18	25
Air velocity, U_{gas} (m/s)	182	182	182	366
Water velocity, U_l (m/s)	7.6	3.6	0	30.5
Reynolds number air jet	1.1×10^5	1.1×10^5	1.1×10^5	2.1×10^6
Reynolds number liquid jet	2.1×10^4	9.7×10^3	0	4.8×10^5
Exit Weber number We_{exit}	1,050	1,103	—	745,000
Air-to-liquid momentum ratio, MR	8.6	38.1	—	10.6
Air-to-liquid velocity ratio, VR	23.9	50.6	—	12
Air-to-liquid mass flowrate ratio, MFR	0.35	0.75	—	0.84

Table 2 Optical characteristics of the phase Doppler instrument

Transmitting optics	
Laser: He-Ne laser	
operating power	35 mW
wavelength	632.8 mm
Beam intersection angle	3.024 degr
Measurement volume length at $1/e^2$ intensity	4.88 mm
Measurement volume diameter at $1/e^2$ intensity	129 μm
Fringe spacing	11.991 μm
Number of fringes	11
Frequency shift	3 MHz
Receiving optics	
Focal length of collimating lens	500 mm
Location of receiving optics from forward scatter angle	30 degr
Equivalent aperture at collimating lens:	
dimension of rectangular aperture	67 × 10.6 mm
separation between aperture 1 and 2	13.3 mm
separation between aperture 1 and 3	26.6 mm
Magnification	1/2
Spatial filter slit width	100 μm
Effective length of measuring volume	312.5 μm
Phase angle-to-diameter conversion factor for channel 1 and 3, without rotation of the plane of the beams	0.973 μm/degr

larger droplets due to the smaller sample size for locations where the number density of large droplets was low.

The representative diameters of the sprays were estimated from the temporal size distribution (number/m^2 s), which is related to the flux of liquid droplets, rather than the spatial (number/m^3), which is related to the number density of the droplets, as explained by Bachalo et al. (1988) and Hardalupas and Taylor (1989). The liquid flux is a conserved quantity and is used by current prediction models for the calculations of local droplet characteristics as explained in detail by Dodge et al. (1987). The representative diameters were the Sauter Mean Diameter (SMD) and the Mass Median Diameter (MMD) defined as:

$$\mathrm{SMD} = \frac{\sum_{i=1}^{N} n_i d_i^3}{\sum_{i=1}^{N} n_i d_i^2} \tag{5}$$

$$\mathrm{MMD} = d_{0.5} = \text{diameter carrying the 50 percent of the cumulative mass flux} \tag{6}$$

where n_i is the number of measurements in the size interval "i" which corresponds to a droplet diameter d_i and N is the total number of intervals. The overall statistical and measurement uncertainty of the mean diameter is expected to be around 5 percent.

The volume flux (m^3 of liquid/m^2 s) of the liquid droplets was measured according to the method of Hardalupas and Taylor (1989) and did not involve droplets larger than the 360 μm set by the size range of the instrument. Uncertainties in the measurement of flux of liquid droplets in sprays have been discussed by Dodge et al. (1987), Bachalo et al. (1988), Hardalupas and Taylor (1989), and Hardalupas et al. (1994), although not in a conclusive way. The size distributions indicated that the number of droplets larger than 300 μm was at least two orders of magnitude smaller than the maximum probability for most of the measurements, so the error to the flux measurement due to the contribution of droplet sizes larger than 360 μm was negligible. The rejection of measurements by the validation procedure of the instrument was larger in the dense region of the spray due to attenuation of the laser beams and occurrence of multiple droplets in the probe volume and resulted in systematic reduction of the flux measurements. At axial distances of around $15D_{gas}$ from the nozzle exit of a single atomizer, the estimated values of the liquid flowrate after integration of the measured radial profiles of liquid flux was around 20 percent lower than the liquid flowrate measured by the rotameter, which is expected from the uncertainties of the phase Doppler instrument in the measurement of the liquid flux (Hardalupas et al., 1994). For this reason, the radial profiles of flux are presented as relative values after normalisation by the local maximum value, as measured by the instrument, and the relative flux is likely to be precise to within 20 percent.

The local average mass fraction f of the gas was defined as:

$$f = \frac{\rho_g U_{gas}}{G + \rho_g U_{gas}} \tag{7}$$

where G and $\rho_g U_{gas}$ are the local liquid and gas fluxes, respectively, and ρ_g is the density of the air. The uncertainties involved in this estimate were of the order of 20 percent, caused by uncertainties in the measurement of the fluxes. The mass fraction of a compound in a mixture quantifies its mass transfer through an area of the flow (Spalding, 1963) and the sum of the mass fractions of the compounds in the mixture should equal unity. The definition of Eq. (7) corresponds to the mass fraction of the fuel, since in the preburners of the SSME the liquid phase corresponds to the oxidiser and the gas to the hydrogen fuel.

Air flow velocities without liquid injection were obtained by seeding the flow with TiO_2 powder and operating the phase Doppler as a laser Doppler system, and the uncertainties were around 1 and 3 percent for the mean and rms values based on the average sample size of 4000. Biasing of the air flow velocity measurements due to lack of seeding particles or small droplets in the air surrounding the sprays was negligible for the mean velocity, and reduced the rms of the velocity fluctuations by less than 5 percent, for measurements at distances larger than around $15D_{gas}$ from the nozzle exit (Schefer et al., 1987). The air flowrate obtained by integration of the radial profile of mean axial velocity of the air flow measured at the exit of the single nozzle was within 15 percent of that measured by the rotameters; this agreement was as good as can be expected with the uncertainties involved in the integration procedure.

3 Results and Discussion

Axial velocity characteristics of droplet sizes in the ranges 6–12 μm and 102–108 μm are referred as 9 and 105 μm in the rest of the text. The 9 μm droplets followed the mean and turbulent flow characteristics of the air flow faithfully at the location of the measurements and the 105 μm droplets indicated the motion of the large droplets, which carried most of the liquid volume flux and did not respond to the air flow. The response characteristics of the droplet sizes to the air flow are evaluated in terms of the mean and turbulent Stokes number, defined as the ratio of the mean flow, T_m, and energy containing eddies, T_e, timescale to the droplet relaxation time, τ, respectively:

$$\mathrm{St}_m = T_m/\tau \tag{8}$$

$$\mathrm{St}_{turb} = T_e/\tau \tag{9}$$

where $T_m = D_{gas}/U_{gas}$ was around 0.06 ms at the nozzle exit and $T_e = L/u'$ (Tennekes and Lumley, 1972) was around 0.04 ms at the nozzle exit, as quantified for length scale of the energy containing eddies $L = 0.1D_{gas}$ and rms of the fluctuations of the velocity vector, u', measured around $0.15U_{gas}$. Values of St_m or St_{turb} larger or around unity imply that droplets can follow the mean or turbulent air flow. The ability of a droplet to respond to the gas flow is characterised by the response time $\tau = \rho_l d^2/18\mu_g$, where ρ_l is the liquid density and μ_g is the dynamic viscosity of the gas. The response time of droplets with diameter 9 μm is around 0.1 ms and suggests that they can respond to

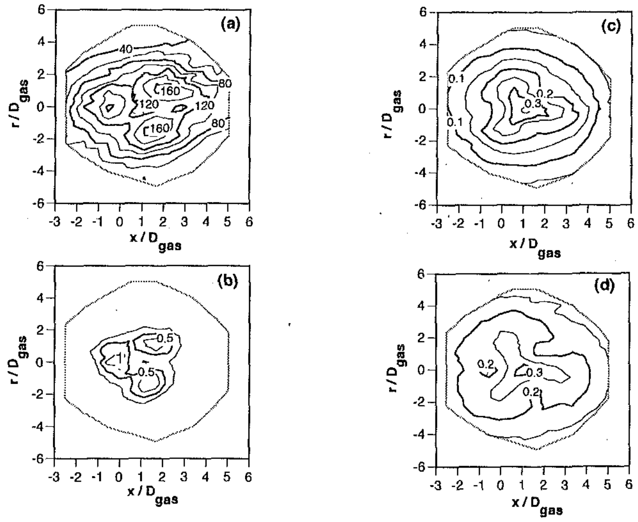

Fig. 3 Contours of (*a*) Sauter mean diameter, (*b*) liquid flux and mean axial velocity of (*c*) 9 μm, and (*d*) 105 μm droplets at axial distance $z/D_{gas} = 23.5$ for flow conditions of case 1 of Table 1

the mean air flow, but not the air flow turbulence at the nozzle exit. The 105 μm droplets did not respond to the air flow since their relaxation time was 15 ms. However, the timescale of the energy containing eddies increased with the axial distance from the nozzle exit, as the air flow developed and the spray width increased, and for a turbulent jet was (Hardalupas et al., 1989):

$$T_e = 3.29 \times 10^{-4}(z/D_{gas})^2(D_{gas}/U_{gas})(u'_{gas}/U_{gas})^{-2} \quad (10)$$

For example from Eq. (10), at $z/D_{gas} = 23.5$ and 33.5 for case 1 of Table 1, $T_e = 0.20$ and 0.30 ms, respectively, and the corresponding turbulent Stokes number for the 9 μm droplets is around 2 and 3 suggesting good response to the air flow turbulence. Therefore, the 9 μm droplets can follow faithfully the air turbulence at the axial stations of the measurements and, as a consequence, they can indicate the turbulence characteristics of the air flow in the presence of the liquid droplets.

The single and multiple spray characteristics were measured at axial distances from the nozzle exit of $z/D_{gas} = 13.4$, 23.5 and 33.5. Since the flow in the multiple spray arrangement was not axisymmetric, the measurements were along the x-direction and along the r-direction for different values of x, as in Fig. 2. The zero value in the x-direction corresponds to the axis of symmetry of nozzle 1, while the axes of nozzles 2 and 3 were at positions $(r/D_{gas}, x/D_{gas})$ of $(-1, 1.68)$ and $(1, 1.68)$, respectively. Detailed spray characteristics are presented along the r-direction at $x/D_{gas} = 1.68$, which passed through the axes of nozzles 2 and 3 and is shown in Fig. 2. Observations in other directions were similar. The mean velocity is normalized by the air velocity averaged over the area of the annulus of a single atomizer, U_{gas}. The radial and axial distances are normalized by the diameter of the air jet, D_{gas}. The radial profiles of volume flux of the droplets are normalized by the local maximum value of the flux, G_m, for the single or the three sprays, as measured by the instrument. The term "single phase" is used in the text for the air flow without injection of liquid. The term "air flow" is used for the characteristics of the 9 μm droplets and indicates the air flow characteristics with liquid injection. The results are presented in two subsections concerned with the comparison between the sprays of the single and multiple atomizer arrangements and the influence of liquid flowrate and axial distance on the spray characteristics of the multiple nozzle arrangements.

(i) Comparison Between the Characteristics of the Single and the Three Sprays Arrangements. The multiple spray characteristics for flow conditions of case 1 of Table 1 are presented in Fig. 3 at z/D_{gas} of 23.5, which confirmed the symmetry of the flow and show that the individual sprays partially maintained their characteristics up to this distance. Figure 3(*a*) shows that maximum values of SMD were around 160 μm on the geometrical axes of the atomizers, where the liquid flux was also maximum. The shear at the interface between the fast moving air jet and the liquid jet at the exit of the nozzles generated small droplets away from the axes of the sprays, which dispersed faster and surrounded the individual sprays and carried a small amount of liquid flux. The larger droplets were generated at the centre after the breakup of the liquid jet, as indicated by the photographic studies of Engelbert et al. (1995), and remained there over a long period of time resulting in larger mean diameters on the axes of the nozzles. However, the sprays interacted mainly at the region between the axes and had larger liquid flux than at the outer region of the flow and SMD values around 120 μm. The contours of the mean axial velocity of the 9 and 105 μm droplets, Figs. 3(*c*) and (*d*), indicate uniform values close to the axes of symmetry of the nozzles and a maximum between them, where increased air flow entrainment accelerated the droplets. At the outer region of the sprays, the large droplets moved faster than the 9 μm droplets due to their inertia.

The comparison between the spray characteristics from multiple and single nozzles was along the direction passing through the axes of nozzles 2 and 3 at $z/D_{gas} = 23.5$, by plotting the single spray characteristics, so that the geometrical axis of the single atomizer coincides with that of nozzle 2 in the multiple spray arrangement. The spray characteristics presented in Fig. 3 suggest that observations in other directions were similar. Figure 4 shows that the characteristics at the outer region, $r/D_{gas} < -2$, of the single and multiple sprays were identical. The mean diameter on the geometrical axes of the nozzles in the three interacting sprays decreased relative to the single spray (Fig. 4(*a*)). The liquid flux profiles for the single or the three sprays, Fig. 4(*b*), show that the width of the individual sprays was not affected in the multiple spray flow and at $z/D_{gas} = 23.5$, the small droplets surrounding the individual spray of nozzle 3 reached the axis of the spray of nozzle 2 and reduced the mean droplet diameter by reducing the relative number of large droplets. The mean diameters in the three sprays were not increased relative to the single spray, which suggests that the influence of droplet coalescence was small during spray merging. The mean and the rms of the fluctuations of the axial velocity of the 9 and 105 μm droplets, Figs. 4(*c*) and (*d*), at the region between the axes of the nozzles, were increased by around two times, respectively, relative to the values of the single sprays, due to spray merging. The similarity between the droplet diameter and velocity characteristics at the outer region, $r/D_{gas} < -2$, of the spray from nozzle 2 and the single spray, Figs. 4(*a*) and (*c*) suggests that the air flow within few nozzle diameters from the nozzle exit was not influenced by the flows of the surrounding nozzles and, therefore, the atomization characteristics of each individual nozzle were not modified.

Figure 4 suggests that the merging of the sprays in the region between the nozzle axes increased the local flux of the air flow faster than the liquid flux, since the large droplets remained over a longer axial distance close to the geometrical axes of the nozzles. The radial distribution of the local mass fraction distribution of the gas at $z/D_{gas} = 23.5$, estimated according to Eq. (7), is presented in Fig. 5(*a*). The local mass fraction in the single spray was low on the axis of the nozzle, where most of the liquid remained, and increased with the radial distance from its axis. In the multiple spray arrangement, the mass fraction increased in the region between the nozzle axes by around 40 percent. The outer region of the sprays had similar mass fractions for the single and the multiple nozzle arrangements confirming that spray merging was mainly responsible for the modification of the single spray characteristics.

(ii) Influence of Axial Distance and Liquid Flowrate on Spray Characteristics. The mean diameters along the r-direction at x/D_{gas} of 1.68, Fig. 6(*a*), show maxima of around

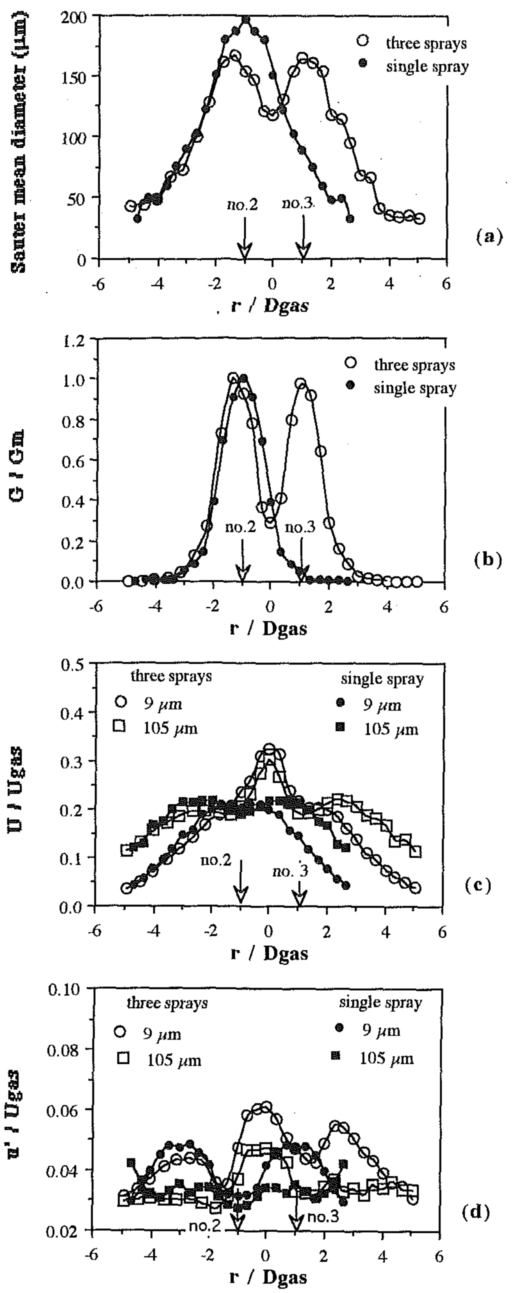

Fig. 4 Comparison between the characteristics of the multiple and single sprays along the *r*-direction at $x/D_{gas} = 1.68$ and axial distance $z/D_{gas} = 23.5$ for flow conditions of case 1 of Table 1; (*a*) Sauter mean diameter, (*b*) the liquid flux, (*c*) mean, and (*d*) rms fluctuations of axial velocity of 9 and 105 µm droplets. The geometrical axis of the single spray has been plotted to coincide with the axis of nozzle 2.

170 and 200 µm for the SMD and the MMD respectively, which occurred on the axes of symmetry of the individual nozzles, which are identified in terms of arrows. The value of the mean diameter at the region between nozzles 2 and 3, $-1 < r/D_{gas} < 1$, was around 120 µm and larger than that at the outer region of the sprays. The mean diameters in the same region remained constant with the increase of axial distance, suggesting negligible influence of droplet coalescence during spray merging. The ratio of the MMD to the SMD was around 1.2, and the size distributions of the sprays followed the root-normal distribution for this ratio as suggested by Simmons (1977) and observed also by Ferrenberg et al. (1985), Lefebvre (1989) and Faeth (1990). The liquid flux profiles of Fig. 6(*b*) show that few droplets existed between the nozzle axes at z/D_{gas} of 13.4, and increased to about 0.7 of the maximum value observed at z/D_{gas} of 33.5. The maxima coincided with the axes of symmetry of the nozzles at the three axial stations. The mean axial velocity of droplets in the region between the axes of the nozzles, Fig. 6(*c*), reached maxima which decreased with increase of droplet size, while minima existed on the axes of the nozzles at z/D_{gas} of 13.4, and gradually disappeared with axial distance. The larger droplets moved faster than the 9 µm droplets at the outer region, $|r|/D_{gas} > 2$, and along straight trajectories defined by their initial conditions (Hardalupas et al., 1989). The slip velocity between small and large droplets was reduced with the axial distance, since the interaction time between droplets and air flow increased. At z/D_{gas} of 33.5, however, the droplet velocity had a single maximum in the central region, so that the droplet velocity characteristics of the individual nozzles had disappeared, while the larger droplets still moved faster than the 9 µm droplets at the outer region. The three sprays could be identified at the last axial distance of the measurements, $z/D_{gas} = 33.5$, in terms of maxima in SMD and liquid flux but not in terms of velocity, which was not, therefore, a good measure of spray development.

Comparison between the velocities of the 9 µm droplets, indicating the characteristics of the air flow in the presence of liquid injection, and the single phase flow shows that the single phase flow developed faster and individual jets could just be identified at z/D_{gas} of 13.4 with a local minimum between the nozzle axes, whereas the 9 µm droplets had a maximum caused by spray merging. This suggests that the increased liquid flowrate delayed acceleration of the air flow close to the axes of each nozzle, since the air flow momentum was used to accelerate the droplets, to allow the characteristics of the individual sprays to be maintained for a longer distance. At the outer region of the sprays, $|r|/D_{gas} > 3$, the 9 µm droplets had velocities similar to those of the single phase, suggesting that the air flow in this region was unaffected by the presence of the liquid jets. Farther downstream, the single phase velocity was similar to that of a

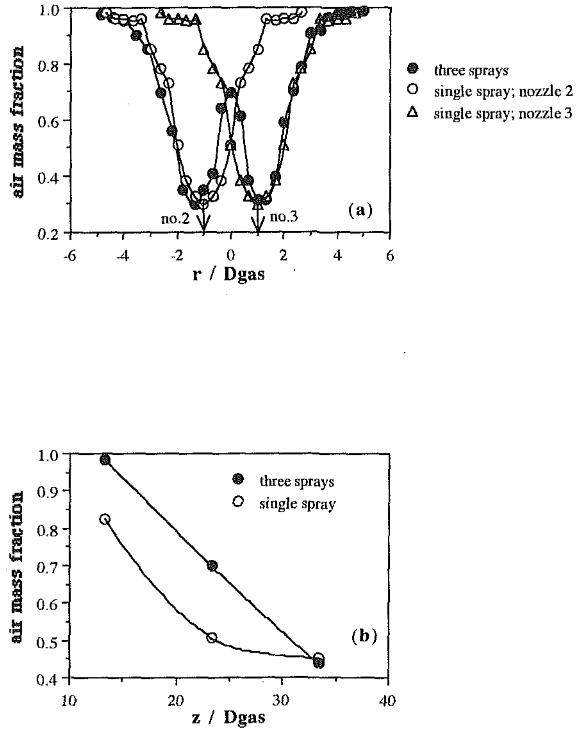

Fig. 5 Comparison between the local air mass fraction of the multiple and single sprays. (*a*) Radial profile along *r*-direction at $x/D_{gas} = 1.68$ and at $z/D_{gas} = 23.5$ and (*b*) along the axial distance from the exit at $(r/D_{gas}, x/D_{gas})$ of (0, 1.68), the middle of the distance between nozzles 2 and 3, for flow conditions of case 1 of Table 1.

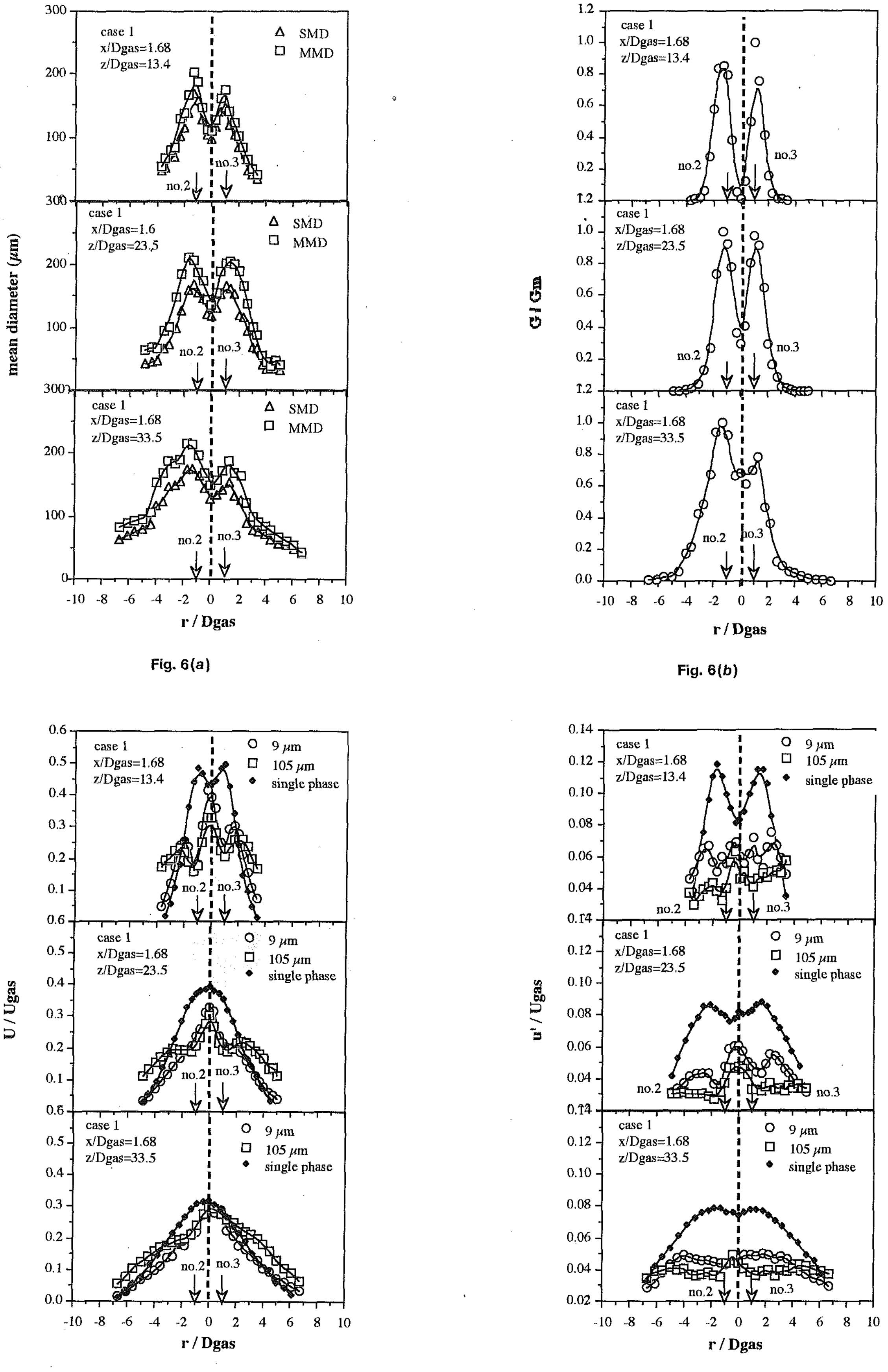

Fig. 6(*a*)

Fig. 6(*b*)

Fig. 6(*c*)

Fig. 6(*d*)

Fig. 6 Radial profiles along the *r*-direction at x/D_{gas} = 1.68 and at axial distances z/D_{gas} = 13.4, 23.5 and 33.5 of (*a*) mean diameters, (*b*) liquid flux, (*c*) mean, and (*d*) rms fluctuations of axial velocity of 9 and 105 μm droplets and single phase flow for conditions of case 1 of Table 1 single jet-like flow with its axis of symmetry at around $x/D_{gas} = 1$, which was the centre of the triangular region between the geometrical axes of the atomizers and at $z/D_{gas} = 33.5$ the air flow was similar to that of the single phase flow.

The rms fluctuations of the axial velocity of the 9 μm droplets were lower on the axes of symmetry of each nozzle, where most of the liquid existed and led to a reduction of the turbulence levels of the air flow, and had local maxima at the region between the axes and towards the outer region of the sprays, $|r|/D_{gas} > 3$, in the shear layers of the jets, Fig. 6(*d*). The similarity of the rms fluctuations of the axial velocity of single and air flow for $|r|/D_{gas} > 3$ at $z/D_{gas} = 13.5$ confirms the ability of the 9 μm droplets to follow the air flow turbulence. The fluctuations of the axial velocity of the large droplets were lower than those of the air close to the nozzle, but became similar farther downstream. This occurred, in contrast to their negligible response to the air flow turbulence, due to the deterministic motion of droplets reaching at the measuring point from different upstream positions with a wide range of axial velocities determined by their initial conditions, as suggested by the "fan-spreading" effect (Hardalupas et al., 1989). The maximum values at the shear layers were reduced with the axial distance from the nozzle and at $z/D_{gas} = 33.5$ the rms of the velocity fluctuations of the air flow was constant in the central region and about half the turbulence levels of the single phase suggesting reduced mixing when the liquid jets are present. However, the rms of the fluctuations of the axial velocity of the air flow was higher than those of the single spray between the nozzle axes, which could enhance the ignition of the mixture in the preburner of the SSME.

The local mass fraction of the gas, estimated in the middle of the distance between nozzles 2 and 3 at $(r/D_{gas}, x/D_{gas})$ of (0, 1.68) according to Eq. (7), is plotted in Fig. 5(*b*) as a function of the axial distance from the nozzle exit. The results show that the local mass fraction of the gas is higher in the multiple nozzle arrangement than the single spray up to $z/D_{gas} = 23.5$ by around 40%. However, at $z/D_{gas} = 33.5$, the progression of the spray merging process resulted in similar local mass fraction for the single and multiple spray arrangements. The result of Fig. 5 is significant for the SSME, since the increase of the mass fraction of the gas, corresponds to an increase of the mass fraction of the fuel in the region between the nozzles, which may influence the ignition location.

The effect of a reduction of the liquid flowrate was examined with the flow conditions of case 2 of Table 1. The mean diameters of the sprays were reduced with the reduction of the liquid flowrate (Fig. 7(*a*)), following the observations for the single sprays, and the maxima of the mean diameter and liquid flux profiles on the axes of symmetry of nozzles 2 and 3, Fig. 7(*a*) and (*b*) could not be detected at z/D_{gas} of 33.5, in contrast to the higher liquid flowrate. The profiles of SMD and MMD at z/D_{gas} of 13.4 had maxima of around 100 and 120 μm respectively and increased with the axial distance to around 110 and 140 μm, respectively, at z/D_{gas} of 33.5, suggesting that droplet coalescence during spray merging with low liquid flowrate resulted in an increase of the droplet diameters by around 15 percent. This was caused by the increased number density of the droplet in the low liquid flowrate case due to the improved atomisation. The mean axial velocities of the 9 and 105 μm droplets, Fig. 7(*c*), had only one maximum at the center at z/D_{gas} of 23.5, where the velocity profiles were similar to that of the single phase. The rms of the fluctuations of the axial velocity of the air flow (9 μm droplets), Fig. 7(*d*), did not have a maximum in the central region, as for the high liquid flowrate case 1, and after $z/D_{gas} = 23.5$ the profile was similar to that of the single phase flow, but the values were about 30 percent lower. It should be noted that the mean axial velocity profiles of the single phase and the air flow were identical at $z/D_{gas} = 33.5$, so the rate of strain $\partial U/\partial r$, the mean axial velocity gradient in the radial direction, was the same. So the reduced turbulence levels of the air flow in this region were not caused by the differences in the mean rate of strain through reduced generation of $\overline{u^2}$ by $[\overline{uv}\partial U/\partial r]$. A possible explanation is that the liquid droplets attenuated the high frequency fluctuations of the turbulence spectrum, while the energy contained in the low frequency eddies was not affected (Owen, 1969; Squires and Eaton, 1990). The faster spray merging with the reduction of the liquid flowrate occurred because the rate of spread of the individual sprays increased and atomization improved (Hardalupas and Whitelaw, 1994). Thus, a decrease of the liquid flowrate by 50 percent increased the interaction between the sprays, by starting the spray merging closer to the nozzle exit, shortening the distance required for the individual spray characteristics to disappear by around 30 percent and increasing the resulting turbulence levels of the air flow by 20 percent, although they remained 30 percent lower than for the single phase flow.

(iii) Implications of the Current Results for the Preburner of the SSME. The current study suggests that spray merging in the region between the axes of the nozzles can increase the gas flow turbulence and the local mass fraction of the gas of the individual sprays. The possibility of the presence of the observed effect in the preburner of the SSME is considered below and its significance on the operation is discussed. The diameter of the gaseous jet is 4.93 mm in the SSME (Table 1) and the distance between the spray axes is around 25 mm, corresponding to $5D_{gas}$, which is wider than $2D_{gas}$ of the current experiment. The gas-to-liquid momentum ratio of the atomizers of the SSME is 10.6, which is similar to the value of 8.6 for the sprays of case 1 of this study. However, for constant momentum ratio of the two streams, the atomization of single atomizers improves with the reduction of the gaseous jet diameter and with the high pressure environment of the SSME and the SMD of liquid oxygen droplets is expected to be around four times lower than for the case 1 of this study (Engelbert et al., 1995). Engelbert et al. (1995) suggested also that the rate of spread of the sprays increased with the reduction of the gaseous jet diameter and, thus, the spray width in the SSME at $z/D_{gas} = 23.5$ is expected to be around two times wider than in this study. Therefore, the smaller distance between the axes of the nozzles for the current atmospheric experiment can compensate the improved atomization and the wider sprays in the SSME and similar spray interaction effects are expected in the preburners.

The hydrogen-to-oxygen mass flowrate ratio of the preburner sprays is around 0.84, and thus the mixture of each individual spray is fuel-rich by about six times above the stoichiometric value of 0.125. This implies that the location of the stoichiometric mass fraction of the individual sprays, which coincides with the flame front, is at a small distance from the axis of the nozzle where most of the oxidiser exists and is surrounded by a fuel-rich region, to ensure than the oxidiser burns completely with the fuel and cannot oxidise the surfaces of the combustor (Huzel and Huang, 1992). In the multiple spray arrangement, the increase of the local mass fraction of gaseous fuel in the region between the nozzle axes may result in a shift of the stoichiometric mass fraction towards larger radial distances from the nozzle axis, where combined with the increased turbulence of the gaseous flow, may influence the location and time of ignition during the startup period. So calculations of the combustion process of single preburner injectors (e.g., Liang et al., 1987) should also consider the effects of the surrounding sprays on the mass fraction distribution when the effect of the injector geometry on the preburner performance is predicted. Since, our results have shown that the turbulence level of the gaseous flow increased with the reduction of the liquid flowrate in the region between the nozzle axes, which is the most likely location for ignition to occur, the ignition characteristics of the preburner may improve by using more injectors with small nozzle diameters, reduced liquid flowrate and at small distances from each other to increase the spray interaction.

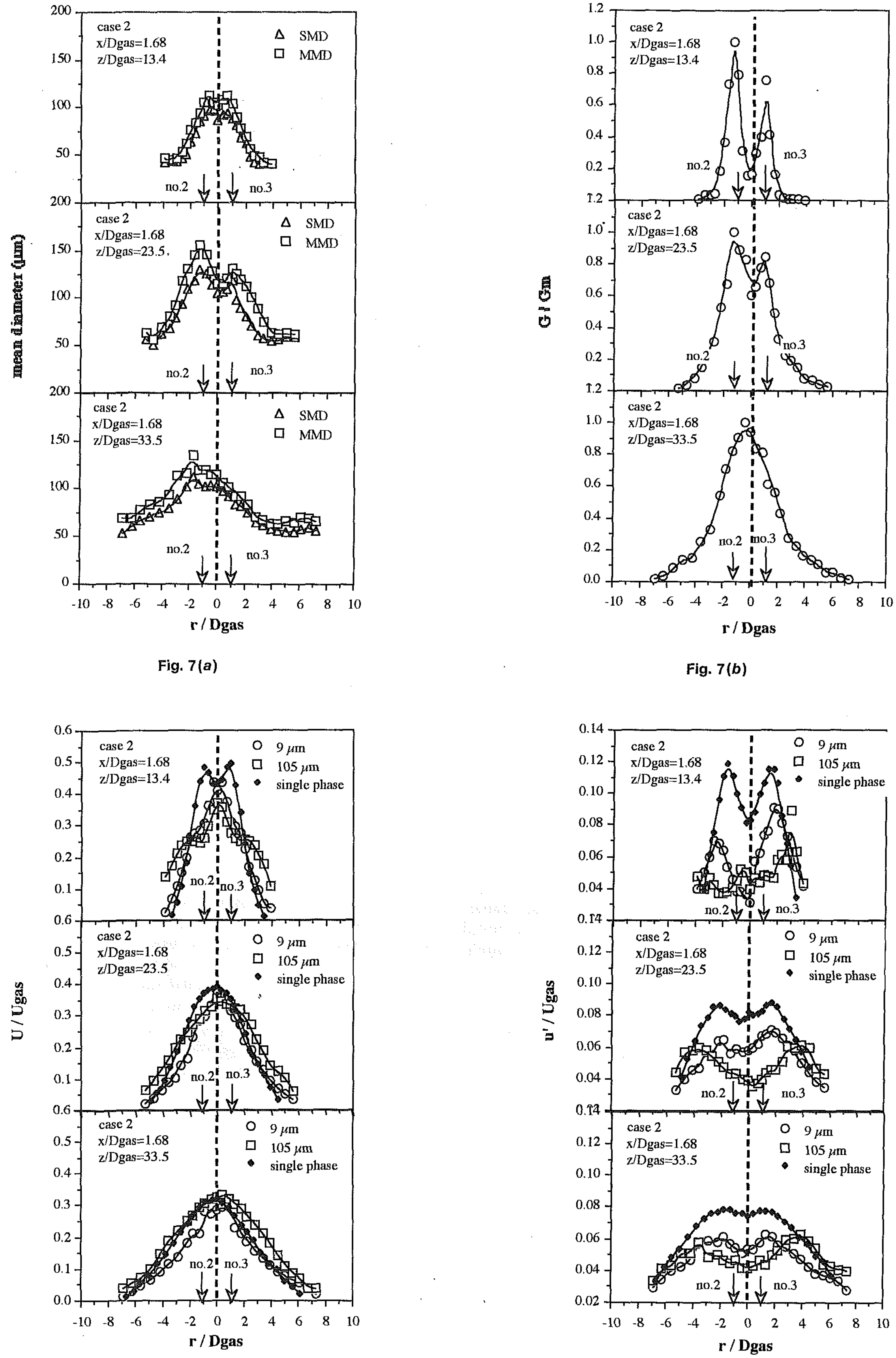

Fig. 7(*a*)

Fig. 7(*b*)

Fig. 7(*c*)

Fig. 7(*d*)

Fig. 7 Radial profiles along the r-direction at $x/D_{gas} = 1.68$ and at axial distances $z/D_{gas} = 13.4$, 23.5 and 33.5 of (*a*) mean diameters, (*b*) liquid flux, (*c*) mean, and (*d*) rms fluctuations of axial velocity of 9 and 105 μm droplets and single phase flow for conditions of case 2 of Table 1

4 Summary and Conclusions

The main findings were as follows:

1. Individual spray characteristics dominated in the initial region of 15 air jet diameters, and maximum mean diameters and liquid flux were observed on the geometrical axes of the nozzles where the mean and the rms fluctuations of the axial velocity of the droplets had local minima. Further downstream, merging of the individual sprays was strong in the region between the nozzle axes, where the mean diameter reduced and the liquid flux, the mean and rms of the fluctuations of the axial velocity of the droplets and the local mass fraction of the gas flow increased relative to the single spray, and, at around 30 gaseous jet diameters, the multiple spray characteristics were modified to a single spray-like flow produced by a nozzle located at the centre of the triangular region between the nozzle axes. The spray characteristics at the outer region of the multiple spray flow were identical to those of the individual sprays. The mean diameter and liquid flux characteristics of the individual sprays existed beyond the mean velocity field and distinct maxima remained in the region of the axes of the nozzles, suggesting that the velocity characteristics of the droplets were not a good indication of the spray development in the downstream region.
2. Decrease of the liquid flowrate by 50 percent, increased atomization by 25 percent, shortened the axial distance from the nozzles where the individual spray characteristics disappeared by 30 percent and increased the air flow turbulence by 20 percent. Droplet coalescence in the spray merging region became significant with the reduction of the liquid flowrate and resulted in an increase of the Sauter mean diameter by 15 percent with the axial distance from the nozzle exit.
3. The turbulence levels of the air flow with liquid injection were lower than those of the air flow without liquid injection and increased with the reduction of the liquid flowrate, even though the corresponding mean axial velocity profiles were identical. Thus, mixing is improved by reducing the liquid flowrate injected by each nozzle.
4. The interacting sprays in the preburner of the space shuttle main engine are not likely to influence the break-up process of the liquid jet of individual nozzles, while the spray characteristics may be altered downstream of the nozzle by the merging of the individual sprays. The region between the nozzle axes is expected to become richer in fuel, where increased levels of gas flow turbulence may enhance ignition during the startup period. The use of an increased number of nozzles with reduced diameter and distance between their axes is recommended to increase the interaction and reduce the liquid flowrate injected by each nozzle and thereby improve the combustion in the preburner.

Acknowledgments

The authors wish to acknowledge financial support from NASA Marshall Space Flight Center, under grant NAS8-38872. Mr. J. R. Laker designed and constructed the electronics of the phase Doppler anemometer and Mr. P. Trowell constructed the experimental facility. We are grateful to Mr. H. Struck and Dr. H. McDonald for many useful discussions during the conduct of this research. The paper was completed, while YH was supported by a 1994 EPSRC Advanced Research Fellowship.

References

Bachalo W. D., Rudoff R. C., and Brena de la Rosa A., 1988, "Mass Flux Measurements of a High Number Density Spray System Using the Phase-Doppler Particle Analyzer," AIAA-paper-88-0236.

Burick R. J., 1972, "Atomization and Mixing Characteristics of Gas/Liquid Coaxial Injector Elements," *Journal of Spacecraft and Rockets,* Vol. 9, pp. 326–331.

Caré I., and Dedoux M., 1991, "Study of an Air Blast Coaxial Atomizer: Experiments and Modelisation," *Proceedings of the 5th International Conference on Liquid Atomization and Spraying Systems* (ICLASS), Gaithersburg, MD, paper 85, pp. 763–770.

Dodge L. G., Rhodes D. J., and Reitz R. D., 1987, "Drop-Size Measurement Techniques for Sprays: Comparison of Malvern Laser-Diffraction and Aerometrics Phase/Doppler," *Applied Optics,* Vol. 26, pp. 2144–2154.

Engelbert C., Hardalupas Y., and Whitelaw J. H., 1995, "Breakup Phenomena in Coaxial Airblast Atomizers," *Proceedings of the Royal Society of London,* Series A, Vol. 451, pp. 189–229.

Eroglu H., and Chigier N. A., 1991, "Initial Drop Size and Velocity Distributions for Airblast Coaxial Atomizers," ASME JOURNAL OF FLUIDS ENGINEERING, Vol. 113, pp. 453–459.

Faeth G. M., 1990, "Structure and Atomization Properties of Dense Turbulent Sprays," *Proceedings of the 23rd Symposium (International) on Combustion,* The Combustion Institute, pp. 1345–1352.

Falk A. Y., 1975, "Coaxial Spray Atomization in Accelerating Gas Stream," NASA CR-134825.

Ferrenberg A., Hunt K., and Duesberg J., 1985, "Atomization and Mixing Study," NASA CR-178751.

Glass M., and Kennedy I. M., 1977, "An Improved Seeding Method for High Temperature Laser Doppler Velocimetry," *Combustion and Flame,* Vol. 29, pp. 333–335.

Hardalupas Y., 1989, "Experiments with Isothermal Two Phase Flows," PhD thesis, University of London.

Hardalupas Y., 1990, "Description of the Fluids Section 'Model 2' phase Doppler Counter," Imperial College, Mechanical Engineering Department, Report no. FS/90/29.

Hardalupas Y., and Taylor A. M. K. P., 1989, "On the Measurement of Particle Concentration Near a Stagnation Point," *Experiments in Fluids,* Vol. 8, pp. 113–118.

Hardalupas Y., and Whitelaw J. H., 1994, "The Characteristics of Sprays Produced by Coaxial Airblast Atomisers," *Journal of Propulsion and Power,* Vol. 10, pp. 453–460.

Hardalupas Y., Taylor A. M. K. P., and Whitelaw J. H., 1989, "Velocity and Particle Flux Characteristics of Turbulent Particle-Laden Jets," *Proceedings of Royal Society of London,* Series A, Vol. 426, pp. 31–78.

Hardalupas Y., Taylor A. M. K. P., and Whitelaw J. H., 1994, "Mass Flux, Mass Fraction and Concentration of Liquid Fuel in a Swirl-Stabilised Flame," *International Journal of Multiphase Flows,* 20 Suppl., pp. 233–259.

Huzel D. K., and Huang D. H., 1992, "Modern Engineering for Design of Liquid-Propellant Rocket Engines," *Progress in Astronautics and Aeronautics,* Vol. 147, p. 105, AIAA, Washington.

Kim K., and Marshall W., 1971, Drop size distributions from pneumatic atomizers. AIChE Journal, 17, pp. 575–584.

Kliafas Y., Taylor A. M. K. P., and Whitelaw J. H., 1990, "Errors due to turbidity in particle sizing using laser Doppler anemometry." ASME JOURNAL OF FLUIDS ENGINEERING, Vol. 112, pp. 142–148.

Lefebvre A. H., 1989, *Atomization and Sprays.* Hemisphere Publishing, New York.

Liang P. Y., Jensen R. J., and Chang Y. M., 1987, "Numerical Analysis of SSME Preburner Injector Atomization and Combustion Processes," *Journal of Propulsion and Power,* Vol. 3, pp. 508–514.

Lorenzetto G., and Lefebvre A. H., 1977, Measurements of droplet size on a plain jet airblast atomizer. *AIAA Journal,* 15, pp. 1006–1010.

Owen P. R., 1969, "Pneumatic Transport," *Journal Fluid Mechanics,* Vol. 39, pp. 407–432.

Priem R. J., and Heidman M. F., 1959, "Vaporization of Propellants in Rocket Engines," *ARS Journal,* Vol. 29, pp. 836–842.

Sankar S. V., Brena de la Rosa A., Isakovic A., and Bachalo W. D., 1991, "Liquid Atomization by Coaxial Rocket Injectors," AIAA paper no. 91-0691.

Sankar S. V., Wang G., Brena de la Rosa, Rudoff R. C., Isakovic A., and Bachalo W. D., 1992, "Characterisation of Coaxial Rocket Injector Sprays Under High Pressure Environments." AIAA paper no. 92-0228.

Schefer R. W., Hartmann V., and Dibble R. W., 1987, "Conditional Sampling of Velocity in a Turbulent Nonpremixed Propane Jet," *AIAA Journal,* Vol. 25, pp. 1318–1330.

Simmons H. C., 1977, "The Correlation of Drop-Size Distributions in Fuel Nozzle Sprays. Part I: The Drop-Size/Volume-Fraction Distribution," ASME: *Journal of Engineering for Power,* pp. 309–314.

Spalding D. B., 1963, *Convective Mass Transfer. An Introduction,* Arnold, London.

Squires K. D., and Eaton J. K., 1990, "Particle Response and Turbulence Modification in Isotropic Turbulence," *Physics of Fluids,* Vol. A2, pp. 1191–1203.

Tate R. W., 1982, "Some Problems Associated With the Accurate Representation of Drop-Size Distributions," *Proceedings of the 2nd International Conference on Liquid Atomization and Spraying Systems* (ICLASS), Madison, WI, pp. 341–351.

Wanhainen J. P., Parish H. C., and Conrad E. W., 1966, "Effect of Propellant Injection Velocity on Screech in 20,000-Pound Hydrogen-Oxygen Rocket Engine," NASA TN D-3373.

Weiss M. A., and Worsham C. H., 1959, "Atomization in High Velocity Airstreams," *ARS Journal,* Vol. 29, pp. 252–259.

Zaller M. M., and Klem M. D., 1991, "Coaxial Injector Spray Characterization Using Water/Air as Simulants," Presented at the 28th JANNAF Combustion Meeting, San Antonio, Texas.

Effects of Inlet Conditions on the Flow in a Fishtail Curved Diffuser With Strong Curvature

M. I. Yaras
Assistant Professor,
Department of Mechanical and
Aerospace Engineering,
Carleton University,
Ottawa, Ontario,
Canada K1S 5B6

The paper presents detailed measurements of the incompressible flow at the exit of a large-scale 90-degree curved diffuser with strong curvature and significant streamwise variation in the cross-section aspect ratio. The diffuser flow path approximates the so-called fish-tail diffuser utilized on small gas turbine engines for the transition between the centrifugal impeller and the combustion chamber. Five variations of the inlet boundary layer are considered. The results provide insight into several aspects of the diffuser flow including: the effect of flow turning on diffusion performance; the dominant structures influencing the flow development in the diffuser; and the effect of the inlet boundary layer integral parameters on the diffusion performance and the exit velocity field. The three-dimensional velocity distribution at the diffuser exit is found to be sensitive to circumferentially uniform alterations to the inlet boundary layer. In contrast, circumferential variations in the inlet boundary layer are observed to have only secondary effects on the velocity field at the diffuser exit. The static pressure recovery is observed to be comparable to the published performance of conical diffusers with equivalent included angle and area ratios. Furthermore, both the static pressure recovery and the total pressure losses are observed to be relatively insensitive to variations in the inlet boundary layer. The physical mechanisms dominating the flow development in the diffuser are discussed in light of these observations.

Introduction

In small gas turbines utilizing a centrifugal impeller as the last compressor stage the designer is confronted with the problem of efficiently diffusing and redirecting the high-kinetic-energy flow between the impeller exit and the combustion chamber. In the pipe diffuser and fishtail diffuser configurations this task is accomplished by diffuser passages wrapped around a radial-to-axial turn (Kenny, 1968; Reeves 1977; Blair and Russo, 1980). To avoid penalties in terms of engine diameter and weight, the diffusion and redirection must be achieved over the shortest possible length. At the same time, it is paramount to achieve high pressure recovery and maintain minimal flow nonuniformity at the diffuser exit, the latter constraint being imposed by the combustion efficiency in the downstream combustion chamber. Some current fishtail diffuser designs incorporate straightening vanes near the diffuser exit in an attempt to reduce the cross flows in the discharging flow at the expense of extra weight and manufacturing difficulties. It is evident that the design of fishtail diffusers involves a difficult trade-off between aerodynamic efficiency, compactness, and discharge conditions suitable for efficient combustion.

While there is a substantial body of published literature devoted to the study of diffuser flows, a relatively small fraction of this deals with curved, diffusing passages. Previous works on diffusing bends include those of Fox and Kline (1962), Sagi and Johnston (1967), Parsons and Hill (1973), McMillan (1982), and Wellborn et al. (1992). However, none of these studies have considered strong curvature or substantial streamwise variation in the cross-sectional aspect ratio, both of which are characteristics of fishtail diffusers. The work of Blair and Russo (1980) is one of the few studies where such geometries were considered. However, the extent of the measurements in that study did not allow for a detailed account of the flow development. This absence of detailed data and the ensuing lack of understanding of the flow physics has hindered optimization of these diffusers. The present work is the first step in an attempt to fill this gap in our existing knowledge of such flows.

The hub-to-shroud nonuniformity of the flow leaving the centrifugal impeller produces highly nonuniform mean-velocity distributions at the entrance of fishtail diffusers. The diffuser flow is further influenced by unsteady effects that arise from the jet-wake type of flow emerging from the impeller passages. Finally, there is the additional complexity introduced by elevated Mach numbers. The present work examines the influence of radial and circumferential mean-velocity nonuniformities at the diffuser inlet on the flow development through the diffuser and the associated performance, in absence of the effects of unsteadiness, compressibility and high levels of inlet turbulence. A systematic examination of these remaining effects is intended in subsequent phases of this research programme.

Finally, while the geometry of the diffuser being examined approximates that of fishtail diffusers utilized on small aero-engines, the observations should prove useful for any fluid dynamics application involving diffusing bends of similar geometries such as hydraulic-turbine draft tubes and steam-turbine exhaust ducts.

Experimental Apparatus

Test Section. The test section is shown schematically in Fig. 1. Longitudinally, the diffuser consists of four sections, with each section further partitioned into symmetric upper and lower halves. The first section provides a conical flow path with an inlet diameter of 193.7 mm and an included angle of 6.15 degrees. In the subsequent three sections the flow path turns by 90 degrees along a centerline with a radius that is 4.36 times the inlet diameter of the diffuser. In these sections the cross-section of the flow path becomes increasingly more oblong with downstream distance while the cross-sectional area continues

---

Contributed by the Fluids Engineering Division for publication in the JOURNAL OF FLUIDS ENGINEERING. Manuscript received by the Fluids Engineering Division November 4, 1995; revised manuscript received June 7, 1996. Associate Technical Editor: Wing Ng.

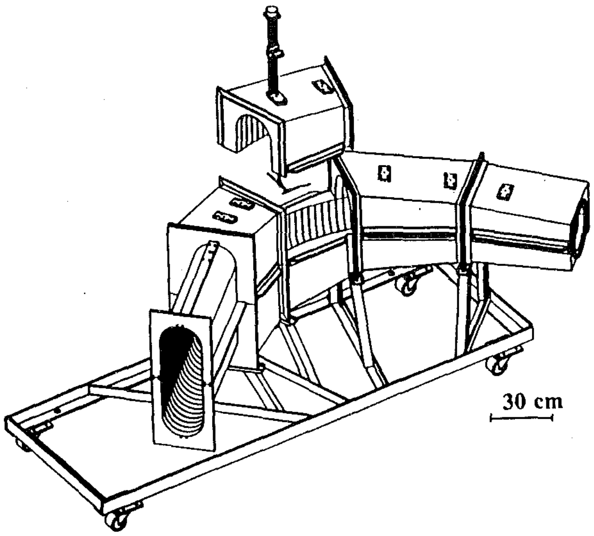

Fig. 1 Schematic of the curved-diffuser test section (reproduced from Saroch, 1996)

to increase linearly until it reaches a size that is 3.42 times the inlet area of the diffuser. The modular construction of the diffuser was necessitated by the limits imposed on the part size by the CNC machine used to manufacture the diffuser and by the requirement of easy probe access to any cross section within the diffuser. MB1000, a resin based material, was used in the construction of the diffuser. This material was chosen for its easy machinability, low moisture absorption, lighter weight than like-substitutes and grain free composition. To produce each half of the diffuser sections, 152 cm × 41 cm × 5 cm boards made out of MB1000 were laminated, the external surfaces were milled and the flow path was carved out on a CNC machine. Aluminum flanges are used to connect the sections to each other. The step-and-groove design of the flanges provides for the alignment of adjacent sections and helps to prevent leakage. Beyond the 90-degree diffusing turn, the cross section of the flow path remains unchanged through the tail duct. This tail duct consists of two symmetric halves and is constructed of galvanized sheet metal contained in an aluminum frame. Pertinent geometric information on the diffuser flow path is summarized in Fig. 2(*b*). This geometry is a scaled version of typical fishtail diffuser geometries utilized on small gas turbine engines, with the inlet of the test section corresponding to the throat of the fishtail diffuser. The large scale of the test section has allowed fine resolution of the flow.

An open-circuit wind tunnel is used as the wind source for the diffuser. A variable-speed centrifugal fan draws in ambient air and delivers it through a honeycomb into a circular settling chamber containing three screens. At the exit of the settling chamber the air passes through two contractions of 9:1 and 4.4:1 contraction ratios. At the exit of the second contraction, the flow enters a PVC pipe that leads to the inlet of the diffuser test section. This entry pipe is made of three longitudinal segments, each 2.623 diameters long.

In the present work, variations in the boundary layer thickness at the diffuser inlet were established by adjusting the length of the entry pipe and by installing complete and partial trip rings at the inlet of the pipe (Fig. 3). These geometric configurations are summarized in Table 1.

Instrumentation. All pressures were measured using capacitive-type pressure transducers. The transducer outputs were converted to digital form, with 12-bit resolution, using a Sciemetric Instruments data acquisition system controlled by a microcomputer.

A motorized traversing gear mounted on the inlet pipe allowed radial traverse of the flow one diameter upstream of the diffuser inlet. For each of the test cases the velocity distribution was measured at 12 evenly-spaced circumferential positions. A pitot probe of 0.5 mm tip diameter was used for these measurements. The static pressure was obtained from a pressure tap on the pipe wall located at the same streamwise position.

The three-dimensional flow in the $\theta = 90$ deg plane of the diffuser was measured with a miniature seven-hole pressure probe used in non-nulling mode. The probe pressures were measured through a scanning valve. The measurement grid consisted of about 1100 data points, yielding a very detailed picture of the flow pattern emerging from the diffuser. The probe tip is of conical geometry with an included angle of 60 degrees. The probe was calibrated in 3-degree steps up to 27 degrees of flow misalignment and the calibration was checked regularly during the experiments. This calibration range was found to be sufficient for measuring the cross flows encountered at the exit of the present test section. The calibration was performed at a Reynolds number corresponding to the mean velocity in the θ

Nomenclature

A = cross-sectional area
B = blockage factor = $1 - (\bar{V}/V_{\mathrm{CL}})_1$
$C_P = (P - P_1)/\frac{1}{2}\rho\bar{V}_1^2$ = static pressure coefficient
$C_{P_0} = ((P_{0_1})_{\mathrm{CL}} - \mathrm{P}_0)/\frac{1}{2}\rho\bar{V}_1^2$ = total pressure coefficient
d = diameter
h = half-height of the diffuser side walls; refer to Fig. 2(*a*)
$H = \delta^*/\theta$ = boundary layer shape factor
L = diffuser centerline length
L_p = entrance pipe length
P = static pressure
P_0 = stagnation pressure
r = radius of the upper and lower walls; refer to Fig. 2(*a*)
r_1 = radius at the diffuser inlet
Re_d = Reynolds number based on the inlet diameter
v = fluctuating component of velocity
V = velocity
$\bar{V}$ = spatially-averaged velocity
x, y, z = orthogonal curvilinear co-ordinates; x axis is tangent to the centerline of the flow path with $x = 0$ at the inlet of the diffuser; refer to Fig. 2(*a*)
α_{xy}, α_{xz} = flow direction in the x–y and x–z planes, respectively
Δr_t = height of the trip ring
Δx_t = thickness of the trip ring
$\Delta\phi_t$ = circumferential extent of the trip ring; refer to Fig. 3
δ = boundary layer thickness
$\delta^* = \int_{r_1}^{r_1-\delta} (1 - V/V_e)dr$ = boundary layer displacement thickness
$\theta = \int_{r_1}^{r_1-\delta} (1 - V/V_e)V/V_e dr$ = boundary layer momentum thickness; also used for the turning angle of the diffuser centerline; refer to Fig. 2(*a*)
ρ = density
ϕ = circumferential coordinate; refer to Fig. 2(*a*)
ϕ_t = circumferential position of the trip ring; refer to Fig. 3

Subscripts

CL = centerline of the pipe, one diameter upstream of the diffuser inlet plane
e = boundary-layer edge value
x = component in the x direction
1 = one diameter upstream of the diffuser inlet
2 = ($\theta = 90$ deg) plane

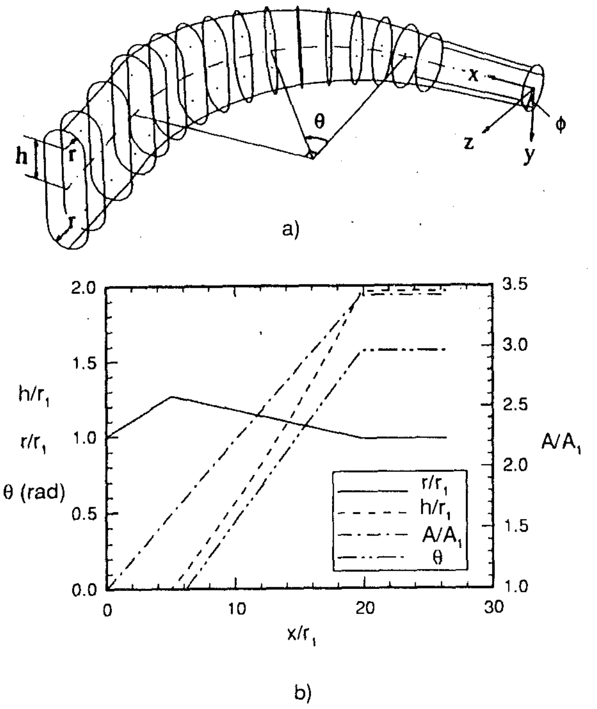

Fig. 2 Geometry of the diffuser flow path

= 90 deg plane of the diffuser. Tests on the variation of the probe calibration with Reynolds number showed only small sensitivity within the range of flow misalignments considered.

An Nth order uncertainty analysis (Moffat, 1982) was performed to establish the error estimates for the dynamic and total pressures and the local flow direction measured with the seven-hole probe. In this analysis, first the uncertainty in the seven pressures of the probe were evaluated. This evaluation accounted for repeatability errors for measurements in the diffuser test section as well as for propagation of uncertainties such as those associated with the pressure-transducer calibration curves. The corresponding error estimates in the measured flow variables were then combined with the errors introduced by the biquadratic interpolation scheme used in conjunction with the calibration curves of the probe. Based on this analysis, the velocity and total pressure extracted from the probe at the diffuser exit are estimated to be accurate to within one percent of the diffuser-inlet centerline velocity and dynamic pressure, respectively. Outside the stalled region of the diffuser flow, the error in the measured flow direction is estimated to be within ±0.9 degrees.

The design of the test section allows motorized traverse of the probe in the y or z directions. For instance, with the traversing gear mounted as shown in Fig. 1, motorized traverses are performed in the y direction. For traversing a complete cross-sectional plane in this configuration, the probe is repositioned manually along the z direction after each motorized traverse in the y direction. Multiple mounting ports for the traversing gear, distributed along the length of the diffuser, allow probe access to cross-sections throughout the diffuser. Similar mounting ports are present on the outer wall of the lower half of each section, providing for motorized traverse in the z direction. When not in use, the probe stem and pressure tubing access holes, each of 6.4 mm diameter, are sealed from the inside with thin adhesive tape. The seven-hole probe data presented in this paper were obtained in the cross sectional plane located at $\theta =$ 90 deg ($x/r_1 = 19.86$). For these measurements the traversing gear was mounted at the first access port on the tail duct, with motorized probe motion in the y direction.

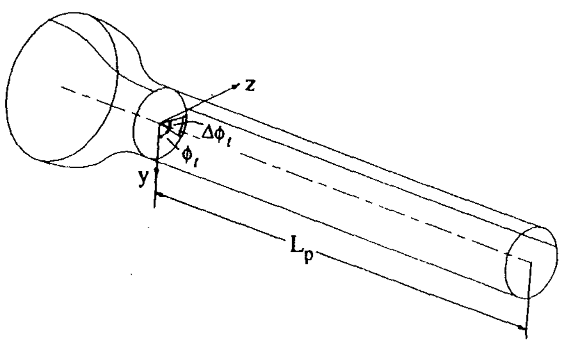

Fig. 3 Geometric configuration upstream of the diffuser inlet

Table 1 Geometric configurations upstream of the diffuser inlet

	L_p/d_1	ϕ_t	$\Delta\phi_t$	$\Delta r_t/r_1$	$\Delta x_t/\Delta r_t$
Case I	7.87	-	360°	0.125	0.8
Case II	7.87	-	-	-	-
Case III	2.62	-	-	-	-
Case IV	7.87	55°	70°	0.237	0.017
Case V	7.87	145°	70°	0.237	0.017

Once the traversing gear is mounted at the appropriate port, fine adjustment of the probe tip position in the streamwise (x) direction is accomplished by sliding the probe in its holder relative to the probe stem. For motorized traverses in the y direction, the manual positioning along the z axis is performed with the aid of an alignment/positioning device designed for use on this test section (Saroch, 1996). This device also provides for referencing the probe position in the y direction and establishing its orientation relative to the curvilinear reference axes shown in Fig. 2. The probe position and its orientation relative to the reference axes are estimated to be accurate to within ±0.20 mm and ±0.1 degrees, respectively.

Experimental Results and Discussion

Diffuser Inlet Flow. All measurements were taken at a Reynolds number of $7.25 \pm 0.1 \times 10^5$ based on the diameter and the mean velocity at the diffuser inlet. The corresponding Mach number was less than 0.2. The integral boundary layer parameters extracted from the pitot probe measurements one diameter upstream of the diffuser inlet are given in Fig. 4. As is evident from these results, the aforementioned geometric variations upstream of the diffuser inlet were able to produce considerable changes in the displacement and momentum thicknesses, with the boundary layer shape factor varying in the range of 1.2 to 1.7. For Cases II and III the integral parameters are observed to vary slightly along the circumference despite the absence of partial trip rings in these cases. These variations were the result of a small asymmetric step at the joint of the contraction and the pipe. For all five cases examined, the velocity distribution outside the boundary layer was essentially uniform, with spatial variations in the velocity magnitude remaining within ±0.5 percent of the centerline velocity, V_{CL}. Seven-hole probe measurements in the same measurement plane confirmed that the velocity distribution remained uniaxial for all the test cases.

In the present work the objective has been to examine the diffuser flow with a variety of boundary layer thicknesses at the inlet. However, the means used to generate these variations had some influence on the turbulence intensity, as depicted in Fig. 5 for Case V. Elevated levels of turbulence intensity are observed in the region of flow downstream of the trip ring. This

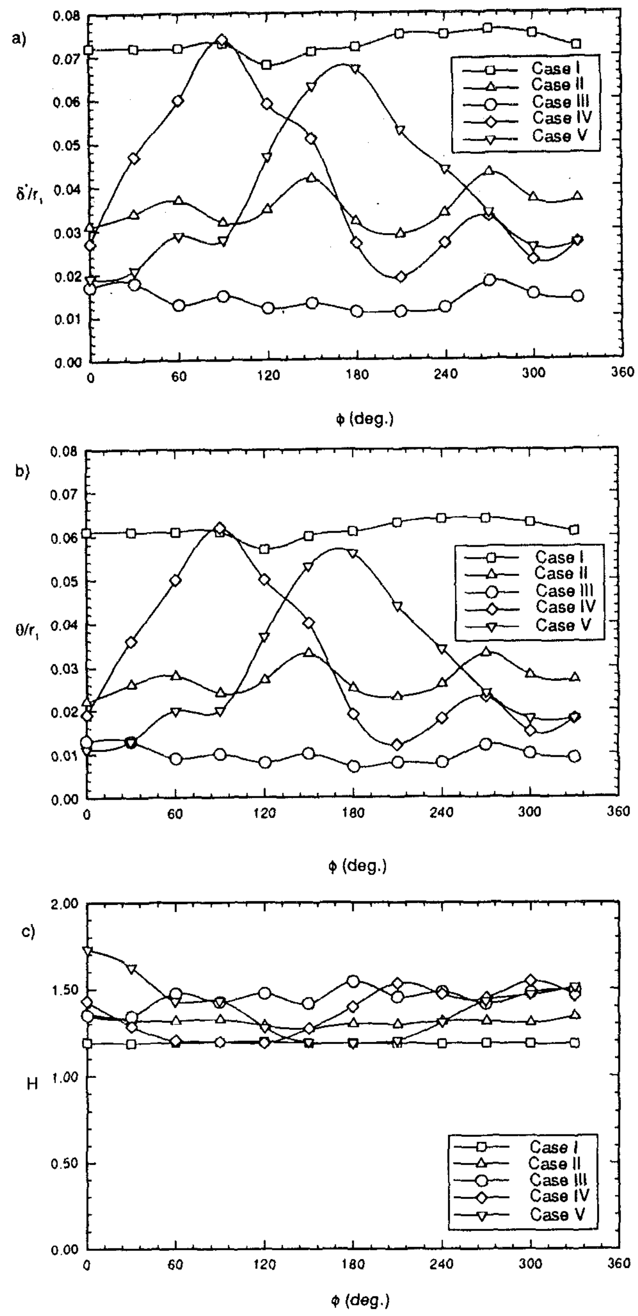

Fig. 4 Integral boundary layer parameters in the inlet measurement plane (uncertainty in $\delta^*/r_1 = \mp 0.002$ and in $\theta/r_1 = \mp 0.002$)

distribution of the streamwise component of turbulence intensity was measured with a single-wire hotwire probe. Increased turbulence at the inlet of straight diffusers generally enhances the pressure recovery of the diffuser (Cutler and Johnston, 1981; Klein, 1981). Augmented mixing caused by increased free-stream turbulence tends to diminish the growth of the boundary layer on the diffuser walls. This, in turn, delays separation and reduces the outlet blockage, thereby yielding improved pressure recovery. In curved diffusers this effect of turbulence is likely to be diminished since the secondary flows caused by the flow turning tend to have a dominating influence on the boundary layer development along the diffuser walls, as will be evident from the exit-plane measurements in the present diffuser.

Diffuser Exit Flow. Figure 6 shows the velocity distribution in the $\theta = 90$ deg plane for all of the test cases. For Case I, the case with the thickest inlet boundary layer, the fluid in close vicinity of the upper and lower walls is seen to migrate towards the inner wall. This is due to the well known imbalance between the centrifugal force and the radial pressure gradient acting on this relatively slow-moving fluid. After travelling some distance along the inner wall, towards the geometric symmetry plane, this fluid moves away from the inner wall and proceeds back toward the upper and lower walls respectively. The result of this motion is a pair of vortices centered along the upper and lower portions of the inner wall. Hereafter these vortices are referred to as vortex-pair 1. A region of fluid, substantially devoid of streamwise momentum, centered along the inner wall is seen to prevent these vortices from extending further toward the symmetry plane. This fluid region, hereafter called the stalled region, is mostly the result of large streamwise adverse pressure gradients combined with diminished turbulent mixing affecting the development of the viscous layer on the convex inner wall.

The fluid in close proximity of the outer wall, possessing the highest streamwise momentum, is seen to migrate toward the upper and lower walls, contributing to the replacement of the low-momentum fluid along these walls that is being absorbed by vortex-pair 1. Along the outer wall the streamwise momentum of the fluid diminishes with increasing distance from the wall. As a result, the fluid further away from the outer wall experiences radial pressure gradients that more than offset the centrifugal force. This, in turn, induces a weak radial cross-flow in the region along the symmetry plane, carrying the fluid toward the stalled region by the inner wall. However, this motion quickly diminishes further away from the symmetry plane as it is counteracted by the cross flow associated with vortex-pair 1. In fact, this interaction is seen to yield a second pair of vortices, hereafter called vortex-pair 2, with a sense of rotation opposite to that of pair 1, positioned closer to the symmetry plane and closer to the outer wall. In this test case this second pair is seen to be very weak.

In contrast to the results of Case I, in the velocity distribution for Case II corresponding to the medium-thickness inlet boundary layer, a vortical cross-flow pattern associated with vortex-pair 1 is no longer clearly identifiable. As in Case I, under the influence of unbalanced pressure gradients, a radially inward migration prevails in the region close to the symmetry plane, away from the outer wall. This time, however, this migration

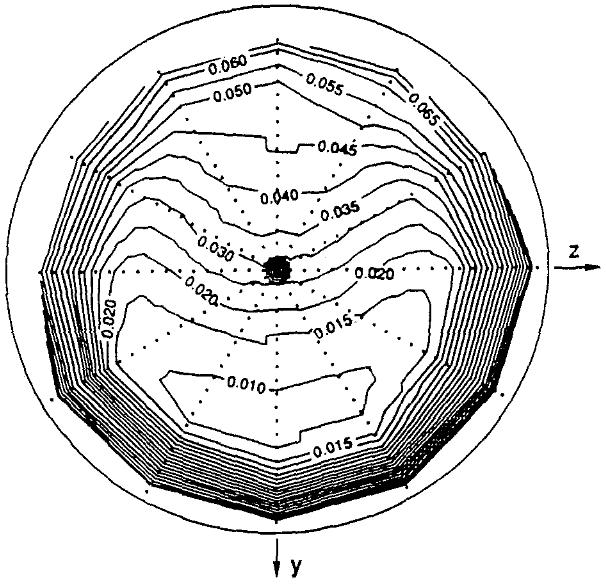

Fig. 5 Turbulence intensity ($(\overline{v^2})^{1/2}/V$) distribution one diameter upstream of the diffuser inlet—Case V (uncertainty in $(\overline{v^2})^{1/2}/V = \mp 5$ percent)

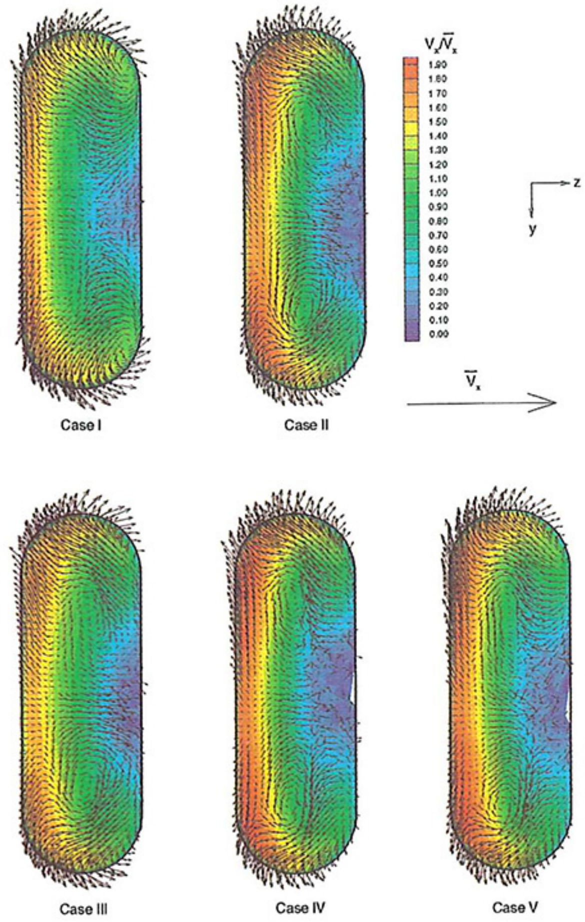

Fig. 6 Velocity distribution in the θ = 90 deg measurement plane (uncertainty in V/V_{CL} = ∓0.01; outside the stalled region, uncertainty in α_{xy}, α_{xz} = ∓0.9 deg)

is much stronger due to the diminished opposition posed by the fluid migrating along the upper and lower walls. This results in a stronger vortex-pair 2 centered further away from the outer wall and the symmetry plane compared to the vortex-pair 2 observed in Case I.

In Case I, vortex-pair 1 carries fluid of relatively high streamwise momentum toward the stalled region by the inner wall, with the resultant mixing tending to reduce the extent of the stall as the flow develops through the diffuser. In Case II, a similar influence on the stalled region is affected by vortex-pair 2. The extent of the stalled fluid in Case I is observed to be considerably less than that in Case II. On the basis of mass conservation, the larger extent of the stalled region in Case II would require the remaining fluid to have relatively higher streamwise momentum. Comparison of the axial velocity distributions for Cases I and II illustrates that this relative elevation in the streamwise momentum is primarily associated with the regions along the upper and lower portions of the outer wall.

The exit-plane velocity distribution corresponding to the thinnest inlet boundary layer (Case III) displays a velocity distribution very similar to that of Case II. One identifiable difference is the slightly reduced extent of the stalled region by the inner wall and the accompanying reduction in the streamwise momentum of the fluid along the outer wall.

Finally, Cases IV and V allow examination of the effects of asymmetric inlet boundary layer distribution on the flow emerging from the diffuser. In both cases the boundary layer integral parameters over about three quarters of the inlet circumference were close to those of Case II. The mass deficit in the boundary layer over the remaining quarter was approximately twice as large (Fig. 4(a)). The inner (ϕ = 90 deg) and upper (ϕ = 180 deg) quarters constituted the quarter with the thicker boundary layer for Cases IV and V, respectively. A close similarity between the exit velocity distributions for Cases IV and II is evident. In all the cases examined so far, the cross flows and the ensuing mixing have been observed to dominantly dictate the development of the flow in the diffuser. This is likely to result in rapid redistribution of the incoming boundary layer fluid. Consequently, it may be argued that the flow development in this diffuser is mostly affected by the thickness of the incoming boundary layer averaged over the circumference, with circumferential variations in this boundary layer having secondary influence. Comparison of the velocity distributions for Cases II and V reveals that this secondary influence is slightly more apparent when the incoming boundary layer is also asymmetric with respect to the geometric symmetry plane of the diffuser.

Diffuser Performance. The overall diffuser performance is conventionally documented in terms of static pressure recovery. Supplementary information on stagnation pressure losses may be used to gain further insight into the physics of the flow. For the present work, the nonuniformity of the total pressure distribution in the inlet and exit planes and the static pressure gradients prevailing within the exit plane require mass-averaged calculation of these quantities:

$$C''_P = \frac{\iint C_P(y,\, z)\rho V_X dydz}{\iint \rho V_x dydz} \tag{1}$$

$$C''_{P_0} = \frac{\iint C_{P_0}(y,\, z)\rho V_x dydz}{\iint \rho V_x dydz} \tag{2}$$

For each of the test cases, the integrated mass flow rates at the inlet and exit measurement planes agreed to within one percent. The inlet static pressure was measured one diameter upstream of the diffuser inlet to avoid any influences due to the diffuser entrance. The exit-plane pressure coefficients therefore include the pressure drop in this pipe segment. The results of the integrations are summarized in Table 2. The uncertainties quoted in this table were obtained through repeated calculation of the mass-averaged pressure coefficients while the pressure coefficients and the axial velocity at individual data points were adjusted within their respective uncertainty ranges.

The net total-pressure loss tabulated in the last column indicates negligible influence of the variations in the inlet boundary layer on the entropy generation within the diffuser. Case III, the case with the thinnest inlet boundary layer, appears to have slightly less loss generation than the remaining cases. However, in light of the levels of uncertainty assessed for the mass-averaged total pressure coefficients, it would not be fitting to attach much physical significance to this trend. Examination of the exit flow revealed a dominant influence of the vortical cross flows on the development of the flow within the diffuser. Through mixing losses and through their influence on the development of the boundary layers along the diffuser walls, these vortical structures would be expected to have considerable effect on the loss generation. In this context, it is interesting to observe similar amounts of loss generation for Case I and the remaining test cases despite the apparent differences in secondary flow development inferred from the measurements in the θ = 90 deg. plane.

The spatial extent of the stalled region by the inner wall containing low-stagnation-pressure fluid was observed to be considerably smaller in Case I in comparison to the other test cases. However, the corresponding differences in the mass-averaged total pressure losses should be considerably less since the mass flow rate associated with this region of flow is quite small.

Examination of the static pressure coefficients in Table 2 reveals only small changes in the static pressure recovery as the inlet boundary layer thickness is varied. Viscous energy dissipation through the diffuser and the inlet and exit flow distortions dictating the effective area ratio are the two factors that may influence the pressure recovery. We have already observed that the total pressure losses remain essentially unaffected by changes in the inlet blockage. Examination of the axial velocity distribution in Fig. 6 reveals that the stalled region by the inner wall is the primary influence on the exit flow distortion. Variation in the relative extent of this stalled region was observed, particularly for Cases I to III. The anticipated trend in the pressure recovery on the basis of this variation is seen to be in agreement with the trend tabulated in Table 2. In any event, the observed variations in the pressure recovery are quite small.

In Table 3 the static pressure recovery for Cases I to III are compared to the recovery of straight conical diffusers of equivalent A_2/A_1 and L/r_1 documented by Dolan and Runstadler (1973).

It is observed that the pressure recovery of the curved diffuser is very close to that of the equivalent conical diffuser, with the curved diffuser slightly outperforming the conical diffuser for the largest inlet blockage. In absence of loss data for an equivalent conical diffuser, a similar comparison of the total pressure losses is not feasible. Nonetheless, the curved diffuser is expected to have somewhat higher loss generation due to the enhanced mixing induced by the cross flows. Even if one ignores this anticipated difference in the total pressure losses, the aforementioned comparison of the static pressure recoveries dictates that the curved diffuser should have at least as high an effective area ratio as the equivalent conical diffuser. Increased exit blockage due to the stalled region by the inner wall of the curved diffuser would tend to deteriorate the pressure recovery. On the other hand, the boundary layer developing along the outer, top and bottom walls is continually thinned by the prevailing cross flows. Based on the pressure recovery data, these two effects appear to offset each other in the present diffuser.

According to the performance charts of Dolan and Runstadler, the equivalent conical diffuser tabulated in Table 2 is longer than the conical diffuser with the optimum pressure recovery for the same area ratio. The less than optimum performance of the equivalent conical diffuser is due to the adverse effect of the boundary layer growth along the extra diffuser length on the effective area ratio. In the case of the curved diffuser, the detrimental effect of such an extra diffuser length on the effective area ratio would be considerably less severe due to the thinning effect of the cross flows on the boundary layers. This is likely one reason for the favourable comparison of the present curved diffuser performance with that of the equivalent conical diffuser in Table 2.

Table 2 Mass-averaged static and total pressure coefficients (uncertainty in $C''_{p_{o_1}} = \mp 0.005$, in $C''_{p_2} = \mp 0.005$ and in $C''_{p_{o_2}} = \mp 0.01$)

	C_{p_2}''	$C''_{p_{o_1}}$	$C''_{p_{o_2}}$	$C''_{p_{o_2}} - C''_{p_{o_1}}$
Case I (B= 0.11)	0.78	0.21	0.35	0.14
Case II (B= 0.06)	0.74	0.10	0.24	0.14
Case III (B= 0.03)	0.76	0.04	0.16	0.12
Case IV (B= 0.07)	0.73	0.11	0.26	0.15
Case V (B= 0.07)	0.74	0.11	0.25	0.14

Table 3 Static pressure recovery coefficients for A_2/A_1 = 3.42 and L/r_1 = 19.86.

	C_{p_2}'' Curved Diffuser $Re_d = 7.25 \times 10^5$	C_{p_2} Conical Diffuser (Dolan & Runstadler) $Re_d = 1.20 \times 10^5$ (*)
B = 0.12	-	0.74
B = 0.11	0.78	-
B = 0.06	0.74	0.75
B = 0.03	0.76	0.76

(*)Reynolds number based on the inlet core velocity.

Conclusions

The flow field at the exit of the 90-degree diffusing bend of strong curvature displayed strong gradients in the axial velocity component with the flow being close to stagnant over a sizable region in the vicinity of the inner wall. Cross-stream pressure gradients lead to the formation of two pairs of vortices. For any of the test cases considered, only one of these pairs dominated the flow field in the exit plane.

For the thickest inlet boundary layer examined, the dominant vortical structures at the exit consisted of the well-known pair of counter rotating vortices, carrying the relatively low-momentum fluid along the upper and lower walls towards the inner wall. For the remaining four test cases, however, a pair of counter rotating vortices, rotating in a sense opposite to that observed in the thick inlet boundary layer case, dominated the flow field. In all of the cases, these vortical cross flows had energizing influence on the stalled fluid centered along the inner wall. Circumferential nonuniformities in the incoming boundary layer were found to have only secondary effects on the axial and cross-flow velocity distributions at discharge.

The mass-averaged stagnation pressure loss through the diffuser was found to be insensitive to variations in the incoming boundary layer. Only small changes in the static pressure recovery were observed with variations in the inlet boundary layer. These changes were consistent with the anticipated adjustments in the effective area ratio of the diffuser, affected by the variations in the spatial extent of the stalled fluid along the inner wall.

The mass-averaged static pressure recovery was found to be comparable to that of straight conical diffusers of equivalent A_2/A_1 and L/r_1. The boundary layers along the outer, upper and lower walls of the curved diffuser were observed to remain thin under the influence of the cross flows. This counteracted the detrimental influence of the low-momentum fluid along the inner wall on the effective exit area of the diffuser. These observations, together with the less-than-optimum pressure recovery of the equivalent conical diffuser, provided explanations for the aforementioned similarity of the pressure recoveries.

Acknowledgments

The author gratefully acknowledges the research grant provided by the Natural Sciences and Engineering Research Council of Canada in support of this project. The contribution of Mr. Michael F. Saroch to the development of the test section is also acknowledged.

References

Blair, L. W., and Russo, C. J., 1980, "Compact Diffusers for Centrifugal Compressors," AIAA-80-1077, presented at the AIAA/SAE/ASME 16th Joint Propulsion Conference.

Cutler, A. D., and Johnston, J. P., 1981, "The Effects of Inlet Conditions on the Performance of Straight-Walled Diffusers at Low Subsonic Mach Numbers—A Review," Stanford University Report PD-26.

Dolan, F. X., and Runstadler, P. W., 1973, "Pressure Recovery Performance of Conical Diffusers at High Subsonic Mach Numbers," NASA Contractor Report 2299.

Fox, R. W., and Kline, S. J., 1962, "Flow Regimes in Curved Subsonic Diffusers," ASME *Journal of Basic Engineering,* Vol. 84, pp. 303–316.

Kenny, D. P., 1968, "A Novel Low Cost Diffuser for High Performance Centrifugal Compressors," ASME 68-GT-38.

Klein, A., 1981, "REVIEW: Effects of Inlet Conditions on Conical-Diffuser Performance," ASME JOURNAL OF FLUIDS ENGINEERING, Vol. 103, pp. 250–257.

McMillan, O. J., 1982, "Mean-Flow Measurements of the Flow Field Diffusing Bend," NASA Contractor Report 3634.

Moffat, R. J., 1982, "Contributions to the Theory of Single-Sample Uncertainty Analysis," ASME JOURNAL OF FLUIDS ENGINEERING, Vol. 104, pp. 250–260.

Parsons, D. J., and Hill, P. G., 1973, "Effects of Curvature on Two-Dimensional Diffuser Flow," ASME JOURNAL OF FLUIDS ENGINEERING, Vol. 95, pp. 349–360.

Reeves, G. B., 1977, "Design and Performance of Selected Pipe-Type Diffusers," ASME 77-GT-104.

Sagi, C. J., and Johnston, J. P., 1967, "The Design and Performance of Two-Dimensional, Curved Diffusers," ASME *Journal of Basic Engineering,* Vol. 89, pp. 715–731.

Saroch, M. F., 1996, "Contributions to the Study of Turbomachinery Aerodynamics, Part I: Design of a Fish-Tail Diffuser Test Section, Part II: Computations of the Effects of AVDR on Transonic Turbine Cascades," Masters thesis, Department of Mechanical and Aerospace Engineering, Carleton University.

Wellborn, S. R., Reichert, B. A., and Okiishi, T. H., 1992, "An Experimental Investigation of the Flow in a Diffusing S-Duct," AIAA-92-3622 presented at the AIAA/SAE/ASME/ASEE 28th Joint Propulsion Conference.

Extension of the Wall-Driven Enclosure Flow Problem to Toroidally Shaped Geometries of Square Cross-Section

L. M. Phinney
Research Graduate Student,
Department of Mechanical Engineering,
University of California at Berkeley,
Berkeley, CA 94720

J. A. C. Humphrey
Professor and Head,
Department of Aerospace and Mechanical Engineering,
University of Arizona,
Tucson, AZ 85721

The two-dimensional wall-driven flow in an enclosure has been a numerical paradigm of long-standing interest and value to the fluid mechanics community. In this paradigm the enclosure is infinitely long in the x-coordinate direction and of square cross-section ($d \times d$) in the y-z plane. Fluid motion is induced in all y-z planes by a wall (here the top wall) sliding normal to the x-coordinate direction. This classical numerical paradigm can be extended by taking a length L of the geometry in the x-coordinate direction and joining the resulting end faces at $x = 0$ and $x = L$ to form a toroid of square cross-section ($d \times d$) and radius of curvature R_c. In the curved geometry, axisymmetric fluid motion (now in the r-z planes) is induced by sliding the top flat wall of the toroid with an imposed radial velocity, u_{lid}, generally directed from the convex wall towards the concave wall of the toroid. Numerical calculations of this flow configuration are performed for values of the Reynolds number ($Re = u_{lid}d/\nu$) equal to 2400, 3200, and 4000 and for values of the curvature ratio ($\delta = d/R_c$) ranging from $5.0 \cdot 10^{-6}$ to 1.0. For $\delta \leq 0.05$ the steady two-dimensional flow pattern typical of the classical (straight) enclosure is faithfully reproduced. This consists of a large primary vortex occupying most of the enclosure and three much smaller secondary eddies located in the two lower corners and the upper upstream (convex wall) corner of the enclosure. As δ increases for a fixed value of Re, a critical value, δ_{cr}, is found above which the primary center vortex spontaneously migrates to and concentrates in the upper downstream (concave wall) corner. While the sense of rotation originally present in this vortex is preserved, that of the slower moving fluid below it and now occupying the bulk of the enclosure cross-section is reversed. The relation marking the transition between these two stable steady flow patterns is predicted to be $\delta_{cr}^{1/4} = 3.58\, Re^{-1/5}$ ($\delta \pm 0.005$).

Introduction

The Problem of Interest. Wall-driven flows in two- and three-dimensional enclosures of rectangular cross-section, also referred to as lid-driven enclosure or cavity flows, have been extensively studied for three main reasons (Prasad and Koseff, 1989): (i) they are idealized representations of flows over cut-outs, repeated ribs, or cavities on the walls of heat exchangers or on the surfaces of aircraft; (ii) the nature of recirculating flow phenomena and their underlying physical mechanisms can be investigated through fundamental studies of the large primary vortex, secondary corner eddies, and Taylor-Görtler vortices present in such flows; (iii) the relatively simple geometry and easily posed boundary conditions for the case of laminar two-dimensional flow have made this an attractive test case for assessing the performance of various numerical schemes developed to solve the Navier-Stokes equations (see, for example, Pollard and Siu, 1982; Choi et al., 1988; Hayase et al., 1992; and Thakur and Shyy, 1993). The relatively large regions of recirculating flow require that numerical schemes represent both the diffusive and convective terms accurately.

In the present investigation, the effect of geometrical curvature is studied in a modification of the "classical" two-dimensional wall-driven straight enclosure flow problem. The motion of a constant property, Newtonian fluid is calculated in the toroidal geometry pictured in Fig. 1 assuming axisymmetry. The curvature ratio, $\delta = d/R_c$, is the ratio of the toroid cross-section dimension to the toroid radius of curvature. A toroid of square cross-section is computationally advantageous for the specification of boundary conditions as in the conventional straight wall-driven enclosure. All of the boundaries coincide with coordinate directions when analyzed in a cylindrical, (r, θ, z), coordinate system. Fluid motion is induced by moving the upper flat wall of the toroid at a constant or radially-dependent radial velocity. This wall is moved radially inwards, toward the center of the toroid, or radially outwards, away from the center of the toroid. In this study, the latter condition is the one of primary interest. For $\delta \rightarrow 0$ the toroid flow configuration transforms into the classical (straight) two-dimensional wall-driven enclosure flow problem. Thus, in the limit of δ approaching zero our numerical methodology can be validated against a well known and universally accepted standard.

Prior Work. Ghia et al. (1982) studied the effectiveness of a multigrid method by solving the vorticity-stream function formulation of the two-dimensional, incompressible Navier-Stokes equations in a straight wall-driven square enclosure flow. Flows with Reynolds numbers ranging from 100 to 10,000 were calculated on grids as fine as 257×257. Their results have been used extensively by subsequent researchers as a reliable benchmark. Nishida and Satofuka (1992) used a fourth-order Runge-Kutta-Gill scheme to time-integrate the vorticity-stream function form of the Navier-Stokes equations which were spatially discretized to tenth-, eighth-, and sixth-order accuracy for Reynolds numbers of 100, 1000, and 3200, respectively. It is

---

Contributed by the Fluids Engineering Division for publication in the JOURNAL OF FLUIDS ENGINEERING. Manuscript received by the Fluids Engineering Division December 20, 1994; revised manuscript received May 23, 1996. Associate Technical Editor: M. M. Sindir.

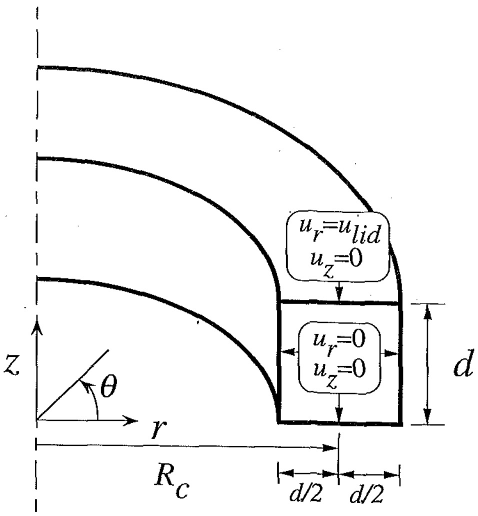

Fig. 1 Coordinate system and boundary conditions used in this study, shown for one-quarter of the toroid. At $z/d = 1$, the flat upper wall or "lid" velocity in the radial direction is fixed to a constant value, u_{lid}, in order to generate Reynolds numbers, Re $= u_{lid}d/\nu$, of 2400, 3200, and 4000. All other velocities are set to zero at the enclosure walls. Flow fields with $u_{lid} \propto 1/r$ were also explored. Note, $u_\theta = 0$ everywhere in the domain.

to be noted that the results of these two investigations converged to steady flow fields in the Reynolds number range studied.

Flow visualization and velocity measurement investigations by Koseff and coworkers (Koseff and Street, 1984, and Prasad and Koseff, 1989) show that end-wall and three-dimensional effects are important in wall-driven rectangular enclosure flows for Reynolds numbers ranging from 3200 to 10,000. The experimental facility in these studies used a belt in contact with the fluid at the top of the enclosure to generate the motion. The depth and span of the enclosure could be varied, and the fluid near the belt could also be heated or cooled. Taylor-Görtler-like vortices were observed in the region of the downstream secondary eddy, and corner vortices were observed at the end walls. These authors found that the transition to turbulent flow occurs in the area around the downstream eddy for Reynolds numbers between 6000 and 8000.

The loss of stability of a two-dimensional, wall-driven enclosure flow perturbed by three-dimensional disturbances due to a Görtler type instability was subsequently predicted and analyzed by Ramanan and Homsy (1994). These authors predict a loss of stability of the base flow due to a long wavelength mode at a critical Reynolds number equal to 594 and a second unstable competing mode with a wavelength close to the enclosure width at Re = 730. The latter result is in reasonable agreement with the experimental data of Aidun et al. (1991).

Koseff and Street (1985) also studied the effects of heating the fluid next to the sliding wall for Richardson numbers, a ratio of the buoyancy to inertial forces, spanning 0.08 to 6.5 for values of the Reynolds number ranging from 1000 to 10,000. Their experiments show that the two-dimensional, wall-driven flow problem which is frequently calculated to verify and test proposed numerical schemes is not strictly realized due to end wall effects.

Several investigators have tried to correctly calculate the three-dimensional characteristics of wall-driven flows in straight enclosures. Iwatsu et al. (1989, 1990) calculated time-dependent flows in a cubical enclosure for Reynolds numbers ranging from 100 to 4000. They did not obtain steady-state solutions for their calculations at Reynolds numbers of 3000 and 4000. Zang et al. (1993) used a modified dynamic subgrid-scale eddy viscosity turbulence model to predict flows at Reynolds numbers of 3200, 7500, and 10,000 and obtained excellent agreement with the experimental data of Prasad and Koseff (1989).

Present Contribution. This is a numerical investigation of steady, two-dimensional, wall-driven flow in a toroidally-shaped enclosure of square cross-section. While steadiness of the fluid motion is the outcome of the calculations, the justification for assuming flow two-dimensionality in the range of Reynolds numbers investigated rests on the findings that: 1) The present transition phenomenon observed in the flow structure does not depend for its existence on a third component of motion. 2) There are practicable geometrical and dynamical conditions for which the transition phenomenon and flow two-dimensionality coexist. 3) Because of the large flow deceleration that takes place adjacent to the sliding wall due to the expansion of the surface normal to the radial direction, the Reynolds number marking the transition between two-dimensional and three-dimensional flow in a toroid is expected to significantly exceed that in a straight enclosure.

The wall-driven flow in a toroidally-shaped enclosure of square cross-section can be realized experimentally and has environmental and electronics cooling applications. A controlled realization of the flow can be accomplished by refining an experiment in which a downwards-directed jet of air is aimed at the center of a horizontally oriented flat block of plastic containing a toroidally shaped cutout at a radius of curvature R_c from the block center. The cutout contains a fluid which can be air also, or a liquid, like water. The axial to radial deflection of the air jet will shear the air-fluid interface and drive the flow in the toroidal cutout.

The remainder of this paper begins by describing the conservation equations in appropriate nondimensional form for the flow in a toroid of square cross-section. The numerical solution methodology and its testing are then discussed. The results obtained for toroids with small curvature ratios are compared to published two-dimensional, wall-driven flows in straight enclosures of square cross-section. The effects of increasing the toroid curvature are then calculated and analyzed. The main results are summarized in the conclusions.

Mathematical Formulation

The equations of motion for an incompressible, constant property, Newtonian fluid are presented in the form best suited

Nomenclature

c_1, c_2 = constants used in the specification of u_{lid}
d = toroid square cross-section dimension
p = pressure
r = radial coordinate
R_c = toroid radius of curvature
Re = Reynolds number, Re $= u_{lid}d/\nu$
t = time
u_{lid} = radial velocity imposed at the $z/d = 1$ surface of the toroid
u_r, u_θ, u_z = velocity components in the radial, circumferential and axial directions
z = axial coordinate
δ = curvature ratio, $\delta = d/R_c$
δ_{cr} = curvature ratio at which the transition between flow patterns occurs
ν = fluid kinematic viscosity
ρ = density of the fluid
Ψ = stream function
θ = circumferential coordinate

Superscripts

$*$ = denotes a nondimensional variable

for describing the flow in the present toroidal configuration. The fixed cylindrical coordinate system (r, θ, z) shown in Fig. 1 is the most appropriate since the boundaries of the domain coincide with the coordinate directions. In keeping with previous two-dimensional analyses, the flows under consideration are expected to be steady, axisymmetric, and devoid of a circumferential velocity component for the range of the parameters explored. Therefore, the relevant equations are the mass, radial momentum, and axial momentum conservation equations.

The equations are nondimensionalized using appropriate scales. The imposed sliding wall or lid velocity, u_{lid}, is used to nondimensionalize the radial and axial velocities. The pressure is nondimensionalized by the density times the square of the imposed lid velocity. The axial coordinate, z, scales with the toroid cross-section dimension, d. However, the radial coordinate, r, is first translated by the radius of curvature minus one-half the toroid cross-section dimension, $R_c - d/2$, and then scaled by the toroid cross-section dimension, d. The nondimensional axial and radial coordinates, z^* and r^*, vary between 0 and 1 when nondimensionalized in this manner. Time is nondimensionalized by multiplying by the lid velocity and dividing by the toroid cross-section dimension. Thus, the above scales are used to define the following nondimensional variables:

$$u_r^* = \frac{u_r}{u_{lid}}, \quad u_z^* = \frac{u_z}{u_{lid}}, \quad p^* = \frac{p}{\rho u_{lid}^2}, \quad z^* = \frac{z}{d},$$

$$r^* = \frac{r - \left(R_c - \dfrac{d}{2}\right)}{d}, \quad \text{and} \quad t^* = \frac{t u_{lid}}{d} \tag{1}$$

In terms of these nondimensional variables the axisymmetric mass, radial momentum, and axial momentum conservation equations are the following:

continuity

$$\frac{\partial u_r^*}{\partial r^*} + \frac{\delta u_r^*}{1 + \delta\left(r^* - \dfrac{1}{2}\right)} + \frac{\partial u_z^*}{\partial z^*} = 0 \tag{2}$$

r-momentum

$$\frac{\partial u_r^*}{\partial t^*} + u_r^* \frac{\partial u_r^*}{\partial r^*} + u_z^* \frac{\partial u_r^*}{\partial z^*} = -\frac{\partial p^*}{\partial r^*} + \frac{1}{\text{Re}}\left(\frac{\partial^2 u_r^*}{\partial r^{*2}} + \frac{\delta}{1 + \delta\left(r^* - \dfrac{1}{2}\right)} \frac{\partial u_r^*}{\partial r^*} - \frac{\delta^2 u_r^*}{\left(1 + \delta\left(r^* - \dfrac{1}{2}\right)\right)^2} + \frac{\partial^2 u_r^*}{\partial z^{*2}}\right) \tag{3}$$

z-momentum

$$\frac{\partial u_z^*}{\partial t^*} + u_r^* \frac{\partial u_z^*}{\partial r^*} + u_z^* \frac{\partial u_z^*}{\partial z^*} = -\frac{\partial p^*}{\partial z^*} + \frac{1}{\text{Re}}\left(\frac{\partial^2 u_z^*}{\partial r^{*2}} + \frac{\delta}{1 + \delta\left(r^* - \dfrac{1}{2}\right)} \frac{\partial u_z^*}{\partial r^*} + \frac{\partial^2 u_z^*}{\partial z^{*2}}\right) \tag{4}$$

where the Reynolds number, Re, and curvature ratio, δ, are Re $= u_{lid} d/\nu$ and $\delta = d/R_c$, respectively.

The curvature ratio has a maximum value of $\delta = 2$ which corresponds to a solid cylinder of height and radius both equal to d. In the limit of δ going to zero, the above equations become the corresponding conservation equations describing the flow in Cartesian coordinates for the standard two-dimensional, straight wall-driven enclosure flow problem. In the computational analyses performed in this study, Reynolds numbers of 2400, 3200, and 4000 were investigated for curvature ratios varying from $5.0 \cdot 10^{-6}$ to 1.0.

The nondimensional, axisymmetric stream function, Ψ^*, is equal to

$$\Psi^* = \frac{\Psi}{d u_{lid} R_c} \tag{5}$$

and satisfies the continuity equation with velocities defined by

$$u_z^* \equiv \frac{1}{1 + \delta\left(r^* - \dfrac{1}{2}\right)} \frac{\partial \Psi^*}{\partial r^*} \quad \text{and}$$

$$u_r^* \equiv \frac{-1}{1 + \delta\left(r^* - \dfrac{1}{2}\right)} \frac{\partial \Psi^*}{\partial z^*} \tag{6}$$

Again, in the limit of small curvature ratios, this stream function reduces to a Cartesian coordinates stream function.

The cylindrical coordinate system, the flow domain, and the boundary conditions for the present problem are drawn in Fig. 1. Constant zero velocities are specified on the fixed walls comprising the domain boundaries. Calculations have been performed with u_{lid} equal to a constant as well as with $u_{lid} \propto 1/r$. The latter condition corresponds to a source expanding radially outwards from $r = 0$. Since a transient solution procedure was employed, the flow inside the entire domain was initially at rest. However, in all of the cases reported a steady-state flow condition was achieved.

Numerical Procedure

The calculations of this study were performed using the CUTEFLOWS numerical procedure. Detailed descriptions of the algorithm's finite differencing schemes and solution methodology are provided in Schuler et al. (1991) and Humphrey et al. (1995). Applications of the code include: flows between corotating disks by Schuler (1990), Humphrey et al. (1992, 1995), Usry (1992), and Iglesias (1994); around bluff bodies by Treidler (1991), Tatsutani et al. (1993), and Devarakonda (1994); and past backward-facing steps by Tatsutani et al. (1992) and Iglesias et al. (1993). A summary of the procedure and of its rigorous testing follow.

CUTEFLOWS calculates unsteady, three-dimensional, constant property flows in either Cartesian or cylindrical coordinates. The algorithm explicitly calculates the time evolution of the mass, momentum, and energy conservation equations in primitive variable form. The energy solution methodology is not relevant to the present isothermal flow study but is given in Iglesias (1994). The spatial finite differencing scheme is globally second-order accurate and is derived using the staggered grid control-volume formulation of Patankar (1980). Diffusion and pressure terms are discretized using second-order central differences, and the convection terms are represented using the locally third-order accurate QUICK scheme of Leonard (1979).

The resulting set of ordinary differential equations is solved in time for the velocity components using a second-order accurate Runge-Kutta predictor-corrector method (RK2). In order to satisfy mass continuity and simultaneously obtain the pressure field, the expected divergence-free velocity field at each new time step is decomposed into a pseudo-velocity vector field that is independent of pressure and a separate pressure contribution, as described by Chorin and Marsden (1979). The pseudo-velocity vector field is then calculated directly using the RK2 algorithm. The pressure contribution is calculated at the end of each half time step using a conjugate gradient method applied to the discrete Poisson equation that results from imposing the divergence-free condition on the velocity field.

The CUTEFLOWS code has been thoroughly tested by reference to a number of two- and three-dimensional flows in Cartesian and cylindrical coordinates. Of the references listed above, especially noteworthy are the calculations performed by Tatsutani et al. (1992) and Iglesias et al. (1993) for the flow past a backward-facing step for isothermal and nonisothermal conditions, respectively. Both of these cases were set up as "Benchmark Problems for Heat Transfer Codes" at consecutive Winter Annual Meetings of the ASME. In particular, Tatsutani et al. (1992) explore the sensitivity of flow field variables to three different (streamwise × transverse) grids corresponding to (250 × 50), (400 × 76), and (500 × 76) nodes, respectively. They find that the solutions on the coarse and intermediate grids come to within 1.0 and 0.6 percent, respectively, of the finest grid, and that the solution on the finest grid agrees to within less than 1 percent with the benchmark solution obtained by Gartling (1990) on an (800 × 40) grid. In addition to tests such as these proving that CUTEFLOWS is capable of generating grid-independent results, we provide below grid-dependence checks which show that much coarser grids suffice to attain comparable levels of accuracy for the present problem.

Results and Discussion

First, the numerical solutions for toroids with small curvature ratios are compared with previously published solutions of the straight wall-driven enclosure flow configuration. Then, the curvature ratio of the toroid is increased to study the effect of curvature on flow behavior. All of the numerical calculations discussed in this section converged to steady-state solutions.

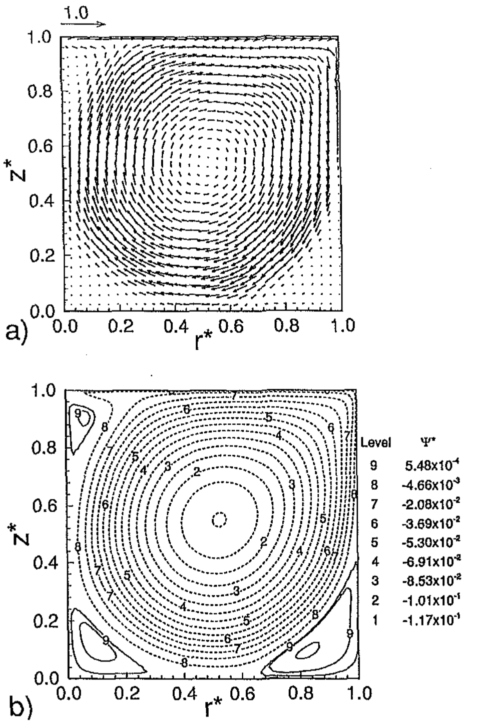

Fig. 2 Outwardly driven flow calculated on a 60 × 60 uniform grid for Re = 3200 and δ = 0.005: (*a*) velocity vectors and (*b*) streamlines

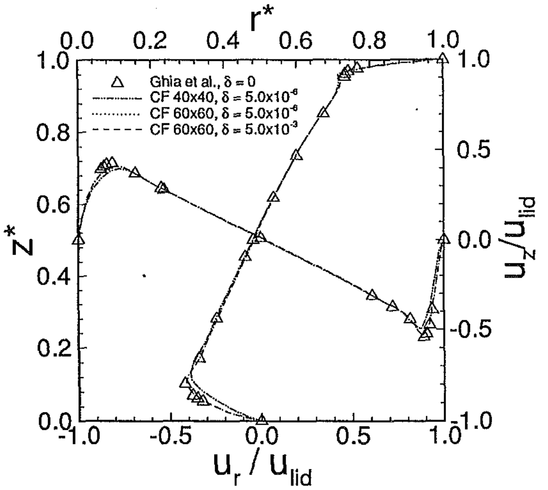

Fig. 3 Outwardly driven flow velocity profiles at the horizontal and vertical centerlines for Re = 3200 calculated on two uniform grids: 40 × 40 and 60 × 60 with $\delta = 5.0 \cdot 10^{-6}$, and 60 × 60 with and $5.0 \cdot 10^{-3}$. The calculations of Ghia et al. (1982) with $\delta = 0$ are included for comparison.

Comparison to Existing Solutions. Figure 2 shows the velocity vectors and streamlines calculated on a 60 × 60 uniform computational mesh at Re = 3200 and $\delta = 0.005$. (For clarity, only every other grid node is plotted in all the velocity vector figures.) The velocity vector and streamline plots exhibit the characteristics of previously studied straight wall-driven enclosure flows. These consist of a large primary vortex or cell occupying the bulk of the enclosure and secondary eddies in the two lower corners and the upper upstream corner. The minimum value of the stream function at the center of the primary vortex agrees within 2.2 and 2.8 percent with the values obtained by Ghia et al. (1982) and Nishida and Satofuka (1992), respectively.

Figure 3 shows velocity profiles calculated along the horizontal and vertical centerlines of the enclosure for flows with Re = 3200 and $\delta = 5.0 \cdot 10^{-6}$ on 40 × 40 and 60 × 60 uniform grids. Also, shown are the results for Re = 3200 and $\delta = 0.005$ from Fig. 2. This comparison reveals that the 60 × 60 grid resolves the boundary layer features of the flow better than the 40 × 40 grid, although the 40 × 40 grid yields profiles in reasonable agreement with the data presented in Ghia et al. (1982). Nonetheless, it was decided to use 60 × 60 grids for all subsequent numerical calculations. It is also clear from these profiles that a curvature ratio equal to 0.005 suffices to reproduce the straight enclosure results since the $5.0 \cdot 10^{-6}$ and $5.0 \cdot 10^{-3}$ velocity profiles calculated on the 60 × 60 grid are indistinguishable, as shown in Fig. 3. Thus, calculations with $\delta = 0.005$ will be representative of essentially "straight" enclosure results in subsequent plots.

Figure 4 shows the effect of changing the radial velocity boundary condition at the upper surface of the toroid. The velocity profiles at the horizontal and vertical centerlines of the enclosure calculated using two different boundary conditions are plotted for curvature ratios of 0.05 and 1.0. The first boundary condition fixes the imposed radial velocity of the upper wall, u_{lid}, to a constant value, c_1. In this case, the value of c_1 is such that a Reynolds number of 3200 is generated. The second boundary condition, $u_{lid} = c_2/r$, corresponds to a source expanding radially outward from $r = 0$. The constant, c_2, is chosen so that the radial velocity imposed at the radial midpoint of the enclosure, $r^* = 0.5$, is equal for the two cases ($c_2 = c_1 R_c$). As shown by the profiles, the small curvature results with $\delta = 0.05$ are indistinguishable for the two cases and only slight differences appear for the strongly curved configuration with $\delta = 1.0$. Clearly, the differences in the velocity profiles are not

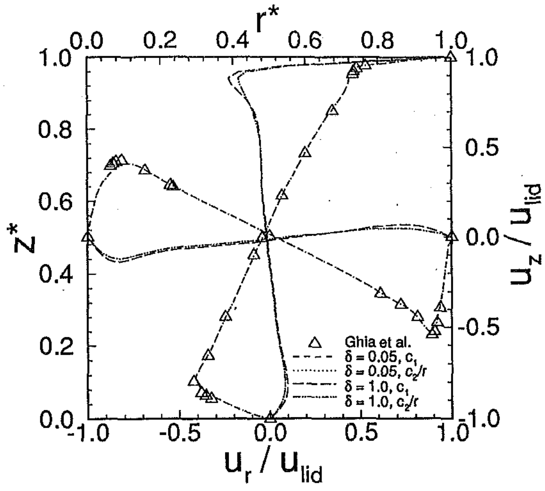

Fig. 4 Outwardly driven flow velocity profiles at the horizontal and vertical centerlines for Re = 3200 with $\delta = 0.05$ and $\delta = 1.0$. Boundary conditions at $z^* = 1.0$ are $u_{lid} = c_1$ and $u_{lid} = c_2/r$, respectively. The calculations of Ghia et al. (1982) with $\delta = 0$ are included for comparison.

substantial. Since the resultant steady-state flow behavior does not depend significantly on the sliding wall boundary condition employed, the remainder of the calculations were performed with the upper wall fixed to a constant radial velocity.

To further check the grid-independence of the numerical results, calculations were performed on a 60 × 60 nonuniform grid for the case in Fig. 4 with $\delta = 1.0$ and $u_{lid} = c_1$ such that Re = 3200. The grid was distributed exponentially in order to double the number of grid nodes at the walls. The solutions calculated for the uniform and nonuniform grids were then compared. The horizontal and vertical centerline profiles of velocity (Phinney, 1994) are practically indistinguishable, and the values for the location and stream function at the center of the primary vortex reveal differences of 2 percent between the two solutions.

Wall-Driven Flow With Curvature Effects. Having established that the numerical procedure accurately predicts wall-driven flows in enclosures of square cross-section with small curvature ratios, curvature effects were then investigated by decreasing the radius of curvature of the toroid, thus increasing its curvature ratio, δ. The Reynolds number for these calculations was maintained at 3200. The steady-state flow patterns exhibited significant changes as the curvature ratio was increased, as seen in the velocity vector and stream function contour plots for curvature ratios of 0.25, 0.256, and 1.0 provided in Figs. 5, 6, and 7, respectively. As the curvature ratio is increased, the primary vortex moves upwards and away from the center of the toroid toward the upper downstream (concave wall) corner from where it drives a larger but weaker counter-rotating vortex now occupying the bulk of the toroid cross-section. At $\delta = 0.25$ the primary vortex has already moved upward significantly, as illustrated by the velocity vectors and streamlines in Fig. 5. If the curvature ratio is increased even slightly above 0.25, the vortex "jumps" into the upper concave wall corner region as shown by the flow patterns in Fig. 6 for $\delta = 0.256$. The strength of the primary vortex is reduced as the curvature ratio is increased. The value of the stream function at the center of the primary vortex for curvature ratios of 0.256 and 1.0 are, respectively, 41 and 45 percent less than the value for the case with $\delta = 0.005$.

Velocity profiles calculated along the horizontal and vertical centerlines for six curvature ratios ranging from 0.005 to 1.0 are plotted in Fig. 8. These results provide additional insight into the effects of increasing the curvature of the toroid. While the calculations for $\delta = 0.005$ agree very well with the two-dimensional, straight wall-driven enclosure results, the calculations for $\delta = 0.2$ start differing and the profiles for $\delta = 0.25$ fall between the small and large curvature ratio results. The calculations for $\delta = 0.256$, 0.333, and 1.0 all exhibit the same general flow patterns, with the primary vortex concentrated in the upper concave wall corner.

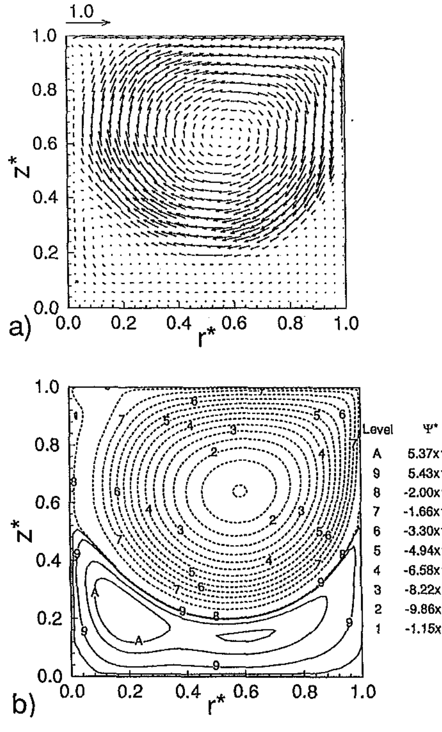

Fig. 5 Outwardly driven flow calculated for Re = 3200 and $\delta = 0.25$: (*a*) velocity vectors and (*b*) streamlines

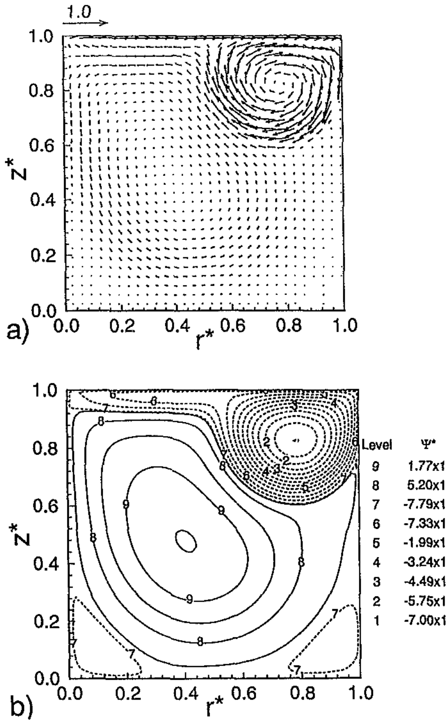

Fig. 6 Outwardly driven flow calculated for Re = 3200 and $\delta = 0.256$: (*a*) velocity vectors and (*b*) streamlines

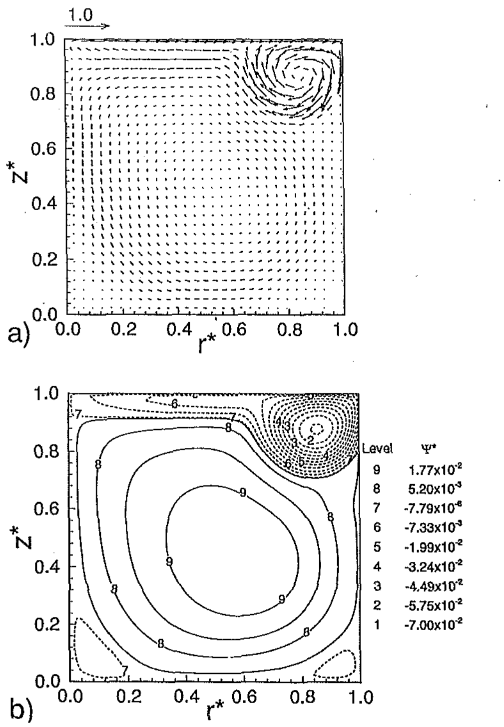

Fig. 7 Outwardly driven flow calculated for Re = 3200 and δ = 1.0; (*a*) velocity vectors and (*b*) streamlines

The r^*-z^* trajectory of the primary vortex center is plotted in Fig. 9 and tabulated in Table 1 for curvature ratios ranging from $\delta = 0.005$ to 1.0 at Reynolds numbers of 2400, 3200, and 4000. The figure shows that at all three Reynolds numbers the small curvature ratio steady-state flow patterns have primary vortices centered near the geometrical center of the enclosure in agreement with the calculations of Ghia et al. (1982) and Nishida and Satofuka (1992). As the curvature ratio is increased, the primary vortex gradually moves upwards and outwards. Then, at a critical curvature ratio, a sudden large change occurs in the location of this primary vortex; the vortex being displaced toward the upper concave wall corner. Further increases in the curvature ratio result in only slight movements of the primary vortex toward this corner.

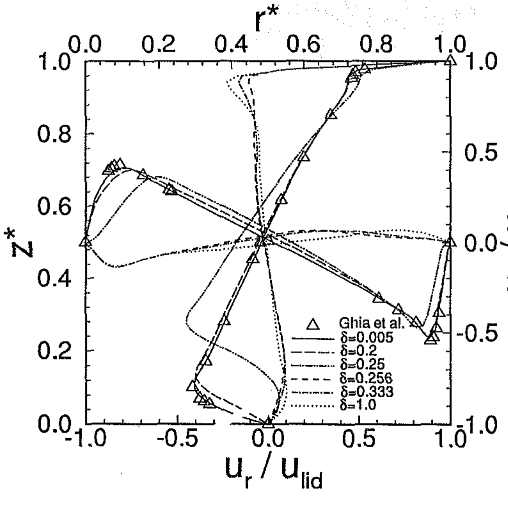

Fig. 8 Outwardly driven flow velocity profiles at the horizontal and vertical centerlines for Re = 3200 with δ = 0.005, 0.2, 0.25, 0.256, 0.333, and δ = 1.0. The calculations of Ghia et al. (1982) with δ = 0 are included for comparison.

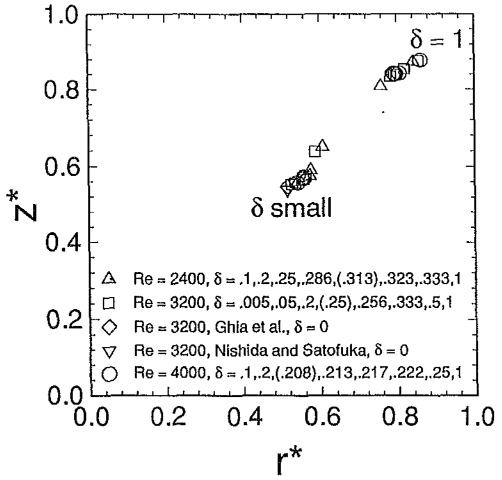

Fig. 9 Location of the primary vortex center for outwardly driven flows at Re = 2400, 3200, and 4000 for a range of curvature ratios, 0.005 ≤ δ ≤ 1.0. The locations of the primary vortex centers for Re = 3200 and δ = 0 calculated by Ghia et al. (1982) and Nishida and Satofuka (1992) are provided for comparison. The parentheses surround the largest value of δ for which the essentially "straight" enclosure two-dimensional steady-state flow pattern exists.

A region of the toroid cross-section exists, between the locations of the centers of vortices exhibiting curvature unaffected (or essentially "straight" enclosure) and curvature-affected (or "curved" enclosure) flow patterns, where no primary vortices are centered. The steady state flow pattern attained is always either the essentially "straight" or the "curved" enclosure pattern shown in the inserts in Fig. 10, with no intermediate flow patterns being observed. The curvature ratio at which the transition from the "straight" enclosure flow pattern to the "curved" enclosure flow pattern occurs is a function of the Reynolds number. Figure 10 graphs this critical curvature ratio as a function of the Reynolds number, the relation being $\delta_{cr}^{1/4} = 3.58$ $\mathrm{Re}^{-1/5}$ ($\delta \pm 0.005$) in the range of the parameters calculated and to the accuracy of the grids used.

As mentioned earlier in order to better resolve the boundary layer at the sliding wall surface, the outwardly driven flow case with Re = 3200 and $\delta = 1.0$ was calculated on a 60 × 60 nonuniform grid. Results very similar to those shown in Fig. 7 were obtained with the conclusion that the increased grid resolution did not significantly impact the resulting flow (Phinney, 1994). Numerical calculations were also performed to investigate the effect of geometrical curvature for cases in which the upper wall of the toroid is moved radially inwards, toward the center of the toroid, with a constant velocity at Re = 3200 (Phinney, 1994). Although slight changes in the steady-state flow pattern are observed, no significant curvature dependence exists for inwardly driven toroidal flows.

The validity of the steady-state flow patterns for the essentially "straight" and "curved" toroid geometries was further demonstrated by performing two additional calculations. The previously calculated steady-state flow fields at $\delta = 1.0$ and $\delta = 5.0 \cdot 10^{-6}$ with Re = 3200 were used as the initial conditions for calculations at the same Re and curvature ratios of $\delta = 5.0 \cdot 10^{-6}$ and $\delta = 1.0$, respectively. Thus, the flow field resulting from the "curved" toroid geometry was used as the initial condition for the essentially straight toroid geometry, and vice versa. In both of these calculations, the final steady-state flow pattern was the pattern calculated for that geometry with the flow field initially at rest. The $\delta = 5.0 \cdot 10^{-6}$ steady-state flow pattern was that for an essentially straight toroid, and the $\delta = 1.0$ steady-state flow pattern was that for a curved geometry with the primary vortex concentrated in the upper concave wall corner. The conclusion of this test is that the amount of curva-

Table 1 Location of the primary vortex centers, (r_c^*, z_c^*), for outwardly driven flows at Re = 2400, 3200, and 4000 for a range of curvature ratios, $0.005 \leq \delta \leq 1.0$. The locations of the primary vortex centers for Re = 3200 and $\delta = 0$ calculated by Ghia et al. (1982) and Nishida and Satofuka (1992) are (0.5165, 0.5469) and (0.5156, 0.5391), respectively

Re = 2400			Re = 3200			Re = 4000		
δ	r_c^*	z_c^*	δ	r_c^*	z_c^*	δ	r_c^*	z_c^*
0.100	0.544	0.560	0.005	0.528	0.553	0.100	0.542	0.558
0.200	0.561	0.571	0.050	0.537	0.557	0.200	0.559	0.569
0.250	0.574	0.575	0.200	0.559	0.566	0.208	0.559	0.573
0.286	0.577	0.590	0.250	0.587	0.639	0.213	0.791	0.842
0.313	0.607	0.651	0.256	0.784	0.833	0.217	0.793	0.840
0.323	0.759	0.807	0.333	0.799	0.838	0.222	0.798	0.840
0.333	0.759	0.807	0.500	0.819	0.853	0.250	0.806	0.842
1.000	0.841	0.872	1.000	0.855	0.875	1.000	0.861	0.877

ture in the toroid geometry determines the steady-state flow pattern at a given Reynolds number.

In concluding this section we note that the straight and curved wall-driven enclosure flows differ in a fundamental way. Due to the area dependence on radius, in the curved toroidal geometry an element of fluid near the sliding wall decelerates as it moves radially outwards. Thus, for the same value of Re, the stagnation pressure of the flow impinging on the concave wall near the upper corner of the toroid is less than that corresponding to the straight enclosure case. In a straight enclosure, the motion of fluid along the sliding wall is driven by friction forces while that in the bulk of the enclosure, defining the primary vortex, is driven primarily by the pressure difference between the upper downstream (concave wall) corner and the upper upstream (convex wall) corner. Due to the radial area expansion, the effect of curvature is to diminish this pressure difference so that the fluid is unable to penetrate as deeply into the enclosure with the consequence that, instead, it induces a weaker, primary vortex located near the upper concave wall corner.

For inwardly driven flows in curved toroidal geometries, the radial dependence of area now works to accelerate fluid near the sliding wall towards the upper downstream (convex wall) corner. This results in a stagnation pressure larger than that corresponding to the straight enclosure case and an overall pressure difference that reinforces a primary vortex revolving about the geometric center of the enclosure.

Conclusions

Numerical calculations of axisymmetric (two-dimensional) wall-driven flows in toroids of square cross-section reveal a striking change in the r-z plane flow patterns as a function of toroid curvature. Here attention is focused primarily on cases with constant wall motions directed radially outwards, from the convex to the concave walls of the toroid. For values of $\delta < \delta_{cr}$ the flow induced resembles that arising in a straight enclosure ($\delta = 0$), consisting of a primary vortex located near the geometric center of the enclosure and with smaller eddies in the two bottom corners as well as the upper upstream corner. For values of $\delta > \delta_{cr}$ the primary vortex "jumps" into the upper concave wall corner of the enclosure, its rotational velocity and size being diminished (relative to that in a straight enclosure) as a result of the radial dependence on area of the outwardly directed flow. In its new position, the primary vortex now drives a larger but weaker counter-rotating vortex located near the geometric center of the toroid. The relationship between the critical curvature ratio and the Reynolds number for which this transition between flow patterns occurs is found to be $\delta_{cr}^{1/4} = 3.58\ \mathrm{Re}^{-1/5}$ ($\delta \pm 0.005$). To the authors' knowledge, these striking findings have not been previously reported.

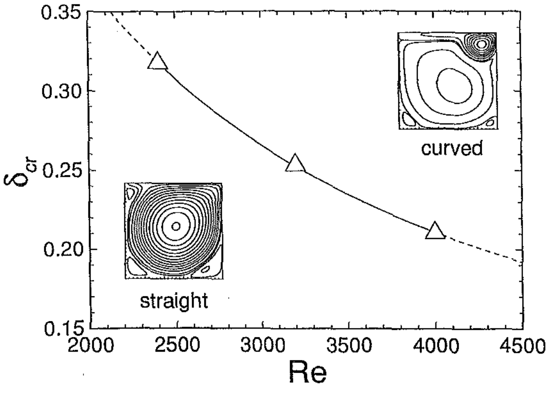

Fig. 10 Flow regime map showing the variation of δ_{cr} with Re separating essentially "straight" from predominantly "curved" enclosure flow patterns in outwardly wall-driven enclosure flows. The transition between flow patterns is fairly abrupt. The curve shown is given by $\delta_{cr}^{1/4} = 3.58\ \mathrm{Re}^{-1/5}$ ($\delta \pm 0.005$).

These findings are not devoid of practical value. They are relevant, for example, to the jet impingement cooling of electronic equipment and to some environmental flows. In a heat transfer application, the sudden displacement and weakening of the primary center vortex in a shear-driven curved enclosure flow will lower the convective heat transfer between the enclosure fluid and its surroundings.

In concluding this paper we note that, according to the linear stability analysis of Ramanan and Homsy (1994), for values of Re < 594 the wall-driven flow in a straight enclosure is stable and two-dimensional; that is, devoid of three-dimensional centrifugally-driven motions. While the corresponding stability analysis has not been performed for the present toroid geometry, because of area-induced radial flow deceleration that takes place adjacent to the sliding wall, the Reynolds number marking the appearance of three-dimensional instabilities in a toroid is expected to significantly exceed the straight enclosure value. Notwithstanding, taking Re = 594 as an estimate of the upper limit for two-dimensional flow in the toroid, this yields a value of $\delta_{cr} = 1.0$ as the lower limit for the straight/curved flow pattern transition shown in Fig. 10. This value of δ_{cr} is well within the limits $\delta = 0$ and 2 which can be realized in the laboratory. The (conservative) conclusion is that for values Re < 594 and $1 < \delta < 2$ the straight/curved flow pattern transition predicted for larger values of Re should correspond to strictly two-dimensional flows.

The toroidal flow configuration analyzed here represents an interesting generalization of the "classical" straight wall-driven enclosure flow paradigm. The propensity of the flow in the toroid to centrifugally-driven instabilities which would render it three-dimensional and possibly unsteady is the subject of continued research by one of the authors (JACH).

Acknowledgments

L. M. Phinney was supported by a National Science Foundation Graduate Fellowship while this research was being conducted. Helpful discussions with S. A. Berger and J. R. Koseff are gratefully acknowledged.

References

Aidun, C. K., Triantafillopoulos, N. G., and Benson, J. D., 1991, "Global Stability of a Lid-Driven Cavity with Throughflow: Flow Visualization Studies," *Physics of Fluids A*, Vol. 3, pp. 2081–2091.

Choi, Y., Humphrey, J. A. C., and Sherman, F. S., 1988, "Random-Vortex Simulation of Transient Wall-Driven Flow in a Rectangular Enclosure," *Journal of Computational Physics*, Vol. 75, pp. 359–383.

Chorin, A. J., and Marsden, J. E., 1979, *A Mathematical Introduction to Fluid Mechanics*, Springer-Verlag.

Devarakonda, R., 1994, "Experimental and Numerical Investigation of Unsteady Bluff Body Flows," Ph.D. thesis, University of California, Berkeley, CA.

Gartling, D. K., 1990, "A Test Problem for Outflow Boundary Conditions—Flow Over a Backward Facing Step," *International Journal for Numerical Methods in Fluids*, Vol. 11, pp. 953–967.

Ghia, U., Ghia, K. N., and Shin, C. T., 1982, "High-Re Solutions for Incompressible Flow Using the Navier-Stokes Equations and a Multigrid Method," *Journal of Computational Physics*, Vol. 48, pp. 387–411.

Hayase, T., Humphrey, J. A. C., and Greif, R., 1992, "A Consistently Formulated QUICK Scheme for Fast and Stable Convergence Using Finite-Volume Iterative Calculation Procedures," *Journal of Computational Physics*, Vol. 98, pp. 108–118.

Humphrey, J. A. C., Schuler, C. A., and Iglesias, I., 1992, "Analysis of Viscous Dissipation in Disk Storage Systems and Similar Flow Configurations," *Physics of Fluids A*, Vol. 4, pp. 1415–1427.

Humphrey, J. A. C., Schuler, C. A., and Webster, D. R., 1995, "Unsteady Laminar Flow between a Pair of Disks Corotating in a Fixed Enclosure," *Physics of Fluids*, Vol. 7, pp. 1225–1240.

Iglesias, I., 1994, "Numerical Investigation of Flow Between a Pair of Disks Corotating in a Cylindrical Enclosure," Ph.D. thesis, University of California, Berkeley, California.

Iglesias, I., Humphrey, J. A. C., and Giralt, F., 1993, "Numerical Calculation of Two-Dimensional, Buoyancy-Assisted Flow Past a Backward-Facing Step in a Vertical Channel," ASME HTD-Vol. 258, pp. 63–72.

Iwatsu, R., Hyun, J. M., and Kuwahara, K., 1990, "Analyses of Three-Dimensional Flow Calculations in a Driven Cavity," *Fluid Dynamics Research*, Vol. 6, pp. 91–102.

Iwatsu, R., Ishii, K., Kawamura, T., Kuwahara, K., and Hyun, J. M., 1989, "Numerical Simulation of Three-Dimensional Flow Structure in a Driven Cavity," *Fluid Dynamics Research*, Vol. 5, pp. 173–189.

Koseff, J. R., and Street, R. L., 1984, "Visualization Studies of a Shear Driven Three-Dimensional Recirculating Flow," JOURNAL OF FLUIDS ENGINEERING, Vol. 106, pp. 21–29.

Koseff, J. R., and Street, R. L., 1985, "Circulation Structure in a Stratified Cavity Flow," *Journal of Hydraulic Engineering*, Vol. 111, pp. 334–354.

Leonard, B. P., 1979, "A Stable and Accurate Convective Modelling Procedure Based on Quadratic Upstream Interpolation," *Computer Methods in Applied Mechanics and Engineering*, Vol. 19, pp. 59–98.

Nishida, H., and Satofuka, N., 1992, "Higher-Order Solutions of Square Driven Cavity Flow Using a Variable-Order Multi-Grid Method," *International Journal for Numerical Methods in Engineering*, Vol. 34, pp. 637–653.

Patankar, S. V., 1980, *Numerical Heat Transfer and Fluid Flow*, Hemisphere.

Phinney, L. M., 1994, "Curvature Effects in Wall-Driven Enclosure Flows," M.S. Report, University of California, Berkeley, CA.

Pollard, A., and Siu, A. L.-W., 1982, "The Calculation of Some Laminar Flows Using Various Discretisation Schemes," *Computer Methods in Applied Mechanics and Engineering*, Vol. 35, pp. 293–313.

Prasad, A. K., and Koseff, J. R., 1989, "Reynolds Number and End-Wall Effects on a Lid-Driven Cavity Flow," *Physics of Fluids A*, Vol. 1, pp. 208–218.

Ramanan, N., and Homsy, G. M., 1994, "Linear Stability of Lid-Driven Cavity Flow," *Physics of Fluids*, Vol. 6, pp. 2690–2701.

Schuler, C. A., 1990, "Investigation of the Flow Between Rotating Disks in an Enclosure," Ph.D. thesis, University of California, Berkeley, California.

Schuler, C. A., Treidler, E. B., and Humphrey, J. A. C., 1991, "CUTEFLOWS (Computing Unsteady Three-Dimensional Elliptic FLOWS): A User's Guide," Report Gold 91-001, Computer Mechanics Laboratory, Berkeley, CA.

Tatsutani, K., Devarakonda, R., and Humphrey, J. A. C., 1993, "Unsteady Flow and Heat Transfer for Cylinder Pairs in a Channel," *International Journal of Heat and Mass Transfer*, Vol. 36, pp. 3311–3328.

Tatsutani, K., Usry, W. R., and Humphrey, J. A. C., 1992, "Numerical Calculation of Two Dimensional Laminar Flow and Heat Transfer for a Backward Facing Step Using CUTE FLOWS," ASME HTD-Vol. 222, pp. 1–6.

Thakur, S., and Shyy, W., 1993, "Some Implementational Issues of Convection Schemes for Finite-Volume Formulations," *Numerical Heat Transfer*, Part B, Vol. 24, pp. 31–55.

Treidler, E. B., 1991, "An Experimental and Numerical Investigation of Flow Past Ribs in a Channel," Ph.D. thesis, University of California, Berkeley, California.

Usry, W. R., 1992, "Investigation of the Flow Between Obstructed Corotating Disks in Enclosures," Ph.D. Thesis, University of California, Berkeley, CA.

Zang, Y., Street, R. L., and Koseff, J. R., 1993, "A Dynamic Mixed Subgrid-Scale Model and its Application to Turbulent Recirculating Flows," *Physics of Fluids A*, Vol. 5, pp. 3186–3196.

Convex Turbulent Boundary Layers With Zero and Favorable Pressure Gradients

(Data Bank Contribution)*

A. C. Schwarz

M. W. Plesniak

School of Mechanical Engineering,
Purdue University,
West Lafayette, IN 47907-1003

A turbulent boundary layer subjected to multiple, additional strain rates, namely convex curvature coupled with streamwise pressure gradients (zero and favorable, ZPG and FPG) was investigated experimentally using laser Doppler velocimetry. The inapplicability of the universal flat-plate log-law to curved flows is discussed. However, a logarithmic region is found in the curved and accelerated turbulent boundary layer examined here. Similarity of the mean velocity and Reynolds stress profiles was achieved by 45 deg of curvature even in the presence of the strongest FPG investigated ($k = 1.01 \times 10^{-6}$). The Reynolds stresses were suppressed (with respect to flat plate values) due primarily to the effects of strong convex curvature ($\delta_o/R \approx 0.10$). In curved boundary layers subjected to different favorable pressure gradients, the mean velocity and normal Reynolds stress profiles collapsed in the inner region, but deviated in the outer region ($y^+ \geq 100$). Thus, inner scaling accounted for the impact of the extra strain rates on these profiles in the near-wall region. Combined with curvature, the FPG reduced the strength of the wake component, resulted in a greater suppression of the fluctuating velocity components and a reduction of the primary Reynolds shear stress throughout almost the entire boundary layer relative to the ZPG curved case.

Introduction

With the desire to achieve higher thrust-to-weight ratios in turbomachines, it becomes increasingly important to understand the fundamental mechanisms of momentum and heat transfer. An increase in turbine performance is coupled with higher turbine inlet temperatures, increased nonuniformity of the inlet temperature distribution, and higher speeds. Due to curved surfaces, low aspect ratio passages and streamwise and spanwise strains, the momentum and heat transfer mechanisms in turbomachinery are challenging to predict.

Due to the complex nature of the flowfield inside a turbine blade row passage, it is important to isolate the effects of various complexities, e.g., interacting strains, in order to make the problem tractable. Since complex turbulent flows cannot be predicted adequately with current computational models, there is a tremendous demand for well-designed experimental investigations. A number of researchers have performed experiments to study the influence of additional rates of strain, e.g., convex and concave curvature (So and Mellor, 1973; Gillis and Johnston, 1983; Muck et al., 1985; Hoffman et al., 1985; and Barlow and Johnston, 1988a, b), as well as adverse and favorable streamwise pressure gradients (Kline et al., 1967; Narayanan and Ramjee, 1969; Narashimha and Sreenivasan, 1979; and Nagano et al., 1991).

The issue of existence of the logarithmic law in complex turbulent boundary layers has received considerable attention. Several investigators have shown that logarithmic regions exist (although the flat-plate log-law constants must be modified) in flows with streamline curvature and longitudinal pressure gradients, even in the case of two strain rates interacting with each other (cf. Smits et al., 1979; Gibson et al., 1984; Gibson, 1984 and 1988; Baskaran et al., 1987; Bandyopadhyay and Ahmed, 1993; and Huang and Bradshaw, 1995). Departures from the log-law have been observed in the case of changing curvature, i.e., from convex to concave curvature as reported by Bandyopadhyay and Ahmed (1993), and also in the presence of a strong, stabilizing favorable pressure gradient (Blackwelder and Kovasznay, 1972). In most of these investigations, two different methods of determining the wall shear stress were employed, e.g., Clauser method along with Preston tube measurements or wall-slope method. In a turbulent flow over a curved hill, Baskaran et al. (1987) found that wall shear stress measurements inferred from the Clauser method agreed to within 2 percent with those obtained using a Preston tube. Barlow and Johnston (1985) compared the Clauser method with the near-wall slope method ($\tau_w = \mu \partial \bar{U}/\partial y|_{y=0}$ in the linear sublayer) in a concave boundary layer ($\delta_o/R \approx 0.055$) and concluded that the difference between these two methods was well within the measurement uncertainties (5 to 8 percent). Moser and Moin (1987), in a DNS study of curved channel flow, showed that convex curvature shifts the mean velocity profile in the logarithmic region above the plane channel value, whereas concave curvature shifts the profile below the plane channel value. The effect of *transverse* convex curvature is to change the slope of the logarithmic region as described by Neves et al. (1994) based on their DNS study, and by a number of experimental studies e.g., Lueptow et al. (1985). In a study of turbulent boundary layers subjected to strong favorable pressure gradients, Blackwelder and Kovasznay (1972) found that the wall shear stress determined using the wall-slope method and the Clauser methods agreed to within 1 percent. Tsuji and Morikawa (1975) also found that the surface shear stress computed from the wall-slope of the mean streamwise velocity component compared well with the values obtained from Clauser's chart. However, they discovered that when the free-stream is accelerated immediately downstream of an adverse pressure gradient

---

* Data have been deposited in the JFE Data Bank. To access the file for this paper, see instructions on p. 883 of this issue.

Contributed by the Fluids Engineering Division for publication in the JOURNAL OF FLUIDS ENGINEERING. Manuscript received by the Fluids Engineering Division June 26, 1995; revised manuscript received May 13, 1996. Associate Technical Editor: P. R. Bandyopadhyay.

region, the mean streamwise velocity departs from the universal logarithmic region earlier than in the case of monotonic acceleration.

One of the first thorough experimental investigations of turbulent flow over curved surfaces with strong curvature ($\delta_o/R \approx 10$ percent), was performed by So and Mellor (1973) in a specially designed, open-return wind tunnel in which all the Reynolds stress components were measured. On the convex wall it was found that the turbulent boundary layer was two-dimensional and that the turbulent shear stress vanished in the outer half of the boundary layer. A zero streamwise pressure gradient was maintained over the convex wall by carefully contouring the opposite wall, except immediately downstream of the onset of curvature, where locally a favorable pressure gradient prevailed. Over the concave wall, evidence of a system of streamwise axial vortices was found. These structures were strong enough to make the flow inherently three-dimensional.

Two experiments with different strengths of curvature ($\delta_o/R \approx 0.10$ and 0.05) were performed by Gillis and Johnston (1983) in a low-speed wind tunnel to study the turbulence structure of the boundary layer that formed over the convex wall, and after 90 deg of turning, its recovery behavior on a flat surface. The streamwise pressure gradient was forced to be zero over the entire test surface, requiring careful design of the wall opposite the curved test wall. Consistent with the results of So and Mellor (1973), they found that the primary Reynolds shear stress was diminished in the outer region of the turbulent boundary layer, and that the shear stress profiles for both experiments collapsed when $-\overline{uv}/u_\tau^2$ was plotted versus distance from the wall normalized with the wall radius of curvature, y/R. This collapse was observed in the downstream portion of the curved test section, indicating that unlike in the flat-plate case, the radius of curvature rather than the boundary layer thickness controls the active turbulence length scales in curved boundary layers with strong curvature (Gillis and Johnston, 1983). It was also shown that the active shear-layer thickness in the downstream region had decreased from its initial value at the onset of curvature.

Many aspects of adverse and favorable, streamwise pressure gradients have been extensively studied for at least two decades and are well known. Adverse pressure gradient can destroy the logarithmic region and significantly change higher-order velocity moments as reported by Nagano et al. (1991), although it is unclear whether or not their turbulent boundary layer was in equilibrium. However, in cases of equilibrium boundary layers, the validity of the "log-law" was established by White and Tiederman (1990) and Koskie (1991).

In groundbreaking experimental work by Kline et al. (1967), the near-wall structure of a turbulent boundary layer with zero, adverse and favorable streamwise pressure gradients was investigated. They identified motions in the viscous sublayer giving rise to "low-speed streaks." These streaks were found to undergo a violent breakup process due to an instability mechanism, resulting in ejections of low-speed fluid from regions very near the wall. This rather complex behavior, known as a turbulent burst, is significant in the production process of turbulence energy and its exchange with the outer portions of the boundary layer. While adverse pressure gradients (APG) have been shown to make bursting more frequent and violent, favorable pressure gradients (FPG) reduce its frequency, and, if sufficiently accelerated ($K = 3.5 \times 10^{-6}$), the bursting process ceases, leading to reverse transition and relaminarization.

In a subsequent study concerning the influence of FPG on reverse transition in a flat plate boundary by Narayanan and Ramjee (1969), mean and fluctuating streamwise velocity profiles, as well as the wall shear stress were measured in a two-dimensional accelerated incompressible turbulent boundary layer. The breakdown of the "logarithmic law" occurs at a value of the pressure gradient parameter $\Delta_P = \nu/(\rho u_\tau^3) \cdot dP/ds \approx -0.02$. It is associated with thickening of the linear sublayer, which occurs before the relaminarization of the mean velocity profiles and is a first sign for the onset of the reverse transition process. The development of the boundary layer downstream of this point was characterized by: (1) increase in the shape factor H; (2) decrease in the skin friction coefficient c_f; and (3) similarity of u^2 profiles in the turbulence decay region.

In the review article by Narashimha and Sreenivasan (1979), the authors describe the influence of highly accelerated flows on the mean statistics and turbulence structures in the boundary layer, especially its tendency of reversion to laminar flow. They suggest a two-layer model, where the turbulence in the outer portion of the boundary layer is rapidly distorted and the Reynolds shear stress is nearly frozen, and the viscous region exhibits random oscillations in response to the forcing provided by the remainder of the original turbulence. In this situation, reversion is a result of the slowly responding Reynolds stresses to the dominating pressure forces in the outer region, accompanied by the generation of a new laminar sub-boundary layer which is stabilized by the strong acceleration.

Overall, there is a lack of detailed information concerning turbulent boundary layers that experience multiple interacting

Nomenclature

c_f = skin friction coefficient, $c_f = 2\tau_w/(\rho U_{pw}^2) = 2(u_\tau/U_{pw})^2$
FPG = favorable pressure gradient
H = shape factor, $H = \delta^*/\theta$
k = acceleration parameter, $k = \nu/U_e^2 \cdot dU_e/ds = -\nu/(\rho U_e^3) \cdot dP/ds$
P = mean static fluid pressure
R = radius of curvature
Re = Reynolds number
Re_θ = momentum thickness Reynolds number, $\mathrm{Re}_\theta = U_{pw}\theta/\nu$
s = streamwise coordinate
s_o = location of onset of curvature
SFPG = strong favorable pressure gradient
$\bar{U}$ = mean streamwise velocity
$U(t)$ = instantaneous streamwise velocity
U^+ = inner normalized streamwise velocity, $U^+ = \bar{U}/u_\tau$
U_c^+ = inner normalized, curvature corrected streamwise velocity, $U_c^+ = (\bar{U})/u_\tau) \cdot (R + y)/R$
U_e = streamwise velocity at edge of boundary layer
U_p = potential flow velocity, $U_p(y) = U_{pw} \cdot R/(R + y)$
U_{pw} = potential flow velocity at the wall
$u(t)$ = instantaneous streamwise velocity fluctuation, $u(t) = U(t) - \bar{U}$
u' = streamwise RMS velocity
u_τ = shear velocity, $u_\tau = \sqrt{\tau_w/\rho}$
$\overline{uv}$ = primary Reynolds shear stress (divided by ρ), $\overline{uv} = \overline{(U(t) - \bar{U}) \cdot (V(t) - \bar{V})}$
$V(t)$ = instantaneous wall-normal velocity
$\bar{V}$ = mean wall-normal velocity
$v(t)$ = instantaneous wall-normal velocity fluctuation, $v(t) = V(t) - \bar{V}$
v' = wall-normal RMS velocity
y = wall-normal coordinate
y^+ = inner normalized wall-normal coordinate, $y^+ = yu_\tau/\nu$
ZPG = zero pressure gradient
Δ_P = pressure gradient parameter, $\Delta_P = \nu/(\rho u_\tau^3) \cdot dP/ds$
α = streamwise angular position in curved test section
β = pressure gradient parameter, $\beta = \delta^*/\tau_w \cdot dP/ds$
δ = boundary layer thickness
δ^* = displacement thickness
ν = kinematic viscosity
ρ = fluid density
θ = momentum thickness

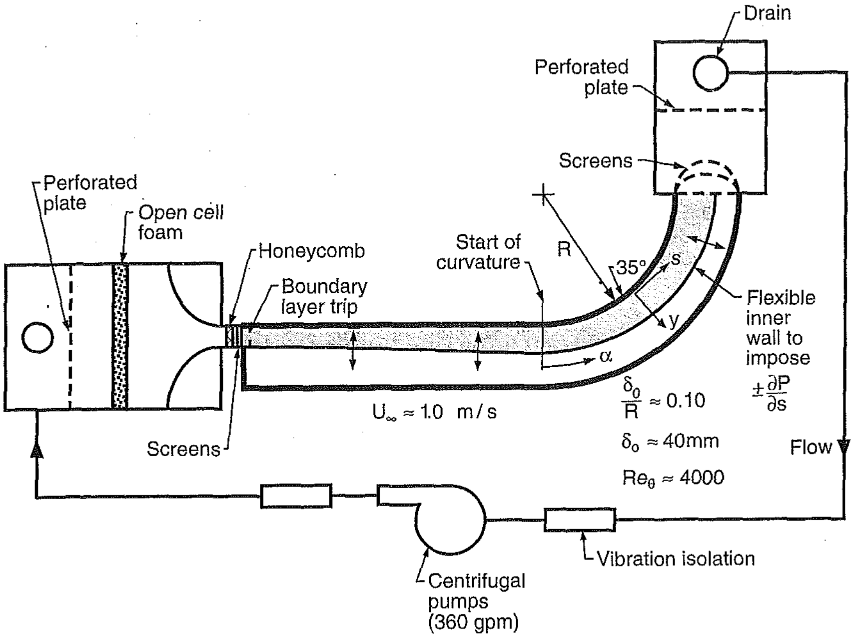

Fig. 1 Schematic of low-speed water tunnel

strain rates, especially in the near-wall region. Furthermore, it is unclear whether pressure gradients and wall curvature interact in a fully nonlinear fashion and to what extent the rapid interaction (i.e., Rapid Distortion Theory) is significant. Therefore, this study examines how interacting radial and streamwise extra rates of strain will affect the momentum transport in a turbulent boundary layer. This information is necessary to obtain a better understanding of the flow physics in these complex flows, and for the development and testing of appropriate turbulence models.

Experimental Facility and Techniques

All of the data were acquired in a recirculating water channel facility (shown schematically in Fig. 1) driven by four centrifugal pumps each rated at 5.7×10^{-3} m^3/s (90 gpm). Softened and filtered water entered the straight test section through a series of screens, into a smooth, two-dimensional contraction section followed by a honeycomb section to reduce large-scale vortical motions in the entrance region. An equilibrium turbulent boundary layer was developed on the smooth wall of the straight, 2.46 m long section upstream of the curved test section. The straight and curved test sections were fabricated from Lexan® and Plexiglas®, with glass windows in both the top and bottom walls for enhanced optical access to the flow region of interest. A flexible wall (constructed from 3.2 mm thick Lexan®) was placed between the measurement wall and opposite side wall to adjust the cross-sectional area, and hence to impose the streamwise pressure gradient, which was a variable parameter in this investigation. The longitudinal pressure gradient in the curved test section was adjusted by rods that were linked to the flexible wall. The flexible wall was adjusted to yield a zero pressure gradient (ZPG) in the straight portion and a zero or favorable pressure gradients (FPG) of different strengths in the curved test section. Pressure taps were installed along the convex wall to measure the imposed streamwise pressure gradients, using a Gilmont® micro-manometer. The boundary layer thickness at the exit of the straight test section was $\delta \approx 40$ mm, resulting in a curvature parameter of $\delta_o/R \approx 0.10$, which comprises a strong curvature.

A two-component laser-Doppler velocimeter (LDV) system was employed for simultaneous measurements of the streamwise and wall-normal instantaneous velocity components, including the near-wall region. The transmitting optics of the two-component, three beam LDV system consisted of a Thermo System Incorporated (TSI®) model 9100-8 velocimeter modified to measure velocity components at ±45° to the mean flow direction. Using a pair of Bragg cells, both monochromatic beams were frequency shifted at 40 MHz to minimize fringe biasing. Operating in the forward scattering mode, near-wall measurements were made possible by inclining the optical axis of the transmitting side by approximately 3° with respect to the measurement wall. The probe volume was 45 μm in diameter and had a spanwise extent of approximately 920 μm, which corresponded to 2 and 40 viscous units, respectively, when normalized with inner variables, u_τ and ν. Spatial and temporal measurement coincidence were achieved by carefully aligning the transmitted beams and the receiving optics, and by setting a coincidence window on the counter processors to ensure that the accepted signal on both channels originated from the same scattering particle passing through the probe volume. The flow was seeded with 0.3 μm diameter fat particles from homogenized cream at a concentration of approximately 2.5 ml/m^3.

In order to calculate reliable statistics (mean and higher order moments), various numbers of statistically independent data realizations were required. For the two-component velocity profiles, 10,000 data points were acquired for each velocity component. Velocity bias can occur in a highly turbulent flow, due to the fact that the probability of measuring a high velocity particle is higher than that of measuring a low velocity particle (McLaughlin and Tiederman, 1973). For all LDV measurements, velocity bias was significantly reduced using the fixed-waiting-time sampling method.

Uncertainty Estimates. The error analysis of the LDV data followed that recommended by Walker and Tiederman (1988), who building on the work of Yanta and Smith (1972), showed that the uncertainty in the estimate for mean statistical quantities depends on both the ensemble size and the RMS level, but it depends solely on the ensemble size for an RMS quantity. A 95 percent confidence interval for Gaussian (or nearly Gaussian) distributions was assumed. Typical uncertainty bounds for the Reynolds stresses are shown in the upper right corner of the appropriate figures. Typical uncertainties on the RMS and mean

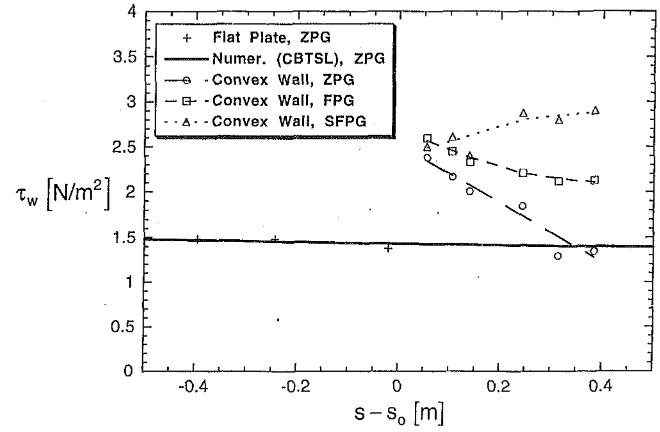

Fig. 2 Streamwise development of the wall shear stress for a turbulent boundary layer on a flat and convex wall

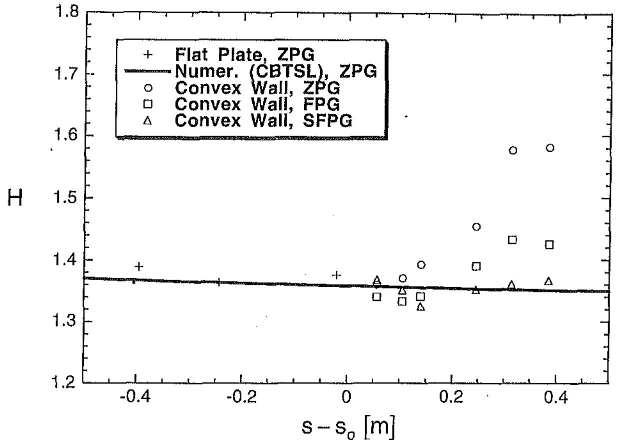

Fig. 3 Streamwise development of the shape factor for a turbulent boundary layer on a flat and convex wall

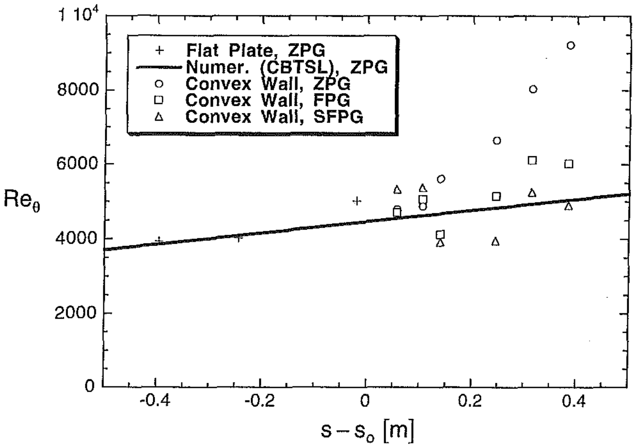

Fig. 4 Streamwise development of the momentum thickness Reynolds number for a turbulent boundary layer on a flat and convex wall

velocities are on the order of the plot symbol sizes, i.e. less than 1 percent, except for the near-wall region ($y^+ \leq 10$), where the measured wall-normal RMS velocity component is significantly overpredicted compared with the direct numerical simulation data by Spalart (1988) and hence is omitted. The maximum uncertainty on the shear stress was typically 12 to 13 percent in the maximum stress region ($y^+ \approx 40–80$). The uncertainty for the mean streamwise velocity component was 0.5 percent. Uncertainty in the shear velocity is less than 1 percent due to the mean streamwise velocity measurements and approximately up to 5 percent due to the additional uncertainty introduced by the Clauser method, which has been used to infer the wall shear stress. The maximum error in estimating $c_f(\propto u_\tau^2)$ is 10 percent. The uncertainties for the pressure gradient parameters are of the same order as the size of the corresponding plotting symbols (1.6 percent for k and 3.8 percent for β).

Experimental Results and Discussion

Two-component velocity data were taken at different streamwise stations along the convex wall in the mid-plane of the test surface, while the flow in the curved test section was exposed to zero and two different favorable streamwise pressure gradients. Streamwise development of the integral parameters as well as the pressure gradient parameters k and β are shown first. Mean and higher-order velocity statistics are presented next. The first set of profiles to be presented were acquired at different streamwise locations along the mid-plane of the convex wall for a strong favorable streamwise pressure gradient. They are compared to a ZPG boundary layer that formed over a smooth flat wall with $\mathrm{Re}_\theta \approx 4000$. The second set of data were acquired at a fixed streamwise location ($\alpha = 35$ deg) with ZPG and two different FPGs. The strengths of the FPGs were $k \approx 0.55 \times 10^{-6}$ (FPG) and $k \approx 1.01 \times 10^{-6}$ (SFPG), respectively, where k is the local acceleration parameter, defined as $k = \nu / U_e^2 \cdot dU_e/ds$.

Mean and Turbulent Statistics. Before the velocity data are presented, several integral quantities along with pressure gradient parameters are shown. In Figs. 2 through 4, the streamwise development of the wall shear stress, the shape factor and the momentum thickness Reynolds number are shown for all data sets that were acquired in the curved test section with different streamwise pressure gradients, including upstream data in the approach flat plate turbulent boundary layer. A finite difference code (CBTSL by Cebeci and Bradshaw, 1977), which solves the thin-shear layer, partial differential equations for laminar and turbulent boundary layers was used to predict the integral quantities for comparison. The agreement between the flat-plate data and the numerical predictions is good. The deviation from the flat plate distribution is apparent as soon as the flow enters the curved test section. As has been observed by a number of investigators (including So and Mellor, 1973, Gillis and Johnston, 1983, and others), the effect of the convex wall is to reduce the wall shear stress and to increase both the shape factor and the momentum thickness Reynolds number. In the presence of favorable streamwise pressure gradients, these effects are counteracted, i.e., the wall shear stress is elevated compared to the ZPG curved case and the other two integral parameters are reduced. The positive shift in the wall shear stress immediately downstream of the onset of curvature can be attributed to a local flow acceleration caused by the sudden change in wall curvature. In Figs. 5(a) and (b), the distributions of the pressure gradients along the test wall are shown in terms of the acceleration parameter, k, and the Clauser equilibrium parameter, β. In this study, care was taken to establish nearly constant levels of pressure gradient along the convex wall, so that rapid changes in the streamwise direction would be minimized.

As mentioned in the introduction, the presence of the ''log-law'' in turbulent boundary layers with one or more additional strains has been widely discussed. In a comprehensive study on the effects of surface curvature by Gibson (1988), it was shown that the logarithmic region existed for the mean streamwise velocity profiles, but that the ''log-law'' constants could be different from the standard values ($\kappa = 0.41$ and $B = 5.0$). As

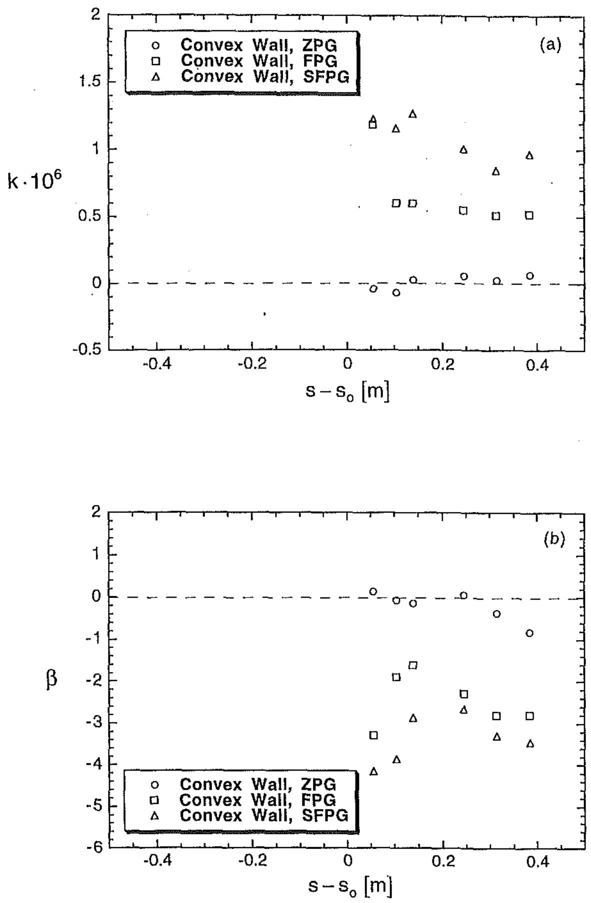

Fig. 5 Streamwise development of the acceleration parameter (*a*) and the Clauser equilibrium parameter (*b*) for a turbulent boundary layer on a flat and convex wall

a result of fitting curved wall profiles to the log-law, where u_τ was determined independently, Gibson recommended a value of $B = 5.78$, while the von Karman constant remained unchanged. Applying this modified value for the intercept to the present data sets (where $\delta_o/R \approx 0.10$ as in Gibson's case) resulted in a lower value of the shear velocity. The original and revised estimates of u_τ are tabulated in Table 1 for the ZPG case. Since the differences in u_τ due to the change in B are on the order of the measurement uncertainty of u_τ (< 5 percent), the present data sets were not "corrected" using the revised intercept. No independent means for measuring u_τ were available, therefore the standard Clauser method was used. Note that this results in an error in estimating c_f of up to 10 percent. However, an advantage of retaining the classical constants is that it facilitates comparison to the vast body of previous work on curved turbulent boundary layers in which the Clauser method had been used (cf. So and Mellor, 1973; Smits et al., 1979; Gillis and Johnston, 1983; Muck et al., 1985; Barlow and Johnston, 1988a, b).

A reference ZPG case was studied prior to investigating the cases with interacting strain rates, but is not presented here for brevity (see Schwarz and Plesniak, 1995). A brief summary of features exhibited by the ZPG profiles follows. As previously reported by other investigators (Gillis and Johnston, 1983 and Gibson et al., 1984), the extent of the logarithmic region was reduced ($30 \leq y^+ \leq 100$) due to the presence of the strong convex curvature. Initially, the wake component in the outer portion of the turbulent boundary layer increased with downstream distance up to $\alpha \approx 45$ deg, then remained constant implying mean flow similarity. Similarity for the Reynolds stresses was also achieved by 45 deg.

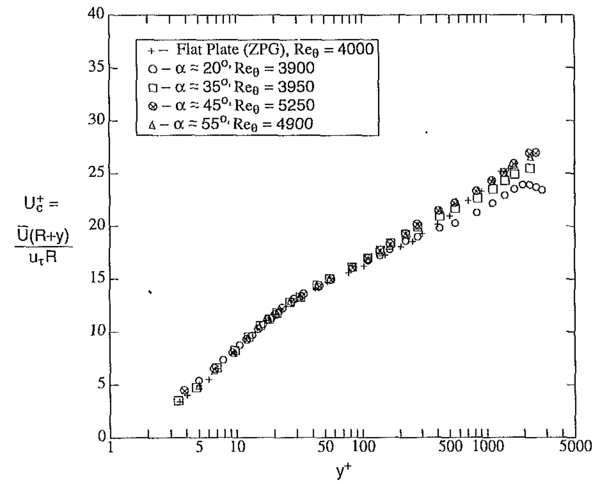

Fig. 6 Mean streamwise velocity profiles in the midplane of a turbulent boundary layer on a flat and convex wall with strong favorable streamwise pressure gradient (SFPG)

The primary peak in the streamwise RMS velocity occurred at the same wall-normal distance ($y^+ \approx 15$) as for the flat plate case. However, the peak values were 14 percent lower than those measured on the flat plate. There was also a dramatic reduction in the primary Reynolds shear stress outside the logarithmic region, which has also been reported by other investigators (So and Mellor, 1973; Gillis and Johnston 1983) and can be attributed to the attenuation of the larger-scale structures in the outer portion of the boundary layer due to the strong stabilizing convex curvature, as observed by Chiwanga and Ramaprian (1993). The primary Reynolds shear stress was as much as 35 percent lower at the first measurement station ($\alpha \approx 20$ deg) compared to the downstream stations. The initial reduction of the primary Reynolds shear stress is attributable to the local favorable pressure gradient near the onset of curvature, which is induced by the sudden change in the wall curvature.

Figures 6 and 7 show the streamwise development for flow over a convex surface with a strong favorable pressure gradient (SFPG). Profiles of the mean streamwise velocity component, shown in Fig. 6, exhibit a similar trend as that observed for the ZPG case along the curved surface, i.e., the wake component increases with downstream distance up to 45 deg, then no further change occurs at the 55 deg location. It should be noted that the overall strength of the wake is significantly reduced in the presence of a strong FPG, which counteracts the wake-enhancing effect of the convex curvature. However, both convex curvature and FPGs have a stabilizing effect on the turbulent boundary layer, reflected by the suppression of the Reynolds stresses in Figs. 7(*a*) and (*b*). Again, there are only slight

Table 1 Calculation of u_τ with different constants in the log-law, $U^+ = 1/\kappa \ln y^+ + B$

α [°]	8	15	20	35	45	55
$B = 5.0$: u_τ [m/s]	0.0489	0.0466	0.0448	0.0423	0.0360	0.0367
$B = 5.78$: u_τ [m/s] Gibson (1988)	0.0467	0.0444	0.0430	0.0403	0.0344	0.0352
Δu_τ in [%]	4.71	4.95	4.19	4.96	4.65	4.26
Δc_f in [%]	9.42	10.03	8.63	10.01	9.49	8.60

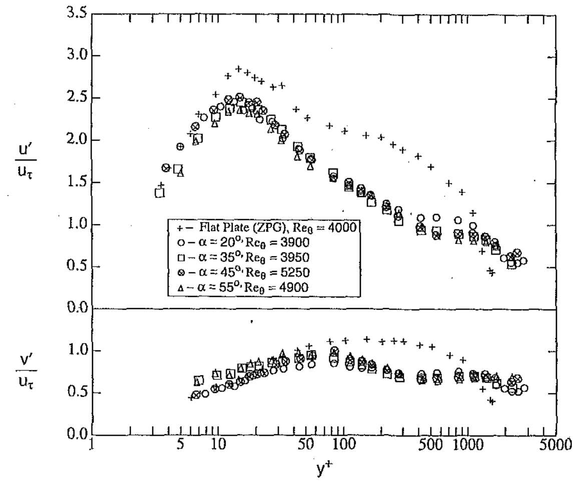

Fig. 7(*a*) Root-mean-square streamwise and wall-normal velocity profiles in the midplane of a turbulent boundary layer on a flat and convex wall with strong favorable streamwise pressure gradient (SFPG)

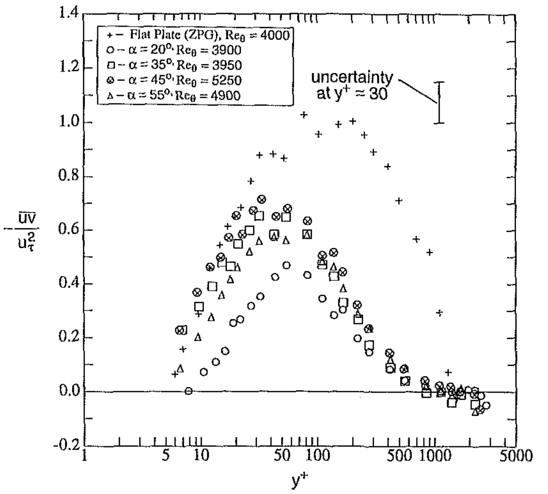

Fig. 7(*b*) Primary Reynolds shear stress profiles in the midplane of a turbulent boundary layer on a flat and convex wall with strong favorable streamwise pressure gradient (SFPG)

changes in the fluctuating (RMS) velocity components between the different axial locations. At the first measurement location ($\alpha \approx 20$ deg), the primary Reynolds shear stress is 27 percent lower than the "asymptotic" downstream values, similar to the ZPG case. These observations indicate that a state of similarity is reached after $\alpha \approx 45$ deg, even in the presence of a strong favorable pressure gradient.

In Fig. 8, the mean streamwise velocity is shown as a function of the normalized wall-normal coordinate with zero and two different favorable streamwise pressure gradients at one fixed streamwise location ($\alpha \approx 35$ deg). Note that the local Re_θ varies as different streamwise pressure gradients are imposed, thus any inherent Reynolds number effects (expected to be small) are coupled with the pressure gradient effects. This particular streamwise distance was chosen because it is downstream of the region that is influenced by a locally strong FPG (due to sudden change in wall curvature) and upstream of regions where confinement effects (due primarily to boundary layer growth) become noticeable. As discussed before, the mean profiles collapse quite well throughout the logarithmic region, whereas the wake component (outer portion of the turbulent boundary layer) is reduced with increasing strength of FPG. The combined curvature and the streamwise pressure gradient effects are more apparent in the outer region ($y^+ > 100$) of these inner-normalized plots. Thus, the inner variables adequately account for the effects of these interacting strain rates in the near-wall region, and all of the profiles collapse onto a single curve. As mentioned previously, favorable pressure gradient has the tendency to oppose the wake-enhancing effect of the convex curvature. On the other hand, both convex curvature and FPG tend to stabilize the turbulence within the boundary layer.

The streamwise and normal RMS velocities, along with the primary Reynolds shear stress (shown in Figs. 9(*a*), (*b*)) illustrate some interesting features of the imposed extra rates of strain. The near-wall behavior ($y^+ \leq 100$) of the normal stress components for interacting strain rates of different magnitude is accounted for by changes in u_τ, except for a reduction of the primary peak in the streamwise RMS velocity. Beyond the logarithmic region, all three Reynolds stresses are reduced relative to the flat plate values. The FPGs augment this effect, especially for the streamwise RMS velocity. The primary Reynolds shear stress completely disappears near the inner edge of the wake region for the flow over the curved surface, regardless of the magnitude of the imposed longitudinal pressure gradient. A further reduction in $-\overline{uv}$ (as high as 45 percent relative to a ZPG) is apparent in the presence of FPGs interacting with the convex curvature throughout almost the entire boundary layer ($10 \leq y^+ \leq 400$).

Conclusions

Mean and higher order velocity statistics were acquired using two-component LDV and analyzed for a turbulent flow over a convex surface with imposed zero and favorable streamwise pressure gradients. While modified constants in the log-law to account for curvature effects were not determined from independent measurements of τ_w, a logarithmic region was observed in the data. Within the logarithmic region (the extent of which was reduced due to the presence of the strong curvature), there were only small changes in the mean streamwise velocity and the normal Reynolds stress components (normalized in inner variables) when different streamwise pressure gradients were coupled with convex curvature. Similarity of the mean and Reynolds stresses was achieved downstream of $\alpha \approx 45$ deg for convex turbulent boundary layers with and without FPG. Inner variable normalization accounted for the effects of the extra strain rates in the near-wall region and resulted in a collapse of the mean and normal stress profiles. On the other hand, in the outer region ($y^+ > 100$) the profiles exhibited the greatest difference under the various imposed strain rates. Favorable

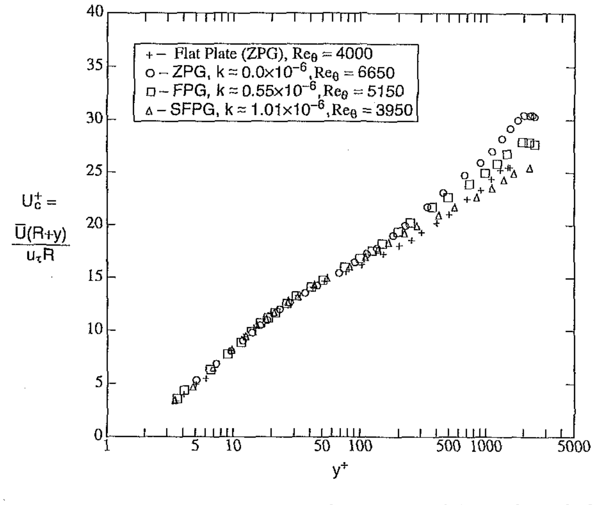

Fig. 8 Mean streamwise velocity profiles in the midplane of a turbulent boundary layer on a flat and convex wall with different streamwise pressure gradients at $\alpha \approx 35$ deg

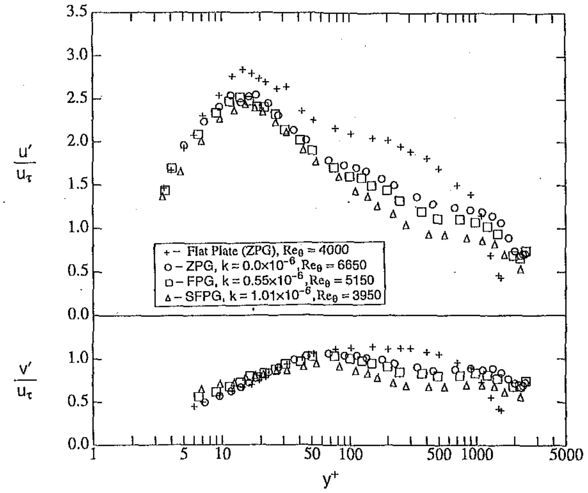

Fig. 9(*a*) Root-mean-square streamwise and wall-normal velocity profiles in the midplane of a turbulent boundary layer on a flat and convex wall with different streamwise pressure gradients at $\alpha \approx 35$ deg

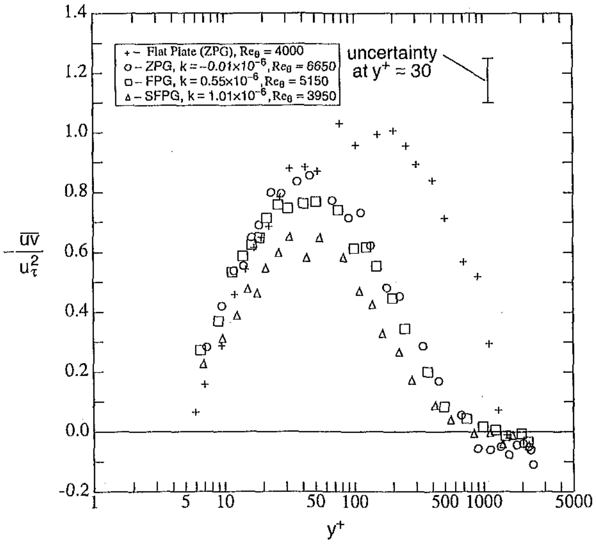

Fig. 9(*b*) *Primary Reynolds shear stress profiles in the midplane of a turbulent boundary layer on a flat and convex wall with different streamwise pressure gradients at $\alpha \approx 35$ deg*

pressure gradient resulted in a reduction of Reynolds stresses beyond $y^+ \approx 100$. Despite the aforementioned success of inner variable normalization, the primary Reynolds shear stress was reduced throughout most of the boundary layer in the presence of a strong FPG.

Data Bank Contribution

The reduced LDV data, consisting of mean and fluctuating velocity profiles and primary Reynolds shear stress profiles, are deposited in the JFE Data Bank. The data tables contain the y-locations (wall-normal distances) along with $\bar{U}$, u', v', and $\overline{uv}$ for every case presented in this paper. Several boundary layer parameters (ν, U_e, dP/ds, k, θ, Re_θ, u_τ, and c_f) are listed below the tabulated profiles. Note that Clauser's method (with $\kappa = 0.41$ and $B = 5.0$) was used to determine the shear velocity, u_τ. All integral parameters were calculated using the Simpson $\frac{1}{3}$ rule.

Acknowledgments

Effort sponsored by the Air Force Office of Scientific Research, Air Force Material Command, USAF, under grant number F 49620-93-1-0003. The U.S. Government is authorized to reproduce and distribute reprints for Governmental purposes notwithstanding any copyright notation thereon. We would also like to thank Dr. S. N. B. Murthy for numerous enlightening discussions and contributions to this work.

References

Bandyopadhyay, P. R., and Ahmed, A., 1993, "Turbulent Boundary Layers Subjected to Multiple Curvatures and Pressure Gradients," *Journal of Fluid Mechanics*, Vol. 246, pp. 503–527.

Barlow, R. S., and Johnston, J. P., 1985, "Structure of Turbulent Boundary Layers on a Concave Surface," Stanford University Report, MD-47.

Barlow, R. S., and Johnston, J. P., 1988a, "Structure of Turbulent Boundary Layers on a Concave Surface. *Journal of Fluid Mechanics*, Vol. 191, pp. 137–176.

Barlow, R. S., and Johnston, J. P., 1988b, "Local Effects of Large-Scale Eddies on Bursting in a Concave Boundary Layer," *Journal of Fluid Mechanics*, Vol. 191, pp. 177–195.

Baskaran, V., Smits, A. J., and Joubert, P. N., 1987, "A Turbulent Flow Over a Curved Hill Part 1. Growth of an Internal Boundary Layer," *Journal of Fluid Mechanics*, Vol. 182, pp. 47–83.

Blackwelder, R. F., and Kovasznay, L. G., 1972, "Large-Scale Motion of a Turbulent Boundary Layer During Relaminarization," *Journal of Fluid Mechanics*, Vol. 53, pp. 61–83.

Cebeci, T., and Bradshaw, P., 1977, *Momentum Transfer in Boundary Layers*, Hemisphere Publishing.

Chiwanga, S. C., and Ramaprian, B. R., 1993, "The Effect of Convex Wall Curvature on the Large-Scale Structure of the Turbulent Boundary Layer," *Experimental Thermal and Fluid Science*, Vol. 6, pp. 168–176.

Gibson, M. M., 1988, "Effects of Surface Curvature on the Law of the Wall," *Near-Wall Turbulence*, 1988 Zoran Zaric Memorial Conference, S. J. Kline and N. H. Afgan, ed., Hemisphere Pub.

Gibson, M. M., 1984, "Effects of Streamline Curvature on Turbulence," *Frontiers in Fluid Mechanics* S. H. Davis, J. L. Lumley, eds. Springer-Verlag, pp. 184–198.

Gibson, M. M., Verriopoulos, C. A., and Vlachos, N. S., 1984, "Turbulent Boundary Layer Flow on a Mildly Curved Convex Surface," *Experiments in Fluids*, Vol. 2, pp. 17–24.

Gillis, J. C., and Johnston, J. P., 1983, "Turbulent Boundary Layer Flow and Structure on a Convex Wall and its Redevelopment on a Flat Wall," *Journal of Fluid Mechanics*, Vol. 135, pp. 123–153.

Hoffman, P. H., Muck, K. C., and Bradshaw, P., 1985, "The Effect of Concave Surface Curvature on Turbulent Boundary Layers," *Journal of Fluid Mechanics*, Vol. 161, pp. 371–403.

Huang, P. G., and Bradshaw, P., 1995, "Law of the Wall for Turbulent Flows in Pressure Gradients," *AIAA Journal*, Vol. 33, No. 3, pp. 624–632.

Kline, S. J., Reynolds, W. C., Schraub, F. A., and Runstadler, P. W., 1967, "The Structure of Turbulent Boundary Layers." *Journal of Fluid Mechanics*, Vol. 30, Part 4, 741–773.

Koskie, J. E., 1991, Turbulence Structure and Polymer Drag Reduction in Adverse Pressure Gradient Boundary Layers. Ph.D. Thesis, Purdue University, West Lafayette, IN.

Lueptow, M. R., Leehey, P., and Stellinger, T., 1985, "The Structure of Turbulent Boundary Layer on a Cylinder in Axial Flow," *Physics of Fluids*, Vol. 28, pp. 3495–3505.

McLaughlin, D. K., and Tiederman, W. G., 1973, "Biasing Correction for Individual Realization of Laser Velocimeter Measurements in Turbulent Flows," *Physics of Fluids*, Vol. 16, pp. 2082–2088.

Moser, R. D., and Moin, P., 1987, "The Effects of Curvature in Wall-Bounded Turbulent Flows," *Journal of Fluid Mechanics*, Vol. 175, pp. 479–510.

Muck, K. C., Hoffman, P. H., and Bradshaw, P., 1985, "The Effects of Convex Curvature on Turbulent Boundary Layers," *Journal of Fluid Mechanics*, Vol. 161, pp. 347–369.

Nagano, Y., Tagawa, M., and Tsuji, T., 1991, "Effects of Adverse Pressure Gradients on Mean Flows and Turbulence Statistics in a Boundary Layer," *8th Symposium on Turbulent Shear Flows*, University of Munich, pp. 2-3-6 to 2-3-6.

Narashimha, R., and Sreenivasan, K. R., 1979, "Relaminarization of Fluid Flows," *Advances in Applied Mechanics*, Vol. 19, Indian Institute of Science, Bangalore, India, pp. 221–309.

Narayanan, M. A. B., and Ramjee, V., 1969, "On the Criteria for Reverse Transition in a Two-Dimensional Boundary Layer Flow," *Journal of Fluid Mechanics*, Vol. 35, part 2, pp. 225–241.

Neves, J. C., Moin, P., and Moser, R. D., 1994, "Effects of Convex Transverse Curvature on Wall-Bounded Turbulence. Part 1. The Velocity and Vorticity," *Journal of Fluid Mechanics*, Vol. 272, pp. 349–381.

Runstadler, P. G., Kline, S. J., and Reynolds, W. C., 1963, "An Experimental Investigation of Flow Structure of the Turbulent Boundary Layer," Report No. MD-8. Dept. Mech. Engr., Stanford University, Stanford, CA.

Schwarz, A. C., and Plesniak, M. W., 1995, "Near-Wall Phenomena in Convex Turbulent Boundary Layers with Zero and Favorable Pressure Gradients," ASME-FED, Vol. 217, pp. 67–74.

Smits, A. J., Matheson, N., and Joubert, P. N., 1983, "Low-Reynolds-Number Turbulent Boundary Layers in Zero and Favorable Pressure Gradients," *Journal of Ship Research*, Vol. 27, No. 3, pp. 147–157.

Smits, A. J., Young, S. T. B., and Bradshaw, P., 1979, "The Effect of Short Regions of High Surface Curvature on Turbulent Boundary Layers," *Journal of Fluid Mechanics,* Vol. 94, part 2, pp. 209–242.

So, R. M. C., and Mellor, G. L., 1973, "Experiment on Convex Curvature Effects in Turbulent Boundary Layers," *Journal of Fluid Mechanics,* Vol. 60, Part 1, pp. 43–62.

Spalart, P. R., 1988, "Direct Simulation of a Turbulent Boundary Layer up to $Re_\theta = 1410$," *Journal of Fluid Mechanics,* Vol. 187, pp. 61–98.

Tsuji, Y., and Morikawa, Y., 1976, "Turbulent Boundary Layer with Pressure Gradient Alternating in Sign," *Aero. Quarterly,* Vol. 27, pp. 15–28.

Walker, D. T., and Tiederman, W. G., 1988, "Turbulence Structure and Mass Transport in a Channel Flow with Polymer Injection," Report PME-FM-88-2, Purdue University, W. Lafayette, IN.

White, J. B., and Tiederman, W. G., 1990, "The Effect of Adverse Pressure Gradient on the Turbulent Burst Structure in Low-Reynolds Number Equilibrium Boundary Layers," *Proceedings of the 12th Symposium of Turbulence,* University of Missouri-Rolla, Rolla, MO, A5.1-A5.8.

Yanta, W. J., and Smith, R. J., 1973, "Measurements of Turbulence Transport Properties with a Laser Doppler Velocimeter," AIAA Paper No. 73-169.

Exploring a Three-Equation R–k–ϵ Turbulence Model

U. C. Goldberg[1]
Member Technical Staff, CFD Department,
Rockwell Science Center,
Thousand Oaks, CA 91360

A low Reynolds number extension of the k–ϵ model is proposed and evaluated. This version has the following attributes: (a) it does not involve wall distance or normal-to-wall directionality; (b) it enforces time scale realisability by preventing it from falling below the Kolmogorov (dissipative eddy) scale, $(\nu/\epsilon)^{1/2}$; (c) it employs a simple wall boundary condition for ϵ. The current approach requires an additional transport equation for the undamped eddy viscosity, R, thus the resulting model is of the three-equation variety. Since wall distance is not used, the proposed model is applicable to arbitrary flow topologies. Predictions using this model are compared with experimental data of several flow cases, with encouraging results.

Introduction

The standard k–ϵ model was developed under the assumption of high turbulence Reynolds number conditions. Over the years numerous suggestions have been proposed for extending its validity to low Reynolds number flow regions, such as near-wall flows. One approach follows the method of Jones-Launder (1972) and Launder-Sharma (1974) in which the dissipation rate of turbulence kinetic energy, ϵ, is replaced by $\tilde{\epsilon} = \epsilon - 2\nu(\partial\sqrt{k}/\partial y)^2$ which, unlike ϵ, vanishes at solid surfaces. In this model the term $S = 2\nu\nu_t(\partial^2 U/\partial y^2)^2$ is added as a source term to the $\tilde{\epsilon}$ transport equation. The presence of the normal-to-wall first and second derivatives in $\tilde{\epsilon}$ and in S, respectively, introduces two disadvantages; numerical and conceptual: these derivatives often create severe numerical "stiffness", limiting the usable size of the time step and increasing the chance of numerical transients severe enough to terminate a computation; they also prevent the model from being pointwise (local) because of the need to find normal-to-wall unit vectors.

Another approach is using the ϵ transport equation unaltered, such as in the Lam-Bremhorst (1981) model, but then the presence of the unnatural wall boundary condition $\epsilon = \nu\partial^2 k/\partial y^2$ becomes the source of numerical difficulties and inability to render the model pointwise.

In both the above approaches two or three near-wall functions are needed to convey the effect of viscous damping and to ensure proper asymptotic behaviour in the viscous sublayer.

This state of affairs regarding low Reynolds number extensions of the standard k–ϵ model has been a source of difficulties and frustration to CFD users attempting to predict real-life flow problems.

More recently, several researchers suggested a hybrid approach, in which the k–ϵ model is combined with a one-equation model, the latter being utilised in near-wall flow regions to cover the low Reynolds number flow regime, obviating the need to modify the standard k–ϵ model formulation. A notable example of this method is the two-layer model of Michelassi (1993). Another hybrid approach is that of Menter (1994) in which the Wilcox k–ω model is used near walls, and the k–ϵ model (translated into k and ω variables) is used away from walls, the two being put in hybrid form by way of blending functions. A common denominator of these hybrid models is the explicit dependance of the blending functions on wall distance; in the 1-eq./2-eq. approach the inner layer model itself involves wall distance in its formulation, restricting the usefulness of such models to relatively simple flow topologies, where wall distance is meaningful.

The present approach extends the k–ϵ model to low Reynolds number flow regimes by combining it with the pointwise k–R model of Goldberg (1994) so that no explicit wall distance is needed, rendering the model applicable to arbitrary geometries. The modification to the standard k–ϵ model is done by (a) using the k equation of the k–R model as the kinetic energy transport equation, in which ϵ is replaced by k^2/R as the dissipation term; (b) limiting the time scale to never fall below the Kolmogorov (dissipative eddy) scale $(\nu/\epsilon)^{1/2}$ [this has been previously suggested by Durbin (1991) and, in a different context, by Goldberg (1991)]; (c) employing a pointwise (local) wall boundary condition for ϵ and a pointwise near-wall damping function. The coupling of k, R, and ϵ renders the current approach a three-equation model.

Model Formulation

The present k–R model is a variant of the one proposed earlier by Goldberg (1994). The transport equation for the undamped eddy viscosity reads

$$\frac{D(\rho R)}{Dt} = \nabla\cdot[(\mu + \mu_t/\sigma_R)\nabla R] + (2 - C_{R1})\frac{R}{k}P - (2 - C_{R2})\rho k - 2\rho\frac{C_\mu}{\sigma_R}\nabla R\cdot\nabla R. \quad (1)$$

The turbulence kinetic energy equation is given by

$$\frac{D(\rho k)}{Dt} = \nabla\cdot[(\mu + \mu_t/\sigma_R)\nabla k] + P - \frac{(\rho k)^2}{\rho R}. \quad (2)$$

The turbulence energy production, $P = -\overline{u_i' u_j'}U_{i,j}$, is used in the linear (Boussinesq) form

$$P = \left[\mu_t\left(\frac{\partial U_i}{\partial x_j} + \frac{\partial U_j}{\partial x_i} - \frac{2}{3}\frac{\partial U_k}{\partial x_k}\delta_{ij}\right) - \frac{2}{3}\rho k\delta_{ij}\right]\frac{\partial U_i}{\partial x_j}. \quad (3)$$

Here U_i are the cartesian mean velocity components; x_i are the corresponding coordinates; ρ is density; μ and μ_t are the dynamic molecular and eddy viscosities, respectively, with $\nu \equiv \mu/\rho$; and D/Dt is the compressive material derivative. The model constants are $C_{R1} = 1.42$, $C_{R2} = 1.83$, $\sigma_R = \kappa^2/(\sqrt{C_\mu}(C_{R2} - C_{R1})) = 1.367$, $\kappa = 0.41$, $C_\mu = 0.09$.

The k–ϵ model in the present work uses Eq. (2) for k. The energy dissipation rate transport equation is given in the form

---

[1] Presently, Senior Scientist, METACOMP Technologies, Inc., Westlake Village, CA 91362.

Contributed by the Fluids Engineering Division for publication in the JOURNAL OF FLUIDS ENGINEERING. Manuscript received by the Fluids Engineering Division May 9, 1995; revised manuscript received May 13, 1996. Associate Technical Editor: J. A. C. Humphrey.

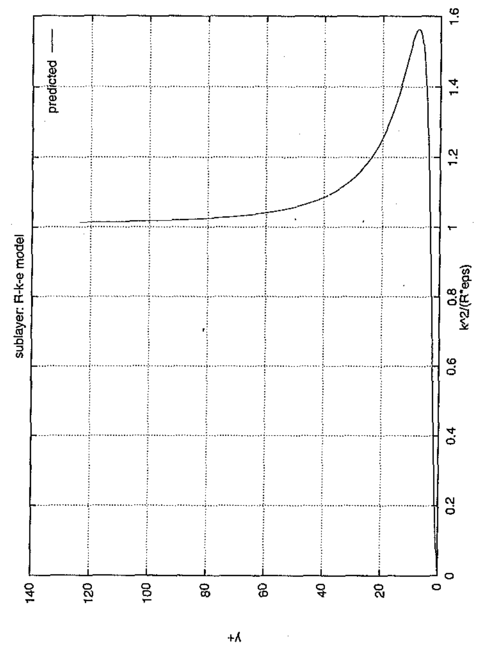

Fig. 1 (*a*) Flat plate flow: profile of the dissipations ratio $k^2/(R\epsilon)$

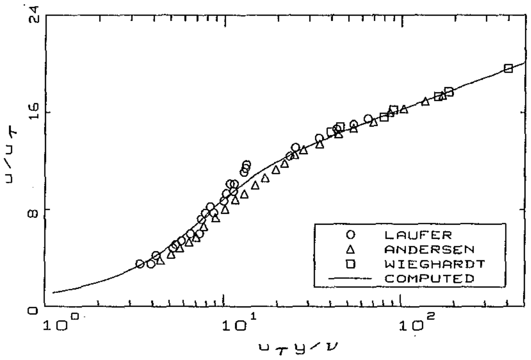

Fig. 1 (*b*) Flat plate flow: near-wall velocity profile

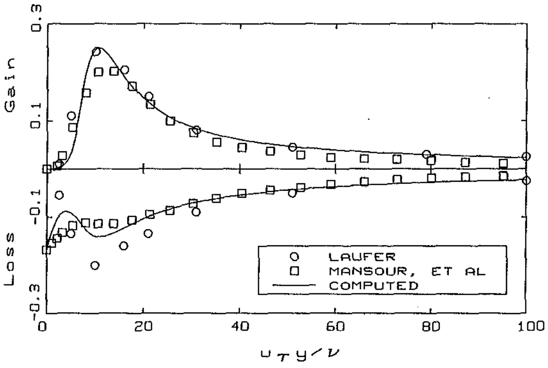

Fig. 1 (*c*) Flat plate flow: near-wall energy balance

$$\frac{D(\rho\epsilon)}{Dt} = \nabla\cdot[(\mu + \mu_t/\sigma_\epsilon)\nabla\epsilon] + T_t^{-1}(C_{\epsilon1}P - C_{\epsilon2}\rho\epsilon), \quad (4)$$

where $\sigma_\epsilon = 1.3$, $C_{\epsilon1} = 1.44$, $C_{\epsilon2} = 1.92$, and turbulence production P given in Eq. (3).

The turbulence time scale, as proposed by Durbin (1991) and (in a different context) by Goldberg (1991), is

$$T_t = \max\{k/\epsilon, C_T(\nu/\epsilon)^{1/2}\} \quad (5)$$

where $C_T = 6$ based on DNS data (see Durbin, 1991). Equation (5) guarantees that the eddy time scale will not be less than the Kolmogorov one, dominant in the immediate vicinity of solid surfaces.

It is noted that when Eq. (1) is derived from the standard k and ϵ equations, two further diffusion terms appear on its RHS, namely $-2C_\mu/\sigma_R[(R/k)^2\nabla k\cdot\nabla k - 2(R/k)\nabla k\cdot\nabla R]$. Since these terms are not used, the resulting R-equation is independent of the k and ϵ equations. This is clearly seen in Fig. 1(*a*) where the ratio of the two dissipation rates, $k^2/(R\epsilon)$, is plotted against y^+ in the case of flat plate near-wall flow. Unlike ϵ, k^2/R tends to vanish at the wall, and it peaks to about 1.6ϵ at $y^+ \approx 8$. As seen in the figure, R tends back to k^2/ϵ only at $y^+ > 100$. Thus using k^2/R as the dissipation term in the k-equation reduces k in near-wall regions much the same as in a regular low-Re k–ϵ model where ϵ is increased for this purpose through multiplying the dissipation term, $C_{\epsilon2}\epsilon$, by a damping function f_2. The use of the extra transport equation, R, introduces such a near-wall effect without the need to use semi ad hoc f_1 and f_2 damping functions (see Lam and Bremhorst, 1981).

The eddy viscosity field is given by

$$\mu_t = C_\mu f_\mu \rho k^2/\epsilon, \quad (6)$$

where the near-wall damping function, f_μ, is given as

$$f_\mu = \tanh(\alpha R_t)/\tanh(\beta R_t) \quad (7)$$

with $R_t = \rho k^2/(\mu\epsilon)$, the turbulence Reynolds number, and $\beta = C_\mu^{3/4}/2\kappa$. The constant $\alpha = 0.0075$ was determined by correlation to flat plate flow data. Note that $f_\mu = \alpha/\beta$ at walls which implies that $\mu_t \sim y^4$ there. This assumption is widely used, for example in Durbin's (1991) k–ϵ–$\overline{v^2}$ model.

The three transport equations, Eqs. (1), (2), and (4), are subject to the following solid wall boundary conditions. The kinetic energy of turbulence vanishes at walls, thus

$$k_w = 0. \quad (8)$$

From DNS data of flat plate and channel flows (Mansour et al., 1988), $\epsilon_w^+ \approx 0.17$. Written explicitly, $\epsilon_w \approx 0.17\nu_w \times (\partial U_t/\partial y_n)_w^2$, where U_t is the local tangential-to-wall velocity component and y_n in the local normal-to-wall direction. The non-pointwise velocity gradient is replaced by the vorticity magnitude, ω, which is tensorially invariant. Thus the final form of the wall boundary condition for ϵ is proposed to read

$$\epsilon_w = 0.17(\nu\omega^2)_w. \quad (9)$$

Finally, since the eddy viscosity vanishes at a solid surface,

$$R_w = 0. \quad (10)$$

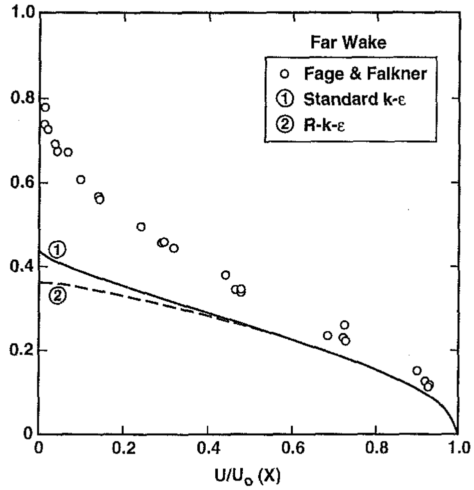

Fig. 2 Far wake flow: velocity profiles

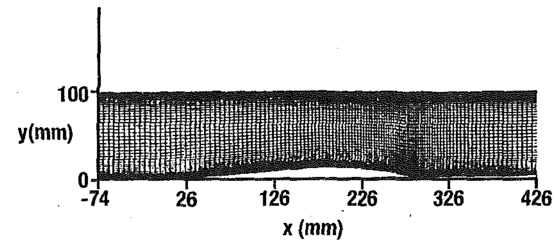

Fig. 3(*a*) Mach 0.615 bump flow: computational grid

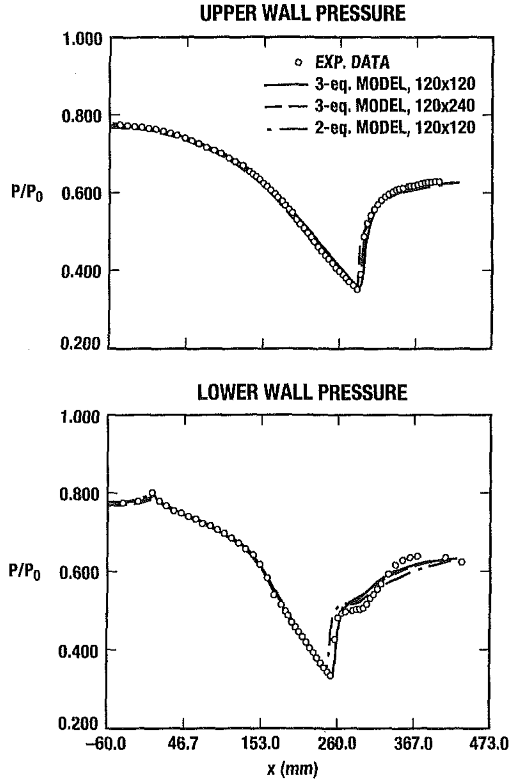

Fig. 3(*b*) Mach 0.615 bump flow: wall pressure profiles

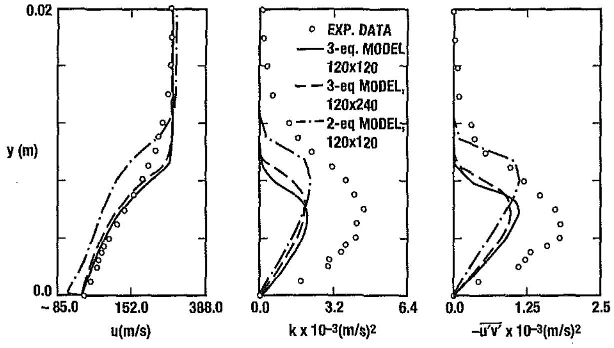

Fig. 3(c) Mach 0.615 bump flow: profiles at x = 330 mm

Freestream and initial conditions for k are usually determined by the level of freestream turbulence, T', through $k_\infty/U_\infty^2 = (3/2)T'^2$, otherwise a value of $k_\infty/U_\infty^2 = 10^{-6}$ is used. Other conditions applicable in the present work are $\epsilon_\infty = 10^{-6}$, and $(\rho R)_\infty = O(\mu_\infty)$, though the last one is not crucial since R is overwritten by the $k-\epsilon$ model.

Flow Examples

The present turbulence model was included in the USA Reynolds-averaged Navier-Stokes (RANS) multiblock structured grid flow solver, which is up to 3rd order accurate, based on an upwind TVD scheme for the convection terms, within a finite volume framework (Chakravarthy et al., 1988). The model was also incorporated into Wilcox's (1993) SUBLAYER and WAKE flow solvers. Four examples are reported here; the two flow cases computed with the RANS solver were initialised with Musker's (1979) turbulent flow velocity profile, corrected for compressibility effects. Initial and inflow k and ϵ profiles were set according to the recommendations set forth in the ETMA Workshop (1994) for these test cases. The computational meshes used here are also those suggested in that workshop.

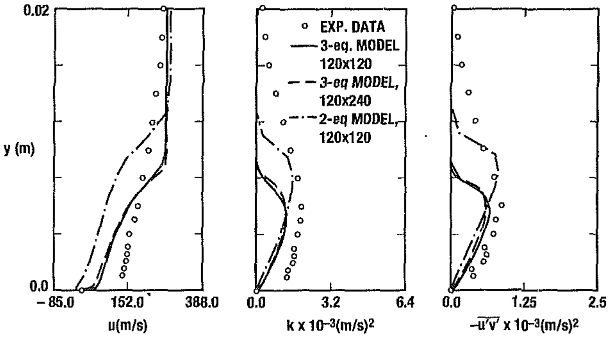

Fig. 3(*d*) Mach 0.615 bump flow: profiles at x = 380 mm

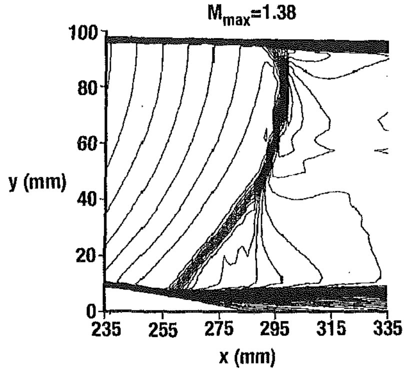

Fig. 3(*e*) Mach 0.615 bump flow: Mach contours

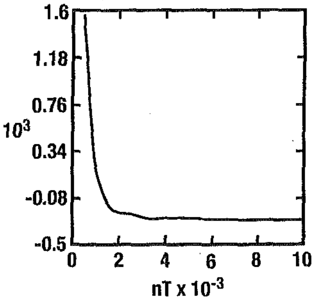

Fig. 3(*f*) Mach 0.615 bump flow: convergence history

Case 1: Flat Plate Sublayer Flow. Wilcox's (1993) SUBLAYER solver was used to compute incompressible near-wall flow over a flat plate. Figure 1(*b*) shows a comparison between prediction of near-wall velocity profile and law-of-the-wall measurements by Laufer (1952), Andersen et al. (1972), and Wieghardt (Coles and Hirst, 1969). Figure 1(*c*) compares predicted near-wall energy balance with experimental data of Laufer (1952) and with DNS results of Mansour et al. (1988).

Case 2: Far Wake Similarity Flow. A far wake flow computation is presented next. Figure 2 shows velocity profile predictions by the current model and by the standard $k-\epsilon$ model.

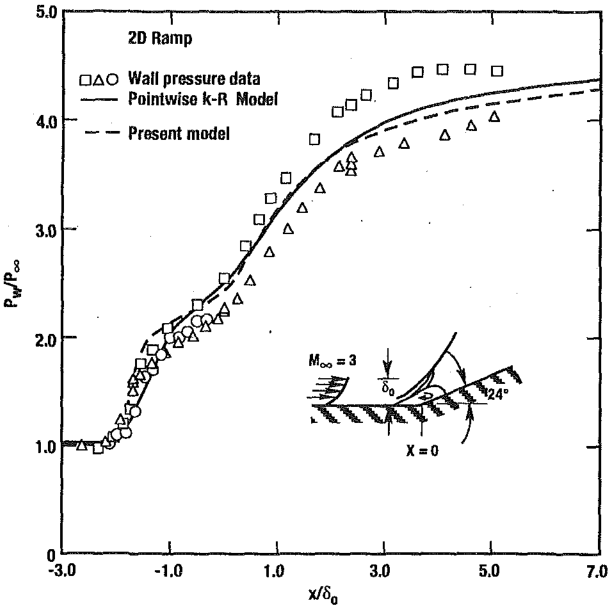

Fig. 4(*a*) Supersonic ramp flow: wall pressure distribution

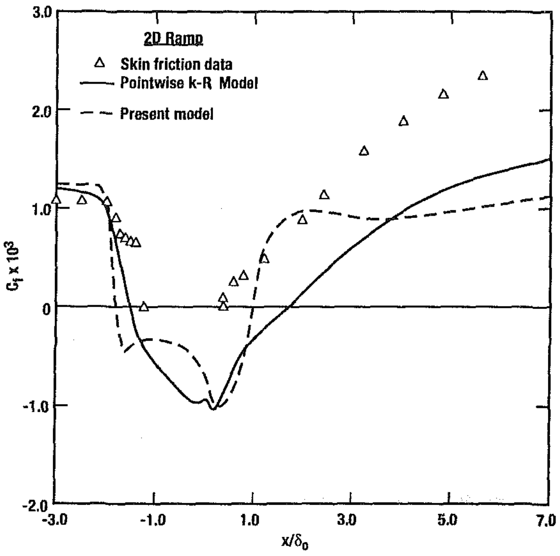

Fig. 4(*b*) Supersonic ramp flow: skin friction distribution

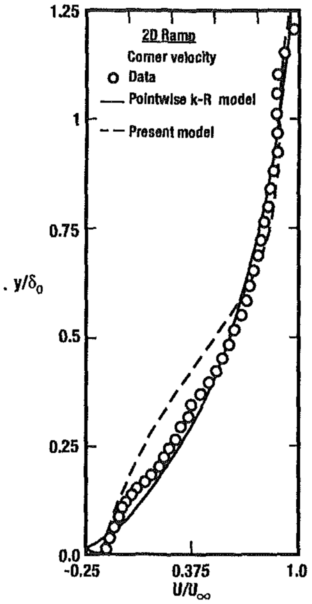

Fig. 4(*c*) Supersonic ramp flow: corner velocity profile

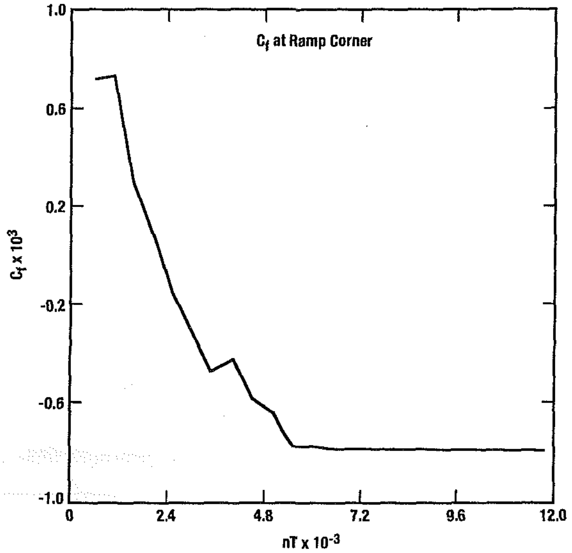

Fig. 4(*d*) Supersonic ramp flow: convergence history

These are compared to measurements by Fage and Falkner (1932). x is the axial coordinate, and y is the normal-to-flow coordinate, measured from the wake centreline. The velocity, U, is normalized by that at the wake centreline, $U_0(x)$, and the normal distance is in similarity form, $\eta = y/\sqrt{Dx/\rho U_\infty^2}$, where D is the momentum defect. Wilcox's (1993) WAKE solver was employed in this computation. The slight difference between the two predictions is solely due to the different values of σ_k in the two models: 1.0 in the $k-\epsilon$ model versus 1.367 in the $R-k-\epsilon$ model. While the agreement with the data is fair at best, the results are nearly independent of the choice of freestream conditions.

Case 3: Transonic Channel Flow Including a Bump. In this case a Mach 0.615 flow enters a two-dimensional channel comprising a flat upper wall and a lower surface which includes a bump-like profile protruding from the otherwise flat wall [see Fig. 3(*a*)]. The inflow total pressure is 96KPa. A transonic λ-shock forms toward the bump trailing edge, and its interaction with the boundary layer induces a separated flow region. Experimental data were taken by Délery and his associates (Délery, 1983). In this experiment the shock location was controlled by an adjustable throat downstream of the bump; since no geometrical details of this throat are provided, computors are instructed to adjust the downstream pressure to replicate numerically the experimental shock location. Inflow conditions were those recommended by the ETMA Workshop (1994), using a 1 mm boundary layer thickness, and adiabatic walls. The computations were done on two grids: a 120×120 grid with 14 points inside the viscous sublayers, first point being located at $y^+ = 0.1$; and a 120×240 grid, with 16 points within the sublayers and finer resolution across the channel. The computational domain extended from $x = -74$ to $x = 426$ mm, and some streamwise grid clustering was imposed, centred at the bump trailing edge, as seen in Fig. 3(*a*). Predictions using the $k-R$ model by itself, on the 120×120 grid, are also included.

Figure 3(*b*) shows comparisons of predictions with experimental data of lower and upper wall pressure profiles. Velocity, turbulence kinetic energy, and Reynolds shear stress profiles, over the lower wall at the reattachment location and downstream of it, are shown in Figs. $3(c-d)$. Figure $3(e)$ shows Mach contours predicted by the present model; the experimentally observed λ-shock is captured fairly well, consistent with the lower wall pressure prediction which exhibits a plateau in the separated flow region. The velocity profiles indicate improved prediction of the extent of the separation bubble by the new model, compared to that by the $k-R$ model. There is no appreciable difference between the "coarse" and "fine" grid predictions.

Figure $3(f)$ is a convergence history plot based on lower wall skin friction in a location within the reversed flow region; nT is the time step counter. This constitutes a more stringent test than monitoring the drop in numerical residuals.

Case 4: Supersonic Ramp Flow. This is the supersonic two-dimensional flow over a 24 deg ramp measured by Settles et al. (1979), with additional data by Dolling and Murphy (1983), and by Selig et al. (1989). An oblique shock, impinging on the boundary layer ahead of the ramp corner (due to upstream influence), induces flow detachment, with subsequent reattachment onto the ramp surface. The origin of the (x, y) cartesian coordinate system is located at the ramp corner, with directions along and normal to the upstream flat plate, respectively. These coordinates are scaled by the boundary layer thickness upstream of the shock, δ_0. Wall pressure (p_w) is scaled by the upstream inflow pressure (p_∞). The computation was done on a 99×99 grid, with at least 8 cells inside the viscous sublayer, first point off the wall being at $y^+ < 1$. The grid was clustered in the x direction too, with $(\Delta x)_{\min} = 0.1\delta_0$, located at the ramp corner.

Numerical predictions of this case are known to be strongly dependent on inflow conditions. The inflow Mach number was 2.84; total temperature 262 K; and static pressure 24 kPa. Wall temperature was 276 K. An equilibrium Musker (1979) velocity profile, corrected for compressibility effects, was used with skin friction coefficient 0.0015, and wake strength parameter $\Pi = 0.55$. The measured upstream boundary layer thickness, $\delta_0 = 0.023$ m, was located at $x/\delta_0 = -3.0$; since the computational inflow was placed at $x/\delta_0 = -21.7$, $\delta = 0.4\delta_0$ was used to match the measured skin friction upstream of the start of the shock/boundary layer interaction. The inflow profiles for k, ϵ, and T are described in the ETMA Workshop Proceedings (1994), with $k_\infty/U_\infty^2 = 10^{-4}$, corresponding to freestream turbulence level $T' = 0.8$ percent.

Figures 4 show predictions and data comparisons of surface pressure, skin friction, and corner velocity profile. A sketch, showing the geometry and some flow features, is seen in Fig. $4(a)$. The figures include predictions using the $k-R$ model. The extent of flow separation is seen in the skin friction plot [Fig. $4(b)$, data of Settles et al.], in the region where $C_f < 0$; the new model predicts the bubble length better than the $k-R$ model does, but it also predicts a slight post-reattachment peak in skin friction. The velocity profile shape in the near-wall portion of the backflow is better predicted by the new model, however, the $k-R$ model's prediction of the bubble height seems closer to the data, judging by Fig. $4(c)$. Figure $4(d)$ is a convergence history plot based on skin friction at the ramp corner.

Conclusions

This paper introduced and tested an $R-k-\epsilon$ model as a low Reynolds number extension of the standard $k-\epsilon$ model. The new turbulence model is pointwise, thus applicable to arbitrary geometries; it enforces time scale realisability; and it incorporates a simple wall boundary condition for ϵ. Comparing predictions by this model with experimental data of several well-documented flow cases demonstrated the feasibility of the present three-equation approach.

Acknowledgment

The author wishes to thank Dr. Dale Ota, Rockwell Science Center CFD Department, for modifying the USA Navier-Stokes solver to handle an arbitrary number of extra transport equations.

References

Andersen, P. S., Kays, W. M., and Moffat, R. J., 1972, "The Turbulent Boundary Layer on a Porous Plate: An Experimental Study of the Fluid Mechanics for Adverse Free-Stream Pressure Gradients," Report No. HMT-15, Dept. Mech. Eng., Stanford University, CA.

Chakravarthy, S. R., Szema, K.-Y., and Haney, J. W., 1988, "Unified 'Nose-to-Tail' Computational Method for Hypersonic Vehicle Applications," AIAA Paper 88-2564.

Coles, D. E., and Hirst, E. A., 1969, "Computation of Turbulent Boundary Layers-1968," AFOSR-IFP-Stanford Conference, II, Stanford University, CA.

Délery, J. M., 1983, "Experimental Investigation of Turbulence Properties in Transonic Shock-wave/Boundary-Layer Interactions," *AIAA Journal*, Vol. 21, pp. 180–185.

Dolling, D. S., and Murphy, M. T., 1983, "Unsteadiness of the Separation Shock Wave Structure in a Supersonic Compression Ramp Flowfield," *AIAA Journal*, Vol. 21, No. 12, pp. 1628–1634.

Durbin, P. A., 1991, "Near-Wall Turbulence Closure Modeling Without 'Damping Functions'," *Theoretical and Computational Fluid Dynamics*, Vol. 3, pp. 1–13.

ETMA Project Workshop, UMIST, Nov. 1994 (document in print).

Fage, A. and Falkner, V. M. (1932) Note on Experiments on the Temperature and Velocity in the Wake of a Heated Cylindrical Obstacle, *Proceedings Royal Society*, London, Series A135, pp. 702–705.

Goldberg, U. C., 1991, "Derivation and Testing of a One-Equation Model Based on Two Time Scales," *AIAA Journal*, Vol. 29, No. 8, pp. 1337–1340.

Goldberg, U. C., 1994, "Toward a Pointwise Turbulence Model for Wall-Bounded and Free Shear Flows," ASME JOURNAL OF FLUIDS ENGINEERING, Vol. 116, No. 1, pp. 72–76.

Jones, W. P., and Launder, B. E., 1972, "The Prediction of Laminarization with a Two-Equation Model of Turbulence," *International Journal of Heat and Mass Transfer*, Vol. 15, pp. 301–314.

Lam, C. K. G., and Bremhorst, K. A., 1981, "Modified Form of $k-\epsilon$ Model for Predicting Wall Turbulence," ASME JOURNAL OF FLUIDS ENGINEERING, Vol. 103, pp. 456–460.

Laufer, J., 1952, "The Structure of Turbulence in Fully Developed Pipe Flow," NACA TM 1174.

Launder, B. E., and Sharma, B. I., 1974, "Application of the Energy-Dissipation Model of Turbulence to the Calculation of Flow Near a Spinning Disc," *Letters in Heat and Mass Transfer*, Vol. 1, pp. 131–138.

Mansour, N. N., Kim, J., and Moin, P., 1988, "Reynolds Stress and Dissipation Rate Budgets in Turbulent Channel Flow," *Journal of Fluid Mechanics*, Vol. 194, pp. 15–44.

Menter, F. R., 1994, "Two-Equation Eddy-Viscosity Turbulence Models for Engineering Applications," *AIAA Journal*, Vol. 32, No. 8, pp. 1598–1605.

Michelassi, V., 1993, "Adverse Pressure Gradient Flow Computation by Two-Equation Turbulence Models," *Engineering Turbulence Modelling and Experiments* 2, W. Rodi and F. Martelli, eds., Elsevier.

Musker, A. J., 1979, "Explicit Expression for the Smooth Wall Velocity Distribution in a Turbulent Boundary Layer," *AIAA Journal*, Vol. 17, pp. 655–657.

Selig, M. S., Andreopoulos, J., Muck, K. C., Dussauge, J. P., and Smits, A. J., 1989, "Turbulence Structure in a Shock Wave/Boundary Layer Interaction," *AIAA Journal*, Vol. 27, No. 7, pp. 862–869.

Settles, G. S., Fitzpatrick, T. J., and Bogdonoff, S. M., 1979, "Detailed Study of Attached and Separated Compression Corner Flowfields in High Reynolds Number Supersonic Flow," *AIAA Journal*, Vol. 17, No. 6, pp. 579–585.

Wilcox, D. C., 1993, *Turbulence Modeling for CFD*, DCW Industries, Inc., La Cañada, CA.

Assessment of the SSG Pressure-Strain Model in Free Turbulent Jets With and Without Swirl

B. A. Younis[1]
Senior Lecturer,
Department of Civil Engineering,
City University,
London EC1V 0HB, United Kingdom

T. B. Gatski
Senior Research Scientist,
NASA Langley Research Center,
Hampton, VA 23681

C. G. Speziale[1]
Professor,
Aerospace and Mechanical
Engineering Department,
Boston University,
Boston, MA 02215

Data from free turbulent jets both with and without swirl are used to assess the performance of the pressure-strain model of Speziale, Sarkar and Gatski, which is quadratic in the Reynolds stresses. Comparative predictions are also obtained with the two versions of the Launder, Reece and Rodi model, which are linear in the same terms. All models are used as part of a complete second-order closure based on the solution of differential transport equations for each nonzero component of $\overline{u_i u_j}$ *together with an equation for the scalar energy dissipation rate. For nonswirling jets, the quadratic model underestimates the measured spreading rate of the plane jet but yields a better prediction for the axisymmetric case without resolving the plane jet/round jet anomaly. For the swirling axisymmetric jet, the same model accurately reproduces the effects of swirl on both the mean flow and the turbulence structure in sharp contrast with the linear models which yield results that are in serious error. The reasons for these differences are discussed.*

1 Introduction

Swirling flows are common in nature as well as in engineering practice (e.g., in tornados, gas-turbine combustors, furnaces, and jet mixers) where a tangential (swirl) velocity is often superimposed on an axially-directed flow to enhance the rate at which it spreads into and entrains from its surroundings. The most basic realization of a practical swirling flow is that of a single axisymmetric swirling jet discharged into infinite, stagnant surroundings. For small values of the Swirl Number S (defined as the ratio of tangential to axial momentum fluxes), the adverse pressure gradients set up by the decaying tangential velocity are insufficient to cause flow reversal and the swirling jet becomes an example of a thin shear layer distorted by the imposition of an extra rate of strain. Flows of this type provide ideal benchmark tests for turbulence closures since their behavior is determined more by turbulent transport than by pressure effects.

The prediction of the free swirling jet has highlighted defects in nearly all current closure models. The sensitivity of the turbulence in a thin shear layer to streamline curvature is not captured by eddy-viscosity models which utilize the Boussinesq linear stress-strain relationship. Adoption of more refined nonlinear relationships such as that of Speziale (1987) are unlikely to lead to drastically improved predictions since they too involve a scalar eddy-viscosity while experiments show this quantity to be highly anisotropic. Second-order closure models, however, are known to reproduce the effects of longitudinal streamline curvature quite accurately (Irwin and Arnot-Smith, 1975; Gibson et al., 1981) and are therefore potentially more suited for swirling flows. The first attempt at the prediction of the free swirling jet with a model of this kind appears to be that of Launder and Morse (1979). Those workers employed the more complete of the two models for the pressure-strain correlation proposed by Launder, Reece and Rodi (1975) (hereafter LRR1) and found that their predictions of the swirling jet experiments of Morse (1980) produced predominantly negative values for the shear-stress component $\overline{uw}$ while the data showed this quantity to be largely positive. This component contributes to the rate of production of $\overline{uv}$ (the shear stress component which governs the radial transport of axial momentum) which, as a result, was also underestimated by the predictions. Not surprisingly, therefore, Launder and Morse reported that compared to a jet without swirl, the "numerical solutions display a reduced rate of spread in contrast to the strong augmentation found in practice." Launder and Morse identified the source of this erroneous result as being due to the mean-strain contribution to the pressure-strain correlation model and demonstrated that improved predictions can be obtained by reducing these terms in the $\overline{uw}$ and $\overline{vw}$ equations by 40 percent. Younis (1984) found that the alternative pressure-strain model of Launder et al. (1975) (sometimes called the IP model but hereafter referred to as LRR2) suffered the same defects as its more complicated counterpart but that the model can be sensitized to swirl by treating the nongradient terms that arise from the transformation of the convective terms into cylindrical coordinates as 'production' and including these in the pressure-strain model. This treatment renders the model dependent on the choice of the coordinate system and cannot therefore be recommended for general applications. Gibson and Younis (1986) obtained satisfactory predictions with the coordinate-invariant form of the LRR2 model by reducing the relative importance of the mean-strain contribution. This was achieved by halving the value of the coefficient C_2, and then using well-established criteria to reoptimize the remaining coefficients. In particular, the value of C_1, the coefficient multiplying the Rotta return-to-isotropy term, was increased from 1.8 to 3.0 in order to keep the value of the important parameter $(1 - C_2)/C_1$ within acceptable limits. The resulting model worked well for a wide variety of complex shear flows including swirling jets, while its performance in benchmark homogeneous and inhomogeneous turbulent flows remained comparable to that of the original model. However, one adverse consequence of moving C_1 farther away

---

[1] Research was supported by the National Aeronautics and Space Administration under NASA Contract No. NAS1-19480 while the author was in residence at the Institute for Computer Applications in Science and Engineering (ICASE), NASA Langley Research Center, Hampton, VA 23681-0001.

Contributed by the Fluids Engineering Division for publication in the JOURNAL OF FLUIDS ENGINEERING. Manuscript received by the Fluids Engineering Division May 5, 1995; revised manuscript received December 15, 1995. Associate Technical Editor: R. W. Metcalfe.

Table 1 Coefficients of the ϵ-equation

Model	C_{ϵ_1}	C_{ϵ_2}	C_ϵ
LRR1	1.44	1.90	0.15
LRR2	1.45	1.90	0.18
SSG	1.44	1.83	0.183

from unity is the increased reliance on the model for wall-reflection effects to obtain the correct relative Reynolds-stress levels in the equilibrium near-wall layer (see Abid and Speziale 1993). C_1' and C_2' (the coefficients associated with the wall-reflection model) were therefore increased to 0.75 and 0.5 from their original values of 0.5 and 0.3, respectively. This practice of giving more prominence to the wall-reflection model runs counter to recent developments in the field which have led to the abandonment of this model altogether in the calculation of wall-bounded flows. Finally, Fu et al. (1987) proposed pressure-scrambling the entire convection terms and not just their non-gradient elements. This is equivalent to omitting the mean-strain part altogether (with $C_2 = 0$) and setting Rotta's coefficient C_1 to 4.5. The need to include the mean-strain part in the model for the pressure-strain correlation is well documented, especially when the effects of buoyancy and streamline curvature are to be properly modeled. It is therefore unlikely that this model will prove adequate when such effects are present.

Even though other closure assumptions (specifically for the turbulent transport and the energy dissipation rate) may well have contributed to the incorrect prediction of the swirling jet, it seems more likely from the foregone that the principal defect lies in the model for the pressure-strain correlations. (Note, for example, that the dissipation rate term does not appear as a sink in the equation for $\overline{uw}$ and cannot therefore be responsible for the negative values obtained for this quantity.) Now since both pressure-strain models of Launder et al. (1975) are linear in the Reynolds stresses, it seemed worthwhile to investigate whether adoption of a non-linear model can produce improvements. Several such models have been proposed in the literature. Recent models include that of Speziale, Sarkar and Gatski (1991) (hereafter SSG), which is quadratic in the Reynolds stresses, and that of Fu et al. (1987) which is cubic in the same terms. The latter is somewhat too complex to implement in general Navier-Stokes solvers and since our ultimate interest is in advancing a model which would be applicable to the confined swirling flows encountered in practical applications, attention was confined to the quadratic model which has already been found to reproduce the correct behavior of a number of wall-bounded flows without the use of empirical wall-reflection terms (Basara and Younis, 1995). The main objective of this work then is to see whether the presence of the quadratic terms in the SSG model provides the "major changes needed in modeling the mean-strain contribution to the pressure strain correlation" deemed necessary by Launder and Morse (1979) to resolve the swirling jet problem. The paper also reports comparative predictions with both the LRR1 and LRR2 models and puts on record the performance of the SSG model in two benchmark flows—namely, the two-dimensional plane and axisymmetric jets without swirl.

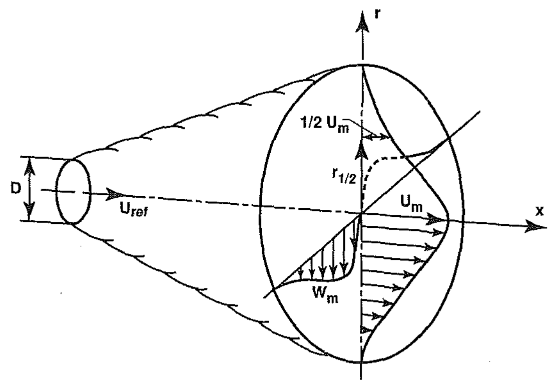

Fig. 1 The swirling free jet. Coordinates and notation

Table 2 Predicted and measured plane-jet spreading rates

	$\frac{dy_{1/2}}{dx}$
Measurements	0.102[1], 0.103[2,3],.0.11[4]
LRR1	0.121 (present), 0.116[5], 0.123[6]
LRR2	0.108 (present), 0.116[5], (0.107–0.111)[7]
SSG	0.0917

[1] Gutmark (1970); [2] Patel (1970); [3] Robins (1971); [4] Haskestad (1965); [5] Launder et al. (1975); [6] Launder and Morse (1979); [7] el Baz et al. (1993).

2 The Turbulence Models

The turbulence models employed in this study are based on the solution of differential transport equations for the Reynolds-stress tensor $\overline{u_iu_j}$ of the form:

$$\overbrace{U_k \frac{\partial \overline{u_i u_j}}{\partial x_k}}^{\text{Convection}} = \overbrace{-\left(\overline{u_i u_k}\,\frac{\partial U_j}{\partial x_k} + \overline{u_j u_k}\,\frac{\partial U_i}{\partial x_k}\right)}^{\text{Production }(P_{ij})}$$

$$\overbrace{-\frac{\partial}{\partial x_k}\left[\overline{u_iu_ju_k} + \frac{1}{\rho}\left(\overline{p'u_i}\,\delta_{jk} + \overline{p'u_j}\,\delta_{ik}\right) - \nu\,\frac{\partial \overline{u_iu_j}}{\partial x_k}\right]}^{\text{Diffusion}}$$

$$\underbrace{-\,2\nu\overline{\left(\frac{\partial u_i}{\partial x_k}\,\frac{\partial u_j}{\partial x_k}\right)}}_{\text{Dissipation}(\epsilon_{ij})} + \underbrace{\overline{\frac{p'}{\rho}\left(\frac{\partial u_i}{\partial x_j} + \frac{\partial u_j}{\partial x_i}\right)}}_{\text{Redistribution }(\Phi_{ij})} \qquad (1)$$

In the above equation, U_k is the mean velocity, u_k is the fluctuating velocity, p is the fluctuating pressure, ρ is the density, and ν is the kinematic viscosity. An overbar denotes a time average.

Diffusion is assumed to be entirely due to the turbulent velocity fluctuations which are modeled here by the Daly and Harlow (1970) gradient-transport hypothesis:

$$-\,\overline{u_iu_ju_k} = C_s\,\frac{k}{\epsilon}\,\overline{u_ku_l}\,\frac{\partial \overline{u_iu_j}}{\partial x_l} \qquad (2)$$

In (2), $k\ (\equiv \frac{1}{2}\,\overline{u_iu_i})$ and ϵ are the turbulent kinetic energy and its dissipation rate, respectively. The coefficient C_s is assigned the value of 0.22, arrived at by Morse (1980) by computer optimization carried out in conjunction with the LRR1 model. The sensitivity of the SSG model to the choice of this value will be checked in Section 4.

The pressure-strain models employed in this paper are:

LRR1 and LRR2 Models

$$\Phi_{ij} = -C_1\epsilon b_{ij} + C_2kS_{ij} + C_3k(b_{ik}S_{jk} + b_{jk}S_{ik} - \tfrac{2}{3}\,b_{kl}S_{kl}\delta_{ij})$$

$$+\ C_4k(b_{ik}W_{jk} + b_{jk}W_{ik}) \qquad (3)$$

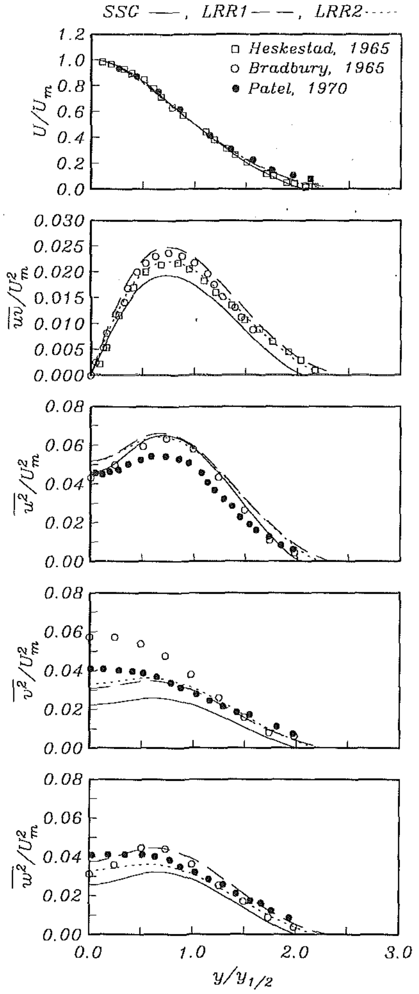

Fig. 2 Predicted and measured cross-stream profiles for the plane free jet

where

LRR1: $C_1 = 3.0, \quad C_2 = \frac{4}{5}, \quad C_3 = 1.75, \quad C_4 = 1.31$

LRR2: $C_1 = 3.6, \quad C_2 = \frac{4}{5}, \quad C_3 = 1.20, \quad C_4 = 1.20$

and b_{ij}, S_{ij}, and W_{ij} are, respectively, the Reynolds-stress anisotropy, mean rate of strain and mean vorticity tensors defined as:

$$b_{ij} = \frac{\overline{u_i u_j}}{\overline{u_q u_q}} - \frac{1}{3}\delta_{ij}$$

$$S_{ij} = \frac{1}{2}\left(\frac{\partial U_i}{\partial x_j} + \frac{\partial U_j}{\partial x_i}\right)$$

$$W_{ij} = \frac{1}{2}\left(\frac{\partial U_i}{\partial x_j} - \frac{\partial U_j}{\partial x_i}\right)$$

SSG Model

$$\Phi_{ij} = -(C_1\epsilon + C_1^*\mathcal{P})b_{ij} + C_2\epsilon(b_{ik}b_{kj} - \tfrac{1}{3}b_{kl}b_{kl}\delta_{ij}) + (C_3 - C_3^* II_b^{1/2})kS_{ij} + C_4k(b_{ik}S_{jk} + b_{jk}S_{ik} - \tfrac{2}{3}b_{kl}S_{kl}\delta_{ij}) + C_5k(b_{ik}W_{jk} + b_{jk}W_{ik}) \quad (4)$$

Table 3 Predicted and measured axisymmetric-jet spreading rates

	$\frac{dr_{1/2}}{dx}$
Measurements	0.086^1, 0.094^2, 0.096^3
LRR1	0.143 (present), 0.135^4, 0.148^5
LRR2	0.119 (present), $(0.112\text{–}0.126)^6$
SSG	0.111

[1] Rodi (1972); [2] Hussein et al. (1994); [3] Panchapakesan and Lumley (1993); [4] Launder and Morse (1979); [5] Musonge (1983); [6] el Baz et al. (1993).

where

$$C_1 = 3.4, \quad C_1^* = 1.80, \quad C_2 = 4.2$$

$$C_3 = \tfrac{4}{5}, \quad C_3^* = 1.30, \quad C_4 = 1.25$$

$$C_5 = 0.40, \quad II_b = b_{ij}b_{ij}, \quad \mathcal{P} = -\overline{u_i u_j}\frac{\partial U_i}{\partial x_j}$$

The SSG model was formulated using a dynamical systems approach; it is topologically the generic form of the commonly used hierarchy of pressure-strain models for two dimensional mean turbulent flows that are homogeneous and in equilibrium. There are three main features that distinguish it from the LRR models: (*a*) the presence of a quadratic slow

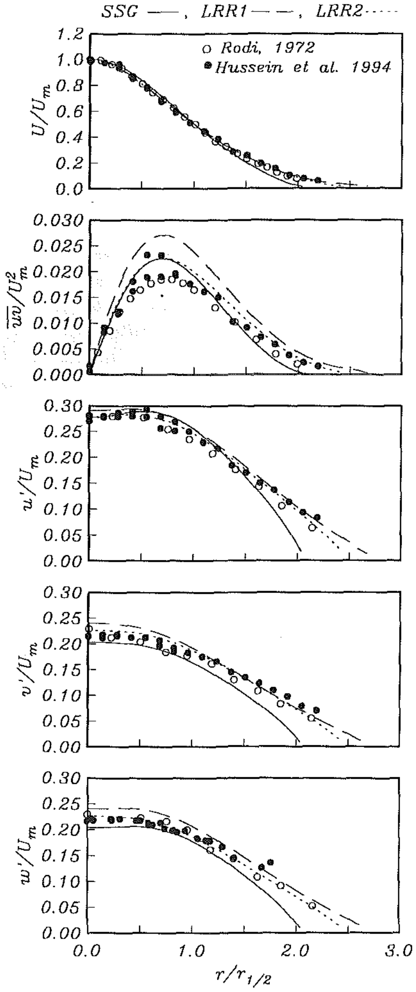

Fig. 3 Predicted and measured cross-stream profiles for the axisymmetric free jet

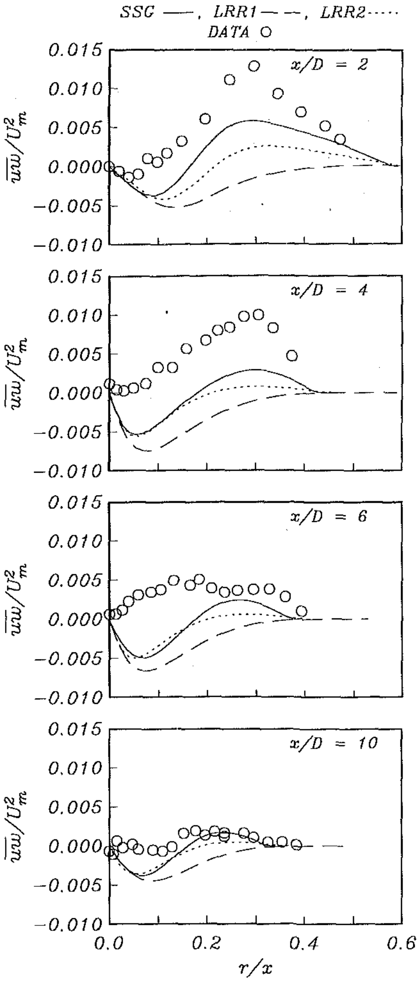

Fig. 4 The swirling free jet. Predicted and measured shear-stress component $\overline{uw}$

term (with coefficient C_2), (*b*) a production-based rapid term that supplements the linear part of the slow pressure strain (with coefficient C_1^*) and (*c*) a variable isotropic rapid term (with coefficient C_3^*). It should also be mentioned that the SSG model was optimized for the description of homogeneous turbulent flows that have combinations of rotational and irrotational strains with the result that it outperforms the LRR models in rotating homogeneous shear flow (Speziale, Sarkar and Gatski, 1991). There is, of course, a strong analogy between flows with a system rotation and those with swirl and this suggests that the effects of the latter may well be better represented by the SSG model.

Closure of the $\overline{u_i u_j}$ equations is completed with the assumption that the dissipation is isotropic at high turbulence Reynolds numbers with the turbulent dissipation rate ϵ (where $\epsilon_{ij} = \frac{2}{3}\epsilon\delta_{ij}$) obtained from the solution of the standard model equation:

$$U_j \frac{\partial \epsilon}{\partial x_j} = \frac{\partial}{\partial x_j}\left(C_\epsilon \frac{k}{\epsilon}\overline{u_j u_l}\frac{\partial \epsilon}{\partial x_l}\right) + C_{\epsilon_1}\frac{\epsilon}{k}\mathcal{P} - C_{\epsilon_2}\frac{\epsilon^2}{k} \quad (5)$$

The coefficients of this equation depend on the model used and are here assigned the values recommended by their originators (see Table 1). The value of C_ϵ appropriate to the SSG model was obtained by the application of a near-wall compatibility relation derived from Eq. (5) (see, for example, Abid and Speziale, 1993).

3 The Solution Procedure

The modeled turbulence equations, transformed into cylindrical-polar coordinates, were solved simultaneously with the mean continuity and momentum equations using the finite-volume marching-integration method of Patankar and Spalding (1970). Incompressible flow conditions were assumed. The solution was started from assumed or, when available, measured distributions for the dependent variables and was then advanced step by step in the predominant flow direction. At each streamwise location, the radial velocity distribution was obtained by integration of the continuity equation while the pressure field was calculated by integration of the boundary-layer form of the radial-momentum equation. In order to ensure that the computed velocities, turbulence quantities and pressure field were fully coupled, iterations were performed at each streamwise location and these were continued till the absolute sum of the residuals for all the dependent variables fell to below 10^{-12}.

For all the results reported in this paper, discretization in the cross-stream direction was by the second-order accurate central-differencing scheme while in the parabolic, streamwise, direction, discretization was by a weighted average approximation which is also second-order accurate. To check the sensitivity of the predictions to the choice of discretization method, further calculations were performed in which convection in the parabolic direction was approximated using the fully-implicit scheme normally employed in boundary-

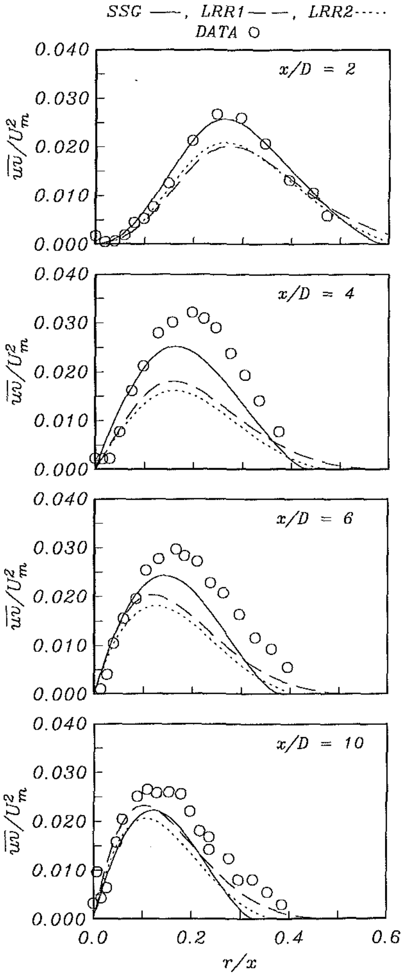

Fig. 5 The swirling free jet. Predicted and measured shear-stress component $\overline{uv}$

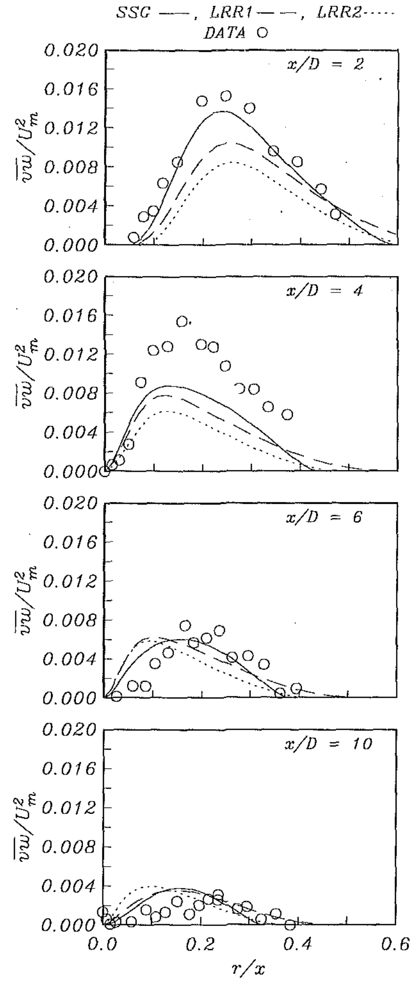

Fig. 6 The swirling free jet. Predicted and measured shear-stress component $\overline{vw}$

layer methods. The outcome of these checks is reported in the Appendix.

In the Patankar and Spalding method, the cross-stream coordinate of the computational domain is a nondimensionalised stream function whose value always lies in between the limits of zero at the axis of symmetry and unity at the free stream. The computational domain (over which the suitably-transformed governing equations are solved) is thus preconstrained while its physical extent expands (or contracts) to match the actual width of the shear layer. This realisation of a flow-adaptive grid ensures that all the computational nodes employed lie within the shear layer and none in the quiescent stream outside it. This practice is both computationally efficient and is also one which alleviates the problem of "edge singularity" discussed by Paullay et al. (1985) in connection with similarity solutions for free jets. This problem is associated with the use of a diffusion model such as that of Eq. (2) is regions of vanishing k and ϵ. In the present application, this problem is confined to the node closest to the free stream (as there are no nodes located within it) and it is resolved there by setting the cross-stream diffusion across the free edge to be exactly equal to the convection rate across it, a practice which is consistent with the limiting forms of the governing equations.

In implementing the Reynolds-stress models in the Patankar and Spalding method, the shear-stress components $\overline{uv}$ and $\overline{vw}$ were solved at grid locations displaced by half a cell from those of the mean velocities in order to prevent uncoupling of the velocity and turbulence fields. The boundary conditions employed were as follows: at the free stream, all the dependent variables were set equal to zero while at the axis of symmetry, the radial gradients of streamwise velocity and the normal stresses were set equal to zero while the transverse velocity and the shear stresses were themselves set equal to zero. The boundary conditions at inlet, and their consequences on the computed solutions, are discussed in the following section.

4 Comparisons With Measurements

We apply the models first to the two-dimensional plane and axisymmetric jets (see Fig. 1) discharged into stagnant surroundings. The calculations were started at the nozzle exit with top-hat profiles for all dependent variables and were continued until the spreading rate became constant and computed profiles (non-dimensionalised by the center-line velocity and half width) ceased to change with further development. These solutions were confirmed to be independent of the assumed inlet conditions. The computational grid consisted of 99 nodes in the cross-stream direction while the forward-step size was limited to 0.5 percent of the local shear-layer half-width (defined as the point where the velocity falls to half of its centerline value). The sensitivity of the computed results to the grid size and to the choice of discretization scheme is reported in the Appendix. The predicted and measured plane jet spreading rates are compared in Table 2. There is considerable scatter in the measured and computed values alike due, for the most part, to the non-attainment of self-preservation or to insufficient grid resolution

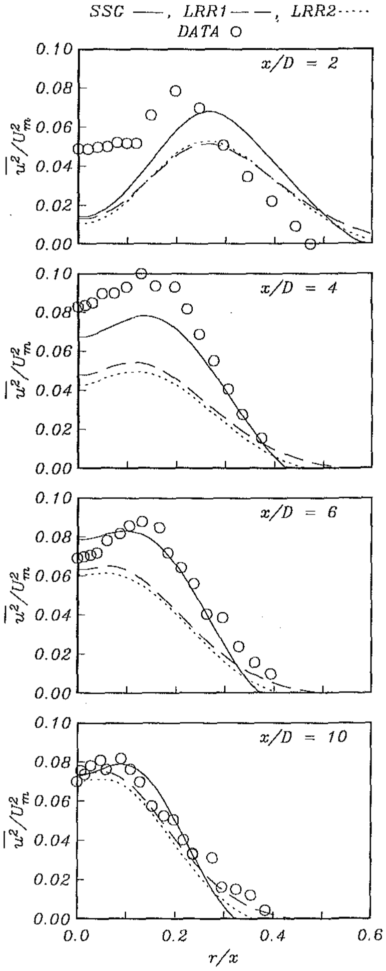

Fig. 7 The swirling free jet. Predicted and measured normal-stress component $\overline{u^2}$

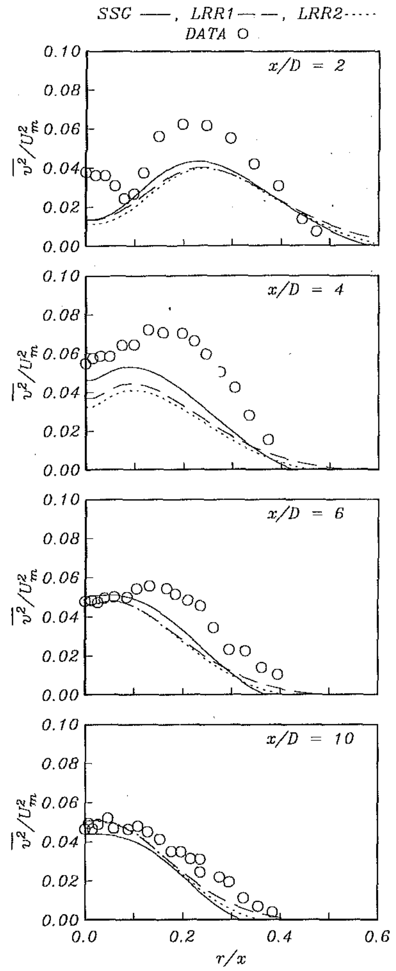

Fig. 8 The swirling free jet. Predicted and measured normal-stress component $\overline{v^2}$

(Launder and Morse used a forward step of 5 percent of the local half-width and attributed the difference with the Launder et al. (1975) result to the "larger forward steps" taken in the latter). The predicted and measured mean and turbulence profiles are compared in Fig. 2. Overall, the SSG model appears to underestimate the measured turbulent stresses which is consistent with the low spreading rate obtained with this model. The reason for this result can clearly be seen from an inspection of the term $-C_1^* \mathcal{P} b_{ij}$ which has no counterpart in the LRR models. This term, while fairly uninfluential for the normal stresses, makes a large and negative contribution to the shear stress equation leading to the reduction of this quantity across the shear layer. A drop in the level of the shear stress reduces the rate of production of turbulent kinetic energy and this in turn lowers the normal Reynolds stresses, either directly through the production term of u^1 or indirectly through reduced transfer of energy via the pressure-strain correlation. It is nevertheless quite encouraging to see that the SSG model yields results that are comparable with the data considering that they were not used in its calibration. The model reproduces the observed turbulence anisotropy on the jet's axis and, in particular, correctly predicts w^2 to be higher than v^2 in contrast with LRR2 which predicts them to be equal.

Following Launder and Morse, we checked the sensitivity of the SSG model to C_s by repeating the calculations with this coefficient reduced by 10 percent of its original value. The effects of this change are to improve the prediction of the spreading rate by about 3 percent (to 0.0943) but only at the expense of causing the turbulent stress profiles to decay much faster to their free-stream levels. Reducing C_s by a similar amount increases the spreading rate by a mere 0.3 percent. These results are very similar to the percentage responses obtained by Launder and Morse and are taken here to mean that the model's performance cannot be significantly improved by fine-tuning the coefficient of the Daly and Harlow model.

Attention is next turned to the axisymmetric jet which was also simulated using 99 cross-stream nodes a forward-step size limited to 0.5 percent of the local width (over 6000 forward steps were used). The numerical accuracy checks are again presented in the Appendix. The predicted and measured spreading rates are compared in Table 3. All the models overestimate this quantity by quite a margin, though the mechanism which has led to the SSG model's underprediction of the plane-jet value is seen here to bring about a closer agreement with the data. The improved agreement is, of course, quite fortuitous but it lends support to the belief that the plane jet/round jet anomaly is not resolvable by further refinement of the pressure-strain model. The SSG model's results for the mean and turbulent profiles, shown in Fig. 3, are broadly the same as the two LRR models.

It has already been mentioned that the plane and axisymmetric jets have not been used in calibrating the coefficients of the SSG model. That was done solely by reference to simple homogeneous shear flow and to grid turbulence. This contrasts with the approach of Launder et al. (1975) and Gibson and Younis (1986) who took the homogeneous flows to provide only a rough guide to the coefficients which were then refined

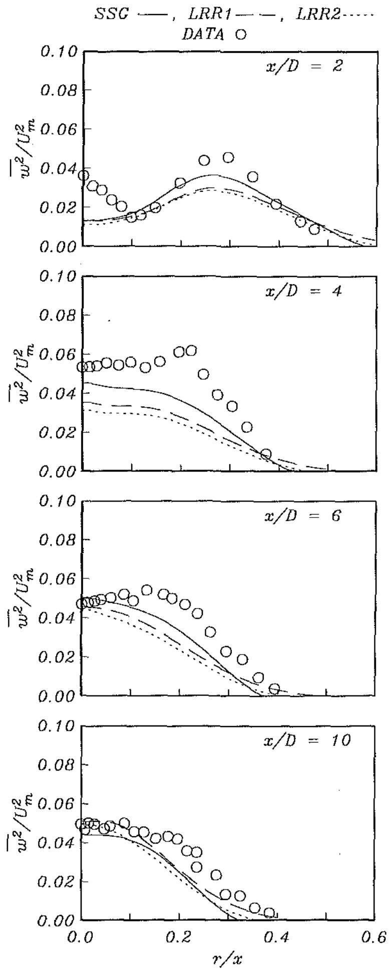

Fig. 9 The swirling free jet. Predicted and measured normal-stress component $\overline{w^2}$

by computer optimization involving a wide range of flows including the plane and axisymmetric free jets.

Attention is turned next to the swirling axisymmetric jets studied experimentally by Morse (1980). This experiment remains the best documented test case for this flow and has recently formed part of the benchmark flows chosen for turbulence-model assessments (Bradshaw et al. 1994). The experiments were performed for two values of the Swirl Number, while the comparisons made here are for the greater of the two ($S = 0.40$) where the effects of swirl are most pronounced. The present calculations were started from $x/D = 0.5$, using the measured mean-velocity and turbulence profiles at this first transverse position. The starting profile for ϵ was deduced from the eddy-viscosity relationship:

$$\epsilon = C_\mu \frac{k^2}{-\overline{uv}} \frac{\partial U}{\partial r} \qquad (6)$$

In the above, the turbulent kinetic energy (k), the shear stress and the mean axial-velocity gradient were substituted for by their measured values and the coefficient C_μ was assigned its usual value of 0.09. The choice of inlet condition for ϵ can materially alter the predicted development of the jet in the near field. We justify the present choice of ϵ inlet condition on the grounds that (a) $C_\mu = 0.09$ is a generally-accepted value for this coefficient, (b) the same inlet condition yielded very satisfactory results for the near-field of the *nonswirling* axisymmetric jet of Morse (1980), (c) this is the same inlet condition as that employed by Launder and Morse and by Gibson and Younis (1986) and, moreover, is the one recommended for the recent turbulence-models benchmarking exercise (Bradshaw et al., 1994), and, (d) the same inlet profile has been used for the linear and the quadratic pressure-strain models and hence differences in their results are directly attributed to their respective formulations rather than to the choice of inlet conditions. All the computations reported below were performed on a grid consisting of 68 cross-stream nodes with a forward step limited to 0.5 percent of the local half width. An assessment of the numerical accuracy of the computed results is presented in the Appendix.

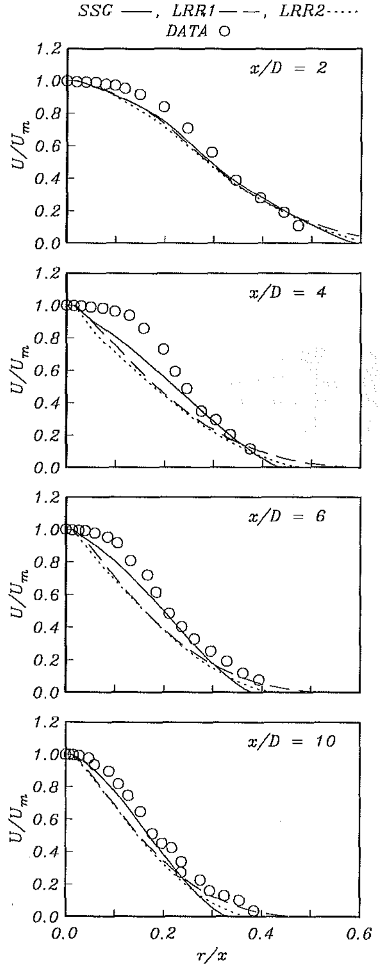

Fig. 10 The swirling free jet. Predicted and measured profiles of mean axial velocity

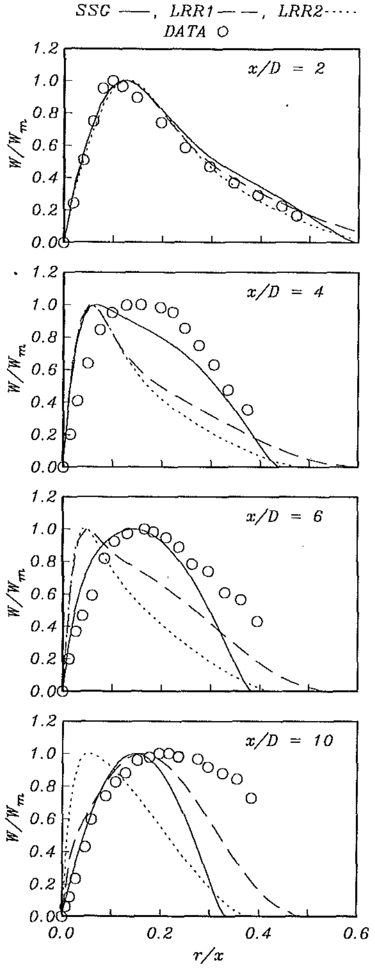

Fig. 11 The swirling free jet. Predicted and measured profiles of mean swirl velocity

We reverse the usual order for presentation of the computed results by starting with the turbulent stresses and in particular the component $\overline{uw}$ predicted by Launder and Morse to be of the wrong sign. Figure 4 compares the predicted and measured profiles of this quantity. The profiles obtained with the LRR1 model correspond very closely to those reported by Launder and Morse using the same model. The quadratic model suffers the same problem as the two linear ones in producing negative values in the region close to the axis ($r/x < 0.1$); however, it is then found to recover, producing positive stress values in the outer parts. In contrast, the linear models predict this quantity to be largely zero (LRR2) or negative (LRR1) throughout the flow. This is a very important result as it will determine the subsequent development of the flow. Its causes can be traced to the form of the pressure-strain models which for $\overline{uw}$ are reproduced below:

$$(\Phi_{\overline{uw}})_{\mathrm{LLR1}} = \underbrace{-3.0\epsilon b_{13} + 1.53 b_{23}\frac{\partial U}{\partial r} + 1.53 b_{12}\frac{\partial W}{\partial r} - 0.22 b_{12}\frac{W}{r}}_{\text{Negative in the outer layer}}$$

$$(\Phi_{\overline{uw}})_{\mathrm{SSG}} = \overbrace{-\left(3.4 + 1.8\frac{\mathcal{P}}{\epsilon}\right)\epsilon b_{13} + 0.825 b_{23}\frac{\partial U}{\partial r} + 0.825 b_{12}\frac{\partial W}{\partial r} - 0.425 b_{12}\frac{W}{r}} + 4.2\{(b_{11} + b_{33})b_{13} + b_{12}b_{23}\}\epsilon \qquad (7)$$

It should first be pointed out that at the starting station, $x/D = 0.5$, $\overline{uw}$ was obtained to be negative in the inner layer and positive in the outer layer (i.e., in between the location of W_m, the maximum tangential velocity, and the free stream). Focusing attention on the outer layer where the differences between the various models are largest, it is immediately clear that all terms in the LRR1 model act as sinks for $\overline{uw}$ which consequently becomes negative (note that only a small part of this component's production rate is positive). In the SSG model, the terms that are counterparts to LRR1 are also always negative, but to a smaller extent as can be seen from the values of the multiplying coefficients. However, the quadratic terms are positive in the outer layer and it is those that are responsible for maintaining $\overline{uw}$ positive in the outer layer.

The consequences of this result on the development of the swirling jet cannot be understated. This can be seen in Fig. 5 where the measurements and predictions of $\overline{uv}$ are compared. The presence of the term $2\,\overline{uw}\,W/r$ in the $\overline{uv}$ transport equation accounts for the differences between the model predictions. A higher value of $\overline{uv}$ is associated with a more rapid expansion of the shear layer and, from continuity, to a faster decay of velocity. Note that the differences between the LRR models and the SSG model are greatest at the early stages of the jet development where the effects of swirl are most pronounced. Downstream, where $\overline{uw}$ will have decayed to about 10 percent of its initial value, the LRR models predict higher $\overline{uv}$ levels—a consequence of their overestimating this quantity in the non-swirling case (Fig. 3).

In Fig. 6 it can be seen that the shear-stress component $\overline{vw}$ which is responsible for the radial diffusion of tangential momentum is also better predicted by the SSG model, particularly at the early stages of development. The predicted and measured normal stresses are compared in Figs. 7–9. The behavior of those quantities and the relative performance of the different models can be explained by the appearance in their transport equations of the shear-stress components already presented. Thus, for example, the higher levels obtained for u^2 by the SSG model are due to the higher values obtained for $\overline{uv}$ which enters into its production.

The predicted and measured profiles of the axial and tangential mean velocities are compared in Figs. 10 and 11. The shapes of the predicted profiles are determined by the distributions of $\overline{uv}$ and $\overline{vw}$ with the fuller profiles obtained using the SSG model corresponding to the higher values of the turbulent shear stresses obtained with that model. Finally, the predicted and measured decay of the maximum axial and tangential velocities in the streamwise direction are compared in Fig. 12. Also plotted there are the computed and measured development of the jet's half width. This parameter is of primary practical interest and is perhaps the most sensitive measure of a model's suitability for swirling-flow calculations. Only the SSG model manages to capture the observed rapid growth of this quantity in the initial region where the effects of swirl are most pronounced. That this should be the case follows from the fact that higher values of $\overline{uv}$ were produced as a result of the quadratic model's better prediction of the sign and magnitude of $\overline{uw}$. The linear models eventually produce a jet half-width value comparable to that measured—but that only occurs far downstream from the nozzle exit, where the importance of swirl has diminished, and the models' tendency to overestimate the spreading rate of the non-swirling jet (see Table 3) comes into play.

5 Conclusions

The performance of the SSG model was tested in the benchmark plane and axisymmetric free jets without swirl, given that neither flow entered into the calibration of the model. Results that were on balance comparable to those of the linear LRR models were obtained. While the SSG model underpredicts the spreading rate of the plane jet by 12 percent, it overpredicts the axisymmetric value by only 17 percent. In the linear models, the overprediction is of the order of 30 percent. The results for the swirling jet obtained from the SSG model constitute a clear

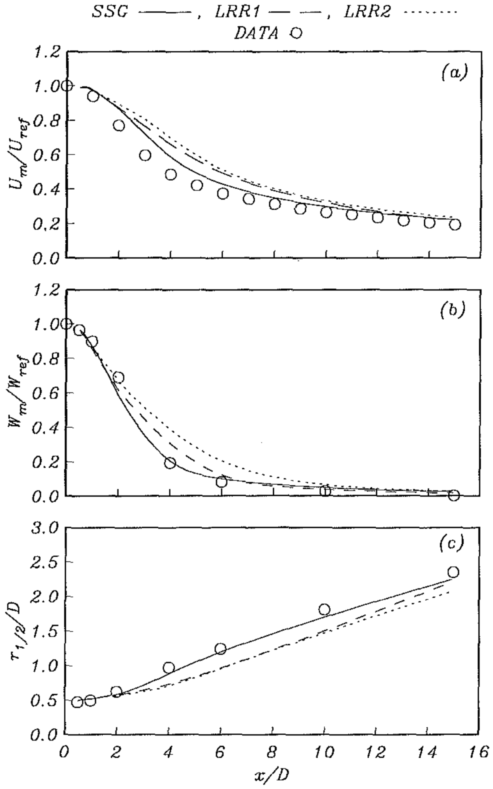

Fig. 12 Predicted and measured streamwise variation of: (a) centerline axial velocity; (b) maximum swirl velocity; (c) jet's half-width

improvement over those obtained with the linear LRR models, most notably in the prediction of $\overline{uw}$ and, consequently, the growth rate of the swirling jet. This improvement is attributed directly to the contribution made by the quadratic slow term in the SSG pressure-strain model and it is interesting to note that the same quadratic term has recently been shown by So et al. (1994) to be essential for the correct prediction of the von Karman constant in flat-plate boundary layer flows when model integration is carried out through the viscous sublayer directly to the wall. It is likely that these terms will also improve the prediction of confined, strongly-swirled flows and, therefore, testing of the SSG model in such geometries will be the subject of a future study.

References

Abid, R., and Speziale, C. G. 1993, "Predicting Equilibrium States with Reynolds Stress Closures in Channel Flow and Homogeneous Shear Flow," *Physics of Fluids A,* Vol. 5, pp. 1776–1782.

Basara, B., and Younis, B. A., 1995, "Assessment of the SSG Pressure-Strain Model in Two-Dimensional Turbulent Separated Flows," *Applied Scientific Research,* Vol. 55, pp. 39–61.

Bradshaw, P., Launder, B. E., and Lumley, J. L., 1994, "Collaborative Testing of Turbulence Models," *Advances in Computational Methods in Fluid Dynamics,* K. N. Ghia, U. Ghia, and D. Goldstein, eds, ASME, New York, FED Vol. 196, pp. 77–82.

Daly, B. J., and Harlow, F. H., 1970, "Transport Equations in Turbulence," *Physics of Fluids,* Vol. 13, pp. 2634–2649.

el Baz, A., Craft, T. J., Ince, N. Z., and Launder, B. E., 1993, On the adequacy of the thin-shear-flow equations for computing turbulent jets in stagnant surroundings," *International Journal of Heat and Fluid Flow,* Vol. 14, No. 2, pp. 164–169.

Fu, S., Launder, B. E., and Leschziner, M. A. 1987, "Modeling Strongly Swirling Recirculating Jet Flow with Reynolds-Stress Transport Closure," *Proc. 6th Symposium on Turbulent Shear Flows,* Toulouse, pp. 17.6.1–17.6.6.

Fu, S., Launder, B. E., and Tselepidakis, D. P., 1987, "Accommodating the Effects of High Strain Rates in Modeling the Pressure-Strain Correlation," *UMIST Report TFD/87/5.*

Gibson, M. M., Jones, W. P., and Younis, B. A., 1981, "Calculation of Turbulent Boundary Layers on Curved Surfaces," *Physics of Fluids,* Vol. 24, pp. 386–395.

Gibson, M. M., and Younis, B. A., 1986, "Calculation of Swirling Jets with a Reynolds Stress Closure," *Physics of Fluids,* Vol. 29, pp. 38–48.

Gutmark, E., 1970, "The Two-Dimensional Turbulent Jet," M.Sc. thesis, Technion-Israel Institute of Technology.

Haskestad, G., 1965, "Hot-Wire Measurements in a Plane Turbulent Jet," ASME *Journal of Applied Mechanics,* Vol. 32, pp. 721–734.

Hussein, H. J., Capp, S. P., and George, W. K., 1994, "Velocity Measurements in a High-Reynolds-Number, Momentum-Conserving, Axisymmetric, Turbulent Jet," *Journal of Fluid Mechanics,* Vol. 258, pp. 31–75.

Irwin, H. P. A. H., and Arnot-Smith, P. A., 1975, "Prediction of the Effects of Streamline Curvature on Turbulence," *Physics of Fluids,* Vol. 18, pp. 624–630.

Launder, B. E., and Morse, A. P., 1979, "Numerical Prediction of Axisymmetric Free Shear Flows with a Reynolds Stress Closure," *Turbulent Shear Flows I,* F. Durst, B. E. Launder, F. W. Schmidt, and J. H. Whitelaw, eds., Springer-Verlag, Berlin, Vol. 1, pp. 279–294.

Launder, B. E., Reece, G. J., and Rodi, W., 1975, "Progress in the Development of a Reynolds Stress Turbulence Closure," *Journal of Fluid Mechanics,* Vol. 68, pp. 537–566.

Morse, A. P., 1980, "Axisymmetric Turbulent Shear Flows With and Without Swirl," Ph.D. thesis, University of London.

Musonge, P., 1983, "The Prediction of Free Turbulent Flows," Ph.D. thesis, University of London.

Panchapakesan, N. R., and Lumley, J. L., 1993, "Turbulence Measurements in Axisymmetric Jets of Air and Helium. Part 1. Air Jet," *Journal of Fluid Mechanics,* Vol. 246, pp. 197–223.

Patankar, S. V., and Spalding, D. B., 1970, *Heat and Mass Transfer in Boundary Layers,* 2nd ed., Intertext-London.

Patel, R. P., 1970, "A Study on Two-Dimensional Symmetric and Asymmetric Turbulent Shear Flows," Ph.D. thesis, McGill University.

Paullay, A. J., Melnik, R. E., Rubel, A., Rudman, S., and Siclari, M. J., 1985, "Similarity Solutions for Plane and Radial Jets Using a $k - \epsilon$ Turbulence Model," ASME JOURNAL OF FLUIDS ENGINEERING, Vol. 107, pp. 79–85.

Robins, A., 1971, "The Structure and Development of a Plane Free Jet," Ph.D. thesis, University of London.

Rodi, W., 1972, "The Prediction of Free Turbulent Boundary Layers by Use of a Two-Equation Model of Turbulence," Ph.D. thesis, University of London.

So, R. M. C., Aksoy, H., Sommer, T. P., and Yuan, S. P., 1994, "Development of a Near-Wall Reynolds-Stress Closure Based on the SSG Model for the Pressure-Strain," *NASA Contractor Report CR-4618.*

Speziale, C. G., 1987, "On Non-Linear $k - l$ and $k - \epsilon$ Models of Turbulence," *Journal of Fluid Mechanics,* Vol. 178, pp. 459–475.

Speziale, C. G., Sarkar, S., and Gatski, T. B., 1991, "Modeling the Pressure-Strain Correlation of Turbulence: An Invariant Dynamical Systems Approach," *Journal of Fluid Mechanics,* Vol. 227, pp. 245–272.

Younis, B. A., 1984, "On Modeling the Effects of Streamline Curvature on Turbulent Shear Flows," Ph.D. thesis, University of London.

APPENDIX

Numerical Accuracy

Checks were made to quantify the sensitivity of the computed solutions to the number of cross-stream grid nodes (N), the forward-step size ($frac = \delta x/\delta_{1/2}$, where $\delta_{1/2}$ is the local shear-layer half width) and the choice of discretization scheme for the convective terms in the parabolic direction ($\alpha = 0.5$ for the second-order weighted scheme; $= 1$ for the first-order implicit scheme). In Table A.1–A.3, Run 1 refers to the values used to obtain the results presented in the main body of the paper. The percent variation is the departure from Run 1 due to the indicated change. The results for all three pressure-strain models were generally similar so only those of the SSG model are presented here.

For the self-similar jets, a sensitive and convenient indicator of numerical accuracy is the jet's spreading rate, and the values of this parameter obtained in the plane- and round-jet tests are presented in Tables A.1 and A.2, respectively.

It is clear from Tables A.1 and A.2 that the computed results reported in Section 4 are not materially altered by doubling the size of the forward step taken in the streamwise direction (Runs 2) nor by halving the number of nodes in the cross-stream direction (Runs 4). Further, the use of a first-order scheme for streamwise convection (Runs 3) is similarly of little consequence, which is not surprising bearing in mind the small step-size taken in the same direction. Inspection of the computed cross-stream profiles revealed percentage changes of the same order as those exhibited by the spreading rates.

Table A.1 Plane-jet accuracy checks

Run	N	frac	α	$\frac{dy_{1/2}}{dx}$	% Var.
1	99	0.005	0.5	0.0917	—
2	99	0.01	0.5	0.092	+0.29
3	99	0.005	1.0	0.09132	−0.41
4	49	0.005	0.5	0.0910	−0.72
5	34	0.01	1.0	0.092	+0.32

Table A.2 Axisymmetric-jet accuracy checks

Run	N	frac	α	$\frac{dr_{1/2}}{dx}$	% Var.
1	99	0.005	0.5	0.111	—
2	99	0.01	0.5	0.1114	+0.37
3	99	0.005	1.0	0.1106	−0.33
4	49	0.005	0.5	0.1102	−0.71
5	34	0.01	1.0	0.112	+0.9

Table A.3 Swirling-jet accuracy checks

Run	N	frac	α	$\frac{dr_{1/2}}{dx}$	% Var.
1	68	0.005	0.5	0.5761	—
2	68	0.01	0.5	0.5801	+0.69
3	68	0.005	1.0	0.5784	+0.4
4	34	0.005	0.5	0.5819	+1.01
5	34	0.01	1.0	0.5811	+.86

For the swirling jet, the values of the half-width at the last measurements station ($x/D = 15$) provide a good measure of the sensitivity of the computed solutions to the grid size and the choice of discretization scheme. The results of the numerical-accuracy tests, shown in Table (A.3), provide an adequate demonstration that the swirling-jet predictions presented in Section 4 are sensibly free of grid-size effects. We have also checked the conservation, in the present simulations, of the momentum fluxes in the axial and tangential directions and found that ratio of the two (i.e., the Swirl No.) varies in Run 1 by only 0.3 percent in between the inlet to the computational domain and the exit from it.

Finally, we have checked that the present computations were unaffected by the flow-adaptive feature of the simulations method by repeating a number of runs with a non-expanding grid (formed of 240 nodes) which contained the entire shear layer at its widest point. This produced no significant changes to the results, an outcome consistent with that obtained by el Baz et al. (1993) from a similar test.

An Investigation of Turbulent Taylor-Couette Flow Using Laser Doppler Velocimetry in a Refractive Index Matched Facility

J. Parker
Research Engineer,
Durametallic Corporation,
2100 Factory Street,
Kalamazoo, MI 49001

P. Merati
Professor and Chair, Department of
Mechanical and Aeronautical Engineering,
Western Michigan University,
Kalamazoo, MI 49008

Turbulent Taylor-Couette flow in an annulus formed by two concentric cylinders with dead end walls was investigated with Laser Doppler Velocimetry (LDV). The test apparatus was designed to provide refractive index matching between the annulus and a working fluid of aqueous sodium iodide. LDV was used to measure the three components of mean velocity and turbulence intensity, concentrating on end wall effects. The flow Taylor and Reynolds numbers were $T = 2.107 \times 10^9$ and $Re = 73{,}440$, respectively. Vector plots of radial-axial component velocities and contour plots of component velocities and turbulence intensities reveal the Taylor vortex flow structure at this high Taylor number.

1 Introduction

Flow in the gap between two concentric cylinders with one or both cylinders rotating has been examined and described since Maurice Couette in 1890 and Geoffrey Taylor in 1923 (Donnelly, 1991). At flow Taylor numbers above a critical value, the steady viscous flow becomes unstable due to perturbations, and alternating toroidal vortices develop. As the rotational speed or Taylor number increases, the vortices can attain various mode shapes and transitions, becoming increasingly turbulent. Geometric dimensions, cylinder rotation, end wall effects, and fluid properties are some of the significant variables which define and maintain Taylor-Couette flow.

A measure of the state of flow is represented by the nondimensional Taylor and Reynolds numbers. Taylor number, T, and Reynolds number, Re, are defined by the following relationships.

$$T = \frac{2\eta^2 d^4}{1 - \eta^2}\left(\frac{\Omega}{v}\right)^2 \qquad (1)$$

$$\mathrm{Re} = \frac{U_s d}{v} \qquad (2)$$

where

η = r_i/r_o, the radius ratio
r_i = inner cylinder radius
r_o = outer cylinder radius
d = $r_o - r_i$, the gap width
Ω = inner cylinder angular velocity
v = kinematic viscosity of the fluid
U_s = $r_i\Omega$, the circumferential speed of the inner cylinder surface

By solving the equations of motion with small perturbations superimposed on the mean flow, the critical Taylor number, T_c, emerges to define the onset of instability and the point at which Taylor vortices form. Previous authors have used different parameters to define Taylor number. We have used the definition (Eq. (1)) of Taylor number and numerical calculations of critical Taylor number stated by Roberts (1965) because of their frequent reference in other publications. Flow regimes are classified under subcritical, critical, and supercritical depending on the magnitude of the Taylor number being less than critical, at critical, and above critical Taylor number, respectively. With the non-dimensional Taylor number ratio T/T_c used to define the flow regimes, turbulent Taylor vortices exist at Taylor numbers greater than $1000T_c$ (Koschmieder, 1993).

Turbulent Taylor-Couette flow has been investigated qualitatively with high-quality flow visualization photographs which display the various modes of vortex formation. Burkhalter and Koschmieder (1972) studied Taylor vortex wavelength and the size of the end wall rings as the gap width, radius ratio, end conditions, and fluids were altered. Their photographs included Taylor number ratios from 0.99 to 11,330. In Burkhalter and Koschmieder (1974), the effects of start-up conditions on the supercritical vortices were examined. In experiments involving Taylor number ratios up to 11,000, they concluded that the Taylor vortex mode is dependent on the cylinder's rotational acceleration.

Smith and Townsend (1982) used hot-wire anemometry and pitot tubes to measure flow velocity and turbulence intensity in turbulent Taylor-Couette flow in the range of $1.0 \times 10^4 < T/T_c < 2.3 \times 10^6$. Because the toroidal vortices are stationary in the axial direction, a small axial flow was introduced to push the vortices past the stationary probe. It was concluded that the toroidal eddies lose their regularity at very high rotation rates and cannot be clearly distinguished at Taylor number ratios greater than 5×10^5.

Fenstermacher et al. (1979) used Laser Doppler Velocimetry to measure the local radial velocity in a chaotic Taylor vortex flow. Although the laser system was aligned to measure the system axial velocity, the vortex radial velocity with respect to its center was recorded. The measurements were limited to an axial line passing through the vortex centers, along $r = (r_i + r_o)/2$.

Barnes et al. (1992) proposed a Taylor vortex flow pattern in a generic seal chamber which acted to wear the inner and outer cylinders at the radial inflow and outflow regions. The

---

Contributed by the Fluids Engineering Division for publication in the JOURNAL OF FLUIDS ENGINEERING. Manuscript received by the Fluids Engineering Division July 5, 1995; revised manuscript received April 1, 1996. Associate Technical Editor: M. Gharib.

investigation focused on the design of an optimum seal chamber which reduces the vortex effects and adds other flow features. Merati et al. (1992) investigated the flow within an ANSI enlarged seal chamber with a rotating impeller on one annulus end and a stationary wall on the other end. It was concluded that one large vortex occupied the chamber and the flow was nonsymmetric.

Considerable experimental research on turbulent Taylor vortex flow has been conducted by Lathrop et al. (1992). They have measured torque on the inner cylinder, wall shear stress on the outer cylinder, and performed flow visualization in the Reynolds number range from 800 to 1.23×10^6. For their experiment, the radius ratio η and the aspect ratio Γ were 0.72 and 11.47, respectively. They have shown how the stable states of vortices changes with Reynolds number and how the vortices gradually disappear at very high Reynolds number. They used 0.1 percent concentration of Kalliroscope for flow visualization and measured distribution functions of fluctuations in shear stress. They did not conduct any velocity measurements at high Taylor number. The present research focuses on measuring the turbulent Taylor-Couette flow at high Taylor number. These studies show that although visualized vortices seem to disappear at high Taylor number due to a high degree of turbulence and mixing, they still exist as measured accurately with LDV. This indicates that a new visualization technique is needed to observe these turbulent vortices.

Careful refractive index matching between the annulus and the working fluid allows non-intrusive measurement systems to map the complete Taylor vortex structure. Refractive index matching is achieved when the fluid mixture has the same refractive index as the annulus such that no refraction exists at the fluid-annulus interface.

Different approaches to refractive index matching are present in the literature and most are unique in terms of application and the selection of solid and liquid materials. Braun et al. (1990) reported using a mixture of Dow Corning mineral silicone oil 556 and Dow Corning mineral oil 550 at 25.0°C to match the refractive index of Plexiglas. Similarly, Northrup et al. (1991) used a mixture of Dow Corning mineral oil 550 and Union Carbide organosilicone L42. Both of these fluid combinations, although inert, have high viscosities and would provide low Taylor number ratios. Thompson (1990) used a mixture of Tetralin and steam-distilled turpentine in a Plexiglas facility. Although low viscosities were reported, the solvent mixture softened and crazed the Plexiglas, reducing the model life. Chen and Kadambi's (1990) experiments with aqueous solutions of sodium iodide found a wide range of refractive indices and the ability to match the refractive index of silica gel ($n = 1.443$). By varying the concentration of sodium iodide up to 60 percent by weight and the solution temperature from 20 to 40°C, the refractive index ranged from 1.333 to 1.487. With such a widely adjustable refractive index, the monitoring and control of the fluid concentration and temperature is critical.

Dybbs and Edwards (1987) evaluated the need for a close match of refractive indices when curved interfaces are encountered by addressing the question "n_1/n_2: How close is close enough?" where n_1 and n_2 are the refractive indices for the solid medium and the fluid, respectively. To define the closeness of match, they developed the equation

$$K' = \sin^{-1}\left(\frac{h}{R}\right) - \sin^{-1}\left(\frac{n_1}{n_2}\frac{h}{R}\right) \qquad (3)$$

where K' is the angular deviation from the horizontal, R is the cylinder radius, and h is the ray height from horizontal. For applications where h/R approaches unity, the refractive index ratio becomes critical. In addition, by monitoring n_1/n_2, the angular deviation can be predicted.

2 Purpose and Application

The primary focus of this research was the investigation of supercritical, turbulent Taylor-Couette flow in a refractive index matched annulus with the inner cylinder rotating. Laser Doppler Velocimetry was used to measure the three components of mean velocity and turbulence intensity. Symmetry conditions of the mean radial and axial velocity were examined for different circumferential planes. Data were collected for both a long and short annulus, where the influence of the end walls was investigated.

The results of this research should satisfy experimental and practical needs for Taylor-Couette flow investigations. Quantitative data for both the long and short annulus lengths can be used to further turbulent Taylor-Couette flow theories and comparisons with Computational Fluid Dynamics predictions. Mechanical seal chamber studies can benefit from the short annulus results for which both end walls are stationary. Finally, this research demonstrates the successful application of an aqueous solution of sodium iodide to match the refractive index of clear acrylic.

3 Facilities, Instrumentation, and Technique

A schematic of the Taylor-Couette flow test apparatus is shown in Fig. 1. The working fluid is located in the annulus region confined between two vertically aligned concentric cylinders and two end walls. Fluid inlet and outlet taps are located at each end of the annulus to provide for fluid changes and facilitate the removal of trapped air. Only the shaft and inner cylinder are free to rotate.

The inner cylinder is a clear acrylic sleeve fixed to a stainless steel shaft at the upper end and centered by a bushing on the lower end. The shaft is suspended by two consecutive pillow blocks at the upper motor coupling end and retained by a low friction bushing at the lower end. The inner cylinder design facilitates the installation of different diameter sleeves. The outer cylinder is a cylindrical bore through a solid 15.24 × 15.24 × 34.67 cm block of clear Plexiglas. To reduce the effects of nonuniform geometry, a radial tolerance of ±0.025 mm was maintained for the inner and outer cylinders.

The upper and lower end walls were also machined from clear acrylic so as not to block the laser beams from measurements in the end wall boundary layers. The lower end wall acts to retain the lower shaft end from radial movement and accommodates optical access from below. What is referred to as the upper end wall is a rectangular ring with close clearances to the inner and outer cylinder diameters. Annulus length is adjusted by changing the length of four steel rods which are fastened between the ring and the upper structural plate. The upper end wall is retained in a rigid fashion such that the rotating inner cylinder and moving fluid do not induce any measurable relative motion. All acrylic surfaces were polished to obtain excellent optical clarity and annealed to relieve residual stresses.

Testing was performed for cylinders with $r_i = 30.96 \pm 0.025$ mm and $r_o = 46.04 \pm 0.025$ mm, providing a gap width of $d = 15.08$ mm and a radius ratio of $\eta = r_i/r_o = 0.672$. These dimensions are characteristic of the inside diameter of an ANSI B73 standard enlarged cylindrical seal chamber and the outside diameter of a Durametallic 48.0 mm CBR Dura Seal (bellows-type mechanical seal). The aspect ratio, Γ, is defined as the ratio of the annulus length to the gap width and was set to 20 and 4. For $\Gamma = 20$, the annulus length was 301.6 mm, and for $\Gamma = 4$, the annulus length was 60.32 mm.

A variable speed motor with a maximum rotation rate of 1750 rpm and accuracy of ±1.0 rpm was connected inline with the shaft through an elastomeric coupling. The entire system was mounted to a rigid bracket and fixed vertically to a rigid wall. Leveling control was provided for all axes. With accurate shaft alignment, vibrations were minimized and did not affect the quality of the results.

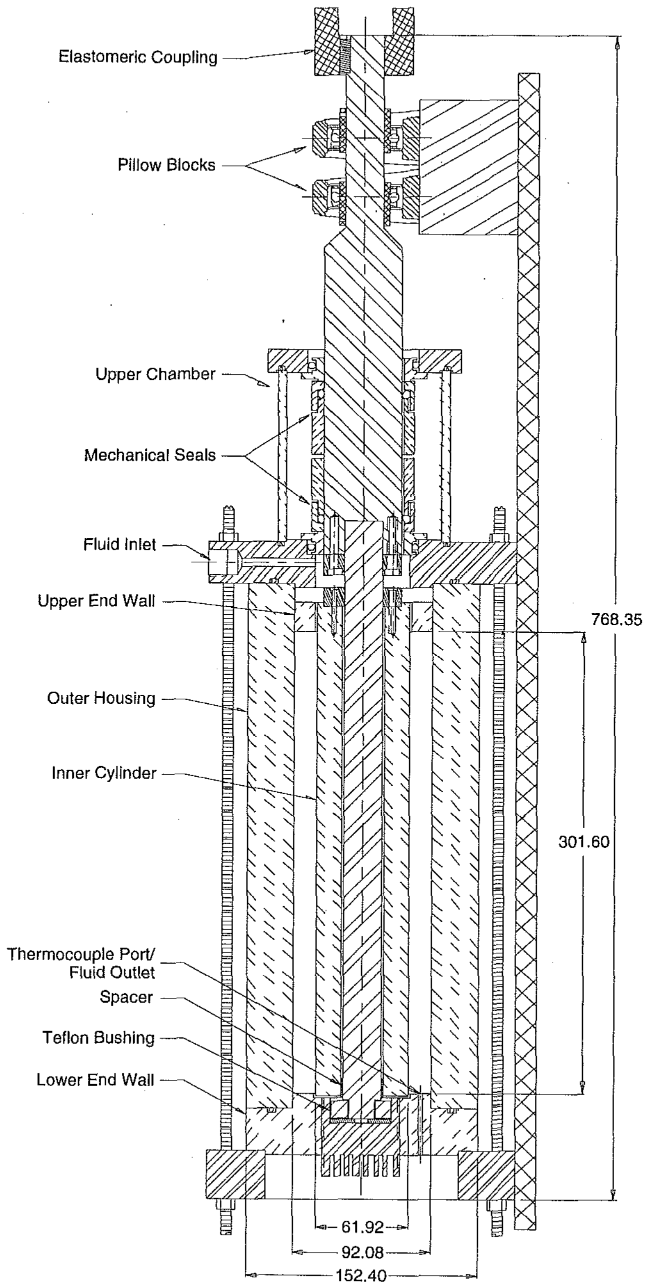

Fig. 1 Section through the apparatus

Leakage paths between stationary components were sealed with o-rings while mechanical seals blocked the leakage paths between rotating and stationary interfaces at the upper end. A separate chamber housing two mechanical seals was flushed with cooling water for the transfer of heat generated at the seal faces. Although the heat generated at the lower bearing was insignificant, an aluminum boot was designed with heat sink fins to remove any frictional heat. Access for a thermocouple was provided axially through the lower end wall such that its position could be adjusted to measure the temperature distribution throughout the length of the annulus. After the entire system reached steady-state equilibrium, a maximum temperature gradient of 2.0 ± 0.1°C was measured along the annulus.

Plexiglas acrylic has an index of refraction of 1.4905 for 514.5 nm wavelength light at 23.4°C. The refractive index of solid sodium iodide is 1.7745, and at its saturation concentration of 64.8 percent by weight in water, the solution refractive index is 1.5025. With the saturated solution as the starting point, water was added to match the refractive index of Plexiglas. Because the refractive index is dependent on temperature, if the operating temperature is known and can be controlled, the mixture concentration can be used to iterate on the best refractive index match. The cooling provided at the annulus ends established a steady-state temperature of 26.7 ± 0.1°C at the lower annulus end and 28.7 ± 0.1°C at the upper end. An Abbe-type refractometer measuring off the sodium D line with a white light source was used for refractive index measurements at the matching temperature.

Sodium iodide releases iodine upon prolonged exposure to light and the fluid turns a brownish color. This effect was counteracted by the addition of small amounts of sodium thiosulfate. Also, upon exposure to air, the mixture slowly crystallizes and can extrude through the smallest crevices. To aid the LDV measurements, metallic coated, 4.0 μm diameter spherical particles were used in the flow as scattering particles. Although these particles provided a reasonable signal-to-noise ratio, they agglomerated in the sodium iodide mixture in about 48 hours and turned the fluid cloudy.

Jacobs et al. (1988) used refractive index matching for LDV measurements on wavy Taylor vortices. These authors addressed the problem of deterioration of the solution, using ascorbic acid instead of sodium thiosulfate. They also used formaldehyde-killed single cell organisms as scattering particles in water and salt solutions. They reported that the advantages over traditional scattering particles are ready availability in large quantities, uniformity in size, monodispersity, and the ability to stay suspended in solution for several days.

For the sodium iodide mixture, the viscosity was measured as $\upsilon = 1.47$ centipoise at 26.7°C and the density was 1.84 gm/cc. The refractive index was maintained at 1.4905 ± 0.0005 for all tests. The index ratio of the acrylic to the fluid falls between $1.0003 < n_1/n_2 < 0.9997$. With the LDV optics providing a maximum $h/R = \sin(82°)$, from Eq. (3), the angular deviation off the horizontal was $K' = 0.12$ deg.

For a radius ratio of $\eta = 0.672$, Roberts (1965) calculated the critical Taylor number as $T_c = 2279$. At an experimental rotational speed of 1200 rpm, the Taylor and Reynolds numbers were $T = 2.107 \times 10^9$ and $Re = 73{,}440$, respectively, and the Taylor number ratio was $T/T_c = 924{,}600$.

For each test, the same start-up procedures were followed to ensure repeatable results. The sodium iodide solution was introduced to the annulus through a port in the lower structural plate, displacing the initial volume of air through a port in the upper structural plate. The variable speed motor was cycled through several speeds and the residual trapped air was released. The motor was then fixed at the desired rotational speed for at least 30 minutes such that an equilibrium fluid temperature of 27.7 ± 0.1°C was reached. Rotational speed was measured by a calibrated strobe light. The fluid temperature and speed were monitored frequently throughout the experiments.

Azimuthal and radial velocities in the r-θ plane are defined as shown in Fig. 2. The axial velocity, defined positive up along the axis of rotation, was measured with the laser beams parallel to the r-z plane. One-component LDV technique measures the velocity component perpendicular to the bisector of the beams and in the plane of the beams. The planar outside surface of the housing avoids asymmetric refraction of light beams as they pass into the chamber. Because the housing and fluid have approximately equal refractive indices, the laser beams encounter refraction only at the flat housing surface. Snell's law was used to predict the location of the measurement volume within the annulus.

Because $n_1 \neq n_2$ and $K_1 \neq K_2$, with respect to Fig. 2, the focal distance from the lens to the measurement volume located in the medium is different than the virtual measurement volume location for $K_1 = K_2$. The new focal distance, F, is calculated through a simple manipulation of Snell's law and the geometric characteristics:

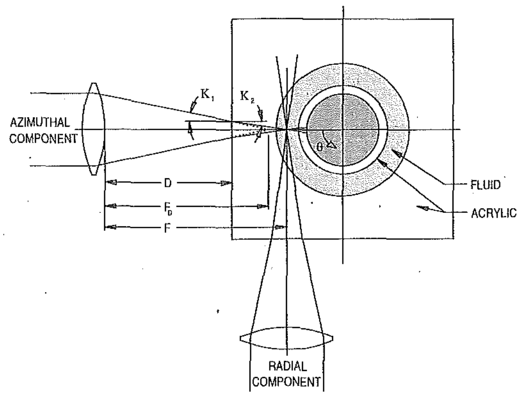

Fig. 2 Beam arrangement for azimuthal and radial component measurements

$$F = F_D \frac{\tan K_1}{\tan K_2} + D\left[1 - \frac{\tan K_1}{\tan K_2}\right] \tag{4}$$

where F_D is the focal distance in air and D is the distance from the front of the lens to the window.

A 23.5 mW argon-ion laser with 514.5 nm wavelength was used with a 122.19 mm focal distance focusing lens. This lens and a 50 mm beam separation provided a half angle $K_2 = 7.729$ deg and fringe spacing of 1.28 μm in the fluid.

4 Results

The primary results of this research were experimental measurements of the three mean velocity components u_r, u_z, and u_θ and their respective Root Mean Square values of the fluctuations u_r', u_z', and u_θ'. Measurements in the $\Gamma = 20$ annulus were obtained only in the lower third of the chamber to concentrate on the extent of the end wall effects. In addition, trapped air bubbles remained in the upper third region of the annulus and could have added uncertainty to the measurements. For the $\Gamma = 4$ case, the entire annulus was investigated. Average component velocities and turbulence intensities were compiled from 2048 samples at each measurement location. Data were recorded in the boundary layer at the inner and outer cylinders; however, the finite size of the probe volume and poor signal-to-noise ratio prohibited fine detail in these regions. The velocities and turbulence intensities presented are non-dimensional with respect to the inner cylinder surface speed of $U_s = 3.89$ m/s.

4.1 Investigation of the Flow Symmetry. Proving the existence of symmetry in the azimuthal direction reduces the need to map the entire three-dimensional annulus. In the $\Gamma = 20$ annulus, the primary and secondary planes are separated by 180 degrees and are referred to as $\theta = 0$ and $\theta = \pi$, respectively. For the symmetry investigation, measurements were obtained at 1.0 mm radial intervals and 10.0 mm axial intervals. Azimuthal velocity, the dominant component, was assumed to follow symmetry and was not measured at $\theta = \pi$.

Figure 3 presents the radial and axial velocities along the annulus gap at $z/d = 0.66$ for $\theta = 0$ and $\theta = \pi$. While the z/d location is presented as an example of the closeness of match between the theta planes, refer to Parker (1995) for the complete series of profiles. While the trends show some random variations greater than the expected uncertainties, the velocities are in general very similar between circumferential planes. At z/d locations less than 4.0, the velocity correlations are best. In measurements above $z/d = 4$, however, increasingly large discrepancies between the theta planes are prevalent. This result may be due to the loss of vortex regularity reported by Smith and Townsend (1982) for very high Taylor number ratios.

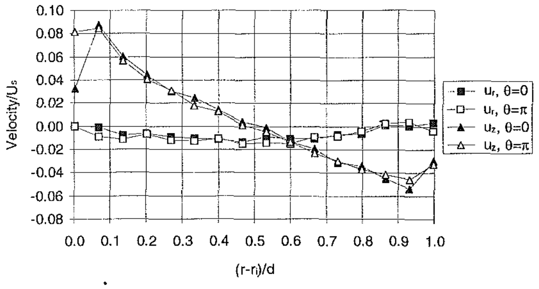

Fig. 3 Radial and axial velocity comparison, $z/d = 0.66$ (uncertainty in radial and axial velocity ±2 percent)

A primary focus of this research was to investigate the effects of end walls on the Taylor vortices. In the region where $z/d < 4.0$, the overall quality of this comparison confirms the axisymmetric behavior of the flow. Therefore, the axial, radial, and azimuthal velocities and turbulence intensities were measured on one r-z plane, $\theta = 0$, and the results are assumed axisymmetric through the circumference.

4.2 Radial-Axial Velocity Vectors. Axial, radial, and azimuthal component data were recorded every one millimeter along the radial axis and every two millimeters axially on the $\theta = 0$ plane. Velocity vectors of radial and axial component velocities are presented in Figs. 4 and 5 for the $\Gamma = 20$ and $\Gamma = 4$ annulus cases, respectively. While the $\Gamma = 4$ case was neatly split into two equal vortex regions, the $\Gamma = 20$ case had 18 vortices in the complete annulus. A symmetry plane at $L/2$

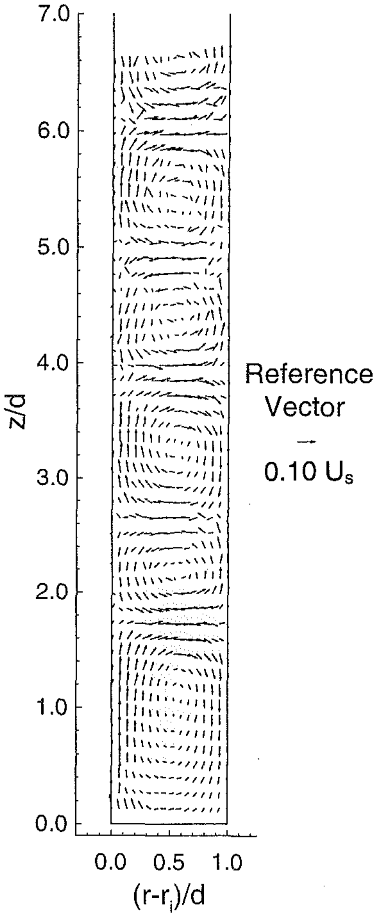

Fig. 4 Radial-axial velocity vectors, $\Gamma = 20$ (uncertainty in radial and axial velocity ±2 percent)

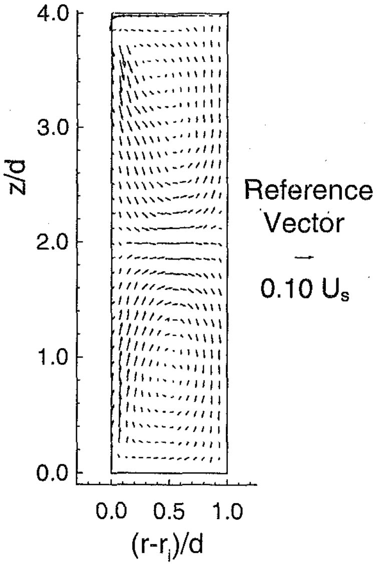

Fig. 5 Radial-axial velocity vectors, Γ = 4 (uncertainty in radial and axial velocity ±2 percent)

was observed for both cases. The vortex center of the top vortex for the Γ = 4 annulus is offset toward the inner cylinder and end wall corner due to the leakage of fluid around the edges of the upper end wall ring. End wall effects are apparent in both cases such that the vortices closest to the end walls are elongated. The inward radial component at the end walls agrees with the conclusions of Koschmieder (1993) for a very long annulus and with Merati et al. (1992) for a short annulus.

Taylor vortices are commonly sized by their wavelength, λ, which is a ratio of the axial length of a pair of vortices divided by the gap width. Typically, wavelength refers to the average Taylor vortex pair size over the entire annulus. Because of the relatively short annulus lengths for which data were recorded, the half wavelength, λ/2, was measured for each vortex and is summarized in Table 1. The half wavelength was measured as the distance between radial outflow and inflow regions, defining one vortex. This approach illustrates the extent of end wall effects through the annulus length. Vortex numbering starts at the lower end wall and increases in the axial direction. The first three vortices for the Γ = 20 case are directly affected by the stationary end wall and each appears to illustrate the transitional stages required to stabilize the radial velocity pattern. Considering the vortices as pairs, the first set is composed of an elongated vortex 1 and a condensed vortex 2. Likewise, the second set consists of vortex 3 longer than vortex 4. In vortex 1, the radial inflow borders the stationary end wall while the radial outflow borders a mating vortex. Consequently, vortex 1 settles into an elongated shape. Vortex 2 compensates for its elongated partner by reducing its size such as to minimize the unit's total length. Similarly, vortex 4 compensates for vortex 3. With the critical wavelength for this flow numerically predicted at $\lambda_c = 2.00$ by Roberts (1965), the local wavelength converges to the critical local wavelength from above as the distance from the end wall increases. The local wavelengths for vortices greater than 5 are expected to remain at 1.06 because of the lack of end wall influence. Literature firmly reports that the wavelength for supercritical vortices is greater than the critical wavelength (Koschmieder, 1993), which confirms the 0.06 experimental difference.

Table 1 Measured vortex size as a function of annulus length

Vortex number	Local wavelength, λ/2	
	Γ = 20	Γ = 4
1	1.72	2.0
2	0.86	2.0
3	1.33	
4	1.06	
5	1.06	

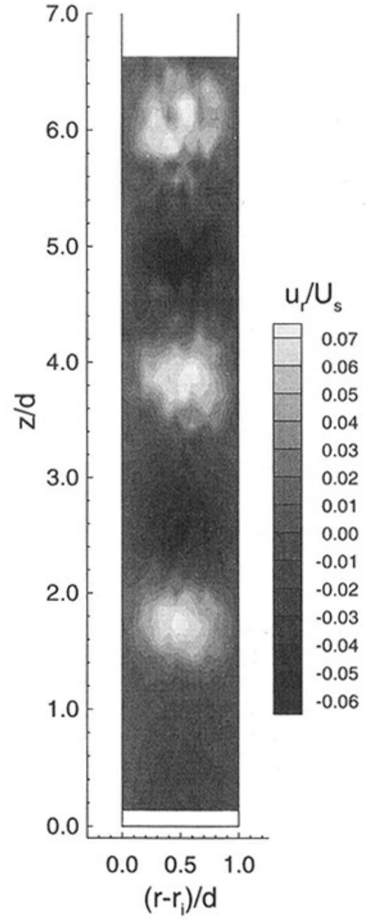

Fig. 6 Radial velocity, Γ = 20 (uncertainty in radial velocity ±2 percent)

4.3 Component Velocity Profiles for the Γ = 20 Annulus. Contours of radial, axial, and azimuthal velocity are plotted in Figs. 6 through 8 for the Γ = 20 annulus. Positive component directions are parallel to the component axes and with positive azimuthal velocity directed into the page.

The maximum radial velocity occurs in the radial outflow regions on adjacent vortices. Centrifugal forces act to increase the outward radial velocity in these regions and impede the returning flow. The axial velocity contours show that the zero velocity point in the radial direction is located at approximately $(r - r_i)/d = 0.6$. This offset from the annulus radial center is also attributed to the centrifugal forces acting to throw fluid away from the inner cylinder.

Up to this point, flow only on the radial-axial plane has been discussed. Without considering the circumferential dimension, the rectangular Taylor vortex cells (with respect to the radial-axial plane) might be regarded independent of the rotating inner cylinder. With the inclusion of the azimuthal velocity, the flow picture becomes much more complex with respect to through-plane activities. Figure 8 maps contours of azimuthal velocity, revealing a significant gradient along the radial axis. Although boundary layer measurements were not possible on the inner and outer cylinders, the azimuthal velocity drops rapidly from the inner cylinder surface speed at the inner cylinder ($u_\theta/U_s =$

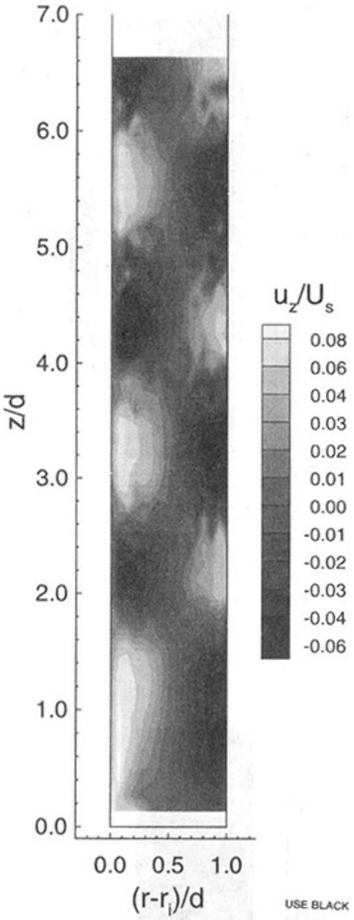

Fig. 7 Axial velocity, $\Gamma = 20$ (uncertainty in axial velocity ±2 percent)

1.0) and ends with zero velocity at the outer cylinder. Over 80% of the mean flow u_θ/U_s is between 0.5 and 0.3.

With respect to the radial-axial velocity vector plots, the fluid at the inner cylinder is moving into the page 12.5 times faster than the maximum axial velocity and does not move into the page at the outer cylinder. Therefore, not only are the fluid particles rotating about their vortex centers while they move in the azimuthal direction, but they also follow an azimuthal shearing gradient between the inner and outer cylinders.

Merati et al. (1995) describe the azimuthal velocity gradient in terms of jet flow: "The regions between the adjacent vortices behave similar to jet flow in redistributing the high speed azimuthal flow near the inner cylinder and the low speed flow near the outer cylinder. In the regions where there is outflow toward the stationary outer cylinder, high speed azimuthal flow is directed toward the outer stationary cylinder. In the regions where the jet flow is toward the inner rotating cylinder, the slow flow is directed toward the inner cylinder."

In a detailed numerical study conducted by Marcus (1984), jet flow phenomenon observed here at a high Taylor number was predicted for low Taylor numbers. Several stable axisymmetric Taylor vortices and several stable non-axisymmetric wavy vortex flows that correspond to one traveling wave were computed. Using the results of the numerical calculations, it was conjectured that the traveling waves were a secondary instability caused by the strong radial motion in the outflow boundaries of the Taylor vortices and were not shear instabilities associated with inflection points to the azimuthal flow. It was demonstrated numerically that at the critical Reynolds number where Taylor-vortex flow becomes unstable to wavy vortex flow, the speed of the traveling wave is equal to the azimuthal angular velocity of the fluid at the center of the Taylor vortices. Werely and Lueptow (1995) conducted PIV measurements at Taylor numbers near the critical flow regime. They observed Taylor vortices, wavy vortex flow and the jet phenomenon predicted by Marcus (1984).

4.4 Component Velocity Profiles for the $\Gamma = 4$ Annulus. Contours of radial, axial, and azimuthal velocity are plotted in Figs. 9 through 11, respectively, for the $\Gamma = 4$ annulus. The radial and axial contours again reveal the circulation of fluid around the upper end wall ring. The two vortices are similar in structure to the first vortex for the $\Gamma = 20$ annulus. The maximum radial velocity at the radial outflow region is half the velocity for the $\Gamma = 20$ case. In addition, the radial velocity at the lower end wall is half the velocity for the $\Gamma = 20$ case. The axial velocity at the inner cylinder is comparable to the $\Gamma = 20$ case, but at the outer cylinder it is again only half the $\Gamma = 20$ value. The stationary end walls act to slow the complete rotational vortex flow except for the axial component at the inner cylinder.

The azimuthal velocity also resembles the $\Gamma = 20$ case such that the azimuthal velocity compensates for a jet flow effect at the radial outflow region at $z/d = 2.0$. In the radial inflow regions along the end walls, the slow azimuthal flow is similarly directed toward the inner cylinder.

4.5 Turbulence Intensity for the $\Gamma = 20$ and $\Gamma = 4$ Annuli. Contours of turbulence intensity for the radial, axial, and azimuthal velocity components in the $\Gamma = 20$ annulus are shown in Figs. 12 through 14, respectively. These contours show that the observed Taylor vortices are turbulent for these Taylor and Reynolds numbers.

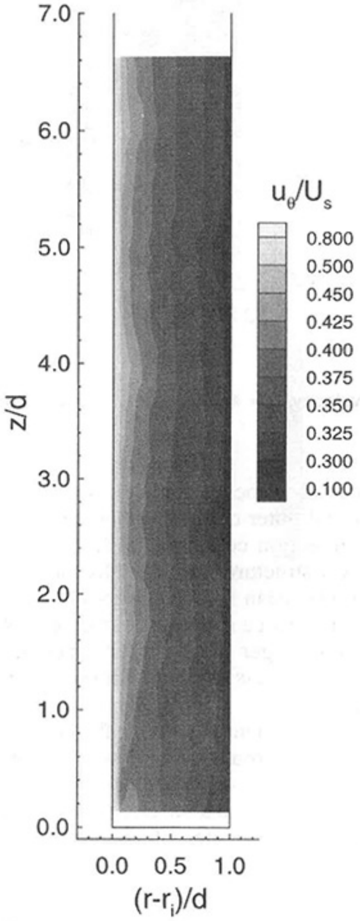

Fig. 8 Azimuthal velocity, $\Gamma = 20$ (uncertainty in azimuthal velocity ±2 percent)

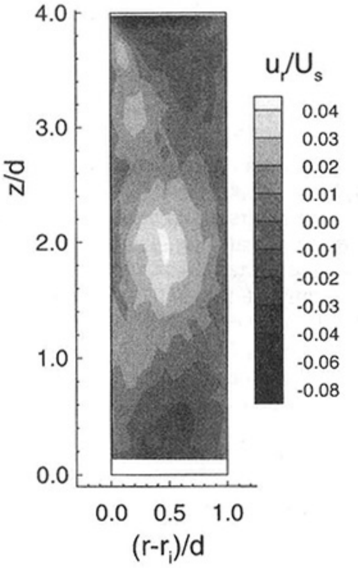

Fig. 9 Radial velocity, $\Gamma = 4$ (uncertainty in radial velocity ±2 percent)

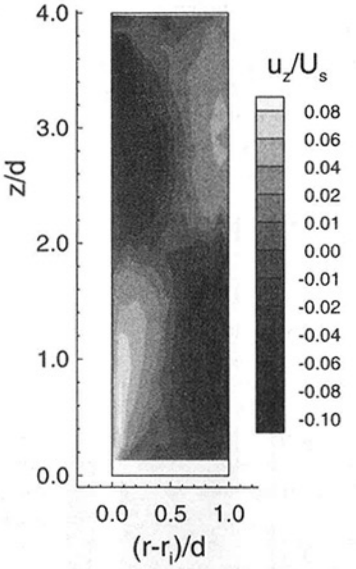

Fig. 10 Axial velocity, $\Gamma = 4$ (uncertainty in axial velocity ±2 percent)

Large azimuthal velocity gradients in the boundary layers near the inner and outer cylinders generate more turbulence in the azimuthal direction compared with the rest of the annulus flow. The jet flow structures produced by the Taylor vortices not only distribute the mean flow contours but also the turbulence intensity contours. Since more turbulence exists near the inner cylinder due to its larger shear, larger zones of high azimuthal turbulence intensity occur at the radial outflow regions near the inner cylinder.

The dominant turbulent flow near the inner cylinder affects the radial and axial turbulence intensity contours as shown in Figs. 12 and 13, respectively. Larger zones of high turbulence intensities for the radial and axial components occur at the radial outflow regions at the center of the gap and near the inner cylinder, respectively.

Figures 15 through 17 display contours of turbulence intensity for the radial, axial, and azimuthal velocity components in the $\Gamma = 4$ annulus. The same jet flow arguments presented for the $\Gamma = 20$ case can be applied to the $\Gamma = 4$ case. In fact, the contours are very similar for any selected set of two vortices for the $\Gamma = 20$ case.

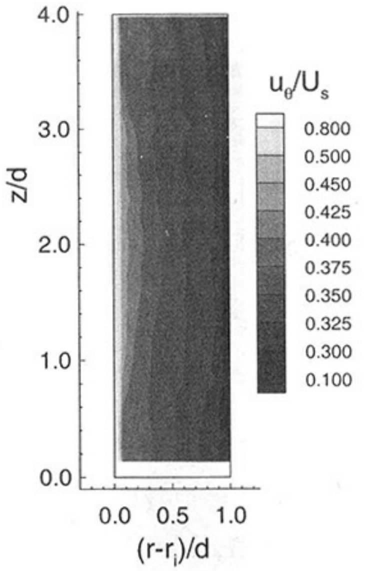

Fig. 11 Azimuthal velocity, $\Gamma = 4$ (uncertainty in azimuthal velocity ±2 percent)

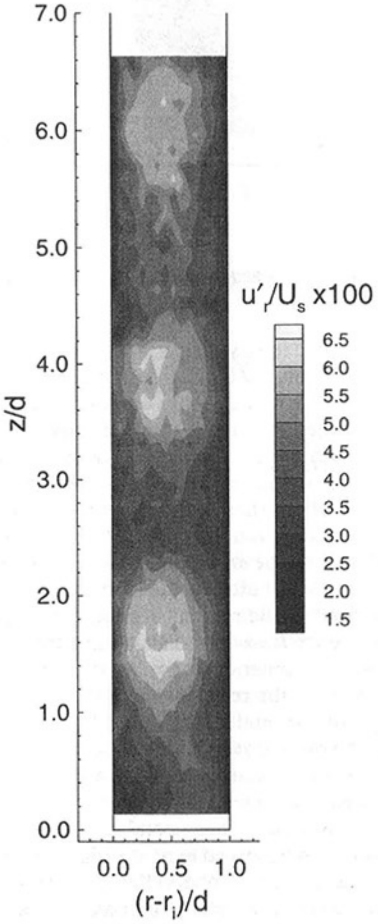

Fig. 12 Radial turbulence intensity, $\Gamma = 20$ (uncertainty in radial turbulence intensity ±5 percent)

5 Conclusions

Refractive index matching provided an annular test apparatus with unrestricted access to study the contained turbulent, Tay-

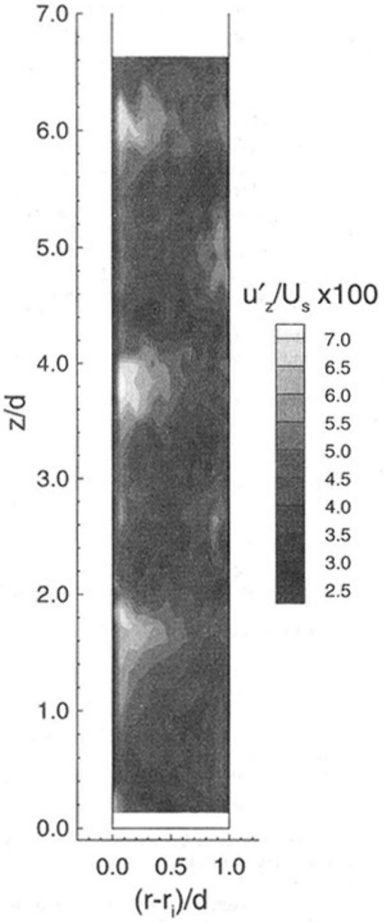

Fig. 13 Axial turbulence intensity, Γ = 20 (uncertainty in axial turbulence intensity ±5 percent)

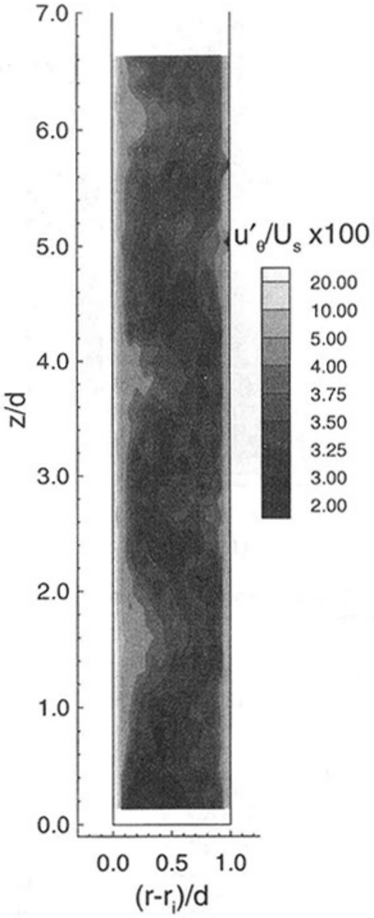

Fig. 14 Azimuthal turbulence intensity, Γ = 20 (uncertainty in azimuthal turbulence intensity ±5 percent)

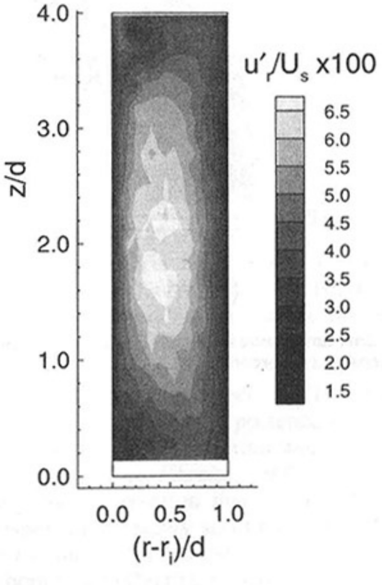

Fig. 15 Radial turbulence intensity, Γ = 4 (uncertainty in radial turbulence intensity ±5 percent)

lor-Couette flow. All optical walls were constructed from clear acrylic and, with a very close refractive index match, the only light refraction occurred at the flat housing surface. An aqueous solution of sodium iodide was used to match the 1.4905 ± 0.0005 refractive index of Plexiglas at 27.0 ± 0.1°C. The annulus consisted of a rotating cylinder aligned within a stationary outer cylinder such that the ratio of inner to outer cylinder radii was 0.672. Annulus length was set at 20 and 4 times the annulus gap. The flow Taylor number was $T = 2.107 \times 10^9$, the Taylor number ratio was $T/T_c = 924{,}600$, and the Reynolds number was $Re = 73{,}440$.

Axial, radial, and azimuthal velocities and turbulence intensities were measured with a one component Laser Doppler Velocimetry system along an azimuthal plane while the inner cylinder rotated at 1200 rpm. Axisymmetric mean velocity conditions in the circumferential direction were investigated by measuring the radial and axial velocity components on two *r-z* planes separated by 180 degrees. Velocity vectors and component velocities for the two planes compared very favorably, supporting the theory of azimuthal symmetry of the mean flow.

Radial-axial velocity vector plots and component velocity contours revealed the Taylor vortex structure. With the annulus length set at 20 times the annulus gap, 18 vortices were observed. Three pairs of Taylor vortices were affected by the end walls before the vortices reached a size equilibrium slightly larger than the predicted critical vortex size. With the annulus length set at 4 times the annulus gap, the two resulting vortices were dominated by the stationary end walls, and the overall velocities were reduced with respect to the long annulus. Jet effects were observed in the distribution of the high velocity mean and turbulence into the radial outflow regions and the low velocity mean and turbulence into the radial inflow regions.

6 Acknowledgments

This paper was based on work supported by the National Science Foundation under grant number MSS-9114453 and the

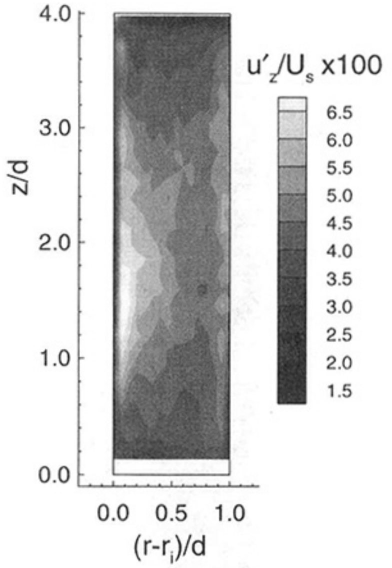

Fig. 16 Axial turbulence intensity, $\Gamma = 4$ (uncertainty in axial turbulence intensity ±5 percent)

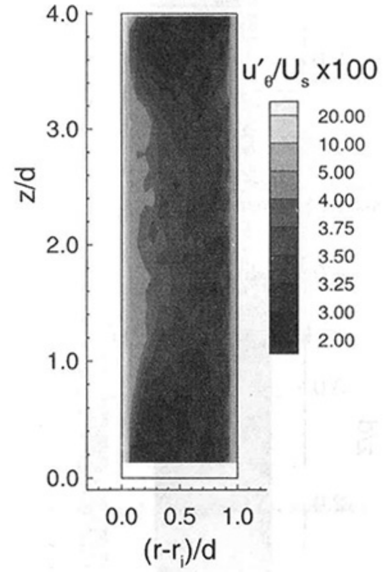

Fig. 17 Azimuthal turbulence intensity, $\Gamma = 20$ (uncertainty in azimuthal turbulence intensity ±5 percent)

Western Michigan University Research Fellows program. The Government has certain rights with this material.

References

Barnes, N. D., Flitney, R. K., and Nau, B. S., 1992, "Mechanical Seal Chamber Design for Improved Performance," *Proceedings of the Ninth International Pump Users Symposium*, Houston, Texas.

Braun, M. J., Canacci, V. A., and Hendricks, R. C., 1990, "Flow Visualization and Quantitative Velocity and Pressure Measurements in Simulated Single and Double Brush Seals," Paper presented at the 45th annual meeting of STLE, Denver, CO.

Burkhalter, J. E., and Koschmieder, E. L., 1972, "Steady Supercritical Taylor Vortex Flow," *Journal of Fluid Mechanics*, Vol. 58, No. 3, pp. 547–560.

Burkhalter, J. E., and Koschmieder, E. L., 1974, "Steady Supercritical Taylor Vortices after Sudden Starts," *Physics of Fluids*, Vol. 17, Nov., pp. 1929–1935.

Chen, R. C., and Kadambi, J. R., 1990, "LDV Measurements of Solid-liquid Slurry Flow Using Refractive Index Matching Technique," *Particulate Science and Technology*, Vol. 8, pp. 97–109.

Donnelly, R., 1991, "Taylor-Couette Flow: the Early Days," *Physics Today*, Nov., pp. 32–39.

Dybbs, A., and Edwards, R. V., 1987, "Refractive Index Matching for Difficult Situations," Paper presented at the Second International Conference on Laser Anemometry—Advances and Applications, Strathclyde, UK., Sept.

Fenstermacher, P. R., Swinney, H. L., and Gollub, J. P., 1979, "Dynamical Instabilities and the Transition to Chaotic Taylor Vortex Flow," *Journal of Fluid Mechanics*, Vol. 94, No. 1, pp. 103–128.

Jacobs, D. A., Jacobs, C. W., and Andereck, C. D., 1988, "Biological Scattering Particles for Laser Doppler Velocimetry," *Physics of Fluids*, Vol. 31, No. 12, pp. 3457–3461.

Koschmieder, E. L., 1993, *Benard Cells and Taylor Vortices*, Cambridge University Press, New York.

Koschmieder, E. L., 1979, "Turbulent Taylor Vortex Flow," *Journal of Fluid Mechanics*, Vol. 93, pp. 515–527.

Lathrop, D. P., Fineberg, J., and Swinney, H. L., 1992, "Turbulent Flow Between Concentric Cylinders at Large Reynolds Number," *Physical Review Letters*, Vol. 68, No. 10, pp. 1515–1518.

Lathrop, D. P., Fineberg, J., and Swinney, H. L., 1992, "Transition to Shear-Driven Turbulence in Couette-Taylor Flow," *Physical Review A*, Vol. 46, No. 10, pp. 6390–6405.

Marcus, P. S., 1984, "Simulation of Taylor-Couette Flow. Part 2. Numerical Results for Wavy-Vortex Flow with One Traveling Wave," *Journal of Fluid Mechanics*, Vol. 146, No. 65.

Merati, P., Jacobs, L., and Parker, J., 1995, "Particle Image Velocimetry in Taylor-Couette Flow," *Proceedings of the 3rd Fluid Dynamics Conference*, Tehran, Iran, Jan.

Merati, P., Parker, J., and Adams, W., 1992, "Turbulent Flow of an Annulus with an Inner Rotating Cylinder and a Dead End Wall," Paper presented at the Thirteenth Symposium on Turbulence, Rolla, MO, Sept.

Northrup, M. A., Kulp, T. J., and Angel, S. M., 1991, "Fluorescent Particle Image Velocimetry: Application to Flow Measurement in Refractive Index-Matched Porous Media," *Applied Optics*, Vol. 30, pp. 3034–3040, July.

Parker, J. C., 1996, "An Investigation of Turbulent Taylor-Couette Flow Using Laser Doppler Velocimetry in a Refractive Index Matched Facility," M. S. thesis, Western Michigan University.

Roberts, P. H., 1965, "The Solution of the Characteristic Value Problem," *Proceedings of the Royal Society of London*, Series A, Vol. 283, pp. 550–556, Jan.

Smith, G. P., and Townsend, A. A., 1982, "Turbulent Couette Flow between Concentric Cylinders at Large Taylor Numbers," *Journal of Fluid Mechanics*, Vol. 123, pp. 187–217.

Thompson, B. E., 1990, "Refractive Index Matching Techniques in Complex Rocket-engine Flow Configurations," Paper presented as SRA Contractor Final Report R89-900072-F, May.

Wereley, S. T., and Lueptow, R. M., 1995, "Measurement of Velocity Fields with Application Toward Two-Phase Flow in a Taylor-Couette Separator," 9th Couette-Taylor Workshop, Boulder, Co, Aug. 7–10.

An Improved Eddy Interaction Model for Numerical Simulation of Turbulent Particle Dispersion

D. I. Graham
Lecturer,
School of Mathematics and Statistics,
University of Plymouth,
Plymouth, PL48AA United Kingdom

Three main effects have been observed in experimental investigations of the dispersion of low concentrations of solid particles in homogeneous turbulent flows, namely the crossing trajectories, inertia, and continuity effects. This paper discusses the development of a simple Lagrangian eddy interaction model to account for all three of these effects. By choosing the length, time, and velocity scales in the model so as to be consistent with the corresponding scales in homogeneous, isotropic, and stationary turbulence, the proper limiting behavior is ensured both for fluid particles and for heavy solid particles. Because only one time step is required per eddy, the computational efficiency of the model is ensured.

Introduction

In fluid/solid flows where the concentration of solid particles is small and/or the particles are distributed over a range of sizes, Lagrangian particle tracking models have been used extensively to model particle dispersion. In such simulations, the fluid and solid phases are treated separately. The solution for the primary flow fluid phase is generally found using one of the standard turbulence models. Trajectories of individual solid particles are then determined by solving the particle equations of motion as each particle moves through the fluid under the influence of drag and other forces. Characteristics of the particulate phase are then determined by statistical averaging over all particle trajectories. A large number of particles is required for statistical reliability of the computational results.

Fluid and particle motions in turbulent flows are, of course, random in nature. Solutions to single-phase turbulent flows are often obtained in terms of average flow velocity, pressure, etc. Lagrangian models used in conjunction with such ''Reynolds-averaged'' primary flow solutions must therefore derive some form of random fluid motions from the mean primary flow solution. Any Lagrangian model considers a (fluid or solid) particle which has some velocity $\boldsymbol{u}_p$ and is surrounded at some arbitrary time by a patch of fluid with velocity $\boldsymbol{u}_f$. The particle and fluid velocities are generally different so that, at some later time, the particle is not necessarily associated with the same fluid patch. Each model specifies a method for determination of the fluid velocity within the fluid patch in which the particle has become located in terms of the fluid velocity in the original patch. In general, the correlations (in space and time) between the fluid velocities in the two different patches are required.

Many different approaches are available in developing Lagrangian models. Examples in the literature include models based upon the Langevin equation (Lu et al., 1993), random Fourier modes (Maxey, 1987), auto-correlation methods (Berlemont et al., 1990), and pdf models (Pozorski and Minier, 1995). However, one of the simplest and most frequently used models is the eddy interaction model (EIM) first introduced by Hutchinson et al. (1971) and developed subsequently by Gosman and Ioannides (1981) and Shuen et al. (1984), among others.

In this model the fluid patch, in which the fluid velocity is assumed to be constant, is a spherical eddy centered at the original location of a solid particle. The instantaneous fluid velocity within the eddy is determined by random sampling using knowledge of the local mean velocity and turbulence intensity. The motion of the particle is determined by integration of the equation of motion of the particle during the eddy interaction. The particle remains influenced by the same eddy until either it escapes the eddy when the distance between the particle and the center of the eddy exceeds the eddy length L_e or the eddy expires when the interaction time exceeds the fluid particle interaction time (fpit) or ''eddy lifetime'' T_e.

On completing an interaction, the particle is assumed to be located at the center of a new eddy, with a different instantaneous velocity. Particle motions are therefore determined by a series of interactions with randomly-oriented eddies and the random fluid velocities within each eddy lead to random particle trajectories. In common with other Lagrangian models, data for the particulate phase are than determined from statistical analysis of the particle tracks.

In nonhomogeneous turbulence, the fpit and eddy length are usually determined as functions of the turbulence kinetic energy and its rate of dissipation. In the following development, however, analysis is restricted for simplicity to the case of homogeneous, isotropic and stationary turbulence (HIST). In this case, the three main effects observed in particle dispersion experiments are:

(i) the crossing trajectories effect, or CTE (Yudine, 1959), whereby particle dispersion in the presence of a drift velocity is reduced compared with the situation with no drift present,

(ii) the inertia effect (Reeks, 1977, Wells and Stock, 1983), namely the observation that, in the absence of body forces, the dispersion of heavy solid particles may exceed the dispersion of the fluid particles themselves,

(iii) the continuity effect (Csanady, 1963), where the dispersion in the direction of a drift velocity exceeds the dispersion at right angles to the drift.

The aim is to develop a simple model which accounts for all of the above effects. In order to aid the development of the model, it is assumed that the drag on a solid particle is given by Stokes' law. The eddy length and fpit are given the constant values L_e and T_e, respectively, and the fluid velocity in each eddy is sampled from a Normal distribution with standard devia-

---

Contributed by the Fluids Engineering Division for publication in the JOURNAL OF FLUIDS ENGINEERING. Manuscript received by the Fluids Engineering Division May 2, 1995; revised manuscript received May 1, 1996. Associate Technical Editor: R. W. Metcalfe.

tion equal to the turbulence intensity u'. Gravity is assumed to act in the x_1 direction.

In this paper, after first of all noting the equations which determine particle dispersion, developments of the eddy interaction model to account for the CTE, the inertia effect and the continuity effect are discussed. The influence of gravity on particle dispersion is then investigated and an integrated model is proposed. Finally, a concluding section discusses the methods and results presented in the paper.

Particle Motion

Assuming that the particle/fluid density ratio is high and assuming no lift forces on a spherical particle, the equation of motion of an individual particle is given by

$$\frac{d\mathbf{u}_p(t)}{dt} = \frac{1}{\tau_r}(\mathbf{u}_f(t) - \mathbf{u}_p(t)) + \mathbf{g}, \tag{1}$$

where t denotes time, $\mathbf{u}_p$, and $\mathbf{u}_f$ are particle and fluid velocities, respectively, τ_r is the Stokesian particle relaxation time and $\mathbf{g} = (g, 0, 0)$ is the acceleration due to gravity. Within a particular eddy in the eddy interaction model, the fluid velocity is assumed to be constant so that, under the assumption of Stokesian drag, Eq. (1) can be integrated analytically to give

$$\begin{aligned}\mathbf{u}_p(t + \delta t)& \\ &= \mathbf{u}_f - (\mathbf{u}_f - \mathbf{u}_p(t))e^{-\delta t/\tau_r} + \mathbf{g}\tau_r(1 - e^{-\delta t/\tau_r}).\end{aligned} \tag{2}$$

The change in position of the particle can also be determined analytically. If the location of the center of the eddy, $\mathbf{X}_f(t)$, and the particle position $\mathbf{X}_p(t)$ are identical at time t, the particle location at time $t + \delta t$ is given by

$$\begin{aligned}\mathbf{X}_p(t + \delta t) = \mathbf{X}_p(t) - (\mathbf{u}_f - \mathbf{u}_p(t))\tau_r(1 - e^{-\delta t/\tau_r})& \\ - \mathbf{g}\tau_r^2(1 - e^{-\delta t/\tau_r} - \delta t/\tau_r) + \mathbf{u}_f\delta t&\end{aligned} \tag{3}$$

A particle crosses an eddy if the separation between the particle and the center of the eddy exceeds the eddy length, i.e.,

$$|\mathbf{X}_p(t + \delta t) - \mathbf{X}_f(t + \delta t)| \geq L_e, \tag{4}$$

where $\mathbf{X}_f(t + \delta t) = \mathbf{X}_f(t) + \mathbf{u}_f\delta t$ is the position at time $t + \delta t$ of the fluid particle located at the center of the eddy.

The long-time dispersion coefficient of the particles in the k direction is determined as

$$D_k = \lim_{t\to\infty} \frac{\langle X_{pk}^2(t)\rangle}{2t}, \tag{5}$$

where $X_{pk}(t)$ is the k-component of the particle displacement at time t and the angled brackets indicate ensemble averaging. The dispersion coefficient is approximated in the following by

$$\bar{D}_k = \frac{\langle X_{pk}^2(t = 2500\tau_L)\rangle}{5000\tau_L}. \tag{6}$$

It is the intention to update particle velocities and positions only once per eddy, thereby ensuring the computational efficiency of the model. It is possible to do this if the time during which a particle interacts with an eddy is known, and the resulting updated quantities are exact in the case of Stokes drag. The interaction time depends on the time taken for a particle to cross an eddy. If it assumed that the influence of gravity on the crossing time is negligible, the crossing time is given by

$$t_c = -\tau_r \log_e(1 - L_e/(|\mathbf{u}_r|\tau_r)), \tag{7}$$

where $\mathbf{u}_r$ is the fluid/particle relative velocity. Clearly, in this case, if $L_e/(|\mathbf{u}_r|\tau_r) > 1$, a particle will never cross an eddy and the particle is trapped by the eddy, in which case the interaction time is set equal to the fpit T_e.

The Crossing Trajectories Effect

The dispersion coefficient of fluid or solid particles in HIST, assuming Stokesian drag, is given by:

$$D_{pk} = u'^2\tau_{pk}^f, \tag{8}$$

where τ_{pk}^f is the integral time scale of the k-component of the fluid velocity following the motion of a (fluid or solid) particle. For fluid particles, the relevant time scale is the Lagrangian integral time scale and the dispersion coefficient is $u'^2\tau_L$. In the presence of gravity aligned in the x_1 direction, for particles for which the drift velocity $V_s = g\tau_r \gg u'$, the integral scale in the x_1 direction is Λ_f/V_s and the dispersion coefficient is given by $u'^2\Lambda_f/V_s$.

The crossing trajectories effect is taken account of in eddy interaction models by forcing the particle to enter a new eddy if the separation between the particle and the center of the eddy is sufficiently large. The analysis of Graham and James (1996) shows that, in HIST, the fpit is related to the Lagrangian integral time scale of the turbulence, τ_L, and the eddy length is related to the Eulerian (longitudinal) integral length scale, Λ_f. For the model considered in the following, $T_e = 2\tau_L$, $L_e = 2\Lambda_f$. Setting these parameters ensures the correct long-time dispersion coefficients both of fluid particles and of heavy particles settling under gravity.

In order to illustrate the CTE, results from the "standard" eddy interaction model, where the time for which a particle interacts with a particle is the minimum of the crossing time and the fpit or eddy lifetime are compared with the analytical results of Reeks (1977, $\gamma = 1$) in Fig. 1. Starting from an initial state in which all particles are located initially at the origin with a velocity equal to the drift velocity V_s, the particle velocity and position at the end of an interaction is updated by using Eqs. (2) and (3) with the time increment δt set equal to the interaction time t_i. The interaction time is determined before the start of each interaction as the minimum of the fpit T_e and the crossing time t_c (which is approximated by Eq. (7)). As noted above, the interaction time for trapped particles is set equal to T_e.

Throughout this paper, following Reeks, lengths are rendered dimensionless by reference to a characteristic length $1/k_0$ and

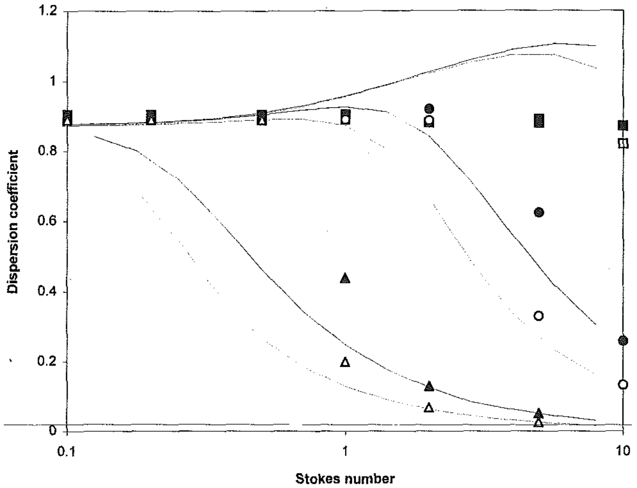

Fig. 1 Dispersion coefficients-standard EIM. Key: EIM: $g = .1$, ■-D_1, □-D_2, $g = 1$, ●-D_1, ○-D_2, $g = 10$, ▲-D_1, △-D_2, ——D_1, ...D_2, Reeks (1977).

time are nondimensionalized by reference to a characteristic time $1/(k_0u')$, where u' is the turbulence intensity and $1/k_0$ is a reference length in the energy spectrum used by Reeks. In these nondimensional variables, Reeks' values for Λ_f and τ_L are given by $\sqrt{(2\pi)}$ and 0.9, respectively. For the simulations, L_e is set to $2\sqrt{(2\pi)}$, T_e equals 1.8 and the eddy velocities are sampled from a Normal distribution with $u' = 1$. The results show clearly that the dispersion coefficients of the low-inertia particles (small τ_r) for which the drift velocity $g\tau_r$ is less than approximately .5, and for "heavy" particles for which the drift velocity exceeds 5, are predicted well.

Although the results should not be expected to agree exactly with Reeks' results due to the different spatial and temporal auto-correlation functions used, the level of discrepancy in the mid-range of drift velocities is suspect. Part of the discrepancy is due to the neglect of gravity in the determination of the crossing time. This aspect is covered in a later section. For the case $g = 0.1$, Reeks' model predicts that the dispersion coefficient increases with increasing τ_r in the range considered in the simulations. The figure shows that the standard EIM is not capable of modeling this increase and a modification of the model which allows for this is described in the next section.

The Inertia Effect

Graham and James (1996) have shown that the standard EIM used in the above simulations always predicts that the particle dispersion coefficient cannot exceed the dispersion coefficient of the fluid particles themselves. This property of the standard EIM is due to the restriction that the interaction time for particles cannot exceed the fpit or "eddy lifetime." However, the experiments of Wells and Stock (1983) and the analytical method used by Reeks (1977) have indicated that, when gravity can be neglected, high-inertia solid particles disperse more rapidly in the long-time limit than fluid particles.

Graham (1996) showed that this inertia effect can be accounted for in the eddy interaction model by allowing the interaction time for solid particles to exceed the fpit. The resulting scheme is similar to the standard eddy interaction model in that, if a particle is trapped, the interaction time is set equal to the fpit. However, if the particle crosses the eddy, the interaction time is determined as the minimum of the crossing time and a maximum interaction time $T_{\max}$ which may differ from T_e. The standard model is retrieved by setting $T_{\max}$ equal to T_e. This choice indicates why it is necessary to avoid the name eddy lifetime for the fpit, since the model allows for particles to interact with eddies for times exceeding this lifetime. The choice of $T_{\max}$ determines the ratio of the Eulerian and Lagrangian integral time scales τ_E/τ_L.

Graham (1996) showed that τ_E is dependent both upon $T_{\max}$ and the turbulence structure parameter defined as $\beta = u'\tau_L/\Lambda_f$. Figure 2 illustrates a contour plot showing the value of $T_{\max}/\tau_L$ required for a given ratio τ_E/τ_L. For small values of β (which corresponds to a large eddy length), $T_{\max}$ is twice τ_E. For example, the value of $T_{\max}$ required to give $\tau_E = 1$ when $\beta = 0.5$ is obtained from Fig. 2 as $T_{\max} = 2$. However, for larger values of β, $T_{\max}$ must exceed $2\tau_E$ in order to lead to an integral time scale *in the model* equal to τ_E. For example, the value of $T_{\max}$ required to give $\tau_E = 1$ when $\beta = 2$ is approximately 2.6. For very large values of β (small eddy lengths), $T_{\max}$ must be significantly larger than τ_E. It should, however, be noted that it is unlikely that β takes on very large values—Reeks (1977) predicts a value between 0 and 0.532 (dependent upon the parameter γ used in Reeks' analysis) for β and, on the basis of experimental results from several authors, Hinze (1975, p424) concludes that the value of β lies below 1.

Figure 3 compares computed dispersion coefficients with the results of Reeks (1977). As in the previous section, nondimensional variables are used leading to $\Lambda_f = \sqrt{(2\pi)}$, $\tau_L = 0.9$ and $\tau_E = \sqrt{(\pi/2)}$. Simulations are therefore made using $\Lambda_f = 2\sqrt{(2\pi)}$, $T_e = 1.8$ and (because the turbulence structure parameter β is small), $T_{\max}$ is twice the value of τ_E i.e., $T_{\max} = 2\sqrt{(\pi/2)}$. The Stokes number is defined as $\mathrm{St} = \tau_r k_0 u'$. Again, the results for fluid-like particles ($\mathrm{St} < 0.5$) and for heavy particles ($\mathrm{St} > 5$) are excellent. In the middle range of St, the dispersion coefficients are generally less than those predicted by Reeks (1977). However, the discrepancies can probably be accounted for by noting the differences in the temporal and spatial auto-correlation functions used in the present work and by Reeks. Overall, it is considered by setting only three parameters, namely, the eddy length, the fluid particle interaction time, and the maximum interaction time, dispersion over the full range of relaxation times is modeled quite well.

Unlike Huang et al. (1993), the maximum interaction time does not depend on the particle relaxation time τ_r. However, the integral fluid velocity time-scale seen by a particle, τ^f_{pk}, does depend on τ_r. This is because particles are trapped if $L_e/(|\mathbf{u}_r|\tau_r) > 1$, so that the proportion of particles which are trapped is dependent upon particle inertia. This leads to inertia-dependence of the dispersion coefficient, as illustrated for example in Fig. 3.

The Continuity Effect

As noted previously, particle dispersion in HIST and under Stokes' drag law is determined by the integral scale of the fluid velocities following the motion of a particle. In the case of the EIM, the integral time scales are determined by the distributions of the particle/eddy interaction times. If the interaction times are the same in each coordinate direction, the dispersion coefficients in each direction will be identical. It is clear that, in order to predict differences in dispersion coefficients, the interaction times must differ in different coordinate directions.

In HIST in which gravity acts in the x_1 direction in a Cartesian system, Csanady (1963) predicts that the "longitudinal" dispersion coefficient of heavy particles in the x_1 direction should be twice the "lateral" dispersion coefficients in the x_2 and x_3 directions. The difference in the dispersion coefficients is due to the difference in the longitudinal and lateral spatial auto-correlation functions in HIST and the difference between these two auto-correlations is due to the continuity equation in the fluid equation of motion (Hinze, 1975). The difference in the dispersion coefficients can therefore be called the continuity effect. Clearly, a scheme should be developed which predicts that, for heavy particles, the integral fluid time scale following particle motions in the lateral directions should be only half of the corresponding time scale in the longitudinal direction. The scheme should predict no differences in the dispersion coefficients for fluid particles.

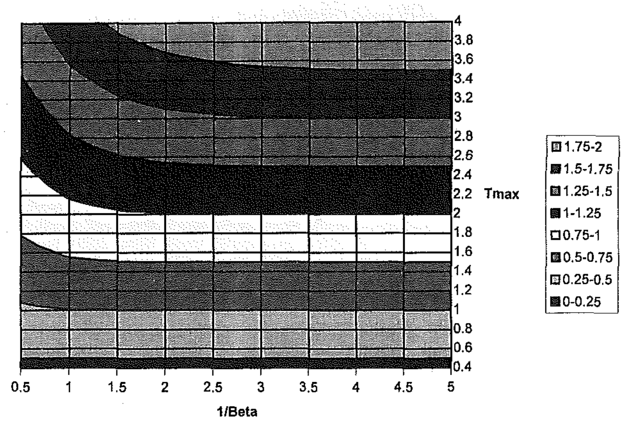

Fig. 2 Contour plot showing τ_E dependence on $T_{\max}$, β

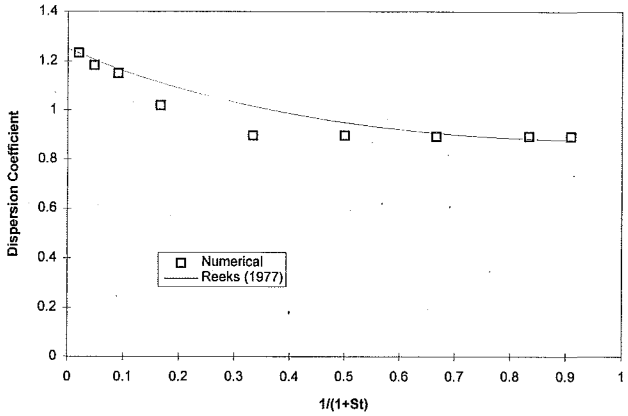

Fig. 3 Inertia effect in modified EIM

Results obtained from such a model are compared with the results of Reeks (1977) in Fig. 1. Here, the interaction time is identical in each coordinate direction for "trapped" particles. If the particle crosses the eddy, on the other hand, the interaction times in directions x_2 and x_3 are exactly half the interaction times in the x_1 direction. The crossing time is again determined by assuming that the influence of gravity is small. For particles with small drift, the dispersion coefficients are correctly predicted to be isotropic, whereas for particles with (dimensionless) drift velocities greater than approximately 1, differences between dispersion coefficients are predicted. For large drift velocities (above 5 in the simulations), the computed lateral coefficients are half of the longitudinal coefficients, as predicted by the analyses of Csanady (1963) and Reeks (1977). The consistency between Reeks' theory and the numerical model of the Eulerian *longitudinal* integral length scales is ensured by the correct choice of eddy length. This method for specifying decreased interaction times in the lateral directions appears to ensure consistency of the *lateral* integral length scales.

Influence of Gravity on Interaction Time

Each model used so far has assumed that the time taken for a particle to cross an eddy can be found by neglecting the influence of gravity on crossing time (though the effects of gravity in updating the particle velocity and position have at all times included the effect of the gravity term). The results of the section concerning the CTE show that neglect of gravity leads to over-predicted dispersion coefficients when compared with the analytical results of Reeks (1977). In this section, different approximations for the crossing time are investigated and compared with a model which accounts for the influence of gravity by numerical solution of the equation for the crossing time. Problems in integrating the CTE, inertia and continuity effects within the model incorporating the influence of gravity on the interaction time are then discussed.

The crossing time is determined as the solution of

$$|\mathbf{X}_p(t+t_c) - \mathbf{X}_f(t+t_c)| = L_e, \tag{10}$$

i.e.,

$$\begin{aligned}&|(\mathbf{u}_f - \mathbf{u}_p(t))\tau_r(1-e^{-t_c/\tau_r})\\ &\qquad - \mathbf{g}\tau_r^2(1-e^{-t_c/\tau_r} - t_c/\tau_r)| = L_e.\end{aligned} \tag{11}$$

It is instructive to look at the two limiting cases $g \rightarrow 0$ and $\tau_r \rightarrow \infty$. In the first case, Eq. (11) reduces to the form

$$|(\mathbf{u}_f - \mathbf{u}_p(t))\tau_r(1-e^{-t_c/\tau_r})| = L_e, \tag{12}$$

which has the solution

$$t_c = -\tau_r \log_e(1 - L_e/(|\mathbf{u}_r|\tau_r)). \tag{13}$$

This is the approximation used in the simulations so far and is ineffective only when the drift velocity is in the range $0.5 < g\tau_r < 2$. When $\tau_r \rightarrow \infty$, Eq. (11) becomes

$$|(\mathbf{u}_f - \mathbf{u}_p(t))t_c| = L_e, \tag{14}$$

for which the solution for the crossing time is given by

$$t_c = \frac{L_e}{|\mathbf{u}_r|}, \tag{15}$$

where $\mathbf{u}_r$ is the relative fluid/solid particle velocity. This is the expression for the crossing time used by Huang et al. (1993).

In the general case, we need to solve the full equation for the crossing time, including the effects of drag and gravity. As noted previously, no analytical solution is available for this general case and so approximate methods must be used. In the following, the method of Regula Falsi has been used to solve the equation for the crossing time. Equation (11) may have several solutions, including negative values for t_c. The required solution is the least positive root.

It should be noted that, if the gravity term is nonzero, particles with finite τ_r can never be trapped by an eddy—given enough time, any particle will cross an eddy. This leads to the major problem in integrating the eddy interaction model to incorporate the inertia effect and the effect of gravity on the crossing time. No particle can ever be trapped if gravity is accounted for, and the crossing time for small particles will inevitably be large. If the interaction time is determined as the minimum of the crossing time and $T_{\max}$, the interaction time for almost-fluid particles is therefore always equal to $T_{\max}$, which can of course be greater than the fpit. This leads to over-prediction of the dispersion coefficient for almost-fluid particles if $T_{\max}$ exceeds T_e.

On the other hand, it can be shown using the analysis of Graham and James (1996), Graham (1996) that for both fluid and heavy particles the dispersion coefficient predicted using Eq. (15) is dependent on β. For $\beta = 0.5$, for example, the dispersion coefficient of fluid particles is 99.5 percent of its true value. However, even for $\beta = 1$, the corresponding dispersion coefficient is only 94 percent of its true value. For larger values of β, estimation of crossing times by the use of Eq. (15) can lead to severe under-prediction of the dispersion coefficient for fluid particles, although, as noted previously, the value of β is not likely to exceed 1.

When the drift velocity is large, the particles cut straight through each eddy and all methods lead to reasonable predictions of the dispersion coefficient. In the middle range, we have seen already by comparison with Reeks' analytical results that neglecting the influence of gravity leads to over-predicted dispersion coefficients and, in this range, the effects of gravity should therefore be incorporated.

There are several methods which could be used to integrate the enhancements discussed here. The method chosen here to ensure the correct diffusion of fluid particles is to neglect the influence of gravity if it can be determined at the outset that its effect should be small. The criterion used here is to neglect the influence of gravity on the crossing time if $\beta g\tau_r/u' < 1$, which can be re-written as $g\tau_r < \Lambda_f/\tau_L$ i.e., if the drift velocity $g\tau_r$ does not exceed an 'average eddy velocity' Λ_f/τ_L. Otherwise, the influence of gravity on the crossing time is determined by numerical solution for the crossing time. Particle/eddy interaction times in the final scheme are determined as follows:

If

$$\beta g \tau_r / u' < 1,$$

gravity is ignored and

$$t_{i1} = t_{i2} = t_{i3} = T_e \quad \text{if} \quad (L_e/(|\mathbf{u}_r|\tau_r) > 1),$$

and

$$t_{i1} = t_{i2} = t_{i3} = \min(t_c, T_{\max}) \quad \text{if} \quad (L_e/(|\mathbf{u}_r|\tau_r) < 1),$$

where

$$t_c = -\tau_r \log_e (1 - L_e/(|\mathbf{u}_r|\tau_r)),$$

otherwise, if

$$\beta g \tau_r / u' > 1,$$

gravity is accounted for and

$$t_{i2} = t_{i3} = t_{i1}/2 \quad \text{if} \quad t_c < T_{\max}$$

$$t_{i2} = t_{i3} = t_{i1} \quad \text{if} \quad t_c > T_{\max}$$

where $t_{i1} = \min(t_c, T_{\max})$, and t_c is found using Eq. (11).

In the above, t_{i1}, t_{i2}, and t_{i3} are the interaction times in the x_1, x_2, and x_3 directions, respectively.

Although the results are not shown here, the results from the method of Huang et al. (1993) (i.e., using Eq. (15) to estimate the crossing time) give reasonably good predictions of Reeks' solution. This is to be expected given the small value of β used in Reeks' solution. The method of Huang et al. should be expected to perform as well as the present method if β is not much greater than about 0.5. It is stressed here that the method developed here is designed to perform well whatever the value of β.

Simulations using this method are compared with Reeks' results in Fig. 4. Recall from previous computations that the values used to enable comparison with Reeks' data are $L_e = 2\sqrt{(2\pi)}$, $T_e = 1.8$, $T_{\max} = 2\sqrt{(\pi/2)}$ and $u' = 1$, so that gravity is included in the determination of the crossing time only if $g\tau_r > 2.79$. The main effects are modeled well. For the case when $g = 0.1$, the effect of gravity on the crossing time is neglected for the range of particle relaxation time considered and the increased dispersion for large St predicted by Reeks' theory is also found in the simulations. For $g = 1$ and $g = 10$, inclusion of the effects of gravity has a clearly beneficial effect on the predictions of the dispersion coefficient when compared with the predictions when gravity is neglected and good agreement is observed to hold between numerical and analytical results over a wide range of conditions.

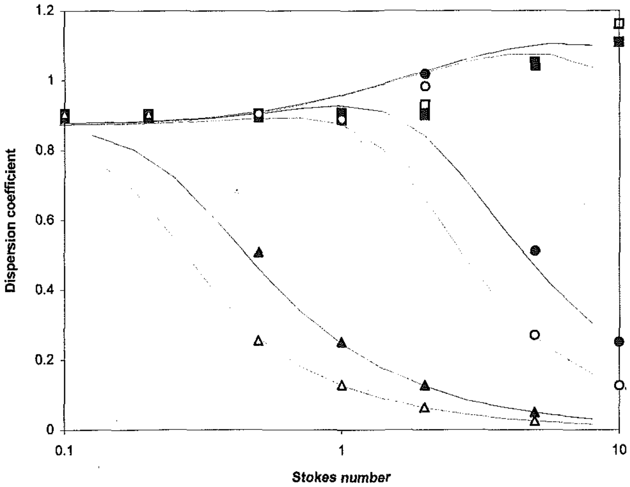

Fig. 4 Dispersion coefficients-integrated model. Key: EIM: g = .1, ■-D_1, □-D_2, g = 1, ●-D_1, ○-D_2, g = 10, ▲-D_1, △-D_2, ——— D_1, ... D_2. Reeks (1977).

Conclusions

The eddy interaction model of Hutchinson et al. (1971), Gosman and Ioannides (1981) has been developed to account for three major effects observed in particle dispersion experiments, namely the crossing trajectories, inertia, and continuity effects. The following conclusions can be drawn:

1. The consistency of the Eulerian integral length scales Λ_f and Λ_g is ensured by choosing $L_e = 2\Lambda_f$ and specifying different interaction times in different co-ordinate directions. The consistency of the Lagrangian time scales τ_L is ensured by choosing $T_e = 2\tau_L$. The consistency of the Eulerian integral time scales is ensured by the correct choice of $T_{\max}$ for a given value of β. When β is small, $T_{\max} = 2\tau_E$.
2. The crossing trajectories effect can be modeled successfully by ensuring the correct choice of eddy length L_e and fluid particle interaction time T_e. Comparisons with other analytical results are improved by accounting for the influence of gravity on the time taken for a particle to cross an eddy.
3. The inertia effect can be modelled by allowing $T_{\max}$, the maximum interaction time for solid particles, to exceed T_e.
4. The continuity effect is accounted for by specifying different interaction times in different coordinate directions.
5. An integrated model which allows for all of the three above effects has been proposed. Good agreement with Reeks' (1977) analytical theory is achieved.

Acknowledgment

The financial support of the UK EPSRC under grant GR/H42 437 is gratefully acknowledged.

References

Berlemont, A., Desjonqueres, P., and Gouesbet, G., 1990, "Particle Lagrangian Simulation in Turbulent Flows," *International Journal of Multiphase Flow*, Vol. 16, pp. 19–34.

Csanady, G. T., 1963, "Turbulent Diffusion of Heavy Particles in the Atmosphere," *Journal of the Atmospheric Sciences*, Vol. 20, p. 201.

Gosman, A. D., and Ioannides, E., 1981, "Aspects of Computer Simulation of Liquid-Fuelled Combustors," *Paper AIAA-81-0323, AIAA 19th Aerospace Sciences Meeting*, St. Louis, MO.

Graham, D. I., 1996, "On the Inertia Effect in Eddy Inter-action Models," *Int. J. Multiphase Flow*, Vol. 22, pp. 177–184.

Graham, D. I. and James, P. W., 1996, "Turbulent Dispersion of Particles using Eddy Interaction Models," *International Journal of Multiphase Flow*, Vol. 22, 157–175.

Hinze, J. O., 1975, *Turbulence*, McGraw Hill, New York.

Huang, X., Stock, D. E., and Wang, L-P., 1993, "Using the Monte-Carlo Method to Simulate Two-Dimensional Heavy Particle Dispersion," *Proc. Third Int. Symposium on Numerical Methods in Multiphase Flows*, pp. 153–160.

Hutchinson, P., Hewitt, G. F., and Dukler, A. E., 1971, "Deposition of Liquid or Solid Dispersions From Turbulent Gas Streams: a Stochastic Model." *Chemical Engineering Science*, Vol. 26, pp. 419–439.

Lu, Q. Q., Fontaine, J. R. and Aubertin, G., 1993, "A Lagrangian Model for Solid Particles in Turbulent Flows," *International Journal of Multiphase Flow*, Vol. 19(2), pp. 347–367.

Maxey, M. R., 1987, "The Gravitational Settling of Aerosol Particles in Homogeneous Turbulence and Random Flow Fields," *Journal of Fluid Mechanics*, Vol. 174, pp. 441–465.

Pozorski, J., and Minier, J-P., 1995, "The PDF Method for Lagrangian Two-Phase Flow Simulations," In *Gas-Particle Flows*, eds D. E. Stock, M. W. Reeks, Y. Tsuji, E. E. Michaelides and M. Gautam, ASME FED Vol. 228, pp. 249–255.

Reeks, M. W., 1977, "On the Dispersion of Small Particles Suspended in an Isotropic Turbulent Fluid," *Journal of Fluid Mechanics*, Vol. 83(2), pp. 529–546.

Shuen, J. S., Solomon, A. S. P., Zhang, Q-F., and Faeth, G. M., 1984, "Structure of Particle-Laden Jets: Measurements and Predictions," *AIAA report AIAA-84-0038, Presented at AIAA 22nd Aerospace Sciences Mtg.*, Reno, Nevada, U.S.A.

Wells, M. R. and Stock, D. E., 1983, "The Effects of Crossing Trajectories on the Dispersion of Particles in a Turbulent Flow," *Journal of Fluid Mechanics*, Vol. 136, pp. 31–62.

Yudine, M. I., 1959, "Physical Considerations on Heavy-Particle Diffusion," *Advances in Geophysics*, Vol. 6, pp. 185–191.

Stability of a Compressible Laminar Wall-Jet With Heat Transfer

O. Likhachev
Research Associate Professor,
Aerospace and Mechanical
Engineering Department,
University of Arizona,
Tucson, AZ 85721

A. Tumin
Associate Professor,
Fluid Mechanics and Heat
Transfer Department,
Tel-Aviv University,
Tel-Aviv,
Israel

The flow of a plane, laminar, subsonic perfect gas wall jet with heat transfer through the wall was investigated theoretically. For the case under consideration the entire surface was maintained at a constant temperature which differed from the temperature of the ambient gas. The velocity and temperature distribution across the flow were calculated for a variety of temperature differences between the ambient gas and the surface. The boundary layer equations representing these flows were solved by using the Illingworth-Stewartson transformation, thus extending the classical Glauert's solution to a thermally non-uniform flow. The effects of heat transfer on the linear stability characteristics of the wall jet were assessed by making the local parallel flow approximation. Two kinds of unstable eigenmodes coexisting at moderate Reynolds numbers are significantly affected by the heat transfer. The influence of cooling or heating on the stability of the flow was expected in view of the experience accumulated in incompressible boundary layers, i.e. heating destabilizes and cooling stabilizes the flows. Cooling of the wall affects the small scale disturbances more profoundly, contrary to the results obtained for the large scale disturbances.

Introduction

Wall jets are used extensively for boundary layer control and film-cooling. Although the flow in these applications is mostly turbulent, laminar wall-jets are often investigated for reasons of clarity and relative ease of analysis. The present theoretical investigation represents such a case. Two kinds of linearly unstable modes coexist in the disturbed isothermal laminar wall-jet at moderate Reynolds numbers based upon the local scales of the mean flow (Chun and Schwartz, 1967; Tsuji et al., 1977; Mele et al., 1986; Cohen et al., 1992; Zhou et al., 1992). One is associated with a boundary layer instability occurring in the vicinity of the wall, and the other with the inviscid, inflectional instability prevailing in the outer part of the flow. The self similar solution for the incompressible and isothermal wall jet (Glauert, 1956) was used in the formulation of the steady flow problem, while the Orr-Sommerfeld equation provided the basis for the linear stability analysis. The more complicated problem of a wall-jet flow stability over convex walls was considered by Floryan (1989). One of the goals of the present investigation was to obtain a self-similar solution for a laminar compressible wall jet which transports heat between the ambient gas and the surface and to calculate the effects of the temperature gradient on the linear stability of the mean flow. The stability characteristics of compressible wall-jets were never analyzed in detail previously.

Self-Similar Mean Flow

Consider a laminar, plane thermal jet of a perfect gas emerging horizontally from a long narrow slit of width h at $x = 0$ along a rigid flat surface $y = 0$ and spreading into a quiescent external gas of constant temperature T_0. The use of the boundary-layer approximation reduces the governing equations to the following form:

$$\frac{\partial \rho u}{\partial x} + \frac{\partial \rho v}{\partial y} = 0 \qquad (1a)$$

$$\rho u \frac{\partial u}{\partial x} + \rho v \frac{\partial u}{\partial y} = \frac{\partial}{\partial y}\left(\mu \frac{\partial u}{\partial y}\right) \qquad (1b)$$

$$\frac{\partial p}{\partial y} = 0 \qquad (1c)$$

$$\rho u \frac{\partial H}{\partial x} + \rho v \frac{\partial H}{\partial y} = \frac{\partial}{\partial y}\left(\frac{\mu}{\mathrm{Pr}} \frac{\partial H}{\partial y}\right) + \frac{\partial}{\partial y}\left(\left(1 - \frac{1}{\mathrm{Pr}}\right) \mu \frac{\partial}{\partial y} \frac{u^2}{2}\right) \qquad (1d)$$

where u and v denote the velocity components in the x and y directions respectively, p the pressure, H the total energy per unit mass of gas, ρ the density and μ the dynamic viscosity. The Prandtl number is defined as $\mathrm{Pr} = \mu/\kappa c_p$, where κ is the thermal conductivity and c_p is the specific heat at constant pressure. For the perfect gas under consideration the equation of state is:

$$p = (c_p - c_v)\rho T. \qquad (2)$$

Considering that under most circumstances the specific heats c_p and c_v are constant the dimensionless total energy can be expressed as

$$\bar{H} = \bar{T} + \frac{(\gamma - 1)}{2} M_0^2 \bar{u}^2 \qquad (3)$$

where the bar denotes dimensionless variables and $\gamma = c_p/c_v$ and the enthalpy of the surrounding gas $I_0 = c_p T_0$ was chosen as the appropriate energy scale. The Mach number $M_0 = u_m/a_0$

Contributed by the Fluids Engineering Division for publication in the JOURNAL OF FLUIDS ENGINEERING. Manuscript received by the Fluids Engineering Division August 10, 1995; revised manuscript received August 12, 1996. Associate Technical Editor: W. S. Saric.

is defined by the ratio between the characteristic velocity $u_m(x)$ (defined below) and the speed of sound waves in the surrounding gas a_0 whose undisturbed density and viscosity are denoted by ρ_0 and μ_0 respectively. Equations (1) and (2) and the absence of an external pressure gradient provide another important relationship:

$$\rho T = \rho_0 T_0 = \text{const.} \tag{4}$$

The boundary conditions stemming from the geometry are:

$$\begin{aligned} y = 0:&\quad u = v = 0; \\ y \to \infty:&\quad u \to 0, \quad T \to T_0. \end{aligned} \tag{5}$$

Additional boundary conditions for the energy equation are specified by the condition of heat transfer through the wall.

By limiting the proposed solutions to the case where the Prandtl number is equal to 1, the last term on the right-hand side of (1*d*) can be eliminated, thereby creating the possibility of a self-similar solution of Eq. (1*d*) as will be shown below.

The continuity Eq. (1*a*) enables one to introduce a Stokes stream function Ψ such that:

$$\begin{aligned} \frac{\partial \Psi}{\partial y} &= \rho u \\ \frac{\partial \Psi}{\partial x} &= -\rho v. \end{aligned} \tag{6}$$

In an attempt to broaden the self-similar solution introduced by Glauert (1956) for the incompressible and isothermal case, we considered the following possibility: the velocity $(u, v) \propto x^a$, the jet thickness $L \propto x^b$. We introduced dimensionless variables by writing

$$\begin{aligned} (u, v) &= U(\hat{u}, \hat{v}) \\ \Psi &= \mu_0 \bar{\Psi} \end{aligned} \tag{7}$$

and we used a coordinate transformation

$$\begin{aligned} x &= \frac{\mu_0 \bar{x}}{\rho_0 U} \\ \eta &= \frac{(1-b)U}{\mu_0 \bar{x}^b} \int_0^y \rho dy \end{aligned} \tag{8}$$

(the velocity scale U will be defined in Eq. (12)). This transformation, which is similar to Illingworth-Stewartson transformation for boundary layer flow, allows one to decouple the hydrodynamic and thermal problems reducing the transformed equations to the isothermal form provided the viscosity coefficient is proportional to the temperature.

The dimensionless stream function $\bar{\Psi}$ was chosen to have the same form as Glauert's:

$$\bar{\Psi} = \bar{x}^{(1-b)} f(\eta) \tag{9}$$

thus, by substituting (8) and (9) into the x-momentum, Eq. (1*b*), one gets:

$$(Cf'')' + ff'' + \alpha(f')^2 = 0 \tag{10}$$

where derivatives with respect to η are denoted by primes, $C = \rho\mu/\rho_0\mu_0$-commonly referred to as the Chapman–Rubesin factor and,

$$\alpha = \frac{2b-1}{1-b}. \tag{10a}$$

The boundary conditions are:

$$\begin{aligned} \eta = 0:&\quad f = f' = 0 \\ \eta \to \infty&\quad f' \to 0. \end{aligned} \tag{11}$$

Taking into account (4) one gets that $C = 1$ whenever $\mu \propto T$; Eq. (10) thus becomes identical to the isothermal case considered by Glauert (1956). This equation has a nontrivial solution satisfying the boundary conditions (11) only when $\alpha = 2$, from which it follows that $a = -\frac{1}{2}$, $b = \frac{3}{4}$. Glauert's integral constraint, F, by being an invariant of the flow, enables one to define a characteristic velocity for this special case:

$$F = \int_0^\infty \rho u \left(\int_y^\infty \rho u^2 dy \right) dy = \left(\frac{\mu_0}{\rho_0} \right)^2 \frac{U}{40} = \text{const.} \tag{12}$$

In the particular case where the surface temperature is kept at a constant level T_w, after taking into account all restrictions mentioned above, the energy Eq. (1*d*) may be written in a self-similar form:

$$G'' + f(\eta)G' = 0 \tag{13}$$

which is subject to the boundary conditions

$$\begin{aligned} \eta = 0:&\quad G = T_w \\ \eta \to \infty:&\quad G \to 1. \end{aligned} \tag{14}$$

The solution of the Eq. (13) may be written as

$$\begin{aligned} G(\eta) &= T_w + \frac{1 - T_w}{D} \int_0^\eta \exp\left[-\int_0^\eta f(\eta')d\eta' \right] d\eta \\ D &= \int_0^\infty \exp\left[-\int_0^\eta f(\eta')d\eta' \right] d\eta. \end{aligned} \tag{15}$$

Since the self-similar solution of Eq. (1) is based on a transformation of variables which extends Glauert's solution to non-isothermal wall-jets, an inverse coordinate transformation is required in order to get the velocity and temperature distributions in the physical space:

$$y = \frac{4\mu_0}{\rho_0 U} \times \bar{x}^{3/4} \int_0^\eta \left[G(\eta) - \frac{\gamma - 1}{2} M_0^2(\bar{x}) \left(\frac{f'(\eta)}{f'_{\max}} \right)^2 \right] d\eta. \tag{16}$$

The velocity and length scales chosen by Glauert (1956) were based on the conservation of the outer momentum flux F (defined in (12)) leading to $U = 40\, F\rho_0^2/\mu_0^2$ and $L = \mu_0/(\rho_0 U)$. The traditional velocity and length scales used in the linear stability analysis are simpler because the analysis assumes that the steady flow is a priori determined. Conforming with the convention, we also chose the maximum velocity in the wall-jet, $u_m(\bar{x})$, the outer transverse coordinate at which this velocity was reduced to ½ of its value, $Y_{m/2}$, and the temperature of ambient gas, T_0, as being the appropriate scales of the problem. The calculated velocity and temperature distributions for different values of wall temperature T_w and for local Mach number $M_0(\bar{x}) = 0.8$ and Prandtl number $\text{Pr} = 1$ are plotted in Fig. 1(*a*, *b*). The results indicate that a hot surface enhances the lateral rate of spread of the wall jet for a prescribed momentum loss. This implies that a given loss of momentum causes a larger deceleration for a lower density fluid.

Stability Analysis

Method of Solution. Stability analysis is carried out by assuming that the flow is locally parallel and that the amplitude of the perturbation is small. These assumptions allow us to describe the disturbances in terms of the usual linearized Navier-Stokes equations provided the wavelength of the perturbation is small relative to the longitudinal scale of the nonuniformity of the basic flow.

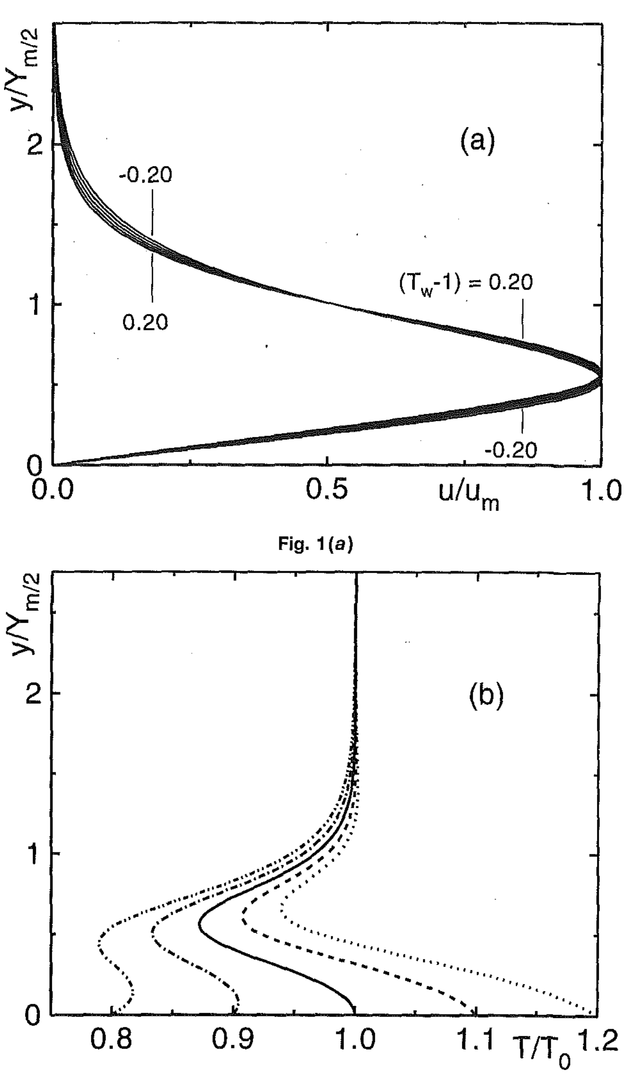

Fig. 1(*a*)

Fig. 1(*b*)

Fig. 1 Dimensionless profiles of velocity (*a*) and temperature (*b*) for different values of wall temperature

When the disturbances are two-dimensional there are only two unknown velocity components, $\tilde{u}(x, y, t)$, $\tilde{v}(x, y, t)$, a pressure disturbance $\tilde{p}(x, y, t)$ and temperature disturbance $\tilde{\theta}(x, y, t)$. The form of the particular solution of linearized Navier-Stokes equations is assumed to be

$$\tilde{q}(x, y, t) = A_q(x) \cdot \hat{q}(x, y) \cdot \exp[i(\alpha x - \omega t)] \quad (17)$$

where $A_q(x)$ are the proper local scales of velocity, pressure and temperature introduced in the preceding chapter; $\hat{q}(x, y)$ belongs to the eigenvector of solutions of the linearized Navier-Stokes equations with assumption of local parallel flow; α is complex while ω is the real frequency.

Making use of linearized equations (1) and the particular form of solution (17) and the local parallel assumption one can get the following set of six ordinary differential equations of first order:

$$\frac{d\vec{Z}}{dy} = H_s \vec{Z} \quad (18)$$

where H_s is a 6×6 matrix; $\vec{Z}$ is a column-vector with six components: $Z_1 = \hat{u}$, $Z_2 = \partial \hat{u}/\partial y$, $Z_3 = \hat{v}$, $Z_4 = \hat{p}$, $Z_5 = \hat{\theta}$, $Z_6 = \partial \hat{\theta}/\partial y$.

The set of equations (18) must be solved subject to the boundary conditions:

$$y = 0: \quad Z_1 = Z_3 = Z_5 = 0$$

$$y \to \infty: \quad |Z_j| \to 0, \quad (j = 1, \ldots, 6). \quad (19)$$

The fourth-order Runge-Kutta method and Gram-Schmidt orthogonalization procedure for linear independent particular solutions were used to get numerical solutions of Eqs. (18). An eigenvalue α has been found by the "shooting procedure" which satisfies the boundary conditions (19).

The Stability of a Thermal Wall-Jet Over an Isothermal Plate. The curves of neutral stability ($\alpha_i = 0$) are shown in Fig. 2(*a*, *b*), where ω is plotted versus $\mathrm{Re} = u_m Y_{m/2}/\nu$ for different values of the parameter $\Theta = (T_w - 1)$. The results of the computations for the cold surface $\Theta \leq 0$ are shown in figure 2(*a*) while the results for $\Theta \geq 0$ are plotted in Fig. 2(*b*). At low Re there is one unstable mode which at high values of ω (i.e. near the upper branch of the neutral stability diagram) possesses a maximum amplitude of the streamwise velocity components, $|\tilde{u}|_{\max}$, near the surface and is thus dominated by the conditions near the wall. The instabilities near the lower branch of the neutral stability curve are dominated by the inflection point in the outer part of the velocity profile and have their

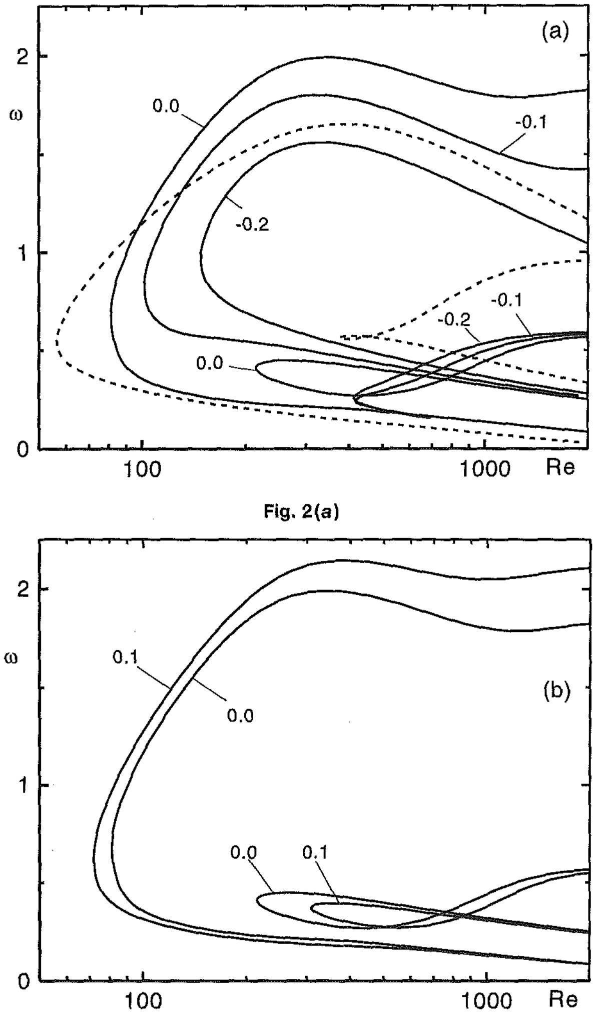

Fig. 2(*a*)

Fig. 2(*b*)

Fig. 2 Neutral diagrams at different wall temperature $\Theta = (T_w - 1)$ at $M_0 = 0.8$: (*a*) for cold surface $\Theta < 0$; (*b*) for $\Theta > 0$. Dashed curve corresponds to Glauert's solution

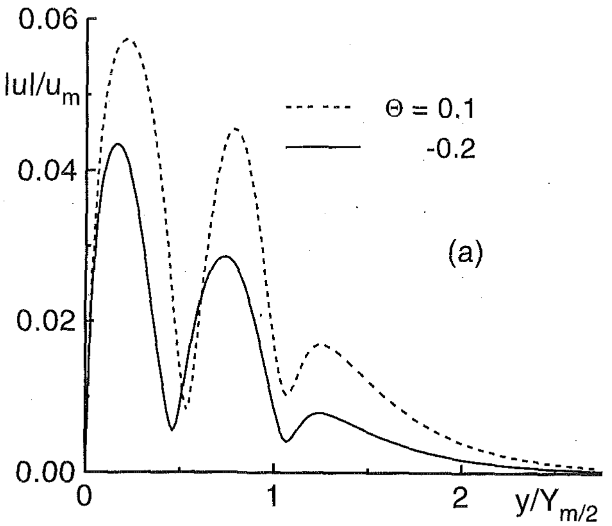

Fig. 3(*a*)

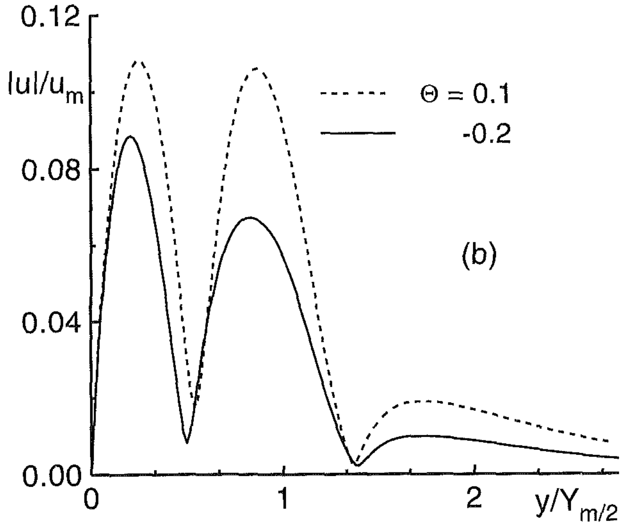

Fig. 3(*b*)

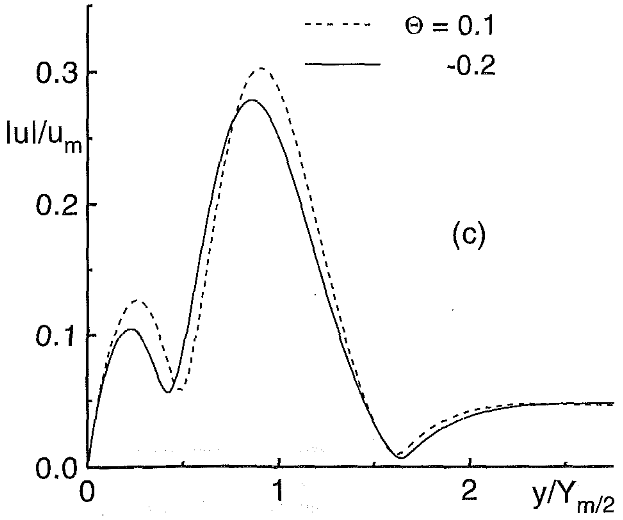

Fig. 3(*c*)

Fig. 3 Distribution of the streamwise velocity component for the inner mode: (*a*) $\omega = 1.5$ and (*b*) $\omega = 0.5$; and for the outer mode: (*c*) $\omega = 0.2$ at Re = 500; $M_0 = 0.8$

maximum amplitude in that region. All amplitude distributions are affected by viscosity due to the no-slip condition at the surface.

At high Reynolds numbers (e.g., Re > 400), the wall-jet possesses two different unstable modes which overlap in the low-range of the unstable frequencies. The region of overlap depends mostly on Re but is also dependent on the temperature of the surface; a cold surface shifts the region of overlap towards higher values of ω. The amplitude distributions of the streamwise perturbations across the flow at moderate Reynolds numbers are shown in figure 3(*a*, *b*, *c*) which reflect the dependence of the two modes on viscosity. The outer mode, which is mostly inviscid, contains a secondary peak in amplitude close to the wall while the inner mode contains a secondary peak close to the inflection point. The second unstable mode starts at $\mathrm{Re}_{\mathrm{crit.II}} \approx 400$ regardless of cooling. A cool surface has a strong effect on the upper branch of the neutral stability diagram dampening most of the high frequency perturbations. It has little effect on the second unstable mode (ut supra the outer mode) and on the second critical Re which remains around $\mathrm{Re}_{\mathrm{crit.II}} \approx 400$ provided $\Theta \leq 0$. At $\Theta > -0.1$ there is an inner stable region which is completely contained within the unstable zone. The size of this region in the Re − ω plane increases with decreasing Θ and for $\Theta \approx -0.1$ joins the stable zone existing below the lower branch of the main neutral curve. The existence of a small, stable, inner-region in the isothermal wall jet was reported pre-

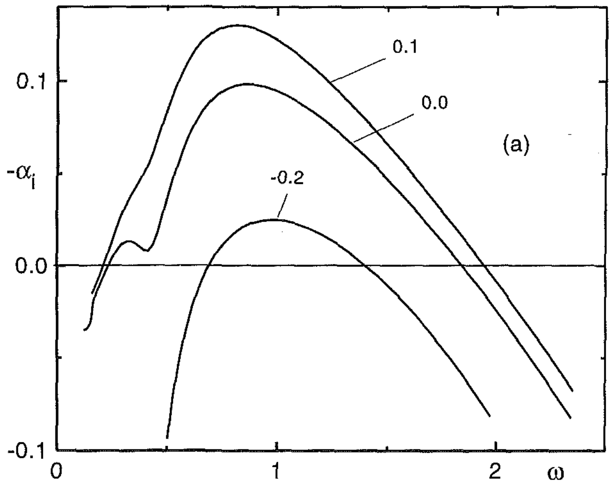

Fig. 4(*a*)

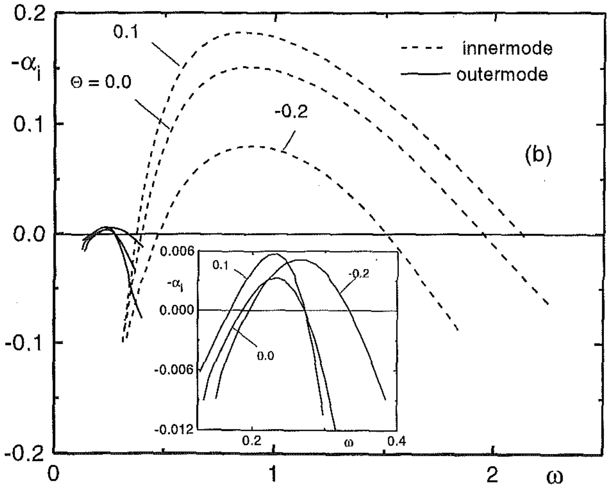

Fig. 4(*b*)

Fig. 4 The amplification rates of the disturbances for different values Θ at $M_0 = 0.8$, Pr = 1: (*a*) Re = 200; (*b*) Re = 500

viously by several authors (Chun and Schwartz, 1967; Tsuji et al., 1977; Mele et al., 1986; Cohen et al., 1992; Zhou et al., 1992); it is restricted to a narrow zone in figure 2(*a*). Larger inner stable zones exist at $\Theta \geq -0.1$ for the case under consideration and the size of these zones of linear stability of the compressible wall-jet decreases with increasing Θ.

The neutral stability diagrams for the flow over a heated wall (Fig. 2(*b*)) are similar to the ones in the isothermal case except that the upper branches of the inner neutrally stable modes are shifted toward higher frequency while the outer mode is little affected by the heating. The broadening of the unstable region to higher frequencies at moderately low Re implies that heating destabilizes the wall layer without affecting the outer flow. The critical Reynolds number is altered by the heating because it is dominated by the viscous mode.

The amplification rates of the disturbances are shown in Fig. 4(*a*, *b*) for different values of Θ, for two Reynolds numbers: Re = 200 and 500. At the low Reynolds number there is just one unstable region having two peaks of the amplification rate, provided $0 > \Theta > -0.1$, which belong to the different physical mechanisms of hydrodynamic instability. Both the high and low frequency extents of the amplified region and their rate of amplification are significantly affected by Θ. One may thus deduce that the amplification of both the large-scale and small-scale perturbations is very sensitive to the temperature differential between the ambient gas and the surface at low Reynolds numbers. At larger Re the inner mode is affected by heat transfer more profoundly, though it too has little effect on the outer mode.

Conclusions

The present analysis indicates that the velocity distribution in a compressible wall jet and its sensitivity to small disturbances are affected by the temperature differential across it. Two kinds of unstable eigenmodes are present in the flow: one, associated with the outer flow, resembles a free, shear-layer instability; the other (associated with the inner flow region) resembles a boundary layer instability. These modes cannot, however, be separated in a clear way since both of them are affected by the no-slip condition at the surface. The effect of cooling and heating the surface are felt first in the inner layer where the wall jet is sensitive to the high frequency, periodic perturbation. One may state that heating destabilizes the region near the surface while cooling stabilizes it. On the other hand, the large-scale perturbations associated with the outer flow are almost unaffected by heat transfer at moderate Reynolds numbers.

Acknowledgments

The authors are grateful to Prof. I. Wygnanski for formulation of the problem and for useful discussion of the results. This work was supported in part by Guaestela scholarship of Rashi foundation (for A. Tumin) at Tel-Aviv University and in part by grants from AFOSR (contract number AFOSR-94-1-0131) and from DOE (contract number DE-FG03-93).

References

Chun, D. H., and Schwarz, W. H., 1967, "Stability of the Plane Incompressible Viscous Wall Jet Subjected to Small Disturbances," *Physics of Fluids*, Vol. 10, pp. 911–915.

Cohen, J., Amitay, M., and Bayly, B. J., 1992, "Laminar-Turbulent Transition of a Wall Jet Flows Subjected to Blowing and Suction," *Physics of Fluids A*, Vol. 4, pp. 283–289.

Floryan, J. M., 1989, "Görtler Instability of Wall Jets," *AIAA Journal*, Vol. 27, pp. 112–114.

Glauert, M. B., 1956, "The Wall Jet," *Journal of Fluid Mechanics*, Vol. 1, pp. 625–643.

Mele, P., Moganti, M., Scibila, M. F., and Lasek, A., 1986, "Behaviour of Wall Jet in Laminar-to Turbulent Transition," *AIAA Journal*, Vol. 24, pp. 938–939.

Tsuji, Y., Morikawa, Y., Nagatani, T. and Sakou, M., 1977, "The Stability of a Two-Dimensional Wall Jet," *Aeronautical Quarterly*. Vol. XXVIII, pp. 235–246.

Zhou, M. D., Rothstein, J., and Wygnanski, I., 1992, "On the Hydrodynamic Stability of the Wall Jet," *Proceedings, 11th Australasian Fluid Mechanics Conference*, M. R. Davis and G. J. Walker, eds., University of Tasmania, pp. 407–410.

Pulsatile Laminar Flow in a Viscoelastic System

A. Lardigue
Postdoctoral.

S. Bennis
Professor.

Ecole de Technologie Supérieure,
4750, avenue Henri Julien,
Montréal, Quebec, Canada,
H2T 2C8

This work involves the study of Newtonian transitory and permanent flow regimes in a rigid tube that has been extended to include a viscoelastic enclosure. Variable pressures are applied at the free end of the tube. The problem is solved analytically by direct integration of the Navier-Stokes equations. In addition to the nondimensional parameter γ_1 introduced previously by other authors, we found a new nondimensional parameter γ_2 which also governs the fluid flow. This parameter may be interpreted as the ratio of the and the membrane viscosity force to the fluid friction force. The effects of small values of the membrane viscosity only attenuate the oscillating effect when inertia dominates on fluid friction force. When the membrane viscosity is important, however, it may cancel out the inertial effect resulting in a damped aperiodic flow. When the fluid friction force predominates, the membrane viscosity slows down an already damped aperiodic flow. All these types of flow are well characterized by well defined intervalls of variation of γ_1 and γ_2. In addition to the transitory flow regime, we also consider permanent pulsatile flow. An experimental device makes it possible to validate the theoretical assertions in the particular case of a pulsed pressure.

1 Introduction

Interest is currently growing in transitory flow regimes in cylindrical tubes for industrial applications, where the possibilities are as varied as the end conditions permit. Oscillatory flows in circular pipes were analyzed by Womersley (1955), Atabek and Chang (1961). Great attention has been given to Atabek's solution formulas of velocity profiles and pressure distributions, as they have been quoted in the literature such as McDonald (1974) and Fung (1981). Their analysis was based on linearization of the Navier-Stokes equations. Non-newtonian fluids and viscoelastic materials have already been carried out by Briley and McDonald (1984), Barnes et al. (1971), and Obrecht (1976). In particular, Lieber and Giddens (1987) considered the treatment of velocity disturbances in pulsatile flow but without taking into account the elastic enclosure. More recently, Giddens and Nerem (1988) have studied flow in the cardiovascular system. For a fluid mechanician, this means solving the three-dimensional Navier-Stokes equations for a system of viscoelastic tubes and enclosures.

In the work described here, the transitory and permanent flow regimes of viscous fluids in a rigid horizontal tube are studied. One of the ends of the tube is connected to a viscoelastic enclosure and the other is subjected to a variable pressure. One of the important applications of the present work is the extra-body circulation. In such an operation, the cardiac and pulmonary functions are stopped. Then a pump and an oxygenator fulfil the functions of the heart and the lung. To represent this system, two main modifications are introduced in the work of Bennis (1993), who focused on a single elastic enclosure and one step change in pressure: (i) the first one consists in using a viscoelastic enclosure that represents faithfully the behavior of the human body; (ii) the second one consists in adding to the step change a pulsed pressure that represents the permanent regime.

2 The Problem and Its Mathematical Representation

The system under study consists of a rigid tube of length L and radius a (Fig. 1). One end of the tube is sealed by a flexible enclosure, the membrane of which displays viscoelastic behavior of the Kelvin Voigt type, such that:

$$\Delta P = K_1 \Delta V + K_2 \frac{d(\Delta V)}{dt} \qquad (1)$$

where ΔP and ΔV represent the change in pressure and in volume, respectively, in the flexible enclosure. K_1 and K_2 are related to the modulus of elasticity and the coefficient of viscosity of the enclosure membrane, respectively. The pressure applied at the free end of the tube is given by:

$$P = P_0 f(t) \qquad (2)$$

where $f(t)$ is some function of time. To resolve the problem, we assume that:

(i) The fluid, is Newtonian, incompressible with kinematic viscosity ν and density ρ;
(ii) The flow is laminar and parallel;
(iii) The end effects are negligible.

A similar study based on the Laplace transform presented by Bennis (1993) shows that the velocity profile is given by the following equation:

$$w(r, t) = 16\alpha \sum_{i=1}^{\infty} \frac{\chi_i^2}{\Phi(\chi_i)} \frac{J_0(r/a\chi_i) - J_0(\chi_i)}{J_0(\chi_i)} \times \int_0^t f(t - t') e^{-\chi_i^2 t' \nu / a^2} dt' \quad \text{with} \quad \alpha = \frac{P_0}{4\rho L}$$

and

$$\Phi(\chi_i) = \frac{\chi_i^8 - 2\gamma_2\chi_i^6 + (2\gamma_1 + 8\gamma_2 + \gamma_2^2)\chi_i^4 - (12\gamma_1 + 2\gamma_1\gamma_2)\chi_i^2 + \gamma_1^2}{\gamma_1 - \gamma_2\chi_i^2} \qquad (3)$$

$w(r, t)$ is the longitudinal fluid velocity component
r is the radial distance from the tube's center
t is the time and K is the stiffness coefficient of the enclosure

---

Contributed by the Fluids Engineering Division for publication in the JOURNAL OF FLUIDS ENGINEERING. Manuscript received by the Fluids Engineering Division March 16, 1995; revised manuscript received June 3, 1996. Associate Technical Editor: J. A. C. Humphrey.

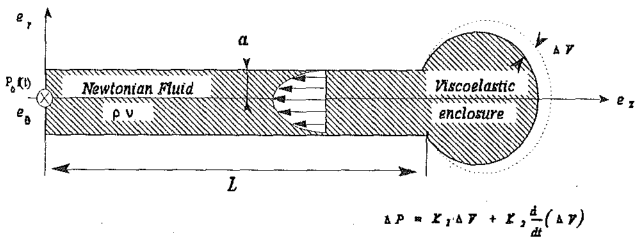

Fig. 1 System under study

The χ_i represent the roots of the following equation:

$$\gamma_1 = \varphi(\chi, \gamma_2) = \frac{\chi^4 J_0(\chi)}{J_2(\chi)} + \gamma_2 \chi^2 \quad \text{with}$$

$$\gamma_1 = \frac{\pi a^6 K_1}{\rho v^2 L}; \quad \gamma_2 = \frac{\pi a^4 K_2}{\rho v L} \tag{4}$$

γ_1 represents the ratio of the inertial forces to the forces due to fluid friction (viscosity forces). γ_2 represents the ratio of the fluid friction forces of the membrane to the fluid friction forces of the fluid (ratio of the viscosity of the membrane to the viscosity of the fluid).

To obtain the numerical values of the velocity, we must solve Eq. (4), the roots of which depend on the two nondimensional parameters γ_1 and γ_2.

To solve Eq. (4), three formula manipulation programs are used: PC Matlab, Macsyma, and Matematica. In the simplest case, the algorithm uses Newton's method, and in the other cases the algorithm, which was created by T. Dekker, uses a combination of bisection, secant and inverse quadratic interpolation methods. An Algol 60 version, with some improvements, is given in Brent (1973). A Fortran version is given in Forsythe (1976).

In the case of flow responding to a step change in pressure ($f(t) = 1$), relation (3) becomes:

$$w(r, t) = 16\beta \sum_{i=1}^{\infty} \frac{1}{\phi(\chi_i)} \frac{J_o(r/a\chi_i) - J_o(\chi_i)}{J_o(\chi_i)} e^{-\chi_i^2 t\nu/a^2}$$

$$\text{with} \quad \beta = \frac{a^2 P_0}{4\rho\nu L} \tag{5}$$

It can be easily shown that under these conditions the difference in pressure between the upstream and downstream ends of the tube is written in the form:

$$\frac{\Delta P_0(t)}{P_0} = -4 \sum_{i=1}^{\infty} \frac{\chi_i^2}{\phi(\chi_i)} e^{-\chi_i^2 t\nu/a^2} \tag{6}$$

In the case of flow subjected to a pulsed pressure consisting in the superposition of a series of pressure sine curves on a step change in pressure; P is expressed by:

$$P = P_0 f(t) = P_0(1 + \epsilon \cos(\omega t + \theta)) \tag{7}$$

Evaluating the integral of relation (3), using integration-by-parts, the expression for the velocity then becomes:

$$w(r, t) = 16\beta \sum_{i=1}^{\infty} \frac{1}{\phi(\chi_i)} \frac{J_0(r/a\chi_i) - J_0(\chi_i)}{J_0(\chi_i)}$$

$$\times ((1 + \epsilon \cos(\theta - \psi_i) e^{-\chi_i^2 t\nu/a^2} + \epsilon \sin(\omega t + \theta - \psi_i))$$

with

$$\tan(\psi_i) = \frac{\omega a^2/v}{\chi_i^2} \tag{8}$$

where ψ_i represents the phase shift caused by each root χ_i. In steady state condition, Eq. (8) simplifies to that of Womersley (1955) and Milnor (1982).

It can be easily shown that under these conditions the difference in pressure between the upstream and downstream ends of the tube is written in the form:

$$\frac{\Delta P_0(t)}{P_0} = -4 \sum_{i=1}^{\infty} \frac{\chi_i^2}{\phi(\chi_i)} ((1 + \epsilon \cos(\theta - \psi_i) e^{-\chi_i^2 t\nu/a^2}$$

$$- 4 \sum_{i=1}^{\infty} \frac{\chi_i^2}{\phi(\chi_i)} (\omega a^2/v) \epsilon \sin(\omega t + \theta - \psi_i)) \tag{9}$$

The first term on the right-hand side of Eq. (9) represents the transitory regime, while the second gives the pressure under a steady-state regime.

3 Experimental Device

The experimental device used by Bennis (1993) has been adapted to the present case, adding a pressure pulsor. Figure 2 displays the various elements of the experimental device: a rigid horizontal tube made of plexiglass of length $L = 4$ m and of diameter $2a = 1.27\ 10^{-2}$ m (1/2 in.) is connected at its downstream end to a plexiglass chamber in the shape of a truncated cone sealed off by an elastic membrane ($K_1 = 6.9108$ N/m^5) and at its upstream end to a plexiglass reservoir. Two openings are made in this container. The first, a large-sized opening, is sealed off by a piston connected to a pulsor. The other, a small-diameter opening, makes it possible to connect the container to a compressed-air booster. Velocity is measured by a laser velocimeter. A Bragg cell is used to detect the direction of the flow. Pressure is measured by means of pressure sensors at both the upstream and downstream ends of the tube.

In the theoretical development, the section of the tube of length L is assumed to belong to a tube of infinite length. In fact, the limitation of the length of the tube introduces a singular loss of head, which is added to other losses caused by irregularities in installation. The corrections made by calculation are found to be long and delicate operations. However, a qualitative study of the losses in head shows that in steady-state regimes flow velocities are weak, and singular head losses can be neglected. In transitory regimes, however, a singular loss of head becomes important, and a fixed damping factor is therefore introduced for the initial experiment and kept constant for all the others.

4 The Influence of Viscoelastic Enclosure (γ_2) on the Type of Flow

For an elastic enclosure ($\gamma_2 = 0$), Bennis (1993) introduced a critical value of γ_1 ($\gamma_{1co} = 11.799745 \pm 10^{-6}$) and showed that if the fluid friction is greater than the inertial force ($\gamma_1 < \gamma_{1co}$), then all the roots of Eq. (4) are real. Thus, during a step change in pressure, the fluid flows in the same direction, resulting in a damped aperiodic flow. By contrast, if the inertial forces predominate ($\gamma_1 > \gamma_{1co}$), then Eq. (4) admits two complex conjugate roots in addition to the infinite number of real

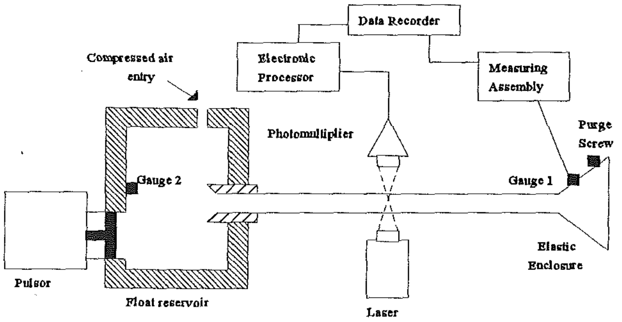

Fig. 2 Experimental device

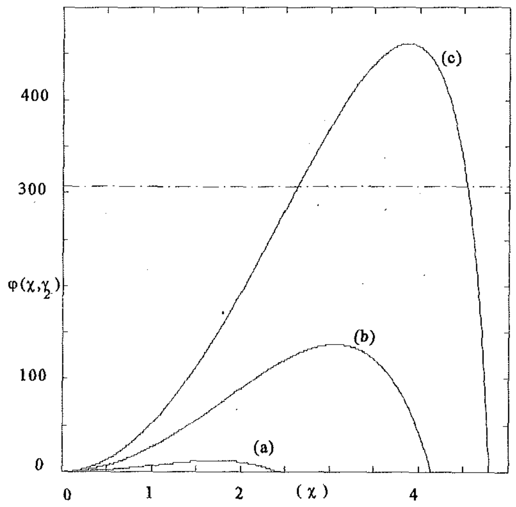

Fig. 3 Evolution of function $\varphi(\chi, \gamma_2)$ (*a*): $\gamma_2 = 0$, (*b*): $\gamma_2 = 20$, (*c*): $\gamma_2 = 45$

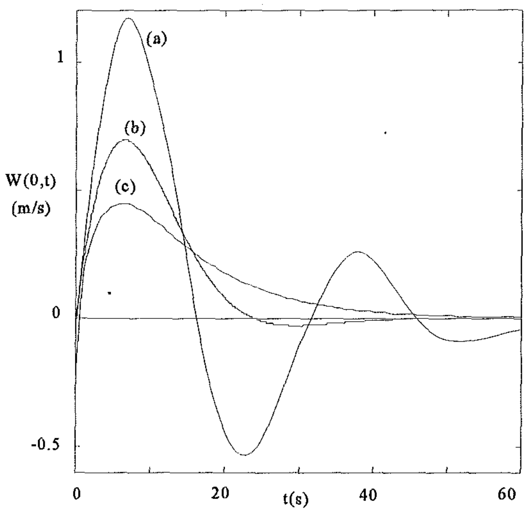

Fig. 4 Velocity at the center of the tube, in the case of a step change in pressure. (*a*): $\gamma_2 = 0$, $\gamma_1 = 307$, $\gamma_{1co} = 11.8$; (*b*): $\gamma_2 = 20$, $\gamma_1 = 307$, $\gamma_{1co} = 137$; (*c*): $\gamma_2 = 45$, $\gamma_1 = 307$, $\gamma_{1co} = 468$

roots. We therefore observe, again for a step change in pressure, a reversal of the flow, resulting in a damped oscillating flow.

In the work described here, the study is generalized to the case of a viscoelastic enclosure ($\gamma_2 \neq 0$). In the following section, we will also develop the case of a pulsed pressure.

We propose to study the influence of γ_2 on this type of flow. If the roots of Eq. (4) are all real, the result is a damped aperiodic flow. If two of the roots are complex, the result is a damped oscillating flow.

$$\varphi(\chi, \gamma_2) = \varphi(\chi, 0) + \gamma_2 \chi^2 \tag{10}$$

The function $\varphi(\chi, \gamma_2)$ is the sum of the function $\varphi(\chi, 0)$, previously considered in the case of an elastic enclosure, and of the term $\gamma_2 \chi^2$. This corrective term, which is due to the viscous character of the membrane, does not modify the way in which the function $\varphi(\chi, \gamma_2)$ works, but only amplifies the value of the relative maximum. We may conclude that $\varphi(\chi, \gamma_2)$ has the same variations and the same asymptotes as $\varphi(\chi, 0)$. It suffices, therefore, to introduce a critical value $\gamma_{1c} > \gamma_{1co}$, a function of γ_2 to render this discussion analogous to the case of the elastic enclosure.

The following example provides an illustration: The case of $\gamma_1 = 307$ is examined for different values of γ_2. A study of the variation of the function $\varphi(\chi, \gamma_2)$ (Fig. 3) shows that for $\gamma_2 = 20$, Eq. (4) admits complex roots (curve b), while for the value $\gamma_2 = 45$, Eq. (4) admits only real roots (curve c). Figure 4 shows the effect of this parameter on the velocity profile at the center of the tube for the same values of γ_2. We note that for an elastic membrane, the viscosity forces are weak in comparison with the inertial forces, resulting in a damped oscillatory flow (curve a). On the other hand, for a membrane with very little viscosity, the viscosity forces are not capable of offsetting the inertial forces. The flow therefore remains damped oscillatory, but with an attenuated frequency (curve b). Finally, for a highly viscous membrane, the viscosity forces of the membrane are added to the viscosity forces of the fluid and cancel out the effects of the inertial forces, resulting in a damped aperiodic flow (curve c).

For an elastic membrane, the theoretical results are validated by experiment. For this, the theoretical loss of head given by equation 6 is compared to the loss of head experimentally by sensor 1 (Fig. 5). The theoretical and experimental results agree well, proving on the one hand that the theory has been validated experimentally and, on the other, that the correction factor for the singular head loss does in fact take this phenomenon into account.

We may conclude that the introduction of the viscous nature of the membrane enhances the fluid friction effects of the system. The effects of small values of membrane viscosity only attenuate the oscillatory effect due to inertia. When these friction forces predominate, however, they cancel out the inertial effect, resulting in a damped aperiodic flow.

5 The Case of Flow Subjected to a Pulsed Pressure

We now propose to study the simultaneous influence of the pulsation ω and the inertia (γ_1) on the mode of flow. In order to do this, we consider a fluid that is highly viscous ($\gamma_1 > \gamma_{1co}$), and whose response to a step change in pressure would be damped aperiodic. Figure 6 gives the evolution of the velocity at the center of the tube for a relatively high pulsation frequency. We find the identical evolution in the case of a step change in pressure (damped aperiodic), but perturbed by a wave of the same frequency as the excitation. Figure 7 (curve a) gives the evolution of the velocity at the center of the tube, this time for a slower pulsation frequency. We note that during the transitory regime, the velocity oscillates. This is explained by the long period of excitation, which is of the same order as the duration of the transitory regime. In addition, the value of the pulsation

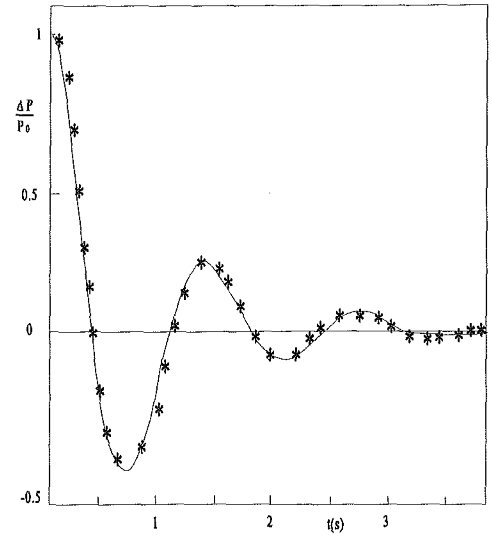

Fig. 5 Comparison with experiment. Water at 25°C, $\gamma_2 = 0$, $\gamma_1 = 59021$, $\gamma_{1co} = 11.8$, —: Theory (Eq. 6) (*): Experiment (sensors 1, 2)

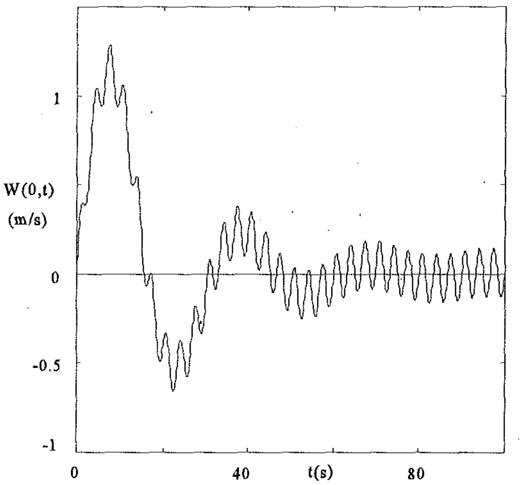

Fig. 6 Evolution of the velocity at the center of the tube. $\gamma_1 = 307$, $\gamma_2 = 0$, $\omega = 2\pi/3$, $f(t) = 1 + \cos(\omega t)$

does not influence the duration of this regime (Fig. 6 and Fig. 7). This is directly linked to the natural frequency of the system. As far as the steady-state regime is concerned, we note (and this applies to all the cases) that the velocity oscillates at the same frequency as the excitation, but with a phase shift (Fig. 7, curves a and b). For an elastic membrane, the theoretical results are validated by experiment.

Pressure sensor 2, located upstream of the conduit, measures the pressure generated by the pulsor. By comparing this with the theoretical form (Eq. (8), the values P_0, ϵ, and θ provided by the pulsor can be deduced. Subsequently, the theoretical loss of head given by Eq. (9) is compared to the loss of head given by experiment with the help of sensors 1 and 2 (Fig. 8). Comparison between the two cases reveals an averaged error of 7 percent.

As far as the amplitude of the oscillations is concerned, we note that the experimental results are in agreement with the theory. A study of the relative errors shows that the mean square of deviations is 0.22 percent relative to the maximal amplitude. We also note that the mean square deviation is 0.43 percent relative to the maximal amplitude.

6 Conclusion

The theoretical study has allowed us to obtain the exact solution to the problem from the direct integration of the Navier Stokes equations. A new nondimensional parameter γ_2 which govens the fluid flow is introduced. This parameter may be interpreted as the ratio of the fluid friction force and the membrane viscosity force to the inertial force. Like γ_1, γ_2 is a function of the geometric data of the system, the physical and mechanical properties of the fluid, the coefficients of elasticity and viscosity and the rheological model attributed to the flexible enclosure involved. The effect of membrane viscosity on the regime of flow has been examined. In addition to the transitory flow regime, the permanent pulsatile flow has also been studied. An experimental device has been designed and built to validate the theoretical assertions.

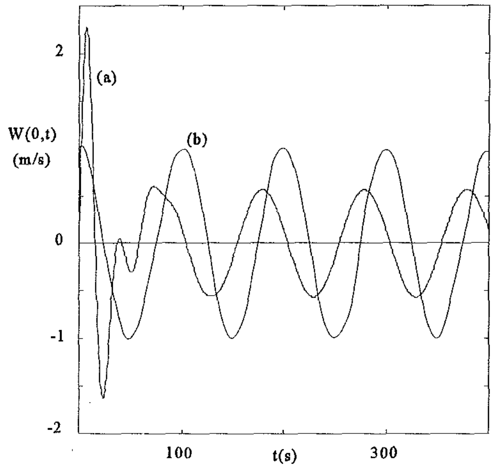

Fig. 7 (*a*): Evolution of the velocity at the center of the tube. (*b*): Evolution the standardized pressure $(P - P_0)/P_0$. $\gamma_1 = 307$, $\gamma_2 = 0$, $\omega = 2\pi/100$, $f(t) = 1 + \cos(\omega t)$

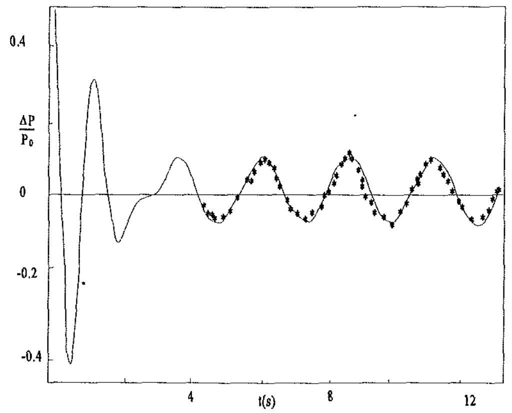

Fig. 8 Comparison with the experiment. Water at 25°C, $\gamma_2 = 0$, $\gamma_1 = 59021$, $\gamma_{1c0} = 11.8$, **—: Theory (Eq. (9)) (*): Experiment (sensors 1, 2)** $P_0 = 1.48$ m, $\epsilon = 0.222$, $\omega = 2.512$, $\theta = 0.5$

Acknowledgments

We wish to thank the reviewers for several useful comments and suggestions. This project was supported by the Natural Sciences and Engineering Council of Canada and the École de technologie supérieure.

References

Atabek, H. B., and Chang, C. C., 1961, "Oscillatory Flow Near the Entry of a Circular Tube," *Z. Angrw, Math. Phys.*, Vol. XII, pp. 185–201.

Barnes, H. H., Townsend, P., and Walter, K., 1971, "On Pulsatile Flow of Non Newtonian Liquid," *Rheologica Acta*, Vol. 10, pp. 517–527.

Bennis, S., 1993, "A New Approach to the Dynamic Parameter Estimation of a Viscoelastic System," ASME JOURNAL OF FLUIDS ENGINEERING, Vol. 115, pp. 153–161.

Bennis, S., 1983, "Ecoulements transitoires dans un tube rigide prolongé par une enceinte viscoélastique," Thèse de doctorat en mécanique, Institut nationale Polytechnique, Toulouse.

Brent, R., 1973, *Algorithms for Minimization Without Derivatives*, Prentice-Hall.

Briley, W. R., and MacDonald, H., 1884, "Tree-Dimensional Viscous Flows with Large Secondary Velocity," *Journal of Fluid Mecanics*, Vol. 144, pp. 47–77.

Forsythe, G. E., Malcolm, M. A., and Moler, C. B., 1976, *Computer Methods for Mathematical Computations*, Prentice-Hall.

Fung, Y. C., 1981, Biomechanics, *Mechanical Properties of Biological Materials*, Springer-Verlag, New York.

Giddens, D. P., and Nerem, R. M., 1988, "Challenging Computationnal Problems in Cardivascular Fluid Mechanics," *Computational Methods in Bioengineering*, presented at the Winter Annual Meeting of ASME, pp. 21–28.

Lieber, B. B., and Giddens, D. P., 1987, "On the Treatement of Velocity Disturbances in Pulsatile Flow." *Proceedings of the International Conference on Fluid Mecanics*, Peking Press, Beijing, pp. 1005–1009.

McDonald, D. A., 1974, *Blood Flow in Arteries*, Edward Arnold Ltd.

Milnor, W. R., 1982, "Pulsatile Pressure and Flow," *Hemodynamics*, pp. 97–134.

Obrecht, B., 1976, "Comportement dynamique de systèmes en régime non permanent. Etude d'un modèle hydraulyque, application à la biomécanique," Thèse de Doctorat Sciences Physique, Strasboug, France.

Womersley, J. R., 1955, "Method for the calculation of velocity, rate of flow and viscous drag in arteries when the pressure gradient is known," *Journal of Physiol.*, Vol. 127, pp. 553–563.

Mixed Convection in Micropolar Boundary-Layer Flow Over a Horizontal Semi-Infinite Plate

I. A. Hassanien
Associate Professor,
Department of Mathematics,
Faculty of Science, Assiut Uiversity,
Assiut, Egypt

A boundary layer analysis is presented to study the effects of buoyancy-induced streamwise pressure gradients on laminar forced convection heat transfer to micropolar fluids from a horizontal semi-infinite flat plate. The transformed boundary-layer equations have been solved numerically. The effects of the buoyancy force, material parameters, and viscous dissipative heat on the friction factor, total heat transfer, displacement thickness, and wall couple stress, as well as the details of the velocity, microrotation, and temperature fields are discussed. A comparison has been made with the corresponding results for Newtonian fluids. Micropolar fluids display drag reduction and reduced heat transfer rate as compared with Newtonian fluids. Also the micropolar properties of the fluid are found to play an important role in controlling flow separation. Furthermore, it is observed that, for high values of the buoyancy and material parameters, the flow and thermal fields are significantly affected by the presence of viscous dissipation heat.

Introduction

In studying forced convective heat transfer over a horizontal surface, it is customary to neglect the effects of buoyancy forces. Such a practice may not be justified when the velocity is small and the temperature difference between the surface and the ambient fluid is large. This is because the buoyancy forces arising from the temperature difference induce a longitudinal pressure gradient, which in turn modifies the flow field and hence the rate of heat transfer from the surface. Thus, predictions of the heat transfer coefficients in the combined convection regime are of practical interest, as are the conditions under which the buoyancy forces first become significant.

In contrast to the problem of combined convective heat transfer along a vertical flat plate or cylinder, less attention has been given to studies of buoyancy force effects on laminar forced convection over a horizontal flat plate. Mori (1961) and Sparrow and Minkowycz (1962) were the first investigators to treat this problem by using a perturbation series in terms of the buoyancy parameter. Raju et al. (1984) and Schneider and Wasel (1985) have studied the mixed convection on a horizontal plate by integrating the boundary layer equations by finite difference schemes. The mixed convection problem for a prescribed heat flux at the wall has been studied by Mucoglu and Chen (1978) and Hussain and Afzal (1988). In particular, self-similar solutions have been studied by Schneider (1979) and Merkin and Ingham (1987) for a wall temperature prescribed as an inverse square root of the distance from the leading edge. In a related problem of similar solutions for mixed convection on a horizontal plate Afzal and Hussain (1984) have shown that the solutions are dual with a turning point where the shear stress is still finite. This conclusion was also supported from the solutions of de Hoog et al. (1984) and the work of Raju et al. (1984).

The above investigations for the case of classical Newtonian fluids do not give satisfactory results (Hoyt and Fabula (1964) and Vogel and Patterson (1964)) if the fluid is a heterogeneous mixture such as liquid crystals, ferro liquid, or a liquid with polymer additives. These are realistic and important from a technological point of view. In order to study the behaviour of such types of complex fluids, Eringen (1966) proposed the theory of micropolar fluids. This theory includes the effects of local rotary inertia and couple stresses, which are not present in the theory of Newtonian fluids. A fluid with suspensions, polymeric fluid, liquid crystals, and animal blood may be characterized as micropolar fluids (see Tozeren and Skalak, 1977; Riha, 1979; and Liu, 1970). Eringen (1972) extended the micropolar fluid theory to the theory of thermomicropolar fluids. The boundary layer concept in such fluid was first studied by Peddieson and McNitt (1970).

Convective heat transfer in a micropolar fluid through a vertical channel and through a horizontal parallel plate channel has been studied by Balaram and Sastry (1973) and Maiti (1975), respectively. Sastry and Maiti (1976) studied the problem of free and forced convective heat transfer in a micropolar fluid in an annulus and vertical pipes. In all these studies (Balaram and Salary, 1973; Maiti, 1975; and Sastry and Maiti, 1976) boundary layer concepts in convective flow are not taken into account. Jena and Mathur (1981) studied the free convection in the boundary-layer flow of a micropolar fluid past a nonisothermal vertical flat plate. Quite recently, Hassanien and Gorla (1990) analyzed the combined forced and free convection in micropolar boundary layer fluid flow over a horizontal cylinder. More recently, Hassanien et al. (1994) studied the mixed convection in micropolar boundary layer flow on a vertical slender cylinder.

The aim of the present work is to study the laminar boundary-layer mixed convection flow of a micropolar fluid over a horizontal plate. Similarity solutions are obtained for the case of a wall temperature that is inversely proportional to the square root of the distance from the leading edge. Numerical results are presented for range of values of the material parameters and the buoyancy parameter of the fluid.

Basic Equations

The equations of conservation of mass, linear momentum, angular momentum, and energy are given by Erigen (1972) in Cartesian tensor notation for an incompressible thermo-micropolar fluid:

$$v_{i,i} = 0 \tag{1a}$$

$$\rho \dot{v}_i = \rho f_i + t_{ki,k} \tag{1b}$$

Contributed by the Fluids Engineering Division for publication in the JOURNAL OF FLUIDS ENGINEERING. Manuscript received by the Fluids Engineering Division November 22, 1994; revised manuscript received May 13, 1996. Associate Technical Editor: D. P. Telionis.

$$\rho j \dot{\sigma}_i = \rho 1_i + \epsilon_{ikh} t_{kh} + m_{ki,h} \quad (1c)$$

$$-\rho \dot{e} + t_{kh} b_{kh} + m_{kh} \sigma_{h,k} + q_{k,k} + \rho h = 0 \quad (1d)$$

Here $b_{kh} = v_{h,k} - \epsilon_{khr}\sigma_r$, a superposed dot denotes the material derivative, v, σ, $e(T)$ are the fluid velocity, particle spin vector and internal energy, respectively, T is temperature; ρ the density, j the microinertia constant, t_{ki} the stress tensor, f_i the body force, 1_i the body couple, m_{ki} the couple stress tensor, q_k the heat flux vector and h and the heat supply. The constitutive equations of Eringen (1996) are:

$$t_{kh} = -p\delta_{kh} + \mu(v_{k,h} + v_{h,k}) + k(v_{h,k} - \epsilon_{kha} v_a) \quad (2a)$$

$$m_{kh} = \alpha v_{r,r} \delta_{kh} + \beta v_{k,h} + \gamma v_{h,k} + \alpha_c \epsilon_{khm} T_{,m} \quad (2b)$$

$$q_k = k_c T_{,k} + \beta_c \epsilon_{khm} \sigma_{h,m}, \quad (2c)$$

where p is the pressure and, in general, μ, k, α, β, γ are constant viscosity coefficients, α_c, k_c, β_c are heat conduction coefficients and δ_{kl} the Kroneker delta. The material constants must satisfy the following inequality (see Eringen, 1996))

$$\left.\begin{array}{c} 0 \le 2\mu + k, \quad 0 \le k, \quad 0 \le k_c, \quad 0 \le 3\alpha + \beta + \gamma \\ 0 \le \gamma + \beta, \quad (\alpha_c - \beta_c T^{-1})^2 \le 2k_c T^{-1}(\gamma - \beta) \end{array}\right\} \quad (3)$$

The equations for thermo-micropolar fluid are now obtained by inserting Eqs. (2a)–(2c) into (1a)–(1d).

In the following section, a Cartesian coordinates xyz with the velocity vector $\mathbf{v} = [u(x, y), v(x, y), o]$ and the microrotation vector $\boldsymbol{\sigma} = [0, 0, \sigma(x, y)]$ are used. The boundary-layer approximation in the common manner but with the modification of pressure variation across the boundary layer being equal to the hydrostatic pressure in the temperature disturbed fluid is applied.

Analysis

Consider here a semi-infinite horizontal flat plate aligned with a uniform free stream with velocity U_∞, density ρ_∞ and temperature T_∞. The coordinates are chosen such that x represents the distance along the plate from its leading edge and y represents the distance normal to the surface. The flow over the plate is considered to be planar, laminar and steady. Following Eringen (1966 and 1972) and taking into account the hydrostatic pressure variation normal to the plate, assuming constant transport coefficients and applying the Boussinesq approximation, we obtain the following boundary layer equations:

Mass

$$\frac{\partial u}{\partial x} + \frac{\partial v}{\partial y} = 0 \quad (4a)$$

Momentum:

$$u \frac{\partial u}{\partial x} + v \frac{\partial u}{\partial y} = \left(\nu + \frac{k}{\rho}\right) \frac{\partial^2 u}{\partial y^2} + \frac{k}{\rho} \frac{\partial \sigma}{\partial y} \pm g\beta_\infty \frac{\partial}{\partial x} \left[\int_y^\infty (T - T_\infty) dy\right] \quad (4b)$$

Angular Momentum:

$$u \frac{\partial \sigma}{\partial x} + v \frac{\partial \sigma}{\partial y} = \frac{\gamma}{\rho j} \frac{\partial^2 \sigma}{\partial^2 y} - \frac{k}{\rho j} \left[2\sigma + \frac{\partial u}{\partial y}\right] \quad (4c)$$

Energy:

$$u \frac{\partial T}{\partial x} + v \frac{\partial T}{\partial y} = \alpha_c \frac{\partial^2 T}{\partial^2 y} + \left(\frac{\mu + k}{\rho c_p}\right) \left(\frac{\partial u}{\partial y}\right)^2 \quad (4d)$$

in which u and v are the velocity components in the x and y directions, respectively, T is the fluid temperature, g is the gravity acceleration, and β_∞ is the thermal expansion coefficient of the fluid in the undisturbed state. The last term on the right-hand side of Eq. (4b) is the buoyancy-induced streamwise pressure gradient. The plus and minus signs preceding that term pertain, to the flow above and below the plate, respectively. The appropriate boundary conditions are:

$$\begin{array}{l} u = v = 0, \quad \sigma = 0, \quad T = T_w(x) \quad \text{at} \quad y = 0, x > 0 \\ u \to U_\infty, \quad \sigma \to 0 \quad \text{and} \quad T \to T_\infty \quad \text{as} \quad y \to \infty \end{array} \quad (5)$$

Equations (4a)–(4d) are first transformed into a dimensionless form, by the following dimensionless variables:

$$X = x/L, \quad Y = \mathrm{Re}^{1/2} y/L; \quad U = u/U_\infty; \quad V = \mathrm{Re}^{1/2} v/U_\infty$$

$$\sigma_1 = U_\infty \mathrm{Re}^{1/2} \sigma / L; \quad \theta = \frac{T - T_\infty}{T^*} \quad \text{and} \quad \mathrm{Re} = U_\infty L/\nu \quad (6)$$

where Re is the Reynolds number, T^* represents a characteristic temperature difference between plate and free stream, and L is the value of the x-coordinate where $T_w - T_\infty = T^*$. If the wall temperature is constant, L can be chosen arbitrarily. Proceeding with the analysis, we introduce the following transformation (originally used by Schneider, 1979; Merkin and Ingham, 1987 in Newtonian fluid) as

$$\eta = Y X^{-1/2}, \quad \psi = X^{1/2} f(\eta)$$

$$\sigma_1 = X^{-1/2} g(\eta), \quad \theta = \theta_w \phi(\eta), \quad (7)$$

Nomenclature

t_{ki} = stress tensor
m_{ki} = couple stress tensor
q_k = heat flux vector
Ar = Archimedes number
Pr = Prandtl number
Δ, λ, B = micropolar fluid parameters
Ec = Eckert number
f = reduced stream function, Eq. (7)
σ_1 = angular velocity
g = dimensionless microrotation
j = microinertia per unit mass
p = pressure
l = plate length
L = value of x where $T_w - T_\infty = T^*$
Q = heat exchanged between plate and fluid
Re = Reynolds number, $u_\infty L/\nu$
St = Stanton number, $Q_w/\rho_\infty u_\infty c_p T^* L$
Ω = buoyancy parameter, $AR/\sqrt{\mathrm{Re}}$
U, V = dimensionless velocity components, Eq. (6)
u, v = velocity component in x, y directions
X, Y = dimensionless Cartesian coordinates, Eq. (6)
x, y = Cartesian coordinates
T = temperature
T^* = characteristic temperature difference between plate and free stream
ρ = density of the fluid
ν = kinmatic viscosity
δ^* = displacement thickness
η = similarity varible, Eq. (7)
τ = shear stress
ψ = dimensionless stream function, Eq. (7)
θ = $(T - T_\infty)/T^*$
ϕ = reduced temperature difference, Eq. (7)

Subscript

w = surface condition
∞ = condition far away from the surface

where the wall temperature distribution has the form

$$\theta_w = X^{-1/2}. \tag{8}$$

In terms of the new variables, it can be shown that the velocity components are given by:

$$\left.\begin{aligned} U &= \partial\psi/\partial Y = f' \\ V &= -\partial\psi/\partial X = \frac{1}{2\sqrt{x}}(\eta f' - f) \end{aligned}\right\} \tag{9}$$

Introducing expression in Eq. (7) into Eqs. (4*b*)–4(*d*) gives

$$2(1+\Delta)f''' + ff'' + 2\Delta g' + \Omega\eta\phi = 0 \tag{10a}$$

$$\lambda g'' + \tfrac{1}{2}(f'g + g'f) - \Delta\cdot B(2g + f'') = 0 \tag{10b}$$

$$\frac{2}{\Pr}\phi'' + \mathrm{f}\phi' + \mathrm{f}'\phi + \Delta\,\mathrm{Ec}\sqrt{\mathrm{x}}\cdot(f'')^2 = 0 \tag{10c}$$

The primes above denote differentiation with respect to η only; Pr is the Prandtl number; Ec is the Eckert number; Δ; λ and B are the micropolar fluid parameters, i.e.,

$$\Delta = k/\mu; \quad \lambda = \gamma L/\mu j; \quad B = L\nu/jXU_\infty,$$
$$\Pr = \nu/\alpha; \quad \mathrm{Ec} = \mathrm{U}_\infty^2/(T^*c_p), \tag{11}$$

and Ω is the buoyancy parameter defined as

$$\Omega = \mathrm{Ar}/\mathrm{Re}^{1/2}, \tag{12}$$

in which Ar is the Archimedes number, $\mathrm{Ar} = gL\beta_\infty T^*/U_\infty^2$.

The transformed boundary conditions are given by:

$$f(0) = 0, \quad f'(0) = 0, \quad f'(\infty) = 1 \tag{13a}$$

$$g(0) = 0, \quad g(\infty) = 0 \tag{13b}$$

$$\phi(0) = 1 \quad \text{and} \quad \phi(\infty) = 0 \tag{13c}$$

Equation (10*a*) reduces to the well known Blasuis equation for $\Omega = 0$ (no buoyancy) and $\Delta = \lambda = B = 0$ (Newtonian fluid). Also for Newtonian fluid when Ec = 0, Eqs. (10*a*) and (10*c*) together with appropriate boundary conditions (13*a*) and (13*c*) reduce to the results given by Schneider (1979) and Merkin and Ingham (1987). For Newtonian fluids, Eq. (10*b*) has no significance and is omitted.

It is clear from Eq. (10*c*) that, when the effect of dissipative heat is neglected, the solution become of the similar type and Eq. (10*c*) can be integrated at once. Using the boundary condition (13*c*) at $\eta \to \infty$, we obtain

$$\frac{2}{\Pr}\phi' + f\phi = 0. \tag{14}$$

This first-order differential equation can be formally integrated to give

$$\phi = \exp\left(-\frac{\Pr}{2}\int_0^\eta f\,d\eta\right) \tag{15}$$

where the boundary condition (13*c*) at $\eta = 0$ has already been satisfied. From the numerical point of view, however, it is preferable to use equation (14) instead of Eq. (15). The skin-friction coefficient can be expressed as

$$\begin{aligned} C_f &= \tau_w(\rho_\infty U_\infty^2) \\ &= (\mathrm{Re}X)^{-1/2}(1+\Delta)f''(0), \end{aligned} \tag{16}$$

where $\tau_w = (\mu + k)\partial u/\partial y|_{y=0}$.

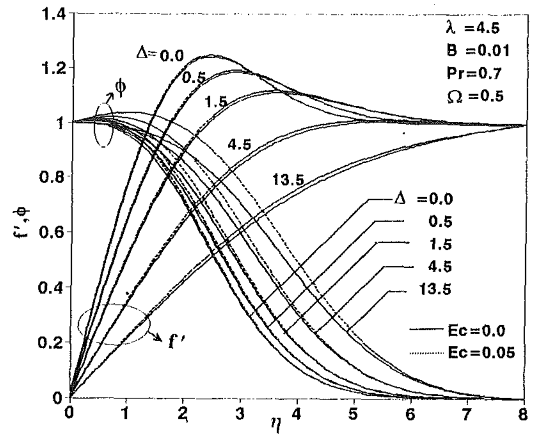

Fig. 1 Velocity and Temperature profiles as a function of η for various values of material parameter Δ

The total heat transfer Q_w is determined with the help of the heat flux equation

$$Q_w = \rho_\infty c_p \int_0^\infty [(T - T)u]_{x=l}\,dy, \tag{17}$$

where l is the length of the plate (not to be confused with L, i.e. the characteristic length of the wall temperature distribution) and c_p is the specific heat capacity at constant pressure. Introducing the dimensionless variables of Eq. (6) and applying the similarity transformation (7) we obtain the relation

$$\sqrt{\mathrm{Re}}\,\mathrm{St} = \int_0^\infty \phi f'\,d\eta = \text{const}, \tag{18}$$

where the Stanton number

$$\mathrm{St} = Q_w/\rho_\infty U_\infty c_p T^* L,$$

is referred to the characteristic length of the wall temperature distribution. According to Eq. (18) the Stanton number is independent of the plate length l, thereby confirming the statement that the total heat transfer takes place at the leading edge.

Finally, the displacement thickness δ^* can be calculated from the relation

$$\begin{aligned} \delta^* &= \int_0^\infty \left(1 - \frac{u}{U_\infty}\right)dy = \sqrt{\frac{\nu x}{U_\infty}}\int_0^\infty [1 - f'(\eta)]\,d\eta \\ &= \sqrt{\frac{\nu x}{U_\infty}}\lim_{\eta\to\infty}[\eta - f(\eta)] \end{aligned} \tag{19}$$

Numerical Solution and Discussion

Equations (10*a*)–(10*c*) with the boundary conditions (13*a*)–(13*c*) have been solved using Runge-Kutta integration scheme in conjunction with the Newton-Raphson Shooting method with Δ, λ, Ω, B, Ec, and Pr as prescribed parameters. The double precision arithmetic was used in all computation. A step size of $\Delta\eta = 0.001$ was selected.

Figures 1–2 represents the distributions of the velocity, microrotation and temperature within the boundary layer, here we have chosen $\lambda = 4.5$, $B = 0.01$, $\Omega = 0.5$, $x = 0.1$ and $\Pr = 0.7$. As the material parameter Δ increases, it is observed that the boundary layer thickness increases, the velocity distribution becomes more linear, the inflection point for the angular velocity distribution moves farther away from the surface. The magnitudes of the maximum values of the angular velocity increase with increasing material parameter Δ. It may be observed that the presence of microelements in micropolar fluid reduces the rate of heat transfer as compared with a Newtonian fluid. On the other hand, the presence of viscous dissipation has very little effect on the flow field for small value of Δ. However, for large values of Δ and Ω, the skin-fraction and Stanton number as well as temperature distribution results, are signifi-

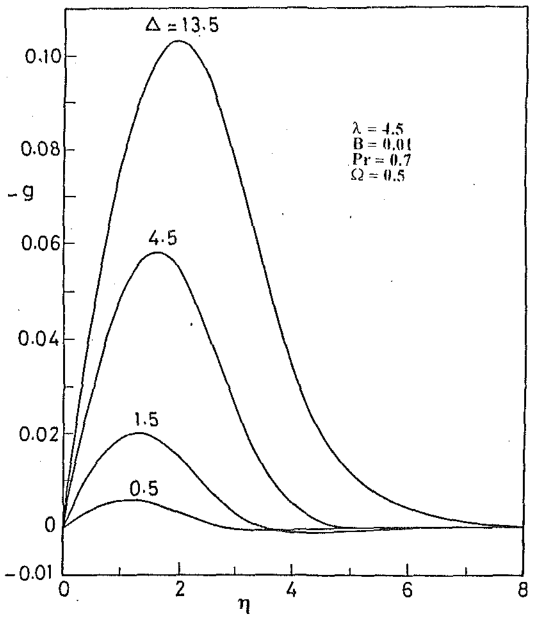

Fig. 2 Angular velocity distribution as a function of η for various values of material parameter Δ with Ec = 0.0

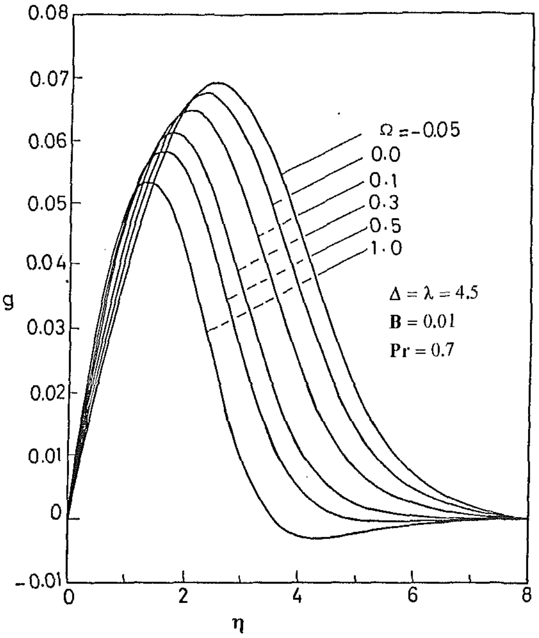

Fig. 4 Angular velocity distribution as a function of η for various values of buoyancy parameter Ω with Ec = 0.0

cantly affected by the presence of viscous dissipation term. This observation can be seen from Figs. (1), (7), and (8).

Figures 3–4 display the effect of the buoyancy parameter Ω on the distribution of velocity, angular velocity and temperature within boundary layer. As the buoyancy force increases, the velocity distribution assumes a more uniform shape and large values of the buoyancy parameter result in an overshoot of the velocity within the boundary layer. The angular velocity is largely influenced by the buoyancy parameter and its magnitude changes the sign in a portion of the boundary layer when Ω becomes very large.

It is interesting to note that $\phi'(0) = 0$ for all values of buoyancy parameter and for both Newtonian and micropolar fluids, cf. temperature distribution Figs. 1, 3. This result, which follows directly from Eq. (14) together with the boundary conditions (13a), indicates that there is no local heat transfer at the plate surface for all $X > 0$. Nevertheless, although dissipation has been neglected from Eq. (14), the temperature of the fluid changes during the flow process. The paradox is resolved by recalling that the similarity solution requires a singular behaviour of the wall temperature at $X = 0$, cf. Eq. (8). Thus all the heat necessary to change the fluid temperature must be transferred at the singular point $X = 0$, which is the leading edge of the plate (Schneider, 1979). In order to circumvent the difficulties linked to the singularity at the leading edge, the total heat transfer Q_w is determined with help of the heat flux equation (see Eq. (18)). The evaluation of such quantities requires only the information contained in Fig. 5 and Table 1. Table 1 present the results for $f''(0)$, $g'(0)$, $\sqrt{\mathrm{Re}}$ St and δ^* for different values of Δ and λ when $B = 0.01$, Pr = 0.7, Ec = 0.0 and $\Omega = 0.5$. Results for the local wall shear stress, wall couple stress, and Stanton number are presented against the buoyancy parameter in Figs. 5–7 for both the Newtonian and micropolar fluids. The results indicate that, for positive values of Ω (i.e., plate temperature larger than free-stream temperature) there is a fa-

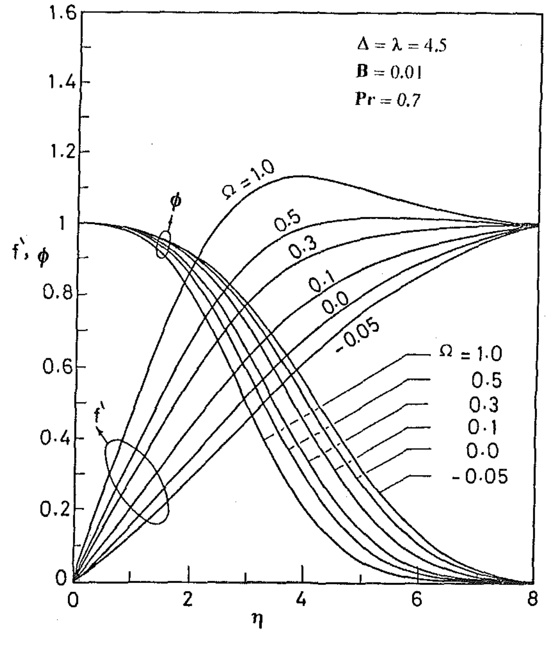

Fig. 3 Velocity and Temperature profiles as a function of η for various values of buoyancy parameter Ω

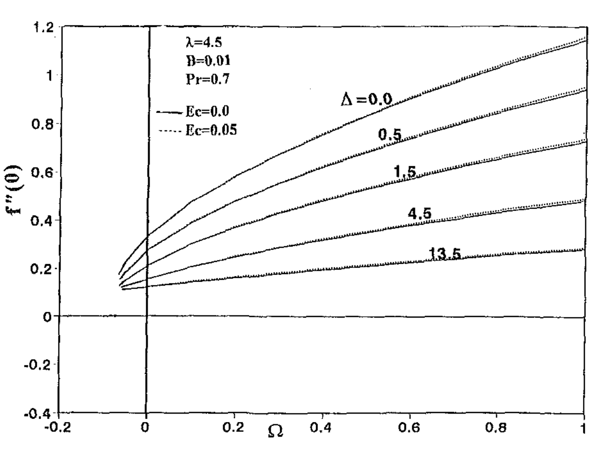

Fig. 5 Dimensionless wall shear stress, $f''(0)$ as a function of the buoyancy parameter Ω for various material parameter Δ

Table 1 Values of $f''(0)$, $g''(0)$, $\sqrt{\text{Re}}$ St and $\sqrt{U_\infty/\nu x}\,\delta^*$ for various values of λ and Δ with $\Omega = 0.5$, $B = 0.01$, Ec = 0.0 and Pr = 0.7

λ	Δ	$f''(0)$	$-g'(0)$	$\sqrt{\text{Re}}$ St	$\sqrt{U_\infty/\nu x}\,\delta^*$
0.0	0.0	0.83161	—	2.21165	0.14248
0.5	0.5	0.68102	0.01012	2.14695	0.36889
	1.5	0.52366	0.02776	2.0506	0.74484
	4.5	0.33502	0.06511	1.8880	1.52801
	13.5	0.18651	0.09942	1.7233	2.40914
1.5	0.5	0.68154	0.00330	2.14660	0.36978
	1.5	0.52640	0.01201	2.04695	0.75386
	4.5	0.34331	0.02466	1.86775	1.59962
	13.5	0.19793	0.04526	1.66541	2.61865
4.5	0.5	0.68119	0.00108	2.14643	0.37019
	1.5	0.52720	0.00301	2.04533	0.75894
	4.5	0.33440	0.00735	1.85596	1.64812
	13.5	0.22020	0.01646	1.62781	2.76157
13.5	0.5	0.68187	0.00140	2.14637	0.37039
	1.5	0.52845	0.00103	2.04478	0.76126
	4.5	0.35196	0.00271	1.85236	1.66592
	13.5	0.21988	0.00670	1.61655	2.80745

vorable pressure gradient above the plate due to the buoyancy effects. The wall shear stress, wall couple stress and Stanton number are larger than that of the non-buoyant case. For negative values of Ω (i.e., the plate temperature smaller than free-stream temperature), the opposite is true. Also the results indicate that at a certain negative value of Ω, the separation condition $f''(0) = 0$, would be satisfied. For each value of Δ it can be seen from Fig. 5 that, below a certain critical value of Ω there is no similarity solution of the boundary layer equation as used in this paper. Hence the presence of microelements are found to be an important application in the control of flow separation. In comparison to the results for Newtonian fluid, it is noticed that micropolar fluids display drag reduction and heat transfer rate reduction.

Figure 8 shows the limit value of the displacement thickness. It is interesting to note that the displacement thickness is negative for relatively large values of the buoyancy parameter Ω, (corresponding to strong heating of the plate). This is a consequence of local velocity that is larger than the free stream velocity, cf. velocity profiles for $\Omega > 0.5$ in Fig. 3. For a given Ω, the displacement thickness is higher in the case of thermomicropolar fluid than for a Newtonian fluid.

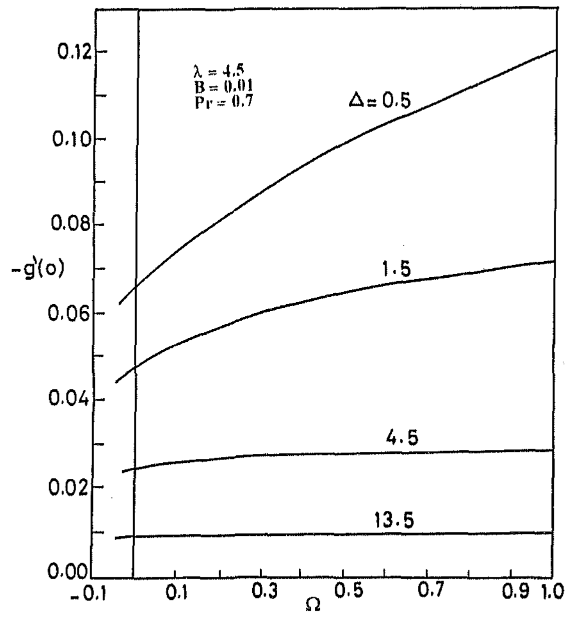

Fig. 6 Dimensionless wall couple stress, $g'(0)$ as a function of the buoyancy parameter Ω for various material parameter Δ

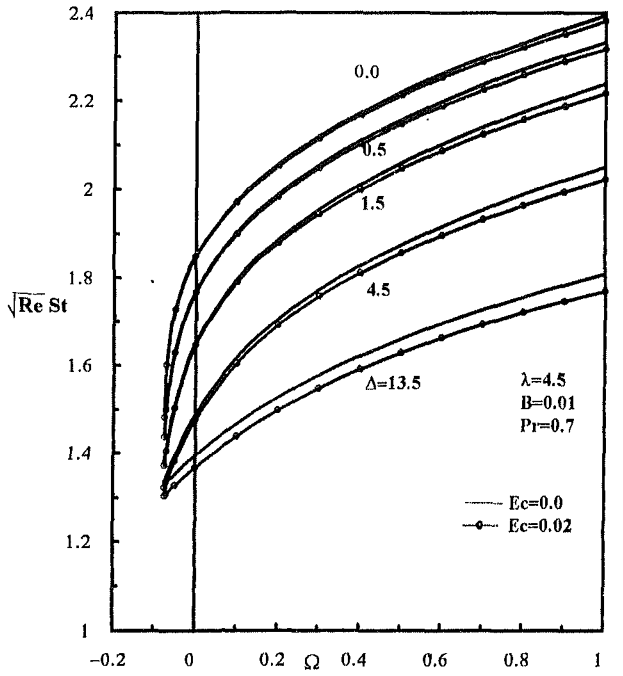

Fig. 7 Total heat transfer at the plate (Stanton number St) as a function of the buoyancy parameter Ω for various material parameter Δ

Concluding Remarks

The effect of buoyancy-induced stream wise pressure gradients on forced convection boundary layer flow over a horizontal plate has been analyzed by similarity solutions when the wall temperature is inversely proportional to the square root of the distance from the leading edge. The buoyancy affects on velocity profiles and significant velocity overshoot beyond the free-stream value is observed at higher values of the buoyancy parameter in the buoyancy assisting flow. Although the wall temperature is different from the free-stream temperature there is no local heat transfer at the wall except in the singular point at the leading edge due to assumption of $\theta = X^{-1/2}$. The total heat transfer is finite, independent of the plate length, and is calcu-

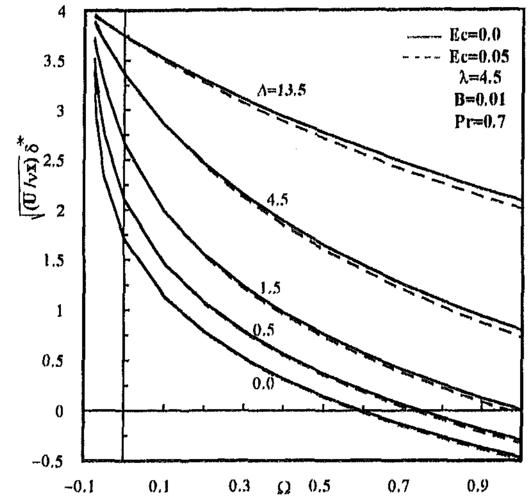

Fig. 8 Effect of buoyancy parameter Ω and material parameter Δ on the displacement thickness δ^*

lated by applying the heat flux equation. A comparison with the results obtained for a Newtonian fluid reveals that the microelements present in the fluid reduce the skin-friction and heat transfer and also play an important role in controlling of separation. The displacement thickness is also given which become negative when the plate is sufficiently heated. Further, the displacement thickness in a micropolar fluid is larger than that of a Newtonian fluid.

Acknowledgment

The author is grateful to Prof. G. E. Karniadakis for the helpful advice.

References

Afzal, N., and Hussain, T., 1984, "Mixed Convection Over Horizontal Plate," *International Journal of Heat Mass Transfer,* Vol. 66, pp. 240–241.

Eringen, A. C., 1966, "Theory of Micropolar Fluids," *Journal Mathematics and Mechanics,* Vol. 16, pp. 1–18.

Eringen, A. C., 1972, "Theory of Thrmomicropolar Fluids," *Journal of Mathematical Analysis and Applications,* Vol. 38, pp. 480–496.

Hassanien, I. A., and Gorla, R. S. R., 1990, "Mixed Convection Boundary Layer Flow of a Micropolar Fluid Near a Stagnation Point on a Horizontal Cylinder," *International Journal of Engineering Science,* Vol. 28, pp. 153–161.

Hassanien, I. A., Mansour, M. A., and Gorla, R. S. R., 1994, "Combined Convection on a Vertical Slender Cylinder in a Micropolar Fluid," *Warme und Stoffubertragung,* Vol. 29, pp. 355–359.

deHoog, I. R., Laminger, B., and Weiss, R., 1984, "A Numerical Study of Similarity Solution for Combined Forced and Free Convection," *Acta Mechanica,* Vol. 51, pp. 139–149.

Hoyt, J. W., and Fabula, A. G. U. S., 1964, "The Effect of Additives on Fluid Friction," U.S. Naval Ordinance Test Station Report.

Hussain, T., and Afzal, N., 1988, "Mixed Convection Boundary Layer Flow on a Horizontal Plate in a Uniform Stream," *International Journal of Heat Mass Transfer,* Vol. 31, pp. 2505–2516.

Jena, S. K., Mathur, M. M., 1981, "Similarity Soultions for Laminar Free Convection flow of Thermomicropolar Fluid Past a Non-isothermal Vertical Plate," *International Journal of Engineering Science,* Vol. 19, pp. 1431–1439.

Liu, C. Y., 1970, "On Trbulent flow of micropolar Fluids," *International Journal of Engrg. Science,* Vol. 8, pp. 457–466.

Maita, G., 1975, "Convection Heat Transfer in Micropola Fluid Flow Through a Horizontal Parallel Plate Channel," *Journal of Mathematics and Mechnics (ZAMM),* Vol. 55, pp. 85–92.

Merkin, J. H., and Ingham, D. B., 1987, "Mixed Convection Similarity Solutions on a Horizontal Surface," *Journal of Applied Mathematics and Physics (ZAMP),* Vol. 38, pp. 102–115.

Mori, Y., "Buoyancy Effects in Forced Laminar Convection Flow Over a Horizontal Flat Plate," ASME *Journal Heat Transfer,* Vol. 83, pp. 479–482.

Mucoglu, A., and Chen, T. S., 1978, "Mixed Convection on a Horizontal 'Plate With Uniform Surface Heat Flux," *Proc. 6th International Journal of Heat Mass Transfer Cofrannce,* Vol. 1, pp. 85–90, Hemisphere, Washington, DC.

Peddiesin, J., and McNitt, R. P., 1970, "Boundary-Layer Theory for Micropolar Fluid," *Recent Advaces in Engineering Science,* Vol. 5, pp. 405–426.

Raju, M. S., Liu, X. Q., and Law, C. K., 1984, "A Formulation for Combined Forced and Free Convection Past Horizontal and Vertical Surface," *International Journal of Heat Mass Transfer,* Vol. 27, pp. 2215–2224.

Riha, P., 1979, "Thory of Mixtures of Microfluids," *Acta Techinca, Ceskoslovenska Akademmie Ved,* Vol. 24, pp. 389–396.

Sastry, V. U., and Maiti, G., 1976, "Numerical solution of combined convection heat transfer of micropolar fluid in an annulus of Two vertical Pipes," *International Journal of Heat Mass Transfer,* Vol. 19, pp. 207–211.

Schneider, W., 1979, "A Similarity Soultion for Combined Forced and Free Convection Flow Over a Horizontal Plate," *International Journal of Heat Mass Transfer,* Vol. 22, pp. 1401–1406.

Schneider, W., and Wasel, M. G., 1985, "Breakdown of the Boundary-Layer Approximation for Mixed Convection Above a Horizontal Plate," *International Journal of Heat Mass Transfer,* Vol. 28, pp. 2307–2313.

Sparrow, E. M., and Minkowycz, W. J., 1962, "Buoyancy Effects on Horizontal Boundary-Layer Flow and Heat Transfer," *International Journal of Heat Mass Transfer,* Vol. 5, pp. 505–511.

Tozeren, A., and Skalak, R., 1977, "Micropolar Fluid as Models for Suspensions of Rigid Spheres," *International Journal of Engineering Science,* Vol. 15, pp. 511–524.

Vogel, W. M., and Patterson, A. M., 1964, "An Experimental Investigation of The Effect of Additives Injected into Boundary Layer of an Underware Body," Pacific Naval Lab. of the Defence Research Board of Canada Report 64-2

Computation of Unsteady Separated Flow Fields Using Anisotropic Vorticity Elements

S. A. Huyer
Mechanical Engineer.
Mem ASME

J. R. Grant
Physicist.

Hydrodynamics Branch,
Naval Undersea Warfare Center,
Newport, RI 02841

A novel computational methodology to compute two-dimensional unsteady separated flow fields using a vorticity based formulation is presented. Unlike traditional vortex methods, the elements used in this method are designed to take advantage of the natural anisotropy of most external flows. These vortex elements are disjoint and of compact support. The vorticity is uniform over rectangular elements whose initial thickness is set by a diffusion length scale. The elements are a mathematical construction which enables the vorticity of the flow to be created and followed numerically, and the Biot-Savart integral to be performed. This integral specifies the associated velocity field. Since the vorticity of a single element is of finite extent, the velocity associated with an element is given by a nonsingular expression. Viscous diffusion effects are modeled using random walk and the advection term is computed by transporting the vorticity elements with the local velocity field. Consequently, this Lagrangian mesh continually evolves through time. Since pressure does not explicitly appear in the formulation, surface pressures are computed using a stagnation enthalpy formulation. These elements are used to compute vorticity production, accumulation, transport and viscous diffusion mechanisms for unsteady separated flow fields past a pitching airfoil. Dynamic stall vortex initiation and development were examined and compared with existing experimental data. Surface pressure data and integrated force coefficient data were found to be in excellent agreement with experimental data. Effects of geometry were provided with baseline calculations of the unsteady flow past an impulsively started cylinder. Both qualitative and quantitative comparisons with experimental data for equivalent test conditions establish the applicability of this approach to depict unsteady separated flow fields.

1 Introduction

There are several advantages to using vortex element methods to compute complex flows. For many external flows, the vorticity is concentrated in relatively small regions of the fluid. A vorticity based formulation thus reduces the need to grid large portions of the flow field; instead, calculation points are concentrated in the regions where vorticity is present. For irrotational free streams, specification of inflow or outflow boundary conditions is unnecessary. Lagrangian representation of the evolving vorticity field is well-suited to moving boundaries, and transformation of the governing equations to noninertial reference frames is unnecessary. Artificial diffusion of vorticity due to representation by a finite grid is avoided. Perhaps most important for separated flow problems characterized by large vortex coherent structures, a Lagrangian mesh is able to locally adapt to the resolution demands of the flow field. Sethian (1990) and Speziale (1987) list some other advantages of this formulation.

Wall-bounded flow, particularly at high Reynolds number, is an important example of anisotropy of length scale. Grid-based methods take advantage of this feature near the wall in bounded flow by setting the point spacing smaller normal to the wall than tangent to the wall. However, traditional Lagrangian discrete vortex element methods (e.g., Chorin, 1973; Leonard, 1980; Anderson and Greengard, 1985; Sethian and Ghoniem, 1988; Winckelmans and Leonard, 1993) are based on isotropic elements. In flows where anisotropy is appreciable, this isotropy diminishes the ability of traditional methods to fully realize the striking economy of computational points which Lagrangian approaches allow. We summarize here an investigation of a two-dimensional Lagrangian vorticity method which uses elements that adapt to the anisotropy of the flow. This technique was found to compute the instantaneous lift on an airfoil undergoing a single pitch at $\mathrm{Re}_c = 40{,}000$ to an accuracy comparable to that reported by Visbal and Shang (1988) and Ghia et al. (1992) for grid-based calculations.

These vortex elements are disjoint and of compact mathematical support. The vorticity is uniform over a rectangle whose original width is set by a diffusion length scale. The endpoints of the elements move independently with the local flow and the total circulation is conserved when the element stretches or compresses. When the two endpoints of an element move further apart than a specified criterion, the element is divided into two shorter elements, so that resolution is maintained. Since the endpoints of one element are not connected to those of other elements, gaps and overlaps occur in the support of the vorticity field. The elements are a mathematical construction which enables the vorticity of the flow to be created and followed numerically, and the Biot-Savart integral to be performed. This integral specifies the associated velocity field. Since the vorticity of a single element is of finite extent, the velocity associated with an element is given by a nonsingular expression. Traditional methods require setting a core radius in order to regularize an otherwise singular expression.

Use of anisotropic elements to compute boundary layer flow was investigated by Chorin (1978), where the elements were infinitely thin and a boundary layer approximation was made to the Biot-Savart integral. More recently, Huyer et al. (1993) computed flow past a three-dimensional wing using infinitely thin three-dimensional elements and the full Biot-Savart integral. This study found the time-averaged spanwise variation in

---

Contributed by the Fluids Engineering Division for publication in the JOURNAL OF FLUIDS ENGINEERING. Manuscript received by the Fluids Engineering Division May 22, 1995; revised manuscript received April 23, 1996. Associate Technical Editor: A. F. Ghoniem.

lift on the wing to agree with a boundary element method estimate. However, in the full expression, the singularities at the element edges due to the thinness of the element generated significant noise in the instantaneous velocity field. Consequently, another motivation for studying anisotropic elements of finite thickness is the absence of a singularity in the expression for their associated velocity. An alternative anisotropic element to the rectangular ones used here is the elliptical element of uniform vorticity proposed by Teng (1986). They distorted the elements using the flow strain rate instead of moving element endpoints independently. However, division of such elements to maintain resolution is less straightforward than with rectangular elements.

The evolution of vorticity is specified by the vorticity equation, written for two-dimensional flow in (7). This equation states that the development of the vorticity field depends on advection and diffusion. For this investigation, the effects of viscosity as specified by the diffusion term in (7) was developed from the following considerations. Pressure force on various bodies along with some aspects of wake geometry are used to validate the present method. Satisfactory comparison of these computed features with observation requires a faithful depiction of the coherent structures in the near wake and a reasonable prediction of the separation point. Viscous effects are dominant near the body surface and our scheme described in Section 2 for production of vorticity at the surface is based on these processes. Once produced, the role of viscosity in the development of these key features is secondary to that of the advection term in (7) which is accurately accounted for by moving the endpoints of the elements with the local flow. Consequently, we were content for this study to use a simply implemented model for viscous effects in the flow, namely, a random walk algorithm. While such algorithms can be quite accurate (e.g., Hald, 1986), it is recognized that achievement of this accuracy requires a large number of points undergoing a random walk. A primary motive for employing a Lagrangian approach, however, is reduction of the number of points needed due to the adaptivity of the Lagrangian points. Thus for the present calculations, the random walk algorithm depicts the qualitative effects of viscosity in the flow, but it is not expected to provide high quantitative accuracy. Yet the overall error in the calculation of features of interest should be small due to the slightness of viscous effects, and the agreement of the calculation results with observation supports this hypothesis.

A problem associated with the direct calculation of the velocity of each element using the Biot-Savart integral is the N^2 increase in CPU time (where N is the number of elements for each time step). Christiansen (1973), Aref and Zawadzki (1989) and Smith and Stansby (1988) (among others) overcome this problem by using the vortex-in-cell method. In this method, the vorticity on points in a given cell are interpolated on fixed grid points. While the high CPU times due to the N^2 calculations are avoided, reintroducing a grid into the computation recalls many of the difficulties inherent with grid based methods. An alternate approach is to accelerate the Biot-Savart integration by the use of a multipole expansion where the effects of distant elements are summed together and nearby elements are computed directly. This method was used by Greengard and Rokhlin (1987); it was modified and applied to the present problem for use with our anisotropic elements. This accelerated computation allows for the treatment of significantly more elements while requiring considerably less computational time.

The work described here has at least three novel aspects. These include the use of compact, disjoint, anisotropic elements which deform according to the local flow strain. A stagnation enthalpy formulation is used to compute instantaneous surface pressure. Other methods require a stream function approach (e.g., Smith and Stansby, 1988) to compute surface pressure. Finally, the problem of unsteady separation past a pitching airfoil is examined. This problem has been computed using finite difference methods (Visbal and Shang, 1988). But previous vortex blob methods (Shih et al., 1992) provided only qualitative comparisons regarding the individual vortex structures. The present method provides quantitative force data comparisons as well.

The unsteady flow field produced by an impulsively started cylinder provides baseline calculations to determine geometry effects. Unsteady flow development about a cylinder has been well documented and the ability of the present technique to accurately depict this flow lends credibility to the current formulation. Computation of unsteady flow past an airfoil undergoing a single pitch motion demonstrate the ability of this method to compute separated flows past stationary and maneuvering bodies. Moreover, this computation displays the particular utility of Lagrangian approaches for maneuvers and other situations where the body moves relative to the free stream. Qualitative results are presented by displaying element velocity vector plots and computing the stream function of the flow field. Unsteady and time averaged pressure and unsteady lift and drag are presented as well. Quantitative and qualitative data are compared with known experimental data sets for equivalent test cases.

2 Formulation

Satisfaction of the Velocity Boundary Conditions. A surface representation of a NACA 0015 airfoil section was constructed by connecting 200 line segments from body coordinates. This is typical of the way bodies are defined for flow computations by the code. The airfoil chord is of nondimensional length 1.0. Each segment on the body surface carries two velocity generators: a surface vorticity distribution lying in the plane of the segment and a potential source. The sources are needed, mathematically, to ensure that the no-flux boundary conditions are satisfied. Uhlman and Grant (1993) showed that as the number of segments representing the surface vorticity increases, the strengths of the sources approach zero. The sources are therefore a result of the finite discretization of the surface vorticity distribution. Both distributions are taken to be uniform over an individual segment and lie in an infinitely thin sheet on the surface. Thus the vorticity strength parameter characterizing a panel is the velocity jump across the panel. The velocity due to a potential source σ and vorticity strength (velocity jump) $\bar{\gamma}$ on a contour C is

Nomenclature

c = nondimensional unit chord length
U_∞ = nondimensional unit freestream velocity
t = nondimensional time
Δt = nondimensional time step
H = stagnation enthalpy
C_p = pressure coefficient = $(p - p_\infty)/\frac{1}{2}\rho U_\infty^2$
C_l = lift coefficient
C_d = drag coefficient
α = angle of attack
α^* = pitch rate (rad/s)
α^+ = nondimensional pitch rate = $\alpha^* c/U_\infty$
Re = Reynolds number = $U_\infty c/\nu$
ν = kinematic viscosity
σ = surface source strength
γ = surface vortex sheet strength
ω = vorticity
$\tilde{u}$ = element velocity
St = Strouhal number = fc/U_∞
θ = cylinder azimuth angle referenced from stagnation point

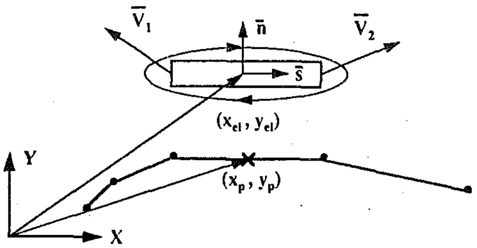

Fig. 1 Vorticity Element Geometry

$$\vec{u}(\vec{x}) = \frac{-1}{2\pi}\int_C \frac{\sigma(\vec{x}')(\vec{x}-\vec{x}')}{|\vec{x}-\vec{x}'|^2}\,d\vec{x}' \tag{1}$$

$$+ \frac{1}{2\pi}\int_C \frac{\vec{\gamma}(\vec{x}')\times(\vec{x}-\vec{x}')}{|\vec{x}-\vec{x}'|^2}\,d\vec{x}'$$

$$= \sum_{n=1}^{N}\{-\sigma_n\vec{B}_n + \vec{\gamma}_n \times \vec{B}_n\} \tag{2}$$

where σ_n and $\vec{\gamma}_n$ are the strengths for panel n of length l_n, the body is defined by N panels, and

$$\vec{B}_n = \frac{1}{2\pi}\int_{l_n} \frac{|\vec{x}-\vec{x}'|}{|\vec{x}-\vec{x}'|^2}\,dx' \tag{3}$$

The integral $\vec{B}_n$ may be evaluated analytically and is given in Appendix A.

For a body defined by N panels, there are $2N$ unknowns. Requiring the total velocity (that due to these surface panels as well as all other velocity generators) to be zero at the control point (centroid) of each segment produces an equivalent number of equations. However, the integral of vorticity over a bounded volume is zero when the velocity vanishes on the bounding surface. This property requires that the integral of the vorticity over the body surface be zero. Total circulation about the body will still be generated depending on the instantaneous vorticity distribution in the boundary layer. Similarly, the integral of the surface potential source over the body surface is zero by continuity. Because of these constraints (one source, one vorticity component) this set of $2N + 2$ equations is an overdetermined set. The matrix solution for the surface strengths is formulated via Lagrange multipliers so that the $2N$ boundary conditions on velocity are satisfied in a least-squares sense and the integral constraints are met exactly.

Shedding of Vorticity From the Surface. The transfer of vorticity from the surface into the flow is accomplished in the algorithm by the creation of rectangular vorticity elements lying just above the body surface (Fig. 1). After each element is produced at the surface, it is placed directly above the surface and has initial thickness equal to a viscous diffusion length scale $\sqrt{2\nu\Delta t}$ where ν is the kinematic viscosity and Δt the time step. The elements have the same length as the respective segment over which they lie. The total vorticity is derived from the surface slip velocity which satisfies the no-slip, no flux boundary conditions. The vorticity is computed to satisfy the relation:

$$\vec{\omega}\cdot dA = \vec{\gamma}\cdot dl \tag{4}$$

where A is the element area and $\vec{\omega}$ the vorticity.

Immediately after vorticity is shed in this fashion, minimal surface vorticity is required to satisfy the no-slip velocity boundary condition. As the elements move away from their original position through advection and viscous diffusion (random walk), increased surface vorticity is required to satisfy these boundary conditions until eventually the new vorticity is shed into the flow by creation of a new family of elements. Shedding of vorticity elements every time step was found to add an unnecessarily large number of elements into the calculation. The reason is that since the previous family of elements are in close proximity, the strength of the elements required to satisfy the no-slip boundary conditions was small. Consequently, they had very little influence on the flow. Similar results were obtained by shedding families of elements every three time steps. This allowed for similar flow computations using significantly fewer elements.

Calculation of Velocity. The velocity field induced by each element is determined by the Biot-Savart integral:

$$\vec{u}(\vec{x}) = \frac{1}{2\pi}\int_S \frac{\vec{\omega}\times(\vec{x}-\vec{x}')}{|\vec{x}-\vec{x}'|^2}\,d^2x \tag{5}$$

In the present work, vorticity is uniform over the rectangular support of each element, so this integral may be written:

$$\vec{u}(\vec{x}) = \sum_n \frac{\vec{\omega}_n}{2\pi}\times\int_{S_n}\frac{(\vec{x}-\vec{x}')}{|\vec{x}-\vec{x}'|^2}\,dS_n \tag{5a}$$

where ω_n is the z-component of vorticity of the nth element having area S_n. The integral was evaluated and the result is shown in Appendix A. The velocity at any point is the sum of this expression and the surface contribution (2).

This treatment of the Biot-Savart integral (5) and vorticity equation (7) differs from that in the traditional vortex method. In the traditional method, the vorticity is written as a sum of overlapping vortex blobs, so that the velocity has the form (e.g., Chorin, 1973; Sethian and Ghoniem, 1988; Sethian, 1991; Knio and Ghoniem, 1990; Winckelmans and Leonard, 1993):

$$\vec{u}(\vec{x}) = \sum_n \frac{\vec{\Omega}_n\times(\vec{x}-\vec{x}_n)}{2\pi|\vec{x}-\vec{x}_n|^2}K\left(\frac{|\vec{x}-\vec{x}_n|}{\delta}\right) \tag{6}$$

Here the sum is over all vortex elements, located at the points x_n and having amplitudes Ω_n, respectively, and K is a function related to the distribution of vorticity in the element. Because of the overlapping of elements, the amplitude Ω_n is not the vorticity at x_n. In the traditional method the calculation proceeds by evolving these amplitudes by an equation having the form of (7). Theoretical analysis (Beale and Majda, 1982a,b; Anderson and Greengard, 1985) has shown the convergence of this method to a solution of (7), on regularly-spaced or otherwise pre-set points. This convergence depends on the relative size of the separation between neighboring points and the size δ of the distribution of vorticity within the element, that is, the amount of overlap. As noted by Beale (1986) and others, the accuracy of this expression diminishes as the points x_n become irregularly and arbitrarily spaced. The elements in the present scheme only incidentally overlap, and a convergence criteria based on overlap is not required for convergence. Indeed, one motivation for pursuing the reported work, in addition to formulating a technique using anisotropy is the development of algorithms that do not depend on overlap criteria for convergence.

There are limitations in the present method which assumes the vorticity to be constant over compact rectangular elements. Effectively, gaps between the elements are created. Let S_n be the area of element n and let Q_n be its share of the surrounding space between neighboring elements, i.e., its share of the gap between neighbors. One might suppose that the leading term in the error introduced by allowing gaps to form would have for this element of the order $Q_n/(S_n + Q_n)$. Fortunately, in regions of high vorticity concentration (as seen in the vortex cores and close to the surface) there is almost 100 percent coverage of vorticity elements over the region. In regions where the vorticity is less and spatially distributed over a larger region, elements may cover only 25 percent of the total area. The computed velocity compared to experiment was found to be quite accurate as will be seen in the next section. The process of determining the element strength using the no-slip condition maintains proper values of circulation. Consequently, the strength of elements are greater by an amount proportional to the relative size of the gaps in the local distribution of elements. Therefore, in regions of high vorticity, element amplitudes should be close to the actual vorticity and in regions of low or spatially diffuse vorticity, local amplitudes are likely greater than the corresponding vorticity. The total circulation, however, will remain the same.

Evolution of the Vorticity Field. The evolution of vorticity is prescribed by the vorticity equation, which is, in two-dimensions:

$$\frac{\partial \omega}{\partial t} = -(\bar{u}\cdot\nabla)\omega + \nu\nabla^2\omega \qquad (7)$$

The terms on the right describe the change in vorticity at a point through advection and diffusion, respectively. The effect of advection is accounted for by moving the element control points with the local velocity. In the algorithm, each end point (see Fig. 1) is advected separately allowing for lengthening or shortening as well as rotation of the element. To conserve total vorticity, the total circulation, defined as $\omega \cdot dA$, must remain constant. To achieve this, the thickness of the element varies to keep dA constant as the element becomes longer or shorter.

In order to maintain spatial resolution, an upper limit is set on maximum element length. Close to the body, the maximum element length is twice its original length. As the elements advect away from the body, the maximum element length is equal to twice its original length multiplied by the absolute value of the distance to the element. Therefore, if the element is five chord lengths away from the body, the maximum size of the element is ten times its original length. Regardless, maximum absolute element size was set to 0.25. If the element exceeds this threshold, it is split into two elements of equal length. This effectively maintains spatial resolution of the vorticity field.

Continual division of certain elements causes the elements which are left to eventually become so thin that they effectively contain a singularity. A minimum thickness bound was then desired to avoid this singularity. The minimum thickness bound was chosen to be based on a diffusion length scale $\sqrt{\nu/|\omega|}$ and was arrived at from dimensional analysis. After this minimum thickness is reached, the thickness of the element remains constant and the total area of the element increases with a corresponding decrease in vorticity in order to satisfy conservation of circulation. Unfortunately, this technique can add additional diffusion of the vorticity field since the area of the element effectively increases. This effect was found to be generally small, however, since few elements reach this minimum thickness bound.

Element division can generate a large number of elements. Since the corresponding high level of spatial resolution may not be needed in certain parts of the flow (e.g., regions of low or constant vorticity), an amalgamation algorithm was written to offer control of the total number of new elements generated. If two elements cross, they are amalgamated in such a way that both linear and angular momentum is conserved. Linear momentum is conserved by setting the new element centroid to the weighted average of the centroids of the two elements amalgamated. Angular momentum is conserved by accounting for the circulation of each element as well as its moment of inertia (due to the fact that it is rectangular in shape) and its orientation in space. The total circulation of the new element will be the sum of the circulation of the elements amalgamated. The length, thickness and orientation of the new element can then be computed from the aforementioned considerations.

As elements are advected by the flow, there will be times when the control points and endpoints are located inside the body. In addition, during amalgamation, there will be times that a new element point can lie inside the body. If any parts of the element lie inside the body, significant errors result as the no-slip no-flux boundary conditions are computed and the corresponding surface and vortex sheet strengths calculated. A penetration algorithm was therefore written to insure that element points lie outside the body. If a point (control and/or end point) lies comes to within half the diffusion length scale ($\sqrt{2\nu\Delta t}$) to the body, that point is 'pushed out' so that it is half the diffusion length scale distance above the body.

Random walk of the element control points (e.g., Chorin, 1973) was used to include the effects of viscous diffusion. In this method, the random walk has a standard deviation of $\sqrt{2\nu\Delta t}$.

Time stepping of the element vorticity strengths and of the element control points is done using a standard predictor-corrector scheme, with one correction applied to the predictor step.

Computation of Surface Pressure. Surface pressure was computed according to the method formulated by Uhlman (1992) based on stagnation enthalpy:

$$\beta H + \oint_C H \frac{\partial}{\partial n}\ln\left(\frac{1}{r}\right)dl = -\oint_C \left\{\hat{n}\cdot\frac{\partial \bar{u}}{\partial t}\ln\left(\frac{1}{r}\right) + \nu\frac{\bar{r}\cdot(\hat{n}\times\bar{\omega})}{r^2}\right\}dl + \iint_V \frac{\bar{r}\cdot[\bar{u}\times\bar{\omega}]}{r^2}\,dV \qquad (8)$$

where:

$$H = \frac{p - p_\infty}{\rho} + \frac{1}{2}[\bar{u}^2 - \bar{U}_\infty^2] \qquad (9)$$

is the stagnation enthalpy. The left-hand side of the equation represents a matrix formulation which needs to be decomposed on the first time step only. The right hand side accounts for the pitching motion of the body and the volume vorticity. Solution of the above equation yields the stagnation enthalpy. On the surface, $\bar{u} = 0$ (relative to the airfoil) due to the no-slip and no-flux boundary conditions so the pressure coefficient can be expressed as:

$$C_p = 1.0 + 2.0{*}H \qquad (10)$$

Integration of the unsteady surface pressure yielded unsteady lift and drag coefficient data.

Fast Multipole Method. In order to increase the resolution of the surface as well as the flow field, it was necessary to compute the interactions of a large set of vorticity elements. The fast multipole method allowed us to compute the flow field due to the increased number vorticity elements in reasonable CPU times. The full derivation of the calculation used in this paper is based on the method presented by Greengard and Rokhlin (1987). A nonadaptive box structure is used to organize the vortices in order to compute the far-field influence. A nonadaptive box structure was used for simplicity and allowed for significant reduction in memory requirements. Since elements and not blobs were used, integration in the far field was approximated by using six point vortices weighted and located at the Gauss points. The final expression for each velocity component has the form:

$$\Psi = \sum_{n=0}^{\infty}\sum_{m=0}^{n} B_{n-m,m}h^{n-m}k^{m} \qquad (11)$$

An expression for the far-field influence of all vorticity elements in terms of a set of coefficients, B, and local coordinates relative to the box center, h, k, for each box in the field was thus formulated. At least 1000 elements were needed to justify use of the fast calculation.

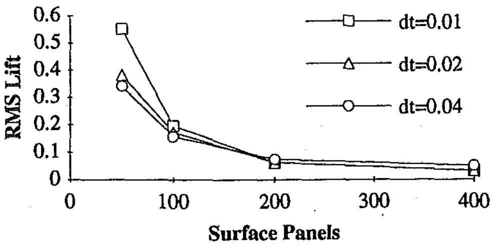

Fig. 2 Effect of Surface Panel Resolution

Sources of Error. In the present methodology, sources of error may be identified and some were quantified. One source of error is due to the multipole expansion. Calibration and error tests were conducted for the multipole expansion with details of the results found in Huyer et al. (1994b). Tests demonstrated an optimal minimum box size of ten times maximum element length. Six point vortices were used to model each vorticity element and were used to approximate the exact integral in the far-field. The circulation of all the point vortices was equal to the circulation of the vorticity element and the weights and locations of the point vortices were determined by the rules of Gauss quadrature. This resulted in a ''modeling'' error of approximately 10^{-7} (scaled by unit freestream). Maximum and average errors in velocity relative to a unit freestream velocity were found to be less than 10^{-3} and 10^{-4}, respectively. For 20,000 elements, the direct calculation required 948 CPU seconds compared with 20 CPU seconds for the accelerated calculation. A direct calculation for vortex blobs would require approximately 120 seconds for 20,000 elements. Direct evaluation of the integral for the present elements is significantly more complex compared with the integral for vortex blobs. This fact underlies the importance of using the accelerated calculation.

The nature of vorticity element calculations make specific error analyses difficult. Errors will exist due to finite discretization of the surface, maximum element thicknesses, maximum element length amalgamation criteria, vortex shedding rate and time step multipole expansion and discretization of the vorticity field. The last item results in errors in the treatment of the Biot-Savart integral (5). There is a truncation error associated with the assumption that the vorticity is uniform over an individual element. This error scales with the cube of a typical length of the element (Grant et al., 1995) but cannot globally be assessed. In order to approximate the sum effect of all numerical errors, examination of root mean square (RMS) lift values at zero angle of attack were conducted. Since the instantaneous lift should be close to zero, RMS lift over a time provides an estimate of the global error. While there will be nonzero RMS lift due to vortex shedding at the trailing edge, these values should asymptote to this non-zero value. Computer runs for various spatial and temporal resolutions were conducted from $t = 0.0$ to $t = 1.0$ and then average and RMS lift values computed. The flow field was computed for surface resolutions of 50, 100, 200, and 400 panels and time steps (Δt) of 0.01, 0.02, and 0.04. These data are presented in Fig. 2 where RMS lift is plotted for the various panel resolutions for the three time steps examined. The lowest RMS values were for 400 panels and time step of 0.01 (RMS = 0.032). A surface resolution of 200 panels and time step of 0.02 yielded an RMS lift of 0.06. The former calculation was predicted to require at least eight times the CPU time of the latter, however. The projected error of the latter was estimated at 1 percent based on maximum lift values and was deemed acceptable. There was also little practical difference in flow field results for time steps of 0.02 or 0.01. Therefore, the present tests used a 200 panel surface resolution and time step of 0.02.

Review of the literature yielded little information of error analysis using vortex blob methods. This seems necessary in order to compare and contrast our present method with the more traditional vortex blob methods. When utilizing the random walk algorithm, there will be a component of ''noise'' at each time step. A high pass filter can be used to quantify the random component, therefore, and project subsequent error due to the random walk. Shih et al. (1992) report results using vortex blob methods to examine flow past a circular cylinder for Re = 250 and 10,000 and for flow past a pitching airfoil. They used approximately 30,000 blobs and a random walk algorithm to simulate viscous diffusion. They estimated the random component in the integrated drag component to be approximately 10 percent of maximum values. Smith and Stansby (1988) used a vortex in cell method to examine flow past an impulsively started cylinder. By a time of 3.0, approximately 38,000 blobs were present in the flow. In spite of smoothing the surface vorticity, a random component of approximately 10 percent of maximum C_d values was still observed for Re = 1,000. We previously reported (Huyer, Grant and Uhlman, 1994a) a random component of drag of approximately 5 percent for Re = 1,000 and 10 percent for Re = 100,000 for flow past a cylinder using only 5000 rectangular vorticity elements. The fast calculation allowed us to use 20,000 elements for the current calculation. Although not shown, the magnitude of the random component dropped below 1 percent for the same two cylinder test cases. As will be seen in Figs. 10 and 11, the integrated lift and drag curves are also quite smooth over time and exhibit a random component of less than 1 percent.

Unsteady flow field development about an impulsively started cylinder was examined for Reynolds numbers of 1000, 3000, and 100,000. Only subcritical Reynolds number were examined since the lack of a turbulence model could not allow for prediction of turbulent boundary layer transition and the drag crisis. Forced unsteady separated flow field development about a NACA 0015 airfoil undergoing a single pitch motion was examined for a Reynolds number (based on chord) of 40,000. Non-dimensional pitch rate, $\alpha^+ = \alpha^* c / U_\infty$, was 0.2. The freestream was impulsively started at $t = -1.0$. Boundary layer development occurred from $t = -1.0$ to 0.0. The airfoil was then pitched about the quarter chord location at $t = 0.0$ from $\alpha = 0$ deg to $\alpha = 60$ deg. The pitch motion ceased at approximately $t = 5.2$ and the flow field was allowed to develop out to $t = 12.0$. All test runs were conducted on the Cray C-90 located at the Waterways Experimental Station in Vicksburg, MS. Cylinder runs took approximately 30 CPU hours; pitching airfoil runs took approximately 20 CPU hours.

3 Results

Flow Past a Cylinder. Figure 3 shows the unsteady flow field development behind a circular cylinder for a Reynolds numbers of 1000 (based on cylinder diameter) from $t = 1.0$–5.0 in increments of 1.0. Element vector plots with the local instantaneous velocity at every fourth vortex element displayed are displayed. Displaying all elements hindered qualitative inspection of the flow.

Two vortices form over the upper and lower region, respectively, behind the cylinder. These vortices appear symmetrical at $t = 1.0$. On the upper surface of the cylinder, the blue vectors indicate clockwise vorticity with weaker vortex elements indicated by the green velocity vectors. There are red vectors present in the vortex indicating that some opposite vorticity was formed on the upper surface. Similarly, the vortex on the lower surface is dominated by red vectors indicating counter-clockwise rotation. Blue vectors are seen as well indicating some opposite vorticity production and entrainment. At $t = 2.0$, a slight asymmetry appears with the vortex on the upper surface becoming elongated compared with the round vortex on the lower surface suggesting initial instability. By $t = 4.0$ and 5.0, the vortices grow larger as the wake develops. In general, note how the Lagrangian mesh evolves with time with additional vorticity

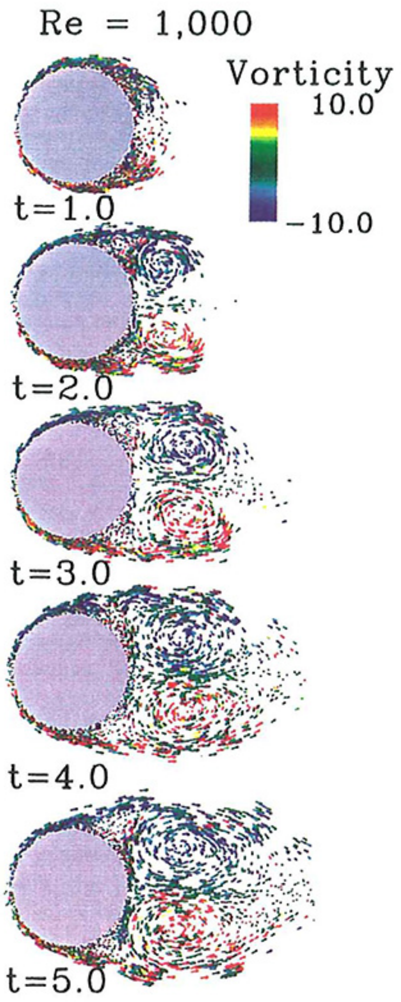

Fig. 3 Initial flow development about a circular cylinder for Re = 1,000 and t = 1.0–5.0 Velocity vectors at every fourth element are plotted and colored by element vorticity

elements introduced into the flow. These vorticity elements accumulate into two well defined vortex structures. By this time in the flow field development, there are approximately 20,000 vorticity elements in the flow. Qualitatively, the flow field is similar to results reported by Bouard and Coutanceau (1980) for equivalent Reynolds numbers.

Comparisons regarding initial wake development were made with experimental data provided by Bouard and Coutanceau (B and C). Numerical simulations were made at Re = 3,000 to exactly match experimental results. Figure 4 shows experimental and predicted values for the length of the vortex wake (L) and x and y coordinates of the vortex centers were determined from the streamline plots and were nondimensionalized based on cylinder diameter. Wake length was defined from the end of the cylinder to the point where the streamlines over the upper and lower surface join. This point is considered to be the point where the streamlines transition from being circular to being oriented in the streamwise direction. The coordinates of the vortex center were taken as the average of the coordinates of the two vortex cores with x referenced from the end of the cylinder and y from the centerline. Reasonably good agreement (discrepancies on the order of 10 percent) between numerical and experimental data were obtained. From t = 1.0 to 3.0, wake length and x coordinate of the vortex core increase approximately linearly with time. The y position of the vortex core, however, remains relatively constant, decreasing minimally to 0.28 at t = 3.0.

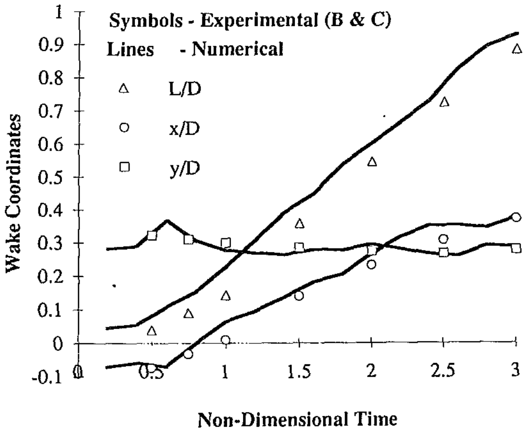

Fig. 4 Unsteady wake development from t = 0 to t = 3.0. Symbols display experimental data by Bouard and Coutanceu (1980) and lines show computed data.

Figure 5 shows wake velocity data obtained using the present computations and compared with the experimental data provided by B and C. Streamwise velocities are plotted and were taken along the cylinder centerline (y = 0.0) from x/D = 1.0 (just above the surface) to x/D = 2.5 where x is referenced from the front of the cylinder. Symbols display the B and C experimental data with the lines showing the numerical results from t = 0.5 to t = 3.0 in increments of 0.5. This plot shows the induced velocities produced by the separated vortex structures and their subsequent development. At t = 0.5, streamwise velocities increase asymptotically from near zero close to the cylinder surface to freestream values by x/D = 2.0. At t = 1.0, reverse flows were seen proximal to the back of the cylinder (x/D = 1.0) to x/D = 1.2. At later times, the magnitude and spatial extent of the reverse flow region increases. At t = 3.0, the magnitude of the reverse flows are approximately −1.4 with the reverse flow region extending out to x/D = 1.9. In general, good agreement between the experimental and numerical results were seen. It does appear that the numerical results under-predict the initial increase in magnitude of the reversed flows after t = 2.0 and also underestimate by approximately 5 percent the asymptotic approach to freestream velocities away from the vortices.

Unsteady lift and drag was computed for Re = 1000 and 100,000. For both cases, sinusoidal variation in lift was seen and was used to estimate Strouhal number. The sinusoidal variation in lift is qualitatively similar to experimental data presented by Bishop and Hassan (1964) for equivalent Reynolds numbers.

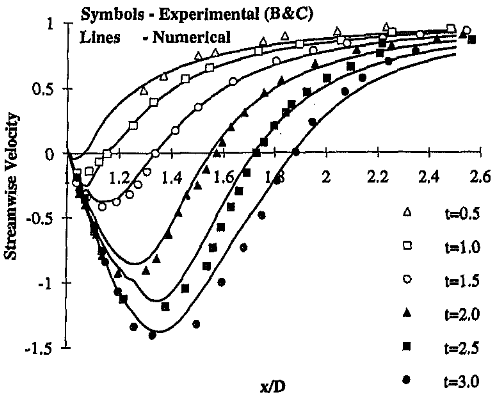

Fig. 5 Unsteady wake velocities at t = 0.5, 1.0, 1.5, 2.0, 2.5 and 3.0. Symbols display experimental data by Bouard and Coutanceu (1980) and lines show computed data.

Table 1 Time averaged quantities

	Cd		RMS Cd		RMS Cl		Strouhal #	
Re	Num	Exp	Num	Exp	Num	Exp	Num	Exp
1,000	1.03	1.05	0.089	0.2	0.67	0.3	0.196	0.21
100,000	0.93	1.1	0.14	0.125	0.61	0.7	0.197	0.2

The average period of lift fluctuation was 5.11 for Re = 1000 and was 5.09 for Re = 100,000 (four shedding cycles). Table 1 shows time averaged quantities of drag, RMS lift and drag and Strouhal numbers compared with experimental data provided by Schlichting (1968), Fleichman and Sallet (1981), and Roshko (1953, 1961) respectively. Overall, these time averaged drag and Strouhal number are in good agreement with experimental results. Relatively poor agreement was seen in RMS values for Re = 1,000. Agreement in RMS quantities was improved as Re was increased to 100,000.

Single Pitch Airfoil. Forced unsteady separated flow field produced by an airfoil undergoing a single pitch motion was examined and compared with equivalent experimental data collected by Helin (1986). Figure 6 shows the evolving Lagrangian mesh at times t = 1.2, 2.6, 4.0 and 5.4 with velocity vectors plotted at every fourth element control point. These times correspond to instantaneous angles of attack of 13.75, 29.8, 45.8, and 60 deg (after the pitch motion stopped).

At t = 1.2, the flow still appears attached over the upper surface with small accumulations of vorticity vectors over the upper surface. The largest magnitude of clockwise vorticity is seen near the leading edge. Alternating clockwise and counterclockwise vorticity accumulations are shed into the airfoil wake. By t = 2.6, a single coherent vortex structure is visible and centered upstream of mid-chord. This dynamic stall vortex structure is characterized by clockwise accumulations of vorticity and large rotational flow velocities. There is also a secondary coherent structure indicated by the small accumulation of counterclockwise vorticity immediately upstream from this vortex, and another region of clockwise vorticity just upstream from the second vortex. By t = 4.0, this vorticity is entrained and contained within a single dynamic stall vortex which dominates the airfoil upper surface. The dynamic stall vortex is shed into the airfoil wake by t = 5.4 with a trailing edge vortex of counterclockwise vorticity dominant near the trailing edge. Notice small accumulations of elements along the outer border of the dynamic stall vortex; this feature is similar to one seen in the visualization plots in Fig. 7 and is probably associated with Kelvin-Helmholtz instability of the shear layer there.

In order to better visualize individual vortex structures, instantaneous streamlines obtained by directly integrating the stream function from the vorticity elements were computed and plotted in Fig. 7. These plots could then be qualitatively compared with smokewire flow visualization photographs taken by Helin (1986) provided care was taken regarding the differences between streamlines and pathlines. These differences include previous motion histories of the smoke particles from an earlier time and inertial effects due to the finite mass of the smoke particles. These differences will be smaller during incipient flow separation and large scale vortex formations due to the forcing of the flow so comparisons seem reasonable. Streamlines are colored based on the value of the stream function, Ψ, with scales shown to the right of each plot.

At t = 1.2, the streamlines indicate attached flow over the upper surface with small shear layer vortices contained in the

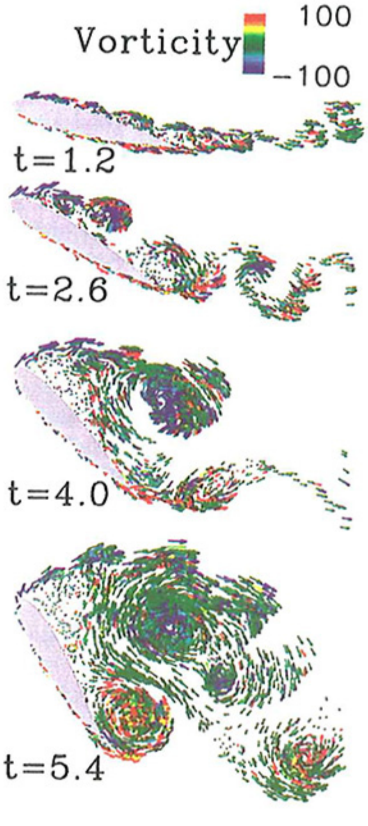

Fig. 6 Initial flow development about a pitching airfoil at t = 1.2, 2.6, 4.0 and 5.4. Velocity vectors at every eighth element are plotted and colored by element vorticity.

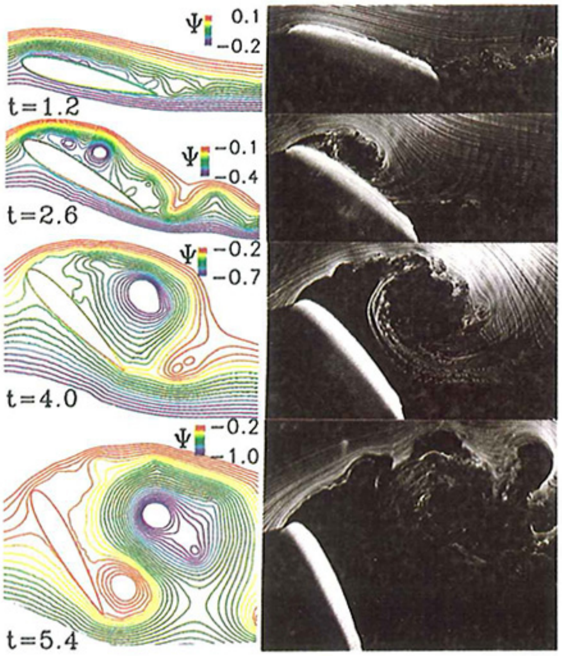

Fig. 7 Streamline visualization and experimental flow visualization by Helin (1986) for test case displayed in Fig. 10. Colored contour plots display constant stream function values.

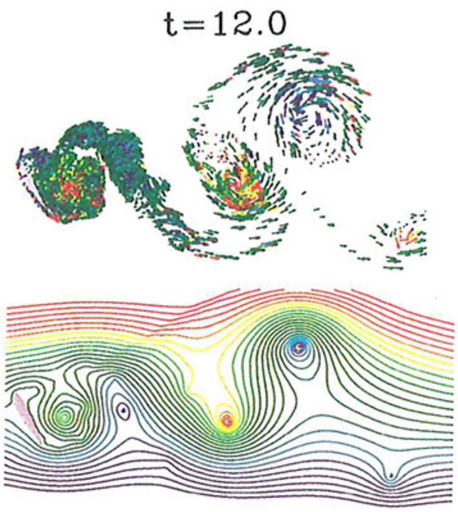

Fig. 8 Instantaneous wake at t = 12.0 comparing element vector plots with streamlines. Vorticity scale is the same shown in Fig. 9; full range stream function values are Ψ = −1.25 to 1.25.

boundary layer in the aft portion of the airfoil. A similar flow field was recorded in the experimental results displayed. At $t = 2.6$, the numerical results predict a dynamic stall vortex centered at midchord with a counter rotating vortex immediately upstream. Similar flow was seen in the visualization data where a small counter-rotating vortex may be inferred from the smoke just upstream of the dynamic stall vortex. The numerical vortex appears slightly smaller compared with that seen experimentally. By $t = 4.0$, a single clockwise vortex dominates the airfoil upper surface in both numerical and experimental results with the size of the vortices comparable. After the pitch motion ceases, the dynamic stall vortex is shed into the wake and a trailing edge vortex is formed. Small vortices around the outer diameter of the vortex can be seen experimentally and are in qualitative agreement with Fig. 6. Although the trailing edge vortex was not seen in this photograph due to lack of smoke, trailing edge vortex formation is seen in other visualization data (Walker et al., 1985a, b). Numerical results slightly underpredict the distance the vortex advects after it is shed into the wake.

Figure 8 shows both vector and streamline plots of the flow field at t = 12.0. Color scales are not shown but the full range of vorticity is −100 to 100 and the full range of the stream function is −1.25 to 1.25. The dynamic stall vortex and trailing edge vortex advect with the local flow as a vortex pair. In addition, alternate vortex shedding can be seen proximal to the airfoil surface with a second leading edge vortex shed in the near wake with a trailing edge vortex attached to the airfoil near the trailing edge. Notice how the division of the elements allows thin vorticity element ‘filaments’ to connect each of the individual vortex structures. This type of connectivity between vortices has routinely been observed in numerous flow visualization experiments (e.g., Freymuth, 1988).

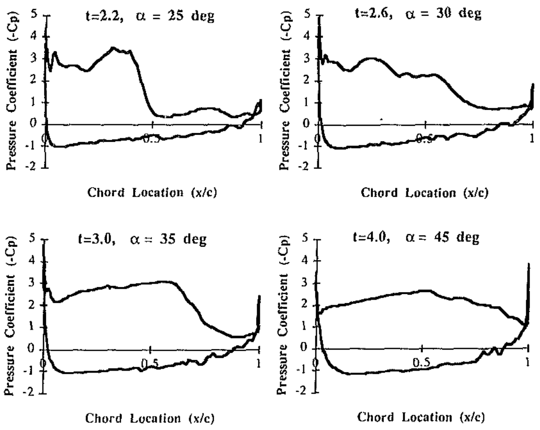

Fig. 9 Surface pressure distributions at t = 2.2, 2.6, 3.0 and 4.0

Surface pressure distributions are presented in Fig. 9 at t = 2.2, 2.6, 3.0, and 4.0 corresponding to instantaneous airfoil angles of attack of 25, 30, 35, and 45 deg. These cases were chosen to illustrate the effect of dynamic stall vortex formation on the surface pressures and subsequent vortex advection into the wake. At α = 25 deg, the suction pressure due to the vortex can be seen upstream of 40 percent chord with suction pressures peaking at $C_p \approx -3.5$ at 30 percent chord. Surface pressures approach zero at stations downstream. At α = 30 deg (see corresponding visualization plots in Figs. 6 and 7), effects of the vortex can be seen past midchord with the suction pressure peak located near 25 percent chord with $C_p = -3.0$. Although the peak values are less, suction pressures influence a greater portion of the upper surface. By α = 35 deg, the pressure distribution over the upper surface becomes flatter with near constant C_p values of approximately −2.5 observed up to 75 percent chord. At α = 45 deg, the dynamic stall vortex is being shed into the wake and nearly constant C_p values of −2.0 are observed over the entire upper surface. A slight peak continues to be observed at midchord implying continued effects, although small, of the dynamic stall vortex. Although not plotted, these pressure peaks due to passage of the dynamic stall vortex are consistent with experimental results presented by Helin (1986) as well as Strickland and Graham (1987).

Surface pressures were integrated to provide unsteady lift (force component normal to the freestream) and drag (force component parallel to the freestream) coefficients which are plotted in Figs. 10 and 11. As a reference, experimental data acquired by Helin (1986) are plotted as well. Experimental data were ensemble averaged over 20 runs and therefore diminish the magnitudes of the peak lift and drag forces as well as other fluctuations which are observed during individual runs. Still, the present numerical results are in good agreement with the experimental results during airfoil pitching. Lift force coefficients exhibit an increase in lift force during airfoil pitch up. A maximum lift of 2.45 was observed at T = 3.0. Experimentally, two “humps” were seen for maximum C_l with $C_{l\max}$ = 2.3 seen at T = 3.0. Afterward lift values decrease and reach a minimum of 0.62 at T = 6.3. Experimentally, minimum lift of 0.67 was seen at T = 6.8. Lift values then increase during formation of the second vortex reaching values of 1.8 from T = 8.5 to 9.5 and decrease again. Experimentally, the magnitude of the second lift peak is 1.2 at t = 10.0. Additional fluctuations in lift are seen during initial formation of subsequent vortices. Direct comparisons with experimental data show the current numerical tech-

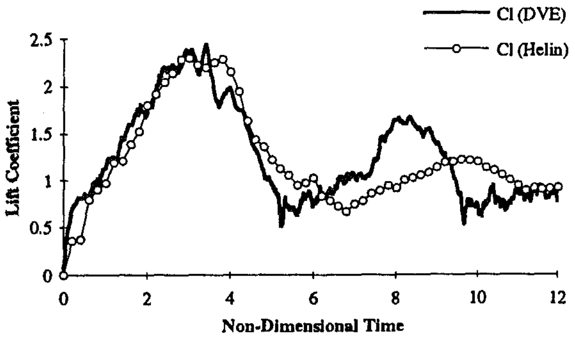

Fig. 10 Unsteady lift force comparisons with experiments by Helin (1986)

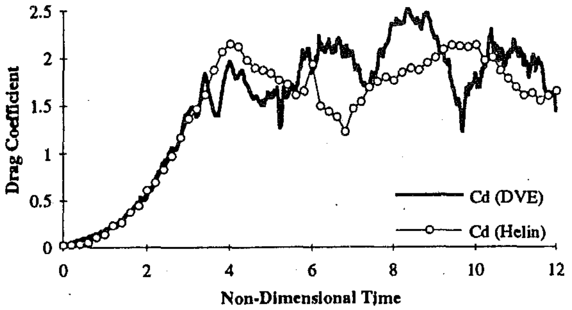

Fig. 11 Unsteady drag force comparisons with experiments by Helin (1986)

nique predicts peak lift forces during pitch up to within 2 percent and over predicts the second lift peak by approximately 20 percent. Temporal persistence of the second lift peak is significantly shorter for the numerical compared with experimental results.

Drag force was plotted as a function of non-dimensional time and is shown in Fig. 11. Again, experimental data are plotted as well to provide a reference. Experimental and numerical data are virtually identical during initial pitch up. At 45 deg angle of attack, numerical lift and drag values are approximately the same at 2.2. Experimentally, C_l and C_d are both 2.15. As the airfoil motion ends, there appears to be fluctuations in drag force. After the pitching motion stops, the current method predicts drag forces approximately 10 percent higher on average than the measured data.

4 Discussion

The goal of the present research was to determine the effectiveness of anisotropic elements in computing unsteady separated flow fields. Test cases of flow past an impulsively started cylinder and of an airfoil undergoing a single pitch motion were used to gauge this effectiveness. This article summarizes the current ability of the present method to predict typically complex flow fields. Unsteady separated flow fields are characterized by localized vorticity distributions away from the surface where the vorticity originates. Velocity based methods would then require adaptive gridding to resolve individual vortex structures. A Lagrangian vorticity based methodology follows the vorticity as it evolves. To demonstrate the potential of the present method, relatively simple surface geometries, test cases and motion histories were chosen where it was known that considerable experimental data exists to provide comparisons.

Anisotropic elements have some distinct advantages over isotropic vortex elements in computing unsteady flow over surfaces. Near a surface, anisotropic elements can satisfy the no-slip boundary condition using far fewer elements, while maintaining the required resolution normal to the surface. As the flow field evolves, shearing of the flow requires addition of isotropic elements to maintain resolution. These anisotropic elements deform with the local flow and stretch to automatically adapt to regions of high shear. As the elements stretch beyond twice their original length, they are divided to maintain spatial resolution. To conserve circulation, the elements effectively become thinner. These elements also require no overlap so when they are divided, they remain disjoint. Even though fewer elements are used in the computation, sufficient spatial resolution is still maintained—especially in regions of high shear. This was especially demonstrated in Fig. 8 where filaments are constructed out of the vorticity elements connecting the leading edge and trailing edge vortices that form. In addition, as the vortex structures advect downstream, they grow in size. Again, division of the vorticity elements maintains the spatial resolution. Although not shown, the aspect ratio (length/thickness) of the elements varies considerably. They can vary from extremely thin (aspect ratios on the order of 100,000) to approximately square elements, a range due to their adaptivity to continually changing flow conditions. Near the vortex cores, square elements approximate the constant vorticity there whereas near the surface or the outer vortex core element aspect ratios are high.

There are two sources of artificial viscosity present in this method which must be considered. Some artificial numerical viscosity is introduced as the elements reach the minimum thickness bound. This effect is dominant in the filaments which connect vortex structures since that is where most of the stretching takes place. The second source is in the amalgamation routine. As elements are amalgamated, artificial diffusion is introduced as the elements are 'forced' to combine. This effect can be reduced, however, by choosing the amalgamation criteria appropriately. In the present algorithm, elements close to the body are only amalgamated if their centroids are within 10 percent of their overall length and only if they are parallel to within 10 deg. The elements then effectively lie on top of each other so amalgamation has minimal effect in terms of the spatial resolution.

One shortcoming of the current method is the inability to deterministically define the Reynolds number (i.e., a quantitative calculation of viscous diffusion). The present algorithm accounts for Reynolds number in four ways: initial thickness of the vortex element, initial placement of the element, random walk of the element and amalgamation criteria. An increase in Reynolds number corresponds to a decreased element thickness and increased element vorticity. The quantity $\omega \cdot dA$ remains constant for all Reynolds numbers. Therefore, the amount of vorticity produced is dependent on instantaneous surface slip velocity alone. An increase in Reynolds number will cause the element to be placed closer to the surface, will decrease the magnitude of the random walk of the element and results in the amalgamation of fewer elements. Qualitatively, Reynolds number effects seem representative of the flow field as a whole. Although not shown, boundary layer thickness was significantly less for Re = 100,000 compared with Re = 1000. The force data presented showed few differences in Reynolds number with unsteady lift and drag data except data were 'noisier' for the higher Reynolds number. Lift data did indicate periodic Strouhal vortex shedding consistent with experimental results (Roshko, 1953, 1961). Initial flow asymmetry, however, was likely due to the random walk diffusion model. Limitations did appear when looking at detailed aspects of the data. Resolution is lost near the surface in the boundary layer and would require additional elements to maintain an accurate diffusion of vorticity. This is especially seen in the upstream regions of the cylinder flow where opposite signed vorticity was observed. Opposite signed vorticity is only expected in the downstream region of the cylinder where secondary vortices are produced. This opposite signed vorticity was found to be due to a lack of surface resolution and the consequence of shedding families of elements every four time steps. Still, the diffusion and shedding models were sufficient to examine the effectiveness of the compact disjoint vorticity elements. Flow field velocities, surface pressure and integrated force data were all found to be smooth for both the cylinder and pitching airfoil test cases. We are currently investigating deterministic diffusion methods. Marshall and Grant (1995) and Huyer and Grant (1995) describe methods to directly account for diffusion by computing the Laplacian on scattered points. Particle exchange algorithms (e.g., Winkelmans and Leonard, 1993) also offer a deterministic method to compute diffusion and will be considered as well.

The present method predicted the initiation, development and shedding of a large scale dynamic stall vortex for a rapidly pitching airfoil. The approximate size and location of this vortex was consistent with experimental data by Helin (1986) as was formation of secondary vortex structures. Coalescence of the primary and secondary vortices into a single dynamic stall vortex, trailing edge vortex formation, vortex pairing and alternate vortex shedding were all consistent with experimental results.

Integrated lift and drag force coefficient data demonstrated the global effects of unsteady vortex formation and compared favorably with experimental data. Lift overshoot was predicted to occur at the same time as was seen in experiments and the magnitude of maximum lift was predicted as well. Lift produced by the formation of the second vortex after the pitch motion ceased was predicted to be numerically more transient and larger in magnitude compared with experimental data. Drag force coefficient data was seen to be virtually identical with experimental data during airfoil pitch up. After the pitching motion had ceased, however, several fluctuations in drag coefficient were observed due to vortex shedding. On average, the drag appears to be slightly larger than experimental results. A possible explanation for this discrepancy may be due to the ensemble averaging used to compile the experimental data; 20 pitching test runs were ensemble averaged. This would have the effect of attenuating larger transients and smoothing out the data. The simulation results display a single run of data. Experimentally, individual runs demonstrate more transient behavior and larger lift peaks compared with the averaged data. In addition, Helin (1986) showed that small changes in pitch rate greatly affected the temporal aspects of dynamic stall vortex formation as well as subsequent vortex formation after the airfoil motion stopped. Averaging 20 runs would further "smooth" the lift and drag fluctuations in the experimental data. Although these fluctuations can still be seen in the numerical data, they were even greater for individual test runs. Another likely explanation is onset of three-dimensionality in the experiments which was noted by Helin as well. It is possible that additional numerical inaccuracies were responsible for some of the small discrepancies observed. Overall, quantitative agreement in terms of average drag and shedding frequency in the cylinder data as well as overall agreement in lift and drag data during airfoil pitch up suggest that the correct amounts of vorticity are shed from the surface and the temporal shedding characteristics are being physically modeled as well.

5 Conclusions

A vorticity based algorithm utilizing anisotropic vorticity elements was used to compute two-dimensional unsteady separated flow fields past a cylinder and a NACA 0015 airfoil undergoing a single pitch motion. Constant vorticity elements were produced at the surface and shed into the flow. Element vorticity magnitudes were determined by simultaneous satisfaction of the no-slip and no-flux boundary conditions at all element control points on the surface. Each element endpoint was advected separately according to a velocity determined by the induced velocities of all the other elements in the field as well as velocities induced due to surface vorticity and source strengths. Vortex production, shedding, diffusion and advection mechanisms together determined the characteristics of the flow field.

Qualitative comparisons with experimental data were made using both vector and streamline plots. These plots demonstrated the effectiveness of the current vorticity based method in predicting the formation of large scale vortex structures. The present method correctly predicted the formation of distinct vortex structures and Karman vortex street for low Reynolds number cylinder flow. This method also correctly predicted initiation and formation of a dynamic stall vortex during airfoil pitch up and subsequent alternate shedding of additional leading and trailing edge vortex structures after the pitching motion ends. Quantitative data output from the code were shown to be in good agreement with experimental data. Calculations of flow past a cylinder revealed good agreement of unsteady wake development and centerline velocities with experiments. Sinusoidal variation in lift was associated with Strouhal-type vortex shedding. Strouhal shedding frequencies and average drag values compared favorably with experimental data. The vorticity based method predicted formation of a leading edge suction pressure peak and subsequent pressure peaks as the dynamic stall vortex passed over the upper surface for the pitching airfoil. Lift overshoot was correctly predicted in both magnitude and time. Additional peaks in lift force were observed during subsequent leading edge vortex formation. Fluctuations in drag force were observed after the airfoil ended its pitching motion. Overall, unsteady pressure, lift and drag data correlated well with experimental data.

Considerable agreement between numerical results utilizing discrete vortex element techniques and experimental results has been demonstrated and there are a number of planned improvements to further enhance the predictive capability of the code. A major focus of future research will be replacement of random walk with a deterministic method for computing diffusion. Ongoing improvements and developments will be presented in future work. Concepts of the present work are currently be extended to examine more complex unsteady separated flows past three-dimensional bodies.

Acknowledgments

This research was supported by the Office of Naval Research, Contract no. 92WX22010, Mr. James A. Fein, Program Manager and by the NUWC Internal Research program, Dr. Ken Lima, Program Manager. Helpful discussions and reviews provided by Drs. James Uhlman and Promode Bandyopadhay at NUWC are greatly appreciated. The authors wish to express their appreciation to the reviewers of this article for their helpful comments.

References

Anderson, C., and C. Greengard, 1985, "On Vortex Methods," *SIAM Journal of Numerical Analysis*, Vol. 22, pp. 413–440.

Aref, H., and Zawadzki, I., 1989, "Comment on Vortex Ring Reconnections," *Proceedings IUTAM Symposium-Topological Fluid Mechanics*, H. K. Moffatt and A. Tsinober, eds., Cambridge, MA.

Bishop, R. E. D., and Hassan, A. Y., 1964, "The Lift and Drag Forces on a Circular Cylinder in a Flowing Fluid," *Proceedings Royal Society of London*, Series A, Vol. 277, pp. 32–50.

Bouard, R., and Coutanceau, M., 1980, "The Early Stage of Development of the Wake Behind an Impulsively Started Cylinder for $40 < Re < 10^4$," *Journal of Fluid Mechanics*, Vol. 101, no. 583.

Chorin, A. J., 1973, "Numerical Study of Slightly Viscous Flow," *Journal of Fluid Mechanics*, Vol. 57, pp. 785–796.

Chorin, A. J., 1973, "Vortex Sheet Approximation of Boundary Layers," *Journal of Computational Physics*, Vol. 27, pp. 428–442.

Christiansen, J. P., 1973, "Numerical Simulation of Hydrodynamics by the Method of Point Vortices," *Journal of Computational Physics*, Vol. 13, pp. 262–379.

Fleischmann, S. T., and Sallet, D. W., 1981, "Vortex Shedding from Cylinders and the Resulting Unsteady Forces and Flow Phenomenon Pat I," *Shock and Vibration Digest*, Vol. 13, No. 10, pp. 9–22.

Freymuth, P., 1988, "Visualizing the Connectivity of Vortex Systems for Pitching Wings," *1st National Congress of Fluid Mechanics*, Cincinnati, OH, July.

Ghia, K. N., Yang, J., Osswald, G. A., and Ghia, U., 1992, "Physics of Forced Unsteady Flow for a NACA 0015 Airfoil Undergoing Constant-Rate Pitch-Up Motion," *Fluid Dynamics Research*, Vol. 10, pp. 351–369.

Grant, J. R., Huyer, S. A., and Uhlman, J. S., 1995, "Solution of the Vorticity Equation on a Lagrangian Mesh Using Triangulation: Computation of the Biot-Savart Integral in Three Dimensions," *Proceedings from Forum on Vortex Methods for Engineering Applications*, Sandia, Albuquerque, N. M., Feb 22–24, pp. 193–209.

Greengard, L., and Rokhlin, V., 1987, "A Fast Algorithm for Particle Simulations," *Mathematics of Computation*, Vol. 47, pp. 387–398.

Hald, O., 1986, "Convergence of a Random Method with Creation of Vorticity," *SIAM Journal of Scientific and Statistical Computation*, Vol. 7, No. 4.

Helin, H. E., 1986, "Experimental Studies on the Dynamic Development and Control of Unsteady Separated Flows," Doctoral thesis, University of Colorado, Boulder, CO.

Huyer, S. A., Grant, J. R., and Uhlman, J. S., 1993, "Numerical Simulation of Three-Dimensional Unsteady Flow Past a Wing Using a Discrete Vortex Element Algorithm," ASME 1993 Fluids Engineering Spring Meeting, Washington, D.C., June.

Huyer, S. A., Grant, J. R., and Uhlman, J. S., 1994a, "A Vortex Element Representation of Two-Dimensional Unsteady Separated Flows," AIAA Paper 94-0075.

Huyer, S. A., Grant, J. R., and Uhlman, J. S., 1994b, "Computation of Unsteady Separated Flow Fields Past an Oscillating Airfoil Using Discrete Vortex Elements," AIAA Paper 94-2257, June.

Huyer, S. A., and Grant, J. R., 1995, "Incorporation of Boundaries for 2D Triangular Vorticity Element Methods," proceedings from Forum on Vortex Methods for Engineering Applications, pp. 211–225, Sandia, Albuquerque, NM, Feb. 22–24.

Leonard, A., 1980, "Vortex Methods for Flow Simulation," *Journal of Computational Physics,* Vol. 37, pp. 289–335.

Marshall, J. S., and Grant, J. R., 1995, "A Lagrangian Collocation Method for Vorticity Transport in Viscous Fluid Flows," proceedings from Forum on Vortex Methods for Engineering Applications, Albuquerque, NM, Feb. 22–24.

Roshko, A., 1953, "On the Development of Turbulent Wakes from Vortex Streets," NACA TN 2913, Mar.

Roshko, A., 1961, "Experiments on the Flow Past a Circular Cylinder at Very High Reynolds Numbers," *Journal of Fluid Mechanics,* Vol. 10, Pt. 3, May, pp. 51–75.

Schlichting, H., 1968, *Boundary Layer Theory,* Sixth Edition, McGraw-Hill, New York, NY, pp. 17, 21 and 32.

Sethian, J. A., and Ghoniem, A. F., 1988, "Validation Study of Vortex Methods," *Journal of Computational Physics,* Vol. 74, pp. 283–317.

Sethian, J. A., 1990, "A Brief Overview of Vortex Methods," Center for Pure and Applied Mathematics, University of California, Berkeley, Report PAM-495, Apr.

Shih, C., Lourenco, L., Van Dommelen, L., and Krothpalli, A., 1992, "Unsteady Flow Past an Airfoil Pitching at a Constant Rate," *AIAA Journal,* Vol. 30, No. 5, May, pp. 1153–1161.

Smith, P. A., and Stansby, P. K., 1988, "Impulsively Started Flow Around a Circular Cylinder by the Vortex Method," *Journal of Fluid Mechanics,* Vol. 104, No. 45.

Speziale, C. G., 1987, "On the Advantage of the Vorticity-Velocity Formulation of the Equations of Fluid Dynamics," *Journal of Computational Physics,* Vol. 73, pp. 476–480.

Strickland, J. H., and Graham, G. M., 1987, "Force Coefficients for a NACA-0015 Airfoil Undergoing Constant Rate Pitch Motions," *AIAA Journal,* Vol. 25, No. 4, pp. 622–624.

Teng, Z. H., 1986, "Variable-Elliptic-Vortex Method for Incompressible Flow Simulation," *Journal of Computational Mathematics,* Vol. 4, No. 3, July, pp. 255–262.

Uhlman, J. S., 1992, "An Integral Equation Formulation of the Equations of Motion of an Incompressible Fluid," Naval Undersea Warfare Center Technical Report 10-086, 15 July.

Uhlman, J. S., and Grant, J. R., 1993, "A New Method for the Implementation of Boundary Conditions in the Discrete Vortex Element Method," ASME 1993 Fluids Engineering Spring Meeting, Washington, D.C., June.

Visbal, M. R., and Shang, J. S., 1988, "Numerical Investigation of the Flow Structure Around a Rapidly Pitching Airfoil," *Proceedings of Workshop II on Unsteady Separated Flows,* FJSRL-TR-88-0004, United States Air Force Academy, Sept. 1988, pp. 91–108.

Walker, J. M., Helin, H. E., and Strickland, J. H., 1985, "An Experimental Investigation of an Airfoil Undergoing Large Amplitude Pitching Motions," AIAA Paper 85-0039, Jan.

Winckelmans, G. S., and Leonard, A., 1993, "Contributions to Vortex Particle Methods for the Computation of Three-Dimensional Incompressible Unsteady Flows," *Journal of Computational Physics,* Vol. 109, pp. 247–273.

APPENDIX A

The integral expression:

$$\vec{B}_n = \frac{1}{2\pi} \int_{l_N} \frac{|\bar{x} - \bar{x}'|}{|\bar{x} - \bar{x}'|^2} \, dx'$$

evaluated over a segment of length $2l$ is given as:

$$\hat{n} \cdot \vec{B} = \tan^{-1}((x - l)/y) - \tan^{-1}((x + l)/y)$$

$$\hat{t} \cdot \vec{B} = \ln((x - l)^2 + y^2)/(x + l)^2 + y^2))$$

where x and y are the normal and tangential field points referenced to the segment centroid. The velocity induced by an element of constant vorticity is given by the integral:

$$\bar{u}(\bar{x}) = \frac{1}{2\pi} \int_C \frac{\bar{\omega} \times (\bar{x} - \bar{x}')}{|\bar{x} - \bar{x}'|^2} \, d\bar{x}'$$

Let x and y be the tangential and normal spatial field points referenced to the element centroid. Also, let the length and thickness of the element be expressed as $2l$ and $2d$, respectively. Then:

$$\begin{aligned}
\hat{t} \cdot \bar{u} = -\frac{\omega}{4\pi} \Bigg\{ & (x - l) \ln \left[\frac{(x - l)^2 + (y + d)^2}{(x - l)^2 + (y - d)^2} \right] \\
& - (x - l) \ln \left[\frac{(x + l)^2 + (y - d)^2}{(x + l)^2 + (y + d)^2} \right] \\
& + 2(y + d) \tan^{-1} \left[\frac{2l(y + d)}{(x + l)(x - l) + (y + d)^2} \right] \\
& - 2(y - d) \tan^{-1} \left[\frac{2l(y - d)}{(x + l)(x - l) + (y - d)^2} \right] \Bigg\}
\end{aligned}$$

$$\begin{aligned}
\hat{n} \cdot \bar{u} = \frac{\omega}{4\pi} \Bigg\{ & (y - d) \ln \left[\frac{(x - l)^2 + (y - d)^2}{(x + l)^2 + (y - d)^2} \right] \\
& - (y + d) \ln \left[\frac{(x - l)^2 + (y + d)^2}{(x + l)^2 + (y + d)^2} \right] \\
& + 2(x + l) \tan^{-1} \left[\frac{2d(x + l)}{(x + l)^2 + (y - d)(y + d)} \right] \\
& - 2(x - l) \tan^{-1} \left[\frac{2d(x - l)}{(x - l)^2 + (y - d)(y + d)} \right] \Bigg\}
\end{aligned}$$

Hitoshi Sato
Graduated Student,
PhD. Department
of Production Engineering,
Graduated School of Science
and Technology.

Xiao Wu Sun

Mamoru Odagawa
Graduated Students,
Graduated Course of
Mechanical Engineering,
Faculty of Engineering.

Kazuo Maeno
Associate Professor,
Department of Mechanical Engineering,
Faculty of Engineering.

Hiroki Honma
Professor,
Department of Mechanical Engineering,
Faculty of Engineering.

Chiba University,
1-33 Yayoi, Inage-ku, Chiba, #263 Japan

An Investigation on the Behavior of Laser Induced Bubble in Cryogenic Liquid Nitrogen

There have been few experimental reports on cryogenic two-phase fluids and cavitation phenomena using the irradiation of pulsed high-power laser. This paper describes an investigation of the behavior of laser induced cavitation bubble in cryogenic liquid nitrogen. The bubble is produced by a pulsed ruby laser focused in the special cryostat. The production, growth, and rebound phenomena of the bubbles are visualized by diffusive shadowgraph technique with an image-converter camera. To compare with the experimental results, a numerical study has also been performed on the dynamics of a single spherical bubble in liquid nitrogen under the conditions of nonequilibrium phase change.

1 Introduction

There have been many studies on the dynamics of cavitation bubbles in liquids of normal temperature range. For the recent research on cavitation, there has been the remarkable experimental method that uses the bubble produced by strong laser pulse (Lauterborn and Bolle, 1975; Alloncle et al., 1993). This method has the merit that the flow fields are not so disturbed to see the individual bubble behavior. In various new technological fields, such as superconductivity technology, space development, and engineering for liquefied natural gas, cryogenic liquids have been important subjects of research, especially regarding cavitation phenomena in relation to their transportation and preservation. For example, if high-speed cryogenic pumps of liquid propellants in aerospace engineering need to be repetitively driven for a long time, the cavitation phenomena will present important problems. In cryogenic fields, the cavitation causes also strong vibration and noise and it affects the performance directly (Reboud et al., 1990; Shimura et al., 1992). Besides, the shock waves produced at bubble generation and at its rebound, and at the liquid microjet in bubble collapse near the wall give damage to the surface of materials. The erosion phenomena in cryogenic liquids will possibly be one of the important problems. Furthermore, in the superconductivity field there is the possibility of high voltage breakdown in cryogenic liquids, where the micro-bubble cavitation will be a key point in such breakdown phenomena. Taking notice of the breakdown as the preproduction of bubble, Yoshino (1980) reported that the breakdown characteristics depend on the molecular structure of liquids. In the case of such liquid as water (H_2O) with nonlinear molecular structure, the electron mobility is related to the breakdown. For linear molecular structure as nitrogen, however, electron avalanche is also important in the short time range as nano-sec order (Kattan et al., 1989; Kattan et al., 1991; Hernandez et al., 1993).

The behavior of bubbles in such cryogenic liquid as nitrogen may differ from that in usual liquid as water, because the latent heat of cryogenic fluid is smaller than normal ones and the cavitation phenomena occur near the equilibrium boiling temperature.

There have been few experimental reports on cryogenic two phase fluids, especially on high-power laser induced cavitation bubbles (Maeno et al., 1990; Maeno et al., 1991; Tomita et al., 1994). This paper deals with an investigation of the behavior of laser induced vapor bubble in cryogenic liquid nitrogen. The bubble is produced by pulsed irradiation of a ruby laser focused in the cryostat. The dynamics of laser induced bubble is visualized by high-speed shadowgraphs of an image-converter camera. The pressure-pulse signal of the bubble motion is measured by a piezoelectric transducer in the liquid nitrogen. To compare with the experimental results, a numerical simulation has also been performed on the dynamics of a single spherical bubble in cryogenic liquid nitrogen with phase change effects. Furthermore, the equation of motion of the bubble with compressibility is also applied and numerical calculations are performed.

2 Experimental Facilities

In the present research, a specially designed cryostat for cavitation experiment as Fig. 1 is used (Maeno et al., 1994; Sato et al., 1994). The cryostat is capable of introduction and focusing of laser beam and also of flow visualization. As the possible experimental liquids, argon or nitrogen are available, and by using the liquid helium as the coolant it is also preferable to have the experiment on liquid hydrogen cavitation. In this report, the experiments have concentrated on cavitation in liquid nitrogen.

Contributed by the Fluids Engineering Division for publication in the JOURNAL OF FLUIDS ENGINEERING. Manuscript received by the Fluids Engineering Division June 29, 1995; revised manuscript received April 23, 1996. Associate Technical Editor: Jong H. Kim.

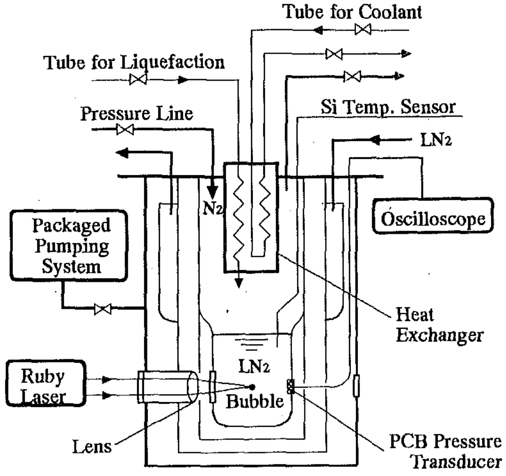

Fig. 1 Experimental apparatus (cryostat)

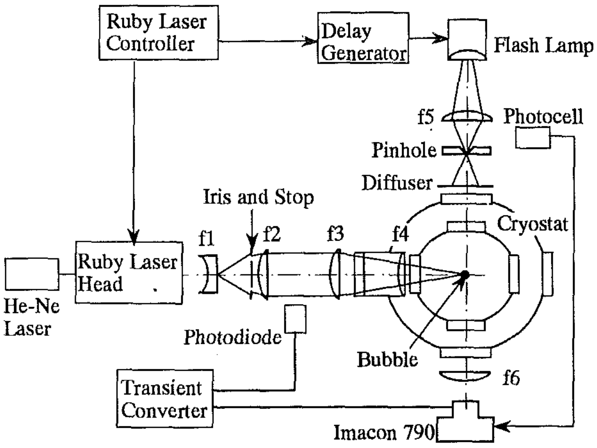

Fig. 2 Optical system for laser focus and visualization

The cryostat has 780 mm in outer height and 280 mm in outer diameter, and inner vessel is 150 mm in height and 38 mm in diameter. Two pairs of windows of 20 mm diameter and 8 mm thickness made of quartz glass are settled for laser-beam introduction and flow visualization. There is a port for pressurization of the experimental liquid in the cryostat by gas to produce the subcooled (nonequilibrium) conditions.

The pressure signal of cryogenic liquid in cryostat can be measured by a piezoelectric gauge (PCB piezotronics, 102A11B, rise time 2 μs, resonant frequency 250 kHz) that is settled at which it does not interfere with the pulsed-laser beam, and the temperature is also monitored by silicon diode thermometer (Scientific Instruments, Inc., Si-400NN).

Figure 2 shows the optical system for laser irradiation and flow visualization. Laser for bubble generation is a Q-switched giant pulse ruby laser (Nihon Kagaku Engng. Ltd., NAL-707P1, 0.8J, 89ns pulse width). The pulsed beam is first expanded by a concave lens with $f_1 = -25$ mm, then the expanded beam becomes parallel through a convex lens with $f_2 = 120$ mm, and the parallel beam is focused through 2 pieces of convex lens with $f_3 = 600$ mm and $f_4 = 70$ mm, and windows into the cryostat. In this experiment, the angle of beam convergence in liquid nitrogen is about 13 deg. In order to improve the energy distribution at the focal point and to limit the aberration of the focusing lens, iris and stop are settled between f_1 and f_2. The visualization of the induced bubble is performed by a flash lamp (Hadland Photonics, HVC-SL) and image-converter camera (Hadland Photonics, Imacon-790) with lens system. In the present experiment diffusive shadowgraph technique is employed.

A synchronization sequence makes it possible to take pictures of the bubble at precise instant with respect to the laser pulse. The output signal of the ruby laser controller is supplied to the laser head and simultaneously to the flash lamp through a delay generator (Sugawara, RE-306) with an adjustable delay. The light of the flash lamp is detected by a photocell whose output signal is used to trigger Imacon-790. The laser pulse, recorded by a photodiode, and the monitor signal of Imacon-790 are displayed on a transient converter (Riken Denshi Co. Ltd., TCFL-8000E) in order to measure the delay between the first picture and the instant of bubble generation.

As for the estimation of accuracy, pressure measurement with piezoelectric element and storage oscilloscope (12bit-1 MHz) resulted in ±1.2 percent uncertainty. The inaccuracy in time by framing mode of image-converter camera was ±1.0 percent, and the bubble radius measurements in framing photograph indicated the maximum uncertainty of ±5.0 percent. In temperature measurement of liquid nitrogen by Keithley digital multimeter the uncertainty was much less than ±1 percent.

3 Numerical Analysis

To compare the experimental results, a numerical analysis of a single vapor bubble in liquid nitrogen has been performed. We consider a spherical bubble with initial radius R_0 containing the vapor in an infinite volume of viscous liquid nitrogen (Maeno et al., 1994; Tomita and Shima, 1979). At time zero, the surrounding pressure increases instantaneously to p_∞ and the bubble begins to collapse. It is assumed that there is no thermodynamic equilibrium between the liquid and the bubble after its motion begins. The effects of inertia of the liquid and the condensation of the vapor are considered. In numerical analysis, the following assumptions are considered, i.e., 1 The effects of gravity and the viscosity of vapor in the bubble are neglected; 2 The bubble maintains its spherical shape during the whole process; 3 Inside the bubble the physical quantities are uniform.

As the equation of motion, the Rayleigh-Plesset equation for incompressible liquid is first used.

$$R\ddot{R} + \frac{3}{2}\dot{R}^2 = \frac{1}{\varrho_\infty}\left(p_v - p_\infty - \frac{2\sigma}{R} - 4\mu\frac{\dot{R}}{R}\right). \quad (1)$$

Nomenclature

c = velocity of sound
D_X, D_Y = diameters of ellipsoidal bubble
p = pressure
r = distance from bubble center
R = bubble radius
$\dot{R}$ = bubble wall velocity ($= dR/dt$)
t = time
T = temperature
U = internal energy
α_M = evaporation/condensation coefficient
γ = specific heat ratio
μ = viscosity
ϱ = density
σ = surface tension for liquid
$\mathcal{R}_v$ = gas constant

Subscripts

L = liquid side at bubble wall
0 = initial condition
v = vapor in bubble
∞ = infinit distance from bubble center

Superscript

* = saturated (equilibrium) conditions

For vapor within the bubble, the equation of state

$$p_v = \varrho_v \mathcal{R}_v T_v, \tag{2}$$

and the equation of energy conservation

$$\frac{d}{dt}\left(\frac{4}{3}\pi R^3 \varrho_v \hat{U}_v\right) = -p_v \frac{d}{dt}\left(\frac{4}{3}\pi R^3\right) - 4\pi R^2 \Delta U_{v\to L}, \tag{3}$$

have been used, where $\hat{U}_v$, $\Delta U_{v\to L}$ are the specific internal energy of vapor, the net rate of the flux of internal energy from the vapor to the liquid, respectively. The mass conservation of vapor in the bubble is indicated by

$$\frac{d}{dt}\left(\frac{4}{3}\pi R^3 \varrho_v\right) = 4\pi R^2 \dot{m}, \tag{4}$$

where $\dot{m}$ denotes the vapor mass transfer rate through the interface per unit time and unit area, and is given as follows (Theofanous et al., 1969; Fujikawa and Akamatsu, 1980),

$$\dot{m} = \frac{\alpha_M}{\sqrt{2\pi \mathcal{R}_v}}\left\{\frac{p_L^*(T_L)}{\sqrt{T_L}} - \frac{p_v}{\sqrt{T_v}}\right\}, \tag{5}$$

The saturation vapor pressure p_L^* is a function of temperature T_L with considering the radius of the surface curvature of bubble, and is given by

$$p_L^*(T_L) = p_{v\cdot\mathrm{sat}}(T_L)\exp\left\{\frac{-1}{\varrho_\infty \mathcal{R}_v T_L}\frac{2\sigma}{R}\right\}. \tag{6}$$

In Eq. (5), α_M is the coefficient of evaporation/condensation, i.e., a nonequilibrium parameter and $\dot{m}$ is strongly influenced by α_M value. In the numerical analysis, it is set in the range of $\alpha_M = 0.0 \sim 1.0$. This parameter is adjustable to compare with the experimental data in section 4.4 and it may relate to real condensation coefficient α_M.

Furthermore, we take the following Keller-Herring equation for compressible liquid (Prosperetti and Lezzi, 1986) in place of Eq. (1).

$$\begin{aligned}(1 - c_\infty^{-1}\dot{R})R\ddot{R} &+ \tfrac{3}{2}(1 - \tfrac{1}{3}c_\infty^{-1}\dot{R})\dot{R}^2 \\ &= \frac{1 + c_\infty^{-1}\dot{R}}{\varrho_\infty}\left\{p_v - \frac{1}{R}(2\sigma + 4\mu\dot{R}) - p_\infty\right\} \\ &\quad + \frac{R}{c_\infty \varrho_\infty}\frac{d}{dt}\left\{p_v - \frac{1}{R}(2\sigma + 4\mu\dot{R}) - p_\infty\right\}.\end{aligned} \tag{7}$$

In solving the equation system only vapor existence is assumed, that is typical for the cryogenic liquid experiments with rather pure conditions. From Eqs. (2), (4), the following relation concerning with p_v is obtained as

$$\begin{aligned}\frac{dp_v}{dt} = p_v\Bigg[&\frac{1}{T_v}\cdot\frac{dT_v}{dt} \\ &- \frac{3}{R}\left\{\dot{R} - \frac{\alpha_M T_v}{p_v}\sqrt{\frac{\mathcal{R}_v}{2\pi}}\left(\frac{p_L^*}{\sqrt{T_L}} - \frac{p_v}{\sqrt{T_v}}\right)\right\}\Bigg].\end{aligned} \tag{8}$$

From Eq. (3) the following equation is derived

$$\begin{aligned}\frac{dT_v}{dt} = \frac{-3T_v}{Rp_v}\Bigg\{&(\gamma_v - 1)p_v\frac{dR}{dt} \\ &+ \alpha_M p_L^*(T_v - T_L)\sqrt{\frac{\mathcal{R}_v}{2\pi T_L}}\Bigg\}.\end{aligned} \tag{9}$$

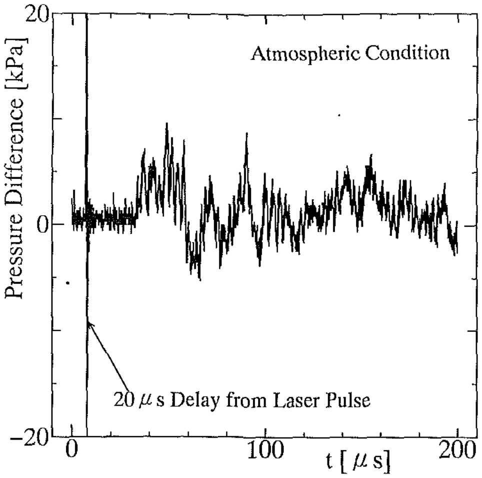

Fig. 3 Pressure signal from transducer

The problem for incompressible liquid is to solve Eqs. (1), (8) and (9), and for liquid compressibility it is to solve Eqs. (7), (8) and (9) numerically with the assumption that the temperature of liquid T_L is approximated to be equal to the infinity value T_∞. These equations are solved by fourth-order Runge-Kutta method with iterative substitution simultaneously from the following initial conditions

$$\left.\begin{aligned} R = R_0 &= R_{\max} \\ \dot{R} &= 0 \\ T_v = T_L &= T_\infty \\ p_v &= p_L^*(T_v) \end{aligned}\right\} \quad \text{at} \quad t = 0. \tag{10}$$

The assumption $T_L = T_\infty$ is, of course, not physically accurate. According to the results by Fujikawa and Akamatsu (1980) for water, the liquid temperature at bubble interface at the strong shrink and rebound of 5 percent of R_0 increases from 293 K to 474 K, which is much smaller value than gas temperature inside the bubble. Therefore, in our relatively weak rebound in liquid nitrogen with small subcooled degree, the temperature increase by the thermal diffusivity effects in liquid can be regarded as so small value, that $T_L = T_\infty$ assumption may not gives us largely deviated results from exact solutions.

4 Results and Discussion

4.1 Measurement of Pressure Variation. With regard to the results of pressure measurement of cryogenic liquid in cryostat, Fig. 3 shows the pressure time variation after 20 μs from the laser pulse under atmospheric conditions. The strong compression wave emitted from the bubble formation is seen to be positive, while the expansion wave, resulting from the reflection of at free surface of the liquid, is negative. Then these pressure waves seem to reflect randomly at the wall of test section and at the liquid-gas interface. The distance from the pressure gauge to focal point is long in 26 mm, so the pressure signal from bubble rebound can not detected clearly. Under pressurized conditions, the generated bubble becomes smaller and it vibrates faster than the one under atmospheric conditions.

4.2 The Behavior of the Bubble. It is known that when a pulsed laser beam is focused in a liquid, the breakdown first occurs and the plasma is formed at the focal point. The breakdown threshold depends strongly on the nature of liquid as well as the characteristics of pulsed laser. For example, Vogel and Busch (1993) have reported that the threshold for breakdown and plasma formation in distilled water was 200 μJ for ns-pulse.

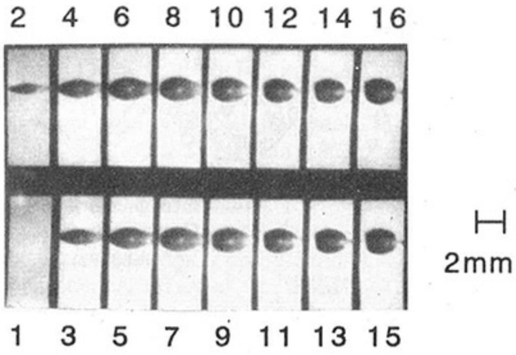

Fig. 4(*a*)

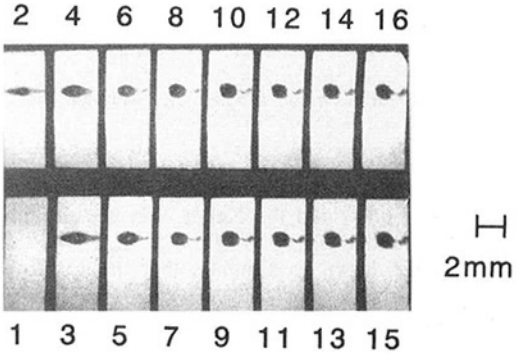

Fig. 4(*b*)

Fig. 4 Diffusive shadowgraphs of induced bubble. These series are taken from 5 μs before laser pulse at 5×10^4 frames/s under (*a*) atmospheric, (*b*) pressurized conditions (Δp = 98 kPa).

In the present experiment, since liquid nitrogen is employed as an experimental fluid, it may be more difficult to have breakdown and plasma formation as its molecular structure has higher threshold than water for ionization and dissociation (Yoshino, 1980; Hernandez et al., 1993). The experimental temperature of liquid nitrogen, however, is much closer to its boiling point than water, so the liquid is much more likely to evaporate. Moreover, the duration and energy of our pulsed ruby laser are larger than those of the experiment by Vogel and Busch (1993), so the breakdown and plasma are actually formed in cryogenic nitrogen. Then after the plasma formation, it turns into the vapor bubble to show the rapid inflation by high temperature and pressure of the plasma, and a shock wave is produced simultaneously.

Figure 4 shows a series of diffusive shadowgraphs of the growth, shrink, and rebound of the bubble in liquid nitrogen taken by Imacon-790. The frame speed is 5×10^4 frames/s and first frame is taken 5 μs before the ruby laser pulse. In Fig. 4(*a*), the shadowgraphs are taken under atmospheric conditions and Fig. 4(*b*) under slightly subcooled conditions that are pressurized by gas nitrogen of +98 kPa just before the laser irradiation.

In Fig. 4(*a*), the generated bubble expands to maximum radius in the seventh frame. Then it slowly shrinks by twelfth frame and rebounds. In Fig. 4(*b*), on the other hand, the bubble expands faster by fourth frame. Then it shrinks faster by seventh frame and rebound. So the motion of bubble under subcooled conditions shows an oscillation with shorter period than that under atmospheric conditions. Furthermore, the bubble sizes of Fig. 4(*b*) are smaller than those of Fig. 4(*a*). Since the focusing angle of the laser beam is large enough to produce a spherical bubble, the initial shape of the bubble is ellipsoidal sphere, and the bubble becomes rather spherical after indicating its maximum shape.

Figure 5 shows also a series of diffusive shadowgraphs of the bubble in cryogenic nitrogen under pressurized conditions (+98 kPa). The frame speed is the same as in Fig. 4, and it is taken from 75 μs after the ruby laser pulse, i.e., the picture series has been taken 80 μs later than Fig. 4(*b*). From the seventh frame in Fig. 5, the instability of the bubble surface is clearly observed, which is the characteristic phenomenon of the motion of the bubble in cryogenic liquid. In the present experiment, the produced bubble in liquid nitrogen is ellipsoidal sphere in the initial stage as mentioned before. So the bubble has inevitably the origin of the second-order mode of its vibrational shape. But the bubble and its surface in cryogenic liquid are strongly influenced by the thermal effects with time, and the oscillation mode seems to be changed from second order to higher order that causes the bubble to collapse with a complicated shape. In about 50 percent of our visualized photographs under pressurized conditions, strong instability of bubble shape after first rebound has been observed depending mainly on the laser power.

4.3 Results of Numerical Calculation for a Single Bubble. Figure 6 presents the calculated results with dimensionless radius for a single spherical bubble under (*a*) atmospheric condition (p_∞ = 101.3 kPa) and (*b*) pressurized condition (p_∞ = 199.3 kPa) with initial bubble radius R_0 = 1.0 mm and T_∞ = 77.23 K. The physical properties in the calculation are indicated Table 1.

The calculations with/without compressibility of the liquid are carried out, and the results are drawn in the same figures. The value of nonequilibrium parameter α_M of phase change is taken from 0.0 (adiabatic) to 1.0 (isothermal). In both of the results in Figs. 6(*a*) and (*b*), the bubble radii seem to oscillate for $\alpha_M = 0.0 \sim 0.1$, but in the results for $\alpha_M = 1.0$ dimensionless radius decreases monotonously. The reason is that the most of vapor within the bubble condenses very fast accompanying with the bubble collapse. This tendency of the bubble motion under subcooled conditions in Fig. 6(*b*) is more remarkable than that under atmospheric conditions in Fig. 6(*a*). In Fig. 6(*b*), the curves under slightly subcooled conditions oscillate more violently than those in Fig. 6(*a*). The rebounds are seen to occur earlier in Fig. 6(*b*) than in Fig. 6(*a*) and these results depend strongly on the value of parameter α_M.

Furthermore, from the curves in Fig. 6(*a*), there is no significant difference between the results of incompressible and compressible liquid calculations. Though it increases in Fig. 6(*b*), its effects is smaller than that of phase change.

4.4 Comparison Between Numerical and Experimental Results. In the present experiments, we consider the shapes of the laser induced bubbles, such as the series of shadowgraphs in Fig. 4 shows to be ellipsoids of revolution, and then we estimate an equivalent radius that the bubble would have if it were a sphere of the same volume. The experimental results for

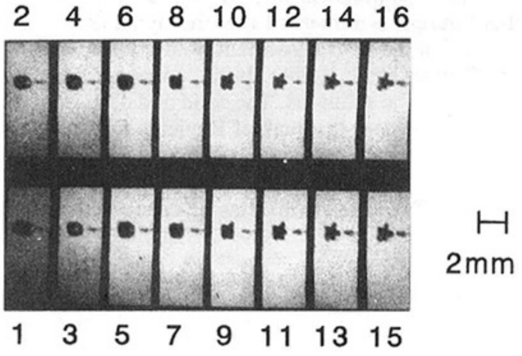

Fig. 5 The instability of bubble surface. The series is taken from 75 μs after laser pulse at 5×10^4 frames/s under pressurized conditions.

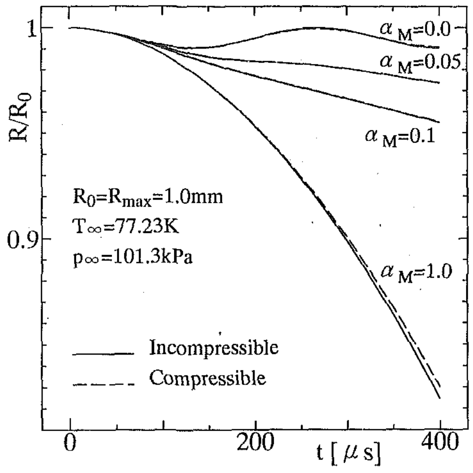

Fig. 6(*a*)

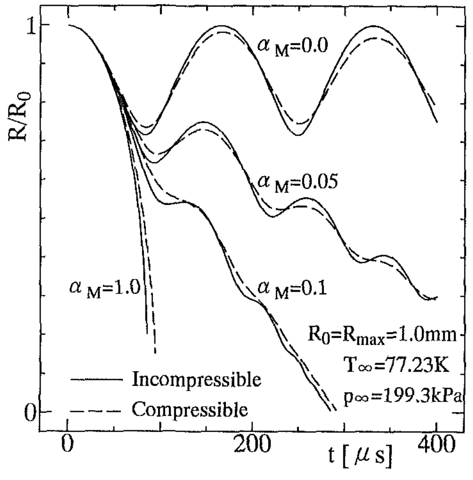

Fig. 6(*b*)

Fig. 6 Calculated time variation of bubble radius. (*a*) Atmospheric, (*b*) Pressurized conditions (Δp = 98 kPa).

temporal motion of a laser induced bubble with $R_{\max}$ of 0.86 ~ 1.10 mm in liquid nitrogen are compared with numerical results, as shown in Fig. 7. Furthermore, the Rayleigh's solution (indicated by the broken curve) for an empty cavity given by the Rayleigh equation (Rayleigh, 1917)

$$R\ddot{R} + \tfrac{3}{2}\dot{R}^2 = \frac{1}{\varrho_\infty}(p_v - p_\infty) \tag{11}$$

is also plotted in Fig. 7, where from $t = 0$ to the maximum radius the solution curve is also folded at the maximum point. This solution is dominated only by inertia in liquid.

In this figure it is remarked that the dynamics in the initial stage of the bubble is in agreement with the folded Rayleigh's solution (Tomita et al., 1994). In the collapse stage, however, data differ from the solutions. The solid and dash-dotted curves, which are drawn from the peak of Rayleigh's solution, indicate

Table 1 Physical properties of cryogenic nitrogen

c_∞	[m/s]	939.6048
γ_v	[—]	1.4559
μ	[Pa s]	1.629×10^{-4}
ρ_v	[Kg/m^3]	4.554
ρ_∞	[Kg/m^3]	809.052
σ	[N/m]	8.916×10^{-3}
$\mathcal{R}_v$	[J/(Kg K)]	350.855

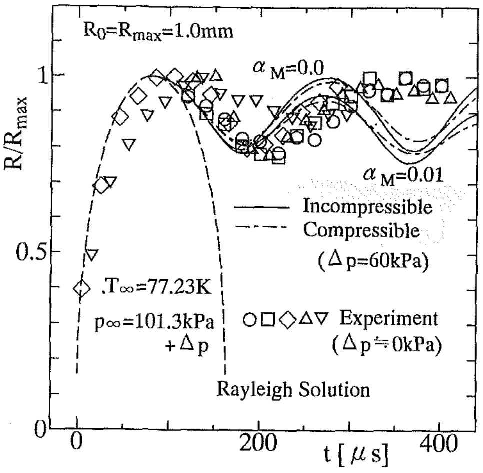

Fig. 7 Comparison of measured bubble radius with numerical results

the numerical solution of Rayleigh-Plesset equation (without liquid compressibility) and the Keller-Herring solution (with compressibility) under Δp = 60 kPa with α_M = 0.0 and 0.01. These curves are drawn to simulate that the first minimum rebounding radii are roughly coinciding with the experimental data. Both compressible and incompressible results, however, deviate largely from the measured data after the first rebound. It is necessary to take the bubble inflating process into account in our numerical analysis.

As mentioned before, the present experimental data in the initial stage are in agreement with the Rayleigh's solution. We estimated that the initial inflating phase of bubble is near adiabatic change, and temperature within the bubble is obtained when the bubble radius is the half of the maximum bubble radius by adiabatic relation. However, if the bubble inflation phase would be exactly adiabatic change, p_v of its half radius of $R_{\max}$ becomes about 2 MPa, and in the calculated curve the peak point that the bubble radius becomes its maximum is much higher than the peak of the Rayleigh's solution. So we assume that the appropriate vapor pressure p_v is 650 kPa. This vapor pressure inside the bubble, considering the term that includes the surface tension in Eq. (1), is firstly obtained to simulate the first maximum radius roughly with α_M = 0.0. The numerical calculation is performed by using the initial conditions as follows,

$$\left.\begin{aligned} R &= R_0\ (= 0.5\ \text{mm}) \\ (R_{\max} &= 1.0\ \text{mm}) \\ \dot{R} &= 0 \\ T_{v0} &= 199.3\ \text{K} \\ T_L &= T_\infty \\ p_{v0} &= 650\ \text{kPa} \\ p_\infty &= 101.3\ \text{kPa} \end{aligned}\right\} \quad \text{at} \quad t = 0 \tag{12}$$

The initial conditions p_{v0}, T_{v0}, and $\dot{R}$ and $R_0 = R_{\max}/2$ seem a crude assumption. In our calculations, the value of p_{v0} was much more sensitive to give the first $R_{\max}/R$ value than T_{v0}, and the value $\dot{R}_0$ gave us sometimes vibrating $R_{\max}$ points giving the excess energy at initial stage. So we have chosen $\dot{R} = 0$ at the smallest initial R in our numerical integration with given range of α_M, and adjusted p_{v0} to simulate the folded Rayleigh curve in the inflation phase with $\alpha_M = 0$.

The obtained results are shown in Fig. 8. The broken curve indicates the Rayleigh's solution as in Fig. 7. The dash-dotted curve presents the results for $\alpha_M = 0$ and the solid curve is for

$\alpha_M = 0.03$. In Fig. 8, the calculated results under the initial conditions of Eq. (12) are in agreement with the experimental results from the peak of the maximum radius to minimum one. The effects of phase change explain well the behavior of induced bubble after taking its first peak. In Figs. 7 and 8, 95 percent of $R/R_{\max}$ data fall within ±9.2 percent error, but near the first shrink and rebound point, there are several scattered data to increase the error range.

The discrepancy between the measured and calculated radii of rebound phase in Figs. 7 and 8 seems to be mainly originated from nonspherical effect of the bubble. In the present study, though we consider the shape of the bubble from its initial stage to be a sphere in calculation, the bubble is ellipsoidal sphere in fact. So the surface area of the bubble in this calculation is smaller than that in the experiment, so the value of α_M is overestimated than that in the real bubble behavior. The time variation of aspect ratio of observed bubble, D_Y/D_X, is plotted in Fig. 9, where D_X is the diameter in the horizontal direction, and D_Y is vertical one. For D_Y/D_X data before the first rebound, they fall within ±5.0 percent error. After the rebound, however, the bubble shape itself shows an instability, and D_Y/D_X data scatter randomly to within ±9.5 percent. The plotted aspect ratio is converged to $D_Y/D_X = 1.0$ (sphere) gradually with time. This ratio during the bubble growth and rebound is smaller than the results of Tomita et al. (1994). The reason is that as mentioned before, the focusing angle of the laser beam is smaller than that of Tomita et al. The present experimental apparatus has been a pioneering setup in cryogenic laser cavitation, and the optical system of focusing was arranged from outside of the cryostat. Therefore, there is the vacuum heat-shield between our optical system and the focal point. That is why our focusing angle is small.

There have been systematic researches on nonspherical shape of the bubble in normal temperature liquids (Kling and Hammit, 1972; Naudé and Ellis, 1961; Plesset and Chapman 1971), and precise discussion on the bubble behavior near rebound phase in the vicinity of solid or free surface boundaries. In our experiments, however, the bubble has very nonspherical shape from the initial inflating stage in liquid nitrogen. Its ellipsoidal revolution shape has the small and large curvature radii, where the former shows the rapid shrink and rebound, the latter indicates much slower shrinking rate. Both effects results in a damped oscillation shape in $R/R_{\max}$ with time. The more precise data comparing with spherical ones will be needed in further discussion. Thermal and phase change effects strongly damps the dynamics of bubble in liquid nitrogen as shown in Fig. 8.

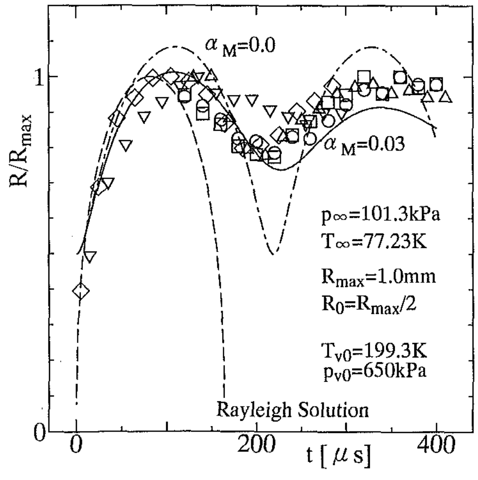

Fig. 8 Comparison of measured bubble radius with numerical results (modified initial conditions)

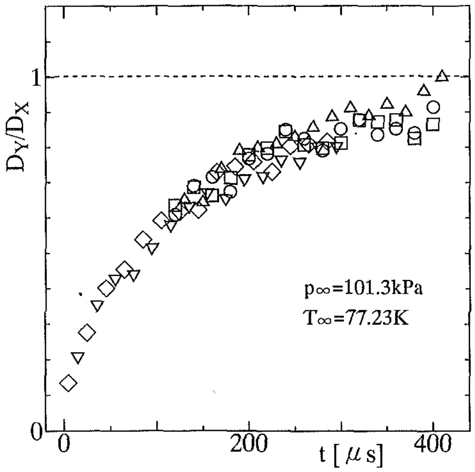

Fig. 9 Time variation of bubble aspect ratio

5 Conclusion

The experimental and analytical investigations of the dynamics of laser induced bubble in cryogenic liquid nitrogen have been carried out. In experiment, the inflation, shrink and rebound phenomena of the laser induced bubble in liquid nitrogen are visualized by diffusive shadowgraph technique with an image-converter camera. From the flow visualization, though the initial stage of the bubble is not spherical one, the time variation of its equivalent radius can be observed. Furthermore, the numerical analysis for a single spherical bubble in liquid nitrogen has been performed by the incompressible Rayleigh-Plesset equation and by the compressible Keller-Herring equation. It is noted that the thermal effects with phase change have the important part on the oscillation of vapor bubble in cryogenic liquid after taking the first maximum point of bubble radius.

Acknowledgment

The authors would like to express their heartful appreciation to Dr. Christophe PRAT, JSPS invited researcher, Chiba university for the fruitful discussions.

References

Alloncle, A. P., Dufresne, D., and Autric, M., 1993, "Visualization of Laser-Induced Vapor Bubbles and Pressure Waves," *Bubble Dynamics and Interface Phenomena,* Blake J. R. et al., eds., Kluwer Academic Publishers, The Netherlands, pp. 365–371.

Fujikawa, S., and Akamatsu, T., 1980, "Effects of the Non-Equilibrium Condensation of Vapour on the Pressure Wave Produced by the Collapse of a Bubble in a Liquid," *Journal of Fluid Mechanics,* Vol. 97, pp. 481–512.

Hernandez-Avila, J. L., Bonifaci, N., and Denat, A., 1993, "Hot Electron Phenomena in Liquid and Gaseous Argon and Nitrogen in Divergent Electric Fields," *Proceedings of 1993 IEEE 11th International Conference on Conduction and Breakdown in Dielectric Liquids,* Fuhr J. and Biller P., eds., pp. A4.57–61.

Kattan, R., Denat, A., and Lesaint, O., 1989, "Generation, Growth, and Collapse of Vapor Bubbles in Hydrocarbon Liquids under a High Divergent Electric Field," *Journal of Applied Physics,* Vol. 66, pp. 4062–4066.

Kattan, R., Denat, A., and Bonifaci, N., 1991, "Formation of Vapor Bubble in Non-Polar Liquids Initiated by Current Pulses," *IEEE Transaction on Electrical Insulation,* Vol. 26, No. 4, pp. 656–662.

Kling, C. L. and Hammit, F. G., 1972, "A Photographic Study of Spark-Induced Cavitation Bubble Collapse," ASME *Journal of Basic Engineering,* Vol. 94, pp. 825–833.

Lauterborn, W., and Bolle, H., 1975, "Experimental Investigations of Cavitation-Bubble Collapse in the Neighborhood of a Solid Boundary," *Journal of Fluid Mechanics,* Vol. 72, pp. 391–399.

Maeno, K., Yokoyama, S., and Hanaoka, Y., 1990, "Study on Laser-Induced Cavitation Bubbles in Cryogenic Liquids," *Proceedings of 17th International Symposium on Shock Waves and Shock Tubes,* AIP-No. 208, pp. 383–388.

Maeno, K., Yokoyama, S., and Hanaoka, Y., 1991, "A Study of Laser-Induced Bubble in Cryogenic Fluid," *Journal of Japan Society for Aeronautical and Space Sciences,* Vol. 39, No. 449, pp. 287–293 (in Japanese).

Maeno, K., Sato, H., Honma, H., and Autric, M., 1994, "On the Behavior of Laser Induced Bubble in Cryogenic Liquids—Experiments and Analysis for Liquid Nitrogen-," *The 2nd International Symposium on Cavitation,* Kato, H., ed., Tokyo Japan, pp. 317–320.

Naudé, C. F. and Ellis, A. T., 1961, "On the Mechanism of Cavitation Damage by Non-hemispherical Cavities Collapsing in Contact with a Solid Boundary," ASME *Journal of Basic Engineering,* Vol. 83, pp. 648–656.

Plesset, M. S. and Chapman, R. B., 1971, "Collapse of an Initially Spherical Vapour Cavity in the Neighborhood of a Solid Boundary," *Journal of Fluid Mechanics,* Vol. 47, pp. 283–290.

Prosperetti, A., and Lezzi, A., 1986, "Bubble Dynamics in a Compressible Liquid.—Part 1. First-Order Theory," *Journal of Fluid Mechanics,* Vol. 168, pp. 457–478.

Rayleigh, L., 1917, "On the Pressure Developed in a Liquid during the Collapse of a Spherical Cavity," *Philosophical Magazine, S.6.* Vol. 34. No. 200. pp. 94–98.

Reboud, J. L., Sauvage-Boutar, E., and Desclaux, J., 1990, "Partial Cavitation Model for Cryogenic Fluids," *Cavitation and Multiphase Flow Forum-1990,* FED-Vol. 98, pp. 165–170.

Sato, H., Maeno, K., Sun, X. W., Odagawa, M., and Honma, H., 1994, "Study on the Behavior of Laser Induced Bubbles in Cryogenic Nitrogen," *Proceedings of 10th International Symposium on Gas Flow and Chemical Lasers,* SPIE Vol. 2502, pp. 530–535.

Shimura, T., Watanabe, M., and Ujino, I., 1992, "Dynamics Response of the Cavitating LE-7 LOX Pump," *Journal of Japan Society for Aeronautical and Space Sciences,* Vol. 40, No. 464, pp. 509–514 (in Japanese).

Theofanous, T. G., Biasi, L., and Isbin, H. S., 1969, "A Theoretical Study on Bubble Growth in Constant and Time-Dependent Pressure Fields," *Chemical Engineering Science,* Vol. 24, pp. 885–897.

Tomita, Y., and Shima, A., 1979, "The Effects of Heat Transfer on the Behavior of a Bubble and the Impulse Pressure in a Viscous Compressible Liquid," *Zeitschrift für Angewandte Mathematik,* Vol. 59, pp. 297–306.

Tomita, Y., Shima, A., Tsubota, M., and Kano, I., 1994, "An Experimental Investigation on Bubble Motion in Liquid Nitrogen," *The 2nd International Symposium on Cavitation,* Kato, H., ed., Tokyo Japan, pp. 311–316.

Vogel, A., and Busch, S., 1993, "Time-Resolved Measurements of Shock-Wave Emission and Cavitation-Bubble Generation in Intraocular Laser Surgery with ps- and ns-Pulses," *Bubble Dynamics and Interface Phenomena,* Blake J. R. et al., eds., Kluwer Academic Publishers, The Netherlands, pp. 105–117.

Yoshino, K., 1980, "Dependence of Dielectric Breakdown of Liquids on Molecular Structure," *IEEE Transaction on Electrical Insulation,* Vol. EI-15, No. 3, pp. 186–200.

Journal of Fluids Engineering

Technical Briefs

Volume Flow-Rate Measurements and Scaling Laws for a Transverse-Inlet Multiple-Disk Fan

M. G. Schlutt[1] **and D. R. Dowling**[2]

The air moving capacity of a transverse-inlet multiple-disk fan has been measured experimentally and the results successfully collapsed with a simple scaling law. The disk fan studied was an array of several hundred closely spaced plastic disks that rotated about a common axis inside an approximately semi-cylindrical housing. A splitter plate lying parallel to the axis of rotation and tangent to the disks separated the inflow and outflow streams. The volume flow rate of air per unit length along the axis of rotation was measured using standard LDV techniques. For disk spacings greater than 1 mm, the volume flow rate was found to be essentially proportional to $\omega\sqrt{hR^3}$, *where* ω = *radian rotation rate of the disks,* h = *disk spacing, and* R = *disk radius. This scaling law was derived from a simple force balance for a small fluid element moving between rotating disks. The Reynolds number of the experiments,* $\omega\sqrt{h^3R}/\nu$, *was varied from* 2×10^2 *to* 10^3. *In addition, the air-moving capability of the disk fan was found to be nearly independent of the geometrical placement of the rotating disks within the fan housing.*

Nomenclature

c_f = skin friction coefficient
D = clearance between the outer disk edges and the curved portion of the housing (mm)
Δp = pressure rise across the fan (Pa)
h = disk spacing (mm)
L = length of the rotating shaft (mm)
μ = fluid viscosity (kg m^{-1} s^{-1})
ν = fluid kinematic viscosity (m^2 s^{-1})
R = disk radius (mm)
Re = Reynolds number = $\omega\sqrt{h^3R/\nu}$
ρ = fluid density (kg m^{-3})
Q = total volume flow rate of the disk fan (m^3 s^{-1})
q = Q/L = volume flow rate per unit length of fan (m^2 s^{-1})
s = angular width of the inlet port (degrees)
U = radial flow scaling velocity = $\omega\sqrt{hR}$ (m s^{-1})
w = angular width of the outlet port (degrees)
ω = rotation rate of the disks (rad/s)
x = location of the outflow velocity measurements (mm)

Introduction

The concept of unbladed steady-flow turbomachinery based on the centrifugal and viscous forces acting on fluid moving between rotating disks has existed since the turn of the century (Tesla, 1913). This class of devices has attracted investigators interested in applications of this technology to pumps and turbines (see Lawn and Rice, 1974; Crawford and Rice, 1974; Bakke and Kreith, 1977; Roddy et al., 1987; and the references contained therein). The emphasis in these previous studies has been on devices that resemble conventional turbomachines with the rotating blade set replaced by a rotating stack of closely spaced parallel disks. The main performance advantage claims of this type of turbomachinery are robust operation with non-Newtonian fluids and multiphase flows, low sensitivity to cavitation, and greater pumping stability (Roddy et al., 1987).

The motivation for this investigation was the noise-reduction benefit from the rotating disks' steady pumping mechanism when compared to traditional fans whose vanes apply oscillatory forces to the moving fluid (see Pierce, 1989; Beranek and Vér, 1992). The results of this study suggest that multiple-disk fans should be able to move enough air for many applications where noise control requirements are dominant. Potential uses include automotive climate control systems, office-equipment cooling, residential appliances, and air-handling systems (for example see: MacGillivray et al., 1995; Bezemek and Mongeau, 1995).

This investigation differs from previous efforts in two important ways. First, the inlet to the multiple-disk fan in this investigation was perpendicular to the axis of disk rotation and not parallel to it (see Fig. 1). This transverse inlet geometry simplifies the construction of the device since the disks can be directly mounted on a solid direct-drive shaft. In the current study, several hundred identical disks were used on a long shaft, $L/R > 10$, so that the inlet and outlet flows from the fan could be considered two dimensional in the plane perpendicular to the axis of rotation of the disks. The second difference concerns emphasis. The focus of this study was the fan's air-moving capability for small Δp. A unique scaling law was developed to collapse the measured volume flow rate data for variations in disk spacing, disk radius, housing-disk clearance, and disk rotation rate for the limit of low pressure rise across the fan. In particular, the dimensionless flow rate was found to be nearly independent of the Reynolds number, suggesting that the dominant fluid-disk interaction is turbulent, and that the results can

---

[1] Project Engineer, Whirlpool Research and Engineering, Monte Road, Benton Harbor, MI 49022.

[2] Assistant Professor, Department of Mechanical Engineering and Applied Mechanics, University of Michigan, Ann Arbor, MI 48109.

Contributed by the Fluids Engineering Division of THE AMERICAN SOCIETY OF MECHANICAL ENGINEERS. Manuscript received by the Fluids Engineering Division January 15, 1996; revised manuscript received August 21, 1996. Associate Technical Editor: J. A. C. Humphrey.

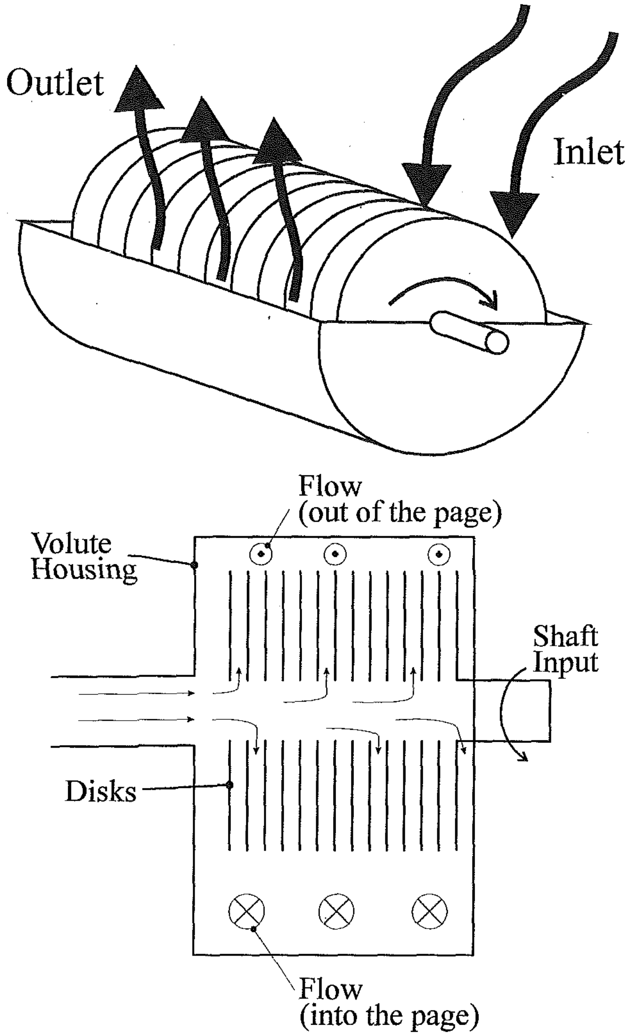

Fig. 1 Drawings of (*a*) perspective view of a transverse-inlet multiple-disk fan and (*b*) cross-sectional view of an axial-inlet multiple-disk pump

be readily scaled to larger higher-speed devices. This approach contrasts with the traditional performance study of Roddy et al. (1987) for a centrifugal water pump utilizing 3 to 11 rotating disks, and involving five dimensionless groups.

Scaling Arguments

The goal of this investigation was to determine how q depends on geometry, rotation speed, and the properties of the moving fluid for a transverse-inlet multiple-disk fan for small Δp. Figure 2 shows a cross sectional schematic of a transverse-inlet multiple-disk fan. If U denotes the mean radial velocity of fluid ejected into the outlet plenum from the edge of the rotating disks, q is readily estimated from:

$$q = wRU. \tag{1}$$

With w and R known (or easily measured), a reliable quantitative prediction of U was sought. A dimensional analysis approach involving nine independent parameters (h, D, R, s, w, L, ρ, μ, and ω) was used to generate a functional prediction for U in terms of six dimensionless groups, i.e.,

$$\frac{U}{\omega R} = F\left(\frac{h}{R}, \frac{L}{R}, \frac{D}{R}, s, w, \frac{\rho\omega Rh}{\mu}\right), \tag{2}$$

where F is an undetermined function. Further parametric reduction is possible with the following simple scaling argument for a cubical fluid element of volume h^3 in contact with flat disks rotating at angular velocity ω. The radial inertial force on the fluid element will be proportional to $\rho h^3\omega^2 R$. Radial fluid motion will be impeded by friction between the fluid element and the disk surfaces. These frictional forces will be proportional to the contact area between the fluid element and the disks = $2h^2$, the local skin friction coefficient = c_f, and the local dynamic pressure, assumed here to be proportional to $\frac{1}{2}\rho U^2$. A scaling law for U can now be developed by proportionally balancing the inertia and friction forces for the fluid element, i.e.,

$$\rho h^3\omega^2 R \propto 2h^2 c_f \frac{1}{2}\rho U^2. \tag{3}$$

Solving for U produces:

$$U \propto \omega\sqrt{\frac{hR}{c_f}}. \tag{4}$$

This relationship defines how the scaling velocity must depend on h and R, so replacing ωR in Eq. (2) by $\omega\sqrt{hR}$ allows to h/R be dropped. In addition, if L/R is large enough to make end effects negligible, it may be dropped from Eq. (2) as well, leaving:

$$U = \omega\sqrt{hR}F\left(\frac{D}{R}, s, w, \frac{\rho\omega R^{1/2}h^{3/2}}{\mu}\right). \tag{5}$$

Here, c_f has been presumed to depend only on Re = $\omega\sqrt{h^3R}/\nu$ so its effects are included through F's dependence on Re. Folding Eq. (5) back into Eq. (1) and absorbing the multiplying w-factor from Eq. (1) into F, establishes the final functional prediction for q:

$$q = \omega R^{3/2}h^{1/2}F\left(\frac{D}{R}, s, w, \frac{\rho\omega R^{1/2}h^{3/2}}{\mu}\right). \tag{6}$$

The relative importance of the first and last two dimensionless groups inside F was experimentally investigated.

Experimental Setup

The experiments were conducted using a single transverse-inlet multiple disk fan whose geometry and rotational speed

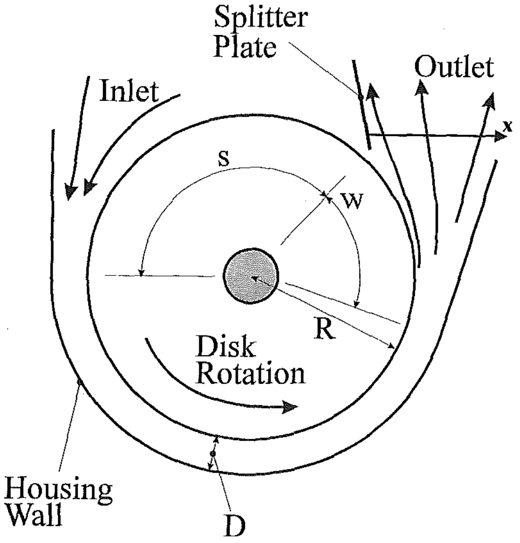

Fig. 2 Schematic of the cross section of a transverse-inlet multiple-disk fan showing the inlet and outlet air flows, splitter plate, housing contour, shaft, and rotating disk circle

Table 1 Dimensional and parametric ranges of the experiments

Parameter	Range	Uncertainty	Dimension
D	3.0–8.0	±0.25	mm
Δp	0–40	±2.	Pa
h	1.0, 2.0, 3.0	±0.1	mm
L	767.	±2	mm
R	45.–55.	±0.025	mm
s	130°	±2	degree
w	65°–75°	±2	degree
Q	0–0.13	±0.007	m^3/s
q	0–0.18	±0.007	m^2/s
U	1.4–4.5	±0.1	m/s
ω	146.6–387.5	±0.4	rad/s
x	0–70	±1.	mm

could be modified. The tested ranges for the dimensional parameters of the fan are given in Table 1. The rotation rate of the fan's Electrocraft servo-motor was feedback set using an Electrocraft Motomatic II controller and held to within ±0.4 rad/s. In cross section, the test fan was essentially identical with the schematic on Fig. 2 except that a finned-grill was placed over the inlet to provide: i) some flow straightening at the inlet, and ii) a small nominal pressure-drop load typical of envisioned disk-fan applications involving air passage through a heat exchanger. The fan's dimensionless specific speed, $N_s = \omega\sqrt{Q}/(\Delta p/\rho)^{3/4}$, was typically above 10.

The measurements were made with a laser-Doppler velocimetry (LDV) system mounted on a linear traverse such that a plane of the outlet flow could be measured at discrete points using the coordinate system depicted in Fig. 2. The position uncertainty of the traversing system was ±1.0 mm. The mean velocity at each measurement point in the fan's outlet flow was determined from 2000 validated bursts taken over approximately 25 seconds with a Dantec Flo-lite system. This sampling window far exceeded any turbulence time scale. All measurements were made at room temperature (20°C) and pressure (101 kPa) with mist seeding from an ultrasonic humidifier.

After verifying that the fan's outflow was two dimensional, the center plane of the fan was selected as the measurement plane. One velocity profile, consisting of thirteen LDV readings equally spaced across the outlet, was measured for each parameter combination. A selection of velocity profile measurements were repeated and found to agree within 1 percent. The measured profiles were numerically integrated using the trapezoidal rule to determine q. A typical velocity profile is shown in Fig. 3 with straight lines between measurements to indicate trapezoidal boundaries. The high speed region occurs near the outer wall of the fan housing.

To further verify the LDV measurements and determine Δp, Q was measured with a Merriam laminar airflow element (model no. 50MC2-4) and an outlet chamber designed and built to conform with ANSI/AMCA standard no. 210-85, and ANSI/ASHRAE standard no. 51-1985. A comparison made between the overall LDV-system measured Q (integrated velocity profile multiplied by total effective length of outlet) and the measurements using the Merriam device showed ±1 percent agreement over the full range of ω when a effective outlet length of $0.93L$ was used to account for end effects. The fan's pressure rise was typically 10 Pa. Fan efficiency was approximately 10 percent.

Volume Flow Rate Results

The scaled measurements of q are plotted on Fig. 4. As the Reynolds number is increased the dimensionless volume flux approaches a constant value ($q \approx \omega\sqrt{hR^3}$) which indicates a Re-independent flow regime, and verifies the effectiveness of the scaling law.

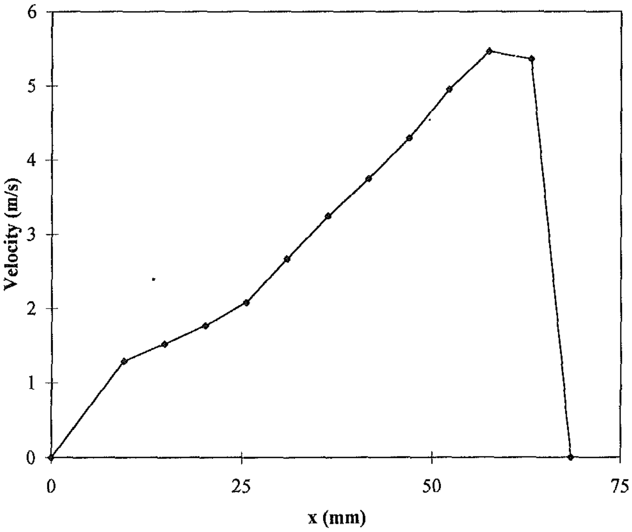

Fig. 3 Typical measured fan-outlet mean velocity profile. See Fig. 2 for the location and orientation of the x-axis. The high-speed portion of the flow occurs near the fan's housing. The lower-speed portion of the flow is nearer to the rotating disks. The measurement uncertainty of each data point is ±1 percent.

The general trend of increased dimensionless volume flux for lower Reynolds numbers shown on Fig. 4 can likely be attributed to changes in c_f. However, scaling the current results to Reynolds numbers below the measured values is not recommended since a no-flow condition existed at the lowest value of h tested (1 mm). This implies that h/R must be greater than approximately 0.02 for proper fan operation. It is hypothesized that this condition is related to the absence of sufficient centrifugal force to destabilize the viscous fluid-disk interaction. Bakke and Kreith (1977) noted a qualitatively similar phenomena in performance studies of an axial-inlet disk pump. However, quantitative comparison isn't possible because the transverse-inlet geometry requires both radially-inward and radially-outward flows to exist simultaneously as the fan functions while the axial-inlet geometry requires only radially-outward flow.

Further examination of Fig. 4 shows that the remaining scatter in the data is primarily caused by variations in the dimensionless clearance ratio D/R. At any Reynolds number, the vertical spread in the measured data consistently indicates that somewhat higher volume fluxes are achieved at larger clearance ratios. The remaining scatter on Fig. 4 is thought to be caused by

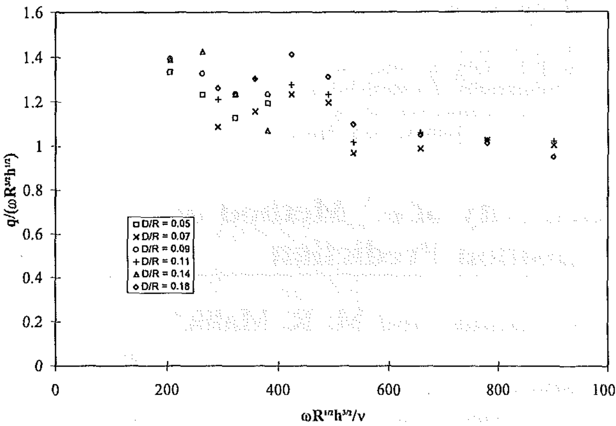

Fig. 4 Transverse-inlet multiple-disk fan dimensionless volume flow rate per unit length versus Reynolds number at low pressure rise across the fan. The vertical placement of each data point is estimated to be ±5 percent uncertain because of mild, but uncontrolled, variations in the pressure drop across the fan inlet.

Re-dependent flow turning in the fan inlet, or variations in the pressure-drop load seen by the fan for the different flow configurations, with larger flow rates producing somewhat larger pressure drops across the fixed-geometry inlet flow straightener. A correction to constant pressure-drop conditions would probably change the vertical placement of the plotted points on Fig. 4 by only a few percent.

As a final note, w was varied from 65° to 75° with little effect on the fan's air-moving performance. Therefore, fan performance is robust regarding reasonable clearance and outlet-size variations, which may make disk fans an attractive alternative to bladed fans and compressors in some applications.

Conclusions

The results presented here lead to two important conclusions concerning the air-moving capability of a transverse-inlet multiple-disk fan operating at high specific speed. (1) The volume flow rate of the fan is proportional to $\omega\sqrt{hR^3}$ once the Reynolds number is high enough. In fact, estimating from $Q = \omega L\sqrt{hR^3}$ is reasonably accurate and conservative. The observed mild Reynolds-number trend in the measurements is likely the result of variations in the effective skin friction coefficient. (2) The fan's volume flow rate performance is robust for moderate changes in geometric parameters related to housing clearance dimension. Hence, this device does not require precision manufacturing and should be nearly insensitive to wear. Additionally, the inherent simplicity and flexibility of the transverse-inlet geometry makes this device easy to package and implement in complete air-handling systems.

Acknowledgments

The authors wish to thank W. S. White and G. Frontini for insightful comments and proof-reading of this manuscript. Suggestions from the techincal reviewers were also appreciated. This research was supported by the Whirlpool Corporation through the Whirlpool Technical Excellence Program with the University of Michigan.

References

Bakke, E., and Kreith, F., 1977, "Disk Pump Performance in Turbulent Flow," ASME Paper No. 77-WA/FE-26.

Beranek, L. L., and Vér, I. L. (eds.), 1992, *Noise and Vibration Control Engineering*, Wiley, New York.

Bezemek, J. D., and Mongeau, L., 1995, "Effects of Installation for Computer Cooling Fans," *Journal of the Acoustical Society of America*, Vol. 98, No. 5, Pt. 2, p. 2885.

Crawford, M. E., and Rice, W., 1974, "Calculated Design Data for the Multiple-Disk Pump Using Incompressible Fluid," ASME Paper No. 74-Pwr-B.

Lawn, M. J., and Rice, W., 1974, "Calculated Design Data for the Multiple-Disk Turbine Using Incompressible Fluid," ASME JOURNAL OF FLUIDS ENGINEERING, Vol. 96, pp. 252–258.

MacGillivray, J. R., Lauchle, G. C., and Swanson, D. C. 1995, "Active Control of Axial Flow Fan Noise," *Journal of the Acoustical Society of America*, Vol. 98, No. 5, Pt. 2, p. 2885.

Pierce, A., 1989, *Acoustics*, Acoust. Soc. Am., Am. Inst. Phys., New York.

Roddy, P. J., Darby, R., Morrison, G. L., and Jenkins, P. E., 1987, "Performance Characteristics of a Multiple-Disk Centrifugal Pump," ASME JOURNAL OF FLUIDS ENGINEERING, Vol. 109, pp. 51–57.

Tesla, N., 1913, "Turbine," U.S. Patent No. 1061206, May 6.

Sensitivity of e^N Method of Transition Prediction

J. A. Masad[1] and M. R. Malik[2]

Introduction

The e^N method (Smith and Gamberoni, 1956, Jaffe et al., 1970) coupled with linear stability theory (LST), remains the most common approach for predicting transition onset on aerodynamic surfaces. In this approach, transition is assumed to occur when the integrated growth rate calculated with LST reaches a certain value. The e^N method is an empirical method that was proposed based on experimental data. The value of N used to correlate transition depends on various parameters such as the level of free-stream disturbances. Therefore, calibration of the value of N with available experimental data is important in correlating transition. The sensitivity of the predicted transition Reynolds number to the chosen value of N is also an important determination. The sensitivity provides a good indication of the level of uncertainty in the value of the predicted transition Reynolds number. We expect that the sensitivity is dependent upon various parameters and conditions, such as the value of N, the Mach number, the surface heat transfer, and wall suction. In this work, we evaluate the sensitivity of the prediction of transition onset under the above mentioned parameters and conditions. The study is restricted to two-dimensional compressible subsonic flows (with a free-stream Mach number M_∞ up to 0.8) without pressure gradients.

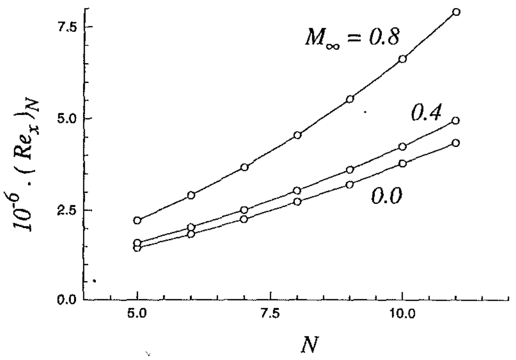

Fig. 1 Variation of N correlated transition Reynolds number with N

Definitions

We denote the sensitivity of the e^N method by σ_N and introduce a definition for it as the rate of change of correlated transition Reynolds number $(\mathrm{Re}_x)_N$ with respect to N divided by the correlated transition Reynolds number. Therefore,

$$\sigma_N = \frac{1}{(\mathrm{Re}_x)_N} \frac{d(\mathrm{Re}_x)_N}{dN} \tag{1}$$

where

$$\mathrm{Re}_x = \frac{U_\infty^* x^*}{\nu_\infty^*} \tag{2}$$

U_∞^* is the dimensional free-stream streamwise velocity, ν_∞^* is the dimensional free-stream kinematic viscosity, and x^* is the dimensional distance measured from the leading edge. The value $(\mathrm{Re}_x)_N$ is the smallest Reynolds number value at which the N factor reaches the value N. Because both $(\mathrm{Re}_x)_N$ and $d(\mathrm{Re}_x)_N/dN$ depend on wall and flow conditions such as suction, heat transfer, and Mach number, σ_N also will depend upon these parameters.

In the results for the effect of suction, the uniform suction velocity v_w is made nondimensional by using the free-stream streamwise velocity U_∞^*; therefore, $v_w = v_w^*/U_\infty^*$. With suction, v_w is negative; for blowing, it is positive. In the results for the

---

[1] Research Scientist, High Technology Corporation, Hampton, VA, 23666. Currently, Engineer, Senior, Lockheed Martin Engineering and Science, NASA Langley Research Center, MS303, Hampton, VA 23681.

[2] Chief Scientist, High Technology Corporation, Hampton, VA, 23666.

Contributed by the Fluids Engineering Division of THE AMERICAN SOCIETY OF MECHANICAL ENGINEERS. Manuscript received by the Fluids Engineering Division July 1, 1996; revised manuscript received July 31, 1996. Associate Technical Editor: W. S. Saric.

Re-dependent flow turning in the fan inlet, or variations in the pressure-drop load seen by the fan for the different flow configurations, with larger flow rates producing somewhat larger pressure drops across the fixed-geometry inlet flow straightener. A correction to constant pressure-drop conditions would probably change the vertical placement of the plotted points on Fig. 4 by only a few percent.

As a final note, w was varied from 65° to 75° with little effect on the fan's air-moving performance. Therefore, fan performance is robust regarding reasonable clearance and outlet-size variations, which may make disk fans an attractive alternative to bladed fans and compressors in some applications.

Conclusions

The results presented here lead to two important conclusions concerning the air-moving capability of a transverse-inlet multiple-disk fan operating at high specific speed. (1) The volume flow rate of the fan is proportional to $\omega\sqrt{hR^3}$ once the Reynolds number is high enough. In fact, estimating from $Q = \omega L\sqrt{hR^3}$ is reasonably accurate and conservative. The observed mild Reynolds-number trend in the measurements is likely the result of variations in the effective skin friction coefficient. (2) The fan's volume flow rate performance is robust for moderate changes in geometric parameters related to housing clearance dimension. Hence, this device does not require precision manufacturing and should be nearly insensitive to wear. Additionally, the inherent simplicity and flexibility of the transverse-inlet geometry makes this device easy to package and implement in complete air-handling systems.

Acknowledgments

The authors wish to thank W. S. White and G. Frontini for insightful comments and proof-reading of this manuscript. Suggestions from the techincal reviewers were also appreciated. This research was supported by the Whirlpool Corporation through the Whirlpool Technical Excellence Program with the University of Michigan.

References

Bakke, E., and Kreith, F., 1977, "Disk Pump Performance in Turbulent Flow," ASME Paper No. 77-WA/FE-26.

Beranek, L. L., and Vér, I. L. (eds.), 1992, *Noise and Vibration Control Engineering,* Wiley, New York.

Bezemek, J. D., and Mongeau, L., 1995, "Effects of Installation for Computer Cooling Fans," *Journal of the Acoustical Society of America,* Vol. 98, No. 5, Pt. 2, p. 2885.

Crawford, M. E., and Rice, W., 1974, "Calculated Design Data for the Multiple-Disk Pump Using Incompressible Fluid," ASME Paper No. 74-Pwr-B.

Lawn, M. J., and Rice, W., 1974, "Calculated Design Data for the Multiple-Disk Turbine Using Incompressible Fluid," ASME JOURNAL OF FLUIDS ENGINEERING, Vol. 96, pp. 252–258.

MacGillivray, J. R., Lauchle, G. C., and Swanson, D. C. 1995, "Active Control of Axial Flow Fan Noise," *Journal of the Acoustical Society of America,* Vol. 98, No. 5, Pt. 2, p. 2885.

Pierce, A., 1989, *Acoustics,* Acoust. Soc. Am., Am. Inst. Phys., New York.

Roddy, P. J., Darby, R., Morrison, G. L., and Jenkins, P. E., 1987, "Performance Characteristics of a Multiple-Disk Centrifugal Pump," ASME JOURNAL OF FLUIDS ENGINEERING, Vol. 109, pp. 51–57.

Tesla, N., 1913, "Turbine," U.S. Patent No. 1061206, May 6.

Sensitivity of e^N Method of Transition Prediction

J. A. Masad[1] and M. R. Malik[2]

Introduction

The e^N method (Smith and Gamberoni, 1956, Jaffe et al., 1970) coupled with linear stability theory (LST), remains the most common approach for predicting transition onset on aerodynamic surfaces. In this approach, transition is assumed to occur when the integrated growth rate calculated with LST reaches a certain value. The e^N method is an empirical method that was proposed based on experimental data. The value of N used to correlate transition depends on various parameters such as the level of free-stream disturbances. Therefore, calibration of the value of N with available experimental data is important in correlating transition. The sensitivity of the predicted transition Reynolds number to the chosen value of N is also an important determination. The sensitivity provides a good indication of the level of uncertainty in the value of the predicted transition Reynolds number. We expect that the sensitivity is dependent upon various parameters and conditions, such as the value of N, the Mach number, the surface heat transfer, and wall suction. In this work, we evaluate the sensitivity of the prediction of transition onset under the above mentioned parameters and conditions. The study is restricted to two-dimensional compressible subsonic flows (with a free-stream Mach number M_∞ up to 0.8) without pressure gradients.

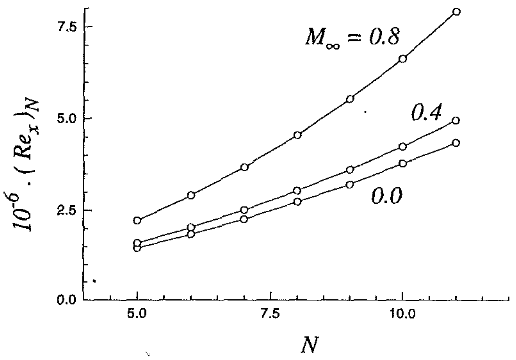

Fig. 1 Variation of N correlated transition Reynolds number with N

Definitions

We denote the sensitivity of the e^N method by σ_N and introduce a definition for it as the rate of change of correlated transition Reynolds number $(\mathrm{Re}_x)_N$ with respect to N divided by the correlated transition Reynolds number. Therefore,

$$\sigma_N = \frac{1}{(\mathrm{Re}_x)_N} \frac{d(\mathrm{Re}_x)_N}{dN} \tag{1}$$

where

$$\mathrm{Re}_x = \frac{U_\infty^* x^*}{\nu_\infty^*} \tag{2}$$

U_∞^* is the dimensional free-stream streamwise velocity, ν_∞^* is the dimensional free-stream kinematic viscosity, and x^* is the dimensional distance measured from the leading edge. The value $(\mathrm{Re}_x)_N$ is the smallest Reynolds number value at which the N factor reaches the value N. Because both $(\mathrm{Re}_x)_N$ and $d(\mathrm{Re}_x)_N/dN$ depend on wall and flow conditions such as suction, heat transfer, and Mach number, σ_N also will depend upon these parameters.

In the results for the effect of suction, the uniform suction velocity v_w is made nondimensional by using the free-stream streamwise velocity U_∞^*; therefore, $v_w = v_w^*/U_\infty^*$. With suction, v_w is negative; for blowing, it is positive. In the results for the

---

[1] Research Scientist, High Technology Corporation, Hampton, VA, 23666. Currently, Engineer, Senior, Lockheed Martin Engineering and Science, NASA Langley Research Center, MS303, Hampton, VA 23681.

[2] Chief Scientist, High Technology Corporation, Hampton, VA, 23666.

Contributed by the Fluids Engineering Division of THE AMERICAN SOCIETY OF MECHANICAL ENGINEERS. Manuscript received by the Fluids Engineering Division July 1, 1996; revised manuscript received July 31, 1996. Associate Technical Editor: W. S. Saric.

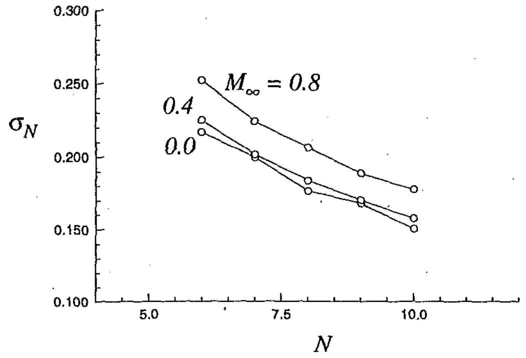

Fig. 2 Variation of sensitivity with N

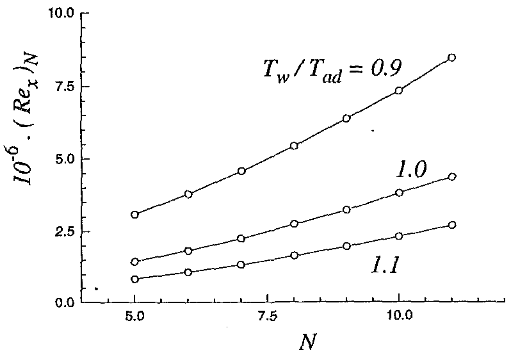

Fig. 5 Variation of N correlated transition Reynolds number with N

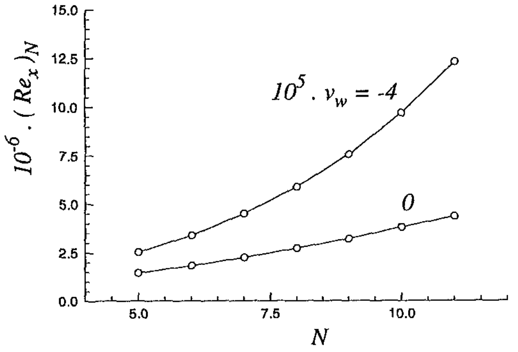

Fig. 3 Variation of N correlated transition Reynolds number with N

effect of heat transfer, temperatures are made nondimensional with the free-stream temperature T_∞^*; therefore, $T = T^*/T_\infty^*$. Here, T_∞^* is taken to be 300 K, the Prandtl number is 0.72, and the variation of viscosity with temperature is governed by the Sutherland formula. The quantities T_w and T_{ad} denote, respectively, the nondimensional actual wall temperature and the nondimensional adiabatic wall temperature. When T_w/T_{ad} is larger than unity, the wall is heated; when it is less than unity, the wall is cooled.

Results

By increasing the free-stream Mach number in the subsonic range, the maximum growth rate (over all frequencies) decreases and the predicted transition Reynolds number increases. The analytical correlation of Masad and Malik (1993) provides an account of the variation of transition Reynolds number with M_∞ in compressible subsonic flow over a flat plate with the e^9 method. The effect of M_∞ on the sensitivity of predicted transition Reynolds number in this work is for M_∞ in the range from 0 to 0.8. Mack (1969) showed that in this approximate range the most amplified instability wave is two dimensional.

The variation of predicted transition Reynolds number with the value N used to correlate transition is shown in Fig. 1 for three values of M_∞. The stabilizing effect of increasing M_∞ at all values of N is obvious. The sensitivity σ_N (Fig. 2) at the same M_∞ decreases with increasing N. Furthermore, σ_N increases as M_∞ increases. In Fig. 2 with $N = 9$, the value of σ_N is 0.168 for $M_\infty = 0$ and 0.189 for $M_\infty = 0.8$. This result implies that the predicted value of $(\mathrm{Re}_x)_N$ will vary by about ±16.8 percent ($M_\infty = 0$) and ±18 percent ($M_\infty = 0.8$) if the correlating N factor was chosen to be 10 or 8 instead of 9.

The application of suction in subsonic flow over a smooth surface reduces the instability growth rates at all frequencies. Although discrete suction might make the boundary layer more receptive to free-stream disturbances, the overall effect of suction is stabilizing; the transition location moves downstream at all values of N (Fig. 3). Suction changes the mean flow by making the velocity profile fuller, which results in a stabilizing effect through the viscous mechanism. The application of suction to aerodynamic surfaces has proved to be a feasible method of laminar flow control (LFC). The feasibility of suction in delaying transition has been demonstrated in both wind-tunnel and flight experiments.

The application of LFC methods is most effective when the flow disturbances are still in the linear regime and before any significant nonlinear or parametric wave interactions set in. Therefore, in suction optimization studies and in the context of the e^N method, one can try to delay the location on an aerodynamic surface at which the N-factor value reaches a low conservative value such as 5. Figure 4 clearly shows that this delay increases the sensitivity. Figure 4 also shows that application of suction increases the sensitivity at all values of N.

Cooling decreases and heating increases the maximum growth rate at all frequencies. Therefore, cooling increases the predicted transition Reynolds number at all values of N (Fig.

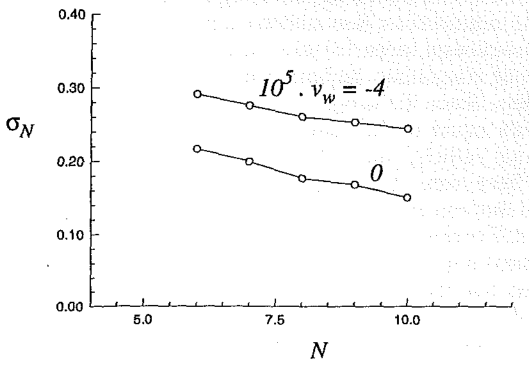

Fig. 4 Variation of sensitivity with N

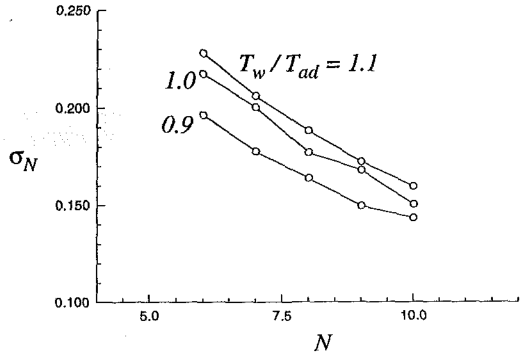

Fig. 6 Variation of sensitivity with N

5). However, the sensitivity to the value of N decreases with cooling and increases with heating when M_∞ is zero (Fig. 6). Initially, this result is unexpected; however, it is caused by the substantially higher value of $(\mathrm{Re}_x)_N$ with wall cooling, which results in lower σ_N (see Eq. (1)). Computations at $M_\infty = 0.8$ show the same trends as can be seen in Fig. 6.

Summary

In summary, the sensitivity of predicted transition Reynolds number with the e^N method decreases as N increases. Furthermore, suction, heating, and increasing Mach number in the subsonic range increase the sensitivity at all values of N.

Acknowledgments

This research is supported by the Laminar Flow Control Project Team, Fluid Mechanics and Acoustics Division, NASA Langley Research Center, Hampton, VA, under contract NAS1-19299.

References

Jaffe, N. A., Okamura, T. T., and Smith, A. M. O., 1970, "Determination of Spatial Amplification Factors and their Application to Predicting Transition," *AIAA Journal,* Vol. 8, pp. 301–308.

Mack, L. M., 1969, "Boundary-Layer Stability Theory," Jet Propulsion Laboratory, Document 900-277, Rev. A., California Inst. of Technology, Pasadena, CA.

Masad, J. A., and Malik, M. R., 1993, "Transition Correlation in Subsonic Flow over a Flat Plate," *AIAA Journal,* Vol. 31, No. 10, pp. 1953–1955.

Smith, A. M. O., and Gamberoni, N., 1956, "Transition, Pressure Gradient and Stability Theory," Report No. ES 26388, Douglas Aircraft Co., El Segundo, CA.

On the Effect of Evaporation on Droplet Drag

R. I. Sujith,[1,2] G. A. Waldherr,[1,3]
J. I. Jagoda,[1] and B. T. Zinn[1]

Nomenclature

D = diameter
k = evaporation constant in the D^2 law, Eq. (2)
Re = Reynolds number
t = time
V = velocity
ρ = density

Subscripts

l = liquid
v = vapor
0 = original quantity

Introduction

This technical note reports measured terminal velocities of evaporating droplets and discusses the effect of evaporation on droplet drag. When a droplet evaporates, there is an outflow of vapor from its surface, which affects the boundary conditions on the droplet surface. Evaporation causes flow separation to occur early, leading to an increase in form drag, known as blowing (Schlichting, 1955).

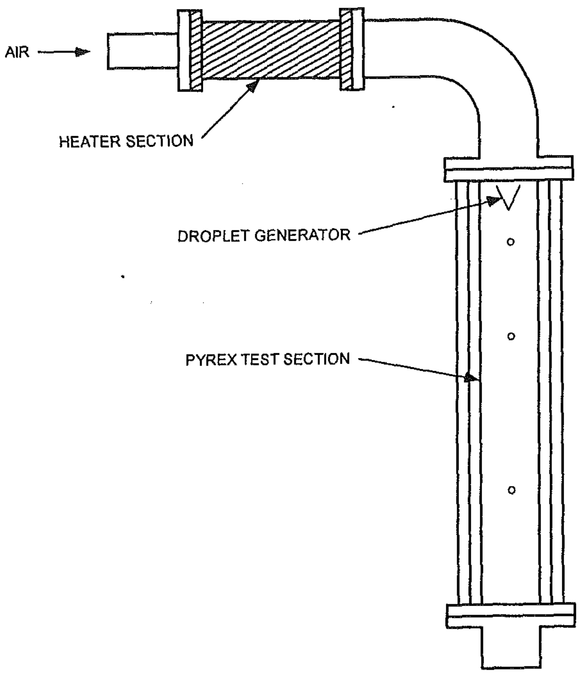

Fig. 1 **Schematic of the experimental setup**

In computations of spray evaporation the drag on the droplets is often modeled as the drag on a sphere, modified to account for the effect of blowing due to evaporation from droplet surface (Gemmen et al., 1990). These modifications are based on numerical studies or experiments performed on stationary droplets (Renksizbulut and Yuen, 1983a and b). Measured terminal velocities of evaporating droplets obtained in this study are compared with terminal velocities calculated theoretically, without accounting for blowing. The significance of the effect of the blowing due to evaporation on droplet drag is then determined from this comparison.

Experimental Setup

The experiment consists of a 52 mm ID duct, with a 60 cm long Pyrex test section, see Fig. 1. A piezo-electric droplet generator (Sujith et al., 1994) is installed at the top of the test section. In order to achieve measurable evaporation rates, the test section was heated using a 3 kW electrical heater installed in the upstream end of the test section. The air flow through the heaters was dehumidified using a drier.

The minimum air flow rate through the heaters to avoid damage produces a mean velocity of 10 m/s in the test section, an order of magnitude higher than the terminal velocity of the droplets. Since the droplets move through the test section at a velocity equal to the sum of the gas velocity and the droplet terminal velocity, their residence time in the test section would have been very short. This would have limited the amount of liquid that can evaporate, and thus, the accuracy of the measurements. Therefore, the apparatus was first preheated to 250°C, the maximum temperature attainable in this test section. The heaters and the airflow were then shut off, before carrying out the evaporation experiments. The temperature in the test section was monitored using a thermocouple.

Droplets moving through the test section were imaged using a Kodak Ektapro 1012 intensified, digital, high speed imaging

---

[1] School of Aerospace Engineering, Georgia Institute of Technology, Atlanta, GA 30332.

[2] Currently, Lecturer, Department of Aerospace Engineering I. I. T. Madras, India 600036.

[3] Currently, G. E. Corporate Research and Development, Building K1-ES104, Schenectady, NY 12301.

Contributed by the Fluids Engineering Division of The American Society of Mechanical Engineers. Manuscript received by the Fluids Engineering Division December 19, 1994; revised manuscript received May 23, 1996. Associate Technical Editor: Jong H. Kim.

5). However, the sensitivity to the value of N decreases with cooling and increases with heating when M_∞ is zero (Fig. 6). Initially, this result is unexpected; however, it is caused by the substantially higher value of $(\mathrm{Re}_x)_N$ with wall cooling, which results in lower σ_N (see Eq. (1)). Computations at $M_\infty = 0.8$ show the same trends as can be seen in Fig. 6.

Summary

In summary, the sensitivity of predicted transition Reynolds number with the e^N method decreases as N increases. Furthermore, suction, heating, and increasing Mach number in the subsonic range increase the sensitivity at all values of N.

Acknowledgments

This research is supported by the Laminar Flow Control Project Team, Fluid Mechanics and Acoustics Division, NASA Langley Research Center, Hampton, VA, under contract NAS1-19299.

References

Jaffe, N. A., Okamura, T. T., and Smith, A. M. O., 1970, "Determination of Spatial Amplification Factors and their Application to Predicting Transition," *AIAA Journal*, Vol. 8, pp. 301–308.

Mack, L. M., 1969, "Boundary-Layer Stability Theory," Jet Propulsion Laboratory, Document 900-277, Rev. A., California Inst. of Technology, Pasadena, CA.

Masad, J. A., and Malik, M. R., 1993, "Transition Correlation in Subsonic Flow over a Flat Plate," *AIAA Journal*, Vol. 31, No. 10, pp. 1953–1955.

Smith, A. M. O., and Gamberoni, N., 1956, "Transition, Pressure Gradient and Stability Theory," Report No. ES 26388, Douglas Aircraft Co., El Segundo, CA.

On the Effect of Evaporation on Droplet Drag

R. I. Sujith,[1,2] G. A. Waldherr,[1,3]
J. I. Jagoda,[1] and B. T. Zinn[1]

Nomenclature

D = diameter
k = evaporation constant in the D^2 law, Eq. (2)
Re = Reynolds number
t = time
V = velocity
ρ = density

Subscripts

l = liquid
v = vapor
0 = original quantity

Introduction

This technical note reports measured terminal velocities of evaporating droplets and discusses the effect of evaporation on droplet drag. When a droplet evaporates, there is an outflow of vapor from its surface, which affects the boundary conditions on the droplet surface. Evaporation causes flow separation to occur early, leading to an increase in form drag, known as blowing (Schlichting, 1955).

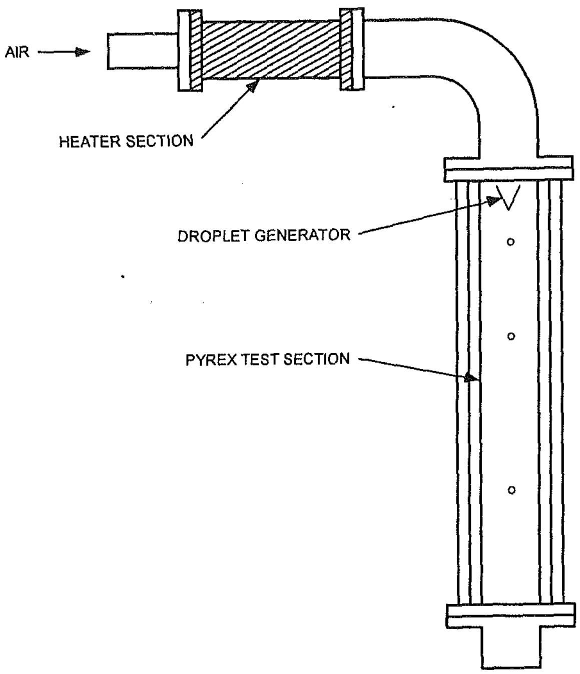

Fig. 1 Schematic of the experimental setup

In computations of spray evaporation the drag on the droplets is often modeled as the drag on a sphere, modified to account for the effect of blowing due to evaporation from droplet surface (Gemmen et al., 1990). These modifications are based on numerical studies or experiments performed on stationary droplets (Renksizbulut and Yuen, 1983a and b). Measured terminal velocities of evaporating droplets obtained in this study are compared with terminal velocities calculated theoretically, without accounting for blowing. The significance of the effect of the blowing due to evaporation on droplet drag is then determined from this comparison.

Experimental Setup

The experiment consists of a 52 mm ID duct, with a 60 cm long Pyrex test section, see Fig. 1. A piezo-electric droplet generator (Sujith et al., 1994) is installed at the top of the test section. In order to achieve measurable evaporation rates, the test section was heated using a 3 kW electrical heater installed in the upstream end of the test section. The air flow through the heaters was dehumidified using a drier.

The minimum air flow rate through the heaters to avoid damage produces a mean velocity of 10 m/s in the test section, an order of magnitude higher than the terminal velocity of the droplets. Since the droplets move through the test section at a velocity equal to the sum of the gas velocity and the droplet terminal velocity, their residence time in the test section would have been very short. This would have limited the amount of liquid that can evaporate, and thus, the accuracy of the measurements. Therefore, the apparatus was first preheated to 250°C, the maximum temperature attainable in this test section. The heaters and the airflow were then shut off, before carrying out the evaporation experiments. The temperature in the test section was monitored using a thermocouple.

Droplets moving through the test section were imaged using a Kodak Ektapro 1012 intensified, digital, high speed imaging

---

[1] School of Aerospace Engineering, Georgia Institute of Technology, Atlanta, GA 30332.

[2] Currently, Lecturer, Department of Aerospace Engineering I. I. T. Madras, India 600036.

[3] Currently, G. E. Corporate Research and Development, Building K1-ES104, Schenectady, NY 12301.

Contributed by the Fluids Engineering Division of THE AMERICAN SOCIETY OF MECHANICAL ENGINEERS. Manuscript received by the Fluids Engineering Division December 19, 1994; revised manuscript received May 23, 1996. Associate Technical Editor: Jong H. Kim.

system. The camera has a resolution of 239 × 192 pixels, and a frame rate of 1000 full frame s/s. (This camera was used because this study was part of an investigation of the behavior of evaporating droplets in an axial acoustic field, which required the high framing rate.) A zoom microscope provides a resolution of 12 μm/pixel, as calibrated using a reticle. This paper includes data for droplet sizes up to 250 μm. The error for 50 μm diameter droplets is significant. However, that for 250 μm droplets is small.

An expanded, attenuated beam from a pulsed copper vapor laser was used as the source of illumination. The 30 ns pulse was short enough to effectively freeze the droplet motion. The laser frequency was adjusted to be a multiple of the camera frequency. The camera gate was adjusted to be 10 μs, which is smaller than the period of the laser pulses. This ensured that only one droplet image was recorded on each frame. The droplets were imaged against a diffusely lit surface behind the test section. The droplet then appears dark against a bright background, which enhances its visibility.

Images acquired by the camera are stored in a circular buffer where the current image replaces the oldest image until triggered. The images are then transferred to a 486 based PC for storage and analysis. The diameter, the coordinates and the velocity of the droplet are obtained using a data analysis program.

Since the droplets are not injected at their terminal velocity the measurements were carried out 42 cm below the droplet generator. This was theoretically and experimentally shown to be far enough for the droplets to have reached their terminal velocity, (Sujith et al., 1994).

In a typical experiment, the apparatus was preheated first to 250°C, the maximum attainable temperature. The heaters and the airflow were then shut off. The temperature drop in the test section was monitored using a thermocouple. The temperature variation along the test section was less than 4°C. Sequences of droplet images were acquired using the camera, and the corresponding temperatures were noted. The field of view is only 3 mm high and the droplet traverses it in about 12 ms. Since the evaporation time of a 100 μm droplet is approximately 450 ms at 200°C, the droplet diameter does not change while in the field of view. Therefore, a quasi-steady approach can be taken, i.e., the droplet can be assumed to fall at its terminal velocity corresponding to its diameter at any instant.

Data for evaporating droplets were acquired at temperatures higher than 100°C. Therefore, the saturation pressure of vapor is one atmosphere or higher. In addition, the air in the test section was dehumidified. Therefore, the relative humidity of the air has only minimal effect.

Results and Discussion

Magnified images of the droplets indicated that the droplets used in this study were perfectly spherical and non-vibrating. No surface waves were visible on their surfaces.

The terminal velocity was calculated theoretically by equating drag and gravitational force (Clift et al., 1978). The following drag correlation, provided by Turton and Levenspiel (1986), which does not contain any corrections for blowing, was used for these calculations:

$$C_D = \frac{24}{\text{Re}}(1 + 0.173\,\text{Re}^{0.657}) + \frac{0.413}{1 + 16300\,\text{Re}^{-1.09}} \quad (1)$$

As a check, the terminal velocity of non-evaporating water droplets at room temperature was experimentally determined and compared to the computed terminal velocities. Figure 2 shows good agreement between the experimental results and theoretical calculations. (The experimental data has a mean scatter of 0.022 m/s and a standard deviation of 0.039 with respect to the theoretical calculation.)

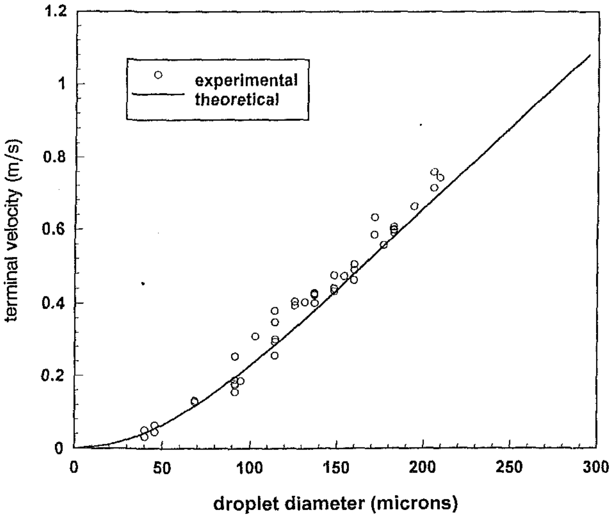

Fig. 2 **Terminal velocity of water droplets as a function of diameter, at room temperature. Uncertainty in the velocity axis (vertical axis) is 0.012 m/s and the uncertainty in the diameter axis (horizontal axis) is 12 microns.**

The dependence of the terminal velocity upon droplet diameter for water droplets is shown in Figs. 3(a) and (b) for different test section temperatures. These figures indicate that the measured data are in good agreement with the theoretical predictions, which did not include the effects of blowing. (The experimental data in Figs. 3(a) and (b) have a mean scatter of 0.041 and 0.047 m/s, and a standard deviation of 0.071 and 0.080 m/s with respect to the theoretical calculation, respectively.) Therefore, effects of blowing, if any, are negligible, at least for ambient temperatures less than 200°C.

The error involved in determining the droplet size and velocity can be determined from the size of the CCD array and the magnification used. For these experiments the error in droplet size is of the order of 10 microns and the error in droplet velocity is of the order of 0.01 m/s, which explains the scatter seen in Figs. 2 and 3(a) and (b). The scatter in the data is of the order of 0.1 m/s which can be attributed to the error in diameter measurements.

The measured terminal velocities are slightly (0.02 to 0.04 m/s) higher than the predicted values. This is true for both, nonevaporating and evaporating droplets. This bias can be attributed to the fact that internal circulation was neglected in these calculations. Clift et al. (1978) have observed that internal circulation is essentially absent in small droplets, whereas it is quite significant in large droplets. However, the droplet sizes at which this transition occurs has not been clearly established. The numerical results by Renkizbulut and Yuen (1983b), which did not take internal circulation into account, also show such a bias.

Terminal velocities were also measured for methanol droplets at room temperature. They are also in good agreement with calculations that did not take blowing into account, see Table 1.

According to the droplet evaporation law, popularly known as the D^2 law,

$$D^2 = D_0^2 - kt \quad (2)$$

Differentiating Eq. (2), the following expression for the rate of change of diameter of the droplet can be obtained.

$$dD/dt = -k/2D \quad (3)$$

Equating the mass flux of the evaporating droplet and the mass flux of the vapor, and using Eq. (3), the following expression for the blowing velocity at the surface of the droplet can be obtained:

$$V_{blowing} = -\frac{\rho_l}{\rho_v}\frac{k}{D} \tag{4}$$

For a 100 μm droplet, at 200°C, with a life time of 440 ms, k is of the order of 2.3×10^{-8} m^2/s (Sujith et al., 1995). Therefore the blowing velocity can be estimated as 0.25 m/s. This velocity is comparable to the droplet terminal velocity for a 100 μm droplet (0.23 m/s at room temperature). Under these circumstances one would expect the effect of blowing on the drag to be significant. However, the terminal velocity, which reflects the droplet drag was not affected.

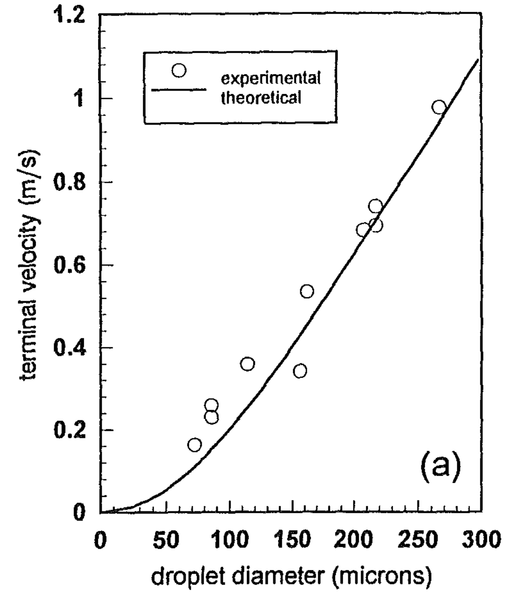

Fig. 3(*a*) Terminal velocity of evaporating water droplets as a function of diameter, for an ambient temperature between 152°C and 161°C. Uncertainty in the velocity axis (vertical axis) is 0.012 m/s and the uncertainty in the diameter axis (horizontal axis) is 12 microns.

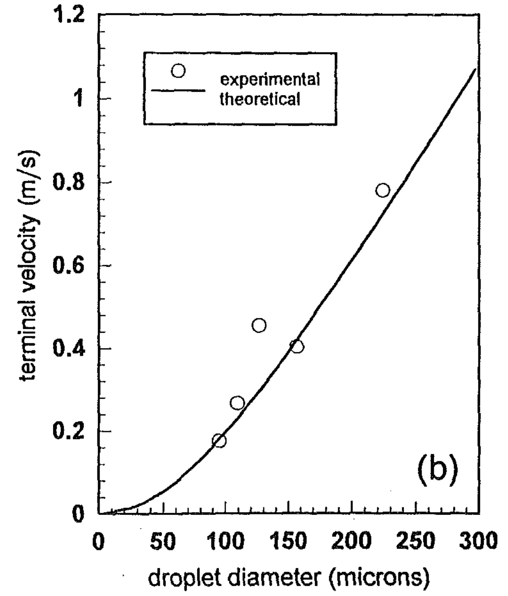

Fig. 3(*b*) Terminal velocity of evaporating water droplets as a function of diameter, for an ambient temperature between 171°C and 178°C. Uncertainty in the velocity axis (vertical axis) is 0.012 m/s and the uncertainty in the diameter axis (horizontal axis) is 12 microns.

Table 1 Terminal velocity of methanol droplets. Uncertainty in the velocity is 0.012 m/s and the uncertainty in the diameter is 12 microns

Diameter (microns)	Terminal velocity (m/s) experimental	Terminal velocity (m/s) theoretical
108.4	0.22	0.25
144.6	0.35	0.36

Emmons (1956) has shown that for a flat plate friction drag is reduced significantly by evaporation. By extending this result to the case of an evaporating droplet, one can argue that while blowing increases the form drag it also decreases the friction drag. These opposite effects appear to approximately cancel each other. As a result it seems that the standard drag curve for solid spheres can be used even for evaporating droplets. This result was shown numerically by Renksizbulut and Yuen (1983b).

Conclusions

In summary, it appears that it may be unnecessary to include any corrections to account for the effect of blowing due to evaporation from the droplet surface when modeling droplet drag.

Acknowledgment

This research was sponsored by the Gas Research Institute. The contract monitor was James Kezerle. Dr. Lawrence Matta helped in the preparation of the manuscript.

References

Clift, R., Grace, J. R., and Weber, M. E., 1978, *Bubbles, Drops and Particles,* Academic Press, p. 113.

Emmons, H. W., 1956, "Thin Film Combustion of Liquid Fuel," *ZAMM,* Vol. 36, pp. 60–71.

Gemmen, R. S., Keller, J. O., and Arpaci, V. S., 1990, "Pulse Combustion: Numerical Analysis of Droplet Mass Transfer Enhancement," *Thermo-Physical Aspects of Energy Conversion,* ASME, AES, Vol. 16, pp. 81–90.

Renksizbulut, M., and Yuen, M. C., 1983a, "Experimental Study of Droplet Evaporation in a High Temperature Stream," ASME *Journal of Heat Transfer,* Vol. 105, pp. 384–388.

Renksizbulut, M., and Yuen, M. C., 1983b, "Numerical Study of Droplet Evaporation in a High Temperature Stream," ASME *Journal of Heat Transfer,* Vol. 105, pp. 389–397.

Schlichting, H., 1955, *Boundary Layer Theory,* McGraw-Hill, New York.

Sujith, R. I., Waldherr, G. A., Jagoda, J. I., and Zinn, B. T., 1994, "Experimental Investigation of the Behavior of Droplets in Axial Acoustic Fields," ASME Winter Annual Meeting, Chicago, Nov. 6–11.

Sujith, R. I., Waldherr, G. A., Jagoda, J. I., and Zinn, B. T., 1995, "Experimental Investigation of the Evaporation of Droplets in Axial Acoustic Fields," AIAA paper no. 95-0495, Aerospace Sciences Meeting, Reno, Nevada, Jan. 9–12.

Turton, R., and Levenspiel, O., 1986, "A Short Note on the Drag Correlation for Spheres," *Powder Technology,* Vol. 47, pp. 83–86.

Numerical Analysis of Slot-Film Cooling: Effectiveness and Flow-Field

S. Sarkar[1] and T. K. Bose[2]

1 Introduction

Components of modern gas turbine engines are exposed to extremely high temperature. Film cooling, which prevents the

---

[1] Assistant Professor, Department of Mechanical Engineering, Bengal Engineering College (Deemed University) Howrah-711 103, India.

[2] Professor, Department of Aerospace Engineering, Indian Institute of Technology, Madras-600 036, India.

Contributed by the Fluids Engineering Division of THE AMERICAN SOCIETY OF

for the blowing velocity at the surface of the droplet can be obtained:

$$V_{blowing} = -\frac{\rho_l}{\rho_v}\frac{k}{D} \quad (4)$$

For a 100 μm droplet, at 200°C, with a life time of 440 ms, k is of the order of 2.3×10^{-8} m^2/s (Sujith et al., 1995). Therefore the blowing velocity can be estimated as 0.25 m/s. This velocity is comparable to the droplet terminal velocity for a 100 μm droplet (0.23 m/s at room temperature). Under these circumstances one would expect the effect of blowing on the drag to be significant. However, the terminal velocity, which reflects the droplet drag was not affected.

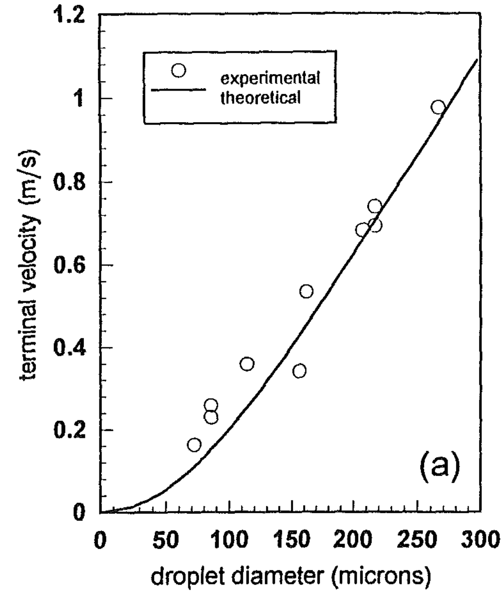

Fig. 3(*a*) Terminal velocity of evaporating water droplets as a function of diameter, for an ambient temperature between 152°C and 161°C. Uncertainty in the velocity axis (vertical axis) is 0.012 m/s and the uncertainty in the diameter axis (horizontal axis) is 12 microns.

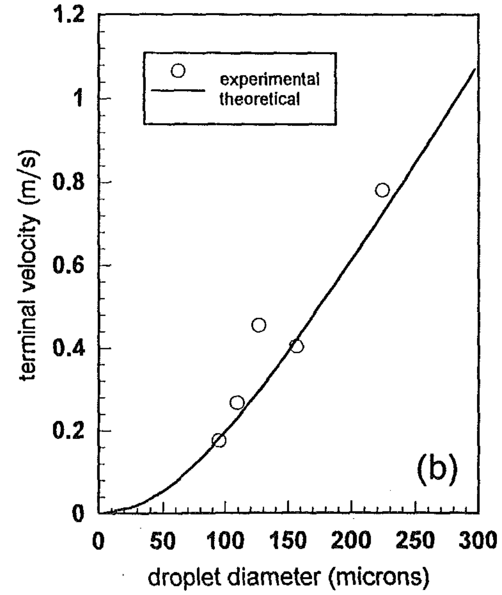

Fig. 3(*b*) Terminal velocity of evaporating water droplets as a function of diameter, for an ambient temperature between 171°C and 178°C. Uncertainty in the velocity axis (vertical axis) is 0.012 m/s and the uncertainty in the diameter axis (horizontal axis) is 12 microns.

Table 1 Terminal velocity of methanol droplets. Uncertainty in the velocity is 0.012 m/s and the uncertainty in the diameter is 12 microns

Diameter (microns)	Terminal velocity (m/s) experimental	Terminal velocity (m/s) theoretical
108.4	0.22	0.25
144.6	0.35	0.36

Emmons (1956) has shown that for a flat plate friction drag is reduced significantly by evaporation. By extending this result to the case of an evaporating droplet, one can argue that while blowing increases the form drag it also decreases the friction drag. These opposite effects appear to approximately cancel each other. As a result it seems that the standard drag curve for solid spheres can be used even for evaporating droplets. This result was shown numerically by Renksizbulut and Yuen (1983b).

Conclusions

In summary, it appears that it may be unnecessary to include any corrections to account for the effect of blowing due to evaporation from the droplet surface when modeling droplet drag.

Acknowledgment

This research was sponsored by the Gas Research Institute. The contract monitor was James Kezerle. Dr. Lawrence Matta helped in the preparation of the manuscript.

References

Clift, R., Grace, J. R., and Weber, M. E., 1978, *Bubbles, Drops and Particles*, Academic Press, p. 113.

Emmons, H. W., 1956, "Thin Film Combustion of Liquid Fuel," *ZAMM*, Vol. 36, pp. 60–71.

Gemmen, R. S., Keller, J. O., and Arpaci, V. S., 1990, "Pulse Combustion: Numerical Analysis of Droplet Mass Transfer Enhancement," *Thermo-Physical Aspects of Energy Conversion*, ASME, AES, Vol. 16, pp. 81–90.

Renksizbulut, M., and Yuen, M. C., 1983a, "Experimental Study of Droplet Evaporation in a High Temperature Stream," ASME *Journal of Heat Transfer*, Vol. 105, pp. 384–388.

Renksizbulut, M., and Yuen, M. C., 1983b, "Numerical Study of Droplet Evaporation in a High Temperature Stream," ASME *Journal of Heat Transfer*, Vol. 105, pp. 389–397.

Schlichting, H., 1955, *Boundary Layer Theory*, McGraw-Hill, New York.

Sujith, R. I., Waldherr, G. A., Jagoda, J. I., and Zinn, B. T., 1994, "Experimental Investigation of the Behavior of Droplets in Axial Acoustic Fields," ASME Winter Annual Meeting, Chicago, Nov. 6–11.

Sujith, R. I., Waldherr, G. A., Jagoda, J. I., and Zinn, B. T., 1995, "Experimental Investigation of the Evaporation of Droplets in Axial Acoustic Fields," AIAA paper no. 95-0495, Aerospace Sciences Meeting, Reno, Nevada, Jan. 9–12.

Turton, R., and Levenspiel, O., 1986, "A Short Note on the Drag Correlation for Spheres," *Powder Technology*, Vol. 47, pp. 83–86.

Numerical Analysis of Slot-Film Cooling: Effectiveness and Flow-Field

S. Sarkar[1] and T. K. Bose[2]

1 Introduction

Components of modern gas turbine engines are exposed to extremely high temperature. Film cooling, which prevents the

---

[1] Assistant Professor, Department of Mechanical Engineering, Bengal Engineering College (Deemed University) Howrah-711 103, India.

[2] Professor, Department of Aerospace Engineering, Indian Institute of Technology, Madras-600 036, India.

Contributed by the Fluids Engineering Division of The American Society of

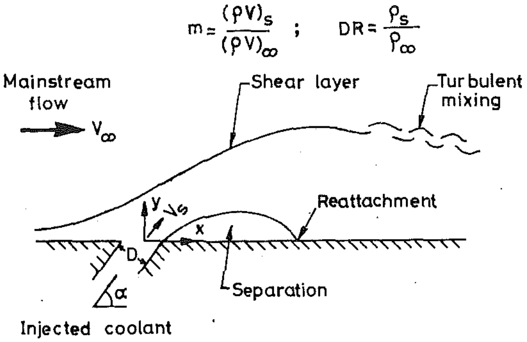

Fig. 1 A general description of flow field

hot gases from reaching a wall and decreases the wall temperature by locally injecting cold fluid, is extensively used to protect such components. The flow-field near the injected coolant jet is very complex with high gradients of velocity, temperature, turbulence intensity and a local flow reversal, Fig. 1. There are different parameters such as injection angle (α), blowing ratio (m), density ratio (DR), incoming boundary layer that affect film cooling processes. In a single study, it is difficult to include all of them. An excellent review by Goldstein (1971) describes some of these factors and earlier experimental investigations on film cooling.

Studies on film cooling are widespread in the literature. Unfortunately, most of these investigations are only devoted to the analysis of surface heat transfer phenomena. A short list representative of such studies are the work of Papell (1960), Petersen et al. (1977), Foster and Lampard (1980), and Sinha et al. (1990). Aerodynamics aspects related to the jet-mainstream interactions and the coolant layer formation are rarely available. Among the very few, Andreopoulos and Rodi (1984) and Pietrzyk et al. (1989) made a detailed turbulence study and aerodynamic description of a jet in a crossflow. As regards of computational studies, most of the published work on the prediction of film cooling considered either parabolic or semi-elliptic solutions. Demuren et al. (1986) used locally-elliptic treatment. There are a limited number of entries such as the work of Patankar et al. (1977) and Jurban (1989) who considered a fully elliptic treatment. Jurban (1989) also stated that one of the serious problems which affect the film cooling prediction is the selection of an appropriate turbulence model.

The experimental work of Papell (1960) is among the very few where the free-stream conditions are representative of the gas turbine environment with free-stream Mach number M_∞ = 0.5 or above, temperature T_∞ = 790 K. In the present study, an attempt is made to numerically simulate the work of Papell. The time-dependent, mass-averaged, compressible Navier-Stokes equations in strong conservation form with a turbulence model are solved, based on an explicit scheme which is applicable for a wide range of Mach numbers. To the authors' knowledge, this is the first time when a density-based flow solver is used to study film cooling whereas all the previous studies have considered pressure-based codes.

As already mentioned, there are different parameters that affect the film cooling performance. This study includes the influence of injection angle and blowing ratio on film cooling and also aims to numerically explore the complex flow-field and heat transfer phenomena due to jet-crossflow interactions. At present, the investigation is limited to a two-dimensional (2-D) simulation.

2 Governing Equations and Numerical Procedure

The unsteady, mass-averaged 2-D Navier-Stokes equations are marched in time using the explicit, second-order accurate time-split, cell-centered finite-volume approach of MacCormack (1972) until the steady state is achieved. Precise control of artificial dissipation is needed to improve the accuracy and stability of solution. Artificial dissipation used here is similar to that of Jameson et al. (1981), which is a blend of second- and fourth-order differences with coefficients that depend on local pressure gradients. Effects of turbulence are incorporated using the Baldwin-Lomax (1978) eddy viscosity model. For comparison, the low-Reynolds-number version of a two-equation ($k - \epsilon$) model of Chien (1982) is also used. It should be noted that, though the $k - \epsilon$ equations have been cast in compressible form, the modeling assumptions invoked here are essentially those for incompressible flow.

A nonuniform Cartesian mesh of 60 in x-direction and 50 in y-direction (generated algebraically, clustering grids near the injection slot and the wall to capture steep gradients of flow variables) is used. A grid sensitivity test revealed that results are sensitive to the number of grids in y-direction and a 60×50 grid was found sufficient to get mesh independent solutions. The first mesh point above the plate surface is chosen such that the average y^+ is of the order of unity.

At the inflow boundary, the static pressure is extrapolated from interior. The exit plane is positioned far downstream of the injection (100D) and a zero gradient condition is applied for all variables at this plane. On the solid surfaces, the no-slip condition is imposed along with vanishing normal temperature gradient to simulate the adiabatic wall condition. Experimental study of Pietrzyk et al. (1989) indicates that a uniform mean velocity profile at the jet exit may be a reasonable approximation of the actual film cooling applications with a short-delivery port. Therefore, across the slot exit a uniform condition is specified, where all the variables are held fixed at the injection conditions. The slot is fixed at a distance of 25D from the inlet plane.

3 Results and Discussion

Figure 2 illustrates the predicted and measured film cooling effectiveness (η) downstream of a normally injected coolant jet for m = 0.5, 1.8 with M_∞ = 0.5; $Re_\infty = 3.65 \times 10^6$/m and DR $\simeq$ 2.0. Although the overall streamwise trend is the same, the predicted value of effectiveness is consistently low at m = 0.5. At a relatively higher blowing ratio of m = 1.8, the prediction is extremely good. Figure 2 also shows that the effectiveness increases in proportion to the injected mass flow rate at large x/D. The under prediction of film cooling effectiveness for a relatively lower blowing ratio may possibly be attributed to the over-predicted mixing by the turbulent model used in the present study. However, the trends of effectiveness are reasonably well predicted by the present computation. On this basis, the

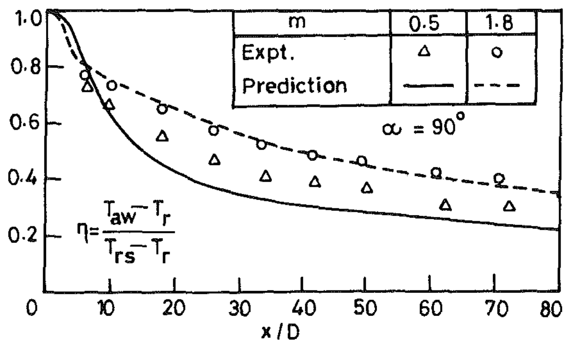

Fig. 2 Streamwise variation of adiabatic film cooling effectiveness, η. Predictions are contrasted with experimental data of Papell (1960).

MECHANICAL ENGINEERS. Manuscript received by the Fluids Engineering Division January 10, 1996; revised manuscript received June 6, 1996. Associate Technical Editor: D. P. Telionis.

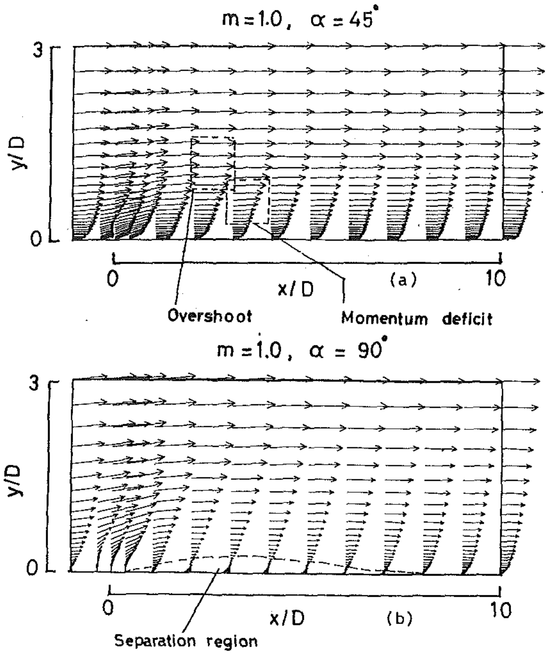

Fig. 3 **Computed velocity profiles downstream of a slot (*a*) $m = 1.0$, $\alpha = 45$ deg; (*b*) $m = 1.0$, $\alpha = 90$ deg**

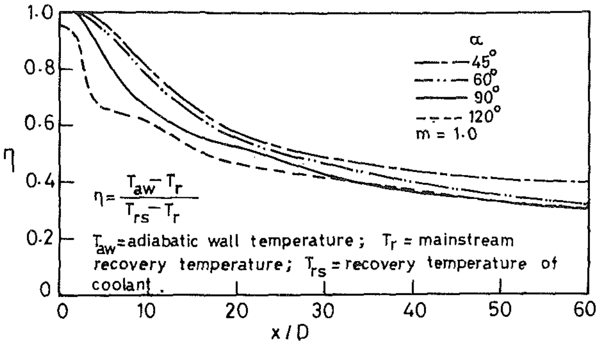

Fig. 5 **Computed streamwise variation of effectiveness indicating effect of injection angle**

variation of flow-field and heat transfer phenomena with changing m and α are investigated numerically.

The computed velocity fields downstream of a slot for angles of injection $\alpha = 45$ and 90 deg with $m = 1.0$ and DR = 2 are shown in Fig. 3. These velocity profiles are very similar to those measured by Pietrzyk et al. (1989) and they clearly demonstrate a near-field wake region and a far-field relaxation region. In the wake region, the velocity profile exhibits two distinguishable zones that is (i) the momentum deficit zone indicating the development of a shear layer between the inner edge of the injected jet and the crossflow and (ii) right above the momentum deficit zone, a region with a slight velocity overshoot caused by the crossflow accelerating over the coolant jet. There is no flow separation downstream of the slot exit at $\alpha = 45$ deg (Fig. 3(*a*)). For the same blowing ratio as α is increased to 90 deg, the aerodynamics of the jet in crossflow changes considerably (Fig. 3(*b*)). The jet penetrates more into the mainstream, bends over, reattaches to the surface forming a separation bubble and subsequently flows downstream approaching boundary layer type flow. Injected coolant undergoes turbulent mixing with the mainstream while crossing over the bubble and at the same time, a small fraction of the injected coolant mass drifts into the recirculating bubble, inducing cooling action near the slot. This attributes to high effectiveness very near the slot exit even with separated flows for 2-D slot injection.

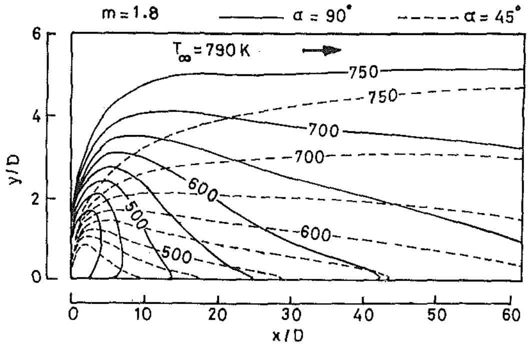

Fig. 4 **Computed temperature contours indicating effect of injection angle**

One important aspect for film cooling processes is the jet trajectory which depends mainly on the injection angle and the momentum ratio. In the present study, temperature field is used to determine the trajectory of the coolant jet. To illustrate the influence of injection angle on the trajectory, the temperature contours due to different injection angles at $m = 1.8$ and DR $\simeq 2$, are superimposed, Fig. 4. This clearly demonstrates that for the low angle of injection, the coolant hugs the surface to be protected, retaining its identity for a larger length. Thus, under this condition, high cooling effectiveness is expected even in the far-field. As the angle of injection increases, the coolant penetrates more into the crossflow resulting in more jet dilution which would cause a rapid decay of film cooling effectiveness. Similarly with the increase of blowing ratio, the coolant tends to retain its wall-jet character and thereby makes a high trajectory.

The distributions of the film cooling effectiveness as the injection angle changes for $m = 1.0$ are illustrated in Fig. 5. When α is increased beyond 60 deg, the effectiveness drops and this effect is prominent in the near field region ($x/D < 30$). As already explained, increased α leads to a higher jet trajectory. The jet penetrates more into the mainflow, subsequently bends over and reattaches to the surface forming a separation bubble. The size of the separation bubble and turbulence mixing increase with increase of α, strongly influencing near field effectiveness. In the far flow region, the effectiveness is strongly determined by the turbulence diffusion and so it is not much affected by larger α. For shallow injection angles ($\alpha \leq 45$ deg), the coolant remains attached to the surface giving comparatively improved effectiveness even in the far field region.

The film cooling effectiveness at $m = 1.0$ and $\alpha = 90$ deg, computed both from the Baldwin-Lomax turbulence model and the $k - \epsilon$ model of Chien are shown in Fig. 6. The results suggest that in the far field region effectiveness predicted by both the models is almost identical, but in the wake region ($x/D < 30$) they differ indicating different predicted mixing characteristics by the two models. However, the overall prediction of film cooling effectiveness by the two-equation model appears to be not much different to that by the Baldwin-Lomax model, which is economical from the computational view-point.

4 Conclusion

A Navier-Stokes analysis is made for the jet-crossflow interactions in an environment representative of film cooling applications in gas turbine practice. The variation of aerodynamics and the complex flow physics with changes in injected mass flow

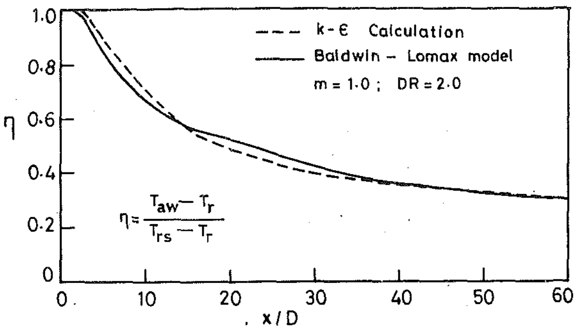

Fig. 6 Comparison of computed streamwise variation of effectiveness from k – ε model and Baldwin-Lomax model

rates and slot angles are captured fairly well by the present calculation.

For large injection angles, the coolant penetrates more into the crossflow resulting in more turbulence generation, followed by enhanced mixing and a rapid turbulent diffusion which leads to a faster decay of film cooling effectiveness in the near field region. A flow reversal also occurs just downstream of the slot exit. For shallow injection angles, the coolant hugs the surface with low turbulence generation and slow mixing rate, retaining its identity for a larger length. This results in high cooling effectiveness even in the far field region. With the increase of blowing ratio, the overall downstream film cooling effectiveness improves due to the thickened thermal layer and more available cold fluid.

References

Andreopoulos, J., and Rodi, W., 1984, "Experimental Investigation of Jets in a Crossflow," *Journal of Fluid Mechanics,* Vol. 138, pp. 93–127.

Baldwin, B. S., and Lomax, H., 1978, "Thin Layer Approximation and Algebraic Model for Separated Turbulent Flows," AIAA paper 78-257, pp. 1–8.

Chien, K., 1982, "Prediction of Channel and Boundary-Layer Flows With a Low-Reynolds Number Turbulence Model," *AIAA Journal,* Vol. 20, No. 1, pp. 33–38.

Demuren, A. O., Rodi, W., and Schönung, B., 1986, "Systematic Study of Film Cooling with a Three-Dimensional Calculation Procedure," ASME *Journal of Turbomachinery,* Vol. 108, pp. 121–130.

Foster, N. W., and Lampard, D., 1980, "The Flow and Film Cooling Effectiveness Following Injection Through a Row of Holes," ASME *Journal of Engineering for Power,* Vol. 102, pp. 584–588.

Goldstein, R. J., 1971, "Film Cooling," *Advances in Heat Transfer,* Academic Press, New York and London, Vol. 7, pp. 321–379.

Jameson, A., Schmidt, W., and Turkel, E., 1981, "Numerical Solutions of the Euler Equations by Finite Volume Methods using Runge-Kutta Time-Stepping schemes," AIAA Paper 81-1259.

Jubran, B. A., 1989, "Correlation and Prediction of Film Cooling from Two Rows of Holes," ASME *Journal of Turbomachinery,* Vol. 111, pp. 502–509.

MacCormack, R. W., and Paullay, A. J., 1972, "Computational Efficiency Achieved by Time Splitting of Finite Difference Operators," AIAA Paper 72-154.

Patankar, S. V., Basu, D. K., and Alpay, S. A., 1977, "Prediction of Three-Dimensional Velocity Field of a Deflected Jet," ASME JOURNAL OF FLUIDS ENGINEERING, Vol. 99, pp. 758–762.

Papell, S. S., 1960, "Effect on Gaseous Film Cooling Injection Through Angled Slots and Normal Holes," NASA TN-D-299.

Petersen, D. R., Eckert, E. R. G., and Goldstein, R. J., 1977, "Film Cooling with Large Density Differences Between the Mainstream and Secondary Fluid Measured by Heat-Mass Transfer Analogy," ASME *Journal of Heat Transfer,* Vol. 99, pp. 620–627.

Pietrzyk, J. R., Bogard, D. G., and Crawford, M. E., 1989, "Hydrodynamics Measurements of Jet in Crossflow for Gas Turbine Film Cooling Applications," ASME *Journal of Turbomachinery,* Vol. 111, pp. 139–145.

Sinha, A. K., Bogard, D. G., and Crawford, M. E., 1990, "Film Cooling Effectiveness of a Single Row of Holes with Variable Density Ratio," ASME Paper No. 90-GT-43.

A Novel Method to Measure Capsule Pressure Gradient in a Pipeline

J. Seaba[1] and G. Xu[1]

Introduction

The transport of capsules through a liquid pipeline is of practical as well as academic interest. Currently, the compaction of coal into cylinders and transporting them through liquid (water) pipelines has been shown to be economically feasible for a number of coal transportation scenarios within the United States (Liu and Marrero, 1995 and Liu, 1993). The study of using coal slurry in place of water for the hydraulic transport of coal logs has also been investigated (Seaba and Xu, 1995), suggesting the transport of other materials heavier than coal may be feasible to transport in their own slurry mixture. To provide predictive tools for hydraulic transport of capsule trains in a turbulent pipe flow more experimental information is needed.

This Tech Brief describes a new pressure measurement technique as applied to the study of capsule train transport. The problem of measuring the capsule pressure drop is complicated by two factors. First, the additional pressure drop due to capsules can be relatively small compared to the magnitude of the pressure drop due to water only (within 15 percent at lift-off velocity). Second, the capsule train length (NL_c) is an order of magnitude smaller than the distance between the pressure taps. This is required to provide a steady-state measurement of the capsule train pressure increase as it moves through the test section. Therefore, depending on the capsule transport regime, a pressure drop increase of only 2 to 3 percent across the test section due to the presence of the capsule train can occur.

The transport of capsules in pipes consist of four regimes (Seaba and Xu, 1995). Regime I occurs at a low bulk fluid velocity when the capsule is stationary at the pipe bottom. The bulk fluid velocity (V_b) is defined as the volumetric flow rate in the pipe divided by the pipe area. Regime II begins when the capsules start to move along the pipe bottom, this is defined as the incipient velocity (V_i) where V_b equals V_i. As the bulk velocity increases, the capsule velocity (V_c) increases, and the difference between the capsule velocity and bulk velocity decreases. Regime III begins when the capsule velocity exceeds the bulk velocity ($V_c > V_b > V_i$). This is possible because sufficient lift (microlift) is developed which, together with the buoyancy, diminishes the contact friction between the capsule and the pipe. Consequently, the capsule is accelerated by the pressure gradient in the pipe to a velocity higher than the bulk velocity ($V_c > V_b$). Regime III continues until the bulk fluid velocity reaches the lift-off velocity (V_L). Regime IV occurs at yet higher velocities when capsules are lifted off the pipe floor moving with their leading nose raised forming an angle from the capsule bottom to the pipe wall (angle of attack). The optimum operational velocity of CLP is between regime III and IV, or at the lift-off velocity of the capsules (Liu, 1981).

For the first time, the pressure increase due to the presence of the capsule train is measured in situ. A new experimental facility was designed and built to measure low pressure increases caused by a laboratory scale capsule train (Seaba and Xu, 1995). The pressure gradient produced by the capsule train

---

[1] Assistant Professor and Graduate Student, respectively, Department of Mechanical & Aerospace Engineering, University of Missouri-Columbia, Columbia, MO 65211.

Contributed by the Fluids Engineering Division of THE AMERICAN SOCIETY OF MECHANICAL ENGINEERS. Manuscript received by the Fluids Engineering Division May 16, 1995; revised manuscript received April 2, 1996. Associate Technical Editor: D. P. Telionis.

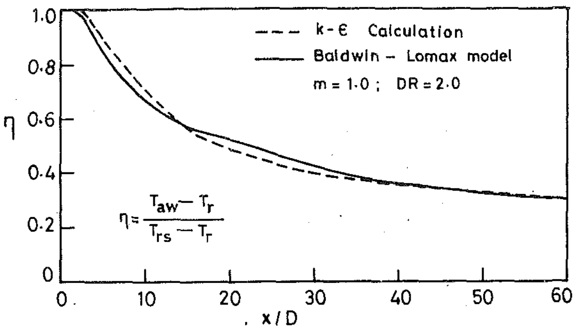

Fig. 6 Comparison of computed streamwise variation of effectiveness from k – ε model and Baldwin-Lomax model

rates and slot angles are captured fairly well by the present calculation.

For large injection angles, the coolant penetrates more into the crossflow resulting in more turbulence generation, followed by enhanced mixing and a rapid turbulent diffusion which leads to a faster decay of film cooling effectiveness in the near field region. A flow reversal also occurs just downstream of the slot exit. For shallow injection angles, the coolant hugs the surface with low turbulence generation and slow mixing rate, retaining its identity for a larger length. This results in high cooling effectiveness even in the far field region. With the increase of blowing ratio, the overall downstream film cooling effectiveness improves due to the thickened thermal layer and more available cold fluid.

References

Andreopoulos, J., and Rodi, W., 1984, "Experimental Investigation of Jets in a Crossflow," *Journal of Fluid Mechanics,* Vol. 138, pp. 93–127.

Baldwin, B. S., and Lomax, H., 1978, "Thin Layer Approximation and Algebraic Model for Separated Turbulent Flows," AIAA paper 78-257, pp. 1–8.

Chien, K., 1982, "Prediction of Channel and Boundary-Layer Flows With a Low-Reynolds Number Turbulence Model," *AIAA Journal,* Vol. 20, No. 1, pp. 33–38.

Demuren, A. O., Rodi, W., and Schönung, B., 1986, "Systematic Study of Film Cooling with a Three-Dimensional Calculation Procedure," ASME *Journal of Turbomachinery,* Vol. 108, pp. 121–130.

Foster, N. W., and Lampard, D., 1980, "The Flow and Film Cooling Effectiveness Following Injection Through a Row of Holes," ASME *Journal of Engineering for Power,* Vol. 102, pp. 584–588.

Goldstein, R. J., 1971, "Film Cooling," *Advances in Heat Transfer,* Academic Press, New York and London, Vol. 7, pp. 321–379.

Jameson, A., Schmidt, W., and Turkel, E., 1981, "Numerical Solutions of the Euler Equations by Finite Volume Methods using Runge-Kutta Time-Stepping schemes," AIAA Paper 81-1259.

Jubran, B. A., 1989, "Correlation and Prediction of Film Cooling from Two Rows of Holes," ASME *Journal of Turbomachinery,* Vol. 111, pp. 502–509.

MacCormack, R. W., and Paullay, A. J., 1972, "Computational Efficiency Achieved by Time Splitting of Finite Difference Operators," AIAA Paper 72-154.

Patankar, S. V., Basu, D. K., and Alpay, S. A., 1977, "Prediction of Three-Dimensional Velocity Field of a Deflected Jet," ASME JOURNAL OF FLUIDS ENGINEERING, Vol. 99, pp. 758–762.

Papell, S. S., 1960, "Effect on Gaseous Film Cooling Injection Through Angled Slots and Normal Holes," NASA TN-D-299.

Petersen, D. R., Eckert, E. R. G., and Goldstein, R. J., 1977, "Film Cooling with Large Density Differences Between the Mainstream and Secondary Fluid Measured by Heat-Mass Transfer Analogy," ASME *Journal of Heat Transfer,* Vol. 99, pp. 620–627.

Pietrzyk, J. R., Bogard, D. G., and Crawford, M. E., 1989, "Hydrodynamics Measurements of Jet in Crossflow for Gas Turbine Film Cooling Applications," ASME *Journal of Turbomachinery,* Vol. 111, pp. 139–145.

Sinha, A. K., Bogard, D. G., and Crawford, M. E., 1990, "Film Cooling Effectiveness of a Single Row of Holes with Variable Density Ratio," ASME Paper No. 90-GT-43.

A Novel Method to Measure Capsule Pressure Gradient in a Pipeline

J. Seaba[1] **and G. Xu**[1]

Introduction

The transport of capsules through a liquid pipeline is of practical as well as academic interest. Currently, the compaction of coal into cylinders and transporting them through liquid (water) pipelines has been shown to be economically feasible for a number of coal transportation scenarios within the United States (Liu and Marrero, 1995 and Liu, 1993). The study of using coal slurry in place of water for the hydraulic transport of coal logs has also been investigated (Seaba and Xu, 1995), suggesting the transport of other materials heavier than coal may be feasible to transport in their own slurry mixture. To provide predictive tools for hydraulic transport of capsule trains in a turbulent pipe flow more experimental information is needed.

This Tech Brief describes a new pressure measurement technique as applied to the study of capsule train transport. The problem of measuring the capsule pressure drop is complicated by two factors. First, the additional pressure drop due to capsules can be relatively small compared to the magnitude of the pressure drop due to water only (within 15 percent at lift-off velocity). Second, the capsule train length (NL_c) is an order of magnitude smaller than the distance between the pressure taps. This is required to provide a steady-state measurement of the capsule train pressure increase as it moves through the test section. Therefore, depending on the capsule transport regime, a pressure drop increase of only 2 to 3 percent across the test section due to the presence of the capsule train can occur.

The transport of capsules in pipes consist of four regimes (Seaba and Xu, 1995). Regime I occurs at a low bulk fluid velocity when the capsule is stationary at the pipe bottom. The bulk fluid velocity (V_b) is defined as the volumetric flow rate in the pipe divided by the pipe area. Regime II begins when the capsules start to move along the pipe bottom, this is defined as the incipient velocity (V_i) where V_b equals V_i. As the bulk velocity increases, the capsule velocity (V_c) increases, and the difference between the capsule velocity and bulk velocity decreases. Regime III begins when the capsule velocity exceeds the bulk velocity ($V_c > V_b > V_i$). This is possible because sufficient lift (microlift) is developed which, together with the buoyancy, diminishes the contact friction between the capsule and the pipe. Consequently, the capsule is accelerated by the pressure gradient in the pipe to a velocity higher than the bulk velocity ($V_c > V_b$). Regime III continues until the bulk fluid velocity reaches the lift-off velocity (V_L). Regime IV occurs at yet higher velocities when capsules are lifted off the pipe floor moving with their leading nose raised forming an angle from the capsule bottom to the pipe wall (angle of attack). The optimum operational velocity of CLP is between regime III and IV, or at the lift-off velocity of the capsules (Liu, 1981).

For the first time, the pressure increase due to the presence of the capsule train is measured in situ. A new experimental facility was designed and built to measure low pressure increases caused by a laboratory scale capsule train (Seaba and Xu, 1995). The pressure gradient produced by the capsule train

---

[1] Assistant Professor and Graduate Student, respectively, Department of Mechanical & Aerospace Engineering, University of Missouri-Columbia, Columbia, MO 65211.

Contributed by the Fluids Engineering Division of THE AMERICAN SOCIETY OF MECHANICAL ENGINEERS. Manuscript received by the Fluids Engineering Division May 16, 1995; revised manuscript received April 2, 1996. Associate Technical Editor: D. P. Telionis.

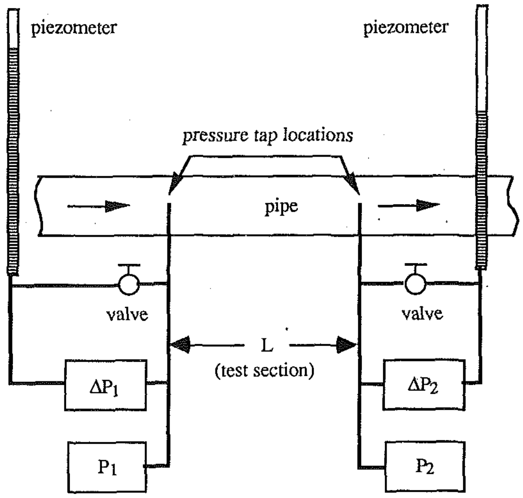

Fig. 1 Schematic of pressure measurement apparatus

provides information which can be directly correlated to the capsule transport regimes, i.e., microlift. This provides data and insight to validate and develop numerical models for capsule transport (Zhai, 1995; Feng et al., 1995; Fujiwara et al., 1994; and Liu and Richards, 1994).

Experimental Approach

A higher pressure gradient is observed as capsules flow in a pipe with water as compared to flow of water in pipe without capsules (Richards, 1992). The total pressure gradient is one of the most important parameters for pipeline use. The total pressure gradient including capsule and fluid in a pipeline is given by Kruyer et al. (1967) as,

$$\left(\frac{dP}{dz}\right)_t = \frac{\Delta P_t - L\left(\frac{dP}{dz}\right)_f}{NL_c} + \left(\frac{dP}{dz}\right)_f \tag{1}$$

where ΔP_t is the total head loss between two pressure taps along the pipeline at a distance L apart. $(dP/dz)_t$ is the total pressure gradient including the presence of both water and capsules, $(dP/dz)_f$ is the pressure gradient of the carrier fluid (water), L_c is the length of the capsule, and N is the number of capsules in the train. The first term on the right side of Eq. (1) is the pressure gradient due to the capsule train only, designated as $(dP/dz)_c$. ΔP_t and ΔP_f are the measured pressure drops with and without capsules, respectively. Equation (1) can be rewritten as,

$$\left(\frac{dP}{dz}\right)_t = \frac{\Delta P_t - \Delta P_f}{NL_c} + \frac{\Delta P_f}{L}. \tag{2}$$

Equation (2) was used by Rhee (1989) and Richards (1992) who measured ΔP_t and ΔP_f, then calculated $(dP/dz)_c$ and $(dP/dz)_t$. However, ΔP_t and ΔP_f are of the same order of magnitude, generating a small difference which is near the accuracy of the pressure transducers. Therefore, disturbances in the flow due to the pump and piping, and accuracy of the pressure transducers limit the assessment of the pressure increase due to the capsule train.

A new technique has been developed to directly measure the increase of pressure due to the capsule train (ΔP_c) as the train moves through the pipe. Figure 1 illustrates the pressure measurement apparatus. Prior to the capsule train entering the test section, the pressure drop between the two pressure taps is due to the water flow only,

$$\Delta P_f = P_1 - P_2. \tag{3}$$

The absolute pressure at each tap is measured (P_1 and P_2) and used to calculate the bulk fluid pressure drop (ΔP_f). A differential pressure transducer is also located at each pressure tap location. The differential pressure transducers are referenced to a piezometer. The piezometers are used to store the steady-state pressure at each pressure tap in the pipeline with no capsules present. A valve between the pressure tap and piezometer is opened to store the steady-state pressure (P_1 and P_2) at each flow rate. Once the piezometers have stored the pipe pressure at each pressure tap the capsule train is released. The readings of the differential pressure transducers (ΔP_1 and ΔP_2) are nearly zero prior to the capsule train reaching the test section. ΔP_1 and ΔP_2 fluctuate slightly due to noise in the test section, the fluctuations are within ±25 Pa for the test facility used in this investigation.

The pressure drop caused by the capsule train and bulk fluid, where the capsule train is in the test section between the pressure taps, is defined by,

$$\Delta P_t = P_1^* - P_2^*, \tag{4}$$

where P^* represents the pressure drop of both the capsule train and water at each tap location. The pressure measurement from each differential pressure transducer (ΔP_1 and ΔP_2) is,

$$\Delta P_1 = P_1^* - P_1, \tag{5}$$

and

$$\Delta P_2 = P_2^* - P_2. \tag{6}$$

The differential pressure transducer measures the pressure difference between the piezometer (P) and each tap location.

The capsule pressure drop is the difference between the total headloss and fluid only pressure drop,

$$\Delta P_c = \Delta P_t - \Delta P_f. \tag{7}$$

Substituting Eqs. (3) and (4) into (7) one obtains,

$$\Delta P_c = (P_1^* - P_2^*) - (P_1 - P_2). \tag{8}$$

Rearranging Eq. (8) yields,

$$\Delta P_c = (P_1^* - P_1) - (P_2^* - P_2). \tag{9}$$

Substituting Eqs. (5) and (6) into (9) defines the capsule pressure drop as,

$$\Delta P_c = \Delta P_1 - \Delta P_2. \tag{10}$$

Therefore, the difference between the differential pressure transducers ($\Delta P_1 - \Delta P_2$) is equivalent to the pressure increase due only to the presence of the capsule train between the pressure taps. This assumes that the flow rate doesn't vary in the test section after the valves between the piezometers and taps are closed. This is not a problem for the constant-head open-loop system used in the investigation of Seaba and Xu (1995).

The capsule and total pressure gradients are calculated by the difference of pressure measurements at each tap location as defined by Eq. (10). Each pressure measurement is taken 1 μs apart, with each tap taken in consecutive order (i.e., P_1 then P_2). The group of pressure measurements are taken in 1 ms time intervals and averaged over a 1 to 2 second time period (time capsule train is between the pressure taps) which corresponds to 100 to 200 data points. The transient pressure fluctuations caused by the capsule train passing the taps are not included in the average pressure measurement. The pressure fluctuations over the averaged time are within ±10 percent. To insure that the capsule train is between the taps, electromike measurements are taken within the test section (Seaba and Xu, 1995). The electromikes produce an analog signal which is calibrated to determine the distance between the capsule and the pipe wall at a given location. This also allows one to define the capsule transport regime by the orientation the capsule to the pipe wall. All instrumentation is connected to a PC based data acquisition system (Xu, 1993).

An ultrasonic flow meter monitors the volumetric flow rate in the test section. The ultrasonic flowmeter was calibrated using a weighing tank (Xu, 1993). The bulk fluid velocity was calculated by dividing the flow rate by the area of the pipe. The uncertainty of the inner pipe dimensions is ±0.03 cm, resulting in an uncertainty of ±2 percent m/s for the bulk flow velocities investigated.

Results and Discussion

To illustrate the utility of this technique, the pressure drop produced by a capsule train is examined in a 50.1 mm inner diameter pipe. The capsule train consists of five capsules with a total length of 50 cm. Each capsule has a specific gravity of 1.3, aspect ratio of 4 (length of capsule divided by capsule diameter), and a diameter ratio equal to 0.75 (diameter of capsule divided by pipe inner diameter). The capsule pressure gradient ($\Delta P_c/NL_c$, second term in Eq. (2)) versus the bulk fluid velocity is shown in Fig. 2. Note that the pressure gradient is along the capsule train in fluid and does not include the section of pipe without capsules.

The capsule transport regimes can be distinguished from the capsule pressure gradient shown in Fig. 2. At the low bulk velocities (1 to 1.7 m/s) the capsule train is dragging along the pipe bottom, increasing the bulk velocity increases the capsule pressure gradient. As the bulk velocity increases, the capsule train begins to lift-off the pipe bottom (microlift) and the capsule pressure gradient begins to decrease. The capsule location relative to the pipe is determined by an electromike (Seaba and Xu, 1995). Therefore, regime III begins at a bulk fluid velocity of 1.7 m/s which correlates to a maximum capsule train pressure gradient of 370 ± 15 Pa/m. For bulk velocities greater than 1.7 m/s, the capsule pressure gradient decreases as the interaction of the capsules with the pipe decrease with increasing bulk velocity.

The total pressure gradient versus bulk fluid velocity for the capsule train, water only, and the Moody diagram at $\epsilon/d = 0.0002$ are illustrated in Fig. 3. The greatest difference between the pure water and capsule total pressure gradients is at 1.7 m/s, where the maximum capsule pressure gradient exists. This difference diminishes at the higher bulk fluid velocities attributed to the decrease in the capsule train pressure gradient. The water pressure gradient versus bulk fluid velocity agrees with the Moody diagram at $\epsilon/d = 0.0002$, this also agrees with the results of Richards (1992) who used the same pipe material in a different test loop.

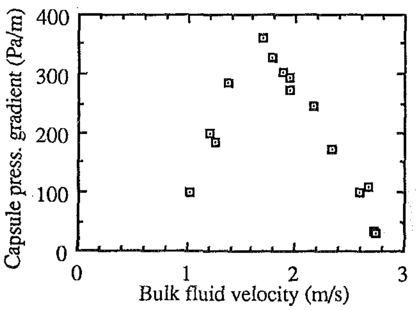

Fig. 2 Capsule train pressure gradient (uncertainty ± 15 Pa/m pipe, ± 2 percent m/s)

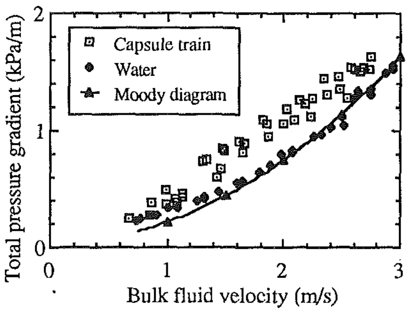

Fig. 3 Total pressure gradient of capsule train (uncertainty ± 0.3 kPa/m, ± 2 percent, m/s)

The experimental repeatability limits the uncertainty of the pressure measurements. The capsule and total pressure gradients are ±15 Pa/m and ±300 Pa/m, respectively. The capsule pressure drop for a 50 cm long capsule train (5 capsules) in a pipeline at a bulk velocity of 2.8 m/s is approximately 245 Pa. The uncertainty for ΔP_c per meter of pipe is ±6 percent (uncertainty divided by the magnitude of measurement) compared to ±67 percent using the technique previously applied (Rhee, 1989 and Richards, 1992). This new method provides sufficient resolution and accuracy to assess short capsule trains (5 capsules) in a laboratory environment.

Conclusions

It has been shown that this new pressure measurement technique is a useful approach to assess capsule train transport. The capsule pressure gradient is measured by the difference of two differential pressure transducers referenced to the total pressure in the pipe flow without capsules. For the first time, the capsule pressure gradient has been measured in situ and capsule transport regimes can be defined from these measurements, i.e., microlift. Further improvement in the accuracy of the pressure measurement system presented is the replacement of the gage pressure transducers, P_1 and P_2 (refer to Fig. 1) with a differential pressure transducer. The measured pressure gradients generated by the presence of the capsule train can be used to validate numerical models.

Acknowledgments

This work has been supported by the NSF sponsored Capsule Pipeline Research Center and the Department of Mechanical & Aerospace Engineering at the University of Missouri-Columbia.

References

Feng, J., Huang, P. Y., and Joseph, D. D., 1995, "Dynamic Simulation of the Motion of Capsules in Pipelines," *Journal of Fluid Mechanics*, Vol. 286, p. 201.

Fujiwara, Y., Tomita, Y., Satou, H., and Funatsu, K., 1994, "Characteristics of Hydraulic Capsule Transport," *JSME International Journal*, Series B, Vol. 37, No. 1, p. 89.

Kruyer, J., Redberger, P. J., and Ellis, H. S., 1967, "The Pipe Flow of Capsules," *Journal of Fluid Mechanics*, Vol. 30, p. 513.

Liu, H., 1981, "Hydraulic Capsule Pipeline," *J. Pipelines*, Vol. 1, p. 11.

Liu, H., 1992, "Hydraulic Behaviors of Coal Log Flow in Pipe," *Proceedings of the 7th International Symposium on Freight Pipelines*, Wollongong, Australia, p. 201.

Liu, H., 1993. "Coal Log Pipeline: Economics, Water Use, Right-of Way, and Environmental Impact," *Proceedings of the 10th Annual Pittsburgh Coal Conference*, p. 23.

Liu, H., and Marrero, T., 1995, "Coal Log Pipeline Transportation of Western Coal: Future Potential," 21st Annual Meeting of Western Coal Transportation Association, Denver, CO, Sept. 11–13. 14 pages.

Liu, H., and Richards, J., 1994, "Hydraulics of Stationary Capsule in Pipe," *Journal of Hydraulic Engineering*, Vol. 120, No. 1, p. 22.

Rhee, K. H., 1989, "Behavior Of Cylindrical Capsules In Fiber-Water Flow In Pipe," Ph.D thesis, Civil Engineering Dept., University of Missouri-Columbia.

Richards, J. L., 1992, "The Behavior Of Coal Log Trains In Hydraulic Transport Through Pipe," M.S. thesis, Civil Engineering Dept., University of Missouri-Columbia.

Seaba, J. P., and Xu, G., 1995, "Capsule Transport in Coal Slurry Medium," ASME Journal of Fluids Engineering, Vol. 117, pp. 691–695.
Xu, G., 1993, "Behavior of Capsules in Slurry Medium in a Pipe," M.S. thesis, Mechanical & Aerospace Engineering Dept., University of Missouri-Columbia.
Zhai, D., 1995, "Computational Analysis of Capsule Transport in Pipe," M.S. thesis, Mechanical & Aerospace Engineering Dept., University of Missouri-Columbia.

Analysis of Mass Transfer in Arctic Plumes (Implications for Global Climate)

A. B. Oertling,[1] S. G. Schwarz,[1] and V. T. John[2]

Plumes recently observed in the Russian Arctic by NOAA satellites provide evidence that gas hydrates may be destabilizing under the ocean floor, transferring into the atmosphere large quantities of light hydrocarbons including methane, a known greenhouse gas. The plumes occur intermittently and are up to hundreds of kilometers long and as much as 30 kilometers wide (Matson, 1986). It was proposed that a downward propagating thermal wave was melting the hydrates located under the Arctic permafrost, releasing the trapped hydrocarbons (Clarke et al., 1990). This thermal wave was due to the decline of the last ice age and the corresponding inundation of the permafrost by the rising sea (MacDonald, 1990; Nisbet, 1992). It was speculated that as the subsurface hydrocarbons were released, pressure built up forcing the migration of methane along geologic fault lines. Eventually the methane reached the sea floor and expanded substantially as it was released into the water. At the surface of the water, this burst of methane formed a large plume. The escape along known fault lines in the area explained the line source observed in the satellite photographs (Kienle et al., 1983).

Methane gas has become a major climate concern as calculations show that its direct effect alone could account for as much as 25 percent of the global warming over the next 100 years (Rotmans et al., 1992). In addition to the direct effects on temperature, there are several potential feedbacks between climate change and methane emissions, not the least of which is the destabilization of methane hydrates accompanying a global temperature increase (IPCC, 1990). As the surface temperature rises, a thermal wave is propagated downward causing the hydrates to melt. The free gas migrates upward and reaches the atmosphere, possibly in the form of the observed plumes. The resulting increase in atmospheric methane contributes to the greenhouse forcing, potentially leading to more hydrate destabilization. This is the nature of the positive feedback process.

Plume Model

In order to assess the potential contribution of methane to the atmosphere, a model is proposed for a plume that mimics the satellite images (Fig. 1). As the thermal wave propagates downward, the hydrate reservoir temperature T_R increases, yielding a temperature-pressure field unsuitable for maintaining methane in hydrate form. Free gas accumulates and increases in pressure until it causes a rupture. It escapes into the sea at the mud line where it vents through approximately 40 m of water. It is released into the atmosphere at a point considered the plume source, having a particular outlet density ρ_o, velocity u_o and plume width b_o. The gas is then subjected to a stratified atmosphere of varying density ρ_∞ and the prevailing wind at velocity u_∞. Important downstream parameters include the plume trajectory, density ρ, velocity u and width b.

We employed a numerical model entitled UDKHDEN (the Universal Davis-Kahnberg-Hirst model, input DENsity version). It is based on the analytical and experimental work of Davis (1975) and Kannberg and Davis (1976), and has been selected by the EPA in their guidelines to predict the behavior of multiple port ocean discharges (Davis, 1990). It uses as a starting point the work of Hirst (1971), who developed an integral model for round, buoyant jets discharged from a point source into a flowing, stratified ambient. It then accounts for plume merging, which provides an effective line source. Both models compare favorably the results of their analyses with the work of Fan (1967), who experimentally investigated the effects of ambient current and stratification on buoyant plume characteristics.

Model Input

The input to the model included plume discharge geometry, velocity, and density. These parameters were varied with the goal of generating a plume matching the height of the plumes depicted in the satellite imagery.

For a reasonable discharge velocity, blow-out conditions were assumed because it was found that velocities resulting from bubbles rising were insufficient for the generation of a 1 km plume. With a sudden rupture, the water column above the gas would be lightened, and the gas would be allowed to vent to the atmosphere. This is commonly referred to as "mud volcanos" or "mud diapirs" (Hovland and Judd, 1988). When methane is formed in the sediments, there is an increase in volume. If the fluids have difficulty escaping from the fine pores of the compacting mud or shales, there will be an increase in pore pressures. If this pressure cannot be released or dissipated, the pressure builds up until it is eventually released by eruption.

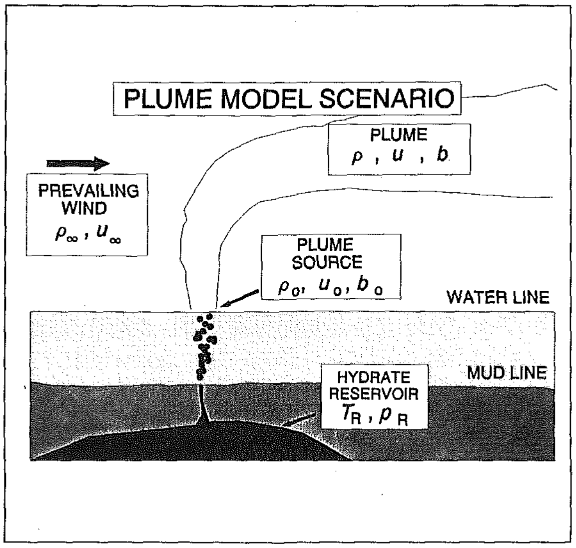

Fig. 1 Plume model scenario

---

[1] PhD Graduate Student and Assistant Professor, respectively, Department of Mechanical Engineering.

[2] Professor, Department of Chemical Engineering.

Tulane University, New Orleans, LA 70118.

Contributed by the Fluids Engineering Division of The American Society of Mechanical Engineers. Manuscript received by the Fluids Engineering Division January 9, 1995; revised manuscript received April 2, 1996. Associate Technical Editor: F. Giralt.

Seaba, J. P., and Xu, G., 1995, "Capsule Transport in Coal Slurry Medium," ASME Journal of Fluids Engineering, Vol. 117, pp. 691–695.

Xu, G., 1993, "Behavior of Capsules in Slurry Medium in a Pipe," M.S. thesis, Mechanical & Aerospace Engineering Dept., University of Missouri-Columbia.

Zhai, D., 1995, "Computational Analysis of Capsule Transport in Pipe," M.S. thesis, Mechanical & Aerospace Engineering Dept., University of Missouri-Columbia.

Analysis of Mass Transfer in Arctic Plumes (Implications for Global Climate)

A. B. Oertling,[1] S. G. Schwarz,[1] and V. T. John[2]

Plumes recently observed in the Russian Arctic by NOAA satellites provide evidence that gas hydrates may be destabilizing under the ocean floor, transferring into the atmosphere large quantities of light hydrocarbons including methane, a known greenhouse gas. The plumes occur intermittently and are up to hundreds of kilometers long and as much as 30 kilometers wide (Matson, 1986). It was proposed that a downward propagating thermal wave was melting the hydrates located under the Arctic permafrost, releasing the trapped hydrocarbons (Clarke et al., 1990). This thermal wave was due to the decline of the last ice age and the corresponding inundation of the permafrost by the rising sea (MacDonald, 1990; Nisbet, 1992). It was speculated that as the subsurface hydrocarbons were released, pressure built up forcing the migration of methane along geologic fault lines. Eventually the methane reached the sea floor and expanded substantially as it was released into the water. At the surface of the water, this burst of methane formed a large plume. The escape along known fault lines in the area explained the line source observed in the satellite photographs (Kienle et al., 1983).

Methane gas has become a major climate concern as calculations show that its direct effect alone could account for as much as 25 percent of the global warming over the next 100 years (Rotmans et al., 1992). In addition to the direct effects on temperature, there are several potential feedbacks between climate change and methane emissions, not the least of which is the destabilization of methane hydrates accompanying a global temperature increase (IPCC, 1990). As the surface temperature rises, a thermal wave is propagated downward causing the hydrates to melt. The free gas migrates upward and reaches the atmosphere, possibly in the form of the observed plumes. The resulting increase in atmospheric methane contributes to the greenhouse forcing, potentially leading to more hydrate destabilization. This is the nature of the positive feedback process.

Plume Model

In order to assess the potential contribution of methane to the atmosphere, a model is proposed for a plume that mimics the satellite images (Fig. 1). As the thermal wave propagates downward, the hydrate reservoir temperature T_R increases, yielding a temperature-pressure field unsuitable for maintaining methane in hydrate form. Free gas accumulates and increases in pressure until it causes a rupture. It escapes into the sea at the mud line where it vents through approximately 40 m of water. It is released into the atmosphere at a point considered the plume source, having a particular outlet density ρ_o, velocity u_o and plume width b_o. The gas is then subjected to a stratified atmosphere of varying density ρ_∞ and the prevailing wind at velocity u_∞. Important downstream parameters include the plume trajectory, density ρ, velocity u and width b.

We employed a numerical model entitled UDKHDEN (the Universal Davis-Kahnberg-Hirst model, input DENsity version). It is based on the analytical and experimental work of Davis (1975) and Kannberg and Davis (1976), and has been selected by the EPA in their guidelines to predict the behavior of multiple port ocean discharges (Davis, 1990). It uses as a starting point the work of Hirst (1971), who developed an integral model for round, buoyant jets discharged from a point source into a flowing, stratified ambient. It then accounts for plume merging, which provides an effective line source. Both models compare favorably the results of their analyses with the work of Fan (1967), who experimentally investigated the effects of ambient current and stratification on buoyant plume characteristics.

Model Input

The input to the model included plume discharge geometry, velocity, and density. These parameters were varied with the goal of generating a plume matching the height of the plumes depicted in the satellite imagery.

For a reasonable discharge velocity, blow-out conditions were assumed because it was found that velocities resulting from bubbles rising were insufficient for the generation of a 1 km plume. With a sudden rupture, the water column above the gas would be lightened, and the gas would be allowed to vent to the atmosphere. This is commonly referred to as "mud volcanos" or "mud diapirs" (Hovland and Judd, 1988). When methane is formed in the sediments, there is an increase in volume. If the fluids have difficulty escaping from the fine pores of the compacting mud or shales, there will be an increase in pore pressures. If this pressure cannot be released or dissipated, the pressure builds up until it is eventually released by eruption.

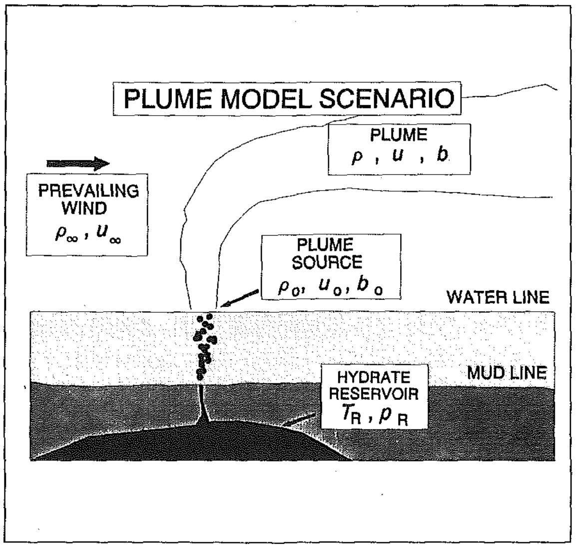

Fig. 1 Plume model scenario

---

[1] PhD Graduate Student and Assistant Professor, respectively, Department of Mechanical Engineering.

[2] Professor, Department of Chemical Engineering.

Tulane University, New Orleans, LA 70118.

Contributed by the Fluids Engineering Division of The American Society of Mechanical Engineers. Manuscript received by the Fluids Engineering Division January 9, 1995; revised manuscript received April 2, 1996. Associate Technical Editor: F. Giralt.

Some of these eruptions have been dramatic, as documented by eyewitness accounts (Hedberg, 1980).

Density estimates were based on the ideal gas law and assumed conditions of pressure and temperature. Allowing thermal exchange between the methane and the seawater, the discharge temperature can be taken as 0°C, the average water temperature in the area (Peixoto and Oort, 1992). This yielded a density of 0.00072 g/cc. With minimal thermal exchange, the discharge temperature is considered a result of rapid expansion of the methane gas. This can be calculated employing the Joule-Thompson coefficient (Budenholzer et al., 1939). Underground pressure was calculated based on a 90 percent filled methane clathrate which has a laboratory density of 0.819 g/cc and occupies 156 m^3 at STP (MacDonald, 1990). Assuming a constant number of moles of methane, a 156 fold increase in volume would provide a 156 fold decrease in pressure. With a surface pressure of 1 atm, this would indicate an underground pressure of 156 atm. The resulting temperature as the methane exits into the atmosphere is calculated to be −74°C, which yields a density of 0.000983 g/cc.

Atmospheric density and velocity distributions were based on upper air temperature and pressure data which were obtained from the closest available weather station located approximately 300 km from Bennett Island (Monthly Climate Data for the World, 1987–1992). Data for February, 1987–1992, were used as this is a typical month for plume sightings. The same data set provided information regarding wind speed, which averaged to a constant 3 m/s from 10 m to about 5000 m.

Results

The results were categorized depending upon which discharge parameter was varied. The discharge conditions for plumes matching the satellite images were used to estimate the methane contribution based on 8.4 plume sightings per year and an average plume duration of 24 hours. This was concluded from a systematic review of plumes sighted in the Bennett Island area during the years 1990–1992 (Buelow, 1993).

In varying the discharge velocity, the discharge density was held constant for a set of computer runs and ranged for a series of sets from 0.00072 g/cc to 0.00098 g/cc. Discharge geometry, constant for an individual set, ranged for a series of sets from 10,000 discharge ports of 1 m in diameter to 500 ports of 20 m in diameter. A sample of the results (Fig. 2) is shown for plumes with initial velocities of at least 20 m/s, as velocities less than that did not produce plumes of significant rise.

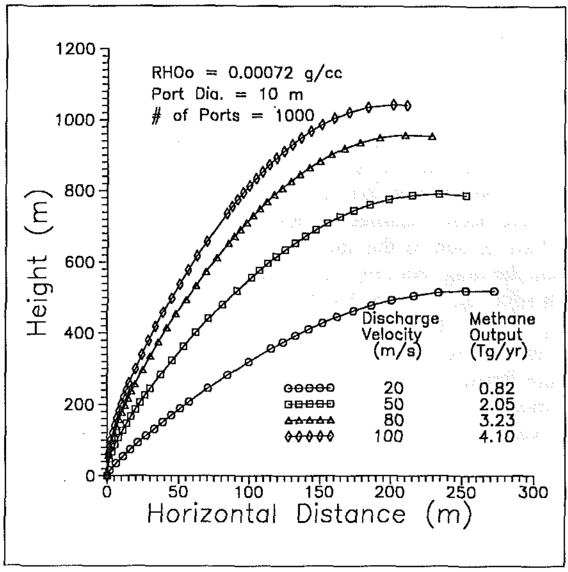

Fig. 2 Plume trajectory with varying discharge velocity

Based on a series of 36 test cases, calculations show a range of 4.10–11.17 Tg/yr of methane discharged to the atmosphere from plumes of approximately 1 km in height. This is equivalent to 0.75–2.03 percent of the estimated annual contribution from all global sources of methane as identified by Rotmans et al. (1992).

In varying the discharge geometry, 27 test cases yield a range of 4.85–11.17 Tg/yr of methane discharged to the atmosphere from plumes of approximately 1 km in height. This is equivalent to 0.89–2.03 percent of the total estimated annual contribution. The range of annual methane discharge resulting from the variation of discharge density is 4.10–5.39 Tg/yr based on 27 additional test cases. This is between 0.75 and 0.98 percent of the total estimated annual contribution.

Conclusion

The goal of this research was to develop a model for a plume that mimics the existing Arctic plumes depicted in satellite imagery. Using this model, the resulting significance of the methane contribution to the overall atmospheric methane budget was estimated.

Results show that the potential methane contribution from plumes matching the satellite photographs was calculated to be between 4.10 and 11.17 Tg/yr. This is equivalent to 0.75–2.03 percent of the estimated annual contribution from all global sources of methane. Considering that this estimate is only for Bennett Island plumes and realizing the existence of known discharges in other Arctic areas, this is certainly a number significant enough to warrant further investigation.

It should be noted that in April, 1992, a joint U.S.-Russian venture was undertaken to sample a plume and determine its composition. They found no elevated levels of methane and concluded that the plumes sighted were meteorological phenomena (Schnell, 1992). It is clear that the clouds sampled are unrelated to methane hydrates, but the existence of a cloud over Bennett Island would not eliminate the possibility of a methane plume being generated by the destabilization of hydrates. There remains the question of plume top temperatures. Infrared imagery indicated that some plumes were as cold as −45°C. This could reasonably be achieved by the hydrate destabilization scenario. It is not likely in the "cloud" scenario (Hufford, 1993). In order to resolve the controversy, a systematic study would be required.

Finally, although the best plume model available was selected to conduct this study, a useful continuation of the research would be more specific tailoring of a model to the Arctic plumes. One could then account for such things as the large scale of the problem and atmospheric turbulence. These in fact describe the limitations of this study.

The final product of this research is a better understanding of the Arctic plume phenomena and its potential relationship to global warming. The results are estimates regarding the possible methane output by these plumes.

Acknowledgment

This research was funded by the U.S. Department of Energy's (DOE) National Institute for Global Environmental Change (NIGEC) through the South-Central Regional Center at Tulane University (DOE Cooperative Agreement No. DE-FCo3-90ER61010.) Financial support does not constitute an endorsement by DOE of the views expressed in this article. We would also like to acknowledge helpful discussions held with Robert G. Watts.

References

Buelow, William J., 1993, personal communication, June.

Budenholzer, R. A., B. H. Sage, and W. N. Lacey, 1939, "Phase Equilibria in Hydrocarbon Systems," *Industrial and Engineering Chemistry*, Vol. 31, No. 3, p. 369.

Clarke, J. W., P. St. Armand, and M. Matson, 1990, "Possible Cause of Plume in the Vicinity of Bennett Island, East Siberian Sea Soviet Far Arctic—An Hypothesis," manuscript.

Davis, L. R., 1975, "Analysis of Multiple Cell Mechanical Draft Cooling Tower Plumes," USEPA, Corvall's Environmental Research Lab., EPA-660/3-75-039.

Davis, L. R., 1990, "A Review of Buoyant Plume Modeling," ASME-AIAA Joint Thermophysics Conference, Heat Transfer Division Symposium, Seattle, WA, 139, 85–99.

Fairbanks, R. G., 1989, "A 17,000-year Glacio-eustatic Sea Level Record: Influence of Glacial Melting Rates on the Younger Dryes Event and Deep-ocean Circulation," *Nature,* Vol. 342, pp. 637–642.

Fan, L. N., 1967, "Turbulent Buoyant Jets into Stratified and Flowing Ambient Fluids," California Institute of Technology, W. N. Keck Laboratory, Report KHR-15.

Hedberg, H. D., 1980, "Methane Generation and Petroleum Migration," Rogerts, W. H., III and Cordell, R. J., eds., *Problems of Petroleum Migration,* American Assoc. Petrol. Geologists, Studies in Geol., No. 10, pp. 179–206.

Hirst, E. A., 1971, "Analysis of Round, Turbulent, Buoyant Jets Discharged to Flowing Stratified Ambients," Oak Ridge National Laboratory, Report ORNL 4685.

Hovland, M., and A. G. Judd, 1988, *Seabed Pockmarks and Seepages,* Graham and Trotman, London, p. 187.

Hufford, G., 1993, personal communication, Oct.

Intergovernmental Panel on Climate Change (IPCC), 1990, Climate Change, The IPCC Scientific Assessment, Houghton, J. T., Jenkins, G. J. and Ephraums, J. J., eds., Cambridge University Press, U.K., p. 18.

Kannberg, L. D., and L. R., Davis, 1976, "An Experimental/Analytical Investigation of Deep Submerged Multiple Buoyant Discharges," USEPA, Corvallis Environmental Research Lab., EPA-600/3-76-101.

Kienle, J., J. G. Roederer and G. E. Shaw, 1983, "Volcanic Event in Soviet Arctic," *EOS,* Vol. 64, 20, p. 377.

Kvenvolden, K. A., and Barnard, L., 1983, "Hydrates of Natural Gas in Continental Margins," J. Watkins and C. Drake, eds., *Studies in Continental Margin Geology,* Mem. 34, Tulsa, OK, American Association of Petroleum Geology, 631–640.

MacDonald, G. J., 1990, "Role of Methane Clathrates in Past and Future Climates," *Climate Change,* Vol. 16, pp. 247–281.

Matson, M., 1986, "Large Plume Events in the Soviet Arctic," *EOS,* Vol. 27, 48, pp. 1372–1373.

Monthly Climate Data for the World, 1983–1991, NOAA, Environmental Data and Information Service, National Climatic Center, Asheville, N.C.

Nisbet, E. G., 1992, "Sources of Atmospheric CH_4 in Early Postglacial Time," *Journal of Geophysical Research,* Vol. 97, No. D12, 12,859–12,867.

Peixoto, Jose P., and Abraham H. Oort, 1992, *Physics of Climate,* American Institute of Physics, New York.

Rotmans, J., M. G. J. den Elzen, M. S. Krol, R. J. Swart and H. J. van der Woerd, 1992, "Stabilizing Atmospheric Concentrations: Towards International Methane Control," *Ambio,* Vol. 21, No. 6, pp. 404–413.

Schnell, R., 1992, personal communication, May.

Velocity Measurements in a Turbulent Non-Newtonian Jet

A. Shekarriz,[1] G. Doulliard,[2] and C. D. Richards[2]

Introduction

The behavior of pseudoplastic and yield-pseudoplastic jets has been of interest for many years. Jets are commonly used for mixing and resuspension of settled slurries and colloidal dispersions within industrial processes. Previous studies of pseudoplastic jet behavior have focused on laminar jets (Gutfinger and Shinnar, 1964; Serth, 1972; Mitwally, 1978; Kumar et al., 1984; and Jordan et al., 1992). In most of these studies the authors attempt to develop similarity solutions for the laminar flow region. Studies of turbulent non-Newtonian jets are primarily limited to drag reducing polymers. A summary of some of the work in this area is given in McComb (1990). Barker (1973) and Serth (1969) performed measurements in jets consisting of dilute polymer suspensions and reported no effect on the mean velocity or turbulent intensity. Shekarriz et al. (1995) used PIV to observe that when the behavior index of a "power-law" fluid is sufficiently low, the jet experiences a very rapid decay at a distance downstream which is directly a function of the nozzle exit velocity.

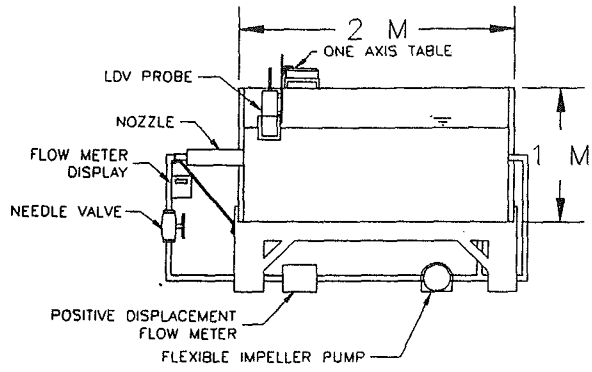

Fig. 1 Experimental apparatus

The objective of this study is to further explore the behavior of submerged pseudoplastic and yield-pseudoplastic jets. Experiments have been designed to encompass turbulent behavior. Four rheological states are studied to provide a range of pseudoplastic behavior. Laser Doppler velocimetry (LDV) is used to map the mean and fluctuating axial velocity field.

Experimental Apparatus and Procedures

The experimental apparatus consisted of a 2 m × 1 m × 1 m tank, a $\frac{1}{3}$ Hp flexible impeller pump, a positive displacement flow meter, a needle valve, and a nozzle. A schematic of the apparatus is shown in Fig. 1. The nozzle consisted of an expansion section, a flow straightener section, and a cosine curved convergence section with a 64:1 area reduction.

The fluid used was an aqueous solution of Carbopol 980®. The concentration of the fluid was varied from 0.025 to 0.10 percent by weight. Samples of the mixtures were saved for rheological characterization before and after the experiments. No measurable differences were observed in fluid rheology before and after the tests. Although measurements by Xie and Hartnet (1992) show that solutions of Carbopol are viscoelastic, they have been classified as purely viscous non-Newtonian fluids. This is due to the fact that solutions of Carbopol do not exhibit the drag reducing behavior observed in other viscoelastic fluids such as Separan. The rheology of the fluid was measured using a controlled strain Bohlin® rheometer. The strain rate was varied from 0.1 to 100 s^{-1} and the temperature of the sample during each measurement was maintained the same as that measured during the jet flow experiments. The rheological data was fit to a Herschel-Bulkley model of the form

$$\tau = \tau_o + K\dot{\gamma}|\dot{\gamma}|^{n-1} \tag{1}$$

in which τ is the shear stress, $\dot{\gamma}$ is the strain rate, K is the consistency index, n is the behavior index, and τ_o is the yield stress of the fluid. The correlation coefficients were all greater than 0.99. The yield stress was 1 Pa for the 0.1 percent concen-

---

[1] Senior Research Engineer, Fluid Dynamics Group, Pacific Northwest Laboratory, Richland WA.

[2] Research Assistant and Assistant Professor, respectively, Mechanical & Materials Engineering Department, Washington State University, Pullman WA 99164-2920.

Contributed by the Fluids Engineering Division of The American Society of Mechanical Engineers. Manuscript received by the Fluids Engineering Division May 24, 1995; revised manuscript received April 23, 1996. Associate Technical Editor: J. A. C. Humphrey.

Clarke, J. W., P. St. Armand, and M. Matson, 1990, "Possible Cause of Plume in the Vicinity of Bennett Island, East Siberian Sea Soviet Far Arctic—An Hypothesis," manuscript.

Davis, L. R., 1975, "Analysis of Multiple Cell Mechanical Draft Cooling Tower Plumes," USEPA, Corvall's Environmental Research Lab., EPA-660/3-75-039.

Davis, L. R., 1990, "A Review of Buoyant Plume Modeling," ASME-AIAA Joint Thermophysics Conference, Heat Transfer Division Symposium, Seattle, WA, 139, 85–99.

Fairbanks, R. G., 1989, "A 17,000-year Glacio-eustatic Sea Level Record: Influence of Glacial Melting Rates on the Younger Dryes Event and Deep-ocean Circulation," *Nature,* Vol. 342, pp. 637–642.

Fan, L. N., 1967, "Turbulent Buoyant Jets into Stratified and Flowing Ambient Fluids," California Institute of Technology, W. N. Keck Laboratory, Report KHR-15.

Hedberg, H. D., 1980, "Methane Generation and Petroleum Migration," Rogerts, W. H., III and Cordell, R. J., eds., *Problems of Petroleum Migration,* American Assoc. Petrol. Geologists, Studies in Geol., No. 10, pp. 179–206.

Hirst, E. A., 1971, "Analysis of Round, Turbulent, Buoyant Jets Discharged to Flowing Stratified Ambients," Oak Ridge National Laboratory, Report ORNL 4685.

Hovland, M., and A. G. Judd, 1988, *Seabed Pockmarks and Seepages,* Graham and Trotman, London, p. 187.

Hufford, G., 1993, personal communication, Oct.

Intergovernmental Panel on Climate Change (IPCC), 1990, Climate Change, The IPCC Scientific Assessment, Houghton, J. T., Jenkins, G. J. and Ephraums, J. J., eds., Cambridge University Press, U.K., p. 18.

Kannberg, L. D., and L. R., Davis, 1976, "An Experimental/Analytical Investigation of Deep Submerged Multiple Buoyant Discharges," USEPA, Corvallis Environmental Research Lab., EPA-600/3-76-101.

Kienle, J., J. G. Roederer and G. E. Shaw, 1983, "Volcanic Event in Soviet Arctic," *EOS,* Vol. 64, 20, p. 377.

Kvenvolden, K. A., and Barnard, L., 1983, "Hydrates of Natural Gas in Continental Margins," J. Watkins and C. Drake, eds., *Studies in Continental Margin Geology,* Mem. 34, Tulsa, OK, American Association of Petroleum Geology, 631–640.

MacDonald, G. J., 1990, "Role of Methane Clathrates in Past and Future Climates," *Climate Change,* Vol. 16, pp. 247–281.

Matson, M., 1986, "Large Plume Events in the Soviet Arctic," *EOS,* Vol. 27, 48, pp. 1372–1373.

Monthly Climate Data for the World, 1983–1991, NOAA, Environmental Data and Information Service, National Climatic Center, Asheville, N.C.

Nisbet, E. G., 1992, "Sources of Atmospheric CH_4 in Early Postglacial Time," *Journal of Geophysical Research,* Vol. 97, No. D12, 12,859–12,867.

Peixoto, Jose P., and Abraham H. Oort, 1992, *Physics of Climate,* American Institute of Physics, New York.

Rotmans, J., M. G. J. den Elzen, M. S. Krol, R. J. Swart and H. J. van der Woerd, 1992, "Stabilizing Atmospheric Concentrations: Towards International Methane Control," *Ambio,* Vol. 21, No. 6, pp. 404–413.

Schnell, R., 1992, personal communication, May.

Velocity Measurements in a Turbulent Non-Newtonian Jet

A. Shekarriz,[1] G. Doulliard,[2] and C. D. Richards[2]

Introduction

The behavior of pseudoplastic and yield-pseudoplastic jets has been of interest for many years. Jets are commonly used for mixing and resuspension of settled slurries and colloidal dispersions within industrial processes. Previous studies of pseudoplastic jet behavior have focused on laminar jets (Gutfinger and Shinnar, 1964; Serth, 1972; Mitwally, 1978; Kumar et al., 1984; and Jordan et al., 1992). In most of these studies the authors attempt to develop similarity solutions for the laminar flow region. Studies of turbulent non-Newtonian jets are primarily limited to drag reducing polymers. A summary of some of the work in this area is given in McComb (1990). Barker (1973) and Serth (1969) performed measurements in jets consisting of dilute polymer suspensions and reported no effect on the mean velocity or turbulent intensity. Shekarriz et al. (1995) used PIV to observe that when the behavior index of a "power-law" fluid is sufficiently low, the jet experiences a very rapid decay at a distance downstream which is directly a function of the nozzle exit velocity.

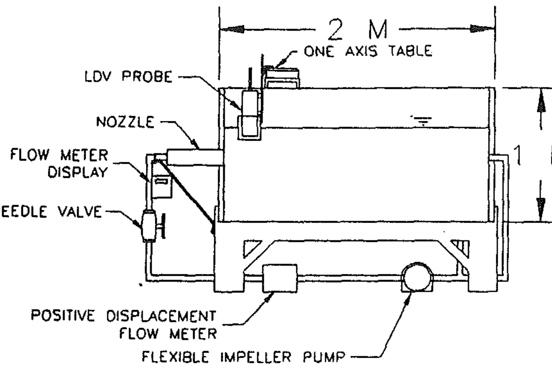

Fig. 1 Experimental apparatus

The objective of this study is to further explore the behavior of submerged pseudoplastic and yield-pseudoplastic jets. Experiments have been designed to encompass turbulent behavior. Four rheological states are studied to provide a range of pseudoplastic behavior. Laser Doppler velocimetry (LDV) is used to map the mean and fluctuating axial velocity field.

Experimental Apparatus and Procedures

The experimental apparatus consisted of a 2 m × 1 m × 1 m tank, a $\frac{1}{3}$ Hp flexible impeller pump, a positive displacement flow meter, a needle valve, and a nozzle. A schematic of the apparatus is shown in Fig. 1. The nozzle consisted of an expansion section, a flow straightener section, and a cosine curved convergence section with a 64:1 area reduction.

The fluid used was an aqueous solution of Carbopol 980®. The concentration of the fluid was varied from 0.025 to 0.10 percent by weight. Samples of the mixtures were saved for rheological characterization before and after the experiments. No measurable differences were observed in fluid rheology before and after the tests. Although measurements by Xie and Hartnet (1992) show that solutions of Carbopol are viscoelastic, they have been classified as purely viscous non-Newtonian fluids. This is due to the fact that solutions of Carbopol do not exhibit the drag reducing behavior observed in other viscoelastic fluids such as Separan. The rheology of the fluid was measured using a controlled strain Bohlin® rheometer. The strain rate was varied from 0.1 to 100 s^{-1} and the temperature of the sample during each measurement was maintained the same as that measured during the jet flow experiments. The rheological data was fit to a Herschel-Bulkley model of the form

$$\tau = \tau_o + K\dot{\gamma}|\dot{\gamma}|^{n-1} \qquad (1)$$

in which τ is the shear stress, $\dot{\gamma}$ is the strain rate, K is the consistency index, n is the behavior index, and τ_o is the yield stress of the fluid. The correlation coefficients were all greater than 0.99. The yield stress was 1 Pa for the 0.1 percent concen-

---

[1] Senior Research Engineer, Fluid Dynamics Group, Pacific Northwest Laboratory, Richland WA.

[2] Research Assistant and Assistant Professor, respectively, Mechanical & Materials Engineering Department, Washington State University, Pullman WA 99164-2920.

Contributed by the Fluids Engineering Division of THE AMERICAN SOCIETY OF MECHANICAL ENGINEERS. Manuscript received by the Fluids Engineering Division May 24, 1995; revised manuscript received April 23, 1996. Associate Technical Editor: J. A. C. Humphrey.

Table 1 Fluid rheological behaviors

Carbopol % mass	τ_o (Pa)	K (Pa s^n)	n	Case
0.100	1.0	2.660	0.39	A
0.075	0.0	0.205	0.64	B
0.050	0.0	0.020	0.90	C
0.025	0.0	0.003	0.97	D

Table 2 Velocity decay and spread rate

Fluid	RE	K_u	δ_u
A	3210	0.147	0.065
B	4750	0.137	0.088
C	4690	0.161	0.089
D	7470	0.166	0.086
Chen and Rodi (1980)		0.161	0.086

tration fluid and was not measurable for the other concentrations. Table 1 summarizes the model parameters for the four fluid concentrations.

The velocity data were obtained via a single-component laser Doppler velocimeter (LDV) with a fiber optic probe of focal length 350 mm. The measurement volume was 3.28×10^{-4} mm^3 and the burst signals were analyzed with a TSI-IFA 750® Doppler burst correlator. The probe was positioned with a traverse table with uncertainties of ±0.05 jet diameters in the radial direction and ±0.125 diameters in the axial direction. Measurements of axial velocity along the centerline were taken for a range of nozzle exit velocities. Radial profiles of axial velocity were acquired at z/d of 20, 40, and 60 diameters. The uncertainty in the mean velocity measurements was ±2 percent. The uncertainty in the rms velocity measurements was ±5 percent. Nozzle exit velocities were controlled with a needle valve and were measured with a flow meter. The uncertainty in the measurement of flow rate was ±10 percent.

Results and Discussion

The centerline decay of mean axial velocity of four turbulent jets representative of cases A–D is compared in Fig. 2. The Reynolds number is calculated from

$$\mathrm{Re} = \frac{\rho U_o^{2-n} d^n}{8^{n-1} K} \tag{2}$$

where ρ is the density, U_o is the bulk exit velocity, d is the nozzle diameter, and n and K are the behavior and consistency index of the Herschel-Bulkley model. The relation used for centerline scaling is

$$\frac{U_o}{U_{cl}} = K_u\left[\frac{z - z_0}{r}\right] \tag{3}$$

where K_u, is the centerline decay rate and z_0 is the virtual origin. Linear least-squares fitting of the centerline values of mean axial velocity were used to obtain the K_u values summarized in Table 2. The correlation coefficients for the regressions were all greater than 0.99. Within experimental uncertainty, the two jets closest to Newtonian behavior (fluids C and D) decay at the rate Newtonian jets do (Chen and Rodi, 1980); whereas, the decay rates of fluids A and B are less.

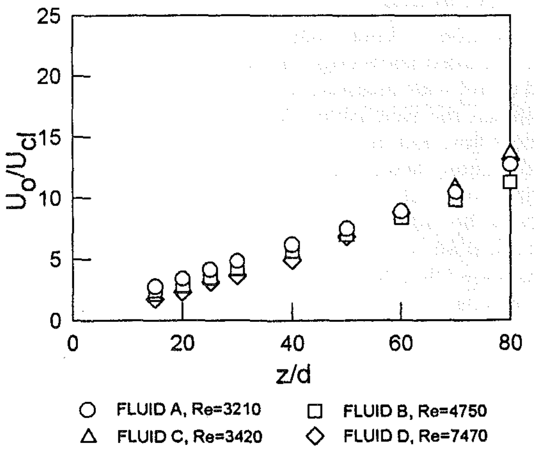

Fig. 2 Centerline decay of mean axial velocity

Radial profiles of mean axial velocity are shown in Fig. 3. The mean velocity is normalized by the centerline value and the radial coordinate by the half-width of the jet, $r_{1/2}$ (the half-width at half-maximum). Also shown plotted is the Gaussian error function

$$\frac{U}{U_{cl}} = \exp(-(r/r_{1/2})^2 \ln 2) \tag{4}$$

form, which data from experimental studies in Newtonian jets conforms to (e.g., So et al., 1990). The plot demonstrates that the data collapse to this form regardless of fluid rheology or axial location.

Half-widths were determined for each of the jets from the radial profiles of mean axial velocity acquired at $z/d = 20$, 40 and 60. The rate of spreading or growth rate, δ_u, is linear in the far field of a Newtonian jet. The values of δ_u shown in Table 2 were obtained from linear regression of $r_{1/2}$ versus downstream distance data for each fluid. The correlation coefficients for each of the regressions were greater than 0.99. Only the jet of fluid A deviates significantly from the value of 0.086 recommended by Chen and Rodi (1980).

Radial profiles of turbulence intensity, u'/U_{cl}, are shown in Fig. 4. The quantity u' is the rms of axial velocity. At $z/d = 20$ the collapse of the data is good. Further downstream, however, at $z/d = 40$ and 60 the data spread out. The turbulence intensity of jets of fluids C and D increases in the downstream direction. Centerline turbulence intensity values increase from 0.21 at $z/d = 20$ to 0.28 at $z/d = 60$. This is evidence that the higher order moments of the velocity field have not yet reached an asymptotic state, or self-similarity. The asymptotic value of turbulence intensity on the centerline of a round Newtonian jet has been shown to be 0.28 (Chen and Rodi, 1980). Thus, although the self-similar region for the turbulence occurs later for these two jets, their behavior is comparable to Newtonian behavior. The jets of fluids A and B display markedly different behavior. The turbulence intensity for the jet of fluid A decreases in the streamwise direction. The centerline turbulence intensity goes from 0.21 at $z/d = 20$ to 0.15 at $z/d = 60$. The profile is narrower and drops off more quickly on the edge of the jet.

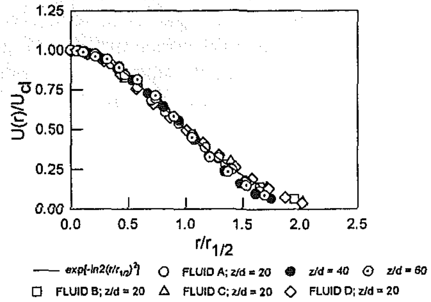

Fig. 3 Radial profiles of mean axial velocity

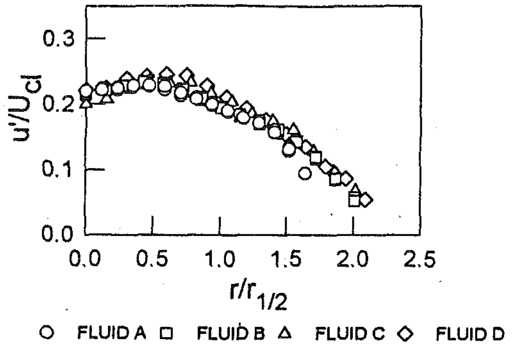

Fig. 4(*a*) *z*/*d* = 20

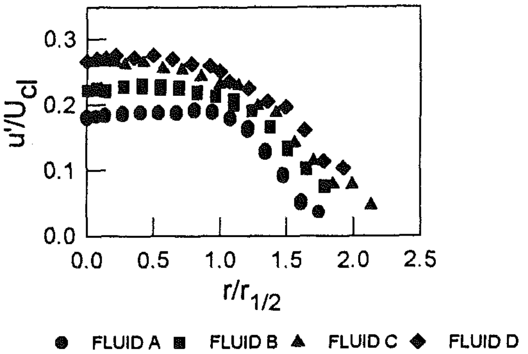

Fig. 4(*b*) *z*/*d* = 40

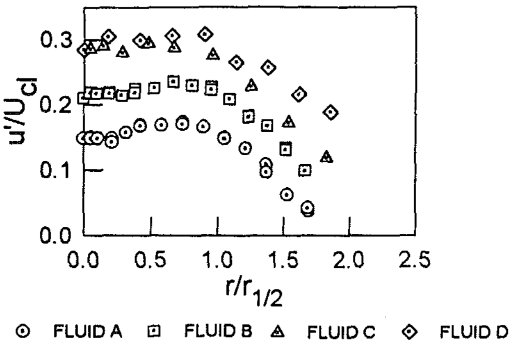

Fig. 4(*c*) *z*/*d* = 60

Fig. 4 Radial profiles of axial turbulence intensity

Although previous measurements in dilute polymer jets (Barker, 1973) showed no effect on turbulence quantities, our results do qualitatively agree with the measurements in grid turbulence of McComb et al. (1977). They found that polymer addition reduced both turbulence intensity and rate of turbulence decay. Flow visualization showed that above a critical threshold concentration small scale turbulence was attenuated. Hibberd et al. (1982) found that small scale turbulence was reduced in a mixing layer, although they did not observe a decrease in turbulence intensity. These investigators have also reported that there appears to be a threshold concentration of polymer required for small scale turbulence suppression. There is, however, disagreement over what the threshold is. Differences in fluid properties may explain this.

Conclusions

Laser Doppler velocimetry has been used to measure the axial components of mean and rms velocity in four jets with different rheological behaviors. This study has extended the range of the experimental data base: results are reported for a fluid with a behavior index of 0.39 and a yield stress of 1 Pa.

The results show significant dampening of the turbulence intensity in the yield-pseudoplastic jet ($n = 0.39$). To a lesser extent, turbulence dampening is also evident in the data of fluid B, a pseudoplastic jet ($n = 0.64$). The effects on the mean velocity field are less substantial.

References

Barker, S. J., 1973, "Laser-Doppler Measurements on a Round Turbulent Jet in Dilute Polymer Solutions," *Journal of Fluid Mechanics*, Vol. 60, pp. 721–731.

Chen, C. J., and Rodi, W., 1980, *Vertical Turbulent Buoyant Jets: A Review of Experimental Data*, Pergamon Press.

Gutfinger, C., and Shinnar, R., 1964, "Velocity Distributions in Two Dimensional Laminar Liquid-into-Liquid Jets in Power-Law Fluids," *AIChE Journal*, Vol. 10, No. 5, pp. 631–639.

Hibberd, M., Kwade, M., and Scharfe, R., 1982, "Influence of Drag Reducing Additives on the Structure of Turbulence in a Mixing Layer," *Rheologica Acta*, Vol. 21, pp. 582–586.

Jordan, C., Rankin, G. W., and Sridhar, R., 1992, "A Study of Submerged Pseudoplastic Laminar Jets," *Journal of Non-Newtonian Fluid Mechanics*, Vol. 41, pp. 323–337.

Kumar, K. R., Rankin, G. W., and Sridhar, K., 1984, "Laminar Length of a Non-Newtonian Fluid Jet," *Journal of Non-Newtonian Fluid Mechanics*, Vol. 15, pp. 13–27.

McComb, W. D., Allen, J., and Greated, C. A., 1977, "Effect of Polymer Additives on the Small-Scale Structure of Grid-Generated Turbulence," *Physics of Fluids*, Vol. 20, pp. 873–879.

McComb, W. D., 1990, *The Physics of Fluid Turbulence*, Oxford, Clarendon Press.

Mitwally, E. M., 1978, "Solutions of Laminar Jet Flow Problems for Non-Newtonian Power-Law Fluids," ASME JOURNAL OF FLUIDS ENGINEERING, Vol. 100, pp. 363–366.

Serth, R. W., 1969, "An Experimental Investigation of the Velocity Field in Axisymmetric Free Turbulent Jets of Non-Newtonian Fluids," Ph.D. dissertation State University of New York at Buffalo.

Serth, R. W., 1972, "The Axisymmetric Free Laminar Jet of a Power-Law Fluid," *Journal of Applied Mathematics and Physics*, Vol. 23, pp. 131–138.

Shekarriz, A., Phillips, J. R., and Weir, T. D., 1995, "Quantitative Visualization of a Submerged Pseudoplastic Jet Using Particle Image Velocimetry," ASME JOURNAL OF FLUIDS ENGINEERING, Vol. 117, pp. 369–373.

So, H. M. C., Zhu, J. Y., Otugen, M. V., and Hwang, B. C., 1990, "Some Measurements in a Binary Gas Jet," *Experiments in Fluids*, Vol. 9, pp. 273–284.

Xie, C., and Hartnett, J. P., 1992, "Influence of Rheology on Laminar Heat Transfer to Viscoelastic Fluids in a Rectangular Channel," *Industrial Engineering Chemical Research*, Vol. 31, pp. 727–732.

Application of Wavelet Analysis to Incident Wind in Relevance to Wind Loads on Low-Rise Structures

M. R. Hajj[1] **and H. W. Tieleman**[1]

1 Introduction

Simulation of wind loads on structures in a wind tunnel requires detailed knowledge of the characteristics of the incident wind in full scale measurements. Such knowledge is particularly significant for establishing an impeccable relation between the incident flow and the wind loads. Measurements of wind speed and direction obtained at the Texas Tech University Wind Engineering Research Field Laboratory (WERFL) show that time series of the different velocity components are characterized by the typical random nature of turbulence. In general, these time series show unsteady characteristics and exhibit high levels of fluctuations.

---

[1] Department of Engineering Science and Mechanics, Virginia Tech, Blacksburg, VA 24061-0219.

Contributed by the Fluids Engineering Division of THE AMERICAN SOCIETY OF MECHANICAL ENGINEERS. Manuscript received of the Fluids Engineering Division November 1, 1995; revised manuscript received August 18, 1996. Associate Technical Editor: F. Giralt.

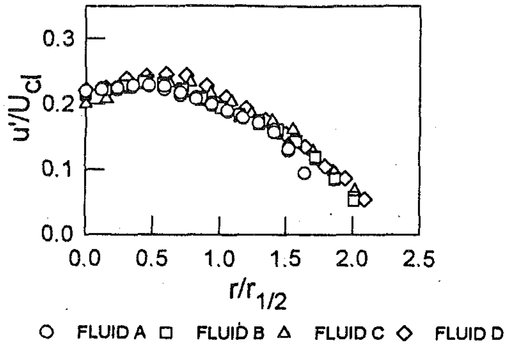

Fig. 4(*a*) $z/d = 20$

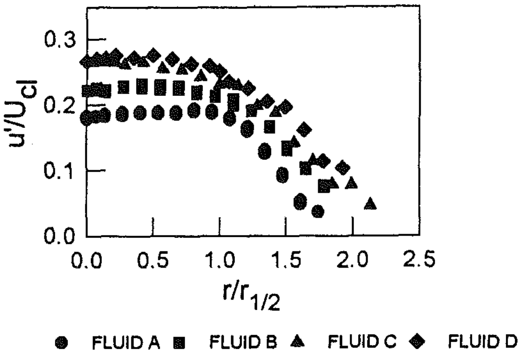

Fig. 4(*b*) $z/d = 40$

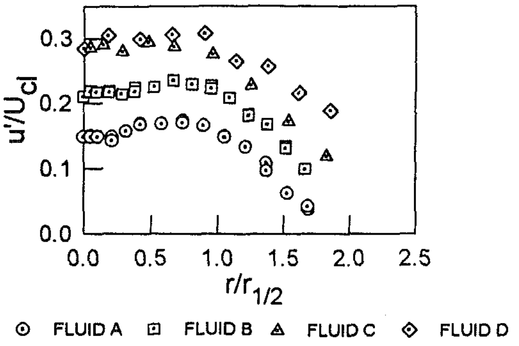

Fig. 4(*c*) $z/d = 60$

Fig. 4 Radial profiles of axial turbulence intensity

Although previous measurements in dilute polymer jets (Barker, 1973) showed no effect on turbulence quantities, our results do qualitatively agree with the measurements in grid turbulence of McComb et al. (1977). They found that polymer addition reduced both turbulence intensity and rate of turbulence decay. Flow visualization showed that above a critical threshold concentration small scale turbulence was attenuated. Hibberd et al. (1982) found that small scale turbulence was reduced in a mixing layer, although they did not observe a decrease in turbulence intensity. These investigators have also reported that there appears to be a threshold concentration of polymer required for small scale turbulence suppression. There is, however, disagreement over what the threshold is. Differences in fluid properties may explain this.

Conclusions

Laser Doppler velocimetry has been used to measure the axial components of mean and rms velocity in four jets with different rheological behaviors. This study has extended the range of the experimental data base: results are reported for a fluid with a behavior index of 0.39 and a yield stress of 1 Pa.

The results show significant dampening of the turbulence intensity in the yield-pseudoplastic jet ($n = 0.39$). To a lesser extent, turbulence dampening is also evident in the data of fluid B, a pseudoplastic jet ($n = 0.64$). The effects on the mean velocity field are less substantial.

References

Barker, S. J., 1973, "Laser-Doppler Measurements on a Round Turbulent Jet in Dilute Polymer Solutions," *Journal of Fluid Mechanics*, Vol. 60, pp. 721–731.

Chen, C. J., and Rodi, W., 1980, *Vertical Turbulent Buoyant Jets: A Review of Experimental Data*, Pergamon Press.

Gutfinger, C., and Shinnar, R., 1964, "Velocity Distributions in Two Dimensional Laminar Liquid-into-Liquid Jets in Power-Law Fluids," *AIChE Journal*, Vol. 10, No. 5, pp. 631–639.

Hibberd, M., Kwade, M., and Scharfe, R., 1982, "Influence of Drag Reducing Additives on the Structure of Turbulence in a Mixing Layer," *Rheologica Acta*, Vol. 21, pp. 582–586.

Jordan, C., Rankin, G. W., and Sridhar, R., 1992, "A Study of Submerged Pseudoplastic Laminar Jets," *Journal of Non-Newtonian Fluid Mechanics*, Vol. 41, pp. 323–337.

Kumar, K. R., Rankin, G. W., and Sridhar, K., 1984, "Laminar Length of a Non-Newtonian Fluid Jet," *Journal of Non-Newtonian Fluid Mechanics*, Vol. 15, pp. 13–27.

McComb, W. D., Allen, J., and Greated, C. A., 1977, "Effect of Polymer Additives on the Small-Scale Structure of Grid-Generated Turbulence," *Physics of Fluids*, Vol. 20, pp. 873–879.

McComb, W. D., 1990, *The Physics of Fluid Turbulence*, Oxford, Clarendon Press.

Mitwally, E. M., 1978, "Solutions of Laminar Jet Flow Problems for Non-Newtonian Power-Law Fluids," ASME JOURNAL OF FLUIDS ENGINEERING, Vol. 100, pp. 363–366.

Serth, R. W., 1969, "An Experimental Investigation of the Velocity Field in Axisymmetric Free Turbulent Jets of Non-Newtonian Fluids," Ph.D. dissertation State University of New York at Buffalo.

Serth, R. W., 1972, "The Axisymmetric Free Laminar Jet of a Power-Law Fluid," *Journal of Applied Mathematics and Physics*, Vol. 23, pp. 131–138.

Shekarriz, A., Phillips, J. R., and Weir, T. D., 1995, "Quantitative Visualization of a Submerged Pseudoplastic Jet Using Particle Image Velocimetry," ASME JOURNAL OF FLUIDS ENGINEERING, Vol. 117, pp. 369–373.

So, H. M. C., Zhu, J. Y., Otugen, M. V., and Hwang, B. C., 1990, "Some Measurements in a Binary Gas Jet," *Experiments in Fluids*, Vol. 9, pp. 273–284.

Xie, C., and Hartnett, J. P., 1992, "Influence of Rheology on Laminar Heat Transfer to Viscoelastic Fluids in a Rectangular Channel," *Industrial Engineering Chemical Research*, Vol. 31, pp. 727–732.

Application of Wavelet Analysis to Incident Wind in Relevance to Wind Loads on Low-Rise Structures

M. R. Hajj[1] **and H. W. Tieleman**[1]

1 Introduction

Simulation of wind loads on structures in a wind tunnel requires detailed knowledge of the characteristics of the incident wind in full scale measurements. Such knowledge is particularly significant for establishing an impeccable relation between the incident flow and the wind loads. Measurements of wind speed and direction obtained at the Texas Tech University Wind Engineering Research Field Laboratory (WERFL) show that time series of the different velocity components are characterized by the typical random nature of turbulence. In general, these time series show unsteady characteristics and exhibit high levels of fluctuations.

---

[1] Department of Engineering Science and Mechanics, Virginia Tech, Blacksburg, VA 24061-0219.

Contributed by the Fluids Engineering Division of THE AMERICAN SOCIETY OF MECHANICAL ENGINEERS. Manuscript received of the Fluids Engineering Division November 1, 1995; revised manuscript received August 18, 1996. Associate Technical Editor: F. Giralt.

Due to the complexities in time series of wind velocity components, spectral decomposition has been used to analyze and characterize wind turbulence and its dynamics. To date, Fourier decomposition has been the main tool used to describe the incident wind and its turbulent characteristics. The underlying process in Fourier decomposition is the representation of the signal onto a set of known complex sinusoids. There are several advantages for frequency domain analyses. First, turbulence scales can be represented by Fourier components and their energy is obtained from the power spectrum. Higher-order moments of the Fourier transform can also be used to quantify linear and nonlinear energy transfer mechanisms among spectral components. Second, estimates of spectral energy in particular frequency bands are statistically independent of estimates of energy at other bands. Third, for large samples of data, Fourier decomposition can be obtained rapidly with FFT techniques.

Having noted some of the advantages of frequency domain analysis, it is important to stress that, while such analysis might be satisfactory in some fields of meteorelogical practice, it is of limited value in characterizing wind flows for simulation of wind loads on structures. The objectives of this technical brief are to discuss some of the shortcomings of Fourier domain analysis and to show how such shortcomings can be overcome by using wavelets. The wavelet representation is more advantageous because it allows one to capture time variations of turbulence scales in wind velocity components. This information is critical for simulation of extreme wind loads on structures.

2 Shortcomings of Fourier Domain Analysis

A typical time series of wind velocity fluctuations is shown in Fig. 1. The sampling rate for this record is 10 Hz and the measurements were made at an elevation of 13 ft. More detailed information about experimental setup and measurement techniques is given in Smith and Mehta (1993). Characterization of these fluctuations is particularly significant for their simulation in a wind tunnel. Among the different parameters that have been used are estimates of integral length scale, *L*, Fourier decomposition, and spectral models. However, these parameters are of limited value in assessing or simulating wind loads.

First, by one definition, the integral length scale is proportional to the spectral density at zero frequency. Thus, this scale depends on correlation-function properties at large lags. Such properties are time-varying and not well known in the atmosphere. Moreover, the length scale is dependent on the method chosen for separation of large-scale and small-scale features (that is on the definition of mean and fluctuations). The integral length scale of the velocity record, shown in Fig. 1, was calculated using different segment lengths and averages. Table 1 illustrates how much the length scale can vary when using different segment lengths and averages. The variations exhibited in Table 1 were also observed in many other records. It is important to note here that this record has been classified stationary by Smith and Mehta (1993). Another method to obtain the integral length scale is to relate it to the frequency $f_{\max}$ at which $fS(f)$ is a maximum. Unfortunately, curves of $fS(f)$ vs frequency, obtained from measurements at WERFL, tend to be quite flat. Therefore, the use of Fourier decomposition to obtain integral length scale for the incident wind is not satisfactory.

Table 1 Variations of integral length scales with segment lengths and averages

Segment length (s) Number of averages	900 1	450 2	300 3	225 4	180 5	150 6
L(m)	132	107	97	108	45	63

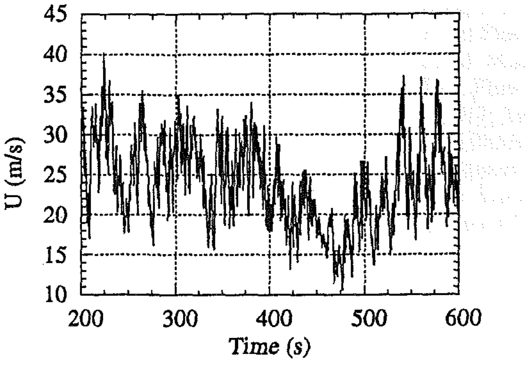

Fig. 1 Time series of the *u*-velocity component for record M 15N432

Second, in order to obtain a good estimate of spectral density functions, averaging over a long period is required. The purpose of this averaging is to reduce the variance of the estimate of these functions. Even when the data is stationary and such averaging is appropriate, an estimate of the power spectrum, obtained over a time of the order of a few minutes, is of limited value in characterizing the relation between the incident flow and wind loads. By examining pressure signals observed on the roof of the experimental building at WERFL, it can be noticed that extreme negative pressure peaks occur over durations that extend up to a maximum of about 5 seconds. This time is much lower than the time needed to obtain a good estimate of the spectrum. Therefore, those peak suction pressures, taking place over a time window of few seconds, cannot and should not be related to spectral characteristics observed over the course of few minutes.

Third, while the Fourier transform is well suited for data analysis when periodic components are expected in the time series, its use for broad-band spectra, such as the wind spectra, is at best confusing and tantalizing. Intermittent events and modulations, that are of interest in relation to wind loads, are usually represented by sinusoids that repeat themselves indefinitely in the Fourier domain. Such a representation or matching may result in wrong conclusions and understanding.

3 Wavelet Analysis and Advantages

The above discussion of frequency-domain analysis shows that frequency decomposition and associated parameters do not give adequate characterization of incident wind. The reason being that frequency decomposition eliminates all temporal information. Such information can be obtained using wavelet analysis where the incident wind is represented in a time-scale domain rather than a Fourier domain.

While frequency analysis is performed by decomposing a signal onto a number of sinusoids, the wavelet analysis is performed by decomposing the signal onto a set of time-localized functions. These basis functions are called wavelets and are obtained from a prototype wavelet by dilations and contractions or scalings. Thus, in wavelets, the notion of a scale replaces the notion of frequency which leads to the so-called time-scale representation. The prototype wavelet can be thought of as a band pass filter. The wavelet transform can either be continuous or discrete. As Farge (1992) states, the wavelet transform yields elegant decompositions of turbulent flows. The Continuous Wavelet Transform offers a continuous and redundant unfolding in terms of space (time) and scale and thus can track coherent structures. The Discrete Wavelet Transform allows an orthonormal projection on a minimal number of independent modes. Such analysis is known as a multiresolution representation and might be used to compute or model turbulent flow dynamics.

In context of studying turbulence content of wind velocity components, the time series shown in Fig. 1 was decomposed by a sequence of low-pass and high-pass filters using Daubechies' orthonormal wavelet bases, DAUB4, into time records of twelve scales. In each iteration of the sequence, the width of the low-

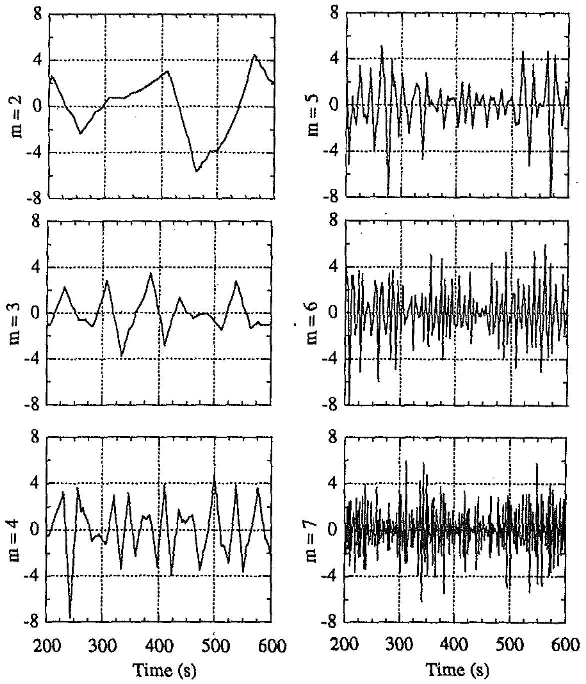

Fig. 2 Time variations of the different turbulent scales in the velocity record shown in Fig. 1

pass filter is halved. This is followed by subsampling by 2 which doubles the scale or halves the resolution. In Fig. 2, the time series for 6 scales are shown. These scales correspond to the spectrum frequency range between 0.02 and 1.25 Hz. The results show important turbulence dynamics in the incident wind. First, the time series for the larger scales, $m = 2$, 3, and 4, show large peaks which implies intermittency events. By comparison with Fig. 1, it can be seen that these events take place near jumps in the velocity signal. Such events can be related to passage of an eddy or occurrence of a wind gust. Currently, we are working on establishing such relations and obtaining a measure of a characteristic time or length scale present in incident wind that is related to the variation level and duration of these events. Second, it is noted that the number of these intermittent events increases at the relatively smaller scales, $m = 6$ and 7. These scales are dynamically quite important and must be simulated in wind tunnel or numerical studies for prediction of suction pressure coefficients and corresponding wind loads. Quantification of the variations of these scales when combined with pressure measurements should lead to a better understanding of the reasons of occurrence of low-pressure peaks.

4 Conclusions

The above results and discussion indicate that wavelet analysis is better suited than the traditional Fourier domain analysis in characterizing wind events that are of important value in determining pressure variations on low-rise structure. Using wavelets, the intermittent events of different scales can be characterized. In the future, we will extend the analysis to come up with characteristic scales and intermittency factors.

Acknowledgment

The authors would like to thank Dr. Kishor Mehta and his staff for providing the WERFL data.

References

1 Farge, M., 1992, "Wavelet Transforms and their Applications to Turbulence," *Annual Review of Fluid Mechanics*, p. 24.

2 Smith, D. A., and Mehta, K. C., 1993, "Stochastic Models for Stationary and Nonstationary Wind Data," *Proceedings of the 7th U.S. National Conference on Wind Engineering*, Los Angeles, CA, June 27–30.

Journal of Fluids Engineering

Discussion

Small Silicon Pressure Transducers for Space-Time Correlation Measurements in a Flat Plate Boundary Layer[1]

P. R. Bandyopadhyay.[2] The authors are to be congratulated for introducing a new technology to turbulence diagnostics and control. Historically, resolution in wall-pressure measurements has not been as great as in velocity-based measurements. Consequently, fruitful relationships between wall-pressure and turbulence are generally lacking. Perhaps this technology will make an impact in this area. It should now be possible to cluster various kinds of wall-sensors and miniaturize them to the viscous sublayer thickness.

There is a need to uncover any systematic behavior that might be lying hidden in the seemingly scattered data sets in Fig. 4. This discusser is interested in offering an explanation. The data in Fig. 4 seem to suggest a trend shown schematically in Fig. 12. It is slightly obscure, but there is a systematic trend in the data, viz., that they come from a family of d^+ $(=dU_\tau/v)$ values. In a recent review of Reynolds number effects,[3] it was concluded that meaningful trends in the inner layer can be extracted only when the sensors are of the order of viscous sublayer thickness. In Fig. 4 also, at all Reynolds numbers, the asymptotic rms values are reached by sensors approaching the size $d^+ = 5$. Furthermore, the slopes of the family of d^+ lines drop as d^+ values are increased (decreasing sensitivity of sensors to Reynolds number effects).

The data in Fig. 4 come from various sources with varying degrees of background noise, differences in signal processing, corrections applied and different inherent errors in the sensors and instrumentation. In other words, the uncertainties in each data set are different and probably not known accurately. There are also gaps in the data. Thus, it would be an useful contribution if the authors in future could systematically vary the sensor dimension (d^+) and the Reynolds number of the flow, and regenerate Fig. 12.

There are two issues regarding the experiment carried out by the authors which need further clarification. In Fig. 9, the authors report a convection velocity that is lower than ever reported: $0.4 < U_c/U_0 < 0.5$. They write that the low values result from the smallness of the sensors. However, in Fig. 10, they have spatial correlations agreeing with those measured using larger transducers. In any case, the low values of the convection velocity is intriguing and need further scrutiny. Finally, could the authors also provide more information on venting? Where is the transducer array vented? How many vents are there and are the vents near the transducer?

R. L. Panton.[4] The measurement of pressure fluctuations under a turbulent boundary layer is a very difficult task. This paper describes tests at a Reynolds number that is high enough for reasonable statistics, but still maintains very good transducer spatial resolution. Another unusual feature is that the spacing between microphones is small; a characteristic that is hard to produce with condenser microphones. I hope that the comments and questions that follow will clarify some issues and be useful in future work from the authors.

First with regard to some details. It would be of interest to know the von Karman constant, additive constant and wake constant for the velocity profiles. Likewise, how was the noise level on Fig. 5 determined?

It is always a problem to identify and account for acoustic noise and free stream oscillations in any facility. The 13 Hz filter seems low compared to the work of others. Is there any more information about these extraneous sources of pressure? The glider work of Panton et al. (1980) and wind tunnel work of Farabee show a rising spectrum at low frequencies. Theoretically one expects such trends if only turbulent pressure sources exist. The current measurements show a flat spectrum.

The verification of the ω^{-1} region of the spectrum is a most important result. This agrees with unpublished work of Wark et al. (1994) and is consistent with the overlap region found in wavenumber-phase velocity space in the recent paper of Panton and Robert (1994). It is not surprising that the extent of the region is small. With data from Panton and Robert (1994) and an assumption that the beginning of the viscous region is $k^+ = 0.1$, one can estimate that the Reynolds number must be $\mathrm{Re}_\tau = u_\tau\delta/\nu = 2400$ for a half of a decade of ω^{-1} to exist.

I am in disagreement with the form of the outer scaling (attributed to Keith et al. (1992)) used in Fig. 6. The ω^{-1} region is an overlap region between inner and outer scaling laws of very specific forms. Consider the inner or viscous dominated portion of the frequency spectrum at the high end. In inner variables the overlap region is

$$\frac{\phi(\omega)}{\rho^2 u_\tau^2 \nu} = C\,\frac{u_\tau^2}{\omega\nu}$$

where C is a constant. There is not any controversy about these variables. Obviously neither ν nor δ are important in this equation and $(\phi(\omega)/\rho^2 u^{*4}/\omega) = C$. If one transform the equation to proper outer variables (Panton and Linebarger (1974), Fig 15) the same form must arise

$$\frac{\phi(\omega)}{\rho^2 u_\tau^3 \delta} = C\,\frac{u_\tau}{\omega\delta}$$

---

[1] By L. Lofdahl, E. Kalvesten, and G. Stemme published in the JOURNAL OF FLUIDS ENGINEERING, Vol. 118, Sept. 1996, pp 457–463.

[2] Naval Undersea Warfare Center, Newport, RI.

[3] Gad-el-Hak, M. and Bandyopadhyay, P. R. 1994, "Reynolds Number Effects in Wall-Bounded Turbulent Flows," Vol. 45, No. 8, pp. 307–366.

[4] Mechanical Engineering, University of Texas, Austin, TX 78712.

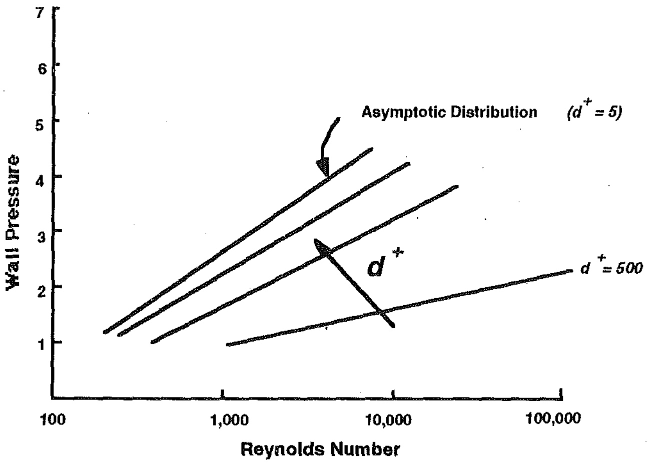

Figure 12 Schematic interpretation of Fig. 4.

The outer length scale is arbitrary; it could be δ^*, or Θ, but u_τ is required. However, if one uses the variables of Fig. 6

$$\frac{\phi(\omega)}{\rho^2 U_\infty^3 \delta^*} = C\left(\frac{u_\tau}{U_\infty}\right)^4 \frac{U_\infty}{\omega\delta^*}$$

Now the new "constant" is a function of Reynolds number; in conflict with the philosophy of the overlap derivation. The physical reason that u^* appears as the important parameter is that the intensity of turbulent fluctuations, which are responsible for the pressure, scale with u^* and not with U_∞. The dynamic pressure $\frac{1}{2}\rho U_\infty^2$ is not important in turbulent boundary layer theory but is associated with the shape of a body or wind tunnel.

If the wavenumber-phase velocity approach of Panton and Robert (1994) yields a correlation relatively independent of Reynolds number, then the frequency spectra will always show a Re dependence in the low frequencies but will still have the ω^{-1} overlap region. These facts were given in unpublished results of Panton (1994).

Comparing convection velocities to U_∞ is only a first approximation and one should expect a Reynolds number effect. The velocities in a boundary layer scale as a defect law $(u - U_\infty)/u_\tau$ in the outer region and u/u_τ in the inner region. In both cases u^* is the proper scale and U_∞ is only a reference in the outer layer.

One result of the paper which is surprising is Fig. 8 for the correlation coefficient as a function of time delay. Previous work of Bull (1967), Willmarth (1962), and Panton et al. (1980) show a far region where R_{pp} is negative. Figure 8 indicates only positive values. Is there an explanation for this?

I surmise from the article that the authors regard the use of pinhole microphones as an open question. Side by side tests of both magnitude and phase response of both pinhole and flush microphones would be of interest to settle this question.

Our knowledge of the viscous dominated region of wavenumber-phase velocity space is very poor. Perhaps an array of transducers such as used in the subject article will provide such information in the future.

Additional References

Panton, R. L., A. L. Goldman, R. L. Lowery, and M. M. Reischman (1980), "Low Frequency Pressure Fluctuations in Turbulent Boundary Layers," *J. Fluid Mechanics,* Vol. 97, pp 299–319.

Panton, R. L. and G. Robert, (1994) "The Wavenumber-Phase Velocity Representation for the Turbulent Wall-Pressure Spectrum" ASME JOURNAL OF FLUID ENGINEERING, Vol. 116, pp. 477–483.

Panton, R. L. (1994) "The Strong Reynolds Number Effect on Frequency Spectra in Turbulent Wall Pressure" *Bulletin of the Am. Phy. Soc.,* Vol. 39, no. 9, p. 867.

C. Wark, S. Gravante, A. Naguib, and H. Nagib (1994) "Inverse-Power Law in Wall-Pressure Spectra Beneath a Turbulent Boundary Layer," *Bulletin of the Am. Phy. Soc.,* Vol. 39, no. 9, p. 1867.

W. L. Keith.[5] The authors have presented a thorough experimental investigation and supporting discussion of turbulent wall pressure fluctuations measured with small silicon pressure transducers. The measurements and analysis presented are very encouraging with regard to the general effectiveness of these new sensors. A significant result is that sensors of $d^+ = 7.2$ produce higher spectral levels than sensors of $d^+ = 21.6$, at the higher frequencies. This result re-opens the question as to the smallest sensor required to adequately resolve the smallest scale pressure producing turbulent structures. The authors compare the contributions to the rms from different portions of the boundary layer with the results of Farabee and Casarella (1991, Phys. Fluids A), in Table 3. Although one would expect a greater contribution from the high frequency region for this investigation, such was not the case. Rather, significantly greater contributions come from the mid and overlap regions, with a smaller contribution from the high frequency region. The spectra compared in Figure 7 show the levels of the present investigation at high frequencies are lower than those of Schewe (1983, JFM) and Farabee and Casarella, which is somewhat unexpected. It is suggested that these differences may reflect the response of the various sensors to the high wavenumbers. Although acoustic calibrations are the most commonly used method, a wavenumber-frequency calibration is actually required. The technology for such a calibration is not available at the present time. An inherent uncertainty therefore exists in all wall pressure measurements due to this effect. Perhaps modeling the response of the small silicon sensors to high wavenumbers and frequencies would be useful. However, such modeling should also be pursued for the sensors of Farabee and Casarella and Schewe, for completeness in the comparison. In conclusion, the authors are to be congratulated on their work, which will undoubtedly lead to further efforts in this area.

T. M. Farabee[6] and M. J. Casarella.[7] The authors are to be commended for providing an interesting and timely study of the application of micromachined pressure sensors for turbulent wall pressure measurements. It is quite encouraging that the authors were able to examine wall pressure fluctuations with such small sensors without suffering from electrical noise floor limitations at higher frequencies. Further studies using these sensors may provide data otherwise unobtainable with current techniques.

There are, however, two issues that should be carefully considered for any future studies. The first issue deals with the characteristics of the flow field. Both background noise and overall flow quality must be well understood for wall pressure measurements. Although the authors mention these subjects no detailed information is provided. Of particular concern is the fact that the measured wall pressures, as displayed in Fig. 6 for example, exhibit the highest low frequency levels for any of the spectra that are shown and there is no observable peak in the mid-frequency range. Such trends are often the result of background noise contamination, or the characteristics of a non-equilibrium flow. The second issue is related to the interpretation of the results presented in Fig. 7. It is reported that the high frequency data, when non-dimensionalized using inner variables, are lower than those of (for example) Farabee and

---

[5] Submarine Sonar Department, Naval Undersea Warfare Center, New London Detachment, New London, CT 06320.

[6] Naval Surface Warfare Center, Code 725, Bethesda, MD 20084-5000.

[7] Mechanical Engineering Department, The Catholic University of America, Washington, D.C. 20064.

Casarella (1991), yet the authors report higher values of RMS pressure. If higher values of RMS pressure are due to an improvement in the resolution of high wavenumber pressures then the frequency content of the spectra shown in figure 7 should exceed that of the comparative data. These issues need to be addressed before the merit of these transducers for wall pressure measurements can be fully established.

Authors' Closure

We would like to thank our colleagues for all comments and positive criticism on our work. Here we also want to state that we sincerely believe that their comments have improved our understanding of the topic and also pin-pointed some difficulties and unanswered questions in the field of wall pressure fluctuations. Below we try to answer the questions raised.

A general comment is the relatively high level of the low frequency part of the spectra. Different origins are suggested like background and acoustic noise, non-equilibrium flow and free stream oscillations. So far, we have not been able to separate these external pressure sources from internal turbulent pressure sources. Hence, the only conclusion we have is that the electrical disturbances and internal sensor noise level are equal to the noise level shown in Figure 5. This was tested by the acoustical shielding of the sensor at a free-stream velocity of 30 m/s and the same noise level as the one shown in Figure 5 was found.

We would particularly like to thank Dr. Bandyopadyay for his constructive suggestion with regard to the interpretation of Figure 4. The suggested Reynolds number and d^+ dependence of the rms values seems plausible. We therefore fully support the interesting finding of a systematical variation of sensor dimension and Reynolds number. Morever, Dr Bandyopadyay also asks about the venting of the pressure sensor arrays. As shown in Figure 1, the vent outlet for each sensor is in the end of the chip opposite the pressure sensor diaphragm, about 3 mm distant. e.g. in Kälvesten et al. (1996) a model developed for sensor modelling shows that this vent channel length is more than sufficient. For the multi-sensor array each pressure sensor has its own vent channels with separate outlets with a spacing of 2 mm. A comment is also made about our low advection velocities. We find it plausible that a small sensor resolves small eddies which are created to a significant extent in the buffer layer where the advecting velocity is lower than further out in the boundary layer.

Professor Panton wants to know how the noise level of Fig. 5 is determined. We obtained this level for the 100 μm sensor mounted in situ inside the wind tunnel and at zero flow. Of course, the noise level of the 300 μm sensor should also have been given in the paper, but this level is very close to that of the 100 μm sensor, within 3 dB, so we omitted the noise level of the 300 μm sensor in order to avoid a cluttered figure. Moreover, Professor Panton suggests using an increased lower frequency limit as has been used by other investigators. We agree, but we also want to point out the difficulties in choosing the frequency cut-off limit. To this end we have no explanation for the only positive values of the correlation coefficient of Fig. 8. We are interested in suggestions concerning a physical interpretation of positive and negative values of this correlation.

Dr. Keith suggests that the unexpected low level of high frequency of the spectra may be due to the various sensors' responses to the high wave-numbers. Furthermore, he concludes that this kind of frequency-wave number calibration method is not available at the present time, but that the sensor modelling for high frequencies and wave numbers would be very useful. The authors agree and thank him for his positive reaction to our paper.

Dr. Farabee and Professor Casarella compare the frequency spectra of Fig. 7 for our investigation to other experiments. They conclude that the high frequency level of our small sensors should be higher than the comparable data. Maybe this is correct, but as Dr. Keith suggests, a wave number-frequency calibration would be required. This issue remains open now.

Additional Reference

Kälvesten, E., Löfdahl, L., and Stemme, G., 1996: Analytical Characterization of Piezoresistive Square-Diaphragm Silicon Microphone, *Sensors and Materials*, Vol. 8, No. 2, pp 113–136.